Ocean Acidification Short Course

November 2-13, 2009

Woods Hole, MA USA

http://www.whoi.edu/courses/OCB-OA

COURSE SYLLABUS

Co-Sponsors

Ocean Carbon & Biogeochemistry (OCB) Project Office*

European Project on Ocean Acidification (EPOCA)

*The Ocean Carbon & Biogeochemistry Project Office gratefully acknowledges the support of the National Science Foundation (NSF), the National Aeronautics and Space Administration (NASA), and the National Oceanic & Atmospheric Administration (NOAA).

COURSE PARTICIPANTS

OCB OCEAN ACIDIFICATION SHORT COURSE: NOVEMBER 2-13, 2009

Name	Affiliation	Email	CO_2 sampling Group A/B/C	CO_2 system measurements Group D/E/F	Biology exp'ts Group G/H/I
Andreas Andersson	BIOS	andreas.andersson@bios.edu	A	D	G
Mark Carls	NOAA / NMFS / Alaska Fisheries Science Center	Mark.Carls@noaa.gov	C	D	H
Caroline Dawber	Department of Earth Sciences, University of Cambridge	cfd25@esc.cam.ac.uk	C	D	H
Sergey Frolov	MBARI	frolovs@mbari.org	A	D	I
Michael Grelaud	ICTA (Institut de Ciència i Tecnologia Ambientals)	mikagrelaud@gmail.com	A	D	I
Iris Hendriks	IMEDEA (CSIC-UIB)	iris@imedea.uib-csic.es	C	D	I
Terrie Klinger	University of Washington	tklinger@uw.edu	A	D	G
Anna McIntyre-Wressnig	Woods Hole Oceanographic Institution	amcintyrewressnig@whoi.edu	B	D	H
Nichole Price	Scripps Institution of Oceanography	nprice@ucsd.edu	B	D	H

OCB OCEAN ACIDIFICATION SHORT COURSE: NOVEMBER 2-13, 2009					
Name	**Affiliation**	**Email**	**CO_2 sampling Group A/B/C**	**CO_2 system measurements Group D/E/F**	**Biology exp'ts Group G/H/I**
Tom Schils	University of Guam Marine Laboratory	tom@schils.be	A	D	G
Nayrah A. Shaltout	National Institute of Oceanography and Fisheries	nshaltout@gmail.com	B	D	I
Rob Whitehead	University of North Carolina Wilmington	whiteheadrf@uncw.edu	A	D	G
Helen Bostock	National Institute of Water and Atmospheric Research	h.bostock@niwa.co.nz	A	E	H
Daniela Danie Böttjer	University of Hawaii	daniela.bottjer@obs-banyuls.fr	B	E	I
Dreux Chappell	University of Rhode Island	dreux@mail.uri.edu	A	E	I
Katharina Fabricius	Australian Institute of Marine Science	k.fabricius@aims.gov.au	A	E	G
Hernan Garcia	NOAA National Oceanographic Data Center	Hernan.Garcia@noaa.gov	B	E	G
Dwight Gledhill	NOAA AOML OCD/CIMAS	dwight.gledhill@noaa.gov	B	E	H

OCB OCEAN ACIDIFICATION SHORT COURSE: NOVEMBER 2-13, 2009					
Name	**Affiliation**	**Email**	**CO_2 sampling Group A/B/C**	**CO_2 system measurements Group D/E/F**	**Biology exp'ts Group G/H/I**
Laetitia Hédouin	Hawaii institute of Marine Biology	laetitia@hawaii.edu	B	E	H
Li-Qing Jiang	NOAA Climate Program Office	Liqing.Jiang@noaa.gov	A	E	H
Clara Manno	Universitetet i Tromsø	clara.manno@uit.no	A	E	I
Shannon Meseck	NOAA-NMFS	Shannon.Meseck@noaa.gov	C	E	I
Daniela Turk	Marine Biology Station, National Institute of Biology	Daniela.Turk@mbss.org	C	E	H
Chip Young	University of Hawaii, Department of Oceanography	charles.young@noaa.gov	C	E	I
Jen Bowen	Princeton University	jlbowen@princeton.edu	C	F	H
Shallin Busch	NOAA - Northwest Fisheries Science Center	Shallin.Busch@noaa.gov	B	F	H
Kristen Davis	WHOI	kadavis@whoi.edu	B	F	G

OCB OCEAN ACIDIFICATION SHORT COURSE: NOVEMBER 2-13, 2009

Name	Affiliation	Email	CO_2 sampling Group A/B/C	CO_2 system measurements Group D/E/F	Biology exp'ts Group G/H/I
Constantin Frangoulis	Inst. of Oceanography, Hellenic Centre for Marine Research	cfrangoulis@her.hcmr.gr	B	F	H
Joaquim I. Goes	Bigelow Laboratory	jgoes@bigelow.org	C	F	I
Xiang-Hui Guo	State Key Lab. of Marine Envir. Science, Xiamen University	xhguo@xmu.edu.cn	C	F	G
Megan Huggett	Hawaii Institute of Marine Biology, University of Hawaii	huggett@hawaii.edu	C	F	G
Anderson Mayfield	University of California, Santa Barbara	mayfield@hawaii.edu	B	F	I
Christina McGraw	Marine and Freshwater Chemistry Group	cmcgraw@chemistry.otago.ac.nz	C	F	G
Moose O'Donnell	Friday Harbor Labs	mooseo@u.washington.edu	A	F	G
Rodrigo Torres	Universidad Austral DE Chile	rtorres@ciep.cl	C	F	I
Pauline Yu	University of California-Santa Barbara	yu.p.chiawen@gmail.com	B	F	G

SAMPLING FOR CO_2 PARAMETERS

GROUP A
Andreas Andersson
Helen Bostock
Dreux Chappell
Katharina Fabricius
Sergey Frolov
Michael Grelaud
Li-Qing Jiang
Terrie Klinger
Clara Manno
Moose O'Donnell
Tom Schils
Rob Whitehead
Meredith White

GROUP B
Daniela Böttjer
Shallin Busch
Kristen Davis
Constantin Frangoulis
Hernan Garcia
Dwight Gledhill
Laetitia Hédouin
Anderson Mayfield
Anna McIntyre-Wressnig
Nichole Price
Nayrah A. Shaltout
Pauline Yu

GROUP C
Jen Bowen
Mark Carls
Caroline Dawber
Joaquim I. Goes
Xiang-Hui Guo
Iris Hendriks
Megan Huggett
Christina McGraw
Shannon Meseck
Daniela Turk
Rodrigo Fernando Torres Saavedra
Chip Young

MEASURING CO_2 PARAMETERS

GROUP D
Andreas Andersson
Mark Carls
Caroline Dawber
Sergey Frolov
Michael Grelaud
Iris Hendriks
Terrie Klinger
Anna McIntyre-Wressnig
Nichole Price
Tom Schils
Nayrah A. Shaltout
Rob Whitehead

GROUP E
Helen Bostock
Daniela Böttjer
Dreux Chappell
Katharina Fabricius
Hernan Garcia
Dwight Gledhill
Laetitia Hédouin
Li-Qing Jiang
Clara Manno
Shannon Meseck
Daniela Turk
Chip Young
Meredith White

GROUP F
Jen Bowen
Shallin Busch
Kristen Davis
Constantin Frangoulis
Joaquim I. Goes
Xiang-Hui Guo
Megan Huggett
Anderson Mayfield
Christina McGraw
Moose O'Donnell
Rodrigo Fernando Torres Saavedra
Pauline Yu

BIOLOGICAL PERTURBATION EXPERIMENTS

GROUP G
Andreas Andersson
Terrie Klinger
Tom Schils
Rob Whitehead
Katharina Fabricius
Hernan Garcia
Kristen Davis
Xiang-Hui Guo
Megan Huggett
Christina McGraw
Moose O'Donnell
Pauline Yu

GROUP H
Mark Carls
Caroline Dawber
Anna McIntyre-Wressnig
Nichole Price
Helen Bostock
Dwight Gledhill
Laetitia Hédouin
Li-Qing Jiang
Daniela Turk
Jen Bowen
Shallin Busch
Constantin Frangoulis

GROUP I
Sergey Frolov
Michael Grelaud
Iris Hendriks
Nayrah A. Shaltout
Daniela Böttjer
Dreux Chappell
Clara Manno
Shannon Meseck
Chip Young
Joaquim I. Goes
Anderson Mayfield
Rodrigo Fernando Torres Saavedra
Meredith White

OCB OCEAN ACIDIFICATION SHORT COURSE: NOVEMBER 2-13, 2009

INSTRUCTOR/TA NAME	AFFILIATION	CONTACT	RELEVANT COURSE CONTENT
DICKSON, ANDREW	SIO	adickson@ucsd.edu	SEGMENT 1: CO_2 system sampling & measurements
DUFORE, CHRIS	USGS	cdufore@usgs.gov	SEGMENT 1: CO_2 system measurements (total alkalinity, pH)
SABINE, CHRIS	NOAA/PMEL	Chris.Sabine@noaa.gov	SEGMENT 1: CO_2 system sampling & measurements
WANG, ALECK	WHOI	zawang@whoi.edu	SEGMENT 1: CO_2 system sampling & measurements
COOLEY, SARAH (TA)	WHOI	scooley@whoi.edu	SEGMENT 1: CO_2 system sampling & measurements
BALCH, BARNEY	BIGELOW	bbalch@bigelow.org	SEGMENT 2: Quantifying calcification
COHEN, ANNE	WHOI	acohen@whoi.edu	SEGMENT 2: Quantifying calcification, larval mollusk exp't
FANGUE, NANN	UC DAVIS	nafangue@ucdavis.edu	SEGMENT 2: Genomics applications for studying physiological responses to ocean acidification

OCB OCEAN ACIDIFICATION SHORT COURSE: NOVEMBER 2-13, 2009

INSTRUCTOR/TA NAME	AFFILIATION	CONTACT	RELEVANT COURSE CONTENT
GATTUSO, JEAN-PIERRE	OBSERVATOIRE OCEANOLOGIQUE-VILLEFRANCHE	gattuso@obs-vlfr.fr	SEGMENT 2: Manipulating the CO_2 system in the laboratory, overview of seacarb
HUTCHINS, DAVE	USC	dahutch@usc.edu	SEGMENT 2: Biogeochemical impacts and feedbacks of ocean acidification
IGLESIAS-RODRIGUEZ, DEBORA	UNIV SOUTHAMPTON, NOC	debora.iglesias-rodriguez@noc.soton.ac.uk	SEGMENT 2: Quantifying calcification and algal/plankton culturing
LANGDON, CHRIS	U MIAMI RSMAS	clangdon@rsmas.miami.edu	SEGMENT 2: Ocean acidification experimental design (field and laboratory), Total alkalinity and infrared DIC measurements (segment 1)
MCCORKLE, DAN	WHOI	dmccorkle@whoi.edu	SEGMENT 2: Larval mollusk experiment
MILLER, WHITMAN	SMITHSONIAN ENVIR RESEARCH CTR	millerw@si.edu	SEGMENT 2: Quantifying calcification
SEIBEL, BRAD	URI	seibel@uri.edu	SEGMENT 2: Physiological effects of ocean acidification
YATES, KIM	USGS	kyates@usgs.gov	SEGMENT 2: CO2SYS experiments

OCB OCEAN ACIDIFICATION SHORT COURSE: NOVEMBER 2-13, 2009

INSTRUCTOR/TA NAME	AFFILIATION	CONTACT	RELEVANT COURSE CONTENT
HOLCOMB, MICHAEL (TA)	WHOI	mholcomb@whoi.edu	SEGMENTS 1 AND 2 (TA measurements, coral exp't)
ROSE, KATHRYN (TA)	WHOI	karose@whoi.edu	SEGMENT 2 (larval mollusk exp't)
WHITE, MEREDITH (TA)	WHOI	meredith@whoi.edu	SEGMENT 2 (larval mollusk, coral, and physiology exp'ts)
DONEY, SCOTT	WHOI	sdoney@whoi.edu	SEGMENT 3: Biogeochemical modeling
KEY, ROBERT	PRINCETON	key@Princeton.EDU	SEGMENT 3: Global data sets
CHANDLER, CYNDY	BCO-DMO/WHOI	cchandler@whoi.edu	SEGMENT 4: Data management
KOZYR, ALEX	CDIAC/ORNL	kozyra@ornl.gov	SEGMENT 4: Data reporting
SCHLITZER, REINER	ALFRED WEGENER INST	Reiner.Schlitzer@awi.de	SEGMENT 4: Ocean Data View

PARTICIPANT LEARNING OUTCOMES

OCB Ocean Acidification Short Course

November 2-13, 2009
Woods Hole, MA USA

Participant Learning Outcomes

Upon completion of the short course, participants will have gained increased knowledge in four areas relevant to OA research: 1) monitoring carbonate chemistry; 2) chemical measurements for CO_2 –perturbation experiments, 3) experimental design of ocean acidification experiments, and 4) data reporting guidelines. Specifically, course participants will gain experience with:

Monitoring the inorganic carbon system in seawater

- Know what systems are currently available to measure different parameters of the inorganic carbon system in seawater
- Know what parameters need to be measured in order to calculate aragonite and calcite saturation state and all other parameters of the carbonate system, using CO2SYS and seacarb
- Know what ancillary seawater measurements are needed to calculate all the parameters of the CO_2/carbonate system
- Know what algorithms can be used as proxies for aragonite and calcite saturation state
- Know the advantages and disadvantages of the different platforms: moored surface sensors, gliders, satellite tracked Lagrangian drifters, underway measurements, autonomous discrete water samplers
- Be familiar with the requirements for maintenance/calibrations/groundtruthing of specific platforms and instruments
- Know what temporal and spatial sampling is required for open-ocean and coastal ecosystems

Measurements of the parameters of the inorganic carbon system in seawater for manipulative CO_2-perturbation experiments

- Know methods to measure dissolved inorganic carbon, total alkalinity, pH and pCO_2 including the accuracy and precision of each method, the use of certified reference materials, the typical sample volume required, and the advantages and disadvantages of each method;

- Know what other variables must be known and at what accuracy to calculate all the parameters of the inorganic carbon system in seawater (temperature, salinity, nutrients, barometric pressure);
- Be able to use CO2SYS, seacarb, or similar programs to calculate all parameters of the inorganic carbon system;
- Appreciate the importance of high quality measurements of the parameters of the CO_2/carbonate system through the propagation of errors in calculations;
- Understand why pH_{NIST} is generally not used in measurements of the seawater CO_2/carbonate system;
- Understand why one cannot assume that bubbling seawater with air of known CO_2 concentration will result in the seawater with the same pCO_2 value (i.e. understand gas exchange rates of unperturbed and perturbed water)
- Understand why the seawater CO_2 chemistry should be monitored throughout the experiment or at least at the beginning and the end of the experiment. Be able to compute or model how the carbonate parameters will change in your experimental system for a given set of assumptions about water volume, surface area, and organism biomass.

Design of ocean acidification experiments

- Advantages and disadvantages of various methods for seawater CO_2 system manipulations- acid additions versus bubbling, acid plus bicarbonate additions, steady state equilibration versus dynamic seawater CO_2 chemistry experimental designs, etc. The need for consideration of how these choices will affect interpretation of experimental results
- Strengths and weaknesses of culture approaches and natural community manipulations- what each can and cannot do.
- Experimental design methodology, including volume scaling issues from beakers to mesocosms to potential in situ approaches; batch versus semi-continuous versus continuous cultures, etc.
- Appreciate the need to consider appropriate acclimation times for short term experiments, and how to address issues of short term acclimation versus long term adaptation and evolution. Molecular approaches for studying population responses to OA.
- The use of different strains/cell lines, and consideration of how responses may be modulated by natural genotypic and phenotypic variability within diverse natural populations.
- Experimental approaches to looking at potential interactions with other variables such as temperature, salinity, light, nutrients, trace metals
- Know the various methods to measure calcification in benthic and planktonic organisms and the advantages and disadvantages of each method (interest? How about other rate measurements?)

- Need for appropriate replication and statistical approaches, standardization and intercomparison among methods of biological rate and standing stock measurements.
- Trade-offs between experiments with many replicate tanks versus single tank or mesocosm experiments that are repeatedly sampled over time.
- Understand appropriate sampling that is needed for frequency and spatial resolution for the carbon species

Data reporting guidelines

- Know units to report for various measurements, accuracy and precision
- Where to submit data

Modeling for scientific use- modeling for policy makers

- Understand the major models that are currently being used scientifically for local, regional and global OA models and the type of data used from experiments and monitoring
- Understand how the models are being used – and what questions are being asked- by policy makers

COURSE LOGISTICS

GETTING HERE AND GETTING SETTLED

DRIVING DIRECTIONS

http://www.mbl.edu/about/visit/directions/directions_drive.html

WALKING DIRECTIONS FROM BUS STOP IN WOODS HOLE TO SWOPE

As soon as you step off the bus at the Woods Hole Bus Stop you will look to your left and see the Leeside Restaurant. Cross the street towards the Leeside past the fire hydrant and sign saying Railroad Ave. You are now on Luscombe Ave. although there is no sign until you walk to the end of the block when you take a left onto Water St. (also no sign). Go straight, as landmarks as you walk you will see on your left: Coffee Obsession, the Fishmonger Restaurant, Smith Lab, Bigelow Lab, and the MBL Visitor Center, until you see on your right MBL Street. Make that right onto MBL Street. Swope is directly in front of you at the end of the block on Eel Pond. You will see the entrance slightly to the left. It can be very windy on this approximately 10-minute walk. Hopefully the weather will cooperate.

CHECK-IN AND IDENTIFICATION BADGES

When you check in at the Swope front desk, you will receive an identification (ID) badge, **which you will need at all times to access the dormitories, the Rowe laboratory (lecture hall and lab), and the cafeteria**. Please carry it with you always. We are providing OCB lanyards (with nametags) for the ID badges to make it easier for you to keep them on you at all times. You will also receive a course syllabus at check-in.

PARKING

You will also receive a temporary MBL parking pass when you check in. Parking will be available in the Swope and/or Stoney Beach Parking Lots (you'll receive directions at check-in – I have also marked these parking lots on the MBL campus map).

LATE ARRIVALS

The Swope Front Desk is typically staffed until 9 pm on Sundays. Sometimes they do leave earlier than that. However, the MBL Watch Staff is on duty 24 hours/day. If you arrive and find the Swope Building locked and staff gone, then you need to

follow the sign on the Main Entrance Door. Use the Emergency phone to the left of the door to call the Watch Staff. The Watch Staff will then come over and issue you your Room Key.

DORMITORIES

Check-in time is 2 pm (arrival date) and check-out time (departure date) is 10 am. MBL Housekeeping will provide fresh linens approximately every four days and fresh towels daily. Bathrooms are cleaned daily and trash is removed daily. Carpet sweeping/vacuuming is done on an as-needed basis. Ethernet data jacks with direct access to the MBL network are available to all dormitories. Please check the Information Technology website (http://www.mbl.edu/it/index.html). Six computers and six phone jacks (for use with laptops with modems) are available in the Swope Center. Wireless is now available. There are coin-operated laundry facilities on the ground floor of Swope and in the basements of Ebert Hall. Detergent vending machines are located in all laundry rooms. Change machines are located in the Swope lobby and in Pilot House. Change for laundry machines is also available at the main desk in Swope.

MEALS

Meals will be served in the Swope Dining Room at the following times:

Breakfast: 7:00-8:30 am (before course begins each morning)
Lunch: 12:00-1:00 pm
Dinner: Served until 7:00 pm (start times vary, see daily schedule)

Don't forget your MBL ID card!! Your package includes dinner on Sunday November 1 through lunch on Friday November 13. If you arrive the day before (10/31) or prior to dinner on Sunday November 1 and/or stay past lunch on Friday November 13, you will need to acquire your own meals outside of MBL. Please refer to the list of local restaurants in your syllabus. Dinner on Sunday November 1 will be served from 5:30-7:00 pm.

Some Suggested Local Restaurants

Woods Hole:

Captain Kidd (bar/restaurant)	77 Water Street	508-548-8563
Coffee Obsession (Internet café)	38 Water Street	508-540-8130
Fishmonger's Cafe	56 Water Street	508-540-5376
Jimmy's Sandwich Shop	22 Luscombe Ave.	508-540-6823
(hot dogs, hamburgers,sandwiches, gourmet pizza: take-out mostly, only a few tables)		
Landfall Restaurant	2 Luscombe Ave.	508-548-1758
Pie in the Sky (bakery, sandwiches)	10 Water Street	508-540-5475
Shuckers World Famous Raw Bar and Cafe	91A Water Street	508-540-3850

Falmouth:

Bangkok Cuisine Thai Restaurant	809 Main St.	508-495-3760
The British Beer Company (pub)	263 Grand Avenue	508-540-9600
Café Villaggio (Italian, some alfresco dining)	188 Main St.	508-540-6400
Casino Wharf FX (water view)	286 Grand Ave.	508-540-6160
Chapoquoit Grill (local favorite)	410 West Falmouth Highway	508-540-7794
Clam Shack of Falmouth	227 Clinton Ave.	508-540-7758
(fried clams, lobster rolls, extremely casual outdoor dining, water view)		
Coonamessett Inn (elegant Cape Cod)	311 Gifford St.	508-548-2300
Firefly Woodfire Grill and Bar	271 Main St.	508-548-7953
Flying Bridge Restaurant (water view)	220 Scranton Ave.	508-548-2700
Golden Swan (Indian cuisine)	323 Main St.	508-540-6580
La Cucina Sul Mare (Italian)	237 Main St.	508-548-5600
Liam Maguire's Irish Pub & Restaurant	273 Main St.	508-548-0285
Nimrod (steaks/seafood/piano bar)	Dillingham Ave.	508-548-5500
Peking Palace (Chinese and Japanese)	452 Main St.	508-540-8204
Quarterdeck Restaurant	164 Main St.	508-548-9900
(bar/restaurant, cozy atmosphere)		
Roobar (steaks/seafood)	285 Main Street	508-548-8600

There are lots of restaurants around. Ask the locals for other recommendations, or if you are looking for something specific.

Last updated October 22, 2009.

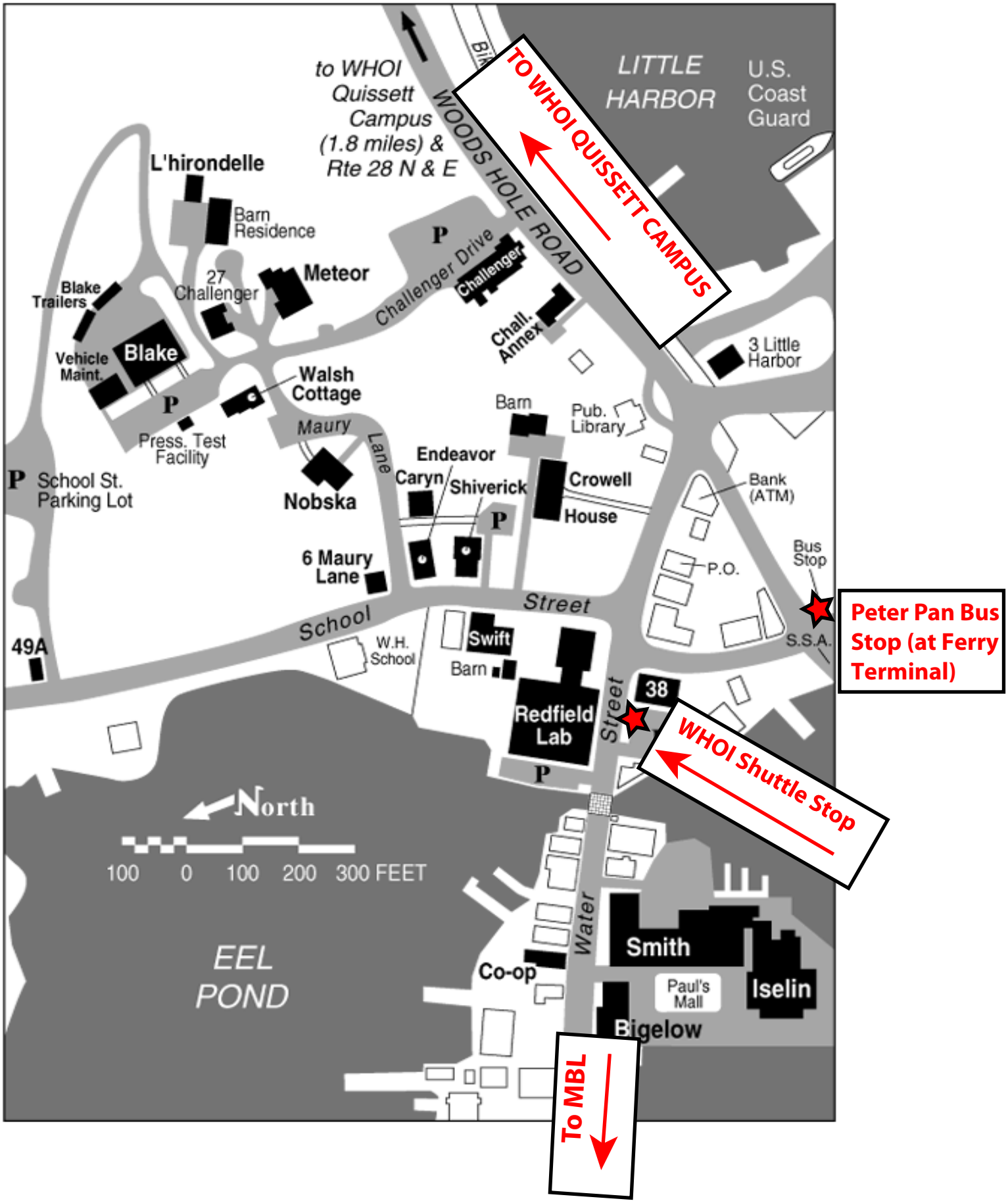
to WHOI
Quissett
Campus
(1.8 miles) &
Rte 28 N & E
WOODS HOLE ROAD
TO WHOI QUISSETT CAMPUS
LITTLE
HARBOR
U.S.
Coast
Guard
L'hirondelle
Barn
Residence
27
Challenger
Meteor
Challenger Drive
Challenger
Chall.
Annex
3 Little
Harbor
Blake
Trailers
Vehicle
Maint.
Blake
Walsh
Cottage
Press. Test
Facility
Maury
Lane
Barn
Pub.
Library
School St.
Parking Lot
Nobska
Endeavor
Caryn
Shiverick
Crowell
House
Bank
(ATM)
6 Maury
Lane
P.O.
Bus
Stop
Peter Pan Bus
Stop (at Ferry
Terminal)
S.S.A.
School
Street
49A
W.H.
School
Swift
Barn
Redfield
Lab
38
Street
WHOI Shuttle Stop
North
100 0 100 200 300 FEET
EEL
POND
Water
Co-op
Smith
Paul's
Mall
Iselin
Bigelow
To MBL


P
Gosnold Rd
Gosnold Rd
Gardiner Rd
Gardiner Rd
Mill Pond
Bigelow St
Spencer Baird Rd
Gardiner Rd
Millfield St
P
Bar Neck Rd
Albatross St
SWOPE
North St.
Shuttle Stop
Mbl St
Woods Hole
Eel Pond Lndg
Great
Harbor Lndg
Albatross St.
MBL St.
ENV. SCI.
CTR
Water St
ROWE
Water St.
LILLIE
Woods Hole
Science
Aquarium
Aquarium of
National Marine
Fisheries
Water St
Marine
Biological
Laboratory
MRC

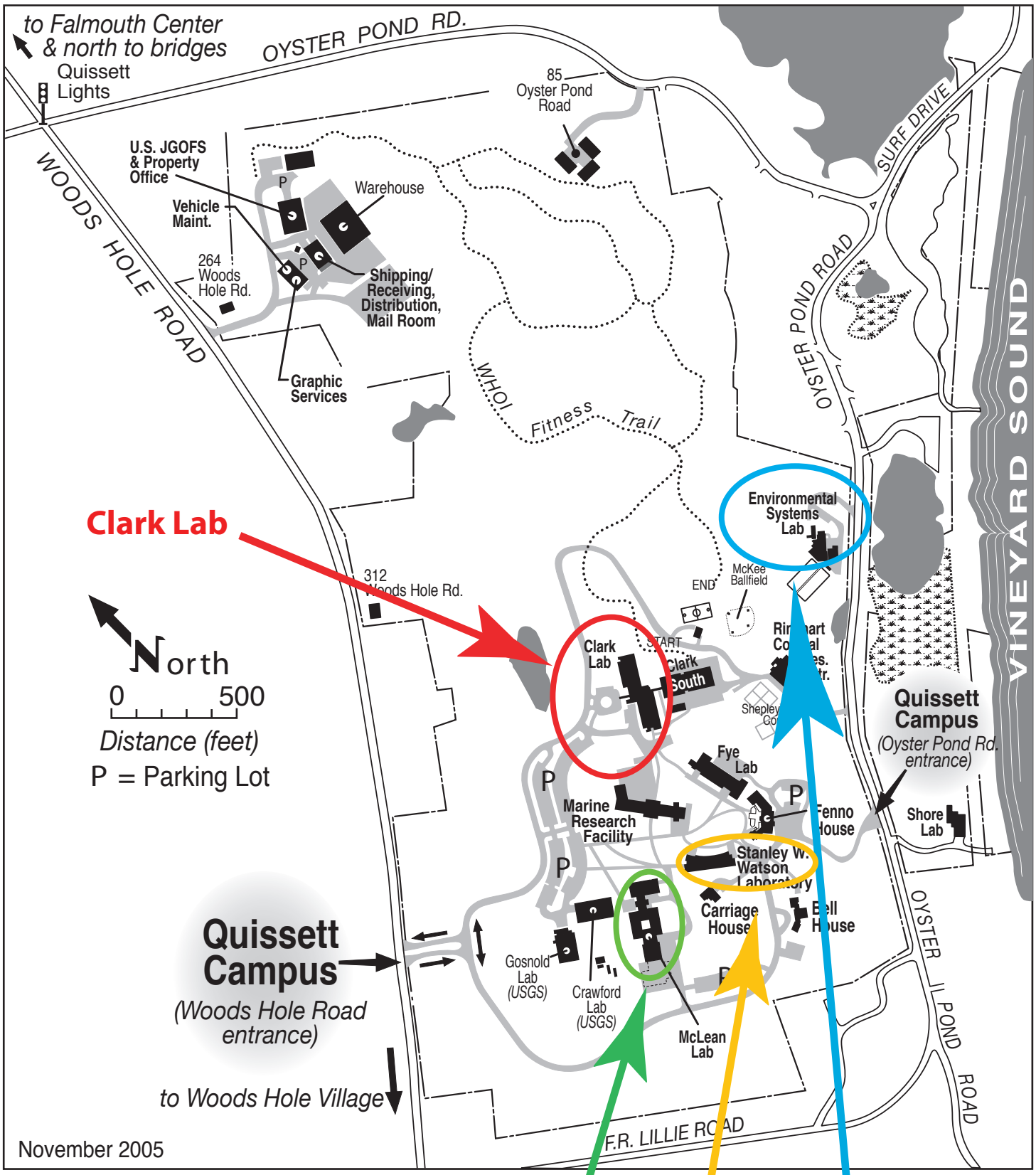
to Falmouth Center
& north to bridges
Quissett
Lights
OYSTER POND RD.
85
Oyster Pond
Road
SURF DRIVE
WOODS HOLE ROAD
U.S. JGOFS
& Property
Office
Vehicle
Maint.
Warehouse
P
264
Woods
Hole Rd.
Shipping/
Receiving,
Distribution,
Mail Room
Graphic
Services
WHOI
Fitness
Trail
OYSTER POND ROAD
VINEYARD SOUND
Clark Lab
312
Woods Hole Rd.
North
0
500
Distance (feet)
P = Parking Lot
Environmental
Systems
Lab
McKee
Ballfield
END
START
Clark
Lab
Clark
South
Quissett
Campus
(Oyster Pond Rd.
entrance)
Fye
Lab
Marine
Research
Facility
Fenno
House
Shore
Lab
Stanley W.
Watson
Laboratory
Carriage
House
Bell
House
Gosnold
Lab
(USGS)
Crawford
Lab
(USGS)
McLean
Lab
Quissett
Campus
(Woods Hole Road
entrance)
to Woods Hole Village
F.R. LILLIE ROAD
OYSTER POND ROAD
November 2005
McLean Lab
Environmental
Systems Lab
Watson Lab

OCEAN CARBON & BIOGEOCHEMISTRY (OCB)
OCEAN ACIDIFICATION COURSE

November 2-13, 2009
Woods Hole, MA USA

MBL Swope Cafeteria Meal Times (highlighted in blue)

Breakfast: 7:00-8:30 am (before course begins each morning)
Lunch: 12:00-1:00 pm
Dinner: Served until 7:00 pm (start times vary, see daily schedule)
Don't forget your MBL ID card!!

Coffee Breaks

All **coffee breaks** will take place in the lobby just outside MBL Speck Auditorium in the Rowe Building. We have the MBL Speck Auditorium for the entire duration of the course. Please feel free to use this space during down time to check email, work, convene smaller meetings, etc.

MBL Wireless Access

Wireless network: MBL-guest
Username: mblguest
Password: mblguest

Important Email Addresses and URLs

Course instructors: **ocb-acid-inst@whoi.edu**
Course participants: **OA-students@whoi.edu**
OCB Ocean Acidification Course Website: **http://www.whoi.edu/courses/OCB-OA**
OCB Ocean Acidification Website: **http://www.whoi.edu/OCB-OA**

Lectures

All lectures will take place in MBL's Speck Auditorium (Rowe building). There are restrooms on the 1st and 3rd floors of the Rowe Building. Please bring your MBL ID card, laptops, notebooks, syllabus, and writing utensils. **Please remember that there will be very few outlets for charging laptops available in the Speck Auditorium, so it is your responsibility to come with a fully charged battery each day.**

Labs

Labs will take place in multiple locations on the WHOI and MBL campuses. See detailed schedule. All buildings have been highlighted on your MBL and WHOI maps. Please bring your MBL ID

card, syllabus, lab coats, lab notebooks, and writing utensils to labs. Please exercise common sense when working in the labs. This means no food/drink, no open-toed shoes, wear long pants, wear your lab coats at all times, wear goggles and nitrile gloves when appropriate (we'll provide these in the labs), be aware of waste disposal protocols (i.e. don't flush hazardous substances, including mercury-poisoned seawater down the drain), and take notice of safety features (building evacuation routes, emergency showers, eye wash stations, and first aid kits). There will be a lab safety briefing on Monday 11/2 from WHOI and MBL officials. Each lab will also have a binder containing important safety information, including MSDSs for all chemicals we're using.

Lab Groups

Participants (36 total) are divided among three groups of 12 throughout the course: **A/B/C for Segment 1 CO_2 sampling; D/E/F for Segment 1 chemistry measurements; G/H/I for Segment 2 experiments**. Group makeup will change throughout the course to distribute participant experience in different areas and provide maximum interaction among participants. **Please see syllabus and/or your nametag for your group assignments.**

Emergency Phone Numbers

MBL campus: Dial 9911
WHOI campus: Dial 2911
Falmouth Hospital Emergency Services: 508-457-3524
Dr. Lee's Falmouth walk-in medical center: 508-540-6790

Transportation

We will provide shuttle service between the WHOI and MBL campuses. **All shuttle activity is highlighted in red.** Several participants and instructors may also have rental cars. Please try to share rides when possible. The MBL shuttle stop will be in front of the Swope building (see MBL campus map). WHOI shuttle drop-off and pick-up locations will be in front of the buildings in which activities are occurring (Clark, McLean, ESL, etc.).

If you miss the OCB/OA Course shuttle between MBL and WHOI

You can walk to the **WHOI shuttle stop** in the parking lot next to Coffee Obsession in Woods Hole village (WHOI shuttle stop is marked on your Woods Hole village map) or in front of the Clark building on the WHOI Quissett Campus. The shuttle is a navy blue van and says "Woods Hole Oceanographic Institution" on it. It is free – if they ask, just tell them you're attending a scientific conference/course at WHOI. The shuttle runs daily between the hours of 8:00 am and 5:40 pm (last shuttle from Woods Hole village to the WHOI Quissett campus). The ride between Woods Hole village and Quissett Campus only takes ~5 minutes, and the schedule is as follows:

Departs Woods Hole village every 20 minutes on the :00, :20, :40
Departs Clark Building (Quissett campus) every 20 minutes on the: 10, :30, :50

If you need help, please don't hesitate to call

Heather Benway	508-289-2838* (office), 541-760-3825 (cell)
Sarah Cooley	508-289-3859* (office), 706-338-6209 (cell)
Mary Zawoysky	508-289-2310* (office)

***If on WHOI campus and using a WHOI phone, just dial last four digits**

SAFETY MATERIALS

OCB Ocean Acidification Course
November 2-13, 2009
Woods Hole, MA USA

General Safety Awareness

Please exercise common sense when working in the labs. This means no food/drink, no open-toed shoes, wear long pants, wear your lab coats at all times, wear goggles and nitrile gloves when appropriate (we'll provide these in the labs), be aware of waste disposal protocols (i.e. don't flush hazardous substances, including mercury-poisoned seawater down the drain), and take notice of safety features (building evacuation routes, emergency showers, eye wash stations, and first aid kits). There will be a lab safety briefing on Monday 11/2 from WHOI and MBL officials.

Each lab will have a binder containing important safety information, including chemical safety handbooks (WHOI and MBL), Material Safety Data Sheets (MSDS) for all chemicals that you will be using in your experiments, and fire/emergency evacuation routes/maps. Please take a few moments to look through the safety binders and orient yourselves with the safety features of each lab, as outlined above. If you have any medical conditions that we should be aware of (for your own safety), please let Heather or Sarah know right away. If you are uncomfortable performing any part of any experiment due to a personal or medical issue, please come and talk with us.

Included in your syllabus is a one-page summary of emergency contacts and procedures for both WHOI and MBL. You will find all other safety materials in the lab safety binders.

WHOI Emergency Procedures

To report an emergency: Dial 2911 or 508-289-2911 (cell phones)

To report Facilities & Services related issues (such as heating problems) see inside back cover

1. Reporting an Emergency

- Remain calm and speak slowly and clearly.
- State your name, building, and location.
- State the nature of the emergency, such as fire, medical, chemical spill, etc.
- State the location of the emergency—be as specific as possible.
- Evacuate to a safe area if there is danger.

2. Evacuation Procedure

- When an evacuation alarm is sounded, immediately exit the facility in a calm and orderly manner through the nearest exit.
- If the nearest exit cannot be used, use the nearest alternate exit.
- Report to your building's assembly area.
- Do not attempt to secure personal property before evacuating.
- Do not attempt to reenter the facility once you have evacuated. Fire and police personnel will perform search and rescue.
- Remain in the assembly area until the facility is cleared for reentry.
- Do not attempt to go home or leave the area until you are accounted for.

3. Fire & Explosion

- Report the emergency—warn others.
- Evacuate immediately.
- Do not attempt to fight the fire unless trained to do so.
- Do not attempt to put out the fire if it is between you and the exit or if you are uncomfortable with the situation.
- If more than one fire extinguisher is needed—evacuate.

4. Medical Emergency

- Report the emergency.
- Make every attempt to comfort the injured person and prevent further injury.
- Only trained personnel should provide first aid treatment to others.

5. Hazardous Chemical Spill

- Report the emergency—warn others.
- Evacuate to a safe area.
- Attend to any person who has been exposed to the material if safe to do so.

6. Violence

- Report the emergency and silence cell phone ringer.
- Stay away from location of violence.
- If you can safely escape, leave immediately. If not, secure yourself in a safe area.
- Never attempt to intervene in a violent incident.

7. Biological/Radiological

- Report the emergency—warn others in the area.
- Attend to injured or contaminated personnel and remove them from further exposure if safe to do so.
- Have potentially contaminated personnel stay in one area until they can be monitored and shown to be free of contamination.
- Prevent entrance to the affected area.

8. Severe Weather

- Facilities monitors National Weather Service reports and notifies departments of severe weather forecasts. Hurricane information is also posted on the Facilities Web site (address questions to x2205). Inclement weather announcements are available on x2120.

Be prepared in the event of an emergency. Remember to:

- Locate the emergency exits and equipment near your work area.
- Locate your assigned assembly area.
- Try to notify a colleague when leaving your work area for an extended period and upon returning to avoid triggering an unnecessary search.

Questions regarding emergency procedures may be directed to the Environmental Health and Safety Office at x3347

MBL SAFETY INFORMATION

http://www.mbl.edu/services/serv_enviro.html

MBL Environmental, Health, & Safety Contacts

- **James Marcello**, Environmental, Health, and Safety Manager, (508) 289-7424, jmarcello@mbl.edu
- **Tim Schorer**, Environmental, Health, and Safety Associate, (508) 289-7192, tschorer@mbl.edu
- **Bill Grossman**, MBL Diving Safety Officer, (508) 289-7433, bgross@mbl.edu
- Env., Health, and Safety Assistant (508) 289-7424

FOR RADIATION OR CHEMICAL EMERGENCIES/SPILLS: DIAL 7424 OR DIAL (508)-277-1933 FOR JIM MARCELLO.

FOR MEDICAL EMERGENCIES: DIAL 9911.

AT-A-GLANCE COURSE SCHEDULE

Lecture = Classroom instruction (unless otherwise noted, all lectures in MBL's Speck Auditorium)
Demo = Instructor physically demonstrates lecture concepts
Hands-on = students practice concepts with computers
Lab = Students participate in hands-on lab activities
Discussion = Group discussion
Tour = Visit site at MBL or WHOI, but no hands-on lab work

Yellow = Segment 1 (Carbonate system measurments)
Blue = Segment 2 (OA experimental set-up: biology/chemistry)
Orange = Segment 3 (Biogeochemical modeling)
Green = Segment 4 (Data reporting)

WEEK 1	NOVEMBER 2 MONDAY	NOVEMBER 3 TUESDAY	NOVEMBER 4 WEDNESDAY	NOVEMBER 5 THURSDAY	NOVEMBER 6 FRIDAY	NOVEMBER 7 SATURDAY	NOVEMBER 8 SUNDAY
Morning Period 1 (8:30-10:00)	**Lecture.** Carbonate system overview (Sabine/Dickson)	**Lecture.** pH and Alkalinity (Dickson)	**Lecture/Discussion.** Quality control and advantages/disadvantages of analytical measurements of CO2 parameters (Dickson/Wang)	**Lecture.** Overview on approaches and tools to manipulate seawater carbonate chemistry (Gattuso)	**Lecture.** Algal culturing overview (Iglesias-Rodriguez)	**Lab.** T2 sampling for corals, pH monitoring for mollusk exp't (Holcomb)	**Free**
Morning Period 2 (10:30-12:00)	**Lecture/Hands-on.** Intro to CO2SYS and seacarb (Sabine and Gattuso)	**Lecture.** Overview on biogeochemical feedbacks (Hutchins)	**Lecture/Discussion.** Implications of uncertainties in equilibrium constants and analytical measurements and choosing optimal parameters to measure for an experiment (Dickson/Sabine)	**Lecture/Demo.** Moored CO2 instrument demo (Sabine)	**Lecture.** Calcification overview (bkgd for coral calcification and larval mollusk exp'ts), methods for measuring coral and bivalve calcification (Cohen/Miller)	**Lecture.** Radioisotope Techniques for measuring coccolithophore calcification (Balch) and PIC methods for quantifying calcification (Iglesias-Rodriguez)	
Afternoon Period (13:30-17:30)	**Lecture/Lab.** Lab safety presentations followed by sampling instruction (movie plus hands-on) and underway pCO2 introduction and demo (Groups A/B/C)	**Lab.** pH and infrared DIC measurements, coulometric DIC setup demo (Groups D/E/F)	**Lab.** TA and DIC measurements (Groups D/E/F)	**Lab/Hands-on.** Lecture/Demo/Hands-On. Theoretical CO2SYS (Yates) experiments and setup for larval mollusk experiments (McCorkle)	**Lab.** Coral calcification setup (Holcomb - Groups G/H/I)	**Lab.** T3 sampling for corals (Holcomb)	**Lab.** T4 sampling for corals and coral exp't breakdown, pH monitoring for mollusks. (Holcomb)
					Tour. Bernhard lab	**Lecture.** Measuring calcification in the field (Langdon)	
Evening Period (19:00-22:00)	**WELCOME RECEPTION AND POSTER SESSION, WHOI Clark 507**		**Lecture.** Overview onf ocean acidification experimental design (Langdon)		**Lab.** Larval mollusk inoculations (White/McCorkle). Coral T1 sampling (Holcomb)		

WEEK 2	NOVEMBER 9 MONDAY	NOVEMBER 10 TUESDAY	NOVEMBER 11 WEDNESDAY	NOVEMBER 12 THURSDAY	NOVEMBER 13 FRIDAY
Morning Period 1 (8:30-10:00)	**Lab.** Larval mollusk harvesting (Cohen/Rose/White)	**Lecture.** Biogeochemical modeling oveview (Doney)	**Lecture/Hands-on.** Large databases (e.g., GLODAP), etc. (Key)	**Lecture.** Introduction to Data Management and Better Practices for Shipboard Data Management (Chandler)	**Lecture.** Data reporting overview (Kozyr)
Morning Period 2 (10:30-12:00)		**Lecture.** Physiology (Seibel)	**Lecture.** Genomics applications to ocean acidification research (Fangue)	**Lecture.** Biogeochemical Modeling Part II (Doney)	**Course wrap-up:** Open discussion and course evaluations
Afternoon Period (13:30-17:30)	**Lecture/Hands-on.** Ocean Data View (Schlitzer)	**Lab.** Larval mollusk microscopy (Cohen/Rose) Cellular pH setups and initial pH measurements (Seibel)	**Lab/Hands-On.** Cellular pH final measurements and respirometry demo (Seibel)	**Synthesis and discussion**	**Departures**
	Tours. MBL Marine Resources Center and Waterbury algal culturing lab		**Lab.** Modeling exercises (Doney)		
Evening Period (19:00-22:00)				**FAREWELL DINNER, MBL**	

Monday, November 2, 2009
Lectures, lab safety talks, sampling, and underway pCO_2 demonstration

Morning

Time	Activity
8:15 am	**Introductory remarks** (Benway/Cooley)
8:30 am	**Lecture**. Overview of the ocean CO_2 system (Sabine) MBL Speck Auditorium
9:00 am	**Lecture.** Introduction to CO_2 chemistry in seawater media (Dickson) MBL Speck Auditorium
9:40 am	**Lecture**. Analytical parameters, and current measurement techniques (Dickson) MBL Speck Auditorium
10:00 am	Coffee Break
10:30 am	**Lecture/Hands-on**. Introduction to CO2SYS (Sabine) MBL Speck Auditorium – bring laptops
11:15 am	**Lecture/Hands-on**. Introduction to seacarb (Gattuso) MBL Speck Auditorium – bring laptops
12:00 pm	Lunch (Swope Cafeteria, MBL)

Afternoon

<table>
<tr><th>Time</th><th>Group A</th><th>Group B</th><th>Group C</th></tr>
<tr><td>1:15 pm</td><td colspan="3">Lecture. WHOI/MBL Chemical Safety training, MBL Speck Auditorium (Poisson - WHOI, Marcello - MBL)</td></tr>
<tr><td>2:00 pm</td><td colspan="3">Lecture/Video. MBL Speck Auditorium:
1) CO_2 water sampling movie (Dickson)
2) Introduction to underway pCO_2 system (Wang)</td></tr>
<tr><td>2:30 pm</td><td rowspan="2">Lab. CO_2 water sampling, Rowe 423/424 (Dickson, Sabine, Cooley)</td><td rowspan="2">Break</td><td>Shuttle MBL to McLean</td></tr>
<tr><td>3:00 pm</td><td rowspan="2">Lab. Underway pCO_2 demo (Wang) (1 hour)</td></tr>
<tr><td>3:30 pm</td><td>Shuttle MBL to McLean</td><td rowspan="2">Lab. CO_2 water sampling, Rowe 423/424 (Dickson, Sabine)</td></tr>
<tr><td>4:00 pm</td><td rowspan="2">Lab. Underway pCO_2 demo (Wang/Cooley) (1 hour)</td><td>Shuttle McLean to MBL</td></tr>
<tr><td>4:30 pm</td><td>Shuttle MBL to McLean</td><td rowspan="2">Lab. CO_2 water sampling, Rowe 423/424 (Dickson, Sabine)</td></tr>
<tr><td>5:00 pm</td><td>Break/Shuttle McLean to MBL (if desired)</td><td rowspan="2">Lab. Underway pCO_2 demo (Cooley) (1 hour) – then walk to Clark</td></tr>
<tr><td>5:30 pm</td><td>Shuttle MBL to Clark (if needed)</td><td>Shuttle MBL to Clark</td></tr>
<tr><td>6:00-8:00 pm</td><td colspan="3">Welcome reception/poster session (WHOI, Clark 507)</td></tr>
<tr><td>8:00 pm</td><td colspan="3">Shuttles from Clark to MBL</td></tr>
</table>

Chris Sabine
Monday, November 2, 2009
Overview of the ocean CO_2 system

a) Review the distribution of carbon species in the ocean
b) Examine the relative effects of biology and physics on carbon
c) Brief review of rising CO_2 in the atmosphere, ocean uptake and storage of CO_2, and the role of the ocean in the global carbon cycle
d) Brief review of changing ocean chemistry and ocean acidification

Helpful Reading:

Doney, S.C., V.J. Fabry, R.A. Feely, and J.A. Kleypas (2009): Ocean acidification: The other CO_2 problem. *Annu. Rev. Mar. Sci.*, 1, doi: 0.1146/annurev.marine.010908.163834, 169–192.

Gruber N, Gloor M, Mikaloff Fletcher SE, Doney CS, Dutkiewicz S, et al. (2009): Ocean sources, sinks, and transport of atmospheric CO_2. *Glob. Biogeochem. Cycles* 23:GB1005.

Sabine CL, Heimann M, Artaxo P, Bakker D, Chen C-TA, et al. 2004. Current status and past trends of the global carbon cycle. In The Global Carbon Cycle: Integrating Humans, Climate, and the Natural World, Scope 62, ed. CB Field, MR Raupach, ch. 2, pp. 17–44b.Washington, DC: Island Press

Sabine, C.L., and T. Tanhua (2009): Estimation of anthropogenic CO_2 inventories in the ocean. *Annu. Rev. Mar. Sci*. [In press]

Takahashi, T., S.C. Sutherland, R. Wanninkhof, et al. (2009): Climatological mean and decadal change in surface ocean pCO_2, and net sea-air CO_2 flux over the global oceans. *Deep-Sea Res. II*, 56(8–10), 554–577.

Estimation of Anthropogenic CO_2 Inventories in the Ocean

Christopher L. Sabine[1] and Toste Tanhua[2]

[1]Pacific Marine Environmental Laboratory/NOAA, Seattle, Washington 98115-6349; email: chris.sabine@noaa.gov

[2]Leibniz-Institut für Meereswissenschaften, Marine Biogeochemie, 24105 Kiel, Germany; email: ttanhua@ifm-geomar.de

Annu. Rev. Mar. Sci. 2010. 2:269–92

The *Annual Review of Marine Science* is online at marine.annualreviews.org

This article's doi: 10.1146/annurev-marine-120308-080947

1941-1405/10/0115-0269$20.00

Key Words

decadal change, ocean biogeochemistry, climate change, carbon cycle

Abstract

A significant impetus for recent ocean biogeochemical research has been to better understand the ocean's role as a sink for anthropogenic CO_2. In the 1990s the global carbon survey of the World Ocean Circulation Experiment (WOCE) and the Joint Global Ocean Flux Study (JGOFS) inspired the development of several approaches for estimating anthropogenic carbon inventories in the ocean interior. Most approaches agree that the total global ocean inventory of C_{ant} was around 120 Pg C in the mid-1990s. Today, the ocean carbon uptake rate estimates suggest that the ocean is not keeping pace with the CO_2 emissions growth rate. Repeat occupations of the WOCE/JGOFS survey lines consistently show increases in carbon inventories over the last decade, but have not yet been synthesized enough to verify a slowdown in the carbon storage rate. There are many uncertainties in the future ocean carbon storage. Continued observations are necessary to monitor changes and understand mechanisms controlling ocean carbon uptake and storage in the future.

INTRODUCTION

CFC: chlorofluorocarbon

C_{ant}: anthropogenic carbon

The global utilization of fossil fuels for energy is rapidly changing the trace gas composition of the Earth's atmosphere, causing a warming from excess CO_2, water vapor, chlorofluorocarbons (CFCs), methane, nitrous oxide, and other greenhouse gases. These anthropogenic gases play a critical role in controlling the Earth's climate because they increase the infrared opacity of the atmosphere, causing the planetary surface to warm. The world's oceans play an important role in the global carbon cycle as they are a vast reservoir of carbon, rapidly exchange carbon with the atmosphere, and take up a substantial portion of anthropogenically released carbon from the atmosphere.

There are only three major reservoirs with natural exchange rates fast enough to vary significantly on the timescale of decades to centuries: the atmosphere, terrestrial biosphere, and the oceans. Of this three-component system, approximately 90% of the carbon is located in the oceans. The oceans are able to hold much more carbon than the other reservoirs because most of the CO_2 that diffuses into the oceans reacts with seawater to form carbonic acid (H_2CO_3) and its dissociation products, bicarbonate (HCO_3^-) and carbonate (CO_3^{2-}) ions.

Seawater carbonate chemistry is governed by a series of chemical uptake, dissolution, and precipitation reactions:

$$Air\text{-}sea\ exchange: CO_{2(atmos)} \leftrightarrow CO_{2(aq)} \quad (1)$$

The equilibration time scale for this exchange is about one year, so on a global scale surface water CO_2 generally increases at close to the same annual rate as the atmosphere (Takahashi et al. 2009). On a finer scale, local physical or biological perturbation events can make surface water CO_2 significantly deviate from atmospheric equilibrium.

$$Reaction\ with\ H_2O: CO_{2(aq)} + H_2O \leftrightarrow H_2CO_3 \leftrightarrow H^+ + HCO_3^- \leftrightarrow 2H^+ + CO_3^{2-} \quad (2)$$

These reactions are relatively rapid, and for most applications, the partitioning of inorganic carbonate species can be assumed to be in equilibrium. For typical surface ocean conditions, about 90% of the total carbon dioxide is in the form of the HCO_3^-, ~9% as carbonate CO_3^{2-}, with only ~1% remaining as undissociated CO_2 (aq) and H_2CO_3.

Although ocean biology plays an integral role in the natural distribution of carbon in the ocean, there is no conclusive evidence that the ocean uptake and storage of anthropogenic carbon, thus far, involves anything other than a chemical and physical response to rising atmospheric CO_2.

On timescales of decades, the rate at which anthropogenic carbon (C_{ant}) is moved into the ocean interior limits the rate of ocean uptake (Sarmiento et al. 1992). The physical mixing time for the ocean is two to three orders of magnitude slower than the mixing time of the atmosphere and is the primary process controlling large-scale CO_2 uptake (Stuiver et al. 1983). Currently the rate of ocean carbon storage does not seem to be keeping pace with the rate of growth in CO_2 emissions (Bindoff et al. 2007). Over hundreds to thousands of years, however, the oceans will be able to absorb 70–80% of CO_2 released to the atmosphere (e.g., Archer & Maier-Reimer 1994, Archer et al. 1997). Over these timescales ocean circulation becomes less of a limiting process and processes like potential changes in ocean biology become important. Chemical neutralization of the CO_2 through the dissolution of calcium carbonate sediments could potentially absorb another 9–15% of fossil fuel release on timescales of tens of thousands of years (Archer et al. 1997). Thus, the role of the ocean in controlling atmospheric CO_2 depends on the timescale being examined and the processes that dominate over those timescales.

To understand the oceans' role in the global carbon cycle and how it might be changing over time, one must understand the rate at which the oceans absorb anthropogenic CO_2 from the atmosphere, referred to as C_{ant} uptake, as well as how and where that CO_2 is stored in the ocean

interior, C_{ant} storage. Uptake is not necessarily the same as C_{ant} storage, because ocean transport can move carbon that is removed from the atmosphere in one place and store that carbon in another place. For example, models suggest that the equatorial Pacific is a region of significant C_{ant} uptake because the equatorial upwelling exposes older waters that have not previously seen the elevated atmospheric CO_2 values. However, relatively little C_{ant} is stored in the equatorial Pacific because the carbon is quickly transported away from the equator and stored in the subtropical gyres (Sarmiento et al. 1992).

Pg C: petagram carbon (peta $\equiv 10^{15}$)

GCM: Global Circulation Model

The techniques for estimating ocean C_{ant} uptake are also different from the techniques for estimating storage. Gruber et al. (2009) recently summarized the latest C_{ant} uptake estimates from a variety of approaches including air-sea CO_2 partial pressure differences, inversion models together with measured changes in ocean interior carbon, changes in atmospheric oxygen together with concurrent measurements of atmospheric CO_2, inversion models together with measured changes in atmospheric CO_2, air-sea $\delta^{13}C$ disequilibrium, deconvolution of atmospheric CO_2 and $\delta^{13}C$, joint atmosphere-ocean inversions, and a suite of prognostic ocean general circulation models. The uptake estimates ranged from 1.5 ± 0.9 to 2.4 ± 0.5 Pg C year^{-1}. Gruber et al. concluded that the latest estimates from all of these techniques for the period of the 1990s and early 2000s were internally consistent within their uncertainties.

This article focuses on C_{ant} storage, not on the uptake that was recently summarized by Gruber et al. (2009). Although the spatial and temporal patterns of C_{ant} uptake may be different from the storage patterns, these two measures of the ocean carbon cycle are closely related to each other. Integrated over large enough time and space domains, the net uptake should be reconcilable with the C_{ant} storage. So far, this has only been possible in a qualitative sense or through inverse calculations using ocean Global Circulation Models (GCMs), but as techniques improve for estimating C_{ant} storage over shorter time intervals, more quantitative comparisons should be possible.

OCEAN CARBON OBSERVATIONS

A significant impetus for ocean biogeochemical research over the past several decades has been to better understand the ocean's role as a sink for anthropogenic CO_2. Ocean uptake estimates in surface waters have the advantage that there are many opportunities to make measurements using research ships, underway measurements from ships of opportunity, autonomous measurements from moorings and drifters, and remote sensing. Air-sea exchange of CO_2 can be measured over short time intervals and with sufficient observations could provide global CO_2 uptake estimates on timescales of months to years. The disadvantage of uptake estimates from surface observations is the very large dynamic range in surface ocean CO_2 values and the uncertainties in air-sea flux parameterizations make it difficult to fully constrain the net global ocean uptake (Wanninkhof et al. 2009). For example, Takahashi et al. (2009) estimate a net CO_2 uptake for the nominal year 2000 as 1.6 ± 0.9 PgC. They attribute most of the uncertainty in the flux estimate to random errors: 13% for uncertainty in the pCO_2 estimates, 30% to the scaling factor for the gas transfer piston velocity parameterization, 20% to uncertainty in the wind speeds, and 35% for the mean rate of change in ocean water pCO_2. The remainder of the error is for the uncertainty in their corrections for systematic biases caused by undersampling and the interpolation method used.

The advantage of using ocean interior measurements to quantify changes in C_{ant} storage is that there is much less variability in the ocean interior. The large seasonal and subseasonal variations in the ocean surface are not seen in the ocean interior, making it much easier to detect long-term secular changes due to C_{ant} accumulation. The major downsides of ocean interior measurements are that they require long oceanographic cruises to collect the necessary interior ocean data, the anthropogenic signal is small compared to the large natural inorganic carbon background in the

ocean (typically less than 1%), and there are several processes that control carbon distributions in the ocean that must be understood and quantified.

GEOSECS: Geochemical Ocean Sections

WOCE: World Ocean Circulation Experiment

JGOFS: Joint Global Ocean Flux Study

Total alkalinity (TA): a measure of the charge balance of seawater (the excess of bases over acids)

Dissolved inorganic carbon (DIC): the sum of dissolved carbon dioxide, carbonic acid, bicarbonate, and carbonate

The Geochemical Ocean Sections (GEOSECS) program of the 1970s provided the first global inorganic carbon data set with consistent, well-documented methods. However, shortly after GEOSECS was completed Broecker et al. (1979) commented that "...unless [inorganic carbon] measurements that are more accurate by an order of magnitude can be made, at least a decade will pass before direct confirmation of the model-based [C_{ant} uptake] estimates will be obtained." These words proved to be true as it has taken more than a decade and more than an order of magnitude improvement in the measurements to produce C_{ant} estimates that were accepted by the carbon cycle community. In the years following GEOSECS, measurement techniques were significantly improved for regional studies like the Transient Tracers in the Ocean (TTO), and South Atlantic Ventilation Experiment (SAVE) in the Atlantic during the 1980s. The next global survey of carbon distributions in the ocean, however, did not occur until the 1990s. At that time two international research programs, the World Ocean Circulation Experiment (WOCE) Hydrographic Program and the Joint Global Ocean Flux Study (JGOFS), collaborated to complete nearly 100 cruises with inorganic carbon measurements (Wallace 2001). It was these data that created a new revolution in assessing C_{ant} from direct measurements of ocean inorganic carbon and other anthropogenic tracers. Many new techniques for evaluating the observations have been developed, but the results have taken a while to make it into the scientific literature.

In the early 2000s the Intergovernmental Panel on Climate Change developed its third assessment report (IPCC 2001). This report had one chapter on observed climate variability and climate change and this chapter contained almost nothing on ocean carbon cycle observations because there were very few published results at that time. The assessment report, in general, relied almost exclusively on indirect approaches and models to estimate the ocean C_{ant} uptake and storage. Also in the early 2000s, the physical and biogeochemical communities organized themselves to initiate an effort to collect full water column boundary to boundary hydrographic and geochemical data along a subset of the cruises that were initially run as part of the WOCE/JGOFS global survey in the 1990s. At least seven countries agreed to coordinate these repeat hydrographic survey cruises to monitor decadal-scale changes in the ocean. For example, the US CLIVAR/CO_2 Repeat Hydrography Program outlined 19 cruises that it will reoccupy on a 10-year rotating basis. The program started in 2003 and is slated to complete its first decadal survey by 2012.

By the time the fourth IPCC assessment report was prepared in 2007, the number of climate observations had grown substantially resulting in three observation-based chapters, including one called Observations: Ocean Climate Change and Sea Level (IPCC 2007). The number of publications and the range of techniques that have been developed to interpret the growing number of ocean carbon observations over the last few years have greatly improved our understanding of the ocean uptake and storage of inorganic carbon.

CARBON UPTAKE AND STORAGE OVER THE LAST TWO CENTURIES

The first anthropogenic CO_2 estimates calculated from direct observations of total alkalinity (TA) and dissolved inorganic carbon (DIC) concentrations were presented about 30 years ago by Brewer (1978) and Chen & Millero (1979). Variations of this approach have been pursued by a large number of investigators in many regions of the world ocean (Chen 1982, Papaud & Poisson 1986, Poisson & Chen 1987, Goyet and Brewer 1993, Goyet et al. 1998). However, the Brewer and Chen/Millero approach (hereafter called the Chen technique) did not find general acceptance, since the uncertainties were generally regarded as too large (e.g., Shiller 1981, Broecker et al. 1985). In 1996, Gruber et al. proposed an approach for estimating anthropogenic CO_2 based on

many of the principles outlined in the Chen technique, but also addressing several of the criticisms of the original approach. This approach (hereafter referred to as the ΔC^* technique) was applied to the GEOSECS, TTO, and SAVE data in the Atlantic Ocean (Gruber et al. 1996, Gruber 1998). The ΔC^* technique was later used to estimate C_{ant} in the Indian, Pacific, and Atlantic oceans using the WOCE/JGOFS data (Sabine et al. 1999, 2002; Lee et al. 2003). Sabine et al. (2004a) combined these WOCE/JGOFS estimates into a global ocean summary of C_{ant}.

Sabine & Feely (2001) compared the Chen and ΔC^* techniques in the Indian Ocean. Application of the Chen technique to the WOCE/JGOFS Indian Ocean data set gave a total C_{ant} inventory that was essentially the same as the ΔC^* inventory, but there were substantial differences in the distributions within the water column depending on the details of how the technique was applied. In 2005, Lo Monaco et al. (2005a) adapted a version of the Chen approach to examine the C_{ant} distributions in the Southern Ocean, south of Africa. Lo Monaco et al. (2005b) compared their results with the ΔC^* estimates and found similar results north of 50°S, but they estimated larger inventories in the high-latitude Southern Ocean.

Both the ΔC^* and Chen techniques are based on the premise that the C_{ant} concentration can be isolated from measured DIC values (C_m) by subtracting the contribution of the biological pumps (ΔC_{bio}) and the physical processes involving the preindustrial end-members and the effects of the solubility pump (C_{phys}):

$$C_{ant} = C_m - \Delta C_{bio} - C_{phys} \quad (3)$$

This general approach is based on the assumption that ocean circulation and the biological pump have operated in steady state since preindustrial times. Both approaches correct for the biological term using changes in alkalinity to estimate the calcium carbonate effect and apparent oxygen utilization (AOU) together with a Redfield ratio to correct for changes due to organic matter decomposition. The main difference between the Chen and ΔC^* techniques is in how the C_{phys} term is handled. The first fundamental difference between the two techniques is that in the Chen approach changes in the properties of the subsurface waters are referenced to the mean deep-water values, whereas the ΔC^* approach divides the water column into isopycnal intervals and references the changes back to the outcrop region for each interval. The ΔC^* technique also takes a different approach to estimating the effects of the solubility pump. Rather than attempting to determine a preformed DIC concentration based on an empirical relationship between temperature and DIC as the Chen method, the C_{phys} term is divided into the DIC the waters would have in equilibrium with a preindustrial atmosphere (C_{eq}) and a term that corrects for the fact that, because CO_2 gas exchange is slow relative to the surface water biological and physical processes that can change CO_2, surface waters are rarely in complete equilibrium with the atmosphere (C_{diseq}).

$$C_{ant} = C_m - \Delta C_{bio} - C_{eq} - C_{diseq} \quad (4)$$

The equilibrium term is by far the largest fraction of the preformed concentration and can be calculated using the equilibrium inorganic carbon constants, alkalinity, and the preindustrial atmospheric CO_2 concentration. The relatively small disequilibrium term can then be estimated on isopycnal surfaces using a time-dependent tracer such as chlorofluorocarbons (CFCs).

Shortly after the ΔC^* approach was published, Goyet et al. (1999) developed a new approach, MIX, that departs from the traditional family of reconstructions based on preformed DIC. The MIX approach uses a multiparameter mixing model (Tomczak & Large 1989) to calculate the relative contributions that a few (basin- or cruise-specific) water mass end members make to each water sample. In Goyet et al.'s application, temperature (T) and salinity (S) were used as conservative parameters and alkalinity and dissolved oxygen (O_2) were used as nonconservative parameters. The mixing model uses each sample's O_2 depletion and alkalinity enrichment relative

Biological pump: the process whereby CO_2 is removed from the surface ocean by biological production and added to the ocean interior when the organisms die and decompose while sinking into the deep ocean

Solubility pump: the process whereby CO_2 is absorbed into cold, high latitude waters that sink into the ocean interior underneath warm, lower latitude waters that cannot hold as much CO_2

to its end member composition to quantify the biological (remineralization) contribution to DIC according to

$$C_{bio} = 0.78^{*}\Delta O_2 + 0.5^{*}\Delta TA \quad (5)$$

GLODAP: Global Ocean Data Analysis Project

Goyet et al. estimate a history of CO_2 changes in each end member as a function of depth from its surface source. The combination of end members' surface DIC changes and depth-penetration scales that best reproduces the present-day DIC distribution at depth is determined iteratively. The MIX approach was first applied to a zonal line in the northern Indian Ocean but was never implemented on a more extensive dataset.

Goyet later developed a different back-calculation method known as the TrOCA method (Touratier & Goyet 2004, Touratier et al. 2007) that uses a quasi-conservative tracer similar to those of NO and PO (Broecker 1974), which is based on a Redfield ratio. C_{ant} is estimated from the difference between the measured TrOCA conservative tracer and a preformed TrOCA tracer. Touratier & Goyet (2004) estimate the preformed TrOCA by regressing TrOCA against potential temperature (θ) in deep Atlantic waters with $\theta < 2.5°C$. These waters are assumed to be free of C_{ant} and the relationship with θ is assumed to hold for the entire Atlantic. In Touratier et al. (2007) the implementation was expanded to regress TrOCA against θ and alkalinity using waters from the Pacific and Indian water where $\Delta^{14}C$ is less than −175 parts per mil (‰). Substantial biases in the TrOCA method has been found by comparing to observational data and model output (Yool et al. 2009).

All observationally based anthropogenic CO_2 methodologies to date rely on the assumption that C_{ant} penetrates the ocean as a passive, inert tracer responding to an evolving history in surface waters. Another approach for estimating C_{ant} is the transit time distribution (TTD) method, which fully exploits this assumption in order to relax other assumptions. The TTD method does not use DIC measurements, thus avoiding large uncertainties in back-calculation approaches related to the biological correction. This approach uses the fact that C_{ant} at any point in the ocean interior should be related to the concentration history of anthropogenic CO_2 at the surface and the spectrum of times it took the water to reach the interior ocean location. The surface history is estimated using the equilibrium inorganic carbon chemistry equations, temperature, the preformed alkalinity (estimated from salinity), and the atmospheric CO_2 record. The transit time distributions are approximated by inverse Gaussian functions based on transient tracers (often CFCs). The approach then only requires measurements of temperature, salinity, and a transient tracer if one assumes that biology is not involved, that circulation is in steady state, and that a single surface source region dominates the interior water so there is no spatial dependency in the source waters. Hall et al. (2004) used a volume-based version of the TTD method to estimate C_{ant} in the Indian Ocean, while Waugh et al. (2004) applied a pointwise version to the subpolar North Atlantic Ocean. Waugh et al. (2006) applied the method to the Global Data Analysis Project (GLODAP) data set (Key et al. 2004) to generate a global C_{ant} estimate.

An approach to scale observed carbon inventory changes between two cruises separated in time to the full anthropogenic storage over the last two centuries has been presented by Tanhua et al. (2007), taking advantage of the exponential nature of the atmospheric Cant increase and exploring the transient steady state concept (Gammon et al. 1982). An exponentially changing tracer will, after a certain time, reach transient steady state, meaning that, e.g., a depth profile of Cant will have constant shape over time, and the concentrations will increase proportionally to the surface layer increase. This way of calculating the Cant concentration is independent from tracer data and circumvents many of the assumptions of the back-calculation methods.

A summary of the long-term Cant estimate approaches is given in **Table 1**. They break down into three general categories: back-calculation, tracer based, and scaled decadal change. There

Table 1 Comparison of methods used to determine long-term C_{ant} storage

	Method	Advantages	Disadvantages
Back-calculation	Chen Technique (Brewer 1978, Chen & Millero 1979)	Based directly on observed DIC concentrations in the ocean. Relies on well-known oceanographic properties. Can be validated in deep water where C_{ant} should be zero.	Need to estimate preindustrial property fields, particularly CO_2 air-sea disequilibrium. Assumes constant stoichiometric ratios. Best done with large data set. Needs water mass age estimates.
	ΔC^* technique (Gruber et al. 1996)		
	LM05 technique (Lo Monaco et al. 2005a)		
	TrOCA (Touratier & Goyet 2004, Touratier et al. 2007)	Based on DIC. Straightforward calculation. Do not need water mass age tracer.	Assumes constant stoichiometric ratios. Preformed values crudely determined.
	MIX (Goyet et al. 1999)	Based on DIC. Does not need water mass age tracer. Can be calculated using data from a single cruise.	Cumbersome water mass analysis. Assumes C_{ant} only increases with depth. Assumes constant stoichiometric ratios.
Tracer based	TTD (Waugh et al. 2004, Hall et al. 2004)	Less sensitive to near-surface biological processes. Will not yield negative Cant values.	This technique cannot detect biological carbon changes. Sensitive to assumptions of mixing and saturation of tracers (e.g., CFCs).
Decadal change	Scaled eMLR (Tanhua et al. 2007)	Based on DIC. No assumptions of preindustrial fields necessary.	Dependent on the assumption of transient steady state. Still limited number of decadal repeat data.

are several variations of the back-calculation methods that use modern DIC measurements and other tracer data to infer the preindustrial carbon distributions and therefore the total inventory of C_{ant}. The tracer-based TTD method and the scaled decadal change approach do not have as many variations. All of these methods have their advantages and disadvantages.

Long-Term C_{ant} Storage

After completion of the WOCE/JGOFS global survey in 1998, a five-year effort was begun to compile and rigorously quality-control the US and international data sets, including a few pre-WOCE data sets in regions that were data limited. The final data set, GLODAP, with 9618 hydrographic stations collected on 95 cruises, provides the most accurate and comprehensive view of the global ocean inorganic carbon distribution available (Sabine et al. 2005). By combining these data with the ΔC^* technique, Sabine et al. (2004a) estimated that 118 ± 19 Pg C had accumulated in the ocean between 1800 and 1994. This inventory accounted for 48% of the fossil fuel and cement manufacturing CO_2 emissions to the atmosphere over that time frame.

A map of the anthropogenic CO_2 ocean column inventory (**Figure 1**) shows that the carbon is not evenly distributed in space. More than 23% of the inventory can be found in the North Atlantic, a region covering approximately 15% of the global ocean. By contrast, the region south of 50°S represents approximately the same ocean area but only has ~9% of the global inventory (Sabine et al. 2004a). Despite the relatively slow equilibration rate for CO_2 in seawater (approximately 1 year versus weeks for oxygen), uptake at the surface does not fully explain the spatial differences

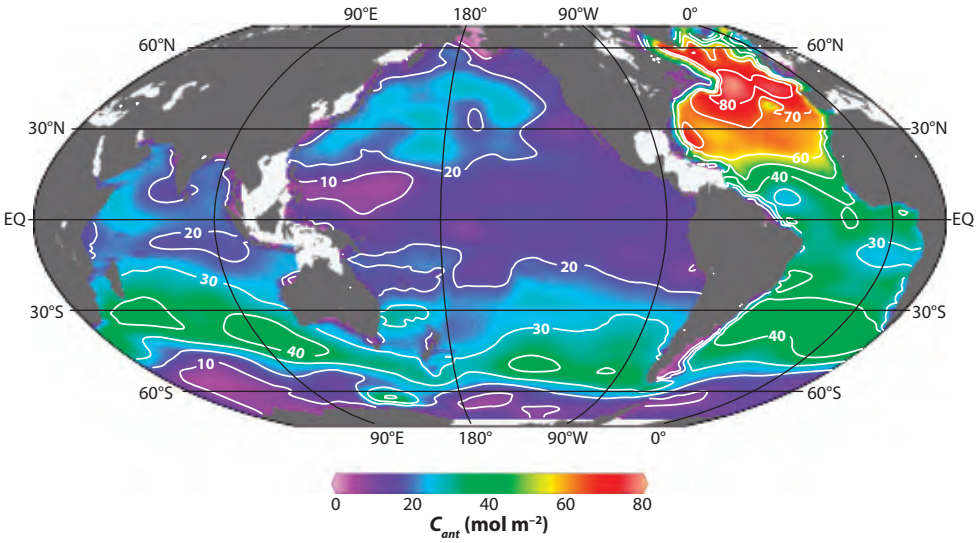

Figure 1

Global map of column C_{ant} (anthropogenic carbon) as given by Sabine et al. (2004a) based on the ΔC^* calculation method of Gruber et al. (1996). Adapted from Sabine et al. (2004a).

in storage. The primary reason for these differences is because of the slow mixing time in the ocean interior and the fact that waters only move into the deep ocean in a few locations. The highest inventories are found in the locations where mode and intermediate waters are moving anthropogenic CO_2 into the ocean interior (e.g., the northern North Atlantic or in the Southern Hemisphere associated with the Subtropical Convergence Zone at 40–50°S; **Figure 1**).

These estimates of ocean C_{ant} have been used to evaluate models (Orr et al. 2001, Matsumoto et al. 2004) and to infer air-sea fluxes of CO_2 (Gloor et al. 2003, Mikaloff-Fletcher et al. 2006). However, there are many uncertainties in the ΔC^* method. Different implementations of the method can yield different results (e.g., Wanninkhof et al. 1999, Lo Monaco et al. 2005b) and there are potential biases due to the assumptions of a single ventilation time, constant disequilibrium, and constant Redfield ratios (Hall et al. 2004, Matsumoto & Gruber 2005).

Waugh et al. (2006) also used the GLODAP data set to estimate the global C_{ant} inventory using the TTD method (**Figure 2*a***). The estimated total inventory in 1994 was 134 Pg C. To evaluate uncertainties in the TTD method, Waugh et al. applied the approach to output from an ocean general circulation model (OGCM) and compared the results to the directly simulated C_{ant}. Outside of the Southern Ocean the predicted C_{ant} closely matched the directly simulated distribution, but in the Southern Ocean the TTD concentrations were biased high. This bias could be due to the TTD assumption of constant disequilibrium and also possibly due to short residence times of Southern Ocean waters, which would accentuate the different equilibration times for CO_2 (~1 year) and the CFCs (~1 week) used for the TTD estimates. The net result was a TTD overestimate of the global inventory by about 20%. Accounting for this bias and other uncertainties, an inventory range of 94–121 Pg C was given by Waugh et al. (2006). This agrees with the inventory of Sabine et al. (2004a). There were, however, differences in the spatial distributions (**Figure 2*b***). The TTD estimates generally gave much higher inventories in the Southern Ocean as previously noted, but there are also differences such as higher inventories in the North Atlantic Deep Water (**Figure 2*b***). The TTD estimates also generally had smaller C_{ant}

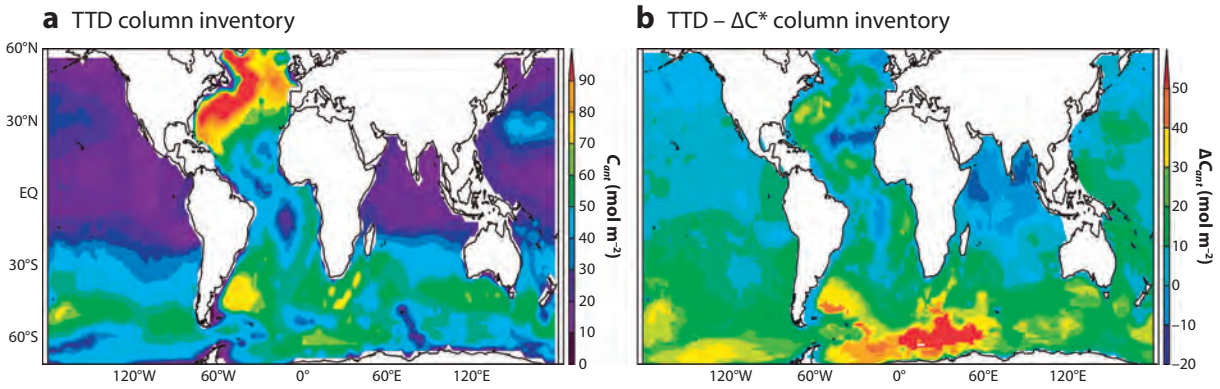

Figure 2

Global map of (*a*) C_{ant} column inventories from transit time distribution (TTD) calculations, and (*b*) difference between TTD and the ΔC* estimates from Sabine et al. (2004a). Adapted from Waugh et al. (2006).

concentrations than ΔC* in the upper ocean and larger at depth, consistent with biases expected in ΔC* given its assumption of a single parcel ventilation time.

The global estimate by Sabine et al. (2004a) approximated the C_{ant} inventories in marginal Seas and the Arctic Ocean due to lack of data, whereas the estimate by Waugh et al. (2006) did not account for those areas at all. The C_{ant} inventory for the Arctic Ocean has later been estimated to 2.5–3.3 Pg C (Tanhua et al. 2009) and for the Mediterranean to 1.7 Pg C (surprisingly high anthropogenic carbon content in the Eastern Mediterranean Sea; A. Schneider, T. Tanhua, A. Körtzinger, and D.W.R. Wallace, unpublished paper) by the TTD method, showing that both of these marginal seas have higher than global average C_{ant} concentrations.

Vázquez-Rodríguez et al. (2009) compared five different approaches along a meridional line in the Atlantic. They found that all the observational methods produced reasonable C_{ant} estimates and inventories for the full length of the Atlantic Ocean. However, south of ~40°S there are significant differences between methods. The uncertainties in C_{ant} estimates due to the method applied are narrow in the subtropics but larger for polar regions. The impact of these discrepancies is most important in the Southern Ocean given its large contribution (up to 12%) to the total inventory of C_{ant} and the larger differences between methods there. A similar result is shown by Álvarez et al. (2009) for a zonal section in the southern Indian Ocean where five methods to estimate C_{ant} were compared to each other and particularly large relative differences were found for the deep waters with a southern origin.

CARBON UPTAKE AND STORAGE OVER THE LAST TWO DECADES

Some of the inherent difficulties in estimating the C_{ant} concentration in the ocean can partly be overcome by comparing repeat measurements in certain ocean regions or along oceanographic sections. At least, any systematic biases tend to cancel out when comparing two estimates using the same assumptions. Typically, comparisons are made on data separated by 10 to 25 years in time, and are measures of the increase in ocean storage in a particular density range, for a particular water mass, or over the whole water column. Since the C_{ant} signal is small in comparison to the background DIC concentration, there are technical difficulties involved in detecting any changes in DIC concentration on timescales less than about a decade. Further, natural small-scale spatial and temporal variability tend to obscure the C_{ant} signal. This type of comparison thus requires

eMLR: extended Multiple Linear Regressions

precise and accurate data. There have been significant advances in this respect over the last few decades, for instance by refining analytical methods and compliance to follow recommended best practices (DOE 1994, Dickson et al. 2007). For carbon measurements, the now common use of Certified Reference Materials (CRMs) has also had a significant positive impact on the consistency of the data.

The WOCE/JGOFS global survey in the 1990s offered the first possibility to detect changes compared to GEOSECS and TTO data. One difficulty in quantifying decadal uptake is that for a large number of historical data, no CRMs were available for DIC and TA measurement (a problem that still exists today for some important measurements, e.g., nutrients). This deficiency can be partly overcome by so-called secondary quality control, i.e., a process where data are objectively studied in order to quantify systematic biases, for which corrections can be made. This is mostly done by comparing measurements from different cruises in the deep ocean where steady state conditions are assumed for the relatively short time interval between cruises (e.g., Gouretski & Jancke 2001, Johnson et al. 2001, Sabine et al. 2005).

Since the time of GEOSECS it has, in principle, been possible to detect changes in ocean carbon content through direct comparisons of measured carbon concentrations in the water column in certain regions. Since several national and international projects are resampling WOCE/JGOFS oceanographic lines with high-quality carbon measurements, more decadal uptake estimates will likely be made in the future. In particular, it opens the possibility of comparing inventory changes with decadal scale changes in the uptake rate, e.g., to distinguish between pre-1990s and post-1990s storage rates.

Just as with estimates of the centennial scale C_{ant} concentrations, there are several methods to calculate decadal scale changes in DIC. One common approach is to compare measured DIC concentrations on surfaces of equal density, and to adjust for changes in dissolution of organic matter and (sometimes) calcium carbonate using oxygen, alkalinity, and/or nutrient data. Another similar method is to calculate the C_{ant} concentrations for two cruises using a back-calculating method, and then consider only the difference between the two estimates. This has the advantage that assumptions such as the preindustrial air-sea disequilibrium become irrelevant, since the two terms will cancel out in the comparison. A multiple linear regression approach (MLR) was introduced by Wallace (1995) where DIC concentration is predicted by several other parameters. This approach compensates for variability in water mass distribution and temporal variability within a water mass. The MLR method was later refined by (Friis et al. 2005) to a method known as extended MLR (eMLR).

As seen above, transient tracers can be used to determine the long term C_{ant} inventory, but they can also be used to evaluate the decadal intentory changes. Once the tracer field is established, the uptake rate can be determined for any time period with the assumption of constant circulation, i.e., that the age field remains constant (e.g., Watanabe et al. 2000). Repeat measurements of transient tracers can account for changes in circulation and specifically address the role of circulation for the storage of C_{ant} (e.g., Steinfeldt et al. 2009). However, the different input histories of C_{ant} and CFCs influences the relationship between the storage rate of the two components, so a rapid increase in CFC concentration is not necessarily associated with a rapid increase in C_{ant} (e.g., Tanhua et al. 2006), if mixing is not explicitly addressed.

Decadal Change in C_{ant} Storage

In the following we will compare some data-based estimates of decadal scale changes in concentration of dissolved inorganic carbon integrated over the whole water column and report this as annual storage change, i.e., in units of mol m^{-2} $year^{-1}$, a measure that includes direct uptake

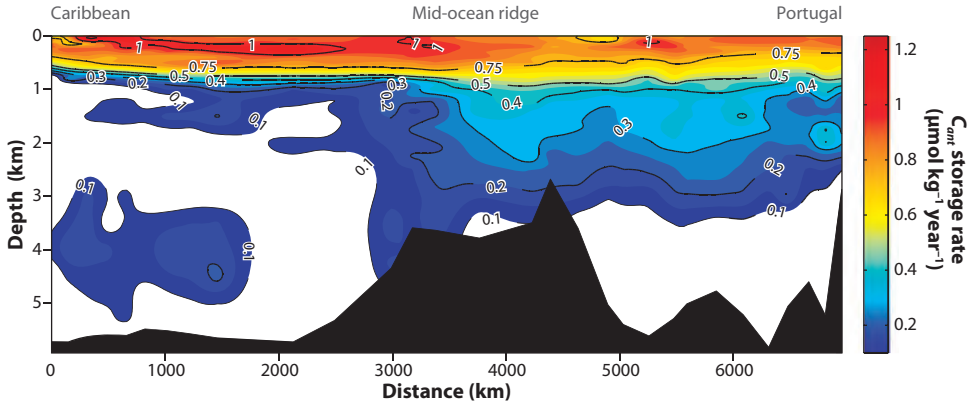

Figure 3

A section of anthropogenic carbon storage rate in the mid-latitude North Atlantic calculated as yearly means of the measured change between 1981 and 2004 with the extended Multiple Linear Regressions (eMLR) method (see cruise j in **Figure 4**; see also Tanhua et al. 2007). Storage changes <0.1 μmol kg^{-1} year^{-1} are left blank.

through the air-sea interface and carbon advected or mixed into the water column from surrounding waters. We will refer to this quantity as storage rate. As an example of the vertical structure of the storage rate, we present a quasi-zonal section of the mid-latitude North Atlantic in **Figure 3**. There are high storage rates for the upper waters, particularly associated with the warm and salty waters of the southwestern part of the section where the buffer capacity is large, and a core of positive storage rates associated with the deep western boundary current in the deep western part of that section. Note that the penetration of C_{ant} is particularly deep in the North Atlantic. If the global oceanic uptake of C_{ant} (∼2.2 Pg C year^{-1}) was evenly distributed over the world ocean, the average storage rate would be ∼0.55 mol m^{-2} year^{-1} (Sabine et al. 2008).

Figure 4, indices a–k, provide an overview of some published data based estimates of storage rates. (*a*) An early work on decadal uptake is provided by Peng et al. (1998) who calculate the C_{ant} storage rates of up to 0.65 mol m^{-2} year^{-1} in the Indian Ocean by comparison of GEOSECS data with data from WOCE (1978–1995). (*b*) Data from GEOSECS was also used by Tsunogai et al. (1993) to calculate storage rates in the Northwest Pacific Ocean between 1974–1991; (*c*) and by Peng et al. (2003) to calculate the storage rate in the Pacific Ocean between 1973–1991 with the MLR approach. The contemporary storage rate studies for the North Pacific are provided by (*d*) Sabine et al. (2008) and (*e*) Murata et al. (2009) that compared cruises from 1991–1993 with cruises in 2005/2006. The highest storage rates found by these two studies in the Northwest Pacific is 0.9 mol m^{-2} year^{-1}, which is lower than both the estimates of Tsunogai et al. (1993) and Peng et al. (2003). The observed differences between early and contemporary storage rates in the North Pacific could be due to technical problems associated with systematic biases in the GEOSECS DIC data. However, it is also possible that there are real trends in storage rate, which would imply a reduction in the C_{ant} storage rate since the mid-1990s while CO_2 has continued to increase faster in the atmosphere.

(*f*) For the South Pacific, a study by Matear & McNeil (2003) used a MLR-based method to compare data from 1968 with data from 1991–1996 along three lines south of Australia and New Zealand. They find high storage rates in the Subantarctic Mode Water and for the Antarctic Intermediate Water (up to ∼0.8 mol m^{-2} year^{-1}), and a large storage rate in the Antarctic Bottom Water for the westernmost section. Despite the different time interval, the storage rates found by

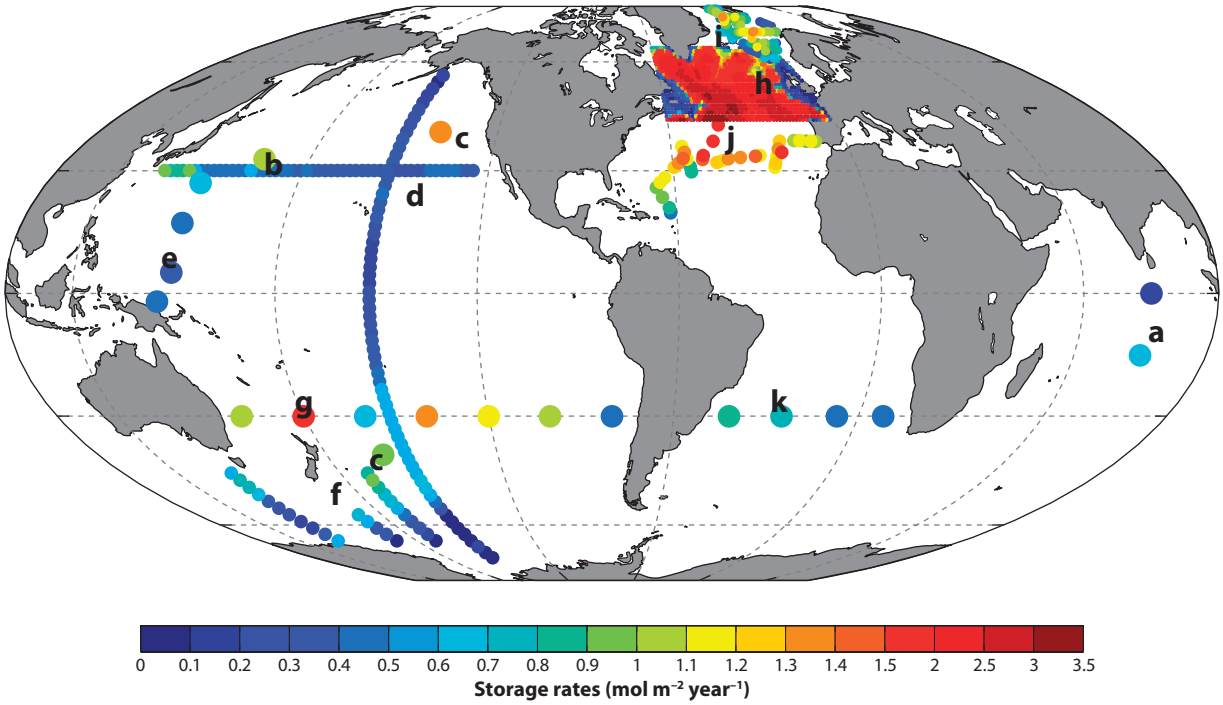

Figure 4

A world map with published data-based estimates of column inventories of anthropogenic carbon storage rates (mol m^{-2} $year^{-1}$).

Index	Data source	Time period	Method
a	(Peng et al. 1998)	1978–1995	Isopycnal, O_2 adjusted
b	(Tsunogai et al. 1993)	1974–1991	Column-integrated change in preformed carbonate
c	(Peng et al. 2003)	1973–1991	MLR
d	(Sabine et al. 2008)	1991/1992–2005/2006; 1994–2004	eMLR
e	(Murata et al. 2009)	1993–2005	Isopycnal, O_2 adjusted
f	(Matear & McNeil 2003)	1968–1991/1996	MLR
g	(Murata et al. 2007)	1992–2003	Isopycnal, O_2 adjusted
h	(Friis et al. 2005)	1981–1997/1999	eMLR
i	(Olsen et al. 2006)	1981–2002/2003	eMLR
j	(Tanhua et al. 2007)	1981–2004	eMLR
k	(Murata et al. 2008)	1992/1993–2003	Isopycnal, O_2 adjusted

Sabine et al. (2008) are similar to the easternmost values by Matear & McNeil. (*g*) A zonal section along 32°S by Murata et al. (2007), however, found slightly higher storage rates than Matear & McNeil using data from 2003 and 1992. Murata et al.'s high storage rates north of New Zealand were attributed to deep-water carbon storage. Even though the methods used by Sabine et al. (2008) and Murata et al. (2007) are different, the storage rates at the crossover point between the two data sets are almost identical.

It seems that only moderate adjustments need to be applied to the 1981 TTO-NAS data (Tanhua & Wallace 2005), and a number of studies have compared the TTO data with modern

data, together covering large parts of the North Atlantic and the Nordic Seas. (*h*) Friis et al. (2005) use data from 1997 and 1999 to calculate the storage rate in the subpolar North Atlantic and to introduce the extended Multiple Linear Regression (eMLR). The eMLR method is later used by (*i*) Olsen et al. (2006) and (*j*) Tanhua et al. (2007) to calculate the storage rate in the Nordic Seas (modern data from 2002/2003) and the mid-latitude North Atlantic (modern data from 2004), respectively. The North Atlantic clearly has the highest storage rate of the world ocean, which is to be expected since this region has the highest inventory of C_{ant} (**Figure 1**).

Figure 4 suggests that the storage rate is highest in the subpolar North Atlantic, slightly lower at lower latitudes and north of the Greenland-Scotland ridge. However, the column inventory is obviously dependent on water depth, and the Nordic Seas tends to be somewhat shallower than the North Atlantic, but the uptake rate might well be variable with time. This is shown by Perez et al. (2008) who reported on C_{ant} changes in the southern part of the Irminger Sea and found significant temporal variability in the storage rates: 0.55 mol m^{-2} $year^{-1}$ between 1981–1991; 2.3 mol m^{-2} $year^{-1}$ between 1991–1997; and 0.75 mol m^{-2} $year^{-1}$ between 1997–2006. Similarly, a study comparing the CFC distributions between 1997–2003 (Steinfeldt et al. 2009) found a dramatic reduction of C_{ant} column inventories in the central Labrador Sea, i.e., storage rates smaller than −2 mol m^{-2} $year^{-1}$. The reason for this is related to weak formation of Labrador Sea Water (LSW) since 1997. The C_{ant} -rich LSW is advected out of the region and replaced with upper LSW and relatively C_{ant}-poor North Atlantic Deep Water. It is unclear if the decrease of Labrador Sea C_{ant} column inventory is part of a long-term trend or part of decadal variability.

(*k*) For the South Atlantic, Murata et al. (2008) finds average storage rates close to the global mean value of 0.55 mol m^{-2} $year^{-1}$, but with significantly higher rates in the western basin. Murata et al. (2008) further found significant storage rates in the Antarctic Bottom Water (AABW) in the eastern part of the section (not visualized in **Figure 4*k***). If the AABW is accounted for, the storage rates would increase to about 1 mol m^{-2} $year^{-1}$ in the eastern basin. As seen before, the concentration of C_{ant} in the AABW continues to be difficult to quantify.

The results presented here clearly demonstrate that detecting decadal changes in carbon inventory is a feasible undertaking, and that these data are good indicators of integrated changes in C_{ant} storage. It is also clear that there are large spatial differences in the storage rates. There are several indications that, in some parts of the ocean, the storage rate is changing on decadal timescales, although it is unclear if this is a trend or variability. There are more cruises planned to complete the current global resurvey of the WOCE/JGOFS lines. Once these cruises are analyzed, a more comprehensive global picture of storage rates will be developed that can be used to evaluate the consistency with the independently derived ocean uptake estimates. Continued monitoring of the changing carbon inventory through repeat hydrography is important for detecting changes in the ocean carbon cycle and developing correct assessments of the anthropogenic carbon stock changes.

CARBON AND CLIMATE FEEDBACKS

We still do not fully understand the global carbon cycle or how the ocean uptake and storage of CO_2 is changing because of the strong interactions between the different parts of the system. Up to this point, the assumption has been that ocean storage of C_{ant} has been controlled by purely physical and chemical processes directly responding to rising CO_2 concentrations in the atmosphere. The average anthropogenic CO_2 fluxes for the period 2000–2005 are indicated by the red arrows in **Figure 5**. The bracketed numbers give natural (black) and anthropogenic (red) inventories. We are just now starting to appreciate that by adding approximately 135 Pg C to the ocean between 1800 and the early 2000s, the resulting changes in seawater chemistry may have

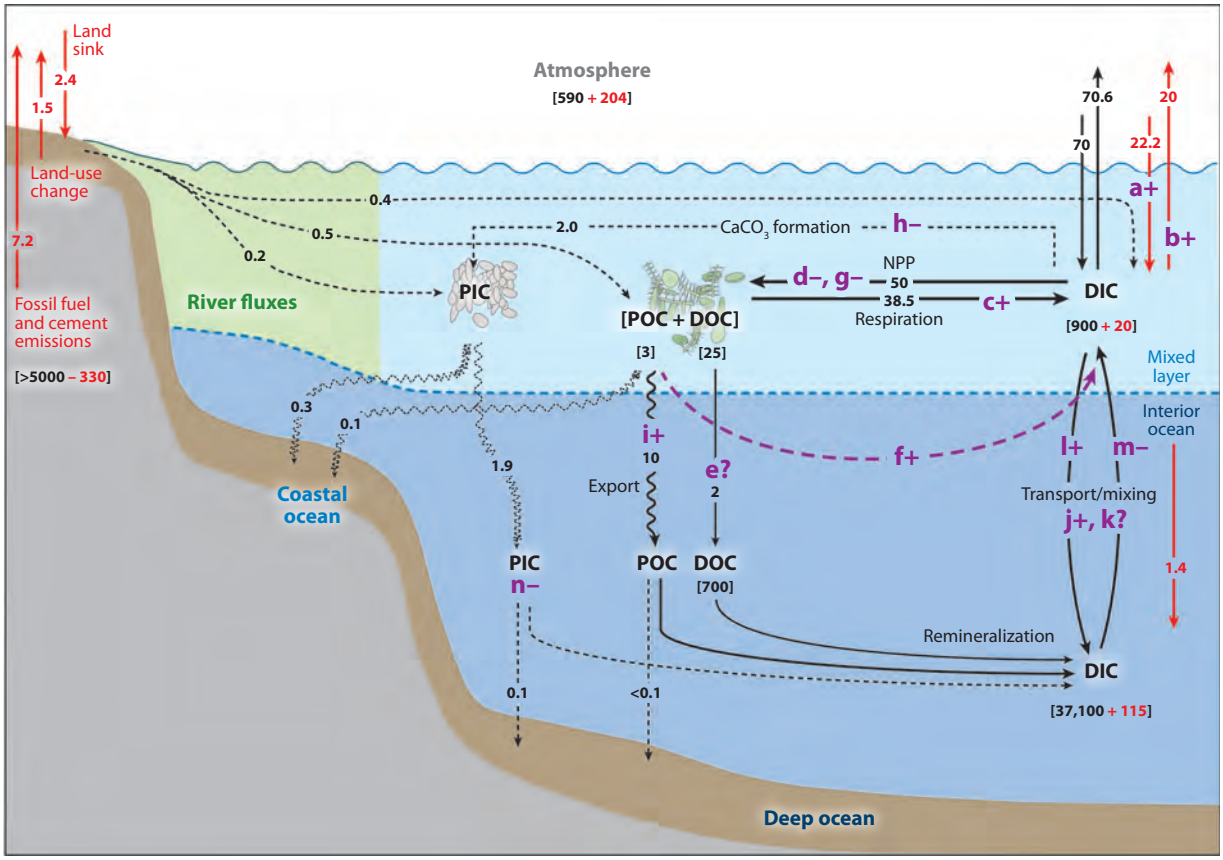

Figure 5

The Global Ocean Carbon Cycle in the early 2000s and feedback mechanisms. Bracketed values denote reservoir size (Pg C), with values in red denoting anthropogenic change. Bracketless values are fluxes (Pg C year^{-1}), with values in red denoting anthropogenic fluxes. Letters in purple denote feedback mechanisms discussed in the text, with plus and minus signs indicating positive and negative feedback loops in terms of atmospheric CO_2 concentration. Abbreviations: a+, decreased buffer capacity; b+, decreased solubility in warmer ocean; c+, enhanced recycling due to warmer ocean; d–, carbon overconsumption; e?, DOM recycling/export; f+, increased denitrification; g–, increased nitrogen fixation; h–, reduced calcification; i+, reduced particle ballast; j+, increased stratification; k?, increased Southern Ocean winds; l+, reduced deep-water formation; m–, reduced upwelling; n–, increased carbonate dissolution; PIC, particulate inorganic carbon; POC, particulate organic carbon; DOC, dissolved organic carbon; NPP, net primary production. Adapted from Sabine et al. (2004b).

a profound impact on the ocean biological and calcium carbonate cycles. A basic schematic of these cycles is shown in **Figure 5**. Changes in one part of the carbon cycle can feed back to affect another part of the carbon cycle (i.e., create a feedback loop) and it is not always clear what the net balance will be. This makes changes in the future role of the ocean in the global carbon cycle very difficult to predict.

Feedback: the process by which a system is modulated, controlled, or changed by the product, output, or response it produces

Part of the problem is that today's global carbon cycle is intimately linked with the structure of the global ecosystems. Carbon is one of the primary currencies exchanged between organisms. As we change the balance of the carbon cycle, it is not clear how these ecosystems might respond. These changes could select against or for particular classes of organisms, causing massive extinctions or population booms. As organisms (including humans) attempt to adapt to these changing conditions, the flows of carbon in and out of the primary reservoirs can be significantly altered,

throwing off the delicate balance observed over the last millennium. Here we present some evidence of feedbacks that are active in the marine carbon system, although we do not pretend to be comprehensive; we will show some of the intriguing and complex feedback systems at work. We refer to mechanisms that enhance the atmospheric CO_2 perturbation as a positive feedback mechanism (shown as plus signs in **Figure 5**), whereas mechanisms that tend to dampen the atmospheric CO_2 perturbation are referred to as negative feedbacks (shown as minus signs in **Figure 5**). The feedback loops discussed below are depicted in purple as a–n in **Figure 5**.

(*a*) There are relatively straightforward and well-understood feedbacks related to the chemistry of the carbonate system. Increased concentration of DIC in seawater and other factors, such as temperature, alkalinity, etc., influence the capacity of the ocean to respond to CO_2 perturbations. One way to consider this is with the Revelle factor:

$$\left(\frac{\delta pCO_2 \Big/ \delta DIC}{pCO_2 \Big/ DIC} \right) \tag{6}$$

Increasing pCO_2 increases the Revelle factor making the ocean less efficient at absorbing more CO_2, i.e., a positive feedback. The Revelle factor for surface waters has already increased by about one unit over the last 250 years (Sabine et al. 2004a).

(*b*) Similarly well understood is the response to increased temperatures; even though the Revelle factor decreases with increasing temperature (everything else constant), the solubility of CO_2 in seawater also decreases with increasing temperature. The latter effect is dominating so that a warmer ocean will lead to reduced CO_2 uptake, i.e., a positive feedback (Goodwin & Lenton 2009).

(*c*) The increased carbon concentration in the photic zone of the ocean has direct effects on biology, with more difficult to quantify feedbacks for the carbon cycle. For instance, experimental evidence indicates a shift in the balance between primary production and heterotrophic consumption of organic matter in warmer water. Enhanced recycling and respiration cause a faster replenishing of the DIC pool in the surface layers and leave less organic carbon for export, thereby potentially weakening the biological pump, i.e., a positive feedback loop induced by warmer surface waters (Wohlers et al. 2009).

(*d*) Similarly, experimental evidence suggests an increased carbon to nitrogen ratio in phytoplankton grown under elevated carbon concentrations (i.e., carbon overconsumption), which would lead to increased export of organic carbon from the mixed surface layer to the deeper part of the ocean (Riebesell et al. 2007), i.e., a negative feedback.

(e) Dissolved organic matter (DOM) tends to have very high carbon to nutrient ratios, particularly for the refractory fraction, and downward transport of DOM is an efficient export mechanism of carbon to the deep ocean (Hopkinson & Vallino 2005). Changes in the DOM cycle or composition can induce potentially significant feedback loops. For instance, increased remineralization depth of labile DOM will provide a negative feedback, whereas decreased near-surface stability of refractory DOM is a positive feedback.

(f) A further feedback loop on the carbon cycle is provided by increased particulate organic carbon (POC) flux to the upper water column associated with carbon overconsumption and lower sinking rates due to reduced calcium carbonate ballast (see below). Taken together, this will likely increase the extent of oceanic oxygen minimum zones (OMZ) (e.g., Hofmann & Schellnhuber 2009, Oeschlies et al. 2008), which implies increased denitrification and hence possible reduced production when this water reaches the surface ocean, creating a positive feedback.

(g) However, it is possible that the nitrate-poor water (relative to phosphate) resulting from the denitrification will stimulate nitrogen fixation in the euphotic zone (Deutsch et al. 2007), i.e., a dampening effect on the positive feedback due to increased OMZs.

pCO_2: the partial pressure of carbon dioxide, which controls the thermodynamic drive for the ocean to exchange carbon with the atmosphere

Denitrification: a process through which nitrate (NO_3^-) is reduced to molecular nitrogen

Nitrogen fixation: a process through which molecular nitrogen is converted to bioavailable nitrate by organisms

Aragonite and calcite: two different forms of calcium carbonate used by marine organisms for shells or skeletal structures

The invasion of anthropogenic CO_2 in the oceans inevitably leads to decreasing pH, lower concentration of carbonate ion, and lowered saturation state for aragonite and calcite, i.e., ocean acidification (e.g., Doney et al. 2008). The largest effects are seen in the upper ocean where most of the anthropogenic CO_2 is stored. High-latitude cold waters are particularly sensitive to decreasing pH since the saturation state of calcite and aragonite tends to be lower than in temperate and tropical waters; i.e., a modest change in the pH might lead to calcite and/or aragonite undersaturation near poles (e.g., Orr et al. 2005). Ocean acidification will likely affect the calcification rate of some organisms. There is experimental evidence that reduced pH leads to decreasing calcification by several, but not all, marine organisms, including cocolitophorides, foraminifers, corals, and pteropods (e.g., Doney et al. 2008, Riebesell et al. 2000). However, it is not clear to what extent calcifying organisms are able to adapt to different carbonate chemistry over many generations (e.g., Langer et al. 2006) or that all calcifying organisms will respond the same way (Iglesias-Rodriguez et al. 2008, Riebesell et al. 2008). Reduced calcification will act on at least two opposing feedback systems for the carbon cycle, (h) and (i).

(h) First, the chemistry of the carbonate system prescribes release of CO_2 during calcification; i.e., less CO_2 will be released under a reduced calcification scenario and act as a negative feedback.

(i) Second, calcium carbonate particles act as ballast for POC sinking from the upper ocean, allowing organic particles to be transported to greater depths before they decompose than they would have without the extra ballast (e.g., Armstrong et al. 2002). It is possible that the particle flux of organic carbon to the deep ocean will be reduced if the calcification rate decreases, creating a positive feedback. It has been shown that even a modest increase in the remineralization depth will reduce atmospheric CO_2 substantially (Kwon et al. 2009).

(j) Changes in climate may act indirectly to affect the uptake of anthropogenic CO_2 via changes in phytoplankton community. For instance, coccolitophores, favored in oligothrophic nutrient-limiting conditions, have a positive feedback effect due to the formation of calcite shells, whereas diatoms that prefer weakly stratified, nutrient-rich environments have a negative feedback since they are responsible for large parts of the biological carbon export. A more stratified ocean in a global warming scenario would tend to reduce the nutrient supply to the photic zone, which in turn would favor the growth of coccolitophores over diatoms; a positive feedback (Cermeno et al. 2008).

(k) Changing climate, with inevitable changes in physical forcing, leads to changes in ocean circulation and properties (salinity and temperature), which will have direct or indirect implications for the carbon cycle. For instance, observations show intensification of Southern Ocean winds during the past decades, and most climate models predict this trend will continue as a response to a warmer world. Further, the Southern Ocean is an important sink for anthropogenic carbon, possibly responsible for ~40% of the total ocean C_{ant} uptake (Sabine et al. 2004a). Le Quere et al. (2007) found, based on atmospheric CO_2 concentrations and an inverse method, that the Southern Ocean sink of C_{ant} has weakened in the last decades compared to expectations from the atmospheric increase of CO_2. However, the study was criticized for the choice of atmospheric CO_2 data and for neglecting important processes regulating the CO_2 air-sea exchange (Law et al. 2008, Zickfeld et al. 2008b). Observational records further indicate that increased wind stress in the Southern Ocean has little effect on the transport in the Antarctic Circumpolar Current and on the meridional overturning circulation since the increased Ekman transport is compensated by an increased eddy flux. Thus, the net effect of increased wind stress on the carbon flux should be quite small (Böning et al. 2008). Non-eddy-resolving ocean models are apparently not able to correctly predict the Southern Ocean response to increased wind forcing and the feedback on the carbon cycle.

(l) Similarly, most climate models predict reduced Meridional Overturning Circulation (MOC) in a future, warmer world. This will choke the transport of surface waters, laden with anthropogenic CO_2, into the deep ocean, a positive feedback.

(m) At the same time, decreased MOC will also reduce upwelling of deep water with high DIC concentration, a negative feedback. The net balance between feedbacks (l) and (m) is still a matter of scientific debate (e.g., Sarmiento & Le Quéré 1996, Zickfeld et al. 2008a). Since the MOC also controls the large-scale supply of nutrients to the surface layer, there are biological ramifications for the carbon cycle in addition to the direct physical transport impacts. Reduced biological export of carbon due to changes in nutrient supplies related to reduced MOC seems to be the dominant impact over circulation changes that leads to a net positive feedback, but with large regional differences (Zickfeld et al. 2008a).

Most of the processes involved in the feedbacks described here are not understood or monitored well enough to determine whether these feedbacks are changing today as a result of climate change and increasing C_{ant} in the ocean. As stated previously, the current scientific paradigm is that anthropogenic CO_2 is entering the ocean as a passive thermodynamic response to rising atmospheric CO_2. The current challenge for the scientific community is to determine whether these feedbacks are occurring and how they will modify the ability of the ocean to store C_{ant} over the next few decades.

LONG-TERM ACCUMULATION OF ANTHROPOGENIC CO_2

By the early 2000s, approximately 330 Pg C had been released to the environment from the burning of fossil fuels (**Figure 5**). There are vast amounts of fossil fuel (>5000 Pg C) remaining in geological formations that can potentially be oxidized to CO_2 by human activities, most of that in the form of coal. In addition to this, there are large deposits (5000–10,000 Pg C) of methane hydrate in permafrost and in deep-sea sediments, the latter location being the dominating source. Although it remains highly uncertain how much of these stores will end up as CO_2 in the atmosphere, we will briefly consider the ocean response to the carbon perturbation on millennial timescales. As seen above, atmospheric CO_2 will equilibrate with the global ocean on centennial timescales and a large fraction of the anthropogenic CO_2 will be stored in the ocean, independently of whether the CO_2 is released to the atmosphere or purposefully placed in the ocean (i.e., ocean sequestration). The ocean has a vast capacity to store CO_2 so it will continue to take up CO_2 as long as it is increasing in the atmosphere. The rate at which this process takes place, and the magnitude of the fraction that dissolves in the ocean, are dependent on the biogeochemical feedback loops and processes discussed in the previous section.

On millennial timescales accumulation of atmospheric CO_2 in the ocean tends to be increased by two additional feedback processes: calcium carbonate ($CaCO_3$) dissolution and silicate ($CaSiO_3$) weathering (e.g., Archer 2005, Archer et al. 1997, Montenegro et al. 2007). As discussed in the previous section, accumulation of CO_2 in the ocean lowers the pH of the ocean and makes the waters more corrosive towards $CaCO_3$ minerals (**Figure 5*n***). Dissolution occurs both in the water column and from sediments, creating a negative feedback to the atmosphere often referred to as $CaCO_3$ compensation (Broecker & Peng 1987). The net effect of $CaCO_3$ dissolution is the restoring of oceanic pH and the increase in the fraction of C_{ant} that can be dissolved in the ocean according to the following equation:

$$H_2O + CO_2 + CaCO_3 \leftrightarrow 2HCO_3^- + Ca^{2+} \tag{7}$$

Further, weathering of silicate-containing igneous rock restores the carbonate system on geological timescales according to the following equation:

$$3H_2O + 2CO_2 + CaSiO_3 \leftrightarrow Ca^{2+} + 2HCO_3^- + Si(OH)_4 \tag{8}$$

This is a slow process; the e-folding timescale for CO_2 relaxation of silicate weathering is on the order 200 to 400 thousand years (e.g., Archer et al. 1997, Sundquist 1991). This process might be more efficient if the hydrological cycle accelerates in a warmer world, but the dynamics of this process is complicated by long timescales invoking glacial/interglacial processes and weathering changes as well as tectonic processes (Archer 2005).

The time until the atmospheric anthropogenic CO_2 burden is reduced to 25% of the total emission is calculated to be 1800 years by Montenegro et al. (2007), but only 300–450 years by Archer (2005) in a different model set-up and experiment type. However, both approaches suggest a long tail in the perturbation, with a mean lifetime of atmospheric anthropogenic CO_2 of 30–35 thousand years found by Archer (2005). Taken together, these two feedback loops tend to restore atmospheric CO_2 levels towards preindustrial levels by increasing the alkalinity and restoring the oceanic buffer capacity. However, on timescales of up to a few millennia, it can be expected that the partitioning between the ocean and atmosphere CO_2 reservoirs will be roughly maintained through restoring of the ocean buffer capacity by $CaCO_3$ dissolution. This leaves a fraction of ~7% of the CO_2 perturbation in the atmosphere for several hundred thousand years for silicate weathering to handle (Archer 2005). However, the magnitude of the ocean C_{ant} fraction is dependent on climate feedbacks such as the amount of ocean heating; warmer water holds less CO_2 than cold water, potentially increasing the airborne fraction up to 15% (Archer 2005). Depending on the future magnitude of the anthropogenic CO_2 emissions, release of anthropogenic CO_2 will result in higher oceanic alkalinity and DIC concentrations, up to roughly 8% increase in oceanic DIC if the majority of available fossil fuel is used.

CONCLUSIONS

The ocean's role as a sink for anthropogenic CO_2 appears to be changing over time and will likely change even more dramatically into the future. Although the uncertainties are fairly large due to necessary assumptions, most approaches agree that the global ocean inventory of C_{ant} was around 120 Pg C in the mid-1990s. This means that nearly half of the CO_2 released into the atmosphere from burning fossil fuels between 1800–1994 ended up in the ocean (Sabine et al. 2004a).

Based on ocean uptake estimates, the global ocean inventory should be increasing by about 2.2 Pg C per year, giving a total inventory of about 135 Pg C in the early 2000s (Gruber et al. 2009). Since 2000, global fossil fuel CO_2 emission has increased at an annual rate of 3.3%, giving a total cumulative emission of approximately 330 PgC by 2006 (Canadell et al. 2007). Thus, the ocean storage of carbon only accounts for ~41% of the total fossil fuel emissisons since the preindustrial. This percentage has droped since the mid 1990s because the rate of ocean carbon uptake does not seem to be keeping pace with the rate of growth in CO_2 emissions (Bindoff et al. 2007). The land use change emissions are highly uncertain, but if they are included as part of the calculation, then the oceans are only absorbing about 25% of the current total anthropogenic emissions (Canadell et al. 2007).

These estimates, however, are strongly dependent on the ocean uptake calculations. Estimates of decadal scale ocean inventory changes consistently show increases in C_{ant} in the water column, but have not been synthesized in a coordinated way to be able to confirm or deny a slowdown in the rate of carbon storage. Unfortunately, the first global estimate of decadal carbon inventory changes will not be available for a few more years, and it will be more than a decade before another survey will be able to make a global evaluation of how the rates of storage are changing based just on ocean interior observations.

Ocean interior observations, however, remain the best mechanism for verifying the changes in ocean C_{ant} inventory. It is extremely difficult to predict how the many possible carbon cycle feedbacks will affect ocean carbon storage; modeling and proxy techniques are limited by our

current understanding of the ocean carbon cycle. It is critically important that we understand how C_{ant} is accumulating in the ocean on timescales relevant to human civilization (years to decades). CO_2 emissions are growing at an ever increasing rate and the momentum of the carbon and climate system is such that decisions made today will still impact the climate for hundreds to thousands of years to come. The best way to improve our understanding is to continue using a broad suite of approaches, with both observations and models, to examine both ocean carbon uptake and ocean carbon storage over a range of timescales.

SUMMARY POINTS

1. With the synthesis of the WOCE/JGOFS data, the first robust global estimates of the total accumulation of Cant were produced. Although the uncertainties are fairly large due to necessary assumptions, most approaches agree that the global ocean inventory of C_{ant} was around 120 Pg C in the mid-1990s.
2. Based on ocean uptake estimates, the global ocean inventory should be increasing by about 2.2 Pg C per year, giving a total inventory of about 135 Pg C in the early 2000s (Gruber et al. 2009). Repeat hydrographic sections are currently being run that will allow an assessment of decadal inventory changes that can be compared to these ocean uptake estimates.
3. Estimates of decadal scale ocean inventory changes consistently show increases in C_{ant} in the water column, but have not been synthesized in a coordinated way to be able to confirm or deny a slowdown in the rate of carbon storage. Ocean interior observations, however, remain the best mechanism for verifying the changes in ocean C_{ant} inventory.
4. It is extremely difficult to predict how the many possible carbon cycle feedbacks will affect ocean carbon storage; modeling and proxy techniques are limited by our current understanding of the ocean carbon cycle.
5. It is critically important that we understand how C_{ant} is accumulating in the ocean on timescales relevant to human civilization (years to decades). CO_2 emissions are growing at an ever increasing rate, and the momentum of the carbon and climate system is such that decisions made today will still impact the climate for hundreds to thousands of years to come.
6. The best way to improve our understanding is to continue using a broad suite of approaches, with both observations and models, to examine both ocean carbon uptake and ocean carbon storage over a range of timescales.

DISCLOSURE STATEMENT

The authors are not aware of any affiliations, memberships, funding, or financial holdings that might be perceived as affecting the objectivity of this review.

ACKNOWLEDGMENTS

T. Tanhua received funding from the EU project CarboOcean (Project 511176-2). The authors acknowledge A. Olsen, J. Pätsch, and R. Sonnerup for providing column inventory change data and suggestions for the text. C. Sabine acknowledges the NOAA's Climate Program Office for support for this work. This is PMEL contribution number 3323.

LITERATURE CITED

Alvaréz M, Lo Monaco C, Tanhua T, Yool A, Oschlies A, et al. 2009. Estimating the storage of anthropogenic carbon in the subtropical Indian Ocean: A comparison of five different approaches. *Biogeosci. Discuss.* 6:729–96

Archer D, Maier-Reimer E. 1994. Effect of deep-sea sedimentary calcite preservation on atmospheric CO_2 concentration. *Nature* 367:260–63

Archer D, Kheshgi H, Maier-Reimer E. 1997. Multiple timescales for neutralization of fossil fuel CO_2. *Geophys. Res. Lett.* 24(4):405–08

Archer D. 2005. Fate of fossil fuel CO_2 in geologic time. *J. Geophys. Res. Oceans.* 110:C09S05

Armstrong RA, Lee C, Hedges JI, Honjo S, Wakeham SG. 2002. A new, mechanistic model for organic carbon fluxes in the ocean based on the quantitative association of POC with ballast minerals. *Deep Sea Res. II* 49:219–36

Bindoff NL, Willebrand J, Artale V, Cazenave A, Gregory JM, et al. 2007. Chapter 5—Observations: Oceanic climate change and sea level. In *Climate Change 2007: The Physical Science Basis. Contribution of Working Group I to the Fourth Assessment Report of the Intergovernmental Panel on Climate Change*, ed. S Solomon, D Qin, M Manning, Z Chen, M Marquis, KB Averyt, et al., pp. 385–428. Cambridge, UK: Cambridge Univ. Press

Böning CW, Dispert A, Visbeck M, Rintoul SR, Schwarzkopf FU. 2008. The response of the Antarctic Circumpolar Current to recent climate change. *Nat. Geosci.* 1:864–69

Brewer PG. 1978. Direct observation of the oceanic CO_2 increase. *Geophys. Res. Lett.* 5:997–1000

Broecker WS. 1974. "NO," a conservative water-mass tracer. *Earth Planet. Sci. Lett.* 23:100–107

Broecker WS, Takahashi T, Simpson HJ, Peng TH. 1979. Fate of fossil fuel carbon dioxide and the global carbon budget. *Science* 206:409–18

Broecker WS, Takahashi T, Peng T-H. 1985. *Reconstruction of Past Atmospheric CO_2 Contents from the Chemistry of the Contemporary Ocean: An Evaluation*, TR020, DOE/OR-857, U.S. Depart. of Energy. 79 pp.

Broecker WS, Peng TH. 1987. The role of $CaCO_3$ compensation in the glacial to interglacial atmospheric CO_2 change. *Glob. Biogeochem. Cycles* 1:15–29

Canadell JG, Le Quere C, Rapauch MR, Field CB, Buitenhuis ET, Ciais P, Conway TJ, Gillett NP, Houghton RA, Marland G. 2007. Contributions to accelerating atmospheric CO_2 growth from economic activity, carbon intensity, and efficiency of natural sinks. *Proc. Nat. Acad. Sci.* 104:18866–70

Cermeno P, Dutkiewicz S, Harris RP, Follows M, Schofield O, Falkowski PG. 2008. The role of nutricline depth in regulating the ocean carbon cycle. *Proc. Nat. Acad. Sci.* 105:20344–49

Chen CTA, Millero FJ. 1979. Gradual increase of oceanic CO_2. *Nature* 277:205–206

Chen C-TA. 1982. On the distribution of anthropogenic CO_2 penetration in the Atlantic and Southern Oceans. *Deep Sea Res.* 29:563–80

Deutsch C, Sarmiento JL, Sigman DM, Gruber N, Dunne JP. 2007. Spatial coupling of nitrogen inputs and losses in the ocean. *Nature* 445:163–7

Dickson AG, Sabine CL, Christian JR, eds. 2007. Guide to best practices for ocean CO_2 measurements. *PICES Spec. Publ.* 3:191

DOE (US Dept. of Energy). 1994. *Handbook of Methods for the Analysis of the Various Parameters of the Carbon Dioxide System in Seawater*, Vers. 2.0, ORNL/CDIAC-74, ed. AG Dickson, C Goyet. Carbon Dioxide Information Analysis Center, Oak Ridge National Laboratory, Oak Ridge, TN

Doney CS, Fabry VJ, Feely RA, Kleypas J. 2008. Ocean acidification: the other CO_2 problem. *Ann. Rev. Mar. Sci.* 1:169–92

Friis K, Körtzinger A, Pätsch J, Wallace DWR. 2005. On the temporal increase of anthropogenic CO_2 in the subpolar North Atlantic. *Deep Sea Res. I* 52:681–98

Gammon RH, Cline J, Wisegarver DP. 1982. Chlorofluoromethanes in the northeast pacific ocean: measured vertical distribution and application as transient tracers of upper ocean mixing. *J. Geophys. Res.* 87:9441–54

Gloor M, Gruber N, Sarmiento J, Sabine CL, Feely RA, Rodenbeck C. 2003. A first estimate of present and preindustrial air-sea CO_2 flux patterns based on ocean interior carbon measurements and models. *Geophys. Res. Lett.* 30(1):1010

Goodwin P, Lenton TM. 2009. Quantifying the feedback between ocean heating and CO_2 solubility as an equivalent carbon emission. *Geophys. Res. Lett.* 36:L15609

Gouretski VV, Jancke K. 2001. Systematic errors as the cause for an apparent deep water property variability: global analysis of the WOCE and historical hydrographic data. *Prog. Oceanogr.* 48:337–402

Goyet C, Adams R, Eischeid G. 1998. Observations of the CO_2 system in the tropical Atlantic Ocean. *Mar. Chem.* 60:49–61

Goyet C, Coatanoan C, Eischeid G, Amaoka T, Okuda K, Healy R, Tsunogai S. 1999. Spatial variation of total alkalinity in the northern Indian Ocean: a novel approach for the quantification of anthropogenic CO_2 in seawater. *J. Mar. Res.* 57:135–63

Goyet C, Brewer PG. 1993. Biochemical properties of the oceanic carbon cycle. In *Modelling Oceanic Climate Interactions. NATO ASI Ser. I*, ed. J Willebrand, DLT Anderson, vol. 11, pp. 271–97. Berlin: Springer

Gruber N, Sarmiento J, Stocker TF. 1996. An improved method for detecting anthropogenic CO_2 in the oceans. *Global Biogeochem. Cycles* 10(4):809–37

Gruber N. 1998. Anthropogenic CO_2 in the Atlantic Ocean. *Glob. Biogeochem. Cycles* 12:165–91

Gruber N, Gloor M, Mikaloff Fletcher SE, Doney CS, Dutkiewicz S, et al. 2009. Ocean sources, sinks, and transport of atmospheric CO_2. *Glob. Biogeochem. Cycles* 23:GB1005

Hall TM, Waugh DW, Haine TWN, Robbins PE, Khaliwala S. 2004. Reduced estimates of anthropogenic carbon in the Indian Ocean due to mixing and time-varying air-sea CO_2 diseqilibrium. *Global Biogeochem. Cycles* 18:GB1031

Hofmann M, Schellnhuber H-J. 2009. Oceanic acidification affects marine carbon pump and triggers extended marine oxygen holes. *Proc. Nat. Acad. Sci.* 106:3017–22

Hopkinson CS, Vallino JJ. 2005. Efficient export of carbon to the deep ocean through dissolved organic matter. *Nature* 433:142–5

Iglesias-Rodriguez MD, Halloran PR, Rickaby REM, Hall IR, Colmenero-Hidalgo E, et al. 2008. Phytoplankton calcification in a high-CO_2 world. *Science* 320:336–40

IPCC. 2001. *Climate Change 2001: The Scientific Basis. Contribution of Working Group I to the Third Assessment Report of the Intergovernmental Panel on Climate Change*, ed. JT Houghton, Y Ding, DJ Griggs, M Noguer, PJ van der Linden, X. Dai, et al. Cambridge, UK: Cambridge Univ. Press. 881 pp.

IPCC. 2007. *Climate Change 2007: The Physical Science Basis. Contribution of Working Group I to the Fourth Assessment Report of the Intergovernmental Panel on Climate Change*, ed. S Soloman, D Qin, D Manning, Z Chen, M Marquis, KB Averyt, et al. Cambridge, UK: Cambridge Univ. Press. 996 pp.

Johnson GC, Robbins PE, Hufford GE. 2001. Systematic adjustments of hydrographic sections for internal consistency. *J. Atmos. Ocean. Technol.* 18:1234–44

Key RM, Kozyr A, Sabine CL, Lee K, Wanninkhof R, Bullister JL, et al. 2004. A global ocean carbon climatology: Results from global data analysis project (GLODAP). *Global Biogeochem. Cycles* 18:GB4031

Kwon EY, Primeau F, Sarmiento JL. 2009. The impact of remineralization depth on the air-sea carbon balance. *Nature Geosci.* 2:630–35.

Langer G, Geisen M, Baumann KH, Klas J, Riebesell U, et al. 2006. Species-specific responses of calcifying algae to changing seawater carbonate chemistry. *Geochem. Geophys. Geosys.* 7:Q09006

Law RM, Matear RJ, Francey RJ. 2008. Saturation of the Southern Ocean CO_2 sink due to recent climate change. *Science* 319:570a

Lee K, Choi S-D, Park G-H, Wanninkhof R, Peng TH, et al. 2003. An updated anthropogenic CO_2 inventory in the Atlantic Ocean. *Glob. Biogeochem. Cycles* 17:1116

Le Quere C, Rodenbeck C, Buitenhuis ET, Conway TJ, Langenfelds R, et al. 2007. Saturation of the Southern Ocean CO_2 sink due to recent climate change. *Science* 316:1735–38

Lo Monaco C, Metzl N, Poisson A, Brunet C, Schauer B. 2005a. Anthropogenic CO_2 in the Southern Ocean: Distribution and inventory at the Indian-Atlantic boundary (World Ocean Circulation Experiment line I6). *J. Geophys. Res.* 110:C06010

Lo Monaco C, Goyet C, Metzl N, Poisson A, Touratier F. 2005b. Distribution and inventory of anthropogenic CO_2 in the Southern Ocean: Comparison of three data-based methods. *J. Geophys. Res.* 110:C09S02

Mikaloff -Fletcher SE, Gruber N, Jacobson AR, Doney SC, Dutkiewicz S, et al. 2006. Inverse estimates of anthropogenic CO_2 uptake, transport, and storage by the ocean. *Glob. Biogeochem. Cycles* 20:GB2002

Matsumoto K, Sarmiento JL, Key RM, Bullister JL, Caldeira K, et al. 2004. Evaluation of ocean carbon cycle models with data-based metrics. *Geophys. Res. Lett.* 31:L07303, doi:10.1029/2003GL018970

Matsumoto K, Gruber N. 2005. How accurate is the estimation of anthropogenic carbon in the ocean? An evaluation of the ΔC^* method. *Global Biogeochem. Cycles* 19:GB3014

Matear RJ, McNeil BI. 2003. Decadal accumulation of anthropogenic CO_2 in the Southern Ocean: A comparison of CFC-age derived estimates to multiple-linear regression estimates. *Global Biogeochem. Cycles* 17:24

Montenegro A, Brovkin V, Eby M, Archer D, Weaver AJ. 2007. Long-term fate of anthropogenic carbon. *Geophys. Res. Lett.* 34:L19707

Murata A, Kumamoto Y, Watanabe S, Fukasawa M. 2007. Decadal increases of anthropogenic CO_2 in the South Pacific subtropical ocean along 32°S. *J. Geophys. Res. Oceans* 112:C05033

Murata A, Kumamoto Y, Sasaki K, Watanabe S, Fukasawa M. 2008. Decadal increases of anthropogenic CO_2 in the subtropical South Atlantic Ocean along 30°S. *J. Geophys. Res. Oceans* 113:C06007

Murata A, Kumamoto Y, Sasaki K, Watanabe S, Fukasawa M. 2009. Decadal increases of anthropogenic CO_2 along 149°E in the western North Pacific. *J. Geophys. Res.* 114:C04018, doi:10.1029/2008JC004920

Oeschlies A, Schulz KG, Riebesell U, Schmittner A. 2008. Simulated 21st century's increase in oxygen suboxia by CO_2-enhanced biotic carbon export. *Glob. Biogeochem. Cycle* 22:GB4008

Olsen A, Omar AM, Bellerby RGJ, Johannessen T, Ninnemann U, et al. 2006. Magnitude and origin of the anthropogenic CO_2 increase and C-13 Suess effect in the Nordic seas since 1981. *Global Biogeochem. Cycles* 20:GB3027

Orr JC, Fabry VJ, Aumont O, Bopp L, Doney SC, et al. 2005. Anthropogenic ocean acidification over the twenty-first century and its impact on calcifying organisms. *Nature* 437:681–86

Orr JC, Maier-Reimer E, Mikolajewicz U, Monfray P, Sarmiento JL, et al. 2001. Estimates of anthropogenic carbon uptake from four three-dimensional global ocean models. *Glob. Biogeochem. Cycles* 15:43–60

Papaud A, Poisson A. 1986. Distribution of dissolved CO_2 in the Red Sea and correlation with other geochemical tracers. *J. Mar. Res.* 44:385–402

Peng T-H, Wanninkhof R, Bullister JL, Feely RA, Takahashi T. 1998. Quantification of decadal anthropogenic CO_2 uptake in the ocean based on dissolved inorganic carbon measurements. *Nature* 396:560–63

Peng T-H, Wanninkhof R, Feely RA. 2003. Increase of anthropogenic CO_2 in the Pacific Ocean over the last two decades. *Deep Sea Res. II* 50:3065–82

Perez FF, Vázquez-Rodríguez M, Louarn E, Padín XA, Mercier H, Ríos AF. 2008. Temporal variability of the anthropogenic CO_2 storage in the Irminger Sea. *Biogeosciences* 5:1669–79

Poisson A, Chen C-TA. 1987. Why is there little anthropogenic CO_2 in the Antarctic Bottom Water? *Deep Sea Res.* 34:1255–75

Riebesell U, Bellerby RGJ, Engel A, Fabry VJ, Hutchins DA, et al. 2008. Comment on "Phytoplankton Calcification in a High-CO_2 World." *Science* 322:1466b

Riebesell U, Schulz KG, Bellerby RGJ, Botros M, Fritsche P, et al. 2007. Enhanced biological carbon consumption in a high CO_2 ocean. *Nature* 450:545–49

Riebesell U, Zondervan I, Rost B, Tortell PD, Zeebe RE, Morel FMM. 2000. Reduced calcification of marine plankton in response to increased atmospheric CO_2. *Nature* 407:364–67

Sabine CL, Key RM, Johnson KM, Millero FJ, Poisson A, et al. 1999. Anthropogenic CO_2 inventory of the Indian Ocean. *Global Biogeochem. Cycles* 13:179–98

Sabine CL, Feely RA. 2001. Comparison of recent Indian Ocean anthropogenic CO_2 estimates with a historical approach. *Global Biogeochem. Cycles* 15:31–42

Sabine CL, Feely RA, Key RM, Bullister JL, Millero FJ, et al. 2002. Distribution of anthropogenic CO_2 in the Pacific Ocean. *Global Biogeochem. Cycles* 16:1083

Sabine CL, Feely RA, Gruber N, Key RM, Lee K, et al. 2004a. The Oceanic sink for Anthropogenic CO_2. *Science* 305:367–71

Sabine CL, Heimann M, Artaxo P, Bakker D, Chen C-TA, et al. 2004b. Current status and past trends of the global carbon cycle. In *The Global Carbon Cycle: Integrating Humans, Climate, and the Natural World, Scope 62*, ed. CB Field, MR Raupach, ch. 2, pp. 17–44b. Washington, DC: Island Press

Sabine CL, Key RM, Kozyr A, Feely RA, Wanninkhof R, et al. 2005. *Global Ocean Data Analysis Project (GLODAP): Results and data*, ORNL/CDIAC-145, NDP-083, Carbon Dioxide Information Analysis Center, Oak Ridge National Laboratory, U.S. Dept. of Energy, Oak Ridge, TN. 110 pp., 6 apps.

Sabine CL, Feely RA, Millero F, Dickson AG, Langdon C, et al. 2008. Decadal changes in Pacific Carbon. *J. Geophys. Res. Oceans* 113:C07021

Sarmiento JL, Orr JC, Siegenthaler U. 1992. A perturbation simulation of CO_2 uptake in an ocean general circulation model. *J. Geophys. Res.* 97:3621–45

Sarmiento JL, LeQuere C. 1996. Oceanic carbon dioxide uptake in a model of century-scale global warming. *Science* 274:1346–50

Shiller AM. 1981. Calculating the oceanic CO_2 increase: A need for caution. *J. Geophys. Res.* 86:11083–11088

Steinfeldt R, Rhein M, Bullister J, Tanhua T. 2009. Inventory changes in anthropogenic carbon from 1997–2003 in the Atlantic Ocean between 20°S and 65°N. *Glob. Biogeochem. Cycle* 23:GB3010, doi:10.1029/2008GB003311

Stuiver M, Quay PD, Ostlund HG. 1983. Abyssal water carbon-14 distribution and the age of the world oceans. *Science* 219:849–851

Sundquist ET. 1991. Steady-state and non-steady-state carbonate silicate controls on atmospheric CO_2. *Quaternary Sci. Rev.* 10:283–96

Takahashi T, Sutherland SC, Wanninkhof R, Sweeney C, Feely RA, et al. 2009. Climatological mean and decadal change in surface ocean pCO_2, and net sea-air CO_2 flux over the global oceans. *Deep-Sea Res. II* 56:554–77

Tanhua T, Biastoch A, Körtzinger A, Lüger H, Böning C, Wallace DWR. 2006. Changes of anthropogenic CO_2 and CFCs in the North Atlantic between 1981 and 2004. *Glob. Biogeochem. Cycles* 20:GB4017

Tanhua T, Körtzinger A, Friis K, Waugh DW, Wallace DWR. 2007. An estimate of anthropogenic CO_2 inventory from decadal changes in ocean carbon content. *Proc. Natl. Acad. Sci.* 104:3037–42

Tanhua T, Wallace DWR. 2005. Consistency of TTO-NAS Inorganic Carbon Data with modern measurements. *Geophys. Res. Let.* 32:L14618

Tanhua T, Jones EP, Jeansson E, Jutterström S, Smethie WM Jr, et al. 2009. Ventilation of the Arctic Ocean: Mean ages and inventories of anthropogenic CO_2 and CFC-11. *J. Geophys. Res. Oceans* 114:C01002

Tomczak M, Large DGB. 1989. Optimum multiparameter analysis of mixing in the thermocline of the Eastern Indian Ocean. *J. Geophys. Res.* 94:16141–49

Touratier F, Goyet C. 2004. Definition, properties, and Atlantic ocean distribution of the new tracer TrOCA. *J. Mar. Syst.* 46:169–79

Touratier F, Azouzi L, Goyet C. 2007. CFC-11, 14C and 3H tracers as a means to assess anthropogenic CO_2 concentrations in the ocean. *Tellus. B* 59:318–25

Tsunogai S, Ono T, Watanabe S. 1993. Increase in total carbonate in the western north pacific water and a hypothesis on the missing sink of anthropogenic carbon. *J. Oceanog.* 49:305–15

Vázquez-Rodríguez M, F. Touratier C, Lo Monaco DW, Waugh XA, Padin R, et al. 2009. Anthropogenic carbon distributions in the Atlantic Ocean: data-based estimates from the Arctic to the Antarctic. *Biogeosciences* 6:439–51

Wallace DWR. 1995. *Monitoring Global Ocean Carbon Inventories*. Texas A & M University, College Station, TX. 54 pp.

Wallace DWR. 2001. Storage and transport of excess CO_2 in the oceans: The JGOFS/WOCE Global CO_2 Survey. In *Ocean Circulation and Climate: Observing and Modelling the Global Ocean*, ed. G Siedler, J Church, J Gould, pp. 489–521. San Diego, CA: Academic Press

Wanninkhof R, Doney SC, Peng TH, Bullister JL, Lee K, Feely RA. 1999. Comparison of methods to determine the anthropogenic CO_2 invasion into the Atlantic Ocean. *Tellus B* 51:511–30

Wanninkhof R, Asher WE, Ho DT, Sweeney CS, McGillis WR. 2009. Advances in quantifying air-sea gas exchange and environmental forcing. *Ann. Rev. Mar. Sci.* 1:213–44

Watanabe YW, Ono T, Shimamoto A. 2000. Increase in the uptake rate of oceanic anthropogenic carbon in the North Pacific determined by CFC ages. *Marine Chemistry* 72:297–315

Waugh DW, Haine TWN, Hall TM. 2004. Transport times and anthropogenic carbon in the subpolar North Atlantic Ocean. *Deep Sea Res. I* 51(11):1475–91

Waugh DW, Hall TM, McNeil BI, Key RM, Matear R. 2006. Anthropogenic CO_2 in the oceans estimated using transit-time distributions. *Tellus B* 58:376–90

Wohlers J, Engel A, Zöllner E, Breithaupt P, Jürgens K, et al. 2009. Changes in biogenic carbon flow in response to sea surface warming. *Proc. Natl. Acad. Sci.* 106:7067–72

Yool A, Oschlies A, Nurser AJG. 2009. A model-based assessment of the TrOCA approach for estimating oceanic anthropogenic carbon. *Biogeosci. Discuss.* 6:7231–93

Zickfeld K, Eby M, Weaver AJ. 2008a. Carbon-cycle feedbacks of changes in the Atlantic meridional overturning circulation under future atmospheric CO_2. *Glob. Biogeochem. Cycles* 22:GB3024

Zickfeld K, Fyfe JC, Eby M, Weaver AJ. 2008b. Saturation of the southern ocean CO_2 sink due to recent climate change. *Science* 319:570

Chapter 2: Current Status and Past Trends of the Global Carbon Cycle

Christopher L. Sabine[1], Martin Heiman[2], Paulo Artaxo[3], Dorothee Bakker[4], Chen-Tung Arthur Chen[5], Christopher B. Field[6], Nicolas Gruber[7], Corinne Le Quéré[2], Ronald G. Prinn[8], Jefferey E. Richey[9], Patricia Romero Lankao[10], Jayant Sathaye[11], Riccardo Valentini[12]

Abstract

Processes relevant to the carbon cycle span the range of scales from molecular to global. They also include a wide range of biological, chemical and physical phenomena, as well as interactions between humans and the environment. To better comprehend and predict potential global carbon cycle changes in the future, we must first appreciate how the system is operating today. Our understanding of the current carbon cycle is improving very rapidly thanks to aggressive research in this field. This chapter examines our current understanding of the global carbon cycle and the processes relevant to controlling atmospheric CO_2 concentrations.

We discuss some recent revisions to the IPCC Third Assessment Report's global carbon budget. For example, oceanic CO_2 sink estimates have been revised from 1.9 to 1.8 Pg C y^{-1} for the 1980s and from 1.7 to 1.9 Pg C y^{-1} for the 1990s. Recent estimates of land use emissions have suggested greater uncertainty in the IPCC values. Updated estimates using traditional approaches have suggested that the land use flux in the 1980s and 90s was higher (2.0 and 2.2 Pg C y^{-1}) than originally suggested by the IPCC budget. However, land use changes determined

[1] NOAA/PMEL, Seattle WA, USA
[2] Max-Planck-Institut für Biogeochemie, Jena, Germany
[3] Universidade de Sao Paulo, Sao Paulo, Brazil
[4] University of East Anglia, Norwich, UK
[5] National Sun Yat-sen University, Kaohsiung, Taiwan
[6] Carnegie Institution of Washington, Stanford CA, USA
[7] University of California-Los Angeles, Los Angeles CA, USA
[8] Massachusetts Institute of Technology, Cambridge MA, USA
[9] University of Washington, Seattle WA, USA
[10] Universidad Autonoma Metropolitana, Mexico City, Mexico
[11] Lawrence Berkeley National Laboratory, Berkeley CA, USA

from remote sensing data suggest lower emissions (0.6 and 1.0 Pg C y^{-1}). A somewhat more detailed budget developed in this chapter uses a land use flux of 1.2 Pg C y^{-1}. The land, ocean, and energy use fluxes are subdivided into components and discussed in this chapter. We discuss the key connections between the reservoirs, including the role of rivers, coastal margins, trade, and non-CO_2 gases in the global carbon cycle. Those processes relevant to controlling atmospheric CO_2 concentrations that may be susceptible to future changes are also discussed.

[12] Disafri- University of Tuscia, Viterbo, Italy

Introduction

In a global, long-term perspective, variations of the atmospheric CO_2 content document the magnitude and speed of climate driven variations, such as the glacial – interglacial cycles (~100 ppm over 420,000 years), but these observations also document a remarkable stability, with variations in atmospheric CO_2 of <20 ppm during at least the last 11,000 years prior to the anthropogenic perturbation (Joos and Prentice 2003). In this longer-term context, the anthropogenic increase of ~100 ppm during the last 200 years is a dramatic alteration of the global carbon cycle. This atmospheric increase is also a graphic documentation of profound changes in human activity. The atmospheric record documents the earth system's response to fossil fuel releases that increased by more than 1200% between 1900 and 1999 (Nakicenovic 2003).

In order to understand and predict future changes in the global carbon cycle, we must first understand how the system is operating today. In many cases, the current fluxes of carbon are a direct result of past processes affecting these fluxes (Nabuurs 2003). Thus, it is important to understand the current carbon cycle in the context of how the system has evolved over time. The Third Assessment Report of the IPCC recently compiled a global carbon budget (Prentice et al. 2001). While that budget reflected the state-of-the-art at that time, this chapter presents a revised budget based on new information from model studies and oceanographic observations. The IPCC-TAR budget focused on the overall carbon balance between the major active reservoirs of land, atmosphere, and ocean. We present in this chapter a somewhat more comprehensive representation of the connections between the reservoirs, together with our current understanding of the biogeochemical processes and human driving forces controlling these exchanges. The key processes relevant to controlling atmospheric concentrations of CO_2 and relevant non-CO_2 gases

(e.g. CH_4, N_2O) that may be susceptible to changes in the future, either through deliberate management or as direct and indirect consequences of global change, are also introduced here.

The Global Carbon Budget

Over the past 200 years, humans have introduced ~ 400 Pg C to the atmosphere through deforestation and the burning of fossil fuels. Part of this carbon was absorbed by the oceans and terrestrial biosphere. Table 1, section 1 shows the global budget recently compiled by the IPCC Third Assessment Report (Prentice et al. 2001). The global carbon budget quantifies the relative importance of these two reservoirs today and the budget uncertainty reflects our understanding of the exchanges between these reservoirs. The IPCC assessment uses the partitioning of the uptake into net terrestrial and oceanic components based primarily on observations of the concurrent global trends of atmospheric CO_2 and oxygen. Since the compilation of the IPCC report, new evidence from model studies and oceanographic observations indicates that this budget should be slightly revised to account for a previously ignored oceanic oxygen flux. This flux is the result of enhanced oceanic mixing, as inferred from observed changes in oceanic heat content (Le Quéré et al. 2003). The revised values are presented in section 2 of Table 1.

The breakdown of the net land-atmosphere flux through the 1990s into emissions from changes in land use and a residual terrestrial sink, based on the updated land use change emissions of Houghton (2003), is given in section 3 of Table 1. This breakdown has recently been challenged based on new estimates of land use change determined from remote sensing data (Table 1, sections 4 & 5). These new estimates lie at the lower end of the uncertainty range of the estimates based on data reported by individual countries (Houghton 2003). If correct, they imply a residual terrestrial sink in the 1990s that is about 40% smaller than previous estimates.

This budget, of course, does not attempt to represent the richness of the global carbon cycle. The land-atmosphere-ocean system is connected by a multitude of exchange fluxes. The dynamical behavior of this system is determined by the relative sizes of the different reservoirs and fluxes, together with the biogeochemical processes and human driving forces controlling these exchanges. Figure 1 shows the globally aggregated layout of the carbon cycle, together with the pools and exchange fluxes that are relevant on time scales of up to a few millennia. Panel "a" in figure 1 presents a basic picture of the global carbon cycle, including the preindustrial (black) and anthropogenic (red) ocean-atmosphere and land-atmosphere exchange fluxes. The anthropogenic fluxes are average values for the 1980s and 1990s. Panel "a" also shows components of the long-term geological cycle and the composite estimates of CO_2 emissions from geological reservoirs (i.e. fossil fuels and the production of lime for cement). Panels "b" and "c" provide more detailed pictures of the ocean and terrestrial fluxes, respectively. Individual component pools and fluxes, including key climatic and anthropogenic drivers, are discussed below and in subsequent chapters.

Although figure 1 focuses primarily on fluxes directly related to CO_2, a number of non-CO_2 trace gases also play significant roles in the global carbon cycle (e.g. CO, CH_4, non-methane hydrocarbons) and/or climate forcing (e.g. CH_4, N_2O, chlorofluorocarbons). The global cycles of these trace gases, which share many of the processes driving the CO_2 cycle, are briefly discussed below.

Reservoir Connections

The background chapters in this volume discuss the various carbon reservoirs and the processes relevant to controlling atmospheric CO_2 and related trace gas concentrations. To

appreciate the Earth's carbon cycle and its evolution, it is necessary to examine the connections among the various carbon pools. This must be done within a framework that provides an integrated perspective across both disciplinary and geographic boundaries, with particular emphasis on the carbon cycle as an integral part of the human-environment system.

Fossil Fuel-Atmosphere Connections

The world energy system delivered approximately 380 EJ (10^{18} J) of primary energy in 2002 (BP Statistical review of World Energy 2003). Of this, 81% was derived from fossil fuels, with the remainder from nuclear, hydroelectric, biomass, wind, solar, and geothermal energy sources (Figure 2). The fossil fuel component released 5.2 Pg C in 1980 and 6.3 Pg C in 2002 (CDIAC, 2003). Cement production is the other major industrial release, which increased to 0.22 Pg C in 1999. The combined release of 5.9 Pg C shown in figure 1a represents an average emission for the 1980s and 90s. Underground coal fires, which are poorly known and only partly industrial, may be an additional as yet unaccounted for source of carbon to the atmosphere as large as cement manufacturing (Zhang et al. 1998). In terms of energy released, the current mix of fossil fuels is approximately 44% oil, 28% coal, and 27% natural gas (figure 2). At current rates of consumption, conventional reserves of coal, oil, and gas (those that can be economically produced with current technology; see figure 1c) are sufficient to last 216, 40, and 62 years, respectively (BP Statistical review of World Energy 2003). If estimates of undiscovered oil and gas fields are included with the conventional reserves, oil and gas lifetimes increase to 101 and 142 years, respectively (Ahlbrandt et al. 2000).

Conventional reserves represent only a fraction of the total fossil carbon in the earth's crust. A much larger quantity of fossil reserves is in tar and heavy oil that cannot be

economically produced with existing technology but is likely to become accessible in the future. The best estimates for total fossil resources that might ultimately be recovered are in the range of 6000 Pg (Nakicenovic 2003; figure 1) or about 5 times the conventional reserves. In addition, vast quantities of methane, exceeding all known fossil fuel reserves, exist in the form of methane hydrates under continental shelf sediments around the world, in the Arctic permafrost, and in various marginal seas. With current technology, however, these reserves do not appear viable as a future energy source.

Although not included in Table 1 or figure 1, combustion of fossil fuels also releases a number of non-CO_2 carbon gases. In particular, carbon monoxide (CO) can be used as an effective tracer of fossil fuel combustion in atmospheric gas measurements. The relative impact of these gases is discussed in a later section.

Land-Atmosphere Connections

The exchange of carbon between the terrestrial biosphere and the atmosphere is a key driver of the current carbon cycle. Global net primary production (NPP) by land plants is about 57 Pg C y^{-1} (figure 1). Of this, about 4 Pg C y^{-1} is in crops. Humans co-opt a much larger fraction of terrestrial NPP, probably about 40%, where co-opting is defined as consuming, removing some products from, or altering natural states of the terrestrial biosphere through ecosystem changes (Vitousek et al. 1986). Total NPP is approximately 40% of gross primary production (GPP), with the remainder returned to the atmosphere through plant respiration. For many purposes, NPP is the most useful summary of terrestrial plant activity. NPP can be assessed with inventories and harvest techniques, and it represents the organic matter passed to

other trophic levels (Lindemann 1941). For other purposes, including isotope studies and scaling from eddy flux, GPP is a more useful index.

Most of the annual flux in NPP is returned to the atmosphere through the respiration of heterotrophs, including micro-organisms, saprophytes, and animals. A smaller fraction, 5-10%, is released to the atmosphere through combustion (Figure 1). Approximately 5% of NPP leaves land ecosystems in organic form, as CH_4 or volatile organic carbon (Prinn 2003). In recent decades, the land was close to carbon neutral (in the 1980s) or was a net sink (in the 1990s) for atmospheric CO_2 (Table 1). This net flux represents a balance between substantial emissions from biomass clearing or fires and enhanced uptake as a physiological response to rising CO_2 or the re-growth of previously cleared areas.

Land plants contain slightly less carbon than the atmosphere; soils contain substantially more (Figure 1). The estimates for soil carbon in figure 1 are higher than shown in previous budgets for two reasons. First, previous budgets estimated soil carbon to a depth of 1 m. Jobaggy and Jackson (2000) extended these to 3 m, adding about 55% to the known stock. Second, previous budgets have ignored carbon in wetland and permanently frozen soils. The exact magnitudes of these stocks are very uncertain. However, the potential for substantial carbon losses from these stocks in coming decades is a strong incentive for careful quantification and further analysis.

Tropical forests contain the largest carbon pool of terrestrial biota (see table 2), and also the largest NPP (Saugier et al. 2001). Averaged over several years, tropical forests traditionally have been believed to be close to carbon neutral, with uptake from NPP balanced by releases from decomposition and fire. The difference between NPP and the sum of all of the processes that release carbon from the land is net ecosystem production (NEP). Recent studies based on in

situ flux measurements and forest inventory techniques indicate net carbon uptake or positive NEP of 100 to 700 gC m^{-2} y^{-1}, corresponding to ~1 Pg C y^{-1} across the tropical evergreen forest biome. The duration and spatial scale of these studies is not yet extensive enough for solid extrapolation. Still, the estimated uptake is in the proper range to compensate for emissions from tropical land use (DeFries et al. 2002; Achard et al. 2002, Foley and Ramankutty 2003). The tropical NEP estimates, however, are also in the range of recent estimates of CO_2 releases from tropical rivers, caused mainly by the decomposition of material transported from the land (Richey 2003). A full carbon accounting has yet to be accomplished, but these individual flux estimates need to be reconciled with top-down estimates from atmospheric inverse modeling studies, which indicate that the overall net carbon balance of the tropical land areas (30°S-30°N) must be close to zero, albeit with large uncertainty ranges (Gurney et al. 2002, Heimann et al. 2003).

Temperate forests cover about 60% of the area of tropical forests and contain the second largest pool of plant carbon. Together, tropical and boreal forests account for approximately 75% of the world's plant carbon and for, 40% of the non-wetland, non-frozen soil carbon (Table 2).

Carbon emissions from land use and land management have increased dramatically over the last two centuries resulting from the expansion of crop land and pasture, infrastructure extension and other effects driven by market growth, pro-deforestation policies, and demographic pressures (Geist et. al. 2001). Prior to about 1950, carbon emissions from land use change were mainly from temperate regions. In recent decades, however, carbon releases from land use change have been concentrated in the topics (Achard et al. 2002; DeFries et al. 2002; Houghton 2003). Cumulative emissions from land use, estimated at approximately 185 Pg C, entail substantial fluxes from every continent except Antarctica (DeFries et al. 1999). Prior to

about 1970, cumulative emissions from land use and land management were larger than cumulative emissions from fossil fuel combustion.

As with fossil fuel combustion, carbon is lost from terrestrial vegetation in a variety of non-CO_2 gases including biogenic VOCs (volatile organic compounds). Globally VOC emissions are 0.2 to 1.4 Pg C y^{-1} (Prinn 2003). For grassland and cultivated land, large emissions of other greenhouse gases such as N_2O, CH_4 and other gases can also occur. These emissions are strongly affected by land management and land use change (Smith 2003; Robertson 2003).

Ocean-Atmosphere Connections

The oceans contain about 50 times more CO_2 than the atmosphere and 10 times more than the latest estimates of the plant and soil carbon stores (figure 1). CO_2 moves between the atmosphere and the ocean by molecular diffusion, when there is a difference between the CO_2 gas pressure (pCO_2) in the oceans and the atmosphere. For example, when the atmospheric pCO_2 is higher than the surface ocean pCO_2, CO_2 diffuses across the air-sea boundary into the seawater. Based on about 940,000 measurements of surface water pCO_2 obtained since the 1960's, the climatological, monthly distribution of pCO_2 in the global surface waters has been calculated with a spatial resolution of 4^o x 5^o (Takahashi et al. 2002). Although the published value for the net air-sea flux indicates a net ocean uptake of 2.1 Pg C for the reference year 1995, this estimate was based on inappropriate wind speed estimates (T. Takahashi, personal communication). The winds used for these estimates correspond to approximately 40m above mean sea level, but the gas exchange coefficient formulas are typically related to winds at 10m above sea level. The near-surface gradient in wind speed is such that the 10m winds are about 1 m s^{-1} slower than the 40m winds. Thus, Takahashi's corrected net global ocean uptake is 1.5 (-

19% to +22%) Pg C for the reference year 1995 (Figure 3). The asymmetrical error estimates reflect the paucity of data on the spatial and temporal variability in sea surface pCO_2 concentrations, plus limitations in the non-linear wind speed parameterizations for the gas exchange coefficient. Ocean models and observations suggest that the interannual variability in the global ocean CO_2 flux is around ±0.5 Pg C y^{-1} (Greenblatt and Sarmiento 2003).

The gross exchanges of CO_2 across the air-sea interface, as shown in figure 1, are much larger than the net flux. The global budget presented in this figure shows the preindustrial oceans as a net source of ~0.6 Pg C y^{-1} to the atmosphere partially offsetting the addition of carbon to the oceans from rivers. The total net modern flux of Takahashi et al. (2002), after the wind speed correction discussed previously (ocean uptake = 1.5 Pg C y^{-1}), is consistent with the modern balance implied by figure 1 (21.9-20 +70-70.6 = 1.3 Pg C y^{-1}), despite the fact that the coastal zones are not well represented in the Takahashi et al. analysis. The coastal zone fluxes represent the largest unknown in the CO_2 balance of the oceans and are a topic of active research (Chen 2003).

During the past decade, significant advances have been made in separating the anthropogenic component from the large background of ocean dissolved inorganic carbon (DIC). Data-based approaches estimate a global inventory of anthropogenic CO_2 in the oceans to be ~112±17 Pg C for a nominal year,1994 (Figure 4) (Lee et al. 2003). Inventories are generally high in the mid-latitudes and lowest in the high latitude Southern Ocean and near the Equator.

The high inventory regions are convergence zones, where waters with relatively high anthropogenic concentrations are moving into the ocean's interior. Roughly 25% of the total inventory of anthropogenic carbon is in the North Atlantic, one of the main regions of deep water formation. The low inventory waters are generally regions of upwelling, where waters with low

anthropogenic concentrations are brought near the surface. The high latitude Southern Ocean generally has very low anthropogenic CO_2 inventories and very shallow penetration. The southern hemisphere mode and intermediate waters at around 40-50°S, on the other hand, contain some of the largest inventories of anthropogenic CO_2. Over 56% of the total anthropogenic CO_2 inventory is stored in the Southern Hemisphere.

Over the long term (millennial time-scales), the ocean has the potential to take up approximately 85% of the anthropogenic CO_2 that is released to the atmosphere. The reason for the long time constant is the relatively slow ventilation of the deep ocean. Most of the deep and intermediate waters have yet to be exposed to anthropogenic CO_2. As long as atmospheric CO_2 concentrations continue to rise, the oceans will continue to take up CO_2. However, this reaction is reversible. If atmospheric CO_2 were to decrease in the future, the recently ventilated waters would start releasing part of the accumulated anthropogenic CO_2 back to the atmosphere, until a new equilibrium is reached.

Land-River-Ocean Connections

Carbon is transported from the land to the oceans via rivers and groundwater. The transfer of organic matter from the land to the oceans via fluvial systems is a key link in the global carbon cycle. Rivers also provide a key link in the geological-scale carbon cycle by moving weathering products to the ocean (figure 1). The conventional perspective is that rivers are simply a conduit for transporting carbon to the ocean. Re-evaluation of this model suggests that the overall transfer of terrestrial organic matter through fluvial systems may be more complex (Richey 2003). A robust evaluation of the role of rivers, however, is complicated by both the diverse dynamics and multiple time constants involved, and the fact that data are scarce, particularly in many of the most impacted systems.

Humans have had a significant impact on the concentrations of carbon and nutrients in river systems. Intensifying agriculture has led to extensive erosion, mobilizing perhaps 10-100 times more sediment, and its associated organic carbon, than undisturbed systems. Sewage, fertilizers, and organic waste from domestic animals also contribute to the carbon and nutrient loads of rivers. Not all of these materials make it to the ocean. Much can be deposited near and along river channels. The retention of particulate material in aquatic systems has increased since preindustrial times because of the proliferation of dams (primarily in the 30-50°N regions), which has increased the average residence time of waters in rivers. If the carbon mobilized via erosion were subsequently replaced by newly-fixed carbon in agriculture, then a sink on the order of 0.5-1.0 Pg C y^{-1} would be created. But organic carbon doesn't move passively through river systems; even very old and presumably recalcitrant soil carbon may be at least partially remineralized in aquatic systems. Remineralization of organic carbon during transport leads to elevated levels of dissolved CO_2 in rivers, lakes, and estuaries worldwide. These high concentrations subsequently lead to out-gassing to the atmosphere on the order of ~1 Pg C y^{-1}, with the majority in the humid tropics (Richey 2003).

Despite the increased particulate retention in rivers, a significant amount of carbon escapes to the ocean. DIC, PIC, DOC, and POC exported from rivers to the coastal ocean are 0.4, 0.2, 0.3, and 0.2 Pg C y^{-1}, respectively (Chen 2003). This includes a pronounced, but difficult to quantify, anthropogenic component. These values are poorly constrained by direct measurements and may represent minimum estimates of inputs to the coastal ocean (Richey 2003). Groundwater discharges, comprising about 10% of the surface flow to the ocean, also contribute poorly known contributions of carbon and nutrients to the coastal oceans.

The final step in the land-to-ocean pathway is the marine fate of fluvial carbon. Previous estimates have suggested that the marginal seas are net heterotrophic. Chen (2003) has suggested that continental shelves are in fact net autotrophic, mostly because of production from coastal upwelling of nutrient rich waters. If this is correct, biological production in the coastal zone may decrease the thermodynamic drive to out-gas the terrestrial carbon delivered by rivers, resulting in greater preservation in the marine environment.

Trade/Commerce Connections

The lateral fluxes of carbon are poorly constrained by measurements and are frequently excluded from models. The river fluxes outlined in the previous section are only beginning to be quantified. The lateral transport of carbon through trade has not been constrained or quantified in global carbon budgets based on inventories of terrestrial carbon stocks and fluxes. Approximately one-third of the 4 Pg C fixed annually through agriculture represents harvested products that are directed toward some form of human or domestic animal consumption (Tschirley and Servin2003). In 2001, $547 million in agriculture and forest-related products entered into international trade, amounting to 9% of total trade (excluding services). Imports and exports of cereals, wood and paper products accounted for about 0.72 Pg C of "embodied" carbon traded in 2000.

As we move from the basic carbon budget presented in Table 1 to a more detailed review of the fluxes shown in figure 1 and to regional assessments of carbon budgets, it becomes increasingly important to recognize and quantify the lateral transports of carbon. The transport of carbon through trade/commerce represents a flux that is nearly as large as the net terrestrial and oceanic sinks. This carbon is assumed to be respired back to the atmosphere, but if the CO_2 is

taken out of the atmosphere on one continent, then transported to another continent before being respired, it can have a significant impact on regional budget assessments.

Embodied carbon represents the carbon that resides directly within the product itself (for cereals, wood and paper, about half of the final weight is carbon). In addition to embodied carbon, at least two other components are usually excluded from estimates of carbon content in international trade. One is the "production" carbon, which comprises the inputs required to produce a final product, primarily energy-related consumption to provide inputs (e.g. pesticides, fertilizers) and processing (e.g. machinery for harvesting, milling, sawing etc.). A second element is the "transport" carbon, which represents the energy costs of transporting the processed products to a final destination. Countries that use intensive production systems and engage in significant exports (primarily in the developed countries) would have higher ratios of carbon content to product mass exported, possibly up to 20%, and would therefore have higher carbon emissions to the atmosphere than currently stated, under a system of full carbon accounting. Other countries would have lower carbon release to the atmosphere under full carbon accounting. Trade/commerce carbon accounting has a political background and differs from budget studies by atmospheric inversion and inventory checks. For example, CO_2 emissions during production and transport of products across regional boundaries would fully and partly, respectively, be accounted for by the country of origin using inventory studies. Inverse models based on atmospheric measurements, however, would reflect the emissions as they were actually distributed over the regions. As we begin to move from the global carbon budget to regional carbon budgets, fluxes like those in trade and commerce will need to be better quantified.

Non-CO_2 Trace Gas Connections

Rising concentrations of a large number of potent anthropogenic greenhouse gases other than carbon dioxide have collectively contributed an amount of radiative forcing comparable to that of CO_2 since pre-industrial times. Many of these non-CO_2 gases (e.g. CH_4, N_2O, CF_2Cl_2, SF_6) are emitted at the earth's surface and contribute directly to this forcing (Prinn 2003). They are characterized by atmospheric lifetimes of decades to millennia (lifetime as used here is the amount of the gas in the global atmosphere divided by its global rate of removal). Other non-CO_2 gases (e.g. isoprene, terpenes, nitric oxide (NO), carbon monoxide (CO), sulphur dioxide (SO_2), dimethyl sulphide ($(CH_3)_2S$), most of which are also emitted at the earth's surface, contribute indirectly to this forcing either through production of tropospheric ozone (which is a powerful greenhouse gas), or tropospheric aerosols (which directly reflect sunlight back to space, absorb it, or indirectly change the reflection properties of clouds). This second group of climatically important non-CO_2 gases is characterized by much shorter lifetimes (hours to months).

The role of non-CO_2 carbon gases is not typically included in global carbon budgets, like the one shown in figure 1, because the sources and sinks for these gases are not well understood. Figure 5 summarizes, albeit with great simplification, the basic cycles and fluxes of the major non-CO_2 trace gases relevant to climate. Note that the emissions of the carbon-containing gases alone contribute about 2.3 Pg C y^{-1} to the carbon cycle (Prinn 2003). To aid the handling of the non-CO_2 gases in the policy processes under the United Nations Framework Convention on Climate Change (UNFCCC), scientists have calculated so-called global warming potentials (GWPs). These dimensionless GWPs, which range from 20 to 20,000 for the major non-CO_2 gases, are intended to relate the time-integrated radiative forcing of climate by an emitted unit mass of a non-CO_2 trace gas to the forcing caused by emission of a unit mass of CO_2. The GWP concept has difficulties, because the removal mechanisms for many gases (including CO_2 itself)

involve complex chemical and/or biological processes, and because the time period (e.g. decade, century) over which one integrates the instantaneous radiative forcing of a gas to compute its GWP is somewhat arbitrary (Manne and Richels 2003). Nevertheless, by multiplying the emissions of each major non-CO_2 greenhouse gas by its GWP, we obtain equivalent amounts of CO_2 emissions, which are comparable to the total actual emissions of CO_2 (e.g. current total emissions of CH_4 and N_2O are equivalent to 3.8 and 2.1 Pg C y^{-1} respectively). For this reason, a "CO_2 emissions only" approach for global warming policy may lead to significant biases in the estimation of global warming abatement costs (Manne and Richels 2003). Thus, a multi-gas approach for studying the carbon cycle and how it relates to climate change needs to be implemented.

Carbon Cycle Processes

To fully understand the significance of the connections described above, as well as the potential that these fluxes might change in the future, one must consider the processes responsible for controlling the fluxes within and between reservoirs. In some cases these processes have already been significantly impacted by human activities. In other cases, they may be vulnerable to climate change in the future.

Terrestrial Processes

On seasonal time-scales the gains and losses from the terrestrial biosphere are reflected in the cyclic variations in atmospheric CO_2 concentrations. Although there is significant interannual variability in the seasonal balance between the gains and losses, it is the trends in this net balance between NPP and carbon losses through decomposition, fires and disturbances that can affect

climate on time-scales of decades to centuries. The scientific community currently believes that the terrestrial biosphere has been acting as a net sink for atmospheric carbon for the past few decades (Foley and Ramankutty 2003). For example, Pacala et al. (2001) recently estimated the carbon sink of the coterminous Unites States using a combination of inventory and atmospheric concentration inversions. They determined a consistent land and atmosphere based carbon sink for the US in the range of 0.37 to 0.71 Pg C y^{-1}. Similar studies have also shown a net sink in Europe (Janssens et al. 2003). The mechanisms underlying the sinks have been the subject of much recent research. The leading hypothesis in the 1970s and 1980s was that the sinks were mainly a result of more rapid plant growth from elevated CO_2 and climate change. This has gradually been replaced with a multi-mechanism explanation, including contributions from changes in forest management, agriculture, long-lived products (e.g. wood), aquatic systems, and nitrogen deposition, in addition to CO_2 fertilization and changes in plant growth/soil carbon pools resulting from climate change (Schimel et al. 2001).

NPP is sensitive to a broad range of factors, including climate, soil fertility, atmospheric CO_2, atmospheric pollutants, and human management. An increase in NPP can lead to a carbon sink, but only if it is not matched by a corresponding increase in carbon losses. In general, processes that promote gradual increases in NPP can lead to carbon sinks, because increases in respiration tend to follow changes in biomass and soil carbon and not NPP directly (Field 1999). For the last 30 years, carbon cycle researchers have hypothesized that gradual increases in NPP in response to the 30% rise in atmospheric CO_2 since preindustrial times explain much or all of the terrestrial sink inferred from atmospheric studies (Bacastow and Keeling 1973). Experimental studies at the ecosystem level often demonstrate accelerated plant growth in response to elevated atmospheric CO_2 (Mooney et al. 1999), but these growth rates only explain

a small fraction of the sink required to balance the global atmospheric CO_2 budget (Friedlingstein et al. 1995). Other factors that can increase NPP, including warming, greater precipitation and humidity, nitrogen deposition, and changes in plant species composition may also contribute to terrestrial carbon sinks.

Processes that retard carbon releases can also lead to terrestrial sinks. Evidence indicates that a substantial fraction of the forest sink in temperate forests is a result of changes in land use and land management. In essence, forests, cut in the past, are regrowing, with a growth rate that is faster than the rate of harvesting (Goodale et al. 2002). Some of this is a result of shifts in land use, especially the abandonment of agriculture over large regions of North America and parts of Europe (Foley and Ramankutty 2003). Fire suppression and the thickening (more trees per unit area) of marginal forests also contribute to increased forest biomass in some areas (Pacala et al. 2001).

Changes in agriculture can also promote terrestrial carbon sinks. Increases in yield, incorporation of crop residue, and areas in perennial crops, as well as a reduction in tillage can all contribute to carbon sinks (Lal et al. 1998).

Recent terrestrial carbon sinks reflect a number of mechanisms (Pacala et al. 2001). The potential for sinks to persist varies from mechanism to mechanism. Sinks due to CO_2 fertilization are likely to persist until NPP is limited by another factor. In some settings, this might occur very soon, and in others it might be far in the future. Sinks caused by forest regrowth saturate as the forests mature (Nabuurs 2003). In general, sinks saturate when increases in NPP are outpaced by increases in the sum of decomposition and combustion. The persistence of terrestrial sinks in the future is by no means assured. Many lines of evidence suggest that the prospect of increasing carbon sources in the terrestrial biosphere is a real possibility (Gruber et al. 2003).

Ocean Processes

Air-sea gas exchange is a physico-chemical process, primarily controlled by the air-sea difference in gas concentrations and the exchange coefficient, which determines how quickly a molecule of gas can move across the ocean-atmosphere boundary (see Le Quéré and Metzl 2003). It takes about one year to equilibrate CO_2 in the surface ocean with atmospheric CO_2, so it is not unusual to observe large air-sea differences in CO_2 concentrations (figure 3). Most of the differences are caused by variability in the oceans due to biology and ocean circulation. The oceans contain a very large reservoir of carbon that can be exchanged with the atmosphere (see figure 1). However, since air-sea exchange can only occur at the surface, the rate at which carbon exchanges between the surface and the ocean interior ultimately regulates how well the atmosphere equilibrates with the ocean as a whole.

Two basic mechanisms control the natural distribution of carbon in the ocean interior: the solubility pump and the biological pump. The solubility pump is driven by two principle factors. First, more CO_2 can dissolve into cold polar waters than in the warm equatorial waters. As major ocean currents (e.g. the Gulf Stream) move waters from the tropics to the poles, they are cooled and can take up more CO_2 from the atmosphere. Second, the high latitude zones are places where deep waters are formed. As the waters are cooled, they become denser and sink into the ocean's interior taking with them the CO_2 accumulated at the surface.

The biological pump also transports CO_2 from the surface to the deep ocean. Growth of phytoplankton uses CO_2 and other chemicals from the seawater to form plant tissue. Roughly 70% of the CO_2 taken up by phytoplankton is recycled near the surface and the remaining 30% sinks into the deeper waters before being converted back into CO_2 by marine bacteria (Falkowski

et al. 1998). Only about 0.1% of the organic carbon fixed at the surface reaches the seafloor to be buried in the sediments. The carbon that is recycled at depth is transported large distances by currents to areas where the waters return to the surface (upwelling regions). When the waters regain contact with the atmosphere, the CO_2 originally taken up by the phytoplankton is returned to the atmosphere. This exchange helps to control atmospheric CO_2 concentrations over decadal and longer time scales.

The amount of organic carbon that is formed and sinks out of the surface ocean is limited by the availability of light and nutrients (mainly nitrate, phosphate, silicate and iron), and by temperature. The plankton types present in the water also play a role. Plankton that bloom create favorable conditions for the formation of fast sinking particles, particularly when they have shells of calcium carbonate or silicate (Klaas and Archer 2002). The formation of calcium carbonate shells impacts carbon chemistry in such a way that it works to counteract the draw-down of CO_2 by soft tissue production. The biological pump also removes inorganic nutrients from surface waters and releases them at depth. Since productivity is limited by the availability of these nutrients, the large-scale thermohaline circulation (THC) of the oceans has a strong impact on global ocean productivity by regulating the rate at which nutrients are returned to the surface.

Up to now, humans have had a relatively small direct impact on the global scale ocean carbon cycle. This is primarily because humans generally only transit across the ocean and because the ocean naturally contains orders of magnitude more carbon than the atmosphere and the terrestrial biosphere. The ocean does, however, act as a significant sink for CO_2 ultimately derived from anthropogenic activities (Table 1). Because biology is not limited by carbon in the oceans, it is thought that increasing CO_2 levels have not significantly impacted ocean biology.

The current distribution of anthropogenic CO_2 is assumed to result from physico-chemical equilibration of the surface ocean with rising atmospheric CO_2 and slow mixing of the anthropogenic CO_2 into the ocean's interior. The long residence time for the deep oceans means that most of the deep ocean waters have not been exposed to the rising atmospheric CO_2 concentrations observed over the last couple of centuries. Although the oceans have the potential to absorb 85% of the anthropogenic CO_2 released to the atmosphere, today's oceans are only at about 15% capacity (Le Quéré and Metzl 2003). Average penetration depth for anthropogenic CO_2 in the global ocean is only about 800 m (Sabine et al. 2002). There is growing evidence, however, that changes in ocean mixing and biology may be occurring as a result of climate change.

Since the solubility of CO_2 is a function of temperature, warming of the ocean will decrease its ability to absorb CO_2. Furthermore, changes in temperature and precipitation may lead to significant alterations of ocean circulation and the transport of carbon and nutrients to and from the surface. Because of its effect on ocean carbon distributions and biological productivity, changes in the THC have been used to help explain past excursions in climate and atmospheric CO_2, including glacial-interglacial and Dansgard-Oeschger events (Joos and Prentice 2003).

Ocean productivity can also be affected by atmospheric inputs that may change as a result of human activity. Iron in oceanic surface waters originates from terrestrial dust deposited over the ocean, deep ocean waters, continental shelves, and to a lesser extent from river inflow. Because of the spatial distribution of dust deposition and other iron sources, large regions of the ocean show a deficit in iron (and to a smaller extent in silicate), although other nutrients are plentiful. These are called High Nutrient Low Chlorophyll (HNLC) regions. There is a potential for enhanced biological productivity in these regions if the ocean can be "fertilized" by iron.

However, the potential for CO_2 reduction in surface waters and in the atmosphere through this artificial sequestration depends on factors like the composition of plankton types and oceanic circulation, and can lead to undesirable side effects (Bakker 2003).

There is also increasing evidence that rising CO_2 levels may directly impact ocean productivity and ecosystem structure. For example, Riebesell et al. (2000) showed a significant reduction in the ability of two different species of coccoliths to secrete calcium carbonate shells under elevated CO_2 conditions. Similar reductions in calcification have been observed in corals and coralline algae. As atmospheric CO_2 concentrations continue to rise, the potential for significantly altering the current balance between the amount of carbon moved into the ocean's interior by the biological pump versus the solubility pump in the ocean increases. The net effect on the ability of the ocean to act as a sink for anthropogenic CO_2 is not clear.

Coastal Ocean

Although the coastal zones, consisting of the continental shelves with depths less than 200m including bays and estuaries, occupy only 10% of the total ocean area, they play a crucial role in the global carbon cycle. Carbon is transported to the coastal zone by riverine inputs and transport of inorganic carbon from the open-ocean. Estuaries and proximal coastal seas are believed to be sources of CO_2, because of the decay of terrestrial organic carbon. However, since the riverine flux of nutrients has risen continually over the past few decades, these areas may now have enhanced biological productivity, and hence, be releasing less CO_2. At present a large fraction (~80%) of the land derived organic and inorganic materials that are transported to the ocean is trapped on the proximal continental shelves (Mackenzie and Ver 2001). The much wider open shelves, on the other hand, probably serve as sinks for atmospheric carbon. A recent

overview suggests that the global coastal waters and marginal seas (extending to a water depth of 200m) are now absorbing about 0.36 Pg C y^{-1} from the atmosphere (Chen 2003).

Across most of the coastal seas and continental margins, surface waters are transported offshore, because of fresh water inputs from land. This surface transport draws nutrient-rich subsurface waters from the open ocean onto the shelves. Such external sources of nutrients support high primary productivity. Most of the organic material produced is respired and recycled on the shelves. The organic matter that is not recycled either accumulates in the sediments or is exported to the slopes and open oceans. The coastal zone may account for 30-50% of the total calcium carbonate accumulation and up to 80% of the organic carbon accumulation in ocean sediments (Mackenzie and Ver 2001). Globally, the shelf seas are estimated to transport 0.6 Pg C y^{-1} of DOC, 0.5 Pg C y^{-1} of POC, and 0.2 Pg C y^{-1} of PIC to the open oceans (Chen 2003). Although these transports have large uncertainties, because of high variability and inadequate data coverage, they represent an important and often neglected link in the global carbon cycle. Shelves and estuaries are also important sources of other greenhouse or reactive gases, such as methane and dimethyl sulfide.

Finally, while humans appear to have had only a small direct impact on the open ocean, they have had a profound and poorly understood impact on the coastal oceans. Furthermore, direct and indirect human perturbations vis-à-vis the continental margins (e.g. pollution, eutrophication, etc.) are likely to have large and dire consequences on marine ecosystems in the future. As much as 40-60% of the world population lives in coastal areas, depending on the definitions and methodologies applied. The coastal regions have the most rapidly growing populations, because of migration from rural areas. Most mega cities in this century will develop in coastal zones, approximately half of them in Asia (IHDP/START, 2000). Such patterns of

urbanization have affected and will continue to affect coastal and marine systems, through processes such as land use change, pressure on infrastructure (water, sewage, and transportation), coastal resource depletion and degradation, eutrophication, and other carbon relevant impacts. Coastal zones support more than 60% of the global commercial fish production (World Resources Institute 1996). It is not clear how these fisheries will be affected by the increasing human pressures on the coastal zone. Additional studies of the coastal zone and the interaction between humans and the coastal biogeochemical systems are needed.

Human Systems

Humans have had a profound impact on carbon cycling in the atmosphere, terrestrial biosphere, and, to a lesser extent, in the oceans. To understand how humans will continue to interact with these reservoirs in the future, one must understand the drivers responsible for how humans interact with the environment.

Energy use has historically been viewed as an essential commodity for economic growth. The paradigm of "grow or die" historically meant increasing demands for additional resources and a commensurate increase in the amount of pollutants released. Over the past thirty years, however, a complex debate has ensued about how to decouple economic growth and resource consumption. Since this debate started, many scholars, policy makers, and nongovernmental organizations have asked themselves how to reshape this paradigm of development. Answers have ranged from doing nothing (business as usual approach) to the slowing and even stalling of economic growth, so as to not exceed the earth's carrying capacity. Carrying capacity here refers to the ability of natural resources and ecosystems to cope with anthropogenic pressures, such as use of renewable natural resources, emission of pollutants, and modification of ecosystem's

structures without crossing "critical thresholds of damage beyond which (these resources) lose their ability for self-renewal and slide inexorably into deeper degradation" (Board on Sustainable Development Policy Division 1999).

Another more tenuous response is based on the idea that one could keep economic growth as a development goal and at the same time find mechanisms aimed at reducing the amount of material input and emissions or aimed at finding replacements for non-renewable or dangerous resources (e.g. fossil fuels). This proposal has resulted in environmental policies and instruments promoting technological innovations aimed at increasing the efficiency of economic activities and at decarbonizing economies.

Energy intensity (the ratio of total domestic energy primary consumption to gross domestic product or physical output) in the US, Japan, and other developed countries has increased far slower than economic growth. China too has made significant gains, and the growth rate of its energy consumption has been half that of its gross domestic product (GDP) growth rate since the early 1980s. While the energy use per unit of GDP has fallen or stabilized since 1970, energy use per capita has increased in most of the developed countries (Sathaye 2003). This statistic may be misleading however, because there has also been a change in consumption and production patterns away from materially intensive commodities towards less intensive services, and production of many of the materially intensive commodities has moved out of the developed countries. This does not necessarily mean that the developed countries are using fewer resources, but the regional distribution of this consumption has changed. Countries belonging to the former Soviet Union (FSU) have also experienced decreases in energy intensity, but for very different reasons. Due to sociopolitical changes, economic activity declined substantially in these countries, resulting in a dramatic decline in energy use and associated carbon emissions.

Over the past century and a half, the use of biomass has successively given way to expanded use of coal, oil, and natural gas as the primary fuels to supply energy (Figure 6). Over the past two decades, the use and share of nuclear and other forms of renewable energy has increased. The carbon intensity (Pg C/GJ) of each successive fuel, beginning with coal, is lower, and this has led to the decarbonization of the global fuel mix over the past century. Critical inventions such as the steam and internal combustion engines, vacuum tubes, airplanes, etc. have accompanied and fostered the use of successive fuels and electricity.

The speed of energy consumption and land use changes have increased during the last two centuries. Three spatial and historical variations of carbon relevant social tendencies need to be considered in developing an understanding of where we are today.

1. Historically, industrialized countries have been the main releasers of carbon from combustion of fossil fuels. Although developing countries are expected to increase their share of emissions, the relocation strategies of corporations based in industrialized regions may actually significantly contribute to increased emissions in these developing countries. In 1925, for example, the United States, Western Europe, Japan, and Australia were responsible for about 88% of the world's fossil fuel carbon dioxide emissions (Houghton and Skole 1990). Data from 1950-1995 indicate that 26 countries fell above the average cumulative emissions figure. These countries include almost all developed, or Annex 1 countries, plus China, India, Brazil and several other larger developing countries that have seen significant growth in foreign investments (Claussen and McNeilly 1998).
2. Until the 20th century, most of the conversion from forest area to cultivated land occurred in the developed countries. During the last few decades, most of the deforestation has occurred in tropical forests.

3. Urbanization, a key driver of energy and land use, was primarily a feature of industrialized nations until the middle of the 20th century. The largest and demographically most dynamic urban agglomerations, like New York, London, and Tokyo were in developed countries. As of the beginning of the 21st century, however, most urban agglomerations are situated in developing countries. These developing nation urban agglomerations have different production systems and living standards than the urban centers in developed countries. These differences impact the carbon emissions of various urban areas (Romero 2003).

Although technology is perceived as the answer to decarbonizing economies, other societal factors work as constraints and windows of opportunity for that purpose (e.g. institutional settings and economic dynamics, see Raupach et al. 2003). In addition, new technological paradigm of production and consumption patterns emerge only over decades. The main energy and production components of the *engineering* epoch, for instance (1850-1940), took at least twenty years to develop. Hence, it will likely take decades to set up alternative energy sources and materials aimed at decarbonizing industrial and agricultural activities. Despite efforts aimed at decoupling economic growth from its carbon impacts, CO_2 emissions from the combustion of fossil fuels and from land-use change have been increasing. Many features of the development trends need to be studied and better understood before opportunities for modifications in life styles, technologies, institutions, and other drivers of carbon emissions can be fully addressed.

Geological Processes

The discussion thus far has focused on reservoirs and processes relevant to human time-scales. With a residence time of about 300 million years, the huge reserves of carbon stored in the sedimentary rocks are not expected to play a large role in the short-term carbon budget. On time-scales greater than 500,000 years, about 80% of the CO_2 exchange between the solid earth and the atmosphere is controlled by the carbonate-silicate cycle (Kasting et al. 1988). In this cycle, atmospheric CO_2 is used to weather calcium-silicate rock minerals on land, which are then transported to the ocean via rivers as calcium and bicarbonate ions. In the oceans, plankton and other organisms incorporate the ions into calcium carbonate shells. A portion of the calcium carbonate is deposited onto the ocean floor, and eventually CO_2 is returned to the atmosphere through volcanic and diagenetic processes.

Vast quantities of carbon stored are in ocean sediments as methane hydrates and as calcium carbonate. The methane hydrates are relatively stable, but could be released, if ocean temperatures increase sufficiently through global warming (Harvey and Huang, 1995). The carbonate sediments are likely to be a significant sink for fossil fuel CO_2 on millennial time-scales (Archer et al. 1999). As the oceans continue to take up anthropogenic CO_2, the CO_2 will penetrate deeper into the water column, lowering the pH and making the waters more corrosive to calcium carbonate. Dissolution of sedimentary carbonates binds the carbon in a dissolved form that is not easily converted back into atmospheric CO_2. Carbonate dissolution is typically thought to occur in the deep ocean, well removed from the anthropogenic CO_2 taken up in the surface waters. In portions of the North Atlantic and North Pacific Oceans, however, anthropogenic CO_2 may have already penetrated deep enough to influence the dissolution of calcium carbonate in the water column and shallow sediments (Feely et al 2002).

Although the processes of CO_2 uptake through weathering and CO_2 release from volcanism and diagenesis appear to have a small net effect on the global carbon-cycle on millennial time-scales, short-term variability in one of these fluxes can impact the carbon cycle on time-scales relevant to humans. For example, explosive volcanic eruptions result in the emission of CO_2, dust, ash and sulfur components. These sulfur particles may rain out and promote acid rain. Atmospheric sulfur particles block sunlight and cool the (regional) climate. Particles that reach the stratosphere reduce global temperatures for several years. The incidental occurrence of cataclysmic volcanic eruptions or the coincidence of several large eruptions (e.g. the eruptions of 1783 or the 1991 Mount Pinatubo eruption) affect the global carbon cycle, directly by their CO_2 emissions and indirectly by their impact on marine and terrestrial primary production (Hamblyn 2001; Sarmiento and Gruber 2002).

Understanding Today's Carbon Cycle

Although our understanding of the contemporary global carbon cycle has increased dramatically over the past few decades, there are many aspects that are still not well understood. Several specific areas where additional studies are needed have been mentioned above. However, there are two general areas of research where our understanding is exceptionally weak and focused research is necessary. One area that needs improvement is understanding regional variability. A second, somewhat related topic is how changes in the carbon-cycle may be linked to different modes of climate variability.

Regional Budgets

Although atmospheric CO_2 concentrations are changing on a global scale, the spatial scales of natural processes as well as the scales of human interventions and the associated societal mechanisms have a profound regional character. Industrialized countries, for instance, dominate fossil fuel CO_2 emissions by direct release and through trade, while developing nations have become the primary CO_2 emitters through land use changes (Romero 2003). Insufficient observations limit our ability to do regional scale assessments globally. However, the potential benefits of such approaches in identifying the biogeochemical and human processes responsible for controlling fluxes makes these studies very important. A regional scale carbon budget assessment also provides a unique opportunity to verify and bridge independent methods and observations made over a range of spatial scales (e.g. top – down atmospheric inversion estimates versus land-based or ocean-based bottom-up observations).

In the land-based bottom-up method, carbon sinks and sources from various ecosystems (forests, croplands, grasslands and organic soil wetlands) are aggregated over all regions to provide a large-scale perspective. The land-based approach can therefore provide information as to which ecosystems and regions are accumulating, and which are losing carbon to the atmosphere. However, the diversity of land mosaics, the complexity of human activities and the lateral transports of carbon in different components make it difficult to provide a comprehensive carbon budget.

Ocean-based bottom-up methods can be used to assess the complex and often competitive controls of heat flux, mixing, and biology on air-sea gas exchange as well as to develop proxies for extrapolating limited observations to larger time and space scales. Monitoring of changes in ocean interior properties can also provide valuable information on surface processes and fluxes.

Atmosphere-based approaches, in contrast, give no information about which ecosystems or processes are contributing to a sink or source, but produce a more consistent large-scale assessment of the net carbon flux to the atmosphere. No one approach holds the key to understanding regional variability in the carbon cycle. A suite of approaches much be used. In addition to providing different, but complementary information, a combination of the bottom-up and top-down methods puts independent constraints on the integrated carbon balance of regional budgets.

The use of multiple approaches can also be used to identify key fluxes that may have been missed by the inventory approach. For example, Janssen et al. (2003) used inventories to estimate that the European continent sink is on the order of 0.11 Pg C y^{-1}, compared with a mean atmospheric inversion estimate of 0.29 Pg C y^{-1}. The discrepancy between these estimates is attributed to the intercontinental displacement of organic matter via trade, emissions of non-CO_2 gases, and a slight overestimation of fossil fuel emissions. This example illustrates the need for comprehensive assessments of the major vertical and lateral fluxes as well as illustrating the power of the multiple approaches for highlighting areas where additional studies are needed.

Variability

Observing and quantifying variability in natural processes and the impact of human interventions is of primary importance for three reasons:

(1) It provides a key diagnostic of how climatic factors and societal dynamics impact exchange fluxes and provides information that is needed for the developing and validating comprehensive process based carbon cycle models that include human dynamics.

(2) Several terrestrial and oceanic carbon cycle components effectively contain a longer-term "memory", i.e. their present state is partly a result of past natural and human perturbations. For example, enhanced fire frequencies or management strategies during a drier past period will be reflected in the age-structure of a present forest, or the carbon content in particular oceanic deep water masses will reflect climate driven variations in deep water formation in the past.

(3) Climate variability often tends to "mask" the slow, longer term signals in the carbon cycle that are of primary interest: i.e. many studies have shown that the uptake rates of the terrestrial biosphere or the ocean are highly variable. In this context, climate variability constitutes a "noise" from which the signals have to be discriminated. Indeed, a significant fraction of the uncertainty in the global budget in Table 1, can be traced to incomplete quantification of possible climate perturbations in the pertinent observations.

On the global scale, climate driven variability can be inferred from atmospheric time series of CO_2 and associated variables, such as $^{13}C/^{12}C$ and O_2/N_2 ratios. Continental or ocean basin scale variations can be detected on time scales of up to several years by means of top-down inversions of atmospheric CO_2 concentration measurements (Heimann et al. 2003). However, it is difficult to separate the terrestrial signals from the ocean signals using these large-scale approaches (Greenblatt and Sarmiento 2003). On land and in the oceans, local-scale direct observations of variability exist from in situ flux measurements at a few time-series stations during the last few years. However, on the regional scale an observational gap exists. The present atmospheric network is not dense enough to resolve carbon sources and sinks on regional scales by atmospheric inversion, while the upscaling of measured in situ oceanic and terrestrial carbon fluxes is extremely difficult. On land, the large heterogeneity of terrestrial ecosystems

and complex atmospheric transport patterns resulting from topography make it difficult to scale up local measurements. In the oceans, the complex interplay between physical and biological controls on sea surface pCO_2 and the dynamics of air-sea exchange complicate the extrapolation of the in situ observations.

Interannual variability in climate leads to large changes in atmospheric temperature and rainfall patterns, as well as changes in ocean surface temperatures and circulation. All of these can have dramatic effects on biological productivity and complex effects on CO_2 exchanges with the atmosphere on land and in the oceans. For example, during El Niño events, the warming of ocean surface waters and reduction in biological productivity in the Equatorial Pacific Ocean should lead to enhanced outgasing of CO_2. However, since the upwelling of carbon rich deep waters, which release CO_2 to the atmosphere, is reduced during El Niños, the net effect is a significant reduction in the outgasing of CO_2 in this region. On the other hand, warmer temperatures and anomalous rainfall patterns during El Niños can lead to increased terrestrial biosphere respiration, forest fires, and droughts. The timing of these effects and the teleconnections between them have a direct impact on atmospheric CO_2 concentrations that are still not completely understood.

Overall, the general consensus is that the interannual variability in air-sea CO_2 fluxes is smaller than that of terrestrial CO_2 fluxes, but the exact amplitude and spatial distributions remain uncertain (Greenblatt and Sarmiento 2003). To better determine these signals, an expanded network of time series CO_2 measurements must be maintained for the atmosphere, oceans and land systems. These measurements, together with intensive process studies, a better use of satellite data, atmospheric observations, and rigorously validated models will help us to better understand the current global carbon cycle and how it is evolving over time.

Conclusions

The current global carbon cycle is in a state of transition. Human activities over the past few centuries have had a profound impact on many aspects of the system. As we begin to assess ways to monitor and potentially manage the global carbon cycle, it is imperative that we better understand how the system, including human dynamics and the biogeochemical processes controlling CO_2 and other carbon gases in the atmosphere, has operated in the past and how it is operating today. How will the land/ocean/atmosphere processes respond to human activities, and what are the societal dynamics that will determine how humans will respond to changes in the land, ocean, and atmosphere systems? Until we can confidently explain and model the contemporary carbon cycle, our ability to predict future changes in atmospheric CO_2 concentrations will always be limited. We have made tremendous progress over the past few decades at reducing the uncertainties in table 1 and figure 1. Many aspects of the system are not, however, fully understood.

References

Achard, F., H. D. Eva, H.-J. Stibig, P. Mayaux, J. Gallego, T. Richards, and J.-P. Malingreau. 2002. Determination of Deforestation Rates of the World's Humid Tropical Forests. Science **297**:999-1002.

Ahlbrandt, T. S., R. R. Charpentier, T. R. Klett, J. W. Schmoker, C. J. Schenk, and G. F. Ulmishek. 2000. Future oil and gas supplies of the world. Geotimes **45**: 24-25.

Archer, D., H. Kheshgi and E. Maier-Reimer. 1999. Dynamics of fossil fuel CO_2 neutralization by marine $CaCO_3$, Global Biogeochem. Cycles, **12**: 259-276.

Bacastow, R., and C. D. Keeling. 1973. Atmospheric carbon dioxide and radiocarbon in the natural carbon cycle. II, Changes from A.D. 1700 to 2070 as deduced from a geochemical reservoir. Pages 86-135 *in* G. M. Woodwell and E. V. Pecan, editors. Carbon and the Biosphere. U.S. Dept. of Commerce, Springfield, Virginia.

Bakker, D. 2003. Storage of carbon dioxide by greening the oceans? Pages (this volume) *in* C. B. Field and M. R. Raupach, editors. Toward CO_2 Stabilization: Issues, Strategies, and Consequences. Island Press, Washington.

Behrenfeld, MJ, JT Randerson, CR McClain, GC Feldman, SO Los, CJ Tucker, PG Falkowski, CB Field, R Frouin, WE Esaias, DD Kolber, and NH Pollack. 2001. Biospheric primary production during an ENSO transition, Science, 291 (5513):2594-2597.

Board on Sustainable Development Policy Division, and National Research Council. 1999. Our common journey: a transition toward sustainability. Washington, DC: National Academy Press.

BP Statistical review of world energy. 2003. <http://www.bp.com/centres/energy/index.asp>.

CDIAC. 2003. Trends Online: A Compendium of Data on Global Change Carbon Dioxide Information Center. Oak Ridge National Laboratory, U.S. Department of Energy, Oak Ridge, Tennessee. <http://cdiac.esd.ornl.gov/trends/trends.htm>.

Claussen, E., McNeilly, L. 1998. equity and global climate change. The complex elements of global fairness. Pew Center on Global Climate Change. http:/www.pewclimate.org/report2.html.

Chen, C-T. A. 2003. Exchanges of carbon in the coastal seas. Pages (this volume) *in* C. B. Field and M. R. Raupach, editors. Toward CO_2 Stabilization: Issues, Strategies, and Consequences. Island Press, Washington.

DeFries, R. S., C. B. Field, I. Fung, J. Collatz, and L. Bounoua. 1999. Combining satellite data and biogeochemical models to estimate global effects of human-induced land cover change on carbon emissions and primary productivity. Global Biogeochemical Cycles **13**:803-815.

DeFries, R. S., R. A. Houghton, M. C. Hansen, C. B. Field, D. Skole, and J. Townshend. 2002. Carbon emissions from tropical deforestation and regrowth based on satellite observations for the 1980s and 1990s. Proceedings of the National Academy of Sciences **99**:14256-14261.

Falkowski, P.G., R.T. Barber, and V. Smetacek. 1998. Biogeochemical controls and feedbacks on ocean primary production. Science **281**: 200:206.

Feely, R.A., C.L. Sabine, K. Lee, F.J. Millero, M.F. Lamb, D. Greeley, J.L. Bullister, R.M. Key, T.-H. Peng, A. Kozyr, T. Ono, and C.S. Wong. 2002. In situ calcium carbonate dissolution in the Pacific Ocean. Global Biogeochem. Cycles, **16(4)**, 1144, 10.1029/2002GB001866

Foley, J.A. and N. Ramankutty. 2003. A primer on the terrestrial carbon cycle: What we don't know, but should. Pages (this volume) *in* C. B. Field and M. R. Raupach, editors. Toward CO_2 Stabilization: Issues, Strategies, and Consequences. Island Press, Washington.

Friedlingstein, P., I. Fung, E. A. Holland, J. John, G. Brasseur, D. Erikson, and D. Schimel. 1995. On the contribution of the biospheric CO_2 fertilization to the missing sink. Global Biogeochemical Cycles **9**:541-556.

Geist, H.J. and Lambin, E.F. 2001. What Drives Tropical Deforestation?, LUCC Report Series 4. http://www.geo.ucl.ac.be/LUCC/lucc.html.

Goodale, C. L., M. J. Apps, R. A. Birdsey, C. B. Field, L. S. Heath, R. A. Houghton, J. C. Jenkins, G. H. Kohlmaier, W. Kurz, S. Liu, G.-J. Nabuurs, S. Nilsson, and A. Z. Shvidenko. 2002. Forest carbon sinks in the northern hemisphere. Ecological Applications **12**:891-899.

Gorham, E. 1991. Northern peatlands - role in the carbon-cycle and probable responses to climatic warming. Ecological Applications **1**:182-195.

Greenblatt, J.B. and J. Sarmiento. 2003. Variability and climate feedback mechanisms in ocean uptake of CO_2. Pages (this volume) *in* C. B. Field and M. R. Raupach, editors. Toward CO_2 Stabilization: Issues, Strategies, and Consequences. Island Press, Washington.

Gruber et al. 2003. The vulnerability of the carbon cycle in the 21st century: An assessment of carbon-climate-human interactions. Pages (this volume) *in* C. B. Field and M. R. Raupach, editors. Toward CO_2 Stabilization: Issues, Strategies, and Consequences. Island Press, Washington.

Gurney, K.R. et al. 2002. Towards robust regional estimates of CO_2 sources and sinks using atmospheric transport models. Nature 415:626-630.

Hamblyn, R., 2001. The invention of clouds. How an amateur meteorologist forged the language of the skies. Picador, New York, 291 pp.

Harvey, L.D.D. and Z. Huang. 1995. Evaluation of the potential impact of methane clathrate destabilization on future global warming. J. Gephys. Res., **100**: 2905-2926.

Heimann, M., C. Rödenbeck, and M. Gloor. 2003. Spatial and temporal distribution of sources and sinks of carbon dioxide. Pages (this volume) *in* C. B. Field and M. R. Raupach, editors. Toward CO_2 Stabilization: Issues, Strategies, and Consequences. Island Press, Washington.

Houghton, R. 2003. Why are estimates of the terrestrial carbon balance so different? Global Change Biology **9**:500-509.

Houghton R.A. and D. L. Skole. 1990. "Carbon". In *The Earth as Transformed by Human Action*, edited by Turner, B. L., II, W. C. Clark, R. W. Kate, J. F. Richards, J. T. Mathews, and W. B. Meyer, Cambridge University Press. Cambridge.

IHDP/START International Human Dimensions Workshop: "Human Dimensions in the Coastal Zones" HDP Proceeding No. 03, September 10-19, 2000, Bonn, Germany, www.ihdp.uni-bonn.de/html/publications/publications.html

Janssens, I., A. Freibauer, P. Ciais, P. Smith, G. Nabuurs, G. Folberth, B. Schlamadinger, R. Hutjes, R. Ceulemans, E. Schulze, R. Valentini, and A. Dolman. 2003. Europe's terrestrial biosphere absorbs 7 to 12% of European anthropogenic CO_2 emissions. Science **300**:1538-1542.

Jobbagy, E., and R. Jackson. 2000. The vertical distribution of soil organic carbon and its relation to climate and vegetation. ECOLOGICAL APPLICATIONS **10**:423-436.

Joos, F. and I.C. Prentice. 2003. A paleo perspective on the future of atmospheric CO_2 and climate. Pages (this volume) *in* C. B. Field and M. R. Raupach, editors. Toward CO_2 Stabilization: Issues, Strategies, and Consequences. Island Press, Washington.

Kasting, J.F., O.B. Toon and J.B. Pollack. 1988. How climate evolved on the terrestrial planets. Sci. Amer. **2**:90-97.

Klaas, C. and D.E. Archer. 2002. Association of sinking organic matter with various types of mineral ballast in the deep sea: Implications for the rain ratio. Global Biogeochem. Cycles **16**(4) 1116, doi:10.1029/2001GB001765

Lal, R., J. M. Kimble, R. F. Follett, and C. V. Cole. 1998. The Potential of U.S. Cropland to Sequester Carbon and Mitigate the Greenhouse Effect. Chelsea Press, Ann Arbor, Michigan.

Lee, K., S.-D. Choi, G.-H. Park, R. Wanninkhof, T.-H. Peng, R.M. Key, C.L. Sabine, R.A. Feely, J.L. Bullister, and F.J. Millero. 2003. An updated anthropogenic CO_2 inventory in the Atlantic Ocean. Global Biogeochem. Cycles [In press].

Le Quéré, C. and N. Metzl. 2003. Natural processes regulating the oceanic uptake of CO_2. Pages (this volume) *in* C. B. Field and M. R. Raupach, editors. Toward CO_2 Stabilization: Issues, Strategies, and Consequences. Island Press, Washington.

Le Quéré, C., O. Aumont, L. Bopp, P. Bousquet, P. Ciais, R. Francey, M. Heimann, C.D. Keeling, R.F. Keeling, H. Kheshgi, P. Peylin, S.C. Piper, I.C. Prentice, and P.J. Rayner. 2003. Two decades of ocean CO_2 sink and variability. Tellus, 55b, 649-656.Lindemann, 1941

Mackenzie, F.T. and L.M. Ver. 2001. Land-sea global transfers. Pages 1443-1453 in J.H. Steele, K.K. Turekian, and S.A. Thorpe editors. Encyclopedia of Ocean Sciences. Academic Press. doi:10.1006/rwos.2001.0073.

Manne, A. and R.G. Richels. 2003. A multi-gas approach to climate policy. Pages (this volume) *in* C. B. Field and M. R. Raupach, editors. Toward CO_2 Stabilization: Issues, Strategies, and Consequences. Island Press, Washington.

Mooney, H. A., J. Canadell, F. S. Chapin, III, J. Ehleringer, C. Körner, R. McMurtrie, W. J. Parton, L. Pitelka, and E.-D. Schulze. 1999. Ecosystem physiology responses to global change. Pages 141-189 *in* B. H. Walker, W. L. Steffen, J. Canadell, and J. S. I. Ingram, editors. The Terrestrial Biosphere and Global Change: Implications for Natural and Managed Ecosystems. Cambridge University Press, Cambridge.

Nakicenovic, N. 2003. Socio-economic driving forces of emissions scenarios. Pages (this volume) *in* C. B. Field and M. R. Raupach, editors. Toward CO_2 Stabilization: Issues, Strategies, and Consequences. Island Press, Washington.

Nabuurs, G. J. 2003. Current consequences of past actions. Pages (this volume) *in* C. B. Field and M. R. Raupach, editors. Toward CO_2 Stabilization: Issues, Strategies, and Consequences. Island Press, Washington.

Pacala, S. W., G. C. Hurtt, R. A. Houghton, R. A. Birdsey, L. Heath, E. T. Sundquist, R. F. Stallard, D. Baker, P. Peylin, P. Ciais, P. Moorcroft, J. Caspersen, E. Shevliakova, B. Moore, G. Kohlmaier, E. Holland, M. Gloor, M. E. Harmon, S.-M. Fan, J. L. Sarmiento, C. Goodale, D. Schimel, and C. B. Field. 2001. Convergence of land- and atmosphere-based U.S. carbon sink estimates. Science **292**:2316-2320.

Prentice, C. et al. 2001. The carbon cycle and atmospheric carbon dioxide, *in* J. Houghton et al. editors. Climate Change 2001: The scientific basis, Contribution of working group I to

the Third Assessment Report of the Intergovernmental Panel on Climate Change. Cabridge University Press, New York, NY, USA.

Prinn, R. G. 2003. Non-CO_2 greenhouse gases. Pages (this volume) *in* C. B. Field and M. R. Raupach, editors. Toward CO_2 Stabilization: Issues, Strategies, and Consequences. Island Press, Washington.

Raupach, M., J. Canadell, D. Bakker, P. Ciais, M. J. Sanz, J. Fang, J. Melillo, P. Romero-Lankao, J. Sathaye, D. Schulze, P. Smith, and J. Tschirley. 2003. Interactions between CO_2 stabilisation pathways and requirements for a sustainable earth system. Pages (this volume) *in* C. B. Field and M. R. Raupach, editors. Toward CO2 Stabilization: Issues, Strategies, and Consequences. Island Press, Washington.

Richey, J. E. 2003. Fluvial systems. *in* C. B. Field and M. R. Raupach, editors. Toward CO_2 Stabilization: Issues, Strategies, and Consequences. Island Press, Washington.

Riebesell, U, I. Zondervan, B. Rost, P.D. Tortell, R.E. Zeebe, and F.M.M. Morel. 2000. Reduced calcification of marine plankton in response to increased atmospheric CO_2. Nature **407** (6802): 364-367

Robertson, G. P. 2003. Towards global CO_2 stabilization: Interactions with the non-CO_2 greenhouse gases. Pages (this volume) *in* C. B. Field and M. R. Raupach, editors. Toward CO_2 Stabilization: Issues, Strategies, and Consequences. Island Press, Washington.

Romero Lankao, P. 2003. Pathways of regional development and the carbon cycle. Pages (this volume) *in* C. B. Field and M. R. Raupach, editors. Toward CO_2 Stabilization: Issues, Strategies, and Consequences. Island Press, Washington.

Sabine, C.L., R.A. Feely, R.M. Key, J.L. Bullister, F.J. Millero, K. Lee, T.-H. Peng, B. Tilbrook, T. Ono, and C.S. Wong. 2002. Distribution of anthropogenic CO_2 in the Pacific Ocean, Global Biogeochem. Cycles **16** (4) 1083, doi: 10.1029/2001GB001639.

Sarmiento, J.L. and N. Gruber. 2002. Sinks for anthropogenic carbon. Physics Today August:30-36.

Saugier, J., J. Roy and H.A. Mooney. 2003. Converging toward a single number? Pages (this volume) *in* C. B. Field and M. R. Raupach, editors. Toward CO_2 Stabilization: Issues, Strategies, and Consequences. Island Press, Washington.

Saugier, B., J. Roy, and H. A. Mooney. 2001. Estimations of global terrestrial productivity: Converging toward a single number? Pages 543-557 *in* J. Roy, B. Saugier, and H. A. Mooney, editors. Terrestrial Global productivity. Academic Press, San Diego.

Schimel, D. S., J. I. House, K. A. Hibbard, P. Bousquet, P. Ciais, P. Peylin, B. H. Braswell, M. J. Apps, D. Baker, A. Bondeau, J. Canadell, G. Churkina, W. Cramer, A. S. Denning, C. B. Field, P. Friedlingstein, C. Goodale, M. Heimann, R. A. Houghton, J. M. Melillo, B. M. III, D. Murdiyarso, I. Noble, S. W. Pacala, I. C. Prentice, M. R. Raupach, P. J. Rayner, R. J. Scholes, W. L. Steffen, and C. Wirth. 2001. Recent patterns and mechanisms of carbon exchange by terrestrial ecosystems. Nature **414**:169 - 172.

Smith, P. 2003. Engineered sinks on land (biological). Pages (this volume) *in* C. B. Field and M. R. Raupach, editors. Toward CO_2 Stabilization: Issues, Strategies, and Consequences. Island Press, Washington.

Takahashi, T., S.C. Sutherland, C. Sweeney, A. Poisson, N. Metzl, B. Tilbrook, N. Bates, R. Wanninkhof, R.A. Feely, C. Sabine, J. Olafsson, and Y. Nojiri. 2002. Global sea-air CO_2 flux based on climatological surface ocean pCO_2, and seasonal biological and temperature effects, Deep-Sea Res. II **49**: 1601-1623.

Tschirley, J. and G. Servin, Carbon transport through international commerece. Pages (this volume) *in* C. B. Field and M. R. Raupach, editors. Toward CO_2 Stabilization: Issues, Strategies, and Consequences. Island Press, Washington.

Vitousek, P. M., P. R. Ehrlich, A. H. Ehrlich, and P. A. Matson. 1986. Human appropriation of the products of photosynthesis. BioScience **36**:368-373.

Whitehouse, 2003

World Resources Institute. 1996. World Resources: A Guide to the Global Environment. Oxford Univ. Press, New York, 365 pp.

Zhang, X. M., C. J. S. Cassells, and J. L. van Genderen. 1998. Multi-sensor data fusion for the detection of underground coal fires. Geologie en Mijnbouw **77**:117.

Zimov, S. A., Y. V. Voropaev, I. P. Semiletov, S. P. Davidov, S. F. Prosiannikov, F. S. Chapin, III, M. C. Chapin, S. Trumbore, and S. Tyler. 1997. North Siberian lakes: A methane source fueled by pleistocene carbon. Science **277**:800-802.

Table 1 The global carbon budget (Pg C y^{-1}). Positive values represent atmospheric increase (or ocean/land sources), negative numbers represent atmospheric decrease (sinks).

	1980s	**1990s**
1. *Prentice et al. 2001*		
Atmospheric increase	+3.3 ± 0.1	+3.2 ± 0.1
Emissions (fossil fuel, cement)	+5.4 ± 0.3	+6.3 ± 0.4
Ocean-atmosphere flux	–1.9 ± 0.6	–1.7 ± 0.5
Net land-atmosphere flux	–0.2 ± 0.7	–1.4 ± 0.7
Land-use change	+1.7 (+0.6 to +2.5)	-
**Residual terrestrial sink*	–1.9 (–3.8 to +0.3)	-
2. *Le Quéré et al. 2003*		
Ocean corrected	–1.8 ± 0.8	–1.9 ± 0.7
Net land-atmosphere flux	–0.3 ± 0.9	–1.2 ± 0.8
3. *Houghton, 2003*		
Land use	+2.0 (+0.9 to +2.8)	+2.2 (+1.4 to +3.0)
Residual terrestrial sink	-2.3 (–4.0 to –0.3)	-3.4 (–5.0 to –1.8)
4. *De Fries et al. 2002*		
Land use	+0.6 (+0.3 to +0.8)	+0.9 (+0.5 to +1.4)
Residual terrestrial sink	-0.9 (-3.0 to 0)	-2.1 (-3.4 to -0.9)
5. *Achard et al. 2002*		
Land use		+1.0 ± 0.2
Residual terrestrial sink		-2.2 (-3.2 to -1.2)

Table 2 Plant carbon, soil carbon, and net primary production in the world's major biomes. Plant carbon is from Saugier et al. (2001). NPP is from Saugier et al. (2001), scaled to give the terrestrial total as the satellite study of Behrenfeld et al. (2001). Soil carbon is from Jobbagy and Jackson (2000), to a depth of 3m. Wetland soil carbon is from (Gorham et al. 1991). Carbon in frozen (non-wetland) soils is from (Zimov et al. 1997).

Ecosystem	Area	NPP	Plant C	Soil C
	(10^6 km^2)	Pg C y^{-1}	Pg C	Pg C
Tropical forests	17.5	20.1	340	692
Temperate forests	10.4	7.4	139	262
Boreal forests	13.7	2.4	57	150
Arctic tundra	5.6	0.5	2	144
Mediterranean shrublands	2.8	1.3	17	124
Crops	13.5	3.8	4	248
Tropical savannas & grasslands	27.6	13.7	79	345
Temperate grasslands	15	5.1	6	172
Deserts	27.7	3.2	10	208
Subtotal	149.3	57.5	652	2344
Wetlands				450
Frozen soils	25.5			400
Total	174.8	57.5	652	3194

Figure 1

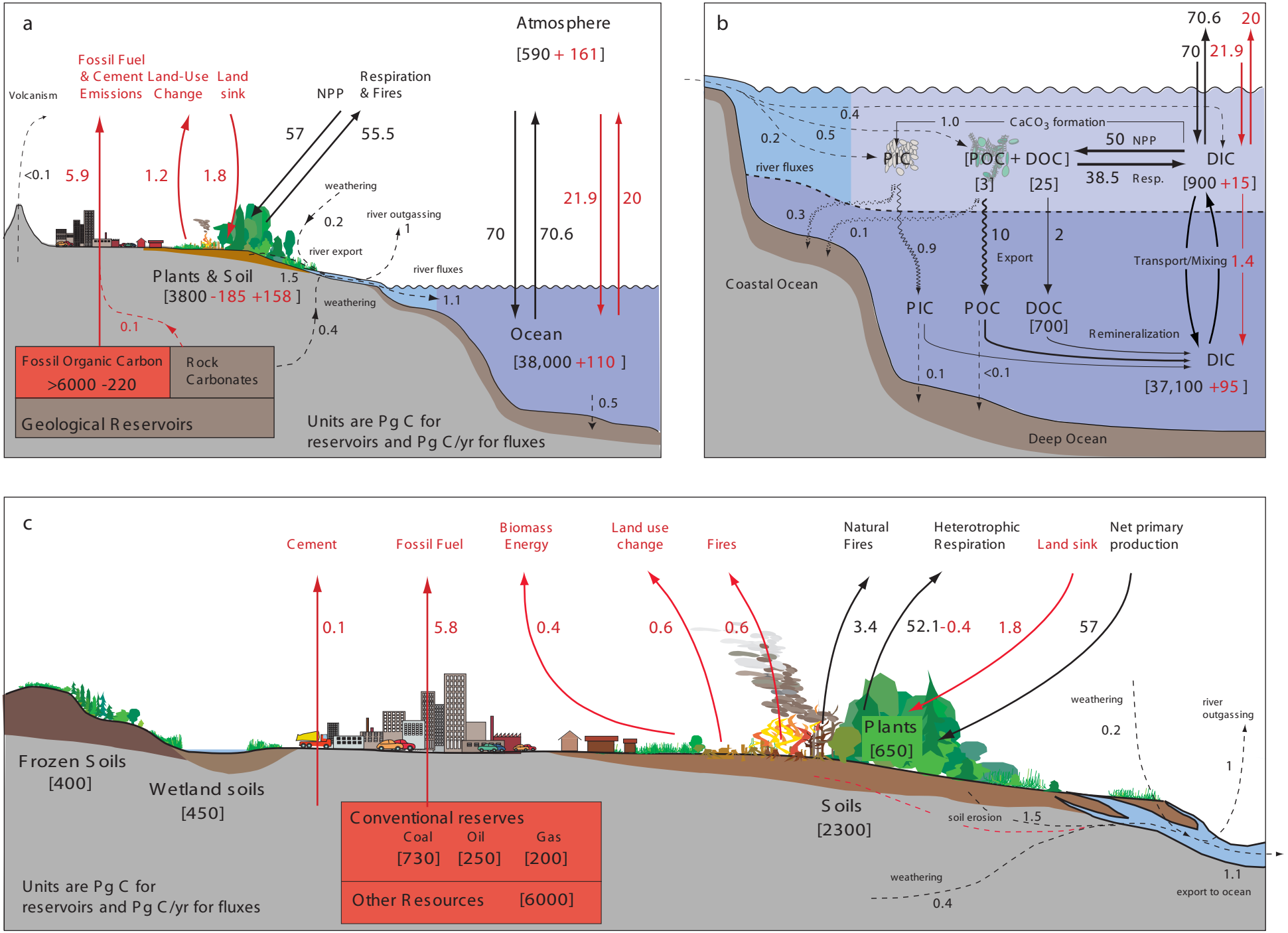
a
Atmosphere
[590 + 161]
Fossil Fuel & Cement Emissions
Land-Use Change
Land sink
Volcanism
NPP
Respiration & Fires
<0.1
5.9
1.2
1.8
57
55.5
weathering
0.2
river outgassing
1
river export
river fluxes
70
70.6
21.9
20
Plants & Soil
[3800 -185 +158]
1.5
weathering
1.1
0.1
0.4
Ocean
[38,000 +110]
Fossil Organic Carbon
>6000 -220
Rock Carbonates
Geological Reservoirs
0.5
Units are Pg C for reservoirs and Pg C/yr for fluxes
b
70.6
20
70
21.9
0.4
1.0
CaCO3 formation
0.2
0.5
50 NPP
river fluxes
PIC
[POC + DOC]
DIC
[3]
[25]
38.5 Resp.
[900 +15]
0.3
0.1
0.9
10
2
Export
Transport/Mixing 1.4
Coastal Ocean
PIC
POC
DOC
[700]
Remineralization
DIC
0.1
<0.1
[37,100 +95]
Deep Ocean
c
Cement
Fossil Fuel
Biomass Energy
Land use change
Fires
Natural Fires
Heterotrophic Respiration
Land sink
Net primary production
0.1
5.8
0.4
0.6
0.6
3.4
52.1-0.4
1.8
57
Plants
[650]
weathering
0.2
river outgassing
1
Frozen Soils
[400]
Wetland soils
[450]
Soils
[2300]
soil erosion
1.5
Conventional reserves
Coal
Oil
Gas
[730]
[250]
[200]
Other Resources
[6000]
weathering
0.4
1.1
export to ocean
Units are Pg C for reservoirs and Pg C/yr for fluxes

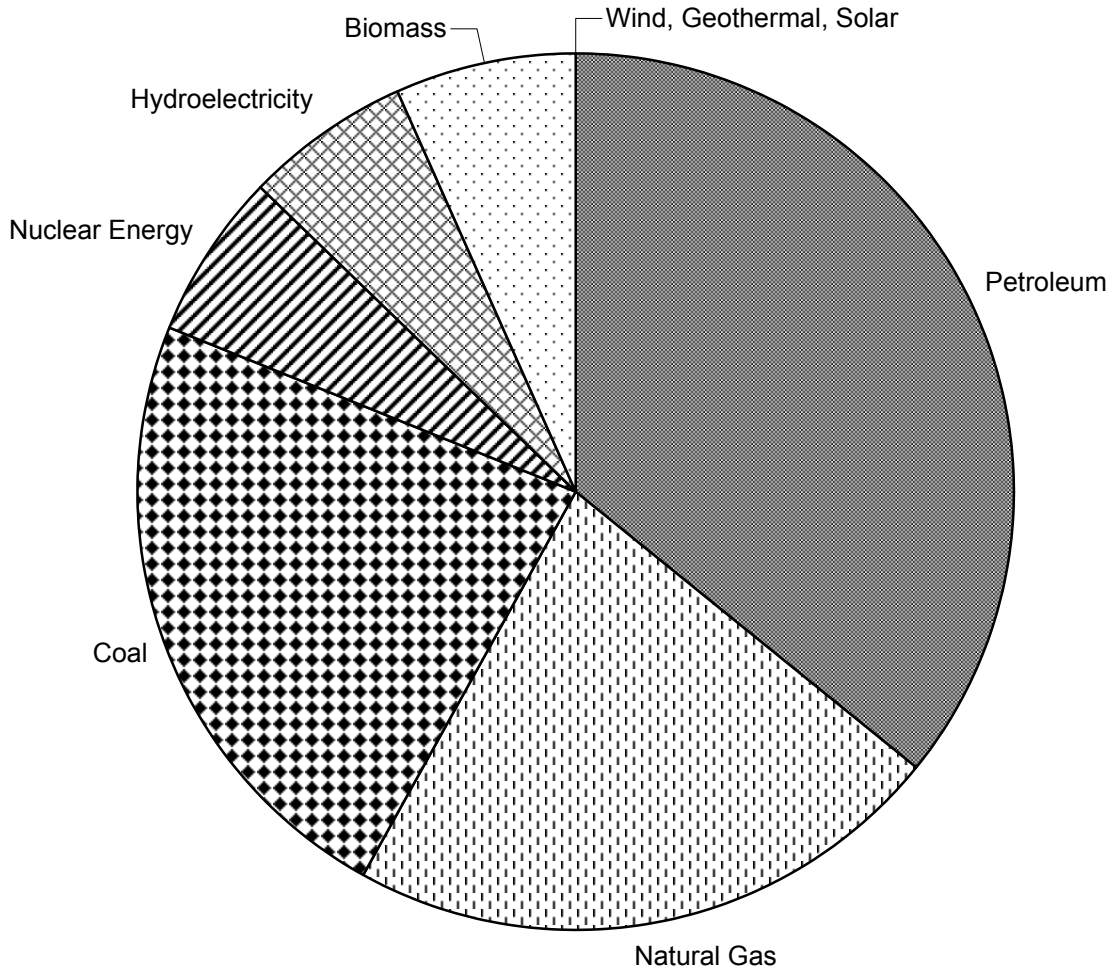
Biomass
Wind, Geothermal, Solar
Hydroelectricity
Nuclear Energy
Petroleum
Coal
Natural Gas

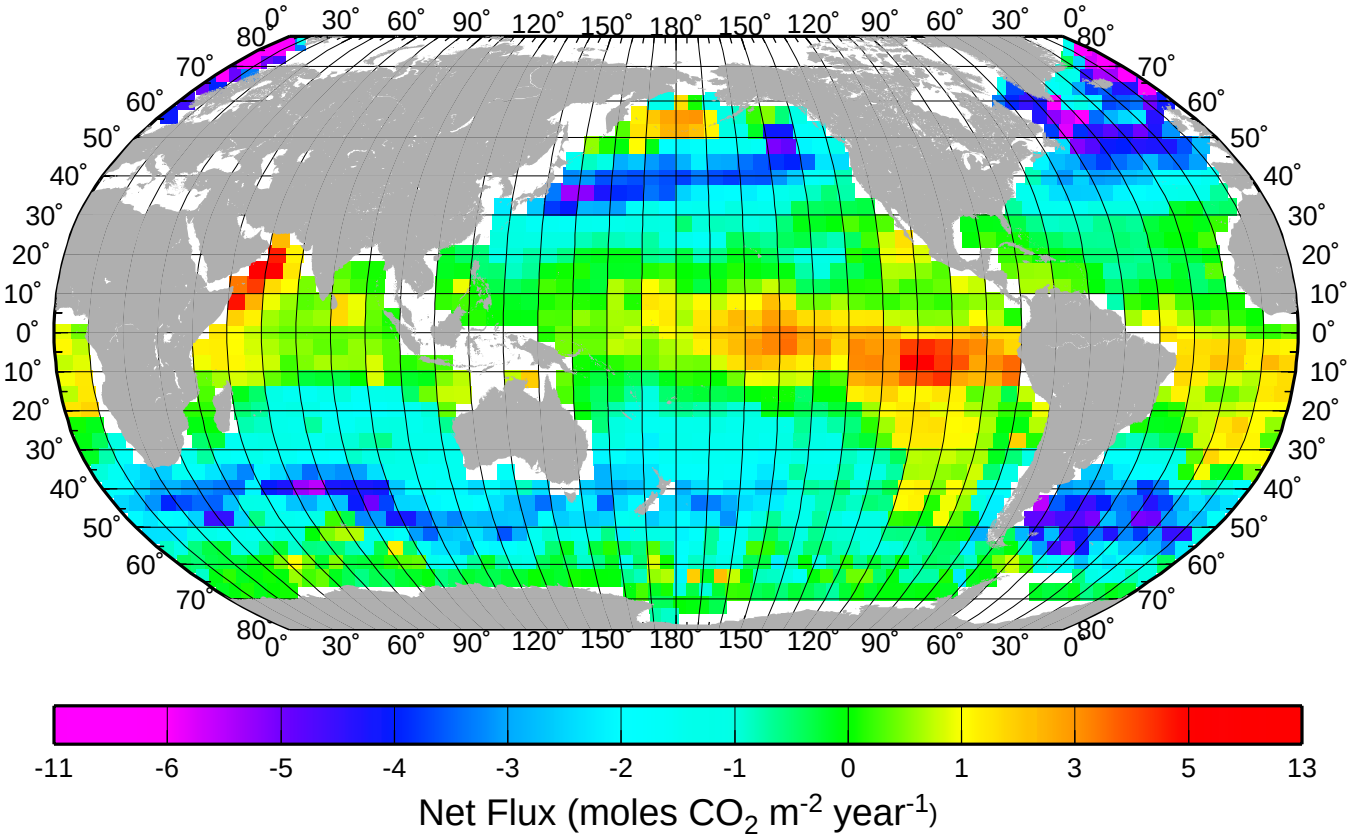
0° 30° 60° 90° 120° 150° 180° 150° 120° 90° 60° 30° 0°
80° 70° 60° 50° 40° 30° 20° 10° 0° 10° 20° 30° 40° 50° 60° 70° 80°
-11 -6 -5 -4 -3 -2 -1 0 1 3 5 13
Net Flux (moles CO2 m-2 year-1)

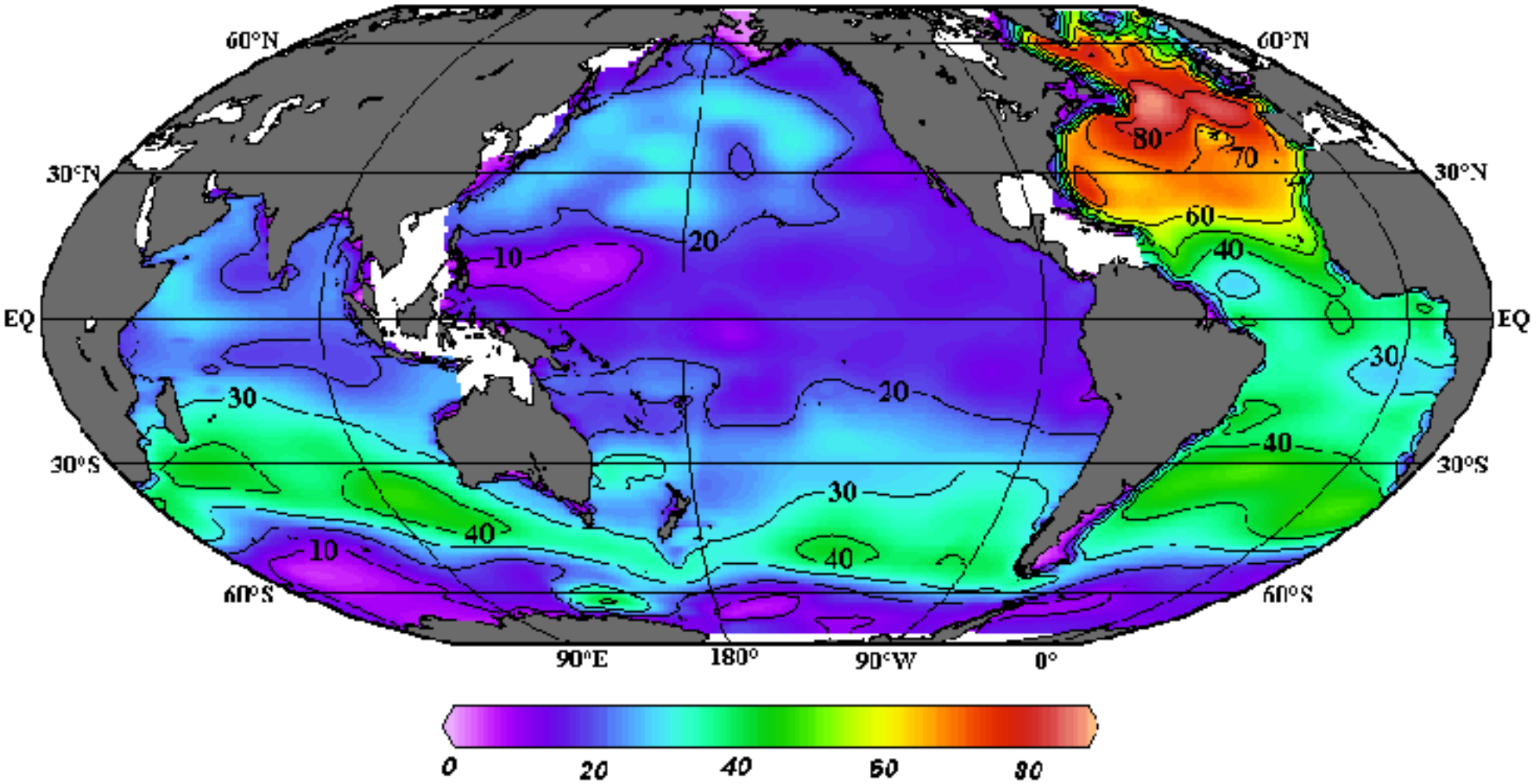
60°N
30°N
EQ
30°S
60°S
90°E
180°
90°W
0°
80
70
60
40
30
20
10
0
20
40
60
80

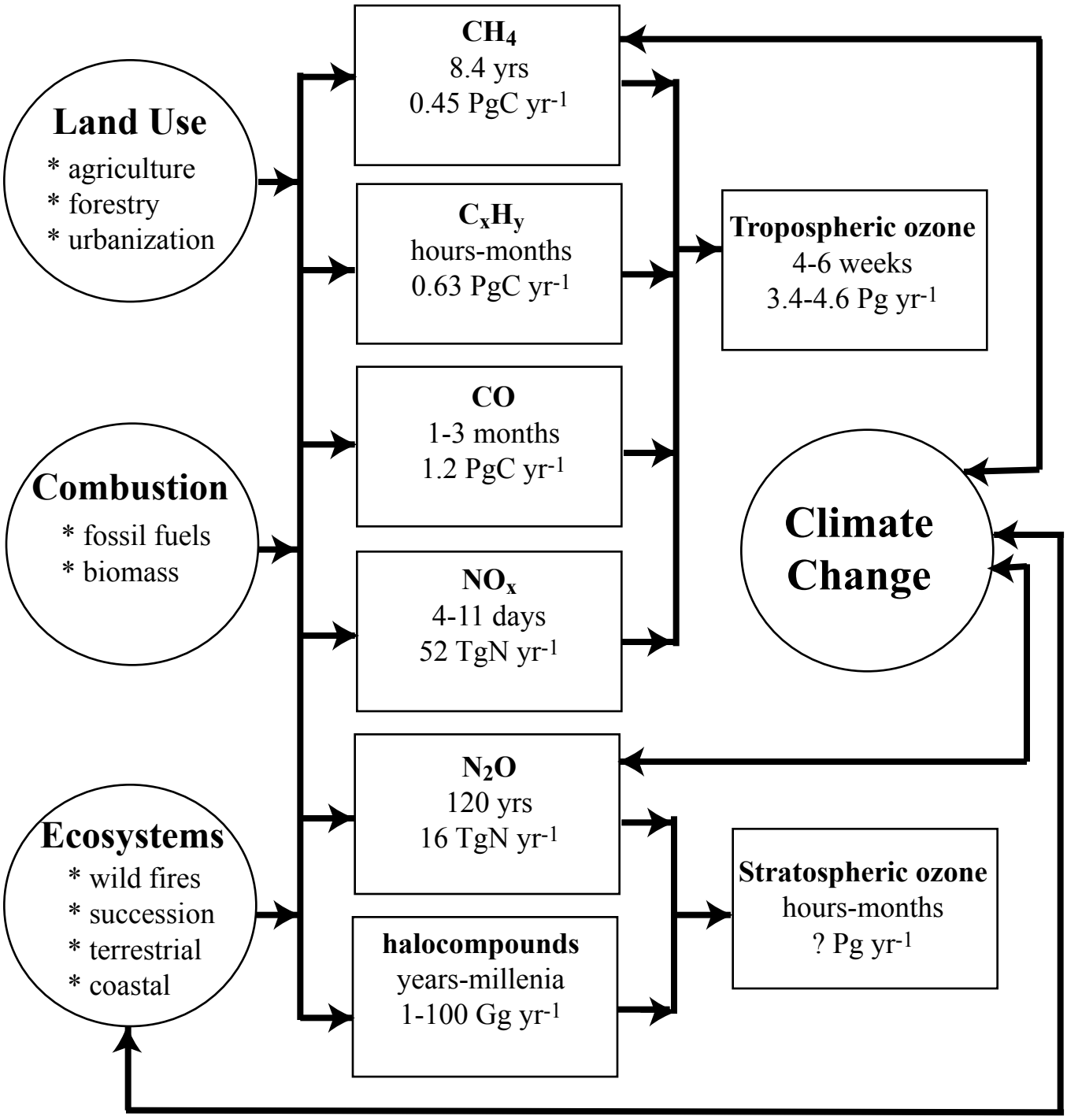
Land Use
* agriculture
* forestry
* urbanization
Combustion
* fossil fuels
* biomass
Ecosystems
* wild fires
* succession
* terrestrial
* coastal
CH4
8.4 yrs
0.45 PgC yr-1
CxHy
hours-months
0.63 PgC yr-1
CO
1-3 months
1.2 PgC yr-1
NOx
4-11 days
52 TgN yr-1
N2O
120 yrs
16 TgN yr-1
halocompounds
years-millenia
1-100 Gg yr-1
Tropospheric ozone
4-6 weeks
3.4-4.6 Pg yr-1
Stratospheric ozone
hours-months
? Pg yr-1
Climate Change

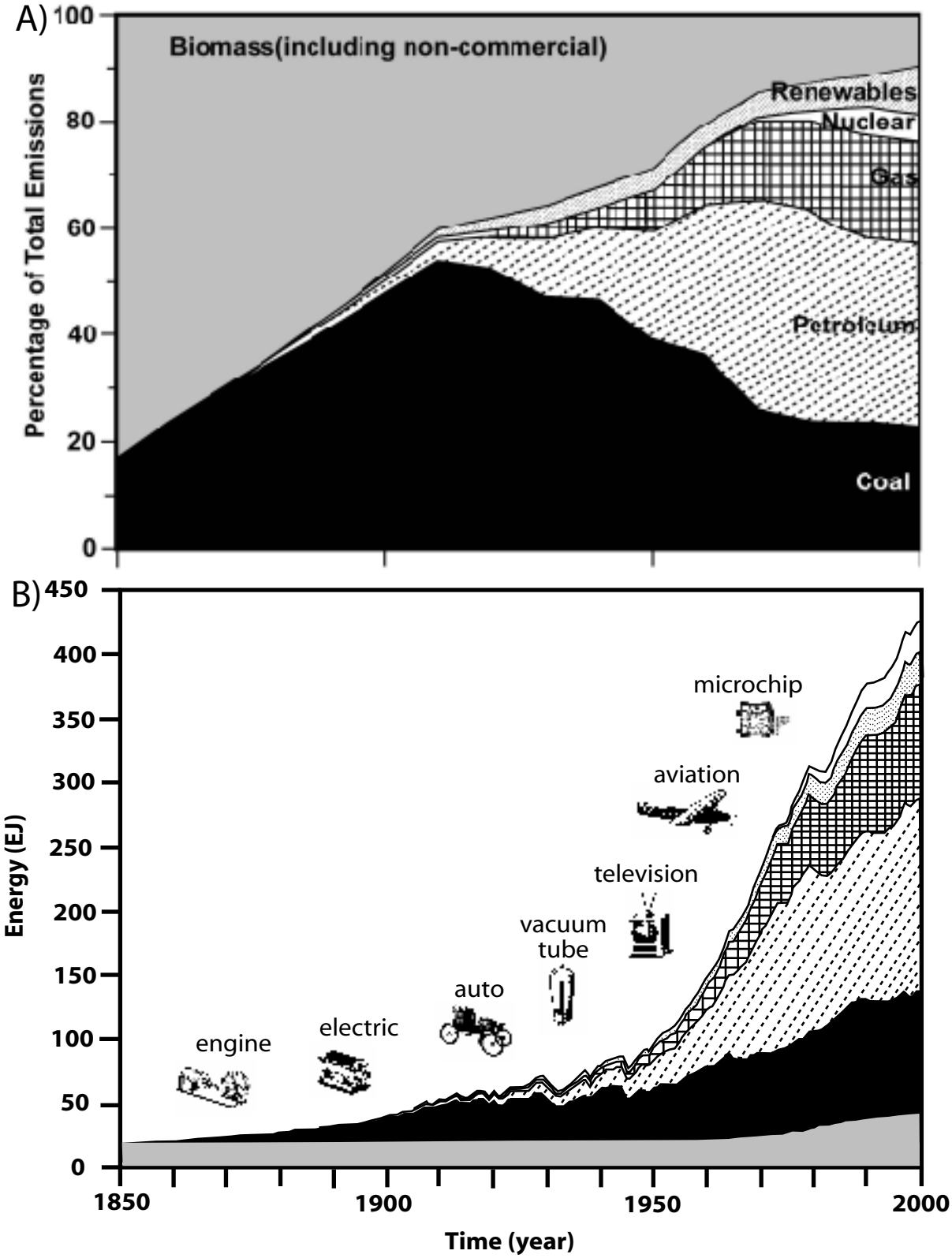
A)
Biomass(including non-commercial)
Renewables
Nuclear
Gas
Petroleum
Coal
Percentage of Total Emissions
100
80
60
40
20
0
B)
Energy (EJ)
450
400
350
300
250
200
150
100
50
0
microchip
aviation
television
vacuum tube
auto
electric
engine
1850
1900
1950
2000
Time (year)

The carbon dioxide system in sea water: equilibrium chemistry and measurements

Andrew G. Dickson

Scripps Institution of Oceanography, University of California, San Diego,
9500 Gilman Drive, La Jolla, CA 92093-0244, USA adickson@ucsd.edu

1 Introduction

The world's oceans can be thought of as a dilute solution of bicarbonate (together with other acid-base species at still lower concentrations) in a salt-water background. In the surface waters of the North Atlantic, for example, the concentration of total dissolved inorganic carbon (the sum of the concentrations of the three coexisting species: bicarbonate ion, carbonate ion, and unionized dissolved carbon dioxide) is only about 2 mmol kg^{-1}. About 90% of this is present as bicarbonate ion, the proportion of carbonate ion is about a factor of 10 less (~10%), and that of unionized carbon dioxide yet another factor of 10 less (<1%). As a result of the equilibria between these various species (see below), sea water is buffered (weakly) with respect to changes in hydrogen ion (present at much lower concentrations: $<10^{-8}$ µmol kg^{-1}).

Accurate measurement of the sea water carbon dioxide system has become a high priority over the last twenty years as scientists have worked to understand just how much of the carbon dioxide (CO_2) created by man's activities has ended up in the ocean, where it is distributed, and how it has changed the chemistry of the oceans. The chemical changes associated with the increase of CO_2 in the oceans are often referred to as *ocean acidification*. As we work to design suitable experiments to understand the biological and ecological consequences of such changes, it is important that the chemistry of CO_2 be well characterized in the various laboratory experiments and field observations that are undertaken. Achieving this requires an understanding of the basic solution chemistry underlying this important process, as well as of the relative merits of the various analytical techniques available to the investigator.

Unfortunately – from the point of view of someone desiring simplicity – in addition to carbon dioxide there are other acid-base systems in sea water that complicate things, particularly in systems that are not typical of the open surface ocean, *i.e.* with low nutrient levels and relatively low amounts of dissolved organic material. The approach I shall take in this section is first to introduce a somewhat simplified view of acid-base chemistry in sea water involving only the primary sea water acid-base systems: carbonic acid, boric acid, and water. These will be discussed in some detail, and used to introduce the classical oceanographic analytical parameters for carbon dioxide studies in sea water: total dissolved inorganic carbon, total alkalinity, pH, and $p(CO_2)$ – the partial pressure of carbon dioxide that is in equilibrium with a water sample. I shall also introduce the concept of calcium carbonate saturation state.

Once this basic sea water chemistry has been presented – and assimilated – it will be appropriate to revisit a number of these topics and to introduce further complexity, so as to indicate how these various concepts can be applied appropriately in the sea water systems that are of interest to investigators in ocean acidification. Finally, I shall present a brief discussion of some of the current (2009) techniques available for the measurement of the various parameters of the sea water carbon dioxide system, and will indicate their advantages and disadvantages. I shall also discuss the advantages and disadvantages of using alternate combinations of parameters to provide a complete description of the composition of a particular sea water sample.

As will become clear, at this time it is not as straightforward as one might wish to characterize the state of a particular sea water sample's carbonate chemistry with a well-constrained

45 measurement uncertainty. Investigators who wish to do high quality work in ocean acidification, but who have little previous experience in sea water CO_2 measurements, would do well to collaborate with a scientist with experience in this area and who has access to a working laboratory that can perform the necessary measurements with the required quality.

2 Basic chemistry of carbon dioxide in sea water

50 2.1 Introduction

Sea water is unique among natural waters in that its relative composition is well defined (see *e.g.*, Millero *et al.*, 2008) and dominated (>99.3% by mass) by a fairly limited number of major ions (Figure 1). The various acid-base species discussed in this section are in the remaining 0.7%, with carbonic acid and boric acid species dominating. As we shall see, this distinction between 55 the *major* ions, that can be considered to make up a background ionic medium, and the various reacting species, that are present at relatively low concentrations, is an important convenience when discussing acid-base chemistry in sea water.

2.2 Acid-base equilibria in sea water

When carbon dioxide dissolves in water, it hydrates to yield carbonic acid, H_2CO_3. This reaction 60 is slow relative to the ionization of H_2CO_3 and it is possible to distinguish between simple dissolved carbon dioxide, $CO_2(aq)$, and the hydrated species, H_2CO_3 (see *e.g.*, Soli & Byrne, 2002). This kinetic process is relevant in some physiological systems and is catalyzed by the enzyme carbonic anhydrase. At equilibrium, the concentration of carbonic acid, $[H_2CO_3]$, is only about $^1/_{1000}$ of the concentration of dissolved carbon dioxide, $[CO_2(aq)]$ and has no special 65 significance to the acid-base equilibria since both are uncharged (Butler, 1998). Here the total concentration of the two unionized species: $[H_2CO_3]$ + $[CO_2(aq)]$, will be abbreviated as the concentration of the hypothetical aqueous species, CO_2^*: $[CO_2^*]$.[1] In acid solutions (pH < 5) CO_2^* is the dominant carbon dioxide species in solution, however at higher pHs it ionizes to form bicarbonate (HCO_3^-) and carbonate (CO_3^{2-}) ions.

70 Thus when carbon dioxide dissolves in sea water it can be considered to react with the water in accordance with the following series of chemical equilibria (Figure 2):

$$CO_2(g) = CO_2^*(aq), \quad (1)$$

$$CO_2^*(aq) + H_2O(l) = H^+(aq) + HCO_3^-(aq), \quad (2)$$

$$HCO_3^-(aq) = H^+(aq) + CO_3^{2-}(aq); \quad (3)$$

75 the notations (g), (l), (aq) refer to the state of the species, *i.e.* a gas, a liquid, or in aqueous solution respectively. Equation (1) refers to the solubility equilibrium of carbon dioxide between air and sea water; equations (2) and (3) are consecutive acid dissociation reactions of dissolved carbon dioxide. Two other important acid-base equilibria in sea water are the dissociation of boric acid and the self-ionization of water:

80

$$B(OH)_3(aq) + H_2O(l) = H^+(aq) + B(OH)_4^-(aq), \quad (4)$$

$$H_2O(l) = H^+(aq) + OH^-(aq). \quad (5)$$

The equilibrium relationships between the concentrations of these various species can then be written in terms of the equilibrium constants:

$$K_0 = [CO_2^*] / f(CO_2), \quad (6)$$

[1] This corresponds to defining the standard states of $CO_2(aq)$ and of H_2CO_3 using the so-called *hydrate convention* (Pitzer, 1961).

$$K_1 = [H^+][HCO_3^-]/[CO_2^*], \quad (7)$$

$$K_2 = [H^+][CO_3^{2-}]/[HCO_3^-], \quad (8)$$

$$K_B = [H^+]\,[B(OH)_4^-]/[B(OH)_3], \quad (9)$$

$$K_W = [H^+]\,[OH^-]. \quad (10)$$

In these equations, $f(CO_2)$ is the fugacity of carbon dioxide in the gas phase (see SOP 24 in Dickson *et al.*, 2007) and brackets represent total stoichiometric concentrations[2] of the particular chemical species enclosed between them, expressed as moles per kilogram of solution. The use of fugacity in equation (6) allows the same equilibrium constant to be used for a wide variety of gas phase compositions (Weiss, 1974). In practice, most applications in ocean acidification studies will involve air containing carbon dioxide that is in equilibrium with the sea water at a total pressure of about 1 atmosphere. This air will thus also contain water vapour that is at its equilibrium concentration (its vapour pressure, approximately). Weiss and Price (1980) defined an alternate relationship, F such that

$$F = [CO_2^*]/x'(CO_2), \quad (11)$$

where $x'(CO_2)$ is the mole fraction of CO_2 present in dry air (*i.e.* after drying to remove the water vapour), and the appropriate corrections for non-ideality have been included implicitly. There are many situations where it is more practical to use this equation directly rather than calculating the correct $f(CO_2)$ value.

These equilibrium constants[3] are functions of the temperature, pressure and salinity of the sea water and have been measured at one atmosphere pressure in a variety of studies (see Millero, 2007). Recommended values are given in Table 1 as a function of salinity and temperature.

2.3 The Saturation State of Calcium Carbonate Minerals in Sea Water

There are three primary biogenic carbonate-containing mineral phases that occur in sea water: aragonite, calcite, and magnesian calcite. Aragonite and calcite are naturally occurring polymorphs of calcium carbonate with differing crystal lattice structures and hence solubilities, aragonite being about 1.5 times more soluble than calcite at 25 °C. Magnesian calcite is a variety of calcite with magnesium ions randomly substituted for the calcium ions in a disordered calcite lattice. At low mole fractions of magnesium (<4%) the solubility of this phase is lower than that of calcite, whereas at high mole fractions (>12%) the solubility is greater than that of aragonite (see Figure 3).

The dissolution equilibria for calcite and aragonite can be written as

$$CaCO_3(s) = Ca^{2+}(aq) + CO_3^{2-}(aq), \quad (12)$$

where (s) indicates the solid phase. The corresponding equilibrium constant is the solubility product

$$K_{sp} = [Ca^{2+}][CO_3^{2-}], \quad (13)$$

---

[2] The *total* stoichiometric concentration of a species is the sum of the concentrations of the *free* species itself, together with the concentrations of all complexes that are formed between that species and the components of the ionic medium (for sea water: H_2O, Na^+, Mg^{2+}, K^+, Ca^{2+}, Cl^-, & SO_4^{2-}).

[3] Strictly, equilibrium expressions such as equations (6) to (10) should be expressed in terms of activities rather than total stoichiometric concentrations in order to be *equilibrium constants*. However, as activity coefficients remain approximately constant for small amounts of reacting species in a background ionic medium, these expressions are valid and correspond to *ionic medium* equilibrium constants where the corresponding standard states are based on a sea water medium of a specified composition (Dickson *et al.*, 1981). Note that the activity of water is assumed to be unity.

where the effect of the different crystal structure of the particular solid phase is now implicit in the solubility product itself. Strictly, aragonite and calcite have different standard Gibbs free energies, thus even when ionic medium standard states are used the solubility products for the two minerals will have different values. It is necessary to indicate the mineral of interest explicitly, *e.g.,*

$$K_{sp}(\text{aragonite}) = [Ca^{2+}][CO_3^{2-}], \quad (14)$$

$$K_{sp}(\text{calcite}) = [Ca^{2+}][CO_3^{2-}]. \quad (15)$$

Clearly these equations cannot both hold true simultaneously. Aragonite is often referred to as a metastable form of calcium carbonate as it is not the form that would be expected at complete thermodynamic equilibrium. Nevertheless it is often convenient to treat the solubility of aragonite in sea water as though it were a stable phase and to apply equation (14) to investigate its saturation state – equation (17) below.

Magnesian calcites can be problematic. Their solubility is not unique, nor do they necessarily form or dissolve congruently (*i.e.*, maintaining the same molar ratio throughout the formation or dissolution process). As a result, they do not really have unique solubility products (see Figure 3). Nevertheless, it is sometimes useful to define *apparent* solubility products for these minerals in sea water (*i.e.*, with essentially fixed proportions of magnesium and calcium ions) as

$$K'_{sp}(\text{mag. calcite}) = [Ca^{2+}][CO_3^{2-}]; \quad (16)$$

the exact value of $K'_{sp}(\text{mag. calcite})$ at any particular salinity and temperature will then depend on the mole fraction of magnesium in the solid (see *e.g.,* Busenberg & Plummer, 1989).

The most common use of such solubility products – particularly in ocean acidification research – is to calculate the saturation state of sea water with respect to a particular calcium carbonate mineral X. The saturation state, $\Omega(X)$, is defined by the expression:

$$\Omega(X) = [Ca^{2+}][CO_3^{2-}] / K_{sp}(X). \quad (17)$$

This expresses the ratio between the observed ion product, $[Ca^{2+}][CO_3^{2-}]$, and its expected value were the solution to be in equilibrium with the particular calcium carbonate mineral. If $\Omega(X) = 1$, the solution is in equilibrium with that mineral phase, if $\Omega(X) > 1$ the solution is supersaturated with respect to that particular mineral phase, and if $\Omega(X) < 1$ it is undersaturated. Insofar as the kinetics of dissolution (and formation) of such minerals have been shown to be functions of saturation state (see *e.g.*, Morse & Arvidson, 2002; Morse *et al.*, 2007) this is a useful parameter for studies of calcification and dissolution.

2.4 Analytical parameters for the carbon dioxide system in sea water

It is usually not practical to measure the individual concentrations of each of these acid-base species in sea water directly so as to get a complete description of the composition of a particular sea water sample. Typically, the concentrations are inferred from a combination of analytical measurements made on the particular sample, together with published values for the various equilibrium constants (Table 1) as well as published information about the boron to salinity ratio of sea water (Table 2).

Salinity and temperature: It is always important to measure salinity and temperature. The various equilibrium constants are all functions of salinity and temperature (see Table 1), and the composition of the solution that is inferred from the various other analytical measurements will depend on these values.

Total dissolved inorganic carbon: The total dissolved inorganic carbon of a sea water sample:

$$C_T = [CO_2^*] + [HCO_3^-] + [CO_3^{2-}], \quad (18)$$

can be measured directly by acidifying the sample, extracting the resulting unionized carbon dioxide, and measuring its amount. The result is expressed in moles per kilogram of solution, and is independent of the temperature (and pressure) of the sample.

Total alkalinity: The total alkalinity of a sample of sea water is a type of mass-conservation expression for hydrogen ion relative to a chosen zero value. For simple, open-ocean surface sea water it can be approximated by the expression:

$$A_T \approx [HCO_3^-] + 2[CO_3^{2-}] + [B(OH)_4^-] + [OH^-] - [H^+]. \quad (19)$$

The total alkalinity of a sea water sample is estimated using some form of acidimetric titration. Again, the result is expressed in moles per kilogram of solution and is independent of the temperature (and pressure) of the sample. Thus although the concentration of each of the individual species making up alkalinity changes when the temperature or pressure changes, the particular linear combination of these concentrations given in equation (19) remains constant.

Hydrogen ion concentration: The hydrogen ion concentration in sea water is reported as a pH:

$$pH = -\lg[H^+]. \quad (20)$$

where $\lg x = \log_{10} x$ (Thompson & Taylor, 2008). Here hydrogen ion concentration is also expressed on a total scale (footnote 2) in moles per kilogram of solution.[4] The pH of a sea water sample can be measured by one of two techniques: a potentiometric technique using an electrode that is sensitive to hydrogen ion together with a suitable reference electrode, and a spectrophotometric technique in which an indicator dye – a dye for which the acid and base forms have different colours – is added to the solution and the pH inferred from the resulting absorbance spectrum. Note that the pH of a particular sample of sea water depends upon its temperature (and pressure). If either of these is changed, the pH will change.

***p*(CO_2):** The partial pressure of carbon dioxide in air in equilibrium with a sea water sample (at a specified temperature). The $p(CO_2)$ of a particular sea water sample is a strong function of temperature, changing about 4.2% per Kelvin.

The partial pressure of a gas in a mixture is given by the expression:

$$p(CO_2) = x(CO_2)\, p\,, \quad (21)$$

where $x(CO_2)$ is the mole fraction of the CO_2 in the gas phase (air), and p is the total pressure. If these are known – usually from direct measurements on the gas phase – it is possible to estimate the corresponding fugacity of CO_2 (see SOP 24 in Dickson *et al.*, 2007). This can then be used with the solubility constant, K_0, in equation (6) to calculate the concentration of dissolved, unionized carbon dioxide, $[CO_2^*]$. The units for fugacity are the same as for pressure, and must correspond to those used to define K_0.

Commonly it is not the $p(CO_2)$ that is measured directly, but rather the mole fraction of CO_2 in air that was in equilibrium with a water sample and which was subsequently dried before measurement. In that case, the function F presented in equation (11) often provides a more convenient way to calculate $[CO_2^*]$ provided that the total pressure is approximately 1 atm. In the inverse case, where sea water is equilibrated with dry air containing a known mole fraction of CO_2 at a total pressure of 1 atm, the same expression may prove useful.

There are a variety of approaches to measuring each of these parameters. At this time, the oceanographic community studying the carbon cycle in the open ocean environment has made available a *Guide to Best Practices for Ocean CO_2 Measurements* (Dickson *et al.*, 2007) that describes the present state-of-the-art techniques for each of these CO_2 parameters.

[4] Strictly pH = –lg {$[H^+]/(\text{mol kg}^{-1})$} so as to allow the taking of the logarithm. This nicety will not be adhered to in this section.

2.5 Calculation of carbon species concentrations in sea water

It is conventional to provide thermodynamic information about acid-base reactions that are written as acid dissociations – equations (2) to (5); however, these are not the only possible ways to write the various reactions. Although it is possible to write many balanced chemical reactions relating the seven individual acid-base species mentioned above (CO_2^*, HCO_3^-, CO_3^{2-}, $B(OH)_3$, $B(OH)_4^-$, H^+ and OH^-), the equilibrium constant for every one of these possible reactions can be calculated from a knowledge of the four simple acid dissociation constants, (7) to (10).

For example, a particularly convenient formulation that encapsulates the equilibrium relationship between the concentrations of the various carbon dioxide species is

$$CO_2^* + CO_3^{2-} + H_2O = 2HCO_3^- : \quad (22)$$

notations in parentheses indicating the state of the various species (g, l, aq, s) are omitted from now on to simplify the various expressions.

An examination of this equation tells us essentially what happens as the dissolved carbon dioxide concentration increases (for example by dissolution of CO_2 from the atmosphere). The additional carbon dioxide reacts with carbonate ion to form bicarbonate ion. The net effect is to increase the concentrations of dissolved carbon dioxide and bicarbonate ion, while decreasing the concentration of carbonate ion. The extent to which this occurs (at any particular salinity and temperature) can be inferred from the equilibrium constant corresponding to reaction (22), which in turn can be derived from equations (7) and (8):

$$K = K_1 / K_2 = [HCO_3^-]^2 / ([CO_2^*][CO_3^{2-}]) . \quad (23)$$

In Figure 4a, I have used equation (22) to construct a contour plot indicating how the concentrations of bicarbonate ion ($[HCO_3^-]$) in sea water media can be viewed as a function of the concentration of dissolved carbon dioxide ($[CO_2^*]$) and of carbonate ion ($[CO_3^{2-}]$) at $S = 35$ and $t = 25$ °C ($T = 298.15$ K). The x-axis is also marked in terms of $f(CO_2)$, which is directly proportional to $[CO_2^*]$ — equation (6).

Another convenient reaction relates carbonate ion directly to the dissolved carbon dioxide:

$$CO_2^* + H_2O = 2H^+ + CO_3^{2-} . \quad (24)$$

The equilibrium constant for this reaction is then the product of K_1 and K_2:

$$K_1K_2 = [H^+]^2[CO_3^{2-}] / [CO_2^*] . \quad (25)$$

Examination of this expression shows that the concentration ratio $[CO_3^{2-}] / [CO_2^*]$ is a function of the hydrogen ion concentration and thus of the pH – equation (20). This is shown in Figure 4b.

If one picks a particular point on these graphs, *i.e.* specifying $[CO_2^*]$ and $[CO_3^{2-}]$, all the other information about the concentrations of the other acid-base species is necessarily defined in terms of the various equilibrium constants (which in turn depend on the salinity and temperature). For example, $[HCO_3^-]$ can be calculated from equation (23) and $[H^+]$ from equation (25). Then once $[H^+]$ is known, $[OH^-]$ can be calculated from equation (10) and the ratio $[B(OH)_4^-] / [B(OH)_3]$ from equation (9). We also know the total boron concentration in the sea water: $[B(OH)_4^-] + [B(OH)_3]$, which varies in direct proportion to the salinity (Table 2), so the individual concentrations of $[B(OH)_4^-]$ and $[B(OH)_3]$ can be estimated. Note too that each of the analytical parameters mentioned above: C_T, A_T, pH, and $p(CO_2)$, can in turn be estimated once these various concentrations are known.

In general therefore, the composition of the carbon dioxide system in any sea water sample is specified completely once one knows the salinity and temperature (and hence the values for all the various equilibrium constants), together with two other concentration-related parameters (in addition to the total boron /salinity ratio). These other concentration-related parameters are

typically chosen from those mentioned above: C_T, A_T, pH, and $p(CO_2)$. The advantages and disadvantages of choosing a particular pair are discussed later in this section.

If one also wishes to estimate the saturation state – equation (17) – with regard to a particular calcium carbonate mineral, in addition to the appropriate solubility product, one also needs the concentration of calcium ion. For unmodified sea waters this too can be estimated from the salinity (Table 2).

There are a variety of programs available to do these calculations. Perhaps the most widely known is CO2SYS which was originally made available as a DOS executable (Lewis & Wallace, 1998), but which is now also available as Excel macros or as MATLAB code at http://cdiac.ornl.gov/oceans/co2rprt.html. Other similar programs are available, for example csys, a series of MATLAB files based on the book by Zeebe & Wolf-Gladrow (2001), is available at http://www.soest.hawaii.edu/oceanography/faculty/zeebe_files/CO2_System_in_Seawater/csys.html; seacarb, a series of routines written in R (Lavigne *et al.*, 2008), is available at http://www.obs-vlfr.fr/~gattuso/seacarb.php; and SWCO2 a package available from Keith Hunter at http://neon.otago.ac.nz/research/mfc/people/keith_hunter/software/swco2/.

When doing such calculations, with or without a standard package, there are two important considerations. First, it is desirable to use the best available values for the equilibrium constants. However, it may not always be clear from a particular program, just which constants have been selected for use. The expressions given in Table 1 are those recommended in the recently published *Guide to Best Practices for Ocean CO_2 Measurements* (Dickson *et al.*, 2007) and are on the *total* hydrogen ion concentration scale. Second, if pH measurements are made, it is essential that the pH be defined in the same way it was for the equilibrium. This is discussed in more detail below.

3 The definition and measurement of pH in sea water

3.1 Introduction

Unfortunately, as noted by Dickson (1984), the field of pH scales and the study of acid-base reactions in sea water is one of the more confused areas of marine chemistry. The primary intent of measuring pH is to use it together with appropriated acid-dissociation constants (and other information – see part 2.5 above) to calculate the speciation of the various acid-base systems in sea water. For a particular acid-dissociation, *e.g.*,

$$HB = H^+ + B^-, \tag{26}$$

the corresponding equilibrium expression can be written in the form

$$pH + \lg K(HB) = \lg\{[B^-]/[HB]\}. \tag{27}$$

If the pH scale is changed, changing the numerical value of pH, the corresponding value of the equilibrium constant must also change, and by the same amount, to ensure that the right hand side of this equation remains constant. It is thus essential that the pH be defined on the same pH scale as that of all acid-dissociation constants that are used with it.

The pH of sea water is best defined in terms of the concentration of hydrogen ion on the total hydrogen ion concentration scale (strictly the activity of hydrogen ion referenced to an *ionic medium* standard state – footnote 3), and that is the approach recommended here. The equilibrium constants recommended in Dickson *et al.* (2007) and provided in this section (Table 1) are also defined using this pH scale.

3.2 The total hydrogen ion concentration scale

A key feature underlying the study of acid-base chemistry in sea water is the (often implicit) use of ionic medium standard states so that it is practical to define equilibrium constants that are based on concentration products, *e.g.,* equations (7) – (10). The pH is defined as

$$\mathrm{pH} = -\lg[\mathrm{H}^+], \tag{20}$$

where the square brackets again imply *total* concentration, that is the sum of the concentration of the *free* species itself, together with the concentrations of all complexes that are formed between that species and the components of the ionic medium (for sea water: H_2O, Na^+, Mg^{2+}, K^+, Ca^{2+}, Cl^-, and SO_4^{2-}).

In the case of hydrogen ion, such complexes occur with water (there are no unhydrated protons present in aqueous solution), and with sulphate ion to form the hydrogen sulphate anion: HSO_4^-. This interaction is usually written as the dissociation:

$$\mathrm{HSO_4^-} = \mathrm{H^+} + \mathrm{SO_4^{2-}}, \tag{28}$$

with the associated equilibrium constant,

$$K_S' = [\mathrm{H^+}]_F[\mathrm{SO_4^{2-}}]/[\mathrm{HSO_4^-}]. \tag{29}$$

The term $[H^+]_F$ indicates that here the hydrogen ion concentration is the *free* concentration (*i.e.*, including only the hydrated forms of the ion), and the prime indicates that the equilibrium constant is defined accordingly. Thus one might expect the total hydrogen ion concentration to be expressed as:

$$[\mathrm{H^+}] = [\mathrm{H^+}]_F + [\mathrm{HSO_4^-}]. \tag{30}$$

Substituting equation (28) in this, gives

$$[\mathrm{H^+}] = [\mathrm{H^+}]_F(1 + [\mathrm{SO_4^{2-}}]/K_S'). \tag{31}$$

The term in parentheses is essentially constant at pH > 5. To ensure that $[H^+] \propto [H^+]_F$ even at lower pHs such as are found in an alkalinity titration or other solutions that have high acid levels, Dickson (1990) proposed that the *total* hydrogen ion scale for sea water be defined as

$$[\mathrm{H^+}] = [\mathrm{H^+}]_F(1 + S_T/K_S'), \tag{32}$$

where S_T is the total amount of sulphate ion present in the sea water and this is the current definition. At pH > 5, equations (31) and (32) are essentially equivalent.

3.3 Measuring total hydrogen ion concentration using a pH cell

The standard potentiometric technique (Dickson, 1993; Dickson *et al.*, 2007) uses the pH cell:

$$\begin{array}{c|c||c|c} \text{reference} \\ \text{electrode} \end{array} \begin{array}{|c} \text{KCl solution} \\ (c \geq 1 \text{ mol dm}^{-3}) \end{array} \begin{array}{||c|} \text{test} \\ \text{solution} \end{array} \begin{array}{|c} \text{electrode reversible} \\ \text{to } \mathrm{H^+(aq)} \end{array}, \tag{A}$$

where typically the electrode reversible to hydrogen ion is a glass electrode, often in a combination format with the associated reference electrode. The pH of a sample is then defined in terms of electromotive force measurements on the sample itself (X) and on a standard buffer solution (S) of assigned pH:

$$\mathrm{pH(X)} = \mathrm{pH(S)} - \frac{E_X - E_S}{RT\ln 10/F}. \tag{33}$$

In this equation pH(X) and pH(S) are the pHs of the sample and standard buffer, respectively; E_X and E_S are the corresponding e.m.f.s obtained with cell (A) on these solutions; T is the measurement temperature (note that both test solution and standard buffer *must* be at the same temperature); and R and F are the gas constant and Faraday, respectively. The primary standard buffer for the measurement of total hydrogen ion concentrations in sea water media is based on 2-amino-2-methyl-1,3-propanediol (Tris) in synthetic sea water, and its pH values are assigned

using Harned cells – cells with hydrogen and silver/silver chloride electrodes (DelValls & Dickson, 1998; Nemzer & Dickson, 1995).

Although it is practical to make up one's own Tris buffers in accordance with the recipe given by Nemzer & Dickson (2005), it is not particularly straightforward and requires some care to ensure values that are in good agreement (0.005) with those published by DelValls & Dickson (1998). It is recommended that such "home-made" buffers be calibrated against a primary standard buffer wherever practical.

A further complication with using such buffers is that, ideally, the salinity of the buffer matches the salinity of the sample being tested. Clearly this is rarely the case, however it has been shown that if the salinity is relatively close (within 5) of the buffer (usually prepared with a nominal salinity of 35), then the likely error is less than 0.01 in pH (Whitfield *et al.*, 1985).

If this electrode-based technique is used to measure pH, the overall uncertainty for the pH measurement is probably less than 0.02 for sea water measurements in the pH range 7.5–8.5, provided that the electrode slope is Nernstian or nearly so (>99%). If the quality of the electrode has not been independently assessed this uncertainty can be larger, but as the pH(S) of Tris buffer is about 8.1, the errors will not be very large within the usual sea water pH range (7.5–8.5).

3.4 Measuring total hydrogen ion concentration using an indicator dye

The spectrophotometric approach to pH measurement involves adding a small amount of a solution of a pH indicator dye to the sea water sample (*e.g.*, Clayton & Byrne, 1993; Dickson *et al.*, 2007). The dye is an acid-base compound such as *m*-cresol purple whose second dissociation:

$$HI^- = H^+ + I^{2-}, \tag{34}$$

occurs at around sea water pH thus ensuring that at sea water pH both species are present in measurable amounts. The expression for the acid-dissociation constant for this dye

$$K(HI^-) = [H^+][I^{2-}]/[HI^-], \tag{35}$$

can be rewritten as

$$pH = -\lg K(HI^-) + \lg\{[I^{2-}]/[HI^-]\}. \tag{36}$$

The spectrophotometric approach uses the fact that the acid and base forms of the indicator have substantially different absorbance spectra. Thus the information contained in the spectrum for the indicator dye in the sea water solution contains sufficient information to estimate the second term on the right hand side of equation (36). The total absorbance at a particular wavelength λ,

$$A_\lambda = \varepsilon_\lambda(HI^-)[HI^-] + \varepsilon_\lambda(I^{2-})[I^{2-}], \tag{37}$$

where $\varepsilon_\lambda(HI^-)$ and $\varepsilon_\lambda(I^{2-})$ are the extinction coefficients at that wavelength of the acid and base forms of the dye, respectively.

Typically absorbance information from two wavelengths (1) and (2) suffices to compute the pH:

$$pH = -\lg K(HI^-) + \lg\left(\frac{A_1/A_2 - \varepsilon_1(HI^-)/\varepsilon_2(HI^-)}{\varepsilon_1(I^{2-})/\varepsilon_1(HI^-) - (A_1/A)\varepsilon_2(I^{2-})/\varepsilon_2(HI^-)}\right). \tag{38}$$

These two wavelengths are usually chosen to correspond to the absorbance maxima for the base (1) and acid (2) forms of the dye. This choice of wavelengths is at once the most sensitive as well as forgiving of minor deviations in wavelength reproducibility. The properties of the indicator dye *m*-cresol purple: equilibrium constant[5] and extinction coefficient ratios, have been described

[5] The paper of DelValls & Dickson (1998) suggests that the buffer used by Clayton & Byrne (1993) to estimate $K(HI^-)$ may have been assigned an inappropriate pH. This has not yet been confirmed. Recent work in my laboratory, however, suggests an additional systematic error may largely counteract the proposed original error.

by Clayton & Byrne (1993). This method is also calibrated by assigning the value of $K(\mathrm{HI}^-)$, in solutions of known $[\mathrm{H}^+]$, ideally using primary standard buffers certified using a Harned Cell.

For the most accurate measurements, it is also important to allow for the pH change contributed by the dye solution (Clayton & Byrne, 1993; Dickson *et al.*, 2007). This is usually minimized by adjusting the pH of that solution to be similar to that of the samples being measured. Unfortunately, it has also been suggested recently that these dyes, when obtained commercially, may have small amounts of coloured impurities that can vary from lot to lot. This will affect the apparent extinction coefficient ratios and can contribute as much as 0.01 to the overall uncertainty of the resulting pH data (Yao *et al.*, 2007). Thus the appropriate overall uncertainty estimate for spectrophotometric pH measurements is probably about 0.01 in pH.

3.5 Other pH scales (that are not recommended for use)

Two other pH scales have been used for sea water measurements in the past:

1. The so-called NBS scale (more correctly now referred to as the IUPAC scale) was based originally on recommendations and primary buffer standards from the US National Bureau of Standards (NBS), renamed the National Institute of Standards and Technology in 1988.
2. The Sea Water pH scale (SWS) which includes fluoride ion in the ionic medium (in addition to sulphate) and thus includes the species HF in the definition of the SWS hydrogen ion concentration:

$$[\mathrm{H}^+]_{\mathrm{SWS}} = [\mathrm{H}^+]_{\mathrm{F}} + [\mathrm{HSO}_4^-] + [\mathrm{HF}], \tag{39}$$

or, more strictly,

$$[\mathrm{H}^+]_{\mathrm{SWS}} = [\mathrm{H}^+]_{\mathrm{F}}(1 + S_{\mathrm{T}} / K'_{\mathrm{S}} + F_{\mathrm{T}} / K'_{\mathrm{F}}), \tag{40}$$

where F_{T} is the total concentration of fluoride ion in the sea water, and is known as the hydrogen ion concentration on the sea water scale (SWS) and K'_{F} is the dissociation constant for HF with hydrogen ion concentration expressed as the *free* concentration.

The uncertainty inherent in using the IUPAC scale for sea water measurements may be as large as 0.05 in pH, even for careful measurements. For the seawater scale, the errors will be approximately the same as for the total scale, provided that measurements are made in a similar fashion. It will however be important to assure oneself that indeed the standard buffer or the indicator dye's pK have been assigned values on this scale. Note that if it is necessary to calculate the amount of hydrogen fluoride in a particular sample, it can be estimated from knowledge of the total hydrogen ion concentration, the total fluoride concentration (proportional to salinity) and the corresponding equilibrium constant.

Whatever pH scale is employed, it is essential that it be used with equilibrium constants defined on the same scale. If one were to use pH measurements on the IUPAC scale with the constants of Table 1 (on the total hydrogen ion scale) an additional systematic error of about 0.15 pH units would be incurred at 25 °C (pH ≈ pH(NBS) – 0.15). For sea water scale pH measurements, the error is about 0.01 units (pH ≈ pH(SWS) + 0.01).

4 Implications of other acid-base equilibria in sea water on sea water alkalinity

4.1 Natural sea water

In addition to the various species detailed above, *i.e.* those from carbon dioxide, boric acid or water, natural sea water can contain a number of other acid-base species in significant amounts. The most common are a variety of minor nutrient species that also have acid-base behaviour (*e.g.*, silicate, phosphate, and ammonia):

$$\mathrm{Si(OH)_4 = H^+ + SiO(OH)_3^-}, \quad (41)$$

$$\mathrm{H_3PO_4 = H^+ + H_2PO_4^- = 2H^+ + HPO_4^{2-} = 3H^+ + PO_4^{3-}}, \quad (42)$$

$$\mathrm{NH_4^+ = H^+ + NH_3}. \quad (43)$$

The dissociation constants for these various equilibria are thus

$$K_{\mathrm{Si}} = [\mathrm{H^+}][\mathrm{SiO(OH)_3^-}]/[\mathrm{Si(OH)_4}], \quad (44)$$

$$K_{1\mathrm{P}} = [\mathrm{H^+}][\mathrm{H_2PO_4^-}]/[\mathrm{H_3PO_4}], \quad (45)$$

$$K_{2\mathrm{P}} = [\mathrm{H^+}][\mathrm{HPO_4^{2-}}]/[\mathrm{H_2PO_4^-}], \quad (46)$$

$$K_{3\mathrm{P}} = [\mathrm{H^+}][\mathrm{PO_4^{3-}}]/[\mathrm{HPO_4^{2-}}], \quad (47)$$

$$K_{\mathrm{NH3}} = [\mathrm{H^+}][\mathrm{NH_3}]/[\mathrm{NH_4^+}]. \quad (48)$$

Although ammonia is typically present at very low amounts (< 1 μmol $\mathrm{kg^{-1}}$) in oxygenated sea water and usually be ignored, the other species are present at significant concentrations in deep water, and can be upwelled to the surface in various regions. In addition, there is the potential for additional organic acid-base species to be present, especially in enclosed systems with significant biological activity (Hernández-Ayon *et al*., 2007; Kim & Lee, 2009).

The net effect is to add additional species into the expression for the total alkalinity of sea water which is rigorously defined (Dickson, 1981) as "... the number of moles of hydrogen ion equivalent to the excess of proton acceptors (bases formed from weak acids with a dissociation constant $K \le 10^{-4.5}$ at 25 °C and zero ionic strength) over proton donors (acids with $K > 10^{-4.5}$) in 1 kilogram of sample." Thus

$$\begin{aligned} A_{\mathrm{T}} = {} & [\mathrm{HCO_3^-}] + 2[\mathrm{CO_3^{2-}}] + [\mathrm{B(OH)_4^-}] + [\mathrm{OH^-}] + [\mathrm{HPO_4^{2-}}] \\ & + 2[\mathrm{PO_4^{3-}}] + [\mathrm{SiO(OH)_3^-}] + [\mathrm{NH_3}] + [\mathrm{HS^-}] + \ldots \\ & - [\mathrm{H^+}]_{\mathrm{F}} - [\mathrm{HSO_4^-}] - [\mathrm{HF}] - [\mathrm{H_3PO_4}] - \ldots \end{aligned} \quad (49)$$

where the ellipses stand for additional minor acid or base species that are either unidentified or present in such small amounts that they can be safely neglected. $[\mathrm{H^+}]_{\mathrm{F}}$ is the *free* concentration of hydrogen ion. (Wolf-Gladrow *et al.* (2007) provide a detailed discussion of the origins of this expression and its application to biogeochemical processes.)

For natural sea water these additional components do not usually complicate the *measurement* of total alkalinity, the value of which can be determined fairly accurately even if the existence of such species is ignored. However, it will affect significantly the *use* of this measured total alkalinity in inferring the composition of the sea water solution (part 2.5). One way to think about this is to consider how much each acid-base system contributes to the total alkalinity of a particular sample. Thus the "phosphate alkalinity" ($[\mathrm{HPO_4^{2-}}] + 2[\mathrm{PO_4^{3-}}] - [\mathrm{H_3PO_4}]$)in most samples (pH range 7–8) is approximately equal to the total concentration of phosphate in the sample, whereas for silicate the "silicate alkalinity" ($[\mathrm{SiO(OH)_3^-}]$) depends strongly on pH, and at pH 8 will be about 3% of the total silicate concentration (less at lower pHs). Ignoring such contributions from these minor acid-base systems is thus equivalent to the alkalinity value being in error by the corresponding amount.

Essentially any computation involving alkalinity requires that (as with borate) that the total concentrations and the various equilibrium constants of all these other acid base systems be known so that they can be accounted for (see Table 2). If they are not well known there will be an inherent uncertainty in the computed speciation. In the case of substantial organic contributions to the alkalinity such information may well not be available, and total alkalinity, though measurable, may not be fully interpretable.

4.2 Modified sea water media – implications for alkalinity

Often when culturing organisms in the laboratory, it will be usual to have high concentrations of these nutrient species (and possibly of ammonia and of various organic acid-base species). If this is indeed the case, it is unlikely that measurements of alkalinity will provide the information desired about the sample's carbon dioxide speciation without significant (and possibly a prohibitive amount of) extra work. This is particularly true if other acid-base species are deliberately added to the culture medium (for example the use of HEPES to control pH). It will then almost certainly be impossible to infer anything useful from an alkalinity measurement and other techniques must be used.

5 Choosing the appropriate measurement techniques

5.1 Introduction

As was discussed in part 2.5, there are no analytical methods that measure directly the individual concentrations of all the various acid-base species that are present in sea water. These concentrations are usually inferred from measurements of salinity, temperature, and at least two of the analytical parameters introduced in part 2.4 in addition to the various other equilibrium constants, *etc*. The question for an investigator then becomes: which two parameters should I choose to measure? Furthermore, what measurement techniques should I use to estimate them?

A key aspect of making appropriate choices is that the measurements chosen be *fit for purpose*, that is, able to achieve the goals: uncertainty, convenience, speed, cost, *etc*., of the ocean acidification study being undertaken. An important first step is to define clearly the purpose for which the measurements are being made and to specify the associated constraints on the uncertainty required of the analytical measurements as well as other necessary considerations.

5.2 Available measurement techniques

In the 1990s a group of US investigators decided to document the techniques that they were using for open ocean studies of the carbon dioxide system in sea water. The resulting Handbook (DOE, 1994) was made available through CDIAC as a printed book, as well as electronically. Recently an effort was made to update this information. This resulting document was published as the *Guide to Best Practices for Ocean CO_2 Measurements* (Dickson *et al.*, 2007) by PICES with additional sponsorship from SCOR, IOC, and US DOE (CDIAC); it is available on the web at: http://cdiac.ornl.gov/oceans/Handbook_2007.html.

This *Guide* provides detailed standard operating procedures for each of the current state-of-the-art techniques for measuring the various parameters of the sea water carbon dioxide system. Unfortunately, none of these techniques can be described as routine. Each requires trained analytical staff to perform the technique described, and much of the instrumentation described in the *Guide* is not commercially available. In fact most such instrumentation in use is, to some degree or another, "home-built" and it involves a significant cost to acquire (or build) a working instrument (including the necessary training of personnel). Furthermore, these instruments have not usually been optimized for ease of use or even ease of maintenance.

Also, the combined standard uncertainty of these various techniques has – as yet – not been evaluated fully, but it is fair to say that on the whole the techniques detailed in the *Guide* are aimed at getting the best possible quality of measurement data for the carbon dioxide system in sea water. Furthermore, many of them have been used extensively in multiple laboratories and there is – within the user community – a reasonable understanding of their uncertainty, as well as of their advantages and disadvantages.

In addition to the techniques outlined in the *Guide*, a few other approaches (see Table 3) are worthy of consideration as being of appropriate quality for ocean acidification studies while being – perhaps – more cost-effective. Instrumentation for some of these techniques is now available commercially (typically from individual scientists who have established companies to build and sell such instrumentation), but – as a result of the limited market for such instrumentation – none of them is available as a "turnkey" system, nor is there a well-developed support infrastructure providing the necessary training or instrument servicing. Furthermore, at this time such techniques have rarely been described with the level of detail outlined in the *Guide* nor have they been independently and rigorously tested.

In Table 4, I provide estimates of the measurement uncertainty for the various primary analytical parameters. These are only for guidance, the magnitudes of these uncertainties depend not only on the measurement technique employed, but also on the metrological traceability of the measured results, as well as on the implementation of the technique in a particular laboratory (skill of analysts, quality assurance program, *etc.*); thus the measurement uncertainty value should be estimated separately by each individual laboratory.

5.3 Quality assurance of measurements

Quality assurance constitutes the system by which an analytical laboratory can assure outside users that the analytical results they produce are of proven and known quality (Dux, 1990). A formal quality assurance program will be required for the carbon dioxide measurements performed in association with ocean acidification studies. A quality assurance program consist of two separate related activities (Taylor, 1987):

Quality control: The overall system of activities whose purpose is to control the quality of a measurement so that it meets the needs of users. The aim is to ensure that data generated are of known accuracy to some stated, quantitative, degree of probability, and thus provides quality that is satisfactory, dependable, and economic.

Quality assessment: The overall system of activities whose purpose is to provide assurance that quality control is being done effectively. It provides a continuing evaluation of the quality of the analyses and of the performance of the associated analytical systems.

These are discussed in detail in the books of Taylor (1987) and of Dux (1990), and a brief description appropriate to ocean carbon dioxide measurements is given in Chapter 3 of Dickson *et al.* (2007). In particular, effective quality control requires at a minimum the following:

- Suitable and properly maintained equipment and facilities,
- Well documented measurement procedures (SOPs),
- Regular and appropriate use of reference materials to evaluate measurement performance,
- Appropriate documentation of measurements and associated quality control information.

As noted above, regular use of reference materials is the preferred approach to evaluating measurement quality. Reference materials are stable substances for which one or more properties are established sufficiently well to calibrate a chemical analyzer or to validate a measurement process (Taylor, 1987). Ideally, such materials are based on a matrix similar to that of the samples of interest, in this case sea water. The most useful reference materials are those for which one or more of the properties have been *certified* as accurate, preferably by the use of a definitive method in the hands of two or more analysts.

The US National Science Foundation has, since 1988, supported my laboratory at the Scripps Institution of Oceanography to produce and distribute such reference materials for the quality control of ocean CO_2 measurements (see Table 5). They should be used regularly to ensure the quality of measurements performed in support of ocean acidification studies.

5.4 Error propagation and its implications

Although, mathematically (in a system without any uncertainties) the use of different combinations of analytical parameters should provide equivalent information, in practice that is not the case. The inherent measurement uncertainties propagate through all further computations aimed at estimating other aspects of the carbon dioxide system in a particular sea water sample. Furthermore such results will include additional measurement uncertainties associated with the various equilibrium constants, and with other information such as the boron/salinity ratio, the total concentration of phosphate, *etc.*

The general relationship between the combined standard uncertainty $u_c(y(x_1,x_2,\ldots,x_n))$ of a value y and the uncertainties of the independent parameters $x_1,x_2,\ldots,x_n$ on which it depends is:

$$u_c(y(x_1,x_2,\ldots,x_n)) = \sqrt{\sum_{i=1,n}\left(\frac{\partial y}{\partial x_i}\right)^2 u(x_i)^2} \qquad (50)$$

where $y(x_1,x_2,\ldots,x_n)$ is a function of several parameters (Ellison *et al.*, 2000), and $u(x_i)$ is the uncertainty in x_i. The various partial derivatives $(\partial y / \partial x_i)$ can be estimated either algebraically (where convenient) or numerically. This is the approach that should be used to estimate the combined measurement uncertainty of an analytical measurement (see Ellison *et al.*, 2000).

In the case of the calculation of some aspect of the carbonate system (*e.g.*, $[CO_3^{2-}]$) from various combinations of the possible analytical parameters, alternate approaches are *not* necessarily equivalent. Dickson and Riley (1978) first pointed out the implications of uncertainties in the various analytical parameters (and in the equilibrium constants) in detail. They chose to rewrite equation (50) in terms of the *relative uncertainties*:

$$\frac{u_c(y(x_1,x_2,\ldots,x_n))}{y} = \sqrt{\sum_{i=1,n}\left(\frac{\partial y}{y}\Big/\frac{\partial x_i}{x_i}\right)^2\left(\frac{u(x_i)}{x_i}\right)^2}\ , \qquad (51)$$

and their Table II provides values of the sensitivity coefficients $\{(\partial y / y)/(\partial x_i / x_i)\}$ for a surface sea water. It is important to note that the values of these sensitivity coefficients, and similarly of the partial differentials $(\partial y / \partial x_i)$, are not constant but depend on the approximate composition of the sea water itself. For particular ocean acidification experiments (whose CO_2 levels are likely to be significantly different from that of the sea waters used in Dickson and Riley) one should plan to estimate them numerically using a program such as CO2SYS.

The uncertainties in the values of the equilibrium constants and other ancillary data such as the boron to salinity ratio are often forgotten. Furthermore, it is usually not straightforward to use CO2SYS (or other easily available software) to estimate the likely contribution of these additional uncertainties. In that case, values provided by Dickson and Riley (1978) provide reasonable estimates of the sensitivity coefficients with respect to K_1 and K_2 (except perhaps when using the measurement pair A_T and C_T).

The principal difficulty in performing a rigorous error propagation to estimate the overall uncertainty of, for example, saturation state is that it is often not straightforward to obtain the necessary information about the uncertainties $u(x_i)$ of the various input data. The marine chemistry community has rarely attempted to estimate the combined standard uncertainty for the various measurement techniques discussed here, instead usually providing only precision information, and then often only data obtained under repeatability conditions, *i.e.* the variability within a single laboratory, over a short time, using a single operator, item of equipment, *etc.* This is necessarily a lot smaller than the combined standard uncertainty for a particular measurement technique (Ellison *et al.*, 2000). Table 4 provides (my personal) estimates of the measurement uncertainties associated with the various parameters. Table 6 uses these values, together with the

sensitivity coefficients estimated by Dickson and Riley (1978) to calculate the relative uncertainties of $[CO_2^*]$ and $[CO_3^{2-}]$ resulting from the various possible pairs of parameters.

As can be seen, the likely relative uncertainty in estimating the concentration of unionized CO_2: $[CO_2^*]$, is always smallest if $p(CO_2)$ is measured directly, and is otherwise of a approximately similar magnitude whichever parameter pair is chosen. Also, the relative uncertainty in $[CO_3^{2-}]$ (or saturation state) is similar for different combinations, with the exception of pH and $p(CO_2)$ where it is twice as large.

5.5 Advantages (and disadvantages) of different parameters

There are a variety of possible metrics for choosing suitable parameter combinations to characterize the sea water composition in an ocean acidification experiment. At present, it is – I feel – fair to say that there is not really an *optimal* choice of parameters. Here I briefly summarize the advantages and disadvantages of each parameter (prices are for 2009 and expressed in US dollars).

Total alkalinity: Equipment for this measurement can be purchased for $10,000–20,000. It is relatively straightforward to use, though troubleshooting can be problematic. It typically has a stable calibration, and reference materials are available. Samples are easy to handle, as gas exchange is not typically a problem. The lowest uncertainty is obtained with sample sizes of about 100 mL, although it is practical to titrate samples that are as small as 15 mL without much difficulty. An analysis takes about 10–15 minutes in all. The most obvious disadvantage is that it is more difficult to interpret alkalinity accurately in samples with high concentrations of nutrients or of dissolved organic material.

Total dissolved inorganic carbon: Equipment for this measurement (using the infra-red technique) can be purchased for $40,000–50,000. It is relatively straightforward to use and quite quick (~10 min per sample), however the calibration is, in many cases, achieved using reference materials and is not highly stable. The sample size needed for analysis is small (<10 mL), however samples must be protected from gas exchange, particularly at higher $p(CO_2)$. Reference materials are available.

pH: Equipment for spectrophotometric pH measurement can be obtained for <$20,000. The procedure is relatively straightforward, and capable of some automation. It is necessary to minimize gas exchange when handling samples. The most obvious disadvantage at this time is the need for concern about the dye purity (Yao & Byrne, 2007) which causes the measurement uncertainty to be about 10 times its reproducibility. At this time, there are only limited amounts of pH reference materials available, though I hope my lab will be able to supply them in larger quantities in the future.

***p*(CO_2):** Equipment for this measurement is typically quite expensive (~$50,000). It usually requires a flowing stream of sea water and is calibrated using cylinders of air with known CO_2 levels. It is cumbersome to set up, but can be relatively straightforward to use once running. One advantage is that such systems are usually designed to run autonomously.

At this time only pH and $p(CO_2)$ can be used for continuous measurement allowing relatively straightforward monitoring of an experiment over time. However, if the experiment is arranged such that the alkalinity of the sea water remains constant (or nearly so), one need only monitor one of these continually, though it will be desirable to measure two parameters explicitly on any discrete samples taken to characterize the experiment.

At this time, I believe that the best combination of parameters for studying the CO_2 system in open ocean water is probably total alkalinity and total carbon. It is straightforward to collect and preserve samples for later analysis, the equipment is reasonably readily available, and reference

materials are also available to ensure metrological traceability. Also, there will be a close link to the extensive set of open-ocean studies that have been, and will be performed in the future.

Nevertheless, there are occasions when an alkalinity measurement will be difficult to interpret. In that case, I believe that the optimal combination of parameters is pH (measured spectrophotometrically) and total dissolved inorganic carbon (measured using infra-red). These two parameters allow a description of the CO_2 system alone (without concern as to other co-existing acid-base systems), equipment for making the measurements is available, and reference materials are also available (though pH reference materials are in shorter supply). This pair can also be applied to study normal sea waters and may well be the best all-round choice.

6 Conclusions and recommendations

As can be seen from the extensive discussion above, sea water acid base chemistry is necessarily complicated. It involves a variety of different acid-base species in addition to the three forms of carbon dioxide: dissolved carbon dioxide, bicarbonate ion, and carbonate ion. Although care has gone into defining and measuring the various equilibrium constants, the uncertainty of these is still discussed extensively (see for example Millero, 1995; Millero *et al.*, 2006).

At present there are four parameters that can be reliably measured for the sea water carbon dioxide system (A_T. C_T, pH, $p(CO_2)$), and one of these, pH, has multiple possible definitions which in turn can result in multiple values for acid-dissociation constants (Dickson, 1984). This section follows the recommendation of the original *Handbook of Methods* . . . (DOE, 1994) and of the more recent *Guide* . . . (Dickson *et al.*, 2007) and recommends use of the so-called *total hydrogen ion concentration scale* to define pH in sea water media. Values of equilibrium constants that correspond to this pH scale are given in Table 1.

The various equilibrium and mass-balance equations that describe the acid-base chemistry of seawater comprise a set of equations with a limited number of linearly independent variables (the rank of the system of equations). It is possible to obtain a complete description of the acid-base composition of a seawater sample at a particular temperature and pressure provided the following is known:

- The salinity and temperature, and hence the solubility constant of carbon dioxide in the sea water as well as the equilibrium constant for each of the acid dissociation reactions that is assumed to exist in the solution,
- The total concentrations for each of these non-CO_2 acid-base systems,
- The values for at least two of the CO_2-related parameters: A_T , C_T , pH, $p(CO_2)$.

At this time, the analytical methods described in the *Guide* . . . (Dickson *et al.*, 2007) are presently the best understood and have the lowest uncertainty. For studies on natural sea water, my recommendation would be to measure A_T and C_T (as samples for these can be preserved easily and the measurements made with low uncertainty). However, as was noted above, there may be samples from ocean acidification experiments where it is not possible to fully interpret an alkalinity measurement. In such cases, it is probably best to measure pH and C_T and this combination is also acceptable for the study of ocean acidification in natural sea waters. However, in that case the uncertainty of the calculated parameters is typically dominated by the uncertainty in the (spectrophotometric) pH measurement, and a total carbon value obtained using a simpler system (such as one based on infra-red measurement) is ideal.

Nevertheless, it is not – as yet – straightforward to make accurate measurements of sea water CO_2 parameters. Most of the methods require trained analysts, and in many cases equipment is not easily available. At this time, it is probably desirable for individuals studying ocean acidification to plan to work closely with a scientist with a good understanding of sea water acid-

base chemistry and with access to a working laboratory that can perform the necessary measurements. Alternately, it may be practical to send samples to a central laboratory for analysis provided that such a laboratory has an appropriate quality assurance program in place, and can provide the results in a timely fashion.

As we move into the future, we need to develop robust analytical techniques that can be used conveniently for ocean acidification studies (involving in many cases smaller samples than are typical for open ocean studies). Although some such techniques already exist (Table 3), they still require additional efforts to document them effectively and to establish a community-wide quality assurance scheme for each technique. Such a scheme will involve:

1. Writing appropriate Standard Operating Procedures for the techniques in use,
2. Interlaboratory comparison exercises to assess the various figures of merit for each technique (trueness and precision),
3. Regular use of certified reference materials to assist in the quality control,
4. Regular laboratory performance testing using blind samples.

To date it is fair to state that few ocean acidification experiments have been conducted where scrupulous care has been directed at the – apparently straightforward – task of measuring the associated carbon dioxide chemistry. Although this may well not be the largest source of uncertainty in such experiments, it is appropriate to plan to control it effectively.

7 References

Buck, R.P., Rondini, S., Covington, A.K., Baucke, F.G.K., Brett, C.M.A., Camoes, M.F., Milton, M.J.T., Mussini, T., Naumann, R., Pratt, K.W., Spitzer, P., & Wilson, G.S., 2002. Measurement of pH. Definition, standards, and procedures. *Pure and Applied Chemistry* **74**:2169–2200.

Busenberg, E. & Plummer, L.N., 1989. Thermodynamics of magnesian calcite solid-solutions at 25 °C and 1 atm total pressure. *Geochimica et Cosmochimica Acta* **53**: 1189–1208.

Butler, J.N., 1998. *Ionic equilibrium: solubility and pH calculations*. (with a Chapter by D.R. Cogley), Wiley-Interscience, New York, 559 pp.

Clayton, T.D., & Byrne, R.H., 1993. Spectrophotometric pH measurements: total hydrogen ion concentration scale calibration of *m*-cresol purple and at-sea results. *Deep-Sea Research I* **40**: 2115–2129.

DelValls, T. A. & Dickson, A. G., 1998. The pH of buffers based on 2-amino-2-hydroxymethyl-1,3-propanediol ('tris') in synthetic sea water. *Deep-Sea Research I* **45**, 1541–1554.

Dickson, A.G., 1981. An exact definition of total alkalinity and a procedure for the estimation of alkalinity and total inorganic carbon from titration data. *Deep-Sea Research* **28A**: 609–623.

Dickson, A.G., 1984. pH scales and proton-transfer reactions in saline media such as sea water. *Geochimica et Cosmochimica Acta* **48**: 2299–2308.

Dickson, A.G., 1993. The measurement of sea water pH. *Marine Chemistry* **44**: 131–142

Dickson, A.G. & Riley, J.P., 1978. The effect of analytical error on the evaluation of the components of the aquatic carbon-dioxide system. *Marine Chemistry* **6**: 77–85.

Dickson, A.G. & Riley, J.P., 1979. The estimation of acid dissociation constants in seawater media from potentiometric titrations with strong base. I. The ionic product of water (K_W). *Marine Chemistry* **7**: 89–99.

Dickson, A.G., Whitfield, M. & Turner, D.R., 1981. Concentration products: their definition, use and validity as stability constants. *Marine Chemistry* **10**: 559–565.

Dickson, A.G., Afghan, J.D. and Anderson, G.C. 2003. Reference materials for oceanic CO_2 analysis: a method for the certification of total alkalinity. *Marine Chemistry* **80**: 185–197.

Dickson, A.G., Sabine, C.L. and Christian, J.R. (Eds.) 2007. Guide to Best Practices for Ocean CO_2 Measurements. *PICES Special Publication 3*, 191 pp.

DOE, 1994. *Handbook of methods for the analysis of the various parameters of the carbon dioxide system in sea water; version 2.* A.G. Dickson & C. Goyet, eds., ORNL/CDIAC-74.

Dux, J.P., 1990. *Handbook of quality assurance for the analytical chemistry laboratory.* 2nd edn., Van Nostrand Reinhold, New York. 203 pp.

Ellison, S.L.R., Rosslein, M. & Williams, A., 2000. *EURACHEM/CITAC Guide: Quantifying uncertainty in analytical measurement. (2nd Edn).* EURACHEM. 120 pp.

Goyet, C. & Snover, A.K., 1993. High-accuracy measurements of total dissolved inorganic carbon in the ocean: comparison of alternate detection methods. *Marine Chemistry* **44**: 235–242.

Hernández-Ayón, J.M., Zirino, A., Dickson, A.G., Camiro-Vargas, T., & Valenzuela, E., 2007. Estimating the contribution of organic bases from microalgae to the titration alkalinity in coastal seawaters. *Limnology & Oceanography, Methods* **5**: 225–232.

Kim, H.-C. & Lee, K., 2009. Significant contribution of dissolved organic matter to seawater alkalinity. *Geophysical Research Letters* **36** doi:10.1029/2009GL040271 (in press).

Lavigne, H., Proye, A., & Gattuso, J.-P., 2008. Seacarb: calculates parameters of the seawater carbonate system. R Package 2.2 (portions of code were contributed by J.-M. Epitalon, A. Hofmann, B. Gentili, J. Orr & K. Soetart). http://www.obs-vlfr.fr/~gattuso/seacarb.php

Lewis, E., & Wallace, D.W.R., 1998. Program Developed for CO_2 System Calculations. ORNL/CDIAC-105. Carbon Dioxide Information Analysis Center, Oak Ridge National Laboratory, U.S. Department of Energy, Oak Ridge, Tennessee.

Mehrbach, C., Culberson, C.H., Hawley, J.E., & Pytkowicz, R.M., 1973. Measurement of the apparent dissociation constants of carbonic acid in seawater at atmospheric pressure. *Limnology & Oceanography* **18**: 897–907.

Morse, J.W., 2007. Calcium carbonate formation and dissolution. *Chemical Reviews* **107**: 342–381

Morse, J.W. & Arvidson, R.S., 2002. The dissolution kinetics of major sedimentary carbonate minerals. *Earth-Science Reviews* **58**: 51–84.

Millero, F.J., 1995. Thermodynamics of the carbon dioxide system in the oceans. *Geochemica et Cosmochimica Acta* **59**: 661–677.

Millero, F.J., 2007. The marine inorganic carbon cycle. *Chemical Reviews* **107**: 308–341.

Milllero, F.J., Graham, T.B., Huang, F., Bustos-Serrano, H., & Pierrot, D., 2006. Dissociation constants of carbonic acid in seawater as a function of salinity and temperature. *Marine Chemistry* **100**: 80–94.

Millero, F.J., Feistel, R., Wright, D.G., & McDougall, T.J., 2008. The composition of standard seawater and the definition of the reference-composition salinity scale. *Deep-Sea Research I* **55**: 50–72.

Neill, C., Johnson, K.M., Lewis, E., & Wallace, D.W.R., 1997. Accurate headspace analysis of fCO_2 in discrete water samples using batch equilibration. *Limnology and Oceanography* **42**: 1774–1783.

Nemzer, B.V. & Dickson, A.G., 2005. The stability and reproducibility of Tris buffers in synthetic seawater. *Marine Chemistry* **96**: 237–242.

Pitzer, K.S. & Brewer, L., 1961. *Thermodynamics (revision of Lewis and Randall),* McGraw-Hill.

SCOR. 1985. *Oceanic CO_2 measurements*. Report of the third meeting of the Working Group 75, Les Houches, France, October 1985.

Soli, A.L. & Byrne, R.H., 2002. CO_2 system hydration and dehydration kinetics and the equilibrium CO_2/H_2CO_3 ratio in aqueous NaCl solution. *Marine Chemistry* **78**: 68–73.

Taylor, J.K., 1987. *Quality assurance of chemical measurements*. Lewis Publishers, Inc., Chelsea, MI, 328 pp.

Thompson, A. & Taylor, B.N., 2008. *Guide for the use of the International System of Units (SI)*. NIST Special Publication 811, 2008 Edition. 85 pp.

Weiss, R.F., 1974. Carbon dioxide in water and seawater: the solubility of a non–ideal gas. *Marine Chemistry* **2**: 203–215.

Weiss, R.F., & Price, B.A., 1980. Nitrous oxide solubility in water and seawater. *Marine Chemistry* **8**: 347–359.

Whitfield, M., Butler, R.A, & Covington, A.K., 1985. The determination of pH in estuarine waters: I. Definition of pH scales and the selection of buffers. *Oceanologica Acta* **8**, 423–432.

Wolf-Gladrow, D.A., Zeebe, R.E., Klaas, C., Körtzinger, A. & Dickson, A.G., 2007. Total alkalinity: the explicit conservative expression and its application to biogeochemical processes. *Marine Chemistry* **106**, 287–300.

Yao, W., Liu, X, & Byrne, R.H., 2007. Impurities in indicators used for spectrophotometric seawater pH measurements: assessment and remedies. *Marine Chemistry* **107**, 167–172.

Zeebe, R.E. & Wolf-Gladrow, D., 2001. *CO_2 in seawater: equilibrium, kinetics, isotopes*. Elesevier, Amsterdam. 346 pp.

800 Table 1. Expressions for calculating equilibrium constants (on the total hydrogen ion scale) as a function of salinity and temperature (Dickson *et al.*, 2007; Millero, 1995; Weiss & Price, 1980).
Note: $I / m^\circ = \dfrac{19.924S}{1000 - 1.005S} \approx 0.02S$; $k^\circ = 1$ mol kg^{-1}.

Equilibrium constant expression	**Equation in text**
$\ln(K_0 / k^\circ) = 93.4517\left(\dfrac{100}{T/\mathrm{K}}\right) - 60.2409 + 23.3585\ln\left(\dfrac{T/\mathrm{K}}{100}\right) + S\left(0.023517 - 0.023656\left(\dfrac{T/K}{100}\right) + 0.0047036\left(\dfrac{T/K}{100}\right)^2\right)$	(6)
$\log(K_1/k^\circ) = \dfrac{-3633.86}{(T/\mathrm{K})} + 61.2172 - 9.67770\ln(T/\mathrm{K}) + 0.011555S - 0.0001152S^2$	(7)
$\log(K_2/k^\circ) = \dfrac{-471.78}{(T/\mathrm{K})} - 25.9290 + 3.16967\ln(T/\mathrm{K}) + 0.01781S - 0.0001122S^2$	(8)
$\ln\left(\dfrac{K_\mathrm{B}}{k^\circ}\right) = \dfrac{-8966.90 - 2890.53S^{1/2} - 77.942S + 1.728S^{3/2} - 0.0996S^2}{(T/\mathrm{K})} + (148.0248 + 137.1942S^{1/2} + 1.62142S) + (-24.4344 - 25.085S^{1/2} - 0.2474S)\ln(T/\mathrm{K}) + 0.053105S^{1/2}(T/\mathrm{K})$	(9)
$\ln\left(K_\mathrm{W}/(k^\circ)^2\right) = \dfrac{-13847.26}{(T/\mathrm{K})} + 148.9652 - 23.6521\ln(T/\mathrm{K}) + \left(\dfrac{118.67}{(T/\mathrm{K})} - 5.977 + 1.0495\ln(T/\mathrm{K})\right)S^{1/2} - 0.01615S$;	(10)
$\ln\left(\dfrac{F}{\mathrm{atm}\ k^\circ}\right) = 218.2968\left(\dfrac{100}{T/\mathrm{K}}\right) - 162.8301 + 90.9241\ln\left(\dfrac{T/\mathrm{K}}{100}\right) - 1.47696\left(\dfrac{T/\mathrm{K}}{100}\right)^2 + S\left(0.025695 - 0.025225\left(\dfrac{T/K}{100}\right) + 0.0049867\left(\dfrac{T/K}{100}\right)^2\right)$	(11)
$K_\mathrm{sp}(\mathrm{aragonite}) = -171.945 - 0.077993(T/\mathrm{K}) + 2903.293(\mathrm{K}/T) + 71.595\lg(T/\mathrm{K}) + (-0.068393 + 0.0017276(T/\mathrm{K}) + 88.135(\mathrm{K}/T))S^{0.5} - 0.10018S + 0.0059415S^{1.5}$	(14)
$K_\mathrm{sp}(\mathrm{calcite}) = -171.9065 - 0.077993(T/\mathrm{K}) + 2839.319(\mathrm{K}/T) + 71.595\lg(T/\mathrm{K}) + (-0.77712 + 0.0028426(T/\mathrm{K}) + 178.34(\mathrm{K}/T))S^{0.5} - 0.07711S + 0.0041249S^{1.5}$	(15)
$\ln(K'_\mathrm{S}/k^\circ) = \dfrac{-4276.1}{(T/\mathrm{K})} + 141.328 - 23.093\ln(T/\mathrm{K}) + \left(\dfrac{-13856}{(T/\mathrm{K})} + 324.57 - 47.986\ln(T/\mathrm{K})\right)\times\left(\dfrac{I}{m^\circ}\right)^{1/2} + \left(\dfrac{35474}{(T/\mathrm{K})} - 771.54 + 114.723\ln(T/\mathrm{K})\right)\times\left(\dfrac{I}{m^\circ}\right) - \dfrac{2698}{(T/\mathrm{K})}\left(\dfrac{I}{m^\circ}\right)^{3/2} + \dfrac{1776}{(T/\mathrm{K})}\left(\dfrac{I}{m^\circ}\right)^2 + \ln(1 - 0.001005S)$,	(29)

Table 1 (continued).

Equilibrium constant expression	Equation in text
$\ln(K_F/k°) = \frac{874}{(T/\mathrm{K})} - 9.68 + 0.111 S^{1/2}$	(44)
$\ln(K_{Si}/k°) = \frac{-8904.2}{(T/\mathrm{K})} + 117.385 - 19.334 \ln(T/\mathrm{K}) + \left(\frac{-458.79}{(T/\mathrm{K})} + 3.5913\right)(I/m°)^{1/2} + \left(\frac{188.74}{(T/\mathrm{K})} - 1.5998\right)(I/m°) + \left(\frac{-12.1652}{(T/\mathrm{K})} + 0.07871\right)(I/m°)^2 + \ln(1 - 0.001005S)$;	(45)
$\ln(K_{1P}/k°) = \frac{-4576.752}{T/K} + 115.525 - 18.453 \ln(T/\mathrm{K}) + \left(\frac{-106.736}{(T/\mathrm{K})} + 0.69171\right) S^{1/2} + \left(-\frac{0.65643}{(T/\mathrm{K})} - 0.01844\right) S$;	(46)
$\ln(K_{2P}/k°) = \frac{-8814.715}{T/\mathrm{K}} + 172.0883 - 27.927 \ln(T/\mathrm{K}) + \left(\frac{-160.340}{(T/\mathrm{K})} + 1.3566\right) S^{1/2} + \left(\frac{0.37335}{(T/\mathrm{K})} - 0.05778\right) S$,	(47)
$\ln(K_{3P}/k°) = \frac{-3070.75}{T/\mathrm{K}} - 18.141 + \left(\frac{17.27039}{T/\mathrm{K}} + 2.81197\right) S^{1/2} + \left(\frac{-44.99486}{T/\mathrm{K}} + 0.09984\right) S$;	(48)
$\ln K_{NH3} = -6285.33/T + 0.0001635T - 0.25444 + (0.46532 - 123.7184/T) S^{0.5} + (-0.01992 + 3.17556/T)\, S$	

805

Table 2. Reference composition of sea water (Millero *et al.*, 2008) at a practical salinity of 35.* To calculate the composition at another salinity, $[\mathrm{Y}]_S = [\mathrm{Y}]_{35} \times (S / 35)$.

Constituent	**Concentration** / **mol kg^{-1}**
Sodium	0.4689674
Magnesium	0.0528171
Calcium	0.0102821
Potassium	0.0102077
Strontium	0.0000907
Chloride	0.5458696
Sulphate	0.0282352
Bicarbonate	0.0017177
Bromide	0.0008421
Carbonate	0.0002390
Borate	0.0001008
Fluoride	0.0000683
Hydroxide	0.0000080
Boric acid	0.0003143
Dissolved carbon dioxide	0.0000096

* The concentrations of the various acid-base species were estimated assuming that the pH = 8.1 (on the sea water scale), and that the A_T = 2300 μmol kg^{-1}. The atmospheric CO_2 fugacity was chosen as 33.74 Pa = 333 μatm, *i.e.* appropriate for the time period the original salinity / conductivity relationship was characterized (see Millero *et al.*, 2008 – p. 59).

Table 3. Methods for the measurement of parameters of the carbon dioxide system in sea water (also see notes below).

Total dissolved inorganic carbon

A. Acidification / vacuum extraction / manometric determination
B. Acidification / gas stripping / coulometric determination
C. Acidification / gas stripping / infra-red detection
D. Closed-cell acidimetric titration

Total alkalinity

E. Closed-cell acidimetric titration
F. Open-cell acidimetric titration
G. Other titration systems

pH

H. Electrometric determination with standard Tris buffer
I. Spectrophotometric determination using *m*-cresol purple

***x*´(CO_2) / *p*(CO_2)**

J. Direct infra-red determination of $x'(CO_2)$

A. This method is used in my laboratory for the certification of reference materials.

B. This is the method described in SOP 2 of Dickson *et al.* (2007). A system for implementing this (VINDTA 3C) is available from Dr. Ludger Mintrop (http://www.marianda.com)

C. This approach has been described in various publications (*e.g.*, Goyet & Snover; 1993). Systems for implementing it are available from Dr. Wei-Jun Cai (http://apolloscitech.com), and from Dr. Ludger Mintrop (AIRICA: http://www.marianda.com).

D. This method is not recommended. If the electrode used is non-Nernstian, a significant error is introduced in the estimation of C_T.

E. This method is described as SOP 3a of Dickson *et al.* (2007). A system for implementing this (VINDTA 3S) is available from Dr. Ludger Mintrop (http://www.marianda.com).

F. This method is used in my laboratory for the certification of reference materials (Dickson *et al.,* 2003). It is described as SOP 3b of Dickson *et al.* (2007), and also as ISO 22718:2008 "Water quality – Determination of total alkalinity in sea water using high precision potentiometric titration."

G. A number of titration systems are now available for this: from the Kimoto Electric Co. (http://www.kimoto-electric.co.jp/english/product/ocean/alkali.html), from Dr. Wei-Jun Cai (http://apolloscitech.com), and from Dr. Chris Langdon (clangdon@rsmas.miami.edu). Although all are described as capable of good repeatability, their reproducibility and uncertainty are unknown.

H. This requires a high-quality pH meter (readable to 0.1 mV, 0.001 in pH) and access to certified Tris buffers. (The method is described in SOP 6a of Dickson *et al.*, 2007).

I. This method is described in SOP 6b of Dickson *et al.* (2007), however see Yao *et al.* (2007).

J. This method is described in SOP 5 of Dickson *et al.* (2007), and requires a significant amount of sea water auch as a flowing stream of sea water: *e.g.*, the system marketed by General Oceanics: http://www.generaloceanics.com/genocean/8050/8050.htm. If however, it is desired to make the measurement on a discrete sample of sea water, the uncertainty is increased to between 0.5 and 1.0%. One such method is described in SOP 4 of Dickson *et al.* (2007); another in a paper by Neill *et al.* (1997).

Table 4. Estimated measurement uncertainties for the measurement of parameters of the carbon dioxide system in sea water (for a single measurement on a sample of surface sea water).

Parameter	**Reference Method**	**State-of-the-art (using RMs)***	**Other techniques (using RMs)**	**Without using RMs†**
Total alkalinity	1.2 µmol kg^{-1}	2–3 µmol kg^{-1}	4–10 µmol kg^{-1}	?
Total dissolved inorganic carbon	1.0 µmol kg^{-1}	2–3 µmol kg^{-1}	4–10 µmol kg^{-1}	?
pH	0.003‡	~0.005‡	0.01–0.03	?
$x'(CO_2)$ / $p(CO_2)$	1.0 µatm	~2 µatm	5–10 µatm	?

* The methods described in Dickson *et al.* (2007), performed by an experienced laboratory with well-trained analysts, and with a good quality assurance program in place.

† If appropriate reference materials are not used, it is usually not practical to assign a measurement uncertainty.

‡ These levels of uncertainty in pH require that the apparent dye extinction coefficient ratios be appropriate to the particular lot of dye being used (see discussion in Yao *et al.*, 2007).

Table 5. Availability of reference materials for the quality control of carbon dioxide measurements in sea water.

Analytical Measurement	Desired Accuracy†	Uncertainty††	Availability
Total dissolved inorganic carbon	± 1 µmol kg^{-1}	± 1 µmol kg^{-1}	Since 1991(a)
Total alkalinity	± 1 µmol kg^{-1}	± 1 µmol kg^{-1}	Since 1996(b)
pH	± 0.002	± 0.003	Since 2009(c)
Mole fraction of CO_2 in dry air	± 0.5 µmol/mol	± 0.1 µmol/mol	Since 1995(d)

† These values are based on considerations outlined in the report of SCOR Working Group 75 (SCOR, 1985). They reflect the desire to measure changes in the CO_2 content of sea water that allow the increases due to the burning of fossil fuels to be observed.

†† Estimated standard uncertainties for the reference materials described here.

(a) Sterilized natural sea water, certified using a definitive method based on acidification, vacuum extraction, and manometric determination of the CO_2 released. Available from UC San Diego (http://andrew.ucsd.edu/co2qc/).

(b) Certified using a definitive method based on an open-cell acidimetric titration technique (Dickson *et al.*, 2003). Available from UC San Diego (http://andrew.ucsd.edu/co2qc/).

(c) Standard buffer solutions based on Tris in synthetic sea water (Nemzer & Dickson, 2005). Available from UC San Diego (http://andrew.ucsd.edu/co2qc/).

(d) Cylinders of air certified by non-dispersive infra-red spectrometry. Available from NOAA/ESRL, Boulder, CO (http://www.esrl.noaa.gov/gmd/ccgg/refgases/stdgases.html). However, gas mixtures certified to a lesser accuracy can be obtained from a variety of manufacturers.

Table 6. Estimated relative uncertainties* in calculating $[CO_2^*]$ and $[CO_3^{2-}]$ (or saturation state) resulting from the measurement uncertainties in Table 4, and based on the sensitivity parameters calculated by Dickson & Riley (1978) for surface sea water. The uncertainties for the various equilibrium constants are assumed to be 0.01 in $\lg K_1$; 0.02 in $\lg K_2$; and 0.002 in $\lg K_0$.

Pair of parameters	**Relative uncertainty**	**Reference Methods**	**State-of-the-art (using RMs)***	**Other techniques (using RMs)**
pH / A_T	$u_c([CO_2^*])/[CO_2^*]$ $u_c([CO_3^{2-}])/[CO_3^{2-}]$	2.6% 3.6%	2.9% 3.7%	6.1–8.7% 5.1–6.5%
pH / C_T	$u_c([CO_2^*])/[CO_2^*]$ $u_c([CO_3^{2-}])/[CO_3^{2-}]$	2.4% 4.1%	2.6% 4.2%	5.6–8.0% 5.7–7.3%
A_T / C_T	$u_c([CO_2^*])/[CO_2^*]$ $u_c([CO_3^{2-}])/[CO_3^{2-}]$	4.9% 0.6%	5.4% 1.7%	5.8–9.3% 2.2–5.5%
pH / $p(CO_2)$	$u_c([CO_2^*])/[CO_2^*]$ $u_c([CO_3^{2-}])/[CO_3^{2-}]$	0.6% 5.3%	0.8% 5.7%	1.5–2.9% 10.6–15.0%
A_T / $p(CO_2)$	$u_c([CO_2^*])/[CO_2^*]$ $u_c([CO_3^{2-}])/[CO_3^{2-}]$	0.6% 3.3%	0.8% 3.3%	1.5–2.9% 3.4–3.8%
C_T / $p(CO_2)$	$u_c([CO_2^*])/[CO_2^*]$ $u_c([CO_3^{2-}])/[CO_3^{2-}]$	0.6% 4.0%	0.8% 4.1%	1.5–2.9% 4.2–4.9%

* These values are certainly not accurate to two significant figures. However, one can easily see the implications of the estimated measurement uncertainties, and can also infer the importance of the uncertainties ascribed to the various equilibrium constants (which dominate the relative uncertainty when using methods with the lowest possible uncertainty.

Figure 1. Composition of reference sea water (Millero *et al.*, 2008) showing quantities in relation to 1 kg of sea water. Modified from http://commons.wikimedia.org/wiki/File:Sea_salt-e-dp_hg.svg

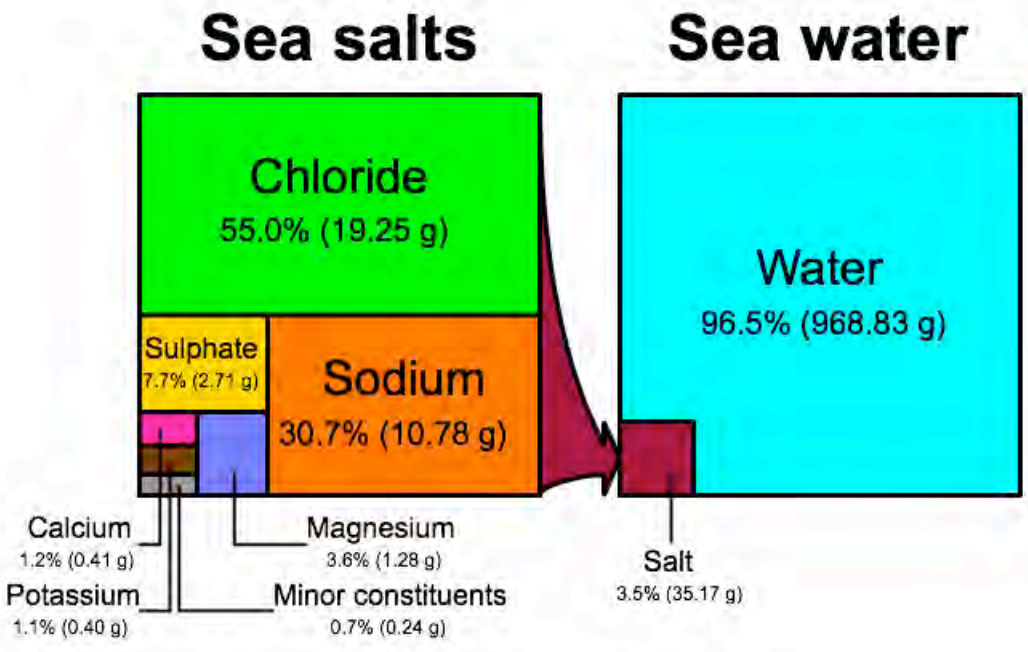

Figure 2. The chemical equilibria of the carbon dioxide system in sea water.

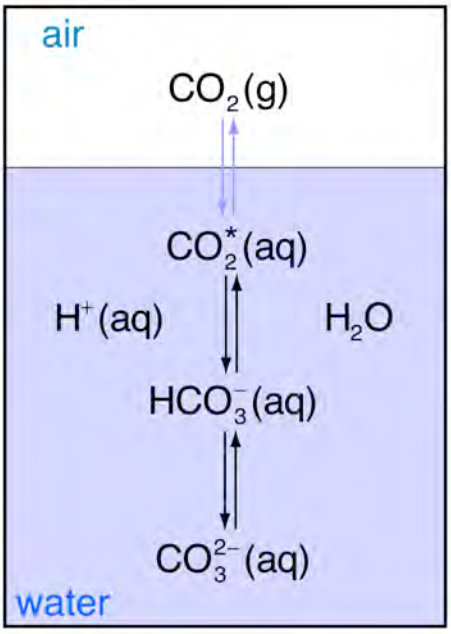

Figure 3. The influence of the mole fraction of magnesium on the solubility of magnesian calcites (after a slide by L.B. Railsback -- http://www.gly.uga.edu/railsback/FundamentalsIndex.html)

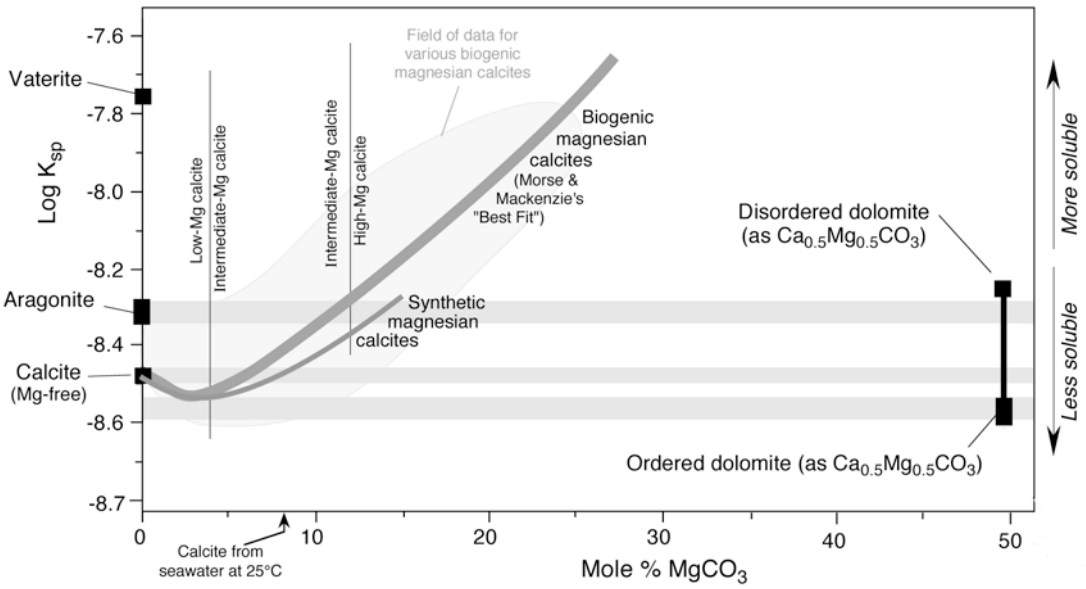

Figure 4a. Plot of contours of constant bicarbonate concentration (µmol kg^{-1}) as a function of $[CO_2^*]$ and $[CO_3^{2-}]$. 4b. Plot of contours of constant pH as a function of $[CO_2^*]$ and $[CO_3^{2-}]$.

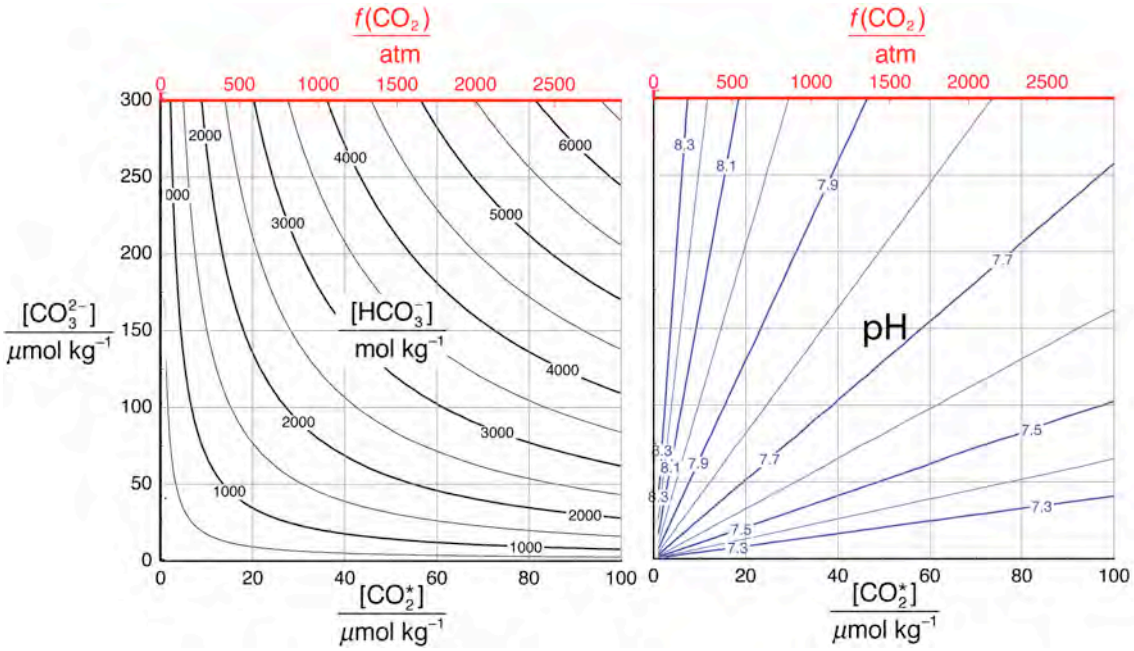

Chris Sabine
Monday, November 2, 2009
Introduction to CO2SYS (lecture) –

a) Brief introduction to CO2SYS and the different versions available
b) Discuss the uses, advantages, disadvantages and pitfalls of CO2SYS
c) Describe the details of the various fields (note: I will be using CO2SYS_ver14.xls)
d) Interactive session where students try calculations on their own computers and we discuss the answers along with any questions, concerns, confusion.

Requirements: Laptop computer with a working version of one of the CO2SYS programs.

Helpful Reading:

Lewis, E., and D. W. R. Wallace. (1998): Program Developed for CO_2 System Calculations. ORNL/CDIAC-105. Carbon Dioxide Information Analysis Center, Oak Ridge National Laboratory, U.S. Department of Energy, Oak Ridge, Tennessee.

Available at: http://cdiac.esd.ornl.gov/oceans/co2rprt.html

Jean-Pierre Gattuso
Monday, November 2, 2009
Introduction to seacarb

Requirements

- The version of the R program suitable with the OS installed on your laptop. Versions for Mac OSX, linux, unix and Windows are available at http://www.r-project.org/

- The R package seacarb. To do that, launch R, go to "Packages & Data:Packages installer", click on "Get list", look for seacarb and click "Install selected"

- Download full seacarb manual at http://cran.at.rproject.org/web/packages/seacarb/index.html

Chris Sabine
Monday, November 2, 2009
CO_2 Water Sampling (lab activity) –

The class will be divided up into three groups of approximately equal size. Each group will spend approximately one hour learning how to collect inorganic carbon samples from a Niskin-type sampling bottle. Every student will fill at least one sample bottle, poison the sample, prepare the ground glass stopper, and seal the bottle for later analysis. We will discuss how sampling differs for different parameters, potential sources of contamination, and how to store the samples after collection. This is a hands-on activity so be prepared to get wet.

Helpful Reading:

Dickson, A.G., Sabine, C.L. and Christian, J.R. (Eds.) 2007. Guide to best practices for ocean CO_2 measurements. PICES Special Publication 3, 191 pp. SOP 1 - Water sampling for the parameters of the oceanic carbon dioxide system.

Available at: http://cdiac.esd.ornl.gov/ftp/oceans/Handbook_2007/sop01.pdf

pH Sampling Instruction
(For discrete spectrophotometric pH measurements)
Instructor: Aleck Wang (Sabine to demonstrate on 11/2)

When sampling, put sampling noodle (silicon tubing about 20 cm) on one end of the cell (10-cm glass cell), put the other end of the noodle to nipple of Niskin bottle (or Carboy bottle), set the cell vertically, push in, get rid of the bubbles by squeezing the noodle and tapping on cell, and when cell is filled up, level the cell. Sometimes a big plume of bubbles rushing out will generate a lot of small bubbles that adhere to the cell wall. If tapping cannot get rid of the bubbles, disconnect the cell and tubing, let the water empty out, then reconnect - this should remove the bubbles.

Rinse one cap, wait ~15 seconds, cap one end, detach tubing, wash the other cap, cap the cell, pull the nipple. Sample is done.

After sampling, rinse the cell with tap water, dry the cell with Kimwipes, and place cell in cell warmer (water bath) within a plastic bag. Wait 30 minutes for the sample to warm up to 20°C. All measurements will be made at 20 or 25°C.

Underway pCO_2 demonstration
Instructor: Aleck Wang (WHOI)

Determination of $p(CO_2)$ in air that is in equilibrium with a continuous stream of sea water (underway measurements)

Methodology

- Non-dispersive infra-red (NDIR) analyzer
  e.g. LiCOR CO_2/H_2O analyzer

- Air-water CO_2 equilibrator
  Rain-type: showerhead + headspace air
  Bubbler type
  Thin film (CO2 gas permeable membrane)

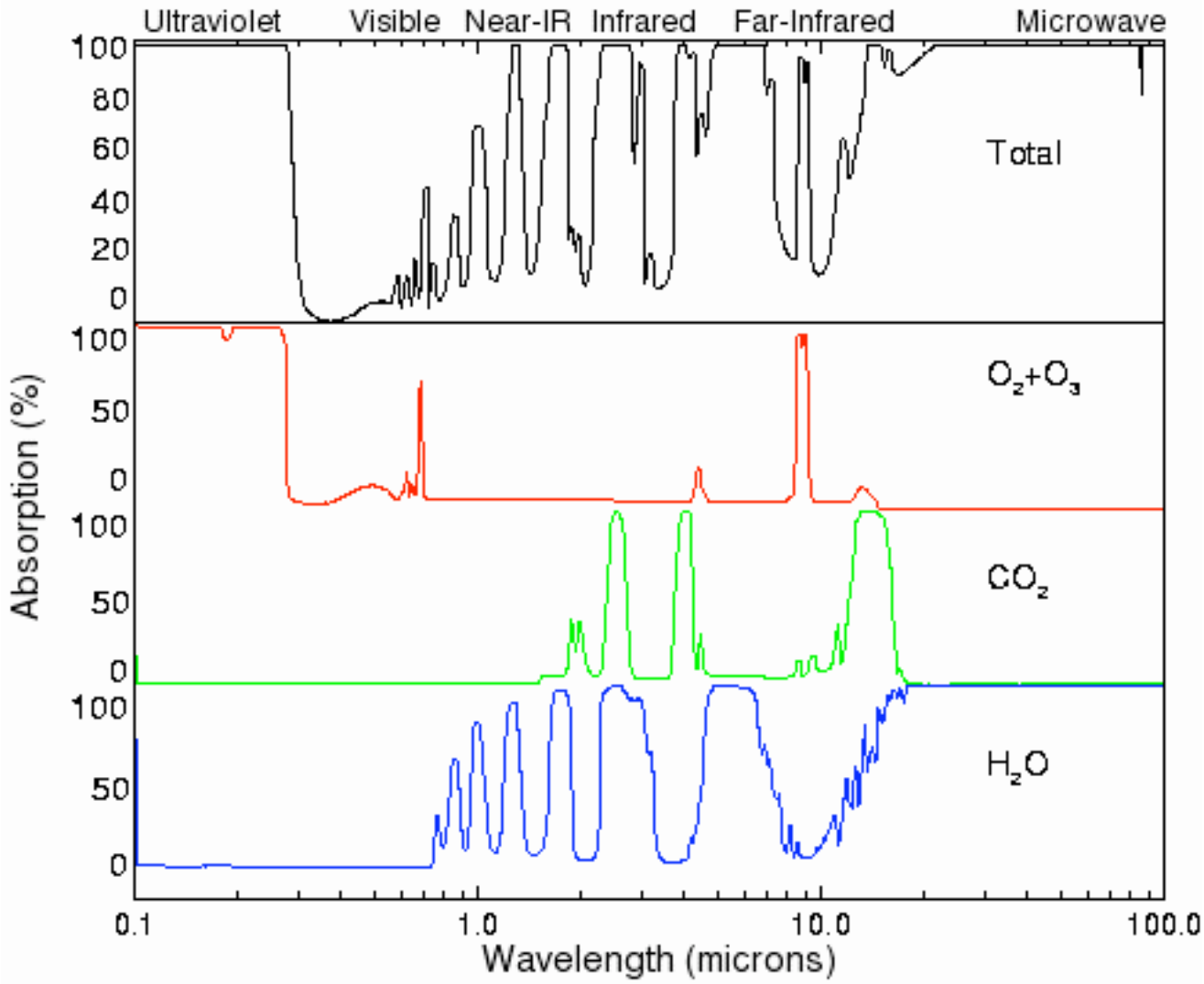
Ultraviolet
Visible
Near-IR
Infrared
Far-Infrared
Microwave
100
80
60
40
20
0
Total
100
50
0
O_2+O_3
100
50
0
CO_2
100
50
0
H_2O
Absorption (%)
0.1
1.0
10.0
100.0
Wavelength (microns)

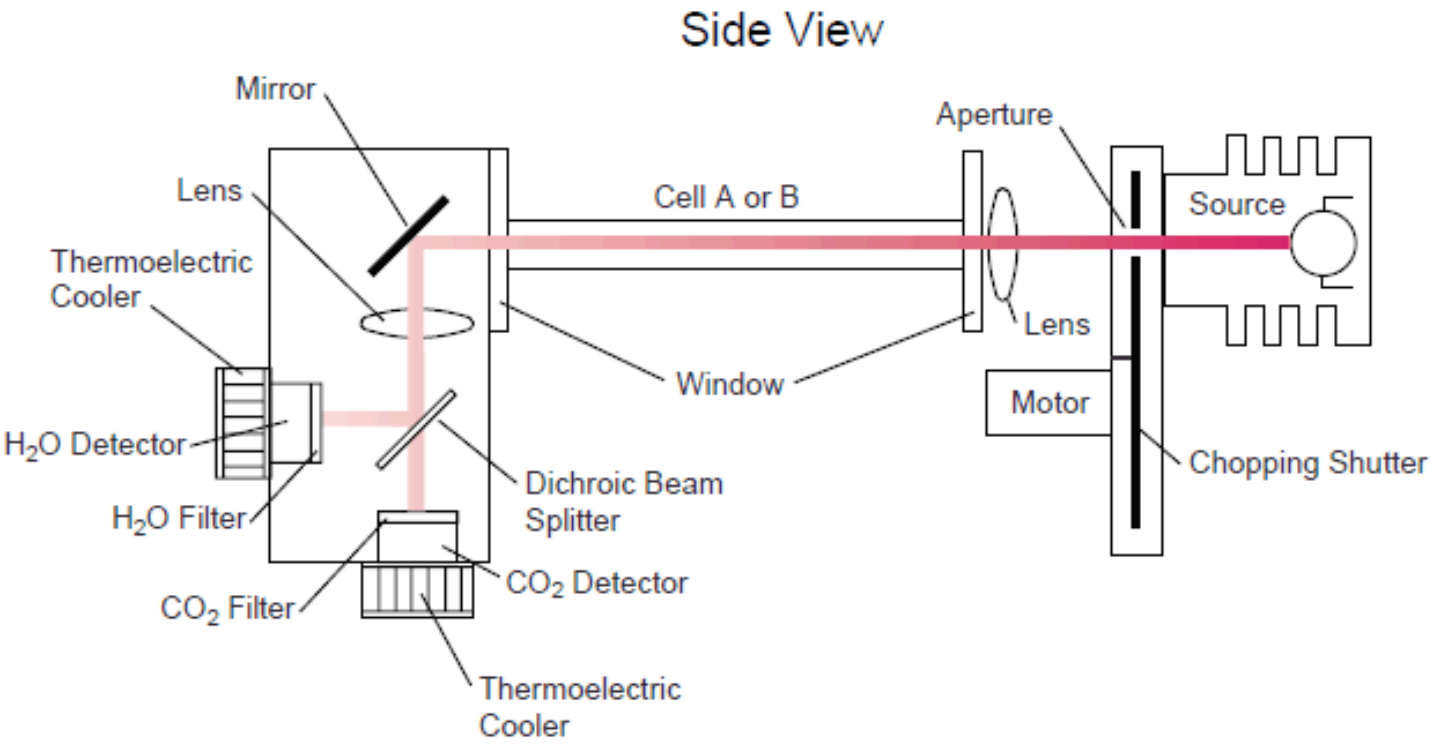

Figure 1-1. Schematic of LI-7000 optical path.

Table 1
Summary of main features of the underway fCO_2 systems "A" through "G" which participated in the exercise

	"A"	"B"	"C"	"D"	"E"	"F"	"G"
Equilibrator							
Design	Shower head	Bubbler	Shower head	Thin film[a]	Showerhead	Bubbler	Showerhead
Total volume	1000 ml	1400 ml	13.1 l	119 ml	11.0 l	36 ml	1200 ml
Water volume	500 ml	1000 ml	2.3 l	21 ml	10.0 l	18 ml	~ 75 ml
Air volume	500 ml	400 ml	10.8 l	98 ml	1.0 l	18 ml	500 ml
Water flow rate	4–6 l min^{-1}	2.0 l min^{-1}	8.0 l min^{-1}	2.0 l min^{-1}	10–15 l min^{-1}	0 l min^{-1}[b]	1.2 l min^{-1}
Air flow rate	0.2 l min^{-1}	0.8 l min^{-1}	0.5 l min^{-1}	1.0 l min^{-1}	0.5 l min^{-1}	0.17 l min^{-1}	0.18 l min^{-1}
Vented?	Yes	Yes	Yes	No[c]	Yes	No	Yes
Time constant[d]	2–3 min	75 s	3–5 min	2–3 min	60–90 s	n/a	Unknown
Mean temperature difference[e]	0.30 ± 0.05	0.30 ± 0.04	0.24 ± 0.02	0.39 ± 0.12	0.17 ± 0.03	0.32 ± 0.03	0.56 ± 0.09
CO_2 measurement							
Method	NDIR	NDIR	NDIR	NDIR	NDIR	NDIR	NDIR
Wet/dry?	Wet	Wet	Dry	Dry	Dry	Dry	Wet
Analyzer calibration							
Number of standard gases	2	2	2	2	4	2[f]	2
Zero gas?	No	Yes	No	No	No	Yes	No
Measurement cycle							
Calibration frequency	6–8 h	6 h	6 h	4–6 h	1.5 h	15 min	2 h
Air measurement frequency	6–8 h	1 h	6 h	4–6 h	0.5 h	n/a	7 min
Interrogation interval	6 s	6 s	1 s	10 s	0.1 s	15 min	0.33 s
Averaging interval	(1[g]) 3 min	1 min	4 min	5 min	1 min	n/a	1 s
Reporting interval	(1[g]) 3 min	1 min	4 min	5 min	~ 13 min	20 min	~ 8 min
Data points per average	10; 30	10	240	33	600	1	3

[a] Film thickness approximately 0.75 mm.
[b] Semi-continuous technique.
[c] Vented only every 20 min.
[d] This is the overall time constant of the system (not the time constant of equilibration).
[e] Mean difference between equilibrator temperature and in situ temperature based on corrected temperature readings (Section 2.3.2).
[f] Standard gas generator was initially calibrated using all six calibration gases; linearity checks are carried out for every sample with only two calibration gases.
[g] Until June 9, 0230 UTC.

(Kortzinger et al., 2000)

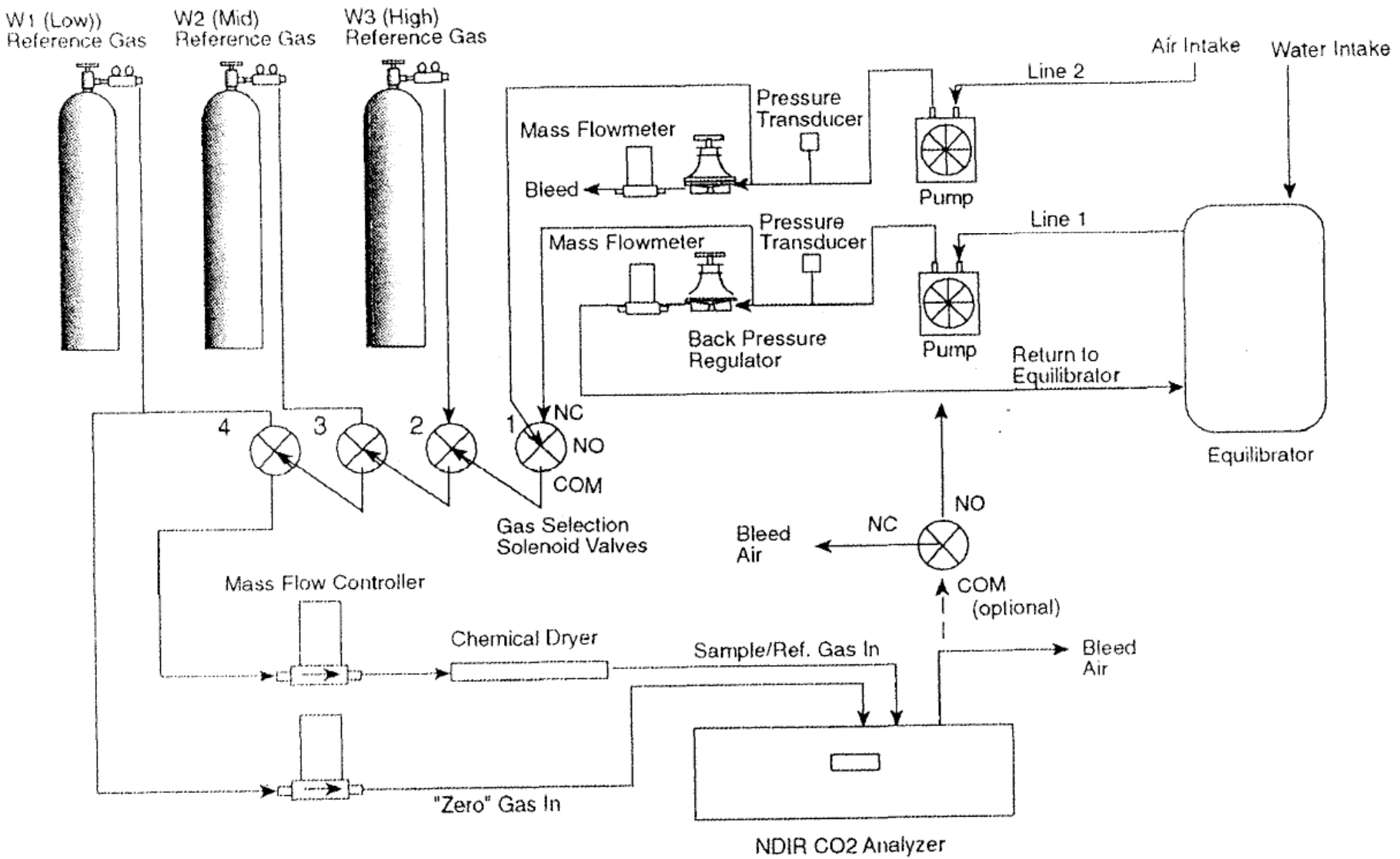

Fig. 1. Schematic of the plumbing of the underway system. For the three-way gas solenoid valves *NC* stands for normally closed, *NO* for normally open, and *COM* for common.

Wanninkhof and Thoning, 1993

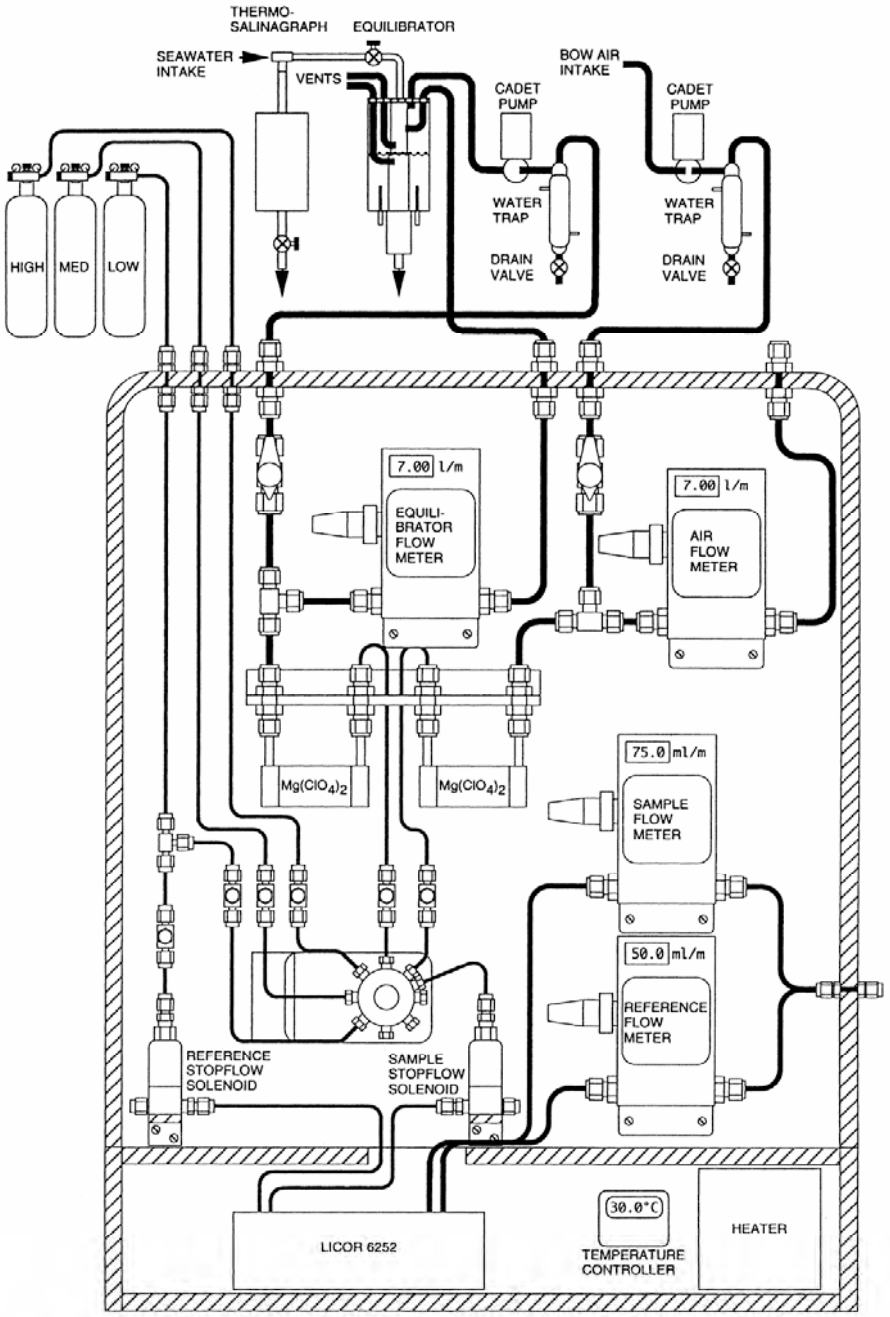

(Feely et al., 1998)

Fig. 1. Schematic diagram of the automated underway pCO_2 system. Seawater-equilibrated air first passes through a cold trap and then through a magnesium perchlorate drying tube to remove water vapor prior to analysis by the Li-Cor™ (model 6252) infrared analyzer.

Annexe

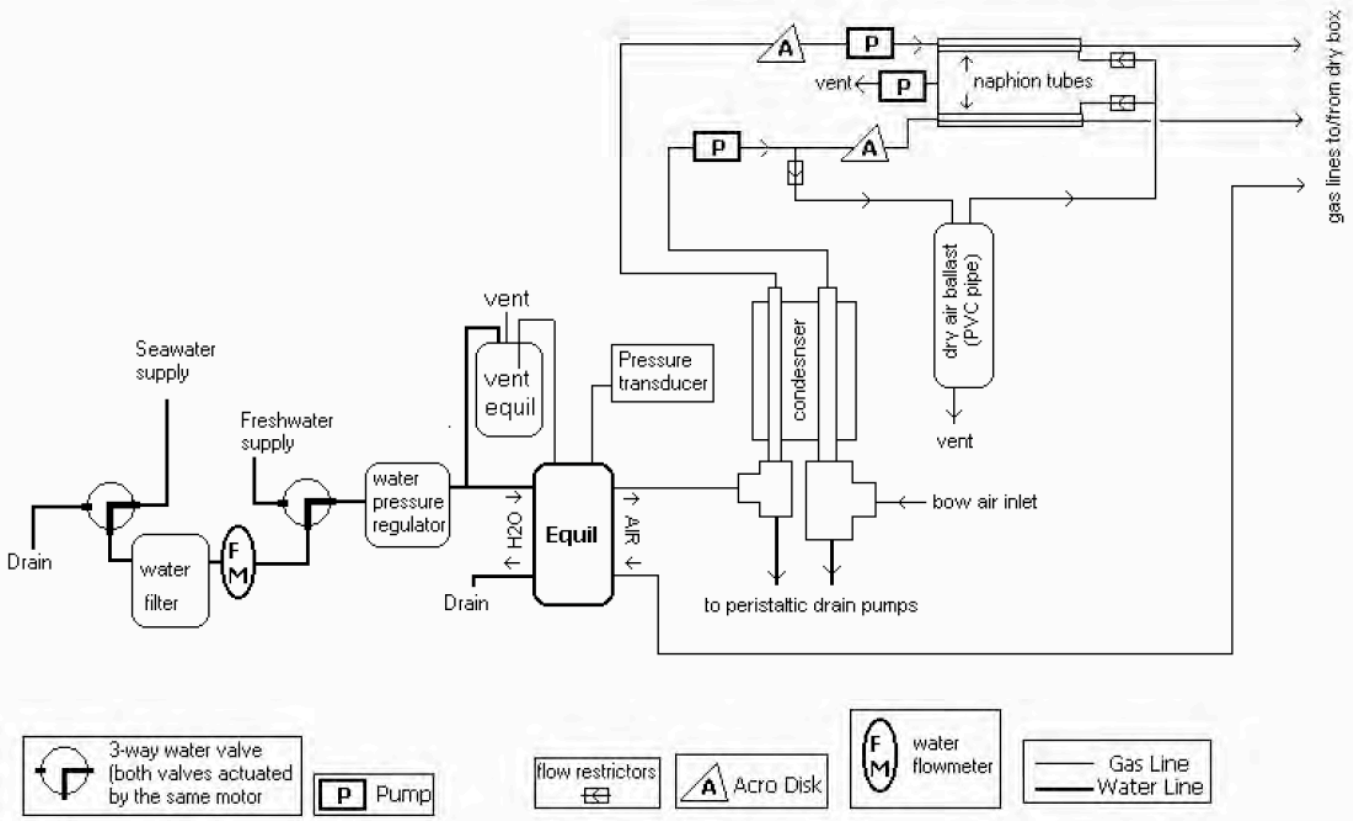

Fig. 1 Schematic showing the layout of the analytical system described here (based on system designed by Craig Neill, Bjerknes Center for Climate Research, Norway).

(2007 CO_2 Handbook)

Through Hull Water Intake Plumbing Option

This package is a Lloyd's approved below water line module, self contained with all exposed parts either stainless steel or plastic. The unit includes a guillotine shut off valve in case of catastrophic failure. The unit collects water a few inches from the hull through the intake pod assembly. Options include an external sea surface temperature sensor, and a chlorine gas generator to eliminate growth of any microorganisms.

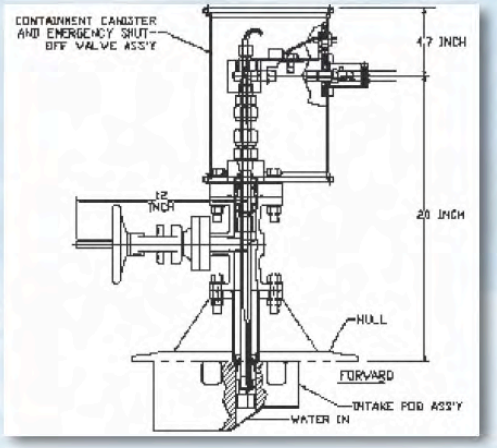

General Oceanics Inc.

Model 8050

pCO_2 Measuring System

Wet Box | Dry Box | Satellite Deck Box

Specifications

Model 8050:

Wet Box: Length 24 inch (61 cm) Width 24 inch (61 cm) Depth 10 inch (25.4 cm)
Dry Box: Length 24 inch (61 cm) Width 24 inch (61 cm) Depth 10 inch (25.4 cm)
Satellite Box: Length 14 inch (35.6cm) Width 10.5 inch (26.7cm) Depth 8 inch (20.4cm)

Note: The User must supply the following items:

1) Main water intake pump and plumbing (interfaces to the wet box), see pump and through hull intake plumbing option above.
2) Calibration gases and connecting lines.
3) Co2 analyzer (Licor 6262 or 7000 recommended)

Introduction

The Model 8050 pCO_2 Measuring System is an autonomous analytical system for measuring carbon dioxide in oceanic surface water.

The system is modeled after instruments previously built by Craig Neill/University of Bergen.

The system may be used on a ship underway or, on a variety of at-sea platforms.

The present pCO2 system operates fully automatically and consists of:

- An equilibrator that balances the CO2 in seawater with a headspace gas that is analyzed
- An infrared analyzer (User Supplied) to quantify the CO2 concentration in the equilibrator headspace and marine air
- A network of valves and pumps that select, control, and monitor flows of seawater, equilibrator headspace, marine air, and CO2 gas standards
- An on deck enclosure that provides a GPS signal, atmospheric pressure measurement and satellite data transfer.
- An integrated notebook computer, computer interface, and software to control valves and pumps and to log data (pressures, temperatures, flows, analyzer response, date, time and position).

General Oceanics Inc.
1295 N.W. 163rd Street
Miami, Florida 33169

Tel: (305) 621-2882
Fax: (305) 621-1710
E-mail:sales@generaloceanics.com
http://www.GeneralOceanics.com

Overview

The system consists of three enclosures: the dry box, the wet box, and the satellite deck box.
The dry box contains a Licor CO2 analyzer (user supplied), electrically actuated valves to control the gas flow through the analyzer, a gas flow sensor, computer and interface with solid-state relays. There are inlets for up to eight gases. Each inlet has a needle valve for adjusting the flow rate. A three-way solenoid valve directs the gas exiting the analyzer towards a vent or towards the equilibrator (when analyzing the equilibrator headspace). The dry box utilizes an RS485 module and cables to communicate with the other two boxes.

The wet box contains main and vent equilibrating chambers, electrically-actuated valves, pressure gauge and regulating valve, reusable water filter, water flow sensor, barometer, temperature probe, condenser unit , two Naphion drying tubes, and three air pumps. After entering the wet box, seawater passes through the reusable filter, which can be automatically back-flushed with fresh water. An adjustable regulating valve after the filter sets the water pressure that is delivered to the equilibrators. The vent equilibrator keeps the CO2 concentration in gas that exchanges with the vent on the main equilibrator close to the concentration in the main headspace. The barometer and temperature probe are attached to the main equilibrator. Seawater drains by gravity out of the wet box.

One of the air pumps in the wet box pulls the headspace gas from the main equilibrator and pushes it through the condenser, a Naphion drying tube and then the CO2 analyzer. Another pump pulls air from an exterior inlet provided and located by the user and pushes the air through a condenser. After the condenser, this gas stream is split towards a vented chamber and towards a drying tube and then the CO2 analyzer. The reduced-humidity air in the vented chamber is pulled through the drying tubes as counter-flow gas by the third air pump.

The weather resistant satellite deck box contains the modem for Iridium satellite communication, a high-precision barometer, a power supply, and data communication modules. A GPS transducer is attached to deck box and data modules. A ten-conductor cable connects the deck box to the dry box (a 25 meter cable is provided; a cable can be up to 1000 meters long, an extra connector is provided for making a cable for a permanent installation). There is a bulkhead tube fitting for connecting a Gill pressure port to the barometer (pressure port not provided).

Schematic of main system components

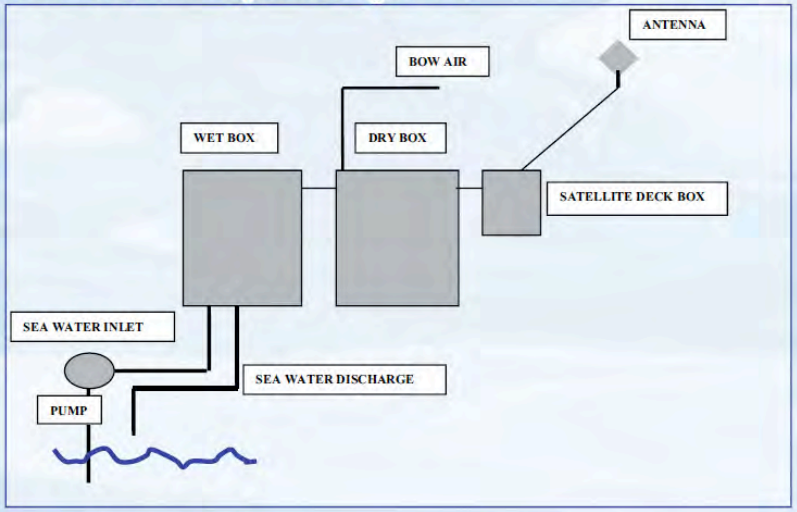

Options

The following options are available for the 8050 pCO2 Measuring System.

Model I8050-7

Idronaut Multiparameter "Flow Through" Sensor Module

The Model I8050-7 Idronaut Multiparameter "Flow Through" Sensor Module, is designed to be integrated into the wet box of the pCO2 system. The instrument is used for the measurement of Conductivity, Temperature, Oxygen, pH and Redox. This advanced instrument is the result of 25 years experience in the design of high technology water quality probes and offers long term sensor stability for unattended data collection, in either fresh or sea water environments. Data can be stored either internally within the probe or directly onto a PC.
The Model I8050-7 Sensor Module comes complete with two thermometers. The first is fitted near the water sampling port, to accurately measure the temperature of the surface waters, while the second is fitted inside the measuring cell to allow salinity calculations.
The unit is housed in a small (102 x 102 x 318 mm) stainless steel unit with an adjacent parallel transparent sensor chamber which can be easily removed for cleaning. The sample volume of the chamber is only 250ml./ which ensures that the system maintains a fast response time. A pressure sensor inside the cell, acts as an accurate flow meter. For ease of maintenance, the flow through conductivity sensor, features Idronaut's well accepted large diameter seven ring quartz cell. This does not require black platinum coating and can therefore be easily cleaned in the field, without the need for recalibration.

Sensor Specifications

	Range	Accuracy	Resolution	Time Constant
Pressure (Flow)	0…..10 dbar	0.2 % full scale	0.03%	50 ms
Temperature	-3…+50 °C	0.003 °C	0.0005 °C	50 ms
Conductivity	0…..64 mS/cm	0.003 mS/cm	0.001 mS/cm	50 ms
Oxygen	0…..25 ppm	0.1 ppm	0.01 ppm	3 s
	0…250% sat.	1% sat.	0.1% sat.	3 s
pH	0…..14 pH	0.01 pH	0.001 pH	3 s
Redox	-1000 to +1000 mV	1 mV	0.1 mV	3 s

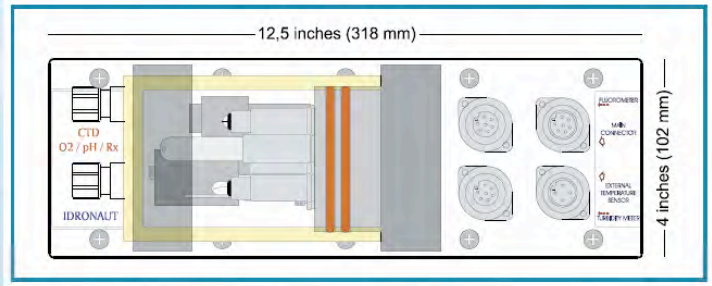

Pump Option

General Oceanics is able to recommend or supply the proper seawater intake pump that best suits your needs.

Please contact us for further information.

Tuesday, November 3, 2009
Lectures, pH and DIC measurements, and video/discussion of coulometric DIC setup

Morning

Time	Activity
8:30 am	**Lecture.** pH and Alkalinity (Dickson) MBL Speck Auditorium
10:00 am	Coffee Break
10:30 am	**Remote Lecture**. Overview of biogeochemical feedbacks (Hutchins) MBL Speck Auditorium
12:00 pm	Lunch (Swope Cafeteria, MBL)

Afternoon

Time	Group D	Group E	Group F
1:15 pm	Shuttle MBL to McLean	**Lab**. pH measurements in Rowe 423/424 (Yates/DuFore at-sea system and electrodes with Sabine/McCorkle)	Break
1:30 pm	**Lab**. Spectrophotometric pH measurements (Wang) and infrared gas analyzer DIC measurements (Langdon) (McLean 203)		
2:00 pm			**Lab**. pH measurements in Rowe 423/424 (Yates/DuFore at-sea system and electrodes with Sabine/McCorkle)
2:15 pm		Shuttle MBL to McLean	
2:30 pm	Shuttle McLean to MBL	**Lab**. Spectrophotometric pH measurements (Wang) and infrared gas analyzer DIC measurements (Langdon) (McLean 203)	
3:00 pm	**Lab**. pH measurements in Rowe 423/424 (Yates/DuFore at-sea system and electrodes with Sabine/McCorkle)		Shuttle MBL to McLean
3:30 pm		Shuttle McLean to MBL	**Lab**. Spectrophotometric pH measurements (Wang) and infrared gas analyzer DIC measurements (Langdon) (McLean 203)
4:00 pm	Break	Break	
4:30 pm			Shuttle McLean to MBL
4:45 pm	**Discussion/Video**: Care and startup of a coulometric DIC system (Cooley/Dickson); MBL Speck Auditorium		
5:30 pm	Dinner (Swope Cafeteria, MBL)		

pH and Alkalinity lecture
Instructor: Andrew Dickson

Please refer to Dickson's CO_2 system chapter "The carbon dioxide system in sea water: equilibrium chemistry and measurements" (already printed under November 2 tab)

Investigating the effects of ocean acidification on carbon, nutrient and trace metal biogeochemistry

Dave Hutchins, University of Southern California

I. Introduction

Why should ocean acidification affect marine biogeochemical cycles?

II. The Nitrogen Cycle

A. Nitrogen fixation

B. Denitrification

C. Nitrification

D. N cycle overview

III. The Phosphorus Cycle

IV. The Silicon cycle

V. Trace metal biogeochemistry

A. Iron and molybdenum

B. Zinc, cadmium and cobalt

VI. Basic biogeochemical measurements for OA experiments

A. Standing stock measurements

1. CHN
2. POP
3. BSi
4. Particulate and dissolved trace metals

B. Rate measurements

1. N_2 fixation
2. CO_2 fixation
3. Nutrient and Fe uptake

4. Nitrification and denitrification

VII. Conclusions

Spectrophotometric determination of the pH of surface seawater at in-situ conditions using the indicator dye thymol blue

C.M. DuFore and K.K. Yates*, U.S. Geological Survey, 600 Fourth Street South, St. Petersburg, FL 33701, kyates@usgs.gov

Schedule of what to expect

- Brief introduction to discuss applications of this method
- Overview of equipment required and flexibility with using similar equipment
- Brief demonstration of technique
- Hands on time for students to make measurements

Equipment list

- Ocean Optics USB2000 linear array spectrometer
- Ocean Optics LS-1 light source
- Ocean Optics 2-m long 400µm diameter optical fibers
- Ocean Optics CUV-UV-10 cuvette holder
- 10 cm pathlength spectrophotometric cells
- 0.2 mm pathlength spectrophotometric cell
- 40 cm drawing tube
- Salinity and temperature probe
- Pipette (0.01 – 0.1 cm^3) and tips
- Stock solution of thymol blue (~2 X 10^{-3} dm^{-3})
- Personal computer with OOIBase32 spectrometer operating software

Background

This procedure describes a method for the spectrophotometric determination of the pH of seawater on the total hydrogen ion concentration pH scale using the sulfonephthalein indicator thymol blue. This indicator is well suited for measurements of oceanic pH ≥ 7.9. Additional information on spectrophotometric determination of the pH of seawater can be found in Dickson et al. 2007 (SOP 6b). Bear in mind that these measurements are performed at in-situ conditions while working on small vessels.

The total hydrogen ion concentration of seawater, $[H^+]_T$, is expressed as moles per kilogram of seawater and includes the contribution from the sulfate ion and is defined as

$$[H^+]_T = [H^+]_F(1+S_T/K_S)$$
$$\approx [H^+]_F + [HSO_4^-]$$

where $[H^+]_F$ is the free concentration of hydrogen ion in seawater, S_T is the total sulfate concentration ($[HSO_4^-] + [SO_4^{2-}]$ and K_S is the acid dissociation constant for HSO_4^-. The pH is then defined as

$$pH_T = -\log[H^+]_T$$

The values of pH are determined by adding an indicator dye to seawater. For sulfonephthalein indicators such as thymol blue, the reaction of interest at seawater pH is the second dissociation

$$K_2 = [H^+]_T[I^{2-}]/[HI^-]$$

where $[HI^-]$ and $[I^{2-}]$ are the concentrations in both protonated and unprotonated thymol blue. The total hydrogen ion concentration of the sample can then be determined:

$$pH_T = pK_2 + \log\{(R-e_1)/(e_2-Re_3)\}$$

where $R = {}_{596}A/{}_{435}A$ (where ${}_{\lambda}A$ is absorbance at wavelength λ in nm) and

$$pK_2 = 4.706\ S/T + 26.3300 - 7.17218\ \log T - 0.017316 \text{ X } S$$

$$e_1 = -0.00132 + 1.600 \text{ X } 10^{-5} T$$

$$e_2 = 7.2326 - 0.0299717 T + 4.600 \text{ X } 10^{-5} T^2$$

$$e_3 = 0.0223 + 0.0003917 \text{ X } T$$

where S = salinity, T = temperature (˚K) and e_1, e_2 and e_3 are the molar absorption ratios of the indicator. It should be noted that the parameter R in the equation above is the ratio of the absorbances produced by thymol blue in seawater at the absorbance maxima of I^{2-} (596 nm) and HI^- (435 nm), and should include measurements made at a non-absorbing wavelength (750 nm for thymol blue) to correct for any baseline shift.

Methods

To begin, be sure to record the salinity and temperature of the sample. Next, draw the sample—using the drawing tube—directly from the Niskin bottle (or other water sampler) into the optical cell. After flushing with several hundred cm^3 of seawater—a flushing time of 15–20 seconds—seal the cell with the Teflon® caps ensuring that there is no headspace.

Clean and dry the exterior of the cell and place it in the cuvette holder and store a reference (blank) measurement. Remove one of the cell caps, add approximately 0.05 cm^3 of concentrated dye (~2 mmol dm^3) to the sample, replace the cap and turn the cell to mix the seawater and dye. The pH of the indicator stock solution should be adjusted to match the anticipated pH range of samples to be analyzed (see below).

Return the cell to the cuvette holder and measure the absorbances at the three wavelengths: a non-absorbing wavelength (${}_{750}A$ for thymol blue) and at the wavelengths corresponding to the absorption maxima of the base (I^{2-}) and acid (HI^-) forms of the dye respectively (${}_{596}A$ and ${}_{435}A$). Cells should be positioned to maintain consistent alignment(s) between baseline and indicator absorbance measurements.

The absorbance measured at a non-absorbing wavelength (A_{750}) is used to monitor and correct for any baseline shift due to error in repositioning the cell, instrumental shifts, etc. This assumes that

the magnitude of any observed baseline shift is identical across the visible spectrum. To do this, subtract the non-absorbing wavelength from each absorbance maxima ($_{596}A$ - A_{750}) and ($_{435}A$ - A_{750}) to obtain the final corrected absorbance value at each wavelength. These final absorbance values, corrected for any observed baseline shifts, are used to calculate R ($_{435}A/_{596}A$), the absorbance ratio which describes the extent of protonation of the dye.

Finally, it is important to analyze collected pH samples immediately. Temperature fluctuations from the time samples are collected to the time of analysis can create significant errors. This method is designed for analysis of samples collected during field deployments on small vessels where a thermostat bath is not available. Note that the system described here is capable of using a temperature-control system using the Ocean Optics CUV-UV-10 cuvette holder.

Example calculation

Using a spreadsheet to calculate the pH of a sample is probably the easiest way for multiple analyses. Here is a quick example to get you started:

$$T = 25.0\ ^{\circ}\text{C, or } 298.15\ ^{\circ}\text{K}$$

$$S = 35.0$$

$$_{435}A = 0.943;\ _{596}A = 0.642\ ;\ A_{750} = 0.001$$

$$\therefore\ R = (0.642 - .001)/(0.943 - 0.001) = 0.6805$$

First we calculate pK_2 as

$$\text{p}K_2 = 4.706\ 35/298.15 + 26.3300 - 7.17218\ \log 298.15 - 0.017316 \text{ X } 35 = 8.5293.$$

Next we calculate the molar absorption ratios:

$$e_1 = -0.00132 + 1.600 \text{ X } 10^{-5} \text{ X } 298.15 = 0.003450$$

$$e_2 = 7.2326 - 0.0299717T + 4.600 \text{ X } 10^{-5} \text{ X } (298.15)^2 = 2.3856$$

$$e_3 = 0.0223 + 0.0003917 \text{ X } 298.15 = 0.1391$$

and thus

$$\text{pH}_T = 8.5293 + \log\{(0.6805 - 0.003450)/(2.3856 - 0.1391 \text{ X } 0.6805)\} = 7.9999$$

Additional information

The addition of indicator dye to the seawater sample will perturb the pH (another acid–base system has been added). Although care is taken to minimize this (by adjusting the dye solution pH), it is desirable to correct for the addition of dye to obtain the best pH measurements.

Although, in principle, the pH perturbation could be calculated from a knowledge of the equilibrium chemistry of the sample and the dye, it is simpler to evaluate the magnitude of the correction empirically. A pair of additions of dye is made to each of a series of seawater samples with different pHs, and the change in the measured ratio ($_{435}A/_{596}A$) with the second addition of indicator solution is determined as a function of the measured value ($_{435}A/_{596}A$) determined after

the first addition of dye using a least-squares procedure (see SOP 23 in Dickson et al. 2007):

$$\Delta({}_{435}A/_{596}A)/V = a + b({}_{435}A/_{596}A)$$

where V is the volume of dye added at each addition. The final, corrected, absorbance ratio is

$$({}_{435}A/_{596}A)_{corr} = ({}_{435}A/_{596}A) - V[a + b({}_{435}A/_{596}A)].$$

When preparing a stock solution of indicator dye it is helpful to monitor and adjust the pH to lessen the effects on sample measurements. The absorbance ratio of the prepared dye, which is directly related to pH, can be measured using a short pathlength (0.20 mm) spectrophotometric cell. To adjust the pH, simply add small amounts of either a weak acid (HCl) or base (NaOH) until the desired R value (pH) is achieved.

Bibliography

Byrne, R.H. and Breland, J.A. 1989. High precision multiwavelength pH determinations in seawater using cresol red. *Deep-Sea Res.* **36**: 803–810.

Byrne, R.H., Robert-Baldo, G., Thompson, S.W. and Chen, C.T.A. 1988. Seawater pH measurements: an at-sea comparison of spectrophotometric and potentiometric methods. *Deep-Sea Res.* **35**: 1405–1410.

Clayton, T.D. and Byrne, R.H. 1993. Spectrophotometric seawater pH measurements: total hydrogen ion concentration scale calibration of m-cresol purple and at-sea results. *Deep-Sea Res.* **40**: 2115–2129.

DelValls, T.A. and Dickson, A.G. 1998. The pH of buffers based on 2-amino-2- hydroxymethyl-1,3-propanediol ('tris') in synthetic sea water. *Deep-Sea Res.* **45**: 1541–1554.

Dickson, A.G., Sabine, C.L. and Christian, J.R. (Eds.) 2007. Guide to best practices for ocean CO_2 measurements. *PICES Special Publication 3*, 191pp.

Dickson, A.G. 1993. The measurement of sea water pH. *Marine Chem.* **44**: 131–142.

Zhang, H. and Byrne, R.H. 1996. Spectrophotometric pH measurements of surface seawater at in-situ conditions: absorbance and protonation behavior of thymol blue. *Marine Chem.* **52**: 17–25.

Additional reading

Clayton, T.D., Byrne, R.H., Breland, J.A., Feely, R.A., Millero, F.J., Campbell, D.M., Murphy, P.P. and Lamb, M.F. 1995. The role of pH measurements in modern oceanic CO2-system characterizations: precision and thermodynamic consistency. *Deep-Sea Res.* **42**: 411-429.

Hunter, K.A. 1998. The temperature dependence of pH in surface seawater. *Deep-Sea Res.* **45**: 1919–1930.

Tapp, M., Hunter, K., Currie, K. and Mackaskill, B. 2000. Apparatus for continuous-flow underway spectrophotometric measurement of surface water pH. *Marine Chem.* **72**: 193–202

Yamazaki, H., Sperline, R.P. and Freiser, H. 1992. Spectrophotometric determination of pH and its application to determination of thermodynamic equilibrium constants. *Anal. Chem.* **64**: 2720–2725.

Yao, W., Liu, X. and Byrne, R.H. 2007. Impurities in indicators used for spectrophotometric seawater pH measurements: Assessment and remedies. *Marine Chem.* **107**: 167–172.

Chris Sabine
Tuesday, November 3, 2009
pH measurements using an electrode (lab activity) –
The class will be divided up into three groups of approximately equal size. Each group will spend approximately one hour learning how to measure seawater pH samples. Every student will have an opportunity to watch how pH electrodes are calibrated and try their hand at making measurements. We will discuss some theory of how electrodes work, the effects of low and high ionic strength solutions on electrodes, long and short term calibrations, how to check for electrode stability, maintaining your electrode. This is a hands-on activity.

Helpful Reading:

Dickson, A.G., Sabine, C.L. and Christian, J.R. (Eds.) 2007. Guide to best practices for ocean CO_2 measurements. PICES Special Publication 3, 191 pp. SOP 6a - Determination of the pH of sea water using a glass/reference electrode cell.

Available at: http://cdiac.esd.ornl.gov/ftp/oceans/Handbook_2007/sop06a.pdf

pH Sampling Instruction
(For discrete spectrophotometric pH measurements)
Instructor: Aleck Wang (Sabine to demonstrate on 11/2)

When sampling, put sampling noodle (silicon tubing about 20 cm) on one end of the cell (10-cm glass cell), put the other end of the noodle to nipple of Niskin bottle (or Carboy bottle), set the cell vertically, push in, get rid of the bubbles by squeezing the noodle and tapping on cell, and when cell is filled up, level the cell. Sometimes a big plume of bubbles rushing out will generate a lot of small bubbles that adhere to the cell wall. If tapping cannot get rid of the bubbles, disconnect the cell and tubing, let the water empty out, then reconnect - this should remove the bubbles.

Rinse one cap, wait ~15 seconds, cap one end, detach tubing, wash the other cap, cap the cell, pull the nipple. Sample is done.

After sampling, rinse the cell with tap water, dry the cell with Kimwipes, and place cell in cell warmer (water bath) within a plastic bag. Wait 30 minutes for the sample to warm up to 20°C. All measurements will be made at 20 or 25°C.

Procedure for discrete spectrophotometric pH measurements

Instructor: Aleck Wang (WHOI)

System: Cary 300 spectrophotometer with thermostated cell holder

Take one sample out of the water bath, and put it in the insulation piece. Never use bare hands to touch the cell body. Once the cell is out of the water bath, put it in the insulation piece as soon as possible. In all the following measurement steps, do it in quick and smooth manner.

Wipe the cell window clean, there should be no visible particles on the window. This first wipe is important to guarantee a good baseline. Take the cell out of the insulation piece and put it in the measurement chamber of the Cary 300.

Take a blank measurement by pressing the "zero" button. You may take several readings after "zero" to check if your baseline is stable (<0.002 Absorbance Units). We use the absorbance readings at three wavelengths for spectrophotometric pH measurements depending on which indicator is used. For thymol blue, the three wavelengths are 434nm, 596nm, and 730nm; for m-cresol purple, they are 434nm, 578nm, and 730nm. Note that we use the reading at 730nm to account for baseline drift for both indicators. After "zero", the absorbance at all three wavelengths should be ~0.000.

After the blank is taken, take the cell out of the insulation piece; open one end of the cell, and insert Gilmont pipet tip into the middle of the cell, and deliver 10 µl of the indicator (thymol blue or m-cresol purple); Cap the cell, wipe the water coming out from both caps. Shake the cell 6 times (left to right motion) then check the window. If there is visible dirt, clean it or just return it to measurement chamber. Put the cell back in the measurement chamber and close the chamber cover. Wait for ~5 mins for the temperature to equilibrate.

Click "start" button to read the absorbance at the three wavelengths we use for pH measurements. We will check the baseline shift first. If the absorbance at 730 nm is within ±0.002 abs units, the baseline is good. Otherwise, you may check the cell to see if the optical window is clean. If the baseline is still not good after you clean the window, then you may never pass the baseline check. You may try it the 2nd time. If you still do not pass the baseline check, just go on with your measurement and mark your sample as "suspicious baseline". Record the absorbance at all three wavelengths.

Scan the sample 4 times. If the standard deviation of the sample pH (calculated from the absorbance at the three wavelengths) you measure 4 times is greater than 0.0004 pH units, then rescan the sample 4 times and record the readings. You may have to repeat several times before you can have a SD within 0.0004 pH units. The cause may be either temperature, or particles inside the cell. Please do not take the cell out to rewipe it. In case you never get a SD within 0.0004 pH units after several tries, you should mark your sample as "quality flag" and move on.

After you finish measuring the sample, check the cell temperature by inserting thermometer tip into the cell. Write down the temperature on the sample sheet provided.

Infrared Gas Analyzer (IRGA) DIC Analyzer

Instructor: Chris Langdon

From: Wang and Cai 2004, L&O 49: 341-352.

The system consists of a non-dispersive infrared CO_2 analyzer (Li-Cor 6262), a precision digital syringe pump, a gas flow controller, and a CO_2 stripping reactor. The syringe pump was used to pump the sample (normally 0.5 ml) and acid (1 ml of 10% H_3PO_4) into the reactor after all of the solution in the previous analysis was purged. The CO_2 extraction system consisted of a gas flow line, the reactor, and a gas-drying unit. The body of the reactor was wrapped with an electronic cooling system, which was set below ~3°C. Thus, a low water vapor pressure was maintained in the reactor. The gas flow was further dried through a $Mg(ClO_4)_2$ plug (about 10 ml). The Li-Cor CO_2 detector was used to measure CO_2 gas concentration. The detector had a baseline noise of <0.3 μatm. Finally, DIC was calculated by integrating the area under the CO_2 curve over time (<2 min). The entire procedure was controlled by a computer. Based on replicate analysis, the precision of the DIC analyzer was 0.10–0.15% of a DIC value or of the total area under the integration curve. The system was calibrated using a known volume (0.1–1.0 ml) of certified reference material (CRM) from A. G. Dickson of Scripps Institution of Oceanography.

Step-by-Step Instructions

1. Turn on the Main Power switch, followed by the power switch on the Li-Cor LI-6262.
2. Make sure the bottom line of the Licor display reads Int. If not:
    a. On Licor, hit Function button, then 09, then enter. Set Channel to 22, Start to Thrsh, Thrsh=1.0, End-Thrsh.
    b. Hit Function, then 04. Set bottom line to Channel 46.
3. Turn on N_2 gas flow (first main valve on top, then small black valve on regulator)
4. Flush syringe twice with Dickson standard, holding syringe upright to flush any air out, then fill halfway.
5. On computer, double-click “DIC62final.exe” icon on desktop.

6. Run Dickson standard: 0.75 mL, 0.5 mL, 0.25 mL and 0.01 mL. Run each volume multiple times until consistent value is repeated. Always read Int value from Licor, ignore the Peak Area on the computer. Record time and temperature each time.
7. Flip each sample upside-down several times to mix before running.
8. Run samples (1.0 mL), recording time and temperature of each analysis.
9. Please enter data both in the logbook and computer spreadsheet.
10. Remember to check the Dickson standard every 5 samples. If it does not agree, we need to figure out why.
11. Also remember to run a Dickson standard at the very end of the day.
12. Before shutting down, run 1.5 mL of DDW as a sample to flush
13. To shut down, turn off N_2 gas first (both valves), LI-6262, and the Main Power switch last.
14. Turn off computer.

Wednesday, November 4, 2009
Lectures, TA and DIC measurements

Morning

Time	Activity
8:30 am	**Lecture**. Quality control of analytical measurements of CO_2 parameters (Dickson) MBL Speck Auditorium
9:00 am	**Discussion**. Advantages and disadvantages of current analytical approaches? How well can you control the CO_2 system in your experiment? (Wang) MBL Speck Auditorium
10:00 am	Coffee Break
10:30 am	**Lecture**. Implications of uncertainties in equilibrium constants and analytical measurements (Dickson) MBL Speck Auditorium
11:00 am	**Discussion**. Choosing the optimal parameters for a particular ocean acidification experiment and learning how well you need to measure the parameters you choose (Sabine) MBL Speck Auditorium
12:00 pm	Lunch (Swope Cafeteria, MBL)

See Wednesday afternoon schedule on next page

Time	Group D	Group E	Group F
1:15 pm	**Lab**. TA measurements in Rowe 423/424 (Yates/DuFore and Langdon systems)	**Lab**. Coulometric DIC demo (Erickson, MBL Envir. Sciences Center 117)	Shuttle MBL to McLean
1:30 pm			**Lab**. Open-cell TA measurements (Wang) (McLean 203)
2:15 pm	Walk to MBL Envir. Sciences Center	Shuttle MBL to McLean	
2:30 pm	**Lab**. Coulometric DIC demo (Erickson, MBL Envir. Sciences Center 117)	**Lab**. Open-cell TA measurements (Wang) (McLean 203)	**Lab**. Small volume open-cell TA measurements (McCorkle/Holcomb) in McCorkle lab (McLean 113)
3:00 pm			Shuttle McLean to MBL
3:15 pm			**Lab**. TA measurements in Rowe 423/424 (Yates/DuFore and Langdon systems)
3:30 pm	Shuttle MBL to McLean	**Lab**. Small volume open-cell TA measurements (McCorkle/Holcomb) in McCorkle lab (McLean 113)	
3:45 pm	**Lab**. Open-cell TA measurements (Wang) (McLean 203)		
4:00 pm		Shuttle McLean to MBL	
4:15 pm		**Lab**. TA measurements in Rowe 423/424 (Yates/DuFore and Langdon systems)	Walk to MBL Envir. Sciences Center
4:30 pm			**Lab**. Coulometric DIC demo (Erickson, MBL Envir. Sciences Center 117)
4:45 pm	**Lab**. Small volume open-cell TA measurements (McCorkle/Holcomb) in McCorkle lab (McLean 113)		
5:15 pm	Shuttle McLean to MBL		
5:30 pm	Dinner (Swope Cafeteria, MBL)		
7:00-8:30 pm	**Lecture**. Overview on experimental design. (Langdon) MBL Speck Auditorium		

Wednesday November 4, 2009

Andrew Dickson's lectures:

1) Quality control of analytical CO_2 measurements
2) Implications of uncertainties in equilibrium constants and analytical measurements lecture

Please refer to Dickson's CO_2 system chapter "The carbon dioxide system in sea water: equilibrium chemistry and measurements" (already printed under November 2 tab)

Discussion Topic:

Advantages and disadvantages of current analytical approaches

pH Measurements

	Spectrophotometric pH	Potentiometric pH
Advantages	“Calibration free”	
Disadvantages		Frequent calibration
When to use		

DIC Measurements

	NDIR-Based	Coulometer-based
Advantages		
Disadvantages		
When to use		

TAlk Measurements

	Closed-cell titration	Open-cell titration
Advantages		
Disadvantages		
When to use		

Discussion Topic:

How well can you control the CO_2 system in your experiment?

Methods to lower pH

	Pros	Cons
Bubbling CO_2		Can it ever reach the target pCO2 level?
Adding acid		
Other methods		

Parameters need to be monitored to define the CO_2 system

	Measurement precisions	Calculation errors
TA-DIC		
TA-pH		
pH-DIC		
pCO2 – DIC (if pCO2 can be monitored)		

Chris Sabine
Wednesday, November 4, 2009
Choosing the Right Parameters to Measure (discussion) –
I will start out with a 10 minute reminder of the different measurable parameters and the pros and cons of different combination pairs. Most of the hour will be used for an open discussion of the types of set-ups and which sampling approaches are best suited for those circumstances. There are many issues that may prevent us from measuring the ideal carbon pairs so this will be an opportunity for a dialogue on how to make the best choices. Students should come prepared with ideas on an experimental set up or monitoring circumstance that they would like to discuss with the class.

Spectrophotometric determination of total alkalinity in seawater using the indicator dye bromocresol purple

C.M. DuFore and K.K. Yates*, U.S. Geological Survey, 600 Fourth Street South, St. Petersburg, FL 33701, kyates@usgs.gov

Schedule of what to expect

- Brief introduction to discuss applications of this method
- Overview of equipment required and flexibility with using similar equipment
- Brief demonstration of technique
- Hands on time for students to make measurements

Equipment List

- Ocean Optics USB2000 linear array spectrometer
- Ocean Optics LS-1 light source
- Ocean Optics 2 m long 400 µm diameter optical fibers
- Custom built PVC housing for spectrophotometric cells
- (2) Ocean Optics 74-UV collimating lenses
- 6.5 cm x 6.5 cm x 6.0 cm optical glass cell (Hellma Cells, Inc.)
- 0.2 mm pathlength spectrophotometric cell
- Sample transfer device
- Stir plate and stir bars
- 10 ml syringe
- Teflon needle
- Gas dispersion tube (Ace Glass, Inc.)
- Ultra high purity N_2 tank with water saturation device
- HCl (~ 0.1 N)
- Ability to measure salinity and temperature
- Pipette (0.01 – 0.1 cm^3) and tips
- ~ 125 cm^3 bottle
- Stock solution of bromocresol purple (~ 4 X 10^{-3} dm^{-3})
- Analytical balance (0.1 mg)
- Certified reference materials (CRM's)
- Personal computer with OOIBase32 spectrometer operating software

Background

The outlined procedures are for the determination of seawater total alkalinity using a rapid scan linear array spectrophotometer. The results are expressed as moles per kilogram of seawater. The method has been shown to produce reliable results for in-situ conditions ranging from salinity values between 29 and 37, and temperature values between 13˚C and 32˚C.

The total alkalinity of a sample of seawater is defined as a difference between the excess concentrations of proton acceptors over proton donors in 1 kilogram of seawater:

$$A_T = [HCO_3^-] + 2[CO_3^{2-}] + [B(OH)_4^-] + [OH^-] + [HPO_4^{2-}]$$

$$+ 2[PO_4^{3-}] + [SiO(OH)_3^-] + [NH_3] + [HS^-] + \ldots$$
$$- [H^+]_F - [HSO_4^-] - [HF] - [H_3PO_4] - \ldots$$

Brackets represent total concentrations of these constituents in solution, $[H^+]_F$ is the free concentration of hydrogen ion, and the ellipses represent additional minor acid or base species that are either unidentified or present in such small amounts that they can be ignored. Additional information can be found in Dickson et al. 2007 (chapter 2).

The total alkalinity (A_T) of a seawater sample that has been acidified and purged of CO_2 can be written as follows:

$$A_T M_{SW} = N_A M_A - [H^+]_{ASW} M_{ASW} - [HI]_{total} \Delta(HI) M_{ASW}$$

where A_T is the alkalinity (mol kg^{-1}(seawater)) of a seawater sample, M_{SW} is the mass of the seawater sample (kg), N_A is the concentration of the added acid (mol kg^{-1}(solution)), M_A is the mass of the added acid, $[H^+]_{ASW}$ is the excess hydrogen ion concentration in the acidified seawater (mol kg^{-1}(seawater)), M_{ASW} is the mass of the acidified seawater calculated as $M_{SW} + M_A$, $[HI]_{total}$ is the total concentration of indicator in both protonated (H_2I, HI^-) and unprotonated (I^{2-}) forms, and $\Delta(HI)$ is a term that accounts for the moles of H^+ gained or lost by the indicator in the final acidified seawater relative to the stock solution from which it is added. For solution pH > ~3, absorbance contributions from H_2I are negligible. The acid-base equilibria for the indicator is described by

$$H^+ + I^{2-} \leftrightarrow HI^-$$

where

$$K_1 = [HI^-]/[H^+][I^{2-}]$$

and [HI-] and [I2-] are the concentrations of the protonated and unprotonated forms of the indicator. The pH of the solution is then given by

$$pH = \log K_1 + \log[I^{2-}]/[HI^-] = \log K_1 + \log\{(R - e_1)/(e_2 - Re_3)\}$$

where R is the ratio of indicator absorbance at two wavelengths ($_{589}A/_{432}A$ for bromocresol purple), K_1 is the formation constant of the indicator and e_1, e_2 and e_3 are the molar absorptivity ratios. The $[H^+]_{ASW}$ and $\Delta(HI)$ terms were measured spectrophotometrically and determined through observations of the absorbance ratios of the sulfonephthalein indicator bromocresol purple. Using bromocresol purple, solution pH_T is given as

$$pH_T = 5.8182 + 0.00129(35 - S) + \log\{(R(25) - 0.00381)/(2.8729 - 0.05104R(25))\}$$

where acid concentrations are in terms of moles per kg of seawater ($pH_T = \log [H^+]_{ASW}$) and

$$R(25) = R(T)\{1 + 0.01869(25 - T)\}$$

where $29 \le S \le 37$ and $13^\circ C \le T \le 32^\circ C$ and $R(T) = {}_{589}A/_{432}A$. Note that the final R value used in the above equation should be corrected for baseline drift by monitoring a non-absorbing wavelength ($_{750}A$) and subtracting from each absorbance maxima ($_{589}A$-$_{750}A/_{432}A$-$_{750}A$).

Absorbances are measured with an Ocean Optics USB2000 linear array spectrometer. Titrations are performed in a square glass cell that is placed inside of a custom built PVC housing consisting of a pair of collimating lenses mounted to the housing. Optical fibers are connected from the collimating lenses to the light source and the spectrometer respectively. Using a rapid scan linear array spectrometer, like the Ocean Optics USB2000, allows for continuous monitoring of solution pH. As such, titrations can be terminated at relatively high pH, such that excess acid terms are very small.

Methods

To begin, place the clean dry cell into the PVC housing located on top of the stir plate and place the stir bar inside. Thoroughly mix the contents of the sample bottle, remove the stopper, and use a Kimwipe® to remove as much grease as possible. Rinse and dry the longer tube of the sample transfer device and insert it into the sample bottle. Using the rubber bulb, pressurize the bottle and flush the tubing with about 20 cm^3 of sample.

Fill the 125 cm^3 plastic bottle with sample and weigh; record the weight to 0.1 mg. Next, carefully pour the sample into the clean glass cell containing the stir bar and set the stir plate to an appropriate setting. Reweigh the now empty sample bottle and subtract this weight from the weight of the original sample bottle containing the sample. This difference is the M_{SW}.

Subsequent to storing a reference (blank), use a pipette to add an appropriate amount of bromocresol purple stock solution to make the final solution concentration approximately 2–3 µM in indicator. A 125 cm^3 sample and a stock solution of ~ 4 x 10^{-3} M of bromocresol purple requires roughly 0.08 cm^3 of indicator.

Weigh a 10 ml syringe fitted with the Teflon needle and filled with ~ 0.1 N HCl and begin dispensing into the spectrometer cell. Begin continuous monitoring of the appropriate wavelengths paying close attention to the calculated *R* value. The color of the solution will start a deep purple and will begin to turn yellow as the pH decreases. Continue titrating the acid until the *R* value approaches ~ 0.07–0.08 (pH ≈ 4.3–4.2).

Purge the solution with N_2 using the gas dispersion tube connected to a water saturation device for at least 5 minutes or until the *R* value stabilizes. Presaturating the N_2 stream with H_2O is recommended in order to prevent solution dehydration with concomitant overestimation of $[H^+]_{ASW}$. During this step continue to monitor the *R* value, adding single drops of acid if the $R > 1$. When using bromocresol purple, a final $R \approx 0.3$ and a pH ≈ 4.8 results in the indicator term ($[HI]_{total}\Delta(HI)M_{ASW}$) being very small (< 0.2 µmol kg^{-1}) and can essentially be ignored.

After the titration is complete, remove the gas dispersion tube and weigh the syringe. Calculate the weight of added acid (M_A) and record the temperature in the spectrometer cell. Record the final absorbance measurements at each wavelength ($_{589}A$, $_{432}A$, $_{750}A$) and remove the baseline offset ($_{589}A$-$_{750}A$/$_{432}A$-$_{750}A$). This is the absorbance ratio $R(T)$ at the measurement temperature (T).

Example calculation

Using a spreadsheet to calculate the total alkalinity is probably the easiest way to organize the data for multiple analyses and simplify calculations. Here is a quick example to get you started:

$T = 24.0$ °C; $S = 34.815$

$$M_{SW} = 124.5362 \text{ g};\ M_A = 2.9165 \text{ g};\ N_A = 0.1006 \text{ mol kg}^{-1}$$

$$_{432}A = 0.260;\ _{589}A = 0.085;\ _{750}A = 0.001$$

$$\therefore\ R = (0.085 - 0.001)/(0.260 - 0.001) = 0.324$$

First we calculate $R(25)$ as

$$R(25) = 0.324(24.0)\{1 + 0.01869(25 - 24.0)\} = 0.330$$

Next we calculate the solution pH as

$$pH_T = 5.8182 + 0.00129(35\text{-}34.815) + \log\{(0.330 - 0.00381)/(2.8729 - 0.05104 \text{ X } 0.330)\}$$
$$= 4.8761$$

and thus

$$A_T = \{(0.1006 \text{ X } 2.9165) - (1.3301 \text{ X } 10^{-5} \text{ X } 127.4527)\}/124.5362 = 2342.3 \text{ µmol kg}^{-1}$$

Additional information

When preparing a stock solution of indicator dye it is helpful to monitor and adjust the pH to lessen the effects on sample measurements. The absorbance ratio of the prepared dye, which is directly related to pH, can be measured using a short pathlength (0.20 mm) spectrophotometric cell. To adjust the pH, simply add small amounts of either a weak acid (HCl) or base (NaOH) until the desired *R* value (pH) is achieved.

Bibliography

Breland, J.B. and Byrne, R.H. 1992. Determination of seawater alkalinity by direct equilibrium with carbon dioxide. *Anal. Chem.* **64**: 2306–2309.

Breland, J.B. and Byrne, R.H. 1993. Spectrophotometric procedures for determination of seawater alkalinity using bromocresol green. *Deep-Sea Res.* **40**: 629–641.

Clayton, T.D. and Byrne, R.H. 1993. Spectrophotometric seawater pH measurements: total hydrogen ion concentration scale calibration of m-cresol purple and at-sea results. *Deep-Sea Res.* **40**: 2115–2129.

Dickson, A.G., Sabine, C.L. and Christian, J.R. (Eds.) 2007. Guide to best practices for ocean CO_2 measurements. *PICES Special Publication 3*, 191pp.

Dickson, A.G., Afghan, J.D. and Anderson, G.C. 2003. Reference material for oceanic CO_2 analysis: a method for the certification of total alkalinity. *Mar. Chem.* **80**: 185-197.

Dickson, A.G. 2001. Reference materials for oceanic CO2 measurements. *Oceanography* **14**: 21-22.

Yao, W. and Byrne, R.H. 1998. Simplified seawater alkalinity analysis: Use of linear array spectrometers. *Deep-Sea Res.* **45**: 1383–1392.

Additional Reading

Clayton, T.D., Byrne, R.H., Breland, J.A., Feely, R.A., Millero, F.J., Campbell, D.M., Murphy, P.P. and Lamb, M.F. 1995. The role of pH measurements in modern oceanic CO2-system characterizations: precision and thermodynamic consistency. *Deep-Sea Res.* **42**: 411–429.

Millero, F.J., Zhang, J.-Z., Lee, K. and Campbell, D.M. 1993. Titration alkalinity of seawater. *Mar. Chem.* **44**: 153-165.

Roche, M.P. and Millero, F.J. 1998. Measurement of total alkalinity of surface waters using a continuous flowing spectrophotometric technique. *Mar. Chem.* **60**: 85-94.

Watanabe, A., Kayanne, H., Nozaki, K., Kato, K., Negishi, A., Kudo, S., Kimoto, H., Tsuda, M. and Dickson, A.G. 2004. A rapid, precise potentiometric determination of total alkalinity in seawater by a newly developed flow-through analyzer designed for coastal regions. *Mar. Chem.* **85**: 75-87.

Yao, W., Liu, X. and Byrne, R.H. 2007. Impurities in indicators used for spectrophotometric seawater pH measurements: Assessment and remedies. *Marine Chem.* **107**: 167–172.

WANG LAB – MCLEAN 203
NOVEMBER 4, 2009
Open-cell TAlk Titration Protocol

System: SEAWATER TOTAL ALKALINITY TITRATOR, MODEL AS-ALK2, Apollo SciTech, Inc.

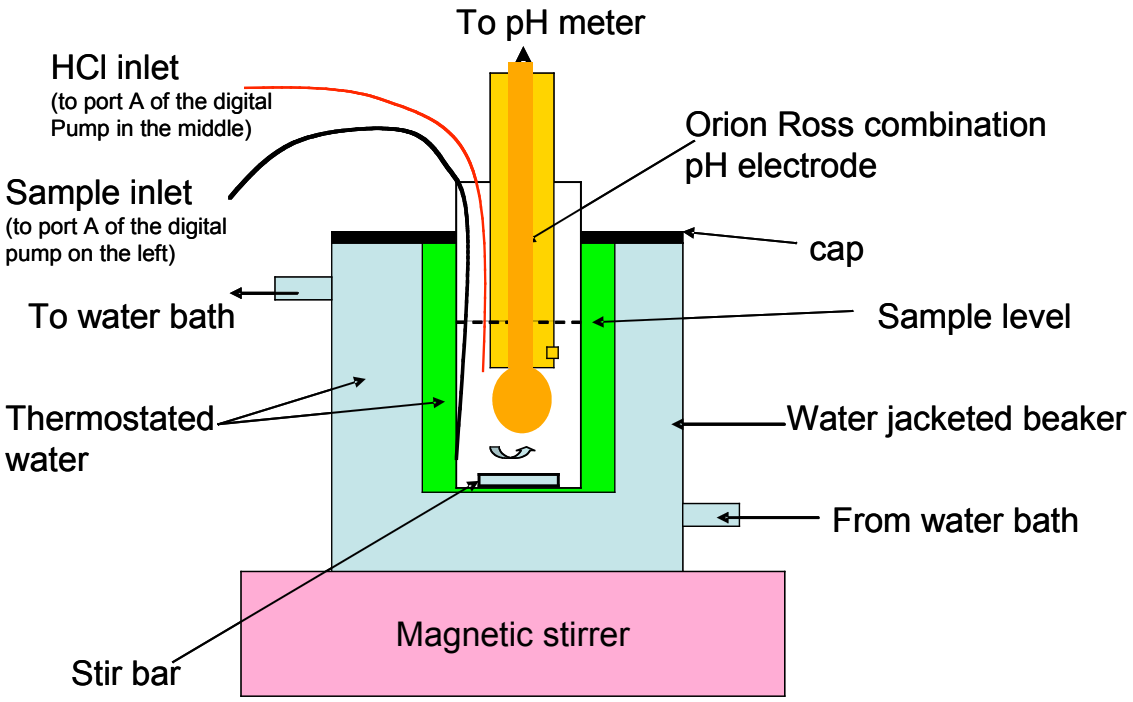

Fig. 1. Illustration of an open cell TAlk titration with a temperature control device

C. OPERATION

C1. Power up

Turn the titrator's power switch on. The indicate light should be on. Also turn the pH meter power on. Check the connection between your PC, the titrator and the pH meter.

C3. Running the analytical program

Under Windows® system use a mouse to select the program "AS-ALK-Star07", and then press "Enter" to run the program.

The program will show a window as below:

A text file: TA_Data\YYMMDD.txt

is being created to save the titration data

which will be used to store titration results. This file is a text file (.txt) and all its columns are separated with TAB key. The file name, YYMMDD.txt, is composed with the current date of the measurement.

After a few seconds, the following screen will show:

Digital Pump is on port COM1 pH Meter is on port COM2
Do you want to change the communication ports (N)?

which requests you to confirm the communication ports. Check the serial cables and type the correct port number (default COM1 for the system and COM2 for the pH meter), then press "Enter", the program will run into the next step.

Computer screen will show:

Initialization of digital pumps

The program will conduct the initialization for the two digital pumps. Note that if there is any liquid left in the syringes it will be pushed out from port "A" of the valve. Be ready to collect the solution with a waste collector.

After initialization the screen displays:

HCl pump is going to be flushed twice Hook HCl solution to port B of HCl pump Make sure to collect the discharged solution When **READY**, Press **ENTER** Key

Before you press "Enter", make sure to link the HCl solution to the port "B" of the pump in the middle, and that the outlet from port "A" is inside the waste collector. Under the control of the program, the syringe will be flushed twice with HCl solution. Then, a main menu of operation will be given.

When the program is running, colored bars will begin to flash on the screen, indicating that the program is working properly.

C4. Analytical procedure

The computer shows the main menu with only two items at this stage:

MENU 1: Calibration of pH electrode & HCl

5：End program

Type the number on the MENU

You have to type "1" to calibrate the system before you start the sample titration.

If the computer has been used previously for this Total Alkalinity (TAlk) titrator, the last calibration information will be loaded and displayed on the screen. You may hit "Y" and "Enter" to finish the calibration if you accept the data shown, or press "Enter" only to get into the calibration procedure.

Note that whenever the program asks for data or string input, the data or string used last time will be shown in light gray color. If you want to accept the number or string shown, you may press "Enter". If you do not want to accept the original data or string shown on the screen, you may input the new data or string. However, once you type any key other than "Enter" you must finish the complete string. You can not share any letters/digits that had been displayed on the screen.

If there are no data saved in the computer, the program will go directly into the calibration procedure.

First, the computer will ask for the temperature of the measurement in degrees Celsius or if you wish to use the ATC temperature sensor. If the titration is conducted with a temperature-controlled water bath, please input the water bath temperature. If the titration is carried on without a water bath (i.e., under room temperature), then, please choose ATC. Under ATC mode, the program corrects temperature variation between the pH electrode calibration and the time of titration.

Then, the program will ask for the calibration of the pH electrode with three standard buffer solutions and inputs of corresponding voltages in mV (see C.5.1 for details).

Next, the program will ask for the HCl standardization. Input the concentration of HCl solution if it is known (choice 1); or you may standardize the HCl concentration by titration with the calibration program using a TAlk standard solution (choice 2) (see C.5.2 for details).

When calibration is done, there will be a new window with the main menu of all the functions as below:

1. Calibration of pH electrode & HCl
2. Seawater Sample (S > 30)
3. Known Salinity Sample
5. End Program

Type the number on the MENU

For seawater alkalinity titration with unknown salinity, you may type 2 and "Enter"; then follow the instruction of the program to input the volume as well as the number of the sample, etc. However, if salinity is known, choice 3 is preferred.

The calibration and measurement should be conducted under the same temperature. Generally, 0.1% precision can be reached in a room with air conditioning, but if you want to have the result with higher quality you should use a constant temperature water bath to control the temperature of titration through the use of water-jackets for the titration vessel, acid and sample bottles. The samples, the TAlk standard, and pH buffer bottles should also be stored in the water bath before use.

For each point of the titration, the pH value will be read by the computer in potential (mV) with the interval of 5 seconds. If the readings are stable, the average of the 4 readings will be given as the final value of the point, otherwise, the computer will keep read every 5 seconds until it is stable, or reaches the time limit for individual point, which is 2 minutes. All the titration data will be displayed on the screen, and renewed instantly.

C5. Standardization

The calibration for the system can be done at anytime when the main menu shows up. Type "1" and "Enter" to enter the calibration procedure.

C5.1 Calibration of the pH electrode

Three pH standard buffer solutions should be used for pH electrode calibration. The quality of the pH electrode is very important for an accurate TAlk titration. We recommend using of Ross Orion pH combination electrode only (Orion cat# 8102BN; or 8102BNUWP).

Standardize the pH electrode with three pH buffers manually. Write down the values of the standard solution and the corresponding potentials, respectively. Input the values to the program when it is prompted. The relationship between pH and potential and the efficiency of the electrode will be calculated. The efficiency of the electrode must be better than 95% to achieve high quality data.

C5.2 Standardization of the HCl solution

Check whether the standard TAlk solution has been connected to the port "B" of the left hand side digital pump. We suggest that you use a HCl solution with the concentration about 0.08 M for seawater applications. [HCl] may be adjusted for other purposes.

There are two choices on the menu for HCl calibration:

1. Known HCl concentration
2. Determine [HCl] by titration with standard solution

Press 1 and input the acid concentration (in mol/L) if you know the exact value. Pressing 2 if the HCl concentration is not known and need be determined through titration of a standard solution such as the Dickson CRM.

Choose function “2”, follow the screen by typing in the volume (e.g., 16 mL) of standard solution each time the titration will use; the name of the standard (e.g., dicksonCRM or Jan04Na2CO3); the concentration of the standard TAlk solution (in mmol/L) and a rough concentration of the HCl solution (e.g., 0.08 mol/L), which will be used to estimate the amount of HCl needed to bring the Alk solution to the first Gran point after the end-point.

Then the program will remind you to connect the TAlk standard to the B-port of the left digital pump and the outlet of port-A to a waster bottle. Then press [Enter]. The left hand side pump syringe will be rinsed with the standard solution for 3 times, twice with 2.5 ml and once with the volume for calibration (or later for sample analysis), and will then suck the solution for analysis. Keep the tubing outlet in the seawater waste container until the syringe is filled to the volume with the standard solution. Now, move the tubing outlet to the titration vessel. Press [Enter] key when the PC screen pop up a prompt. The solution in the syringe then will be transferred to the titration vessel. The PC window will remind you to turn on the stirrer and then to press [Enter] key again. Make sure that the HCl outlet tubing is inside the vessel and the speed of the stirrer is appropriate (no violent stirring!). Press [Enter] to start the titration. The PC will beep when the titration is finished. Meanwhile, the left hand side syringe will suck the standard solution again for the next titration. Turn off the stirrer, remove the titration vessel from the water jacketed beaker on the top of the stirrer, rinse the pH electrode and the HCl outlet tubing with DI water, and then scrape large water drops off them with a piece of Kimwipe tissue. Use another clean & dry vessel for the next titration is preferred. Put a clean & dry stir bar in the vessel and put the vessel back (inside the water jacketed beaker) on the top of the stirrer. Put the pH electrode and the HCl outlet tubing inside the vessel. Put the standard (or later sample) solution outlet in the vessel, press [Enter] key to transfer the solution to the titration vessel. Remove the standard solution outlet tubing from the vessel and press [Enter] key again to start next titration.

During standardization, the first titration result will be discarded. The program will repeat the procedure again and again until the titration results meet the requirement of accuracy (0.08%). Normally, the second and third titration should agree within 0.08%. A high quality pH electrode is critical. The PC will beep to identify that the calibration is done. All the calibration data are saved in the text file. The name of this file is shown on the upper left corner of the screen.

C6. Sample measurement

After calibration, the program show a main menu,

1. Calibration of pH electrode & HCl
2. Seawater Sample (S > 30)
3. Known Salinity Sample
5. End Program

Type the number on the MENU

The following procedure is similar to the standardization. Choose 2 or 3 for seawater sample measurements. You will be asked to select a solution volume (mL) and a sample name/number for the sample to be titrated. The default value will be the volume used for the last sample after first measurement. Then, input the sample number. If you choose 3, you also asked to key in the sample salinity. Then the program will remind you to connect the sample solution to the B-port of the left digital pump and the outlet (A) to the waster bottle.

Afterward, the sample syringe is being rinsed. Please put the sample transferring tubing (from port A of the left hand side pump) into the seawater waste bottle. After rinse, the program will prompt you to put the sample transferring tubing into the titration vessel (the 25-mL vessel with a stir bar in it). Press [Enter], the sample solution will be delivered to the titration vessel. Then, the program will remind you to turn the magnetic stirrer on and, after the [Enter] key is pressed, will start to add HCl to the sample in the titration vessel incrementally. The AS-ALK2 will perform the titration and calculation (end point acid volume and TAlk) according to the automated titration procedure and the Gran titration theory as described in the Background.

When the automated titration is finished, the PC will beep, display the result of the titration and the program will be back to the full MENU. Choosing "2" for seawater measurement again will start for the next sample. You may choose to measure the same water sample twice.

Choose 3 for the samples with known salinity. Beside all the information required for seawater sample, the program will also ask about the salinity of the sample. You may enter an estimated salinity value. We strongly recommend that this mode is used for all open ocean seawater samples with known salinity as it can save time to pre-locate the end point.

If you choose option 3 (Know Salinity Sample) and if the salinity is less than 20, you will be asked to supply a river end-member TA value as well. The default value is 700 μM which is used for salinity > 20. You may alter it to any value. We suggest 350 μM for small coastal plain rivers and low latitude large rivers (i.e., the Amazon), 1000 μM or higher for large mid-latitude rivers (for example, ca.2000 μM for the Mississippi River). Please contact us for your special needs. We will supply you upgraded programs free of charge.

C7. Ending the measurement

After ending the analysis, the screen will show

1. Calibration of pH electrode & HCl
2. Seawater Sample (S > 30)
3. Known Salinity Sample
5. End Program

Type the number on the MENU

Press [5] under the main menu to end the program. The screen will ask you to confirm. You confirm ("1") to finish the measurement. If you are not going to use the titrator for a while,

choose “2” to flush the system with DI water. Supply DI water to the B-ports of both digital pumps and the A-ports of both to the waster to complete the flush. Then power off the titrator and the pH meter.

Protocol for Measuring Total Alkalinity (TA)

Instructor: Chris Langdon

Equipment

Combination pH electrode and reference cell with BNC connector
pH meter/controller
Stepper motor driven 2 ml burette
Water bath and jacketed beaker
Magnetic stirrer and Teflon stir bars

Solutions:	0.1 *N* HCl
	Tris seawater buffer pH_T = 8.089 @ 25.0°C
Recommended:	100 mL polyethylene beakers

Total Alkalinity Protocol –Laboratory

1. Pour 30-40 ml of Tris seawater buffer in beaker
2. Place beaker in jacketed beaker and insert pH electrode, acid dispensing tip and digital temperature probe.
3. Observe mV reading until stable to ± 0.02 mV.
4. Enter temperature and mV reading into TA calculations spreadsheet.
5. Pour 30-40 ml of CRM into beaker and weigh on balance.
6. Place beaker in jacketed beaker and insert pH electrode, acid dispensing tip and digital temperature probe.
7. Enter weight into titrator program.
8. Press Start Titrate button on titrator
9. Titrator will collect mV readings until stability criteria are met. This reading will be used to compute the initial pH of the sample.
10. When the titrator beeps increase the stirring speed to the position marked on the knob.
11. The titrator will now make small HCl additions and observe the resulting pH reading until a pH of 3.0 is reached. This step takes approximately 12 min. At the end the titrator will perform a Gran analysis of the titration data and it will output the first and second equivalence point and the computed TA.
12. If you are using a certified bottle of HCl you can check to see if the TA is within ± 2 µEquiv/kg of the certified value of your CRM. If it is you can proceed to titration of samples. If the normality of the HCl is not precisely known we will compute the normality using the TA calculations spreadsheet. The equation we use is c=1e-6*wt*v2/TA. Repeat the titration of CRMs until you have determined the normality of the HCl to ± 0.0001.
13. Turn off the titrator and turn it back on. Enter the new value for the normality of the HCl.
14. You can now run samples just as you did the CRMs. Be sure to note the weight, temperature, initial mV reading, second equivalence point (v2) and

TA in the TA calculations spreadsheet. The spreadsheet will compute the initial pH on the total pH scale of each sample.

15. If you want to compute the DIC and other carbonate parameters for your samples you can enter the TA and pH into CO2SYS to make the calculations.

Adapted from Guide to Best Practices for Ocean CO_2 Measurements http://cdiac.ornl.gov/oceans/Handbook_2007.html. SOP 6 Measuring Seawater pH and SOP 3b Determination of total alkalinity in seawater using an open-cell.

Outline of Overview of Experimental Design Lecture

Instructor: Chris Langdon

1. Bubbling with CO_2 enriched air or addition of acid and bicarb?
    a. For small systems bubbling is best
    b. For very large systems adding acid and bicarb may be the only way
    c. For experiments underwater adding acid and bicarb may be the way
2. How many treatment levels?
    a. May only be possible to do two if the CO_2 treatments are crossed with one more other factors (present day and year 2100 or 380 and 800 ppm)
    b. If CO_2 is the only factor then the more levels the better because we don't know much about the shape of the response function (380, 560 and 800 for sure and maybe 1000 also 200 if there is interest what may have happened during glacial periods)
3. If you think that saturation state is really the dependent variable then $[Ca^{2+}]$ should also be varied
4. To get at whether control is through pH or CO_2/CO_3^{2-} the pH can be held constant while $[CO_3^{2-}]$ is varied
5. Duration of experiment
    a. Short term experiments to look at for example ocean acidification (OA) effects on fertilization, sperm motility, larval settlement
    b. Long term experiments to look at larval development, growth of adult organisms, acclimation, interactions with other physiological responses
6. Size of the experimental chambers or tanks
        i. Small so you can have lots of replicates
        ii. Large so that the organism under test does not alter the chemistry of the water significantly during the course of the experiment
7. Monitoring the chemistry is essential
    a. With open top systems CO_2 of the gas must be adjusted empirically to achieve the desired level in the experimental tank because of gas exchange
    b. Metabolic activity of the organisms under test will cause diurnal variability in the chemistry that can be minimized by adjusting the biomass to tank volume ratio
    c. If this is a running seawater system then the flow rate will also influence the CO_2 level
    d. At a minimum at the beginning and the end
    e. Ideally throughout the course of the experiment
        i. Withdraw water samples for TA and DIC is generally best
            1. they are very stable
            2. volume needed

ii. Monitor the pCO_2 continuously using an equilibrator with periodic measurements of DIC or TA

Thursday, November 5, 2009
Lectures, moored pCO_2 instrument demo, CO2SYS experiments, and larval mollusk experimental setup

Morning

Time	Activity
8:30 am	**Lecture**. Approaches, tools to manipulate carbonate chemistry (Gattuso) MBL Speck Auditorium (1 hour plus 15 mins for questions/discussion)
9:45 am	Coffee Break
10:15 am	**Lecture/Demo**. Sabine's moored CO_2 instrument demo (MBL Rowe – auditorium for lecture, then to Rowe 423/424 to cycle participants through instrument demo)
12:00 pm	Lunch (Swope Cafeteria, MBL)

Afternoon

Time	Group G	Group H	Group I
1:15 pm	Shuttle MBL to Clark	Shuttle MBL to ESL	Break
1:30 pm	**Lab**. Theoretical CO2SYS experiments (Yates, WHOI Computer Group Training Facility, Clark 141)	**Lab**. Exp't setup (each group does 3 ambient, 3 enriched) for larval mollusk experiment (McCorkle/White, ESL 10)	
2:00 pm			Shuttle MBL to Clark
2:30 pm	Walk Clark to ESL	Break/Walk ESL to Clark	**Lab**. Theoretical CO2SYS experiments (Yates, WHOI Computer Group Training Facility, Clark 141)
2:45 pm	**Lab**. Exp't setup (each group does 3 ambient, 3 enriched) for larval mollusk experiment (McCorkle/White, ESL 10)		
3:30 pm		**Lab**. Theoretical CO2SYS experiments (Yates, WHOI Computer Group Training Facility, Clark 141)	Walk Clark to ESL
3:45 pm	Shuttle ESL to MBL		**Lab**. Exp't setup (each group does 3 ambient, 3 enriched) for larval mollusk experiment (McCorkle/White, ESL 10)
4:00 pm	Break		
4:30 pm		Shuttle Clark to MBL	
4:45 pm			Shuttle ESL to MBL
5:00 pm	Dinner (Swope Cafeteria, MBL)		

Guide for Best Practices in Ocean Acidification Research and Data Reporting

Chapter 1: Sea water carbonate chemistry

Section 1.2: Approaches and tools to manipulate the carbonate chemistry

Jean-Pierre Gattuso[1,2], Kunshan Gao[6], Kitack Lee[3], Björn Rost[4], Kai G. Schulz[5]

(1) Laboratoire d'océanographie, CNRS, B.P. 28, F-06234 Villefranche-sur-mer Cedex, France

(2) Observatoire Océanologique, Université Pierre et Marie Curie-Paris 6, F-06230 Villefranche-sur-mer, France

(3) School of Environmental Science and Engineering, Pohang University of Science and Technology, Pohang, South Korea

(4) Alfred Wegener Institute for Polar and Marine Research, Am Handelshaven 12, 27570 Bremerhaven, Germany

(5) Leibniz Institute for Marine Sciences (IFM-GEOMAR), Düsternbrooker Weg 20, 24105 Kiel, Germany

(6) State Key Laboratory of Marine Environmental Science, Xiamen University, Xiamen, Fujian 361005, China

1.2.1- Introduction

Although the chemistry of ocean acidification is very well understood (see section 1.1), its impact on marine organisms and ecosystems remains poorly known. The biological response to ocean acidification is a recent field of research, the first purposeful experiments have only been carried out as late as the 1980s (Agegian, 1985) and most were not until the late 1990s. The potentially dire consequences of ocean acidification have attracted the interest of scientists and students with a limited knowledge of the carbonate chemistry and its experimental manipulation. Perturbation experiments are one of the key approaches used to investigate the biological response to elevated $p(CO_2)$. Such experiments are based on measurements of physiological or metabolic processes in organisms and communities exposed to seawater with normal and altered carbonate chemistry. The basics of the carbonate chemistry must be understood to perform meaningful CO_2 perturbation experiments (see section 1.1).

Briefly, the marine carbonate system considers CO_2^*(aq)[the sum of CO_2 and H_2CO_3], HCO_3^-, CO_3^{2-}, H^+, OH^-, and several weak acid-base systems of which borate-boric acid ($B(OH)_4^-$, $B(OH)_3$) is the most important. As discussed by Dickson (see section 1.1), if two components of the carbonate chemistry are known all the other components can be calculated for sea water with typical nutrient concentrations at a given temperature, salinity, and pressure. One of the possible pairs is of particular interest because both components can be measured with precision and are conservative in the sense that their concentrations do not change with temperature or pressure. Dissolved inorganic carbon (DIC) is the sum of all dissolved inorganic carbon species while total alkalinity (A_T) equals $[HCO_3^-] + 2\,[CO_3^{2-}] + [B(OH)_4^-] + [OH^-] - [H^+]$ + minor components, and

reflects the excess of proton acceptors over proton donors with respect to a zero level of protons (see section 1.1 for a detailed definition). Analytically, A_T is determined by the titration of sea water with a strong acid and thus can also be regarded as a measure for the buffering capacity of sea water. Any changes in any single component of the carbonate system will lead to changes in several, if not all, other components. In other words, it is not possible to vary a single component of the carbonate system while keeping all other components constant. This interdependency in the carbonate system is important to consider when performing CO_2 perturbation experiments. To adjust sea water to different $p(CO_2)$ levels, the carbonate system can be manipulated in various ways that usually involve changes in A_T or DIC. The goal of this chapter is (1) to examine the benefits and drawbacks of various manipulation methods used to date and (2) to provide a simple software package to assist the design of perturbation experiments.

1.2.2- Approaches and methodologies

Sea water chemistry can be manipulated in various ways that alter parameters of carbonate system differently. The following sections examine the five techniques that are most useful in the context of ocean acidification. To illustrate the discussions, each section below is followed by a numerical example. The R package *seacarb* was used to calculate the carbonate chemistry parameters (Lavigne *et al.*, 2008) and the syntax used for each example is available in Gattuso & Lavigne (2009). Note that other software packages are available (see section 1.1). Calculations were carried out using the first and second dissociation constants of carbonic acid given by Lueker *et al.* (2000). In systems open to the atmosphere, it is assumed that the sea water and

atmosphere are in equilibrium with respect to CO_2 and the target $p(CO_2)$ is the projected value for the year 2100 (Gattuso & Lavigne, 2009; Table 1).

It must be pointed out that the methods described below enable one to set the carbonate chemistry at the beginning of a perturbation experiment. The impact of biological (e.g. photosynthesis, respiration and calcification) and physical processes (e.g. air-sea water exchange of CO_2 and temperature changes) on the carbonate chemistry can distort the initial values and must be taken into account in the experimental design (see section 1.2.4.2).

There are several experimental approaches to adjust sea water CO_2 by either changing DIC at constant A_T (e.g. aeration with air at target $p(CO_2)$, injections of CO_2 saturated sea water and combined additions of $NaHCO_3$ or Na_2CO_3 and HCl) or changing A_T at constant DIC (NaOH and/or HCl additions). Each experiment has different requirements depending on organisms, experimental duration, incubation volumes or sampling intervals and hence one of the possible carbonate chemistry manipulations will probably be favoured.

1.2.2.1- Changing DIC at constant A_T

1.2.2.1.1- Aeration at target p(CO_2)

Bubbling sea water with gases is a very efficient way to manipulate its carbonate chemistry. The *seacarb* function *pgas* estimates the changes in the carbonate chemistry resulting from changes in generated by bubbling gases.

Example: sea water with a $p(CO_2)$ of 384 µatm and an A_T of 2325 µmol kg^{-1} can be bubbled

with a mixture of CO_2 and air with a $p(CO_2)$ of 793 µatm. Salinity is 34.9, temperature is 18.9°C and calculations are done for surface waters. This approach exactly reproduces the values of all parameters of the carbonate system expected in the year 2100 (Table 1).

Two aeration techniques have been used in ocean acidification studies: pH-stat and bubbling with premixed gases. In pH-stat systems, pH is monitored continuously and a controller opens or closes the valves that deliver the gases when pH goes above or below a set value. Gases are then delivered until pH reaches the target value again. Different combinations of gases have been used: (1) air and pure CO_2, (2) CO_2-free air and pure CO_2, and (3) air, CO_2-free air and pure CO_2. CO_2-free air can be produced easily using either molecular sieves or CO_2 scrubbers such as soda lime or NaOH and $Ca(OH)_2$ in low concentrations (C. Hintz, pers. comm.). The pH threshold is calculated using the desired $p(CO_2)$ and total alkalinity which is either assumed to be constant or frequently measured. This method has the potential to compensate for changes in the carbonate chemistry due to photosynthesis and respiration or, in the case of open culture systems, to changes in the chemistry of the source water. However, the air-water gas exchange and CO_2 hydration is relatively slow and the system may not reach equilibrium when there is high biological activity (high biomass to volume ratio). Also, this approach also does not compensate for changes in total alkalinity resulting from the precipitation and dissolution of $CaCO_3$ which occurs between measurements of total alkalinity.

Overall, the carbonate chemistry can be maintained with good efficiency in the culture vessel, usually better than ± 10 µatm. The main drawback of this technique is that the pH electrode must be frequently calibrated in order to correct for drift. Hence, the other technique that involves

bubbling with premixed gases may be attractive. Air with the desired $p(CO_2)$ can be produced using gas mixing pumps or purchased. Another technique would be to maintain atmospheric $p(CO_2)$ to the desired level in the laboratory or in the growth cabinets in which the experiments are carried out (such cabinets for maintaining terrestrial plant are commercially available). A simple air pump can then be used to bubble the experimental sea water. To the best of our knowledge, this technique has not been used yet in the context of ocean acidification.

Aeration of sea water should be used with care for two reasons. First, bubbling may enhance the surface coagulation of organic matter (Engel *et al.*, 2004). This may be critical for studies investigating the response of microbial communities since their metabolism depends on the respective abundance of dissolved and particulate organic matter. This drawback may be avoided by enclosing the community in a dialysis bag maintained in a container bubbled with a gas of the desired $p(CO_2)$ (M. G. Weinbauer, pers. comm.). Such bags are permeable to gases and small molecules but impermeable to larger molecules and particles. It is highly recommended to check that the membranes are chemically neutral as some materials leak unwarranted chemical compounds. Second, some species of phytoplankton, for instance dinoflagellates, are known to be negatively affected by turbulence and especially by continuous bubbling (Shi *et al.*, 2009). For those cases, it is useful to equilibrate the media to the desired $p(CO_2)$ levels prior to the inoculation or use other means to achieve a carbonate system close to reality, i.e. where DIC varies and A_T remains constant.

1.2.2.1.2- Addition of high-CO_2 sea water

DIC and A_T are conservative quantities with respect to mixing (Wolf-Gladrow *et al.*, 2007). Hence, when two water parcels are mixed, the amount of a solute in the mixture equals the sum of the amounts of this solute in the two initial water parcels. The *seacarb* function *pmix* estimates the carbonate chemistry after mixing of two water samples.

Example: one can mix, in a closed system, 0.99623 kg of sea water having an A_T of 2325 µmol kg^{-1}, and $p(CO_2)$ of 384 µatm with 0.00377 kg of sea water having A_T of 2325 µmol kg^{-1} and saturated with CO_2 ($p(CO_2)$ = 1 x 10^6 µatm). The weight fraction of the high-CO_2 sea water relative to the final weight is 3.76 x 10^{-3}. Salinity is 34.9, temperature is 18.9°C and calculations are made for surface waters. This produces sea water with a final $p(CO_2)$ of 793 µatm and all parameters of the projected carbonate chemistry in 2100 are perfectly reproduced.

To the best of our knowledge, this approach has been used only twice. To create a $p(CO_2)$ range from 200 to 1300 µatm, Schulz *et al. (*unpubl.) added about 20 to 200 dm^3 of enriched CO_2 sea water to 60 m^3 mesocosms. C. McGraw (pers. comm., 2009) used this technique in laboratory experiments. As this approach uses water with very high $p(CO_2)$, caution has to be taken to avoid gas exchange during mixing and handling.

1.2.2.1.3- Addition of strong acid as well as CO_3^{2-} and/or HCO_3^-

As will be outlined below, the addition of acid alone does not fully mimic the changes in carbonate chemistry expected during the present century. The addition of CO_3^{2-} and/or HCO_3^- followed by acid circumvents this problem. The first addition elevates DIC to the desired level

and the acid addition (at constant DIC) precisely cancels the increase in A_T resulting from the addition of CO_3^{2-} and/or HCO_3^-.

Example: HCO_3^- (111.2 µmol kg^{-1} of $NaHCO_3$) and CO_3^{2-} (15.3 µmol kg^{-1} of Na_2CO_3) can be added to sea water for which $p(CO_2)$ (384 µatm) and A_T (2325 µmol kg^{-1}) are known, the atmospheric $p(CO_2)$ is 384 µatm, salinity is 34.9, temperature is 18.9°C and calculations are done for surface waters. Then, 14.18 ml kg^{-1} of 0.01 N HCl is added. The first addition raises DIC to the desired level of 2191 µmol kg^{-1} but increases A_T to a value higher than target (2467 vs. 2325 µmol kg^{-1}; Table 1). The subsequent addition of HCl, in a closed system to prevent gas exchange, restores A_T to the desired value without affecting DIC. All carbonate parameters after both additions reach the target values.

1.2.2.2- Addition of strong acids and bases

The addition of a strong acid, such as HCl, or base, such as NaOH, in a system closed to the atmosphere does not alter the concentration of dissolved inorganic carbon but modifies total alkalinity. A_T decreases following addition of an acid whereas it increases following addition of a base.

The change of total alkalinity after addition of a strong acid or base in a system open to the atmosphere is identical to that described above for a closed system. However, the concentration of DIC is modified through CO_2 exchange at the air-water interface. The *seacarb* function *ppH* estimates the changes in the carbonate chemistry during pH manipulations. The change in salinity due to the addition of acid or base is minor and can therefore be neglected.

Example: a volume of 14.08 ml kg^{-1} of 0.01 N HCl is added to 1 kg of sea water having known $p(CO_2)$ (384 µatm) and A_T (2325 µmol kg^{-1}); the atmospheric $p(CO_2)$ is 384 µatm, salinity is 34.9, temperature is 18.9°C and calculations are done for surface waters, assuming that the concentrations of total phosphate and silicate are 0. The target $p(CO_2)$ of 793 µatm is reached in a closed system (Table 1) but the pH is lower than the value expected in 2100 (7.768 vs 7.793, corresponding to a 2.9 % increase in $[H^+]$ that results from the decrease in total alkalinity generated by acid addition). This is an undesirable effect of the direct manipulation of pH as A_T will not change significantly during the course of this century (see the Introduction of this guide and Table 1). As a result, DIC, HCO_3^-, CO_3^{2-} and the $CaCO_3$ saturation states are lower than their target values. However, it is possible to restore A_T to its initial level by adding CO_3^{2-} and HCO_3^-, an approach that is described in section 1.2.1.3.

1.2.2.3- Addition of CO_3^{2-} and/or HCO_3^-

DIC and A_T can be increased by adding CO_3^{2-} in the form of Na_2CO_3 and/or by adding HCO_3^- in the form of $NaHCO_3$. In closed systems, the change in DIC generated by these additions is proportional to the changes in concentration: 1 x $\Delta[CO_3^{2-}]$ and 1 x $\Delta[HCO_3^-]$. The contribution of these anions to A_T is proportional to the production of their charge and concentration. Thus, A_T increases by 2 x $\Delta[CO_3^{2-}]$ and 1 x $\Delta[HCO_3^-]$. The changes in the carbonate chemistry generated by manipulations of total alkalinity therefore depend on the proportion of CO_3^{2-} and HCO_3^- added. This approach can be used to hold pH constant or combined with acid addition to maintain A_T constant (see section 1.2.1.3). The *seacarb* function *pTA* estimates the changes in the carbonate chemistry following addition of CO_3^{2-} and/or HCO_3^-. In an open system, the carbonate system re-

equilibrates through air-sea CO_2 gas exchange after the addition of chemicals but maintains A_T at a level higher to target value.

Example: HCO_3^- (1081 µmol kg^{-1} of $NaHCO_3$) is added to sea water for which $p(CO_2)$ (384 µatm) and A_T (2325 µmol kg^{-1}) are known. No CO_3^{2-} is added, the atmospheric $p(CO_2)$ is 384 µatm, salinity is 34.9, temperature is 18.9°C and calculations are done for surface waters. Results are shown in Table 1. In a closed system, the target $p(CO_2)$ of 793 µatm is reached but all other parameters of the carbonate system are very different from their values expected in 2100. pH is lower than it should be (7.942 vs. 7.993) and A_T, DIC, $[CO_3^{2-}]$ as well as the saturation states of aragonite (Ω_a) and calcite (Ω_c) are higher than the target values and are even higher than the values of the initial sea water. Differences are magnified in open systems.

1.2.2.4- Manipulation of the Ca^{2+} concentration

Although manipulating the calcium concentration is not technically altering the carbonate chemistry *per se*, this approach has been used in the context of ocean acidification. The reason is that some calcifying organisms, such as corals, respond to the calcium carbonate saturation state of sea water Ω which is expressed as:

$$\Omega = [Ca^{2+}{}_{sw}] \times [CO_3^{2-}{}_{sw}] / K_{sp}^*$$

where $Ca^{2+}{}_{sw}$ and $CO_3^{2-}{}_{sw}$ are the concentrations of calcium and carbonate ions in sea water, respectively, and K_{sp}^* is the solubility production at the *in situ* conditions of temperature, salinity and pressure (Zeebe and Wolf-Gladrow, 2001). It can readily be appreciated that the changes in Ω resulting from decrease in $CO_3^{2-}{}_{sw}$ driven by ocean acidification can be mimicked by altering

Ca^{2+}_{sw}. Uncoupling Ω from carbonate chemistry can also be useful, for instance, to examine a possible dependence of photosynthesis on calcification (Gattuso *et al.*, 2000; Trimborn *et al.*, 2007). It is also useful to replenish calcium when its concentration decreases below its natural levels during long-term experiments with calcifiers (Langdon, 2000).

The *seacarb* function *pCa* estimates the changes in Ωc and Ωa resulting from the manipulation of the concentration of Ca^{2+}_{sw}. It is recommended to use the simplified recipe for synthetic sea water described by Gattuso *et al.* (1998) and based on DOE (1994) because it is the basis of the synthetic sea water that has been used to determine a variety of equilibrium constants for use in sea water. Note that the effect of the changes in the calcium concentration on the dissociation constants of carbonic acid and on the solubility production of $CaCO_3$ (BenYaakov & Goldhaber, 1973) may have to be considered.

Example: artificial sea water with a known A_T (2325 µmol kg^{-1}) and DIC (2064 µmol kg^{-1}) and with a calcium concentration set to 6.03 µmol kg^{-1} reproduces well the saturation states of aragonite and calcite expected in 2100 without affecting any of the other parameters of the carbonate system which remain at their 2008 values (Table 1).

1.2.3- Strengths and weaknesses

Three approaches closely mimic the on-going and future changes in the sea water carbonate chemistry: gas bubbling, addition of high-CO_2 sea water, and combined additions of acid and bicarbonate and/or carbonate. All three methods increase dissolved inorganic carbon at constant total alkalinity, a situation that closely resembles the changes in the carbonate chemistry that

occurred during the past 200 years and are expected to continue in the next few hundreds years. All three approaches therefore allow precise control of all carbonate parameters to reach target values at the beginning of a perturbation experiment. Gas bubbling is the easiest to implement and can be used to maintain constant conditions over long periods of time. Note that, in all approaches, biological processes (e.g., photosynthesis, respiration, calcification, dissolution of $CaCO_3$, nutrient uptake and release) can significantly distort the target carbonate chemistry by changing DIC and A_T when experiments are run with high biomass (Rost *et al.*, 2008). Gas bubbling can maintain the concentration of dissolved inorganic carbon constant, provided that the dissolution of CO_2 is faster than its biological uptake, but does not compensate the drift in total alkalinity. Also, in all three methods, calcification can deplete the concentration of Ca^{2+} when the organism-to-volume ratio is high or the incubation time is long.

The approach that adds CO_3^{2-} and/or HCO_3^- appears of limited practical value because most carbonate chemistry variables are from target values. Obviously, due to gas exchange at the air-water interface, only gas bubbling can successfully be used to adjust $p(CO_2)$ and other parameters of the carbonate chemistry in an open system.

Several studies have used acid addition to manipulate the carbonate chemistry. Although this technique enables one to precisely control $p(CO_2)$ in systems closed to the atmosphere, it also alters total alkalinity which results in carbonate parameters distinct from those expected in the future: pH is lower than its target value, DIC remains unchanged (whereas it increases under natural ocean acidification), and the concentrations of bicarbonate and carbonate as well as $CaCO_3$ saturation states are lower than expected. Gattuso & Lavigne (2009) and Schulz *et al.*

(2009) provide a detailed analysis of the similarities and differences between acid addition and DIC manipulations. It is recommended to combine the addition of bicarbonate and/or carbonate, to increase DIC, with acid addition to avoid this drawback.

Iglesias-Rodriguez *et al.* (2008) recently reported that, in contrast to all previous reports, calcification of coccolithophorids increases at elevated $p(CO_2)$. They argued that this is due to the approaches used to manipulate the carbonate chemistry and that the approach of gas bubbling is superior to that of acid addition (Iglesias-Rodriguez *et al.* 2008a and 2008b). The argument is that acid addition does not reproduce the increase of the HCO_3^- concentration generated by natural ocean acidification whereas gas bubbling does. The authors claim that since HCO_3^- may stimulate photosynthesis and, in turn, calcification, experiments which used acid addition and demonstrated that calcification declines at lower pH, confounded the issue. This statement is misleading, although there is no doubt that gas bubbling better mimics the future carbonate chemistry (Table 1). Several previous perturbation experiments were carried out with gas bubbling and also reported lower rates of calcification of coccolithophores at lower pH or higher $p(CO_2)$ (e.g., Sciandra *et al.*, 2003; Delille *et al.*, 2005; Feng *et al.*, 2008). It should also be pointed out that perturbation experiments carried out using gas bubbling can also lead to poor control of the carbonate chemistry, for example when the duration of the experiments is too long, when experiments are run at high biomass, or when the DIC uptake is larger than the dissolution of CO_2 (see above). It therefore seems that the different responses of coccolithophores reported in the literature do not originate from the approach used to manipulate the carbonate chemistry. The situation is clearer in reef-building corals as Schneider *et al.* (2006) measured the rate of

calcification under constant DIC, constant pH and constant $p(CO_2)$ and showed that calcification is controlled by the concentration of CO_3^{2-}, the future value of which is relatively well mimicked by acid addition.

1.2.4- Potential pitfalls and suggestions for improvements

1.2.4.1- Sea water filtration and autoclaving

As filtration can significantly shift the carbonate chemistry of seawater, the carbonate system should be manipulated after filtration. If this cannot be done, samples for carbonate chemistry determination must be taken after filtration to account for any gas exchange. Gentle pressure filtration through a cartridge should be used because vacuum filtration or strong pressure filtration are likely to lead to cell rupture, which in turn increases total alkalinity (see Grasshoff et al., 1999).

Sea water autoclaving should also be performed prior to manipulating the carbonate chemistry. It can severely change the carbonate chemistry as boiling sea water strips off gases and most of DIC is lost. A_T has been reported to change as well. It increases, together with salinity, due to water evaporation. It can also change, may be due to precipitation of carbonate, if autoclaving is performed at high pressure. Overall, $p(CO_2)$ of autoclaved water is initially relatively low and pH quite high. When the sea water cools, some of the DIC is likely to re-dissolve from the headspace into the water phase. When autoclaving natural sea water, it is recommended to sample for DIC and A_T determinations before and after autoclaving in order to ascertain the impact of the operating procedure on the carbonate chemistry. In case of artificial sea water, autoclaving will

not change the carbonate chemistry if it is carried out before additions of $NaHCO_3$ or Na_2CO_3.

1.2.4.2- Reaching and maintaining target values

When sea water is manipulated via bubbling with gases of different $p(CO_2)$, one must ascertain that equilibrium has been reached before starting an experiment. The required time to equilibrium depends on several factors such as the biomass to volume ratio, $p(CO_2)$, gas flow rate, bubble size, volume and shape of the flask and temperature, and may require several days. Since both bottled gas mixtures and CO_2-free air from generators do not contain any water vapor, it is important to humidify the dry air before bubbling in order to minimize evaporation which would increase salinity, itself leading to changes in the parameters of the carbonate system.

Once the carbonate chemistry has reached a target level, it is critical to avoid any process leading to gas exchange between sea water and the atmosphere such as autoclaving, vacuum filtration or temperature changes. Unless the experimental set-up is open and bubbling is running continuously, gas-tight bottles filled without headspace should be used.

When working with high cell densities, processes such as photosynthesis and calcification can severely shift the carbonate chemistry. This problem is most pronounced in closed systems but must also be considered in open systems subject to continuous bubbling because biologically-driven changes can exceed the capability of the regulation system and thus cause a departure from the desired carbonate chemistry. This problem is more pronounced when investigating calcifying systems because calcification decreases A_T. The drawdown of Ca^{2+} might also need to be considered as it could also impact on the $CaCO_3$ saturation state.

1.2.4.3- Contributions of dissolved organic matter, dissolved inorganic nutrients and pH buffers to total alkalinity

During photosynthesis, phytoplankton release dissolved organic compounds containing basic functional groups that readily react with protons during seawater titration, and thereby contribute to total alkalinity. The magnitude of the contribution of dissolved organic compounds to A_T is species-dependent, suggesting that individual phytoplankton species exude dissolved organic compounds with unique proton accepting capacities (Kim and Lee, 2009). This contribution could be significant in perturbation experiments carried out at relatively high biomass:volume ratios. In that case, one might consider the use of calculated carbonate parameters (e.g., total alkalinity from pH and DIC or from $p(CO_2)$ and DIC) rather than the measured total alkalinity.

Some salts such as inorganic nutrients must be considered in experiments manipulating the carbonate chemistry as they contribute to A_T. The use of pH buffers causes large deviations from the natural carbonate chemistry as they increase A_T to values too high for accurate measurements and therefore precludes the calculation of the carbonate system using A_T. DIC and pH or $p(CO_2)$ have then to be used instead. Depending on chemical form and concentration, inorganic nutrient addition can change A_T and/or should be included in carbonate chemistry calculations. Furthermore, possible changes of experimental inorganic nutrient concentrations and speciation and their impact on A_T(for details see Brewer and Goldman (1976); Wolf-Gladrow *et al.* (2007)) highlight the importance of concomitant sampling for nutrients such as phosphate, ammonium and silicate, together with those for carbonate chemistry determination.

Phosphate (PO_4^{3-}) is usually added to sea water as the sodium salt $NaH_2PO_4 \cdot H_2O$ (see Guillard

& Ryther, 1962). Its addition does not alter A_T as the immediate dissociation productions Na^+ and $H_2PO_4^-$ do not contribute to A_T (see eq. X, section 1.1). In other words, as the other three phosphate species are included in A_T, additions of $NaH_2PO_4 \bullet H_2O$ do increase the alkalinity contribution by phosphate but concomitantly reduce the contribution of other A_T components by the same amount, mainly carbonate alkalinity. However, if phosphate is added as phosphoric acid (H_3PO_4), total alkalinity is reduced by one mole per mole of phosphoric acid added. Hence, when calculating carbonate system speciation from measured A_T, the phosphate contribution should be taken into account. However, the error made by ignoring the contribution of phosphate to A_T is negligible at concentrations below 1 μmol kg^{-1}.

Nitrate (NO_3^-) is usually added to sea water as the sodium salt $NaNO_3$ which does not alter A_T. Furthermore, as nitrate has no A_T component, it does not need to be considered when calculating the carbonate system from A_T measurements. However, the addition of nitric acid (HNO_3) decreases A_T. Ammonia is usually added as ammonium chloride (NH_4Cl), which does not change A_T. Nevertheless, since NH_3 contributes to A_T, it must be considered in carbonate chemistry calculations. In practice it can probably be ignored in most cases because of its relatively low concentrations.

Silica in the form of H_4SiO_4 is generally added as the sodium salt $Na_2SiO_3 \bullet 9H_2O$. This changes A_T as SiO_2^{3-} combines with H_2O to form $H_2SiO_4^{2-}$ which quickly converts to $H_3SiO_4^-$ by consuming a proton. At usual sea water pH most of the $H_3SiO_4^-$ further converts to H_4SiO_4, consuming another proton. Therefore, A_T increases by two moles for each mole of Na_2SiO_3 added. Additions of silica to either natural sea water or artificial sea water can be relatively high, in the

100 µmol kg^{-1} range. In these cases it might be advisable to counterbalance the otherwise relatively large increase of A_T by additions of HCl. As $H_3SiO_4^-$ contributes to A_T, it should be included in the carbonate system calculations, although in many cases it can safely be ignored due to is relatively low concentrations at typical sea water pH (see Zeebe and Wolf-Gladrow, 2001).

1.2.4.4- Isotopic labeling of dissolved inorganic carbon

Labeling of the dissolved inorganic carbon (DIC) pool with ^{13}C or ^{14}C requires the same precautions during preparation and handling as described above for carbonate chemistry. In fact, it is a carbonate chemistry manipulation in itself and hence should be the last step in the preparation of an experiment. Any headspace should be avoided as sea water-atmosphere CO_2 gas exchange reduces the concentration of the label.

Even if sea water is close to ambient $p(CO_2)$, any ^{13}C or ^{14}C added would outgas with time, driven by the difference in sea water and atmosphere $^{13}CO_2$ or $^{14}CO_2$ as their atmospheric partial pressure are close to 0: about 4 µatm for $^{13}CO_2$ and 1 x 10^{-13} µatm for $^{14}CO_2$ (calculated according to Coplen *et al.*, 2002 and Nydal & Lövseth, 1996). Therefore, aeration of sea water with air at target CO_2 would increase ^{13}C or ^{14}C outgassing even though $p(CO_2)$ would be kept constant. Furthermore, depending on the amount of ^{13}C or ^{14}C sodium salts added, DIC and A_T and hence $p(CO_2)$ can change significantly.

1.2.4.5- Sampling of carbonate chemistry parameters

Measuring and reporting of at least two quantities of the carbonate system prior, after and ideally

during experiments will ensure constant conditions or reveal possible shifts.

Discrete samples for determination of DIC or pH should be taken with care because CO_2 gas exchange between sample water and atmosphere could otherwise compromise the measurements. Sampling for A_T measurements, however, is not critically influenced by changes in DIC or pH related to gas exchange. Even if the water was stripped of any dissolved inorganic carbon by heating, A_T would stay constant provided that there is no evaporation and salinity remains the same.

Samples should be poisoned for storage (see Grasshoff *et al.* (1999) and Dickson *et al.* (2007) for details) and kept at low temperatures before analysis. Headspaces within DIC or pH sample vials must be avoided. Depending on organism and experimental setup, DIC and A_T measurements should be performed on filtered sea water. For instance, phytoplankton cells grown to relatively high densities in comparison to oceanic waters, can disintegrate during A_T or DIC measurements because of necessary acid additions. This could release A_T or DIC components from the particulate to the dissolved phase and compromise analysis. Furthermore, negatively charged groups in cellular plasma membranes can absorb protons added during A_T titration, thereby compromising the measurement (Kim *et al.*, 2006). Similarly, the study of calcifying organisms can also make DIC and A_T filtration necessary because $CaCO_3$ dissolves during measurements due to acid additions, which artificially increases both DIC and A_T. Filtration of DIC samples must be carried out with care to avoid water-atmosphere CO_2 gas exchange.

1.2.4.6- Headspace and storage

Sea water in which the carbonate system has been manipulated and that is to be used in

experiments should be handled very carefully. Wherever possible, headspace should be avoided as DIC concentrations and speciation will otherwise change through water-atmosphere CO_2 gas exchange if sea water $p(CO_2)$ differs from its atmospheric counterpart (current atmospheric values are about 380 µatm while those inside closed rooms are usually higher). An exception is sea water that is constantly aerated at target $p(CO_2)$ values throughout the experiment. Nevertheless, frequent sampling for at least two carbonate chemistry parameters is necessary for quality control.

Likewise, when storing manipulated sea water prior to the experiment, there should be no headspace. In this respect it is important to keep in mind that temperature variations will change carbonate chemistry. For instance, cooling sea water will initially decrease $p(CO_2)$, while increasing pH. If there is no headspace and the sea water is afterwards adjusted to intended temperatures the carbonate system will shift back to pre-set conditions. This would not be the case if the water was stored with a headspace. The same applies for sea water which was aerated at target CO_2. If aeration is carried out at different temperatures than experimental incubation, $p(CO_2)$ and hence carbonate chemistry speciation will change.

1.2.5- Data reporting

It is essential to report not only on the results obtained, but also on the methods used. The metadata should be included in databases (see section 4.2) in order to enable comparisons of different studies and meta-analysis. Table 2 provides a check list of the information on the manipulation of the carbonate chemistry which should be reported when describing a

perturbation experiment

1.2.6- Recommendations for standards/guidelines

Several factors can collectively affect the success of CO_2 manipulation experiments. Here we make recommendations regarding the method of sea water CO_2 manipulation; the choice of which can be critical in obtaining significant and reproducible results in CO_2 perturbation experiments.

The method of manipulating carbonate chemistry in sea water is of utmost importance. Bubbling sea water with CO_2-enriched air may be the first choice because it is a very efficient way to manipulate sea water carbonate chemistry and, more importantly, exactly mimics carbonate chemistry changes occurring in the years to come; the future scenario for ocean carbon chemistry being an increase in $p(CO_2)$ and DIC (decrease in pH) without alteration of A_T. However, sea water aeration by bubbling may lead to difficulties in phytoplankton cultures (Shi *et al.*, 2009). Bubbling must therefore be sufficiently gentle to cause minimal impact on the phytoplankton assemblage or the cells should be separated from the bubbles by a gas-permeable membrane. Alternative but equally effective methods, when species are highly sensitive to bubbling, is to equilibrate the culture media with air at target $p(CO_2)$ or to mix it with high-CO_2 sea water prior to cell inoculation. Although the later method has yet to be widely tested, it also can exactly mimic changes in carbonate chemistry in the future ocean just as the method of bubbling with high CO_2 gases. A key advantage of this method over the former is that it removes the unwanted effect of bubbling on marine organisms. The third method, equally reliable, is the combined

addition of acid and bicarbonate and/or carbonate (increase in $p(CO_2)$ and DIC, but decrease in pH and A_T) and then addition of Na_2CO_3 and/or $NaHCO_3$ (to restore A_T). This method also yields the conditions predicted to occur in the future ocean. Other methods (manipulation of A_T and Ca^{2+}) can be useful in the context of specific process studies (such as calcification).

1.2.7- Acknowledgements

Thanks are due to A. Dickson, A. Engel, P. Grosjean, C. Langdon, J. Orr, R. Zeebe and the participants of the "Workshop on Best Practices for Ocean Acidification Research and Data Reporting" for very helpful discussions or comments on an early draft of this paper. An anonymous referee as well as L. Hansson and C. Sabine also provided helpful comments on a draft manuscript. This is a contribution to the "European Project on Ocean Acidification" (EPOCA) which receives funding from the European Community's Seventh Framework Programme (FP7/2007-2013) under grant agreement 211384 and CARBOOCEAN (FP6/511176-2).

1.2.8- References

Agegian C. R., 1985. *The biogeochemical ecology of* Porolithon gardineri *(Foslie)*. Ph.D. thesis, University of Hawaii, 178 p.

Ben-Yaakov S. & Goldhaber M. B., 1973. The influence of sea water composition on the apparent constants of the carbonate system. *Deep-Sea Research* 20:87-99.

Coplen T. B., Bohlke J. K., De Bievre P., Ding T., Holden N. E., Hopple J. A., Krouse H. R., Lamberty A., Peiser H. S., Revesz K., Rieder S. E., Rosman K. J. R., Roth E., Taylor P. D. P., Vocke R. D. & Xiao Y. K., 2002. Isotope-abundance variations of selected elements (IUPAC Technical Report). *Pure Applied Chemistry* 74:1987-2017.

Delille B., Harlay J., Zondervan I., Jacquet S., Chou L., Wollast R., Bellerby R. G. J., Frankignoulle M., Borges A. V., Riebesell U. & Gattuso J.-P., 2005. Response of primary

productionion and calcification to changes of pCO_2 during experimental blooms of the coccolithophorid *Emiliania huxleyi. Global Biogeochemical Cycles* GB2023. doi:10.1029/2004GB002318.

Dickson A. G., Sabine C. L. & Christian J. R., 2007. Guide to best practices for ocean CO_2 measurements. *PICES Special Publication* 3: 1-191.

DOE, 1994. *Handbook of methods for the analysis of the various parameters of the carbon dioxide system in sea water*. Carbon Dioxide Information Analysis Center, Oak Ridge National Laboratory.

Engel A., Delille B., Jacquet S., Riebesell U., Rochelle-Newall E., Terbrüggen A. & Zondervan I., 2004. Transparent exopolymer particles and dissolved organic carbon productionion by *Emiliania huxleyi* exposed to different CO_2 concentrations: a mesocosm experiment. *Aquatic Microbial Ecology* 34(1): 93-104.

Feng Y., Warner M. E., Zhang Y., Sun J., Fu F. X., Rose J. M. & Hutchins D. A., 2008. Interactive effects of increased pCO_2, temperature and irradiance on the marine coccolithophore *Emiliania huxleyi* (Prymnesiophyceae). *European Journal of Phycology* 43:87-98.

Gattuso J.-P., Frankignoulle M., Bourge I., Romaine S. & Buddemeier R. W., 1998. Effect of calcium carbonate saturation of sea water on coral calcification. *Global and Planetary Change* 18:37-46.

Gattuso J.-P. & Lavigne H., 2009. Perturbation experiments to investigate the impact of ocean acidification: approaches and software tools. *Biogeosciences* 2121-2133.

Gattuso J.-P., Reynaud-Vaganay S., Furla P., Romaine-Lioud S., Jaubert J., Bourge I. & Frankignoulle M., 2000. Calcification does not stimulate photosynthesis in the zooxanthellate scleractinian coral *Stylophora pistillata. Limnology and Oceanography* 45:246–250.

Grasshoff K., Kremling K. & Ehrhardt M., 1999. *Methods of sea water analysis*. p. New York: Wiley.

Guillard R. R. L. & Ryther J. H., 1962. Studies of marine planktonic diatoms. 1. *Cyclotella nana* Hustedt, and *Denotula confervacea* (Cleve) Gran. *Canadian Journal of Microbiology* 8:229-239.

Iglesias-Rodriguez M. D., Buitenhuis E. T., Raven J. A., Schofield O., Poulton A. J., Gibbs S., Halloran P., R. & de Baar H. J. W., 2008. Response to Comment on "Phytoplankton calcification in a high-CO_2 world". *Science* 322:1466c-1466c.

Iglesias-Rodriguez M. D., Halloran P. R., Rickaby R. E. M., Hall I. R., Colmenero-Hidalgo E., Gittins J. R., Green D. R. H., Tyrrell T., Gibbs S. J., von Dassow P., Rehm E., Armbrust E. V. & Boessenkool K. P., 2008. Phytoplankton calcification in a high-CO_2 world. *Science* 320:336-340.

Kim, H.-C., and K. Lee (2009), Significant contribution of dissolved organic matter to seawater alkalinity, *Geophysical Reseach Letters* 36:L20603. doi:10.1029/2009GL040271.

Kim H.-C., Lee K. & Choi W., 2006. Contribution of phytoplankton and bacterial cells to the

measured alkalinity of sea water. *Limnology and Oceanography* 51:331-338.

Langdon C., Takahashi T., Marubini F., Atkinson M., Sweeney C., Aceves H., Barnett H., Chipman D. & Goddard J., 2000. Effect of calcium carbonate saturation state on the rate of calcification of an experimental coral reef. *Global Biogeochemical Cycles* 14:639–654.

Lavigne H., Proye A. & Gattuso J.-P., 2008. seacarb 2.0, an R package to calculate parameters of the sea water carbonate system. http://cran.r- project.org/web/packages/seacarb/index.html

Lueker T. J., Dickson A. G. & Keeling C. D., 2000. Ocean pCO_2 calculated from dissolved inorganic carbon, alkalinity, and equations for K_1 and K_2: validation based on laboratory measurements of CO_2 in gas and sea water at equilibrium. *Marine Chemistry* 70(1-3): 105-119.

Nydal R. & Lövseth K., 1996. Carbon-14 measurements in atmospheric CO_2 from northern and southern hemisphere sites, 1962-1993. *Environmental Sciences Division Publication* 4582: Oak Ridge, Tennessee: Carbon Dioxide Information Analysis Center.

Rost B., Zondervan I. & Wolf-Gladrow D., 2008. Sensitivity of phytoplankton to future changes in ocean carbonate chemistry: current knowledge, contradictions and research directions. *Marine Ecology Progress Series* 373:227-237.

Schneider K. & Erez J., 2006. The effect of carbonate chemistry on calcification and photosynthesis in the hermatypic coral *Acropora eurystoma. Limnology and Oceanography* 51:1284-1293.

Sciandra A., Harlay J., Lefèvre D., Lemée R., Rimmelin P., Denis M. & Gattuso J.-P., 2003. Response of the coccolithophorid *Emiliania huxleyi* to elevated partial pressure of CO_2 under nitrate limitation. *Marine Ecology Progress Series* 261:111-122.

Shi D., Xu Y. & Morel F. M. M., 2009. Effects of the pH/pCO_2 control method on medium chemistry and phytoplankton growth. *Biogeosciences* 6:1199-1207.

Schulz K. G., Barcelos e Ramos J., Zeebe R. E. & Riebesell U., 2009. CO_2 perturbation experiments: similarities and differences between dissolved inorganic carbon and total alkalinity manipulations. *Biogeosciences* 6:2145-2153.

Trimborn S., Langer G. & Rost B., 2007. Effect of varying calcium concentrations and light intensities on calcification and photosynthesis in *Emiliania huxleyi*. *Limnology and Oceanography* 52:2285-2293.

Wolf-Gladrow D. A., Zeebe R. E., Klaas C., Körtzinger A. & Dickson A. G., 2007. Total alkalinity: The explicit conservative expression and its application to biogeochemical processes. *Marine Chemistry* 106:287-300.

Zeebe R. E. & Wolf-Gladrow D. A., 2001. *CO_2 in sea water: equilibrium, kinetics, isotopes*. 346 p. Amsterdam: Elsevier.

Table 1- Sea water carbonate chemistry in 20087, 2100, and after perturbations intended to simulate year 2100 carbonate chemistry (from Gattuso & Lavigne, 2009). Total alkalinity *(A_T),* partial pressure of CO_2 in sea water ($p(CO_2)$), salinity and temperature were used to derive all other parameters using the *seacarb* package (Lavigne *et al.*, 2008) except for manipulations of the calcium concentration for which DIC was used rather than $p(CO_2)$. Temperature (18.9°C) and salinity (34.9) were assumed to remain constant, the concentrations of total phosphate and silicate were set to 0 and the sea water $p(CO_2)$ was set at 384 µatm in 2007 and 793 µatm in 2100. The main body of the text provides further information. (a): $\times 10^{-9}$ mol kg^{-1}, (b): $\times 10^{-6}$ mol kg^{-1}.

	$pCO_{2\,sw}$ (μatm)	pH_T (–)	$[H^+]$ (a)	TA (b)	DIC (b)	$[CO_2]$ (b)	$[HCO_3^-]$ (b)	$[CO_3^{2-}]$ (b)	Ω_c (–)	Ω_a (–)
Year 2007	384	8.065	8.6	2325	2065	12.8	1865	187	4.5	2.9
Year 2100	793	7.793	16.1	2325	2191	26.4	2055	110	2.6	1.7
Gas bubbling	793	7.793	16.1	2325	2191	26.4	2055	110	2.6	1.7
Addition of high-CO_2 seawater	792	7.793	16.1	2325	2191	26.4	2055	110	2.6	1.7
Addition of CO_3^{2-} and HCO_3^-; closed sys.	793	7.942	11.4	3406	3146	26.4	2901	218	5.2	3.4
Addition of CO_3^{2-} and HCO_3^-; open sys.	384	8.207	6.2	3406	2950	12.8	2580	357	8.5	5.5
Acid addition; closed sys.	793	7.768	17.1	2184	2065	26.4	1940	98	2.3	1.5
Acid addition; open sys.	384	8.042	9.1	2184	194	12.8	1767	167	4	2.6
Addition of:										
CO_3^{2-} and HCO_3^-; closed sys.	400	8.073	8.4	2467	2191	13.3	1977	201	4.8	3.1
followed by acid addition; closed sys.	793	7.793	16.1	2325	2191	26.4	2055	110	2.6	1.7
Manipulation of $[Ca^{2+}]$	384	8.065	8.6	2325	2065	12.8	1866	187	2.6	1.7

Table 2- Check list of the information on the manipulation of the carbonate chemistry which should be reported when describing a perturbation experiment.

530

Method used to manipulate the carbonate chemistry	Which of the methods below was used: - Aeration with air at target $p(CO_2)$ (indicate $p(CO_2)$ level and flow rate) - Addition of high-CO_2 sea water (indicate $p(CO_2)$ and mixing ratio) - Addition of strong acid as well as CO_3^{2-} and/or HCO_3^- (indicate volume and normality of acid added as well as the quantity of inorganic carbon added) - Addition of strong acids and bases (indicate volume and normality) - Manipulation of the Ca^{2+} concentration (indicate the recipe of artificial sea water used)
Type of manipulation	- once before the experiment - continuous control during the experiment
Parameters of the carbonate chemistry	- values at the beginning and end of the experiment. If available, values during the experiment should also be provided - At least two parameters of the carbonate system should be reported together with temperature and salinity - the pH scale must be indicated
History of organisms investigated	- describe the conditions under which the organisms were maintained prior to the experiment. Were they pre-acclimated? If so, indicate the environmental conditions and duration of the pre-acclimation phase.

Biogeosciences, 6, 2121–2133, 2009
www.biogeosciences.net/6/2121/2009/

Biogeosciences

Technical Note: Approaches and software tools to investigate the impact of ocean acidification

J.-P. Gattuso[1,2] **and H. Lavigne**[1,2]

[1]CNRS-INSU, Laboratoire d'Océanographie de Villefranche, BP 28, 06234 Villefranche-sur-Mer Cedex, France
[2]Université Pierre et Marie Curie-Paris 6, Observatoire Océanologique de Villefranche,
06230 Villefranche-sur-Mer Cedex, France

Received: 20 February 2009 – Published in Biogeosciences Discuss.: 21 April 2009
Revised: 9 September 2009 – Accepted: 19 September 2009 – Published: 8 October 2009

Abstract. Although future changes in the seawater carbonate chemistry are well constrained, their impact on marine organisms and ecosystems remains poorly known. The biological response to ocean acidification is a recent field of research as most purposeful experiments have only been carried out in the late 1990s. The potentially dire consequences of ocean acidification attract scientists and students with a limited knowledge of the carbonate chemistry and its experimental manipulation. Hence, some guidelines on carbonate chemistry manipulations may be helpful for the growing ocean acidification community to maintain comparability. Perturbation experiments are one of the key approaches used to investigate the biological response to elevated pCO_2. They are based on measurements of physiological or metabolic processes in organisms and communities exposed to seawater with normal or altered carbonate chemistry. Seawater chemistry can be manipulated in different ways depending on the facilities available and on the question being addressed. The goal of this paper is (1) to examine the benefits and drawbacks of various manipulation techniques and (2) to describe a new version of the R software package *seacarb* which includes new functions aimed at assisting the design of ocean acidification perturbation experiments. Three approaches closely mimic the on-going and future changes in the seawater carbonate chemistry: gas bubbling, addition of high-CO_2 seawater as well as combined additions of acid and bicarbonate and/or carbonate.

Correspondence to: J.-P. Gattuso
(gattuso@obs-vlfr.fr)

1 Introduction

Ocean acidification refers to the on-going decrease in ocean pH as a result of the uptake of anthropogenic carbon dioxide (CO_2) in the ocean. The partial pressure of CO_2 (pCO_2) increases in the atmosphere due to anthropogenic inputs. It has increased by about 40% (267 to 384 µatm) since the beginning of the industrial revolution leading to changes in the Earth's climate and in the functioning of terrestrial ecosystems. The world's oceans currently absorb on average about one metric ton of CO_2 produced by each person every year. It is estimated that the surface waters of the oceans have taken up 118 Pg C, or about 25% of the carbon generated by human activities since 1800 (Sabine et al., 2004). The increase of pCO_2 profoundly affects the seawater carbonate system (Table 1). It increases the concentrations of bicarbonate and dissolved inorganic carbon, and lowers pH, the concentration of carbonate ions (CO_3^{2-}) and the saturation state of the major shell-forming carbonate minerals:

$$CO_2 + CO_3^{2-} + H_2O \rightarrow 2HCO_3^-$$

Surface ocean pH is estimated to have decreased from approximately 8.20 to 8.07 between preindustrial time and the 1990s and may reach 7.79 in 2100 (Table 1). The expression "ocean acidification" refers to the decrease in pH but does not imply that the pH of surface ocean waters will become acidic (below 7.0) any time soon.

Although the chemistry of ocean acidification is very well known, the associated impacts on marine organisms and ecosystems remain poorly known. The impact of low pH on marine organisms started to be investigated several decades ago (e.g. Bouxin, 1926), yet research into the biological response to ocean acidification is still in its infancy: the first

Published by Copernicus Publications on behalf of the European Geosciences Union.

Table 1. Changes in the carbonate chemistry of surface seawater from the Last Glacial Maximum (LGM; 18 ky BP) to 2100. Total alkalinity, CO_2 partial pressure (pCO_2), salinity and temperature were fixed and used to derive all other parameters using the *seacarb* software (Lavigne et al., 2008) and the dissociation constant of carbonic acid of Lueker et al. (2000). It is assumed that the ocean and atmosphere are in equilibrium with respect to CO_2. Values of temperature, salinity, total alkalinity and total phosphate in 1766, 2007 and 2100 are from Plattner et al. (2001) prescribing historical CO_2 records and non-CO_2 radiative forcing from 1766 to 1990 and using the A2 IPCC SRES emissions scenario (Nakićenović and Swart, 2000) thereafter. Temperature during the LGM was set 1.9°C colder than in 2007 (MARGO Project Members, 2009). The LGM salinity was set 1.07 higher than during pre-industrial time (Paul and Schäfer-Neth, 2003). Total alkalinity in the LGM was scaled to salinity while the total phosphate concentration was assumed to be the same as in 1766. pCO_2 in 1766 and 2100 are from Plattner et al. (2001), while values in the LGM and 2007 are from Petit et al. (2001) and Keeling et al. (2008), respectively. The concentration of total silicate is assumed to have remained constant from the LGM to 2100. It was calculated using the gridded data reported by Garcia et al. (2006) between 0 and 10 m and weighing the averages using the surface area of each grid cell. pH is expressed on the total scale.

Parameter	Unit	LGM	1766	2007	2100
Temperature	°C	17.2	18.3	18.9	21.4
Salinity	–	36	34.9	34.9	34.7
Total phosphate	10^{-6} mol kg^{-1}	0.66	0.66	0.63	0.55
Total silicate	10^{-6} mol kg^{-1}	7.35	7.35	7.35	7.35
Total alkalinity	10^{-6} mol kg^{-1}	2399	2326	2325	2310
CO_2 partial pressure (seawater)	µatm	180	267	384	793
$[CO_2]$	10^{-6} mol kg^{-1}	6.26	9.05	12.8	24.7
$[HCO_3^-]$	10^{-6} mol kg^{-1}	1660	1754	1865	2020
$[CO_3^{2-}]$	10^{-6} mol kg^{-1}	299	231	186	118
Dissolved inorganic carbon	10^{-6} mol kg^{-1}	1966	1994	2064	2162
pH_T	–	8.33	8.20	8.07	7.79
$[H^+]$	10^{-9} mol kg^{-1}	4.589	6.379	8.600	16.13
Calcite saturation	–	7.1	5.5	4.5	2.8
Aragonite saturation	–	4.6	3.6	2.9	1.8

purposeful manipulative experiment was carried out only in the 1980s (Agegian, 1985) and others began only in the late 1990s. The potentially dire consequences of ocean acidification have attracted the interest of scientists and students with a limited knowledge of the carbonate chemistry and its experimental manipulation. Hence, some guidelines on carbonate chemistry and its manipulation may be helpful for the growing ocean acidification community in order to ensure that the most adequate approaches are used and that results and subsequent analyses are comparable. The need to standardize measurement of parameters of the carbonate system has been identified (Kleypas et al., 2006), a gap which was recently filled (Dickson et al., 2007). Perturbation experiments are one of the key approaches used to investigate the biological response to elevated pCO_2. They are based on measurements of physiological or metabolic processes in organisms and communities exposed to seawater with normal or altered chemistry. Seawater chemistry can be manipulated using different ways depending on the facilities available and on the question being addressed. Langdon (2000) summarized the state-of-the-art techniques used with reef builders. Here we examine the benefits and drawbacks of current methods and provide a software package to assist the design of perturbation experiments.

2 Method

Detailed information on the carbonate chemistry, including the merit of units and scales, as well as on the measurement methods can be found in Dickson et al. (2007), Zeebe and Wolf-Gladrow (2001) and in the *Guide for Best Practices in Ocean Acidification Research and Data Reporting* in preparation (see http://www.epoca-project.eu/index.php/Best-Practices-Guide/).

The R package *seacarb* was used to calculate the carbonate chemistry parameters. *R* is a free cross-platform language and environment for statistical computing and graphics (R Development Core Team, 2008). The previous version, *seacarb* 1.2.3 (Proye and Gattuso, 2003) is superseded by the recently released version 2.0 (Lavigne et al., 2008). The new version has been updated in order to be fully consistent with the most recent guidelines to best practices for ocean CO_2 measurements (Dickson et al., 2007). All equations are solved analytically except when total alkalinity is one of the two input parameters of the carbonate system that are required. In that case, the concentration of H^+ or dissolved inorganic carbon are solved numerically using the R function *uniroot*. Five new functions have been added to *seacarb* 2.0 to assist the design of ocean acidification perturbation experiments. The syntax of these commands is briefly

described in Appendices A1 to A5. Additional information is available in the help files of the *seacarb* package.

3 Main approaches

The seawater chemistry can be manipulated in various ways in order to alter parameters of the carbonate system. The following sections examine the five techniques that are most useful in the context of ocean acidification. Calculations were carried out using the first and second dissociation constants of carbonic acid given by Lueker et al. (2000). In systems open to the atmosphere, it is assumed that the seawater and atmosphere are in equilibrium with respect to CO_2. It must be pointed out that the methods described below enable to set the carbonate chemistry at the beginning of a perturbation experiment. However, initial values can be altered by biological (e.g. photosynthesis, respiration and calcification) and physical processes (e.g. air-seawater exchange of CO_2 and temperature changes), which must also be taken into account in the experimental design.

3.1 Gas bubbling

Bubbling seawater with gases is an efficient way to manipulate its carbonate chemistry. The *seacarb* function pgas estimates the changes in the carbonate chemistry resulting from changes in pCO_2 generated by bubbling gases.

Example: seawater with a pCO_2 of 384 µatm and total alkalinity (TA) of 2325 µmol kg^{-1} is bubbled with a mixture of CO_2 and air with a pCO_2 of 793 µatm. Salinity is 34.9, temperature is 18.9°C and calculations are made for surface waters. The command needed is:

```
pgas(flag=24, var1=384, var2=2325e-6, pCO2g=793,
S=34.9, T=18.9)
```

This approach exactly reproduces the changes of all parameters of the carbonate system expected in the year 2100 (Fig. 1 and Table 2). Smith and Roth (1979) is perhaps the first publication which manipulated the carbonate chemistry via gas bubbling within a range compatible with that of the on-going ocean acidification.

Two techniques have been used in the context of ocean acidification: pH-stat and bubbling with premixed gases. In pH-stat systems, pH is monitored continuously and a controller opens or closes valves when the pH goes above or below a set value. Gases are then delivered until the pH reaches the set value again. Different combination of gases have been used: (1) air and pure CO_2, (2) CO_2-free air and pure CO_2, and (3) air, CO_2-free air and pure CO_2. CO_2-free air can be produced easily using CO_2 scrubbers such as soda lime or NaOH and $Ca(OH)_2$ (C. J. Hintz, personal communication, 2008). The pH threshold is calculated using the desired pCO_2 and total alkalinity which must either be constant or frequently measured. This method allows one to compensate for any change in the carbonate chemistry due to photosynthesis and respiration or, in the case of open culture systems, to changes in the source water. However, it does not compensate for changes in total alkalinity that would result from precipitation and dissolution of $CaCO_3$ which could occur between measurements of total alkalinity. Hence, the carbonate chemistry can be maintained with good efficiency in the culture vessel, e.g. with variability of pCO_2 better than ± 10 µatm. The main drawback of this technique is that the pH electrode must be frequently calibrated in order to account for drift. Hence, the second technique of bubbling with premixed gases may be attractive. Air with the desired pCO_2 can be produced using gas mixing pumps or purchased.

Another approach would be to control atmospheric pCO_2 to the desired level in the laboratory or growth cabinet in which the experiments are carried out. A simple air pump can then be used to bubble the experimental seawater. To the best of our knowledge, this technique has yet to be used in the context of ocean acidification.

Seawater aeration by bubbling may lead to difficulties in phytoplankton cultures (Shi et al., 2009). It may also enhance the coagulation of organic matter (Engel et al., 2004). This coagulation may be critical for studies investigating the response of microbial communities because their metabolism depends on the respective abundance of dissolved and particulate organic matter. This drawback may be avoided by enclosing the community in a dialysis bag, which is itself enclosed in a container bubbled with a gas having the desired pCO_2 (M. Weinbauer, personal communication, 2008). Such bags are permeable to gases and small molecules in solution but impermeable to larger molecules and particles.

3.2 Addition of high-CO_2 sea water

Dissolved inorganic carbon (DIC) and total alkalinity (TA) are conservative quantities with respect to mixing (Wolf-Gladrow et al., 2007). Hence, when two water parcels are mixed, the amount of a solute in the mixture equals the sum of the amounts of this solute in the two initial water parcels. Hence:

$$[\mathrm{DIC}]_{\mathrm{mixed}} \times M_{\mathrm{mixed}} = [\mathrm{DIC}]_{sw} \times M_{sw} + [\mathrm{DIC}]_{\mathrm{high\ CO_2}} \times M_{\mathrm{high\ CO_2}}$$

$$[\mathrm{TA}]_{\mathrm{mixed}} \times M_{\mathrm{mixed}} = [\mathrm{TA}]_{sw} \times M_{sw} + [\mathrm{TA}]_{\mathrm{high\ CO_2}} \times M_{\mathrm{high\ CO_2}}$$

Where the subscripts "sw" and "high CO_2", respectively indicate concentrations in the normal and high CO_2 seawater. Concentrations are in µmol kg^{-1} and M is the mass in kg. The *seacarb* function pmix estimates the carbonate chemistry after mixing of two water samples.

Example: one mixes, in a closed system, 0.99623 kg of seawater having a TA of 2325 µmol kg^{-1}, and pCO_2 of 384 µatm with 0.00377 kg of seawater having a TA of 2325 µmol kg^{-1} and saturated with CO_2 ($pCO_2 = 1 \times 10^6$ µatm). The weight fraction, wf, is 3.76×10^{-3}. Salinity is 34.9, temperature is 18.9°C

Table 2. Seawater carbonate chemistry in 2007, 2100, and after perturbation. The total alkalinity (TA), partial pressure of CO_2 in seawater ($pCO_{2\,sw}$), salinity and temperature were used to derive all other parameters using the *seacarb* package (Lavigne et al., 2008) except for manipulations of the calcium concentration for which DIC was used rather than $pCO_{2\,sw}$. For simplicity, it is assumed that temperature, salinity and total alkalinity in 2100 are identical to their 2007 values, respectively 18.9°C, 34.9 and 2325×10^{-6} mol kg^{-1}, and the concentrations of total phosphate and silicate were set to 0. The seawater pCO_2 was set to 384 µatm in 2007 (Keeling et al., 2008) and 793 µatm in 2100 (according to the A2 SRES emission scenario; Plattner et al., 2001). The main body of the text provides further information. (a): $\times10^{-9}$ mol kg^{-1}, (b): $\times10^{-6}$ mol kg^{-1}.

	$pCO_{2\,sw}$ (µatm)	pH_T (–)	$[H^+]$ (a)	TA (b)	DIC (b)	$[CO_2]$ (b)	$[HCO_3^-]$ (b)	$[CO_3^{2-}]$ (b)	Ω_c (–)	Ω_a (–)
Year 2007	384	8.065	8.6	2325	2065	12.8	1865	187	4.5	2.9
Year 2100	793	7.793	16.1	2325	2191	26.4	2055	110	2.6	1.7
Gas bubbling	793	7.793	16.1	2325	2191	26.4	2055	110	2.6	1.7
Addition of high-CO_2 seawater	792	7.793	16.1	2325	2191	26.4	2055	110	2.6	1.7
Addition of CO_3^{2-} and HCO_3^-; closed sys.	793	7.942	11.4	3406	3146	26.4	2901	218	5.2	3.4
Addition of CO_3^{2-} and HCO_3^-; open sys.	384	8.207	6.2	3406	2950	12.8	2580	357	8.5	5.5
Acid addition; closed sys.	793	7.768	17.1	2184	2065	26.4	1940	98	2.3	1.5
Acid addition; open sys.	384	8.042	9.1	2184	194	12.8	1767	167	4	2.6
Addition of:										
CO_3^{2-} and HCO_3^-; closed sys.	400	8.073	8.4	2467	2191	13.3	1977	201	4.8	3.1
followed by acid addition; closed sys.	793	7.793	16.1	2325	2191	26.4	2055	110	2.6	1.7
Manipulation of $[Ca^{2+}]$	384	8.065	8.6	2325	2065	12.8	1866	187	2.6	1.7

and calculations are made for surface waters. The command needed is:

pmix(flag=24, var1=384, var2=2325e-6, pCO2s=1e6, wf=3.76e-3, S=34.9, T=18.9)

This produces seawater with a final pCO_2 of 792 µatm (the 1 µatm difference with the target value is due to rounding errors) and all parameters of the carbonate chemistry in 2100 are perfectly reproduced. To the best of our knowledge, this approach has only been used twice: in mesocosms by Schulz et al. (unpublished data) and in the laboratory by C. McGraw (personal communication, 2009). It is therefore not possible to evaluate its pros and cons at this stage.

3.3 Addition of CO_3^{2-} and/or HCO_3^-

Dissolved inorganic carbon and total alkalinity can be increased by adding CO_3^{2-} in the form of Na_2CO_3 and/or by adding HCO_3^- in the form of $NaHCO_3$. In closed systems, the change in DIC generated by these additions is proportional to the changes in concentration: $1\times\Delta CO_3^{2-}$ and $1\times\Delta HCO_3^-$. The contribution of these anions to TA is proportional to the product of their charge and concentration. Thus: TA increases by $2\times\Delta CO_3^{2-}$ and $1\times\Delta HCO_3^-$. The changes in the carbonate chemistry generated by manipulations of total alkalinity therefore depend on the proportion of CO_3^{2-} and HCO_3^- added (Fig. 3). This approach can be used to keep the pH constant or combined with addition of acid to keep TA constant (see Sect. 3.5).

In an open system, the carbonate system re-equilibrates through air-sea CO_2 gas exchange after adding chemicals. At equilibrium:

$$CO_3^{2-} + H^+ \rightarrow HCO_3^- \quad \text{(R1)}$$

$$HCO_3^- + H^+ \rightarrow CO_2 + H_2O \quad \text{(R2)}$$

The *seacarb* function pTA computes the changes in the carbonate chemistry due to addition of CO_3^{2-} and/or HCO_3^-.

Example: HCO_3^- (1081×10^{-6} mol kg^{-1}) is added to seawater for which pCO_2 (384 µatm) and TA (2325 µmol kg^{-1}) are known. No CO_3^{2-} is added. The atmospheric pCO_2 is 384 µatm, salinity is 34.9, temperature is 18.9°C and calculations are made for surface waters. The respective commands in a closed and open system are:

pTA(flag=24, sys=0, var1=384, var2=2325e-6, pCO2a=384, co3=0e-6, hco3=1081e-6, S=34.9, T=18.9)

pTA(flag=24, sys=1, var1=384, var2=2325e-6, pCO2a=384, co3=0e-6, hco3=1081e-6, S=34.9, T=18.9)

Results are shown in Fig. 3 and Table 2. In a closed system, the target pCO_2 of 793 µatm is reached but all other parameters of the carbonate system are very different from their values expected in 2100. pH is higher than it should be (7.942 instead of 7.793) and TA, DIC, $[CO_3^{2-}]$, and the

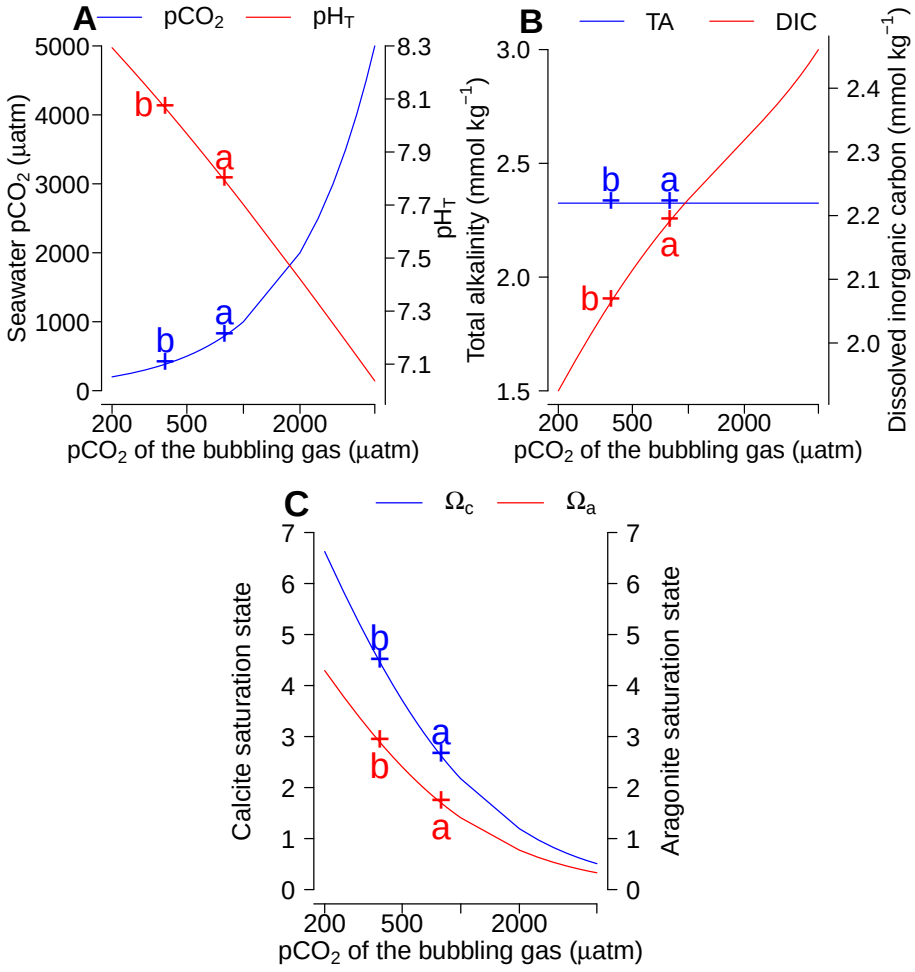

Fig. 1. Effect of bubbling seawater with gases of varying pCO_2 on the carbonate chemistry of seawater as computed with the *seacarb* function pgas. The letters "b" and "a" indicate, respectively, the value of a parameter before and after perturbation for the example described in the text.

saturation states of aragonite and calcite (Ω_a and Ω_c) are higher than the target values. They are even higher than the values of the initial seawater. Those differences are magnified in open systems.

Manipulation of total alkalinity has often been used to investigate the physiological response to changes in the carbonate chemistry (e.g. Swift and Taylor, 1966). Marubini and Thake (1999) used bicarbonate additions to test the hypothesis that the supply of DIC limits coral calcification. Langdon et al. (2000) used this approach in the Biosphere 2 coral reef mesocosm. They added $NaHCO_3$ and Na_2CO_3 to increase the $CaCO_3$ saturation state. Since the experiment lasted several months, additions of $CaCl_2$ were used to restore a normal Ca^{2+} concentration. The manipulations of the Ca^{2+} concentration is described in Sect. 3.6.

3.4 Addition of strong acids and bases

The carbonate chemistry can be manipulated by addition of a strong acid or a strong base, such as HCl and NaOH, which completely dissociate in seawater. Adding of a strong acid or base to a system closed to the atmosphere does not alter the concentration of dissolved inorganic carbon but modifies total alkalinity. TA decreases when adding an acid and increases after addition of a base.

The change of total alkalinity after addition of a strong acid or base in a system open to the atmosphere is identical to that described above for a closed system. However, the concentration of DIC is modified through CO_2 exchange at the air-water interface because the partial pressures of CO_2 in the atmosphere and seawater equilibrate.

The *seacarb* function ppH calculates the changes in the carbonate chemistry during pH manipulations. The change in salinity due to the addition of acid or base is negligible.

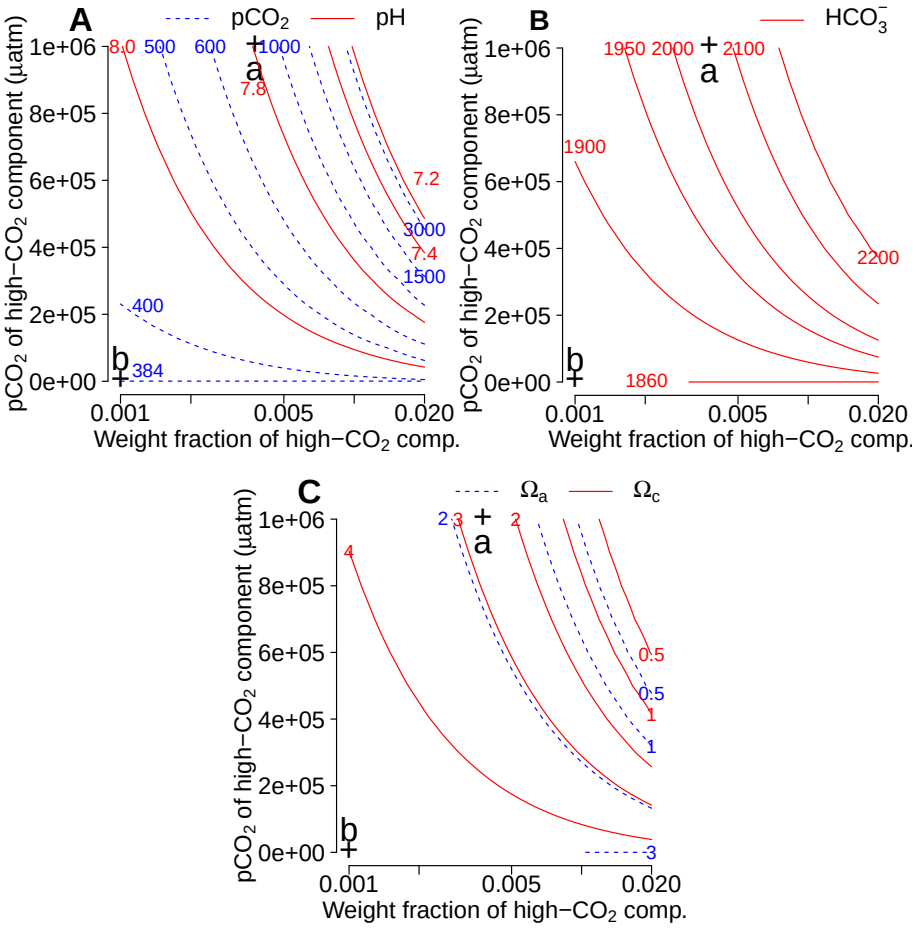

Fig. 2. Effect of mixing with various weight fractions of high-pCO_2 seawater on the carbonate chemistry of seawater in a closed system as computed with the *seacarb* function pmix. The letters "b" and "a" indicate, respectively, the value of a parameter before and after perturbation for the example described in the text.

Example: a volume of 14.08 ml of 0.01 N HCl is added to 1 kg of seawater having a known pCO_2 (384 µatm) and TA (2325 µmol kg^{-1}). The atmospheric pCO_2 is 384 µatm, salinity is 34.9 and temperature is 18.9°C. Calculations are made for surface waters. The commands needed in a closed and open system are:

ppH(flag=24, sys=0, var1=384, var2=2325e-6, pCO2a=384, vol=−14.08e-3, N=0.01, S=34.9, T=18.9)

ppH(flag=24, sys=1, var1=384, var2=2325e-6, pCO2a=384, vol=−14.08e-3, N=0.01, S=34.9, T=18.9)

Results are shown in Fig. 4 and Table 2. The target pCO_2 of 793 µatm is reached in a closed system but the pH is lower than the value expected in 2100 (7.768 instead of 7.793, corresponding to an increase of 2.9% in $[H^+]$ that resulting from the decrease in total alkalinity generated by the addition of acid). This is an undesirable effect of the direct manipulation of pH as TA will not change significantly during the course of this century (Table 1). As a result, DIC, HCO_3^-, CO_3^{2-}, Ω_a and Ω_c are lower than their target values. However, it is possible to restore TA to its initial level by adding CO_3^{2-} and/or HCO_3^-, an approach that is described in Sect. 3.5. Obviously, due to gas exchange at the air-water interface, pCO_2 and other parameters of the carbonate chemistry cannot be successfully adjusted by a one-time addition of acid in an open system.

Addition of acid has often been used in studies of the impact of ocean acidification on organisms. The first purposeful experiment is that of Agegian (1985) who looked at the response of coralline algae.

3.5 Addition of strong acid as well as CO_3^{2-} and/or HCO_3^-

As mentioned in Sect. 3.4, the addition of acid does not allow to fully mimic the changes in carbonate chemistry expected during the present century but the addition of CO_3^{2-} and/or HCO_3^- followed by addition of acid circumvents this

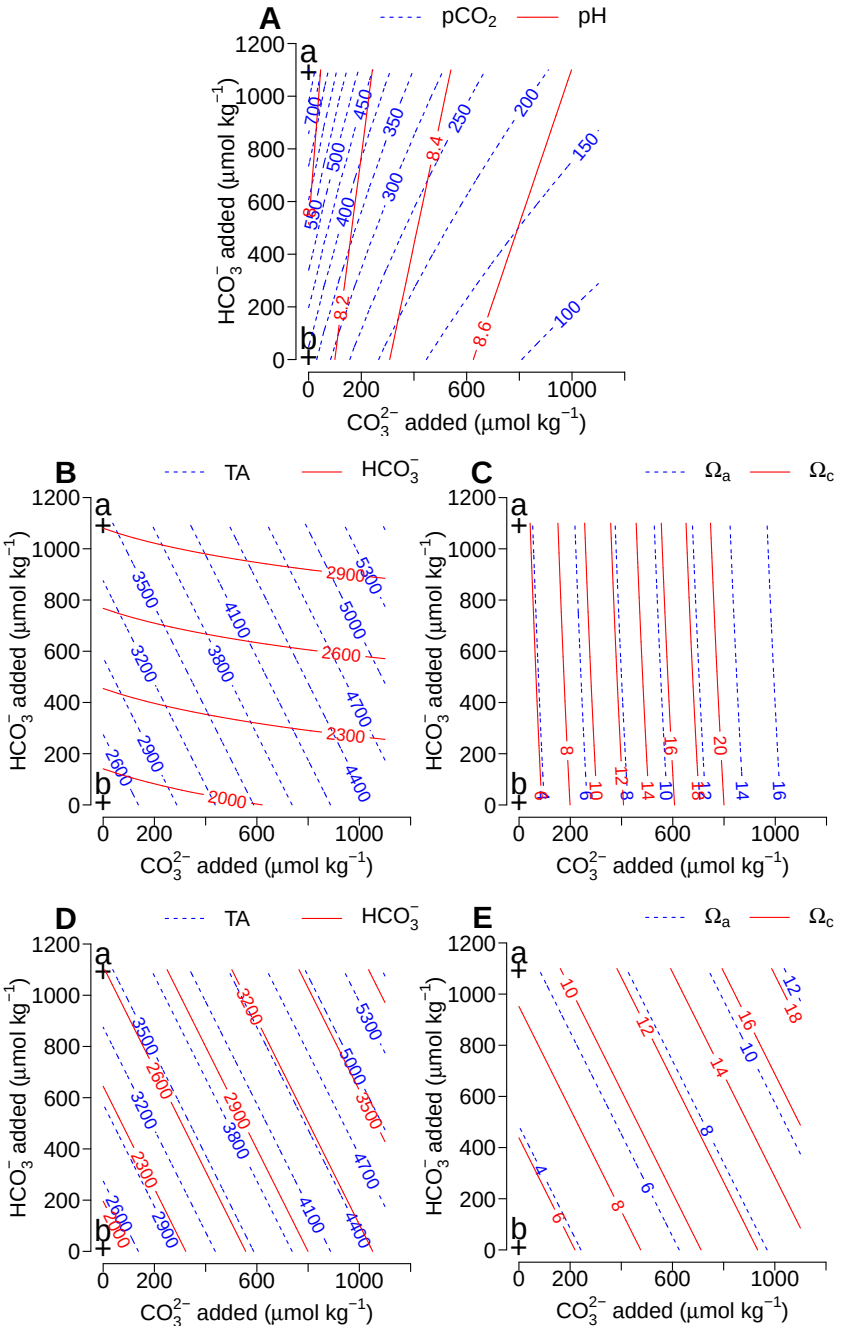

Fig. 3. Effect of adding CO_3^{2-} and/or HCO_3^- on the carbonate chemistry of seawater in closed (**A**, **B** and **C**) and open systems (**D** and **E**) as computed with the *seacarb* function pTA. The letters "b" and "a" indicate, respectively, the value of a parameter before and after perturbation for the example described in the text.

problem. The first addition elevates DIC to the desired level while adding acid (at constant DIC) precisely cancels out the increase in TA resulting from the addition of CO_3^{2-} and/or HCO_3^-.

There is no specific *seacarb* function to handle this approach. The changes in the carbonate chemistry can be calculated using successively the functions pTA and ppH.

Example: HCO_3^- (111.2×10^{-6} mol kg^{-1}) and CO_3^{2-} (15.3×10^{-6} mol kg^{-1}) are added to seawater for which pCO_2 (384 µatm) and TA (2325 µmol kg^{-1}) are known. The atmospheric pCO_2 is 384 µatm, salinity is 34.9, temperature is 18.9°C and calculations are made for surface waters. Then, 14.18 ml of 0.01 N HCl is added. The commands needed are:

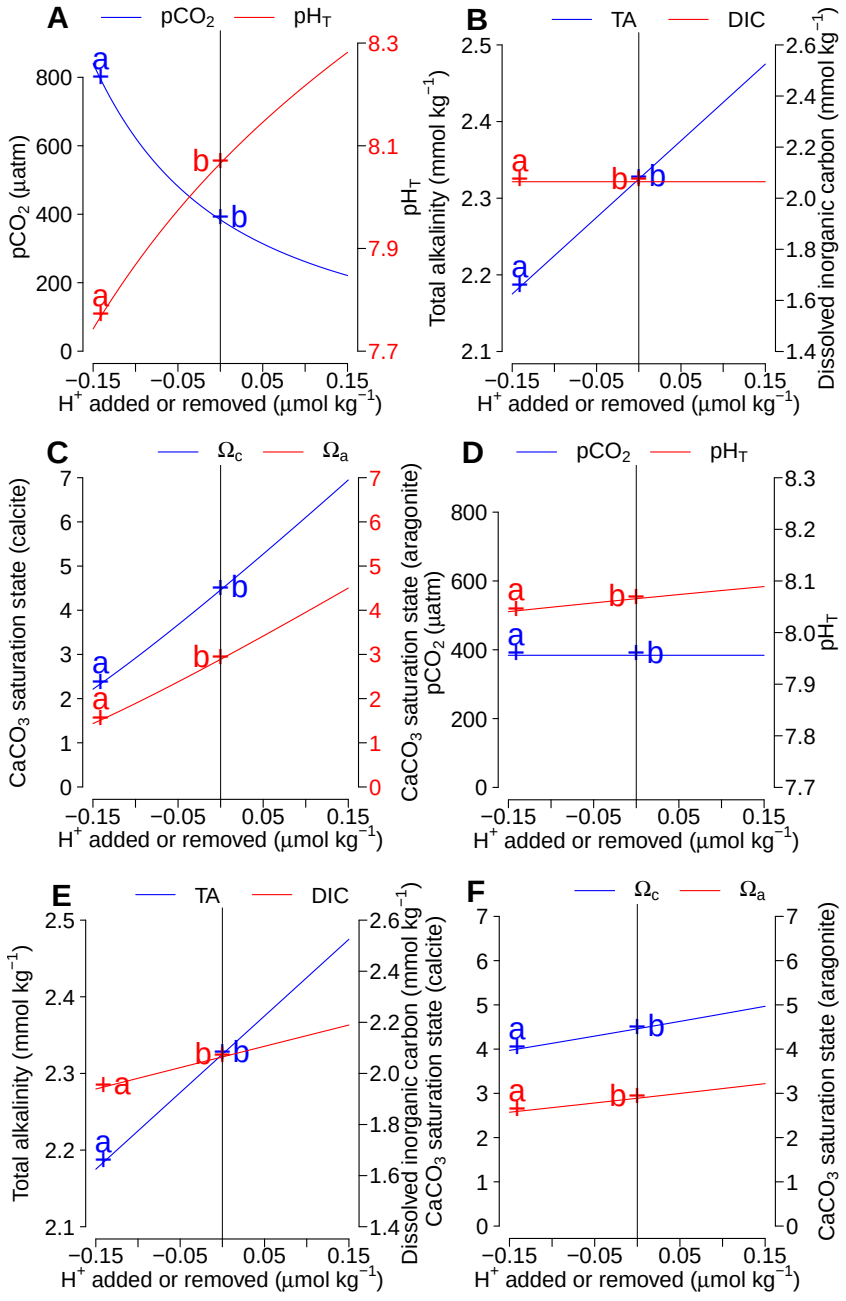

Fig. 4. Effect of adding a strong acid or a strong base on the carbonate chemistry of seawater in closed (**A**, **B** and **C**) and open systems (**D**, **E** and **F**) as computed with the *seacarb* function pgas. By convention, addition of acid is negative whereas addition of base is positive. The letters "b" and "a" indicate, respectively, the value of a parameter before and after perturbation for the example described in the text.

tmp=pTA(flag=24, sys=0, var1=384, var2=2325e-6, pCO2a=384, co3=15.3e-6, hco3=111.2e-6, S=34.9, T=18.9)

ppH(flag=24, sys=0, var1=tmp$pCO2[2], var2=tmp$ALK[2], pCO2a=384, vol=−14.18e-3, N=0.01, S=34.9, T=18.9)

Results are shown in Table 2. The first addition raises DIC to the desired level of 2191×10^{-6} mol kg^{-1} but increases TA to a value higher than the target (2467 vs. 2325×10^{-6} mol kg^{-1}). The subsequent addition of HCl restores TA to the desired value without affecting DIC. After both additions, all carbonate parameters are at the target values (Table 2).

To our knowledge, the first paper which used addition of acid, base and $NaHCO_3$ to manipulate the carbonate chemistry within a range comparable to ocean acidification is that of Borowitzka (1981) who investigated, in the laboratory, the response of photosynthesis and calcification of an articulated coralline red algae.

3.6 Manipulation of the Ca^{2+} concentration

Although manipulating the calcium concentration does not technically alter the carbonate chemistry *per se*, this approach has been used in the context of ocean acidification. The reason is that some calcifying organisms, such as corals, respond to the calcium carbonate saturation state of seawater (Ω) which is expressed as:

$$\Omega = \frac{[Ca^{2+}]_{sw} \times [CO_3^{2-}]_{sw}}{K^*_{sp}}$$

where $[Ca^{2+}]_{sw}$ and $[CO_3^{2-}]_{sw}$ are the concentrations of calcium and carbonate in seawater, respectively, and K^*_{sp} is the solubility product at the *in situ* conditions of temperature, salinity and pressure (Zeebe and Wolf-Gladrow, 2001). It can readily be appreciated that the changes in Ω resulting from the decrease in $[CO_3^{2-}]_{sw}$ driven by ocean acidification can be mimicked by altering $[CO_3^{2-}]_{sw}$. This approach involves the use of artificial seawater (Gattuso et al., 1998). It is recommended to use the simplied synthetic seawater recipe based on DOE (1994) as described by Gattuso et al. (1998) and because it is the basis of the synthetic seawater that has been used to determine a variety of equilibrium constants for use in seawater.

The *seacarb* function pCa estimates the changes in Ω_c and Ω_a resulting from the manipulation of the $[Ca^{2+}]_{sw}$ concentration. Note that this function does not account for the effect of the changes on the calcium concentration of the dissociation constants of carbonic acid and on the solubility product of $CaCO_3$ (Ben-Yaakov and Goldhaber, 1973).

Example: artificial seawater is made with a known TA (2325 µmol kg^{-1}) and DIC (2064 µmol kg^{-1}). The calcium concentration is set to 6.03×10^{-6} mol kg^{-1}. The command needed is:

```
pCa(flag=15, var1=2325e-6, var2=2064e-6,
Ca=6.03e-3, S=34.9, T=18.9)
```

Results are shown in Fig. 5 and Table 2. The saturation states of aragonite and calcite expected in 2100 are well reproduced without affecting any of the other parameters of the carbonate system which remain at their 2008 values.

This approach has been used to investigate the response of corals (Gattuso et al., 1998) and coccolithophores (Trimborn et al., 2007) to changes in the saturation state of calcium carbonate. It has also been used to replenish calcium when its concentration decreases below its natural levels during long-term experiments with calcifiers (e.g. Langdon et al., 2000).

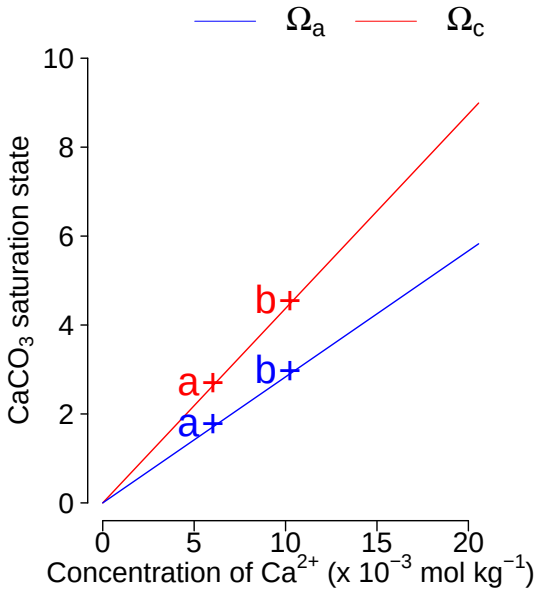

Fig. 5. Calcium carbonate saturation state as a function of the calcium concentration as computed with the *seacarb* function pCa. The letters "b" and "a" indicate, respectively, the value of the calcium carbonate saturation state before and after perturbation for the example described in the text.

4 Discussion and conclusion

Three approaches closely mimic the on-going and future changes in the seawater carbonate chemistry: gas bubbling, addition of high-CO_2 seawater, and combined addition of acid and bicarbonate and/or carbonate. All three methods increase dissolved inorganic carbon at constant total alkalinity, a situation that closely resembles the changes in the carbonate chemistry that have occurred during the last 200 years and are expected to continue during the next few hundreds years. All three approaches therefore offer precise control of carbonate chemistry variables, that reach target values at the beginning of a perturbation experiment. Gas bubbling is the easiest to implement and can be used to maintain constant conditions over long periods of time. However, during bubbling, biological processes (e.g., calcification, dissolution of $CaCO_3$, nutrient uptake and release) can alter the carbonate chemistry by changing total alkalinity even though the concentration of pCO_2 remains constant. Also, in all three approaches, calcification can deplete the concentration of Ca^{2+} when the organism to volume ratio is high or the incubation time long.

The approach of adding CO_3^{2-} and/or HCO_3^- appears to be of limited practical use because most carbonate variables reach values that are far from target values. Several studies have added acid to manipulate the carbonate chemistry. Although this technique offers precise control of pCO_2 in systems closed to the atmosphere, it also alters total alkalinity

which drives other carbonate system variables to levels far from those expected in the future. That is, pH is lower than its target value, DIC remains unchanged (whereas it increases with natural ocean acidification), and the $CaCO_3$ saturation states as well as the concentrations of bicarbonate and carbonate are higher than the target values. To avoid this drawback, it is recommended to first add bicarbonate or carbonate, or both, to increase DIC, before adding acid.

Iglesias-Rodriguez et al. (2008a) have recently reported that, in contrast to previous reports, calcification of the coccolithophore *Emiliania huxleyi* increases at elevated pCO_2. They argued that this is due to the different approaches used to manipulate the carbonate chemistry and that the approach of gas bubbling (changing DIC at constant TA) is superior to the approach of adding acid (changing TA at constant DIC) (Iglesias-Rodriguez et al., 2008a,b). The argument is that the addition of acid does not reproduce the increase in the HCO_3^- concentration occurring from natural ocean acidification whereas gas bubbling does reproduce it. The authors claim that HCO_3^- may stimulate photosynthesis and, in turn, calcification. They conclude that experiments using addition of acid demonstrating that calcification declines at lower pH, confounded the issue. This statement is misleading, although there is no doubt that gas bubbling better mimics the future carbonate chemistry (see above as well as Table 2). In contrast to the claims by Iglesias-Rodriguez et al. (2008a,b), several previous perturbation experiments were also carried out with gas bubbling and reported lower rates of calcification of coccolithophores at lower pH and higher pCO_2 (Sciandra et al., 2003; Delille et al., 2005; Feng et al., 2008). Additionally, the concentrations of CO_2, HCO_3^-, CO_3^{2-}, and H^+ all change in the same direction with both approaches: gas bubbling and acid addition (compare Fig. 1a–c with Fig. 4a–c; Table 2). Hence, the magnitude of biological responses may be different, but should at least tend to go in the same direction. Differences in the two approaches cannot explain biological responses going in opposite directions. Finally, perturbation experiments carried out using gas bubbling can also lead to poor control of the carbonate chemistry, for example, when the experiments last too long or when the biomass-to-volume ratio is too large (see above). Although the cause of the discrepancy in the response of calcification by the coccolithophore *E. huxleyi* to ocean acidification remains a matter of debate (e.g., Riebesell et al., 2008; Shi et al., 2009), it does not appear to be related to the approach used to perform the manipulation of the carbonate chemistry in perturbation experiments.

Fortunately, the situation seems clearer in zooxanthellate scleractinian corals. Schneider and Erez (2006) measured the rate of calcification under constant DIC, constant pH and constant pCO_2 and showed that calcification is controlled by the concentration of CO_3^{2-}, the future value of which is relatively well mimicked by adding acid.

Our goal here has been to provide the appropriate computational tools and to highlight the positive and negative aspects of the different approaches that are used to investigate ocean acidification by perturbing the carbonate chemistry. We have not addressed practical issues that must be taken into account to design and conduct perturbation experiments. To mention just a few: response time, bubbling rate, impact of autoclaving, evaporation, heat flux, impact of nutrients and temperature. These issues, as well as others, will be covered in a *Guide for Best Practices in Ocean Acidification Research and Data Reporting* in preparation (see http://www.epoca-project.eu/index.php/Home/Guide-to-OA-Research/).

Appendix A

A1 Gas bubbling: syntax of pgas

The function pgas calculates the carbonate chemistry after perturbation using the CO_2 partial pressure of the gas used to bubble the medium and the initial total alkalinity which is not altered by gas bubbling. The syntax is:

pgas(flag, var1, var2, pCO2g, S, T, P, Pt, Sit, k1k2, Kf, pHscale)

The input parameters below are required:

- flag: a number (1 to 24) indicating which couple of parameters of the carbonate system is known. For example, flag is 8 when pH_T and total alkalinity are known.
- var1 and var2: the values of the two parameters of the carbonate system prior to the perturbation which are known (pH_T and alkalinity in the example above). See the *seacarb* manual for more details, especially regarding the units.
- pCO2g is the CO_2 partial pressure (in µatm) of the gas used to bubble the medium.
- S: salinity.
- T: temperature in °C
- P: hydrostatic pressure (P; 0 by default). Note that this function was only tested at P=0, that is for surface waters.
- Pt: concentration of total phosphate (mol kg^{-1}; 0 by default).
- Sit: concentration of total silicate (mol kg^{-1}; 0 by default).
- k1k2: "l" for using K_1 and K_2 from Lueker et al. (2000) and "r" for using K_1 and K_2 from Roy et al. (1993), default is "l"

– Kf: "pf" for using K_f from Perez and Fraga (1987) and "dg" for using K_f from Dickson and Riley (1979), default is "pf"

– pHscale: "T" for using the total scale, "F" for using the free scale and "SWS" for using the seawater scale, default is "T"

A2 Addition of high-CO_2 seawater: syntax of pmix

It is important to note that pmix assumes that the initial and high-CO_2 seawater have the same total alkalinity. pmix calculates the carbonate chemistry after perturbation using the final DIC concentration calculated as described in Sect. 3.2 and the initial total alkalinity which is not altered by the mixing. The syntax is:

pmix(flag, var1, var2, pCO2s, wf, S, T, P, Pt, Sit, k1k2, Kf, pHscale)

flag, var1, var2, S, T, P, Pt, Sit, k1k2, Kf and pHscale were defined in Appendix A1. The other input parameters required are:

– pCO2s: pCO_2 of the high-CO_2 water in µatm

– wf: weight fraction of the high-CO_2 seawater vs. final weight

A3 Addition of CO_3^{2-} and/or HCO_3^-: syntax of pTA

For closed systems, the function pTA calculates the carbonate chemistry after perturbation using the final DIC concentration and total alkalinity calculated as described in Sect. 3.3. For open systems, the carbonate chemistry is calculated using atmospheric pCO_2, therefore assuming equilibrium of pCO_2 between air and seawater, and total alkalinity calculated as described in Sect. 3.3 (as is not further altered by air-sea CO_2 exchange). The syntax is:

pTA(flag, sys, var1, var2, pCO2a, co3, hco3, S, T, P, Pt, Sit, k1k2, Kf, pHscale)

flag, var1, var2, S, T, P, Pt, Sit, k1k2, Kf and pHscale where defined above. The other input parameters below are required:

– sys: 0 if the manipulation is carried out in a system closed to the atmosphere or 1 if it is carried out in a system open to the atmosphere (in the latter case, full equilibrium between air and water is assumed).

– pCO2a: the value of atmospheric pCO_2 in μatm. It is only used in systems open to the atmosphere (i.e. sys=1).

– co3: amount of CO_3^{2-} added in mol kg^{-1}.

– hco3: amount of HCO_3^- added in mol kg^{-1}.

A4 Addition of strong acids and bases: syntax of ppH

For closed systems, the function ppH calculates the carbonate chemistry after perturbation using the DIC concentration (which is unchanged by the addition of acid or base) and the total alkalinity which can easily be estimated as strong acids and bases completely dissociate in seawater. For open systems, the carbonate chemistry is calculated using atmospheric pCO_2, therefore assuming equilibrium of pCO_2 between air and seawater, and the total alkalinity after addition of acid or base as it is not further altered by air-sea CO_2 exchange. The syntax is:

ppH(flag, sys, var1, var2, pCO2a, vol, N, S, T, P, Pt, Sit, k1k2, Kf, pHscale)

flag, sys, var1, var2, pCO_2a, S, T, P, Pt, Sit, k1k2, Kf and pHscale were defined above.

The other input parameters required are:

– vol: the volume of acid or base added in liter. By convention, it is given a negative sign for additions of acid and a positive sign for additions of base.

– N: the normality of the acid or base (mol kg^{-1}).

A5 Manipulation of the Ca^{2+} concentration: syntax of pCa

The function pCa calculates the carbonate chemistry using the standard equations of Dickson et al. (2007) except that the actual calcium concentration is used rather than the standard concentration of $0.01028 \times (S/35)$ mol kg^{-1}. The syntax is:

pCa(flag, sys, var1, var2, Ca, S, T, P, Pt, Sit, k1k2, Kf, pHscale)

flag, var1, var2, S, T, P, Pt, Sit, k1k2, Kf and pHscale were defined above. Ca is the calcium concentration in mol kg^{-1}.

Acknowledgements. Thanks are due to G.-K. Plattner for providing model outputs, to P. Grosjean, J. C. Orr, U. Riebesell, K. Schulz and R. E. Zeebe for useful comments on an early draft of this paper, as well as to A. Dickson, A. Engel, C. Langdon, H.-O. Pörtner and the participants of the "Workshop on Best Practices for Ocean Acidification Research and Data Reporting" for helpful discussions. This work is a contribution to the "European Project on Ocean Acidification" (EPOCA) which receives funding from the European Community's Seventh Framework Programme (FP7/2007–2013) under grant agreement 211384, the BOOM project funded by the *Agence Nationale de la Recherche* (ANR-05-BIODIV-004) and CARBOOCEAN (FP6/511176-2).

Edited by: A. Boetius

The publication of this article is financed by CNRS-INSU.

References

Agegian, C. R.: The biogeochemical ecology of *Porolithon gardineri* (Foslie), Ph.D. thesis, University of Hawaii, 1985.

Ben-Yaakov, S. and Goldhaber, M.: The influence of sea water composition on the apparent constants of the carbonate system, Deep-Sea Res., 20, 87–99, 1973.

Borowitzka, M. A.: Photosynthesis and calcification in the articulated coralline red algae *Amphiroa anceps* and *A. foliacea*, Mar. Biol., 62(1), 17–23, 1981.

Bouxin, H.: Action des acides sur le squelette des larves de l'oursin *Paracentrotus lividus*. Influence du pH, C. R. Soc. Biol., 94, 453–455, 1926.

Delille, B., Harlay, J., Zondervan, I., Jacquet, S., Chou, L., Wollast, R., Bellerby, R. G. J., Frankignoulle, M., Borges, A. V., Riebesell, U., and Gattuso, J.-P.: Response of primary production and calcification to changes of pCO_2 during experimental blooms of the coccolithophorid *Emiliania huxleyi*, Global Biogeochem. Cy., 19, GB2023, doi:10.1029/2004GB002318, 2005.

Dickson, A. G. and Riley, J. P.: The estimation of acid dissociation constants in seawater media from potentiometric titrations with strong base. I. The ionic product of water, Mar. Chem., 7, 89–99, 1979.

Dickson, A. G., Sabine, C. L., and Christian, J. R.: Guide to best practices for ocean CO_2 measurements, PICES Special Publication, 3, 1–191, 2007.

DOE: Handbook of methods for the analysis of the various parameters of the carbon dioxide system in sea water, version 2, ORNL/CDIAC; location is Oak Ridge, Tennessee, 1994.

Engel, A., Delille, B., Jacquet, S., Riebesell, U., Rochelle-Newall, E., Terbrggen, A., and Zondervan, I.: Transparent exopolymer particles and dissolved organic carbon production by *Emiliania huxleyi* exposed to different CO_2 concentrations: a mesocosm experiment, Aquat. Microb. Ecol., 34(1), 93–104, 2004.

Feng, Y., Warner, M., Zhang, Y., Sun, J., Fu, F., Rose, J., and Hutchins, D.: Interactive effects of increased pCO_2, temperature and irradiance on the marine coccolithophore *Emiliania huxleyi* (Prymnesiophyceae), Eur. J. Phycol., 43, 87–98, 2008.

Garcia, H., Locarnini, R., Boyer, T., and Antonov, J.: World Ocean Atlas 2005. Volume 4: Nutrients (phosphate, nitrate, silicate), in: NOAA Atlas NESDIS 64, edited by: Levitus, S., 1–396, US Government Printing Office, Washington, DC, 2006.

Gattuso, J.-P., Frankignoulle, M., Bourge, I., Romaine, S., and Buddemeier, R. W.: Effect of calcium carbonate saturation of seawater on coral calcification, Global Planet Change, 18, 37–46, 1998.

Iglesias-Rodriguez, M., Halloran, P., Rickaby, R., Hall, I., Colmenero-Hidalgo, E., Gittins, J., Green, D., Tyrrell, T., Gibbs, S., von Dassow, P., Rehm, E., Armbrust, E., and Boessenkool, K.: Phytoplankton calcification in a high-CO_2 world, Science, 320, 336–340, 2008a.

Iglesias-Rodriguez, M. D., Buitenhuis, E. T., Raven, J. A., Schofield, O., Poulton, A. J., Gibbs, S., Halloran, Paul, R., and de Baar, H. J. W.: Response to Comment on Phytoplankton calcification in a high-CO_2 world, Science, 322, 1466c–1466c, 2008b.

Keeling, R., Piper, S., Bollenbacher, A., and Walker, J.: Atmospheric CO_2 records from sites in the SIO air sampling network, in: Trends: a compendium of data on global change, Oak Ridge National Laboratory, US Department of Energy, 2008.

Kleypas, J. A., Feely, R. A., Fabry, V. J., Langdon, C., Sabine, C. L., and Robbins, L. L.: Impacts of ocean acidification on coral reefs and other marine calcifiers: a guide for future research, Institute for the Study of Society and Environment (ISSE) of the University Corporation for Atmospheric Research (UCAR), Boulder, Colorado, 2006.

Langdon, C.: Review of experimental evidence for effects of CO_2 on calcification of reef builders, in: Proceedings of the 9th International Coral Reef Symposium, 1091–1098, Bali, 2000.

Langdon, C., Takahashi, T., Marubini, F., Atkinson, M., Sweeney, C., Aceves, H., Barnett, H., Chipman, D., and Goddard, J.: Effect of calcium carbonate saturation state on the rate of calcification of an experimental coral reef, Global Biogeochem. Cy., 14, 639–654, 2000.

Lavigne, H., Proye, A., and Gattuso, J.-P.: seacarb 2.0, an R package to calculate parameters of the seawater carbonate system, online available at: http://cran.r-project.org/web/packages/seacarb/index.html, 2008.

Lueker, T. J., Dickson, A., and Keeling, C. D.: Ocean pCO_2 calculated from dissolved inorganic carbon, alkalinity, and equations for K1 and K2: validation based on laboratory measurements of CO_2 in gas and seawater at equilibrium, Mar. Chem., 70(1–3), 105–119, 2000.

MARGO Project Members: Constraints on the magnitude and patterns of ocean cooling at the Last Glacial Maximum, Nat. Geosci., 2, 127–132, 2009.

Marubini, F. and Thake, B.: Bicarbonate addition promotes coral growth, Limnol. Oceanogr., 44(3), 716–720, 1999.

Nakićenović, N. and Swart, R. (eds.): Special report on emissions scenarios : a special report of Working Group III of the Intergovernmental Panel on Climate Change, Cambridge University Press, Cambridge, 2000.

Paul, A. and Schäfer-Neth, C.: Modeling the water masses of the Atlantic Ocean at the Last Glacial Maximum, Paleoceanography, 18, 1058, doi:10.1029/2002PA000783, 2003.

Perez, F. F., and Fraga, F.:Association constant of fluoride and hydrogen ions in seawater, Mar. Chem., 21, 161–168, 1987.

Petit, J. R., Jouzel, J., Raynaud, D., Barkov, N., Barnola, J.-M., Basile, I., Bender, M., Chappellaz, J., Davis, J., Delaygue, G., Delmotte, M., Kotlyakov, V., Legrand, M., Lipenkov, V., Lorius, C., Pépin, L., Ritz, C., Saltzman, E., and Stievenard, M.: Vostok ice core data for 420,000 years, vol. Contribution Series #2001-076, NOAA/NGDC Paleoclimatology Program, 2001.

Plattner, G., Joos, F., Stocker, T., and Marchal, O.: Feedback mechanisms and sensitivities of ocean carbon uptake under global warming, Tellus B, 53, 564–592, 2001.

Proye, A. and Gattuso, J.-P.: seacarb, an R package to calculate parameters of the seawater carbonate system, http://cran.r-project.org/web/packages/seacarb/index.html, 2003.

R Development Core Team: R: A Language and Environment for

Statistical Computing, R Foundation for Statistical Computing, Vienna, Austria, online available at: http://www.R-project.org, ISBN 3-900051-07-0, 2008.

Riebesell, U., Bellerby, R. G. J., Engel, A., Fabry, V. J., Hutchins, D. A., Reusch, T. B. H., Schulz, K. G., and Morel, F. M. M.: Comment on "Phytoplankton calcification in a high-CO_2 world", Science, 322, 1466b–1466b, 2008.

Roy, R. N., Roy, L. N., Vogel, K. M., Porter-Moore, C., Pearson, T., Good, C. E., Millero, F. J., and Campbell, D. M.: The dissociation constants of carbonic acid in seawater at salinities 5 to 45 and temperatures 0 to 45°C, Mar. Chem., 44, 249–267, 1993.

Sabine, C., Feely, R., Gruber, N., Key, R., Lee, K., Bullister, J., Wanninkhof, R., Wong, C., Wallace, D., Tilbrook, B., Millero, F., Peng, T., Kozyr, A., Ono, T., and Rios, A.: The oceanic sink for anthropogenic CO_2, Science, 305(5682), 367–371, 2004.

Schneider, K. and Erez, J.: The effect of carbonate chemistry on calcification and photosynthesis in the hermatypic coral *Acropora eurystoma*, Limnol. Oceanogr., 51, 1284–1293, 2006.

Sciandra, A., Harlay, J., Lefèvre, D., Lemée, R., Rimmelin, P., Denis, M., and Gattuso, J.-P.: Response of the coccolithophorid *Emiliania huxleyi* to elevated partial pressure of CO_2 under nitrate limitation, Mar. Ecol.-Prog. Ser., 261, 111–122, 2003.

Shi, D., Xu, Y., and Morel, F. M. M.: Effects of the pH/pCO_2 control method on medium chemistry and phytoplankton growth, Biogeosciences, 6, 1199–1207, 2009, http://www.biogeosciences.net/6/1199/2009/.

Smith, A. D. and Roth, A. A.: Effect of carbon dioxide concentration on calcification in the red coralline alga *Bossiella orbigniana*, Mar. Biol., 52, 217–225, 1979.

Swift, E. and Taylor, W. R.: The effect of pH on the division rate of the coccolithophorid *Cricosphaera elongata*, J. Phycol., 2, 121–125, 1966.

Trimborn, S., Langer, G., and Rost, B.: Effect of varying calcium concentrations and light intensities on calcification and photosynthesis in *Emiliania huxleyi*, Limnol. Oceanogr., 52, 2285–2293, 2007.

Wolf-Gladrow, D. A., Zeebe, R. E., Klaas, C., Körtzinger, A., and Dickson, A. G.: Total alkalinity: The explicit conservative expression and its application to biogeochemical processes, Mar. Chem., 106, 287–300, 2007.

Zeebe, R. E. and Wolf-Gladrow, D. A.: CO_2 in seawater: equilibrium, kinetics, isotopes, Elsevier, Amsterdam, 2001.

Chris Sabine
Thursday, November 5, 2009
PMEL Moored CO_2 System (lecture/lab activity) –
I will begin with a short overview of the theory of the moored CO_2 measurement. I will show examples of the kinds of data that we have been getting from the system and the pros and cons of this system versus other moored CO_2 systems. We will then move into the lab and I will demonstrate the different components of the system, how to operate the system, and the different functions available. Students will be able to ask questions about the system and its operation.

Helpful Reading:
http://www.pmel.noaa.gov/co2/moorings/

http://www.battelle.org/seaology/

CO2SYS Practice Exercise: Ocean Acidification Perturbation Experiments

K.K. Yates, U.S. Geological Survey, 600 Fourth Street South, St. Petersburg, FL 33701, kyates@usgs.gov

Materials needed:

- Laptop computer with CO2SYS installed
- Notebook and pencil
- Calculator/or use Excel for "quick" calculations

Outline

Introductory discussion

- Brief re-iteration of approaches for perturbation experiments and focus for CO2SYS exercise
- Take home messages
- Overview of practice exercises

Hands-on practice with CO2SYS

- Participants will walk through CO2SYS calculations for experimental practice sets 1 and 2 (of table 1), practice sets 3 and 4 are for discussion only, or can be used for practice at home.
- Walk through calculations for acid and CO_2 gas additions

Discussion

- Results, problems/common mistakes, solutions
- Potential chemical effects on biology
- Potential biological effects on chemistry

Practice Exercises

This practice exercise uses the carbonate speciation program CO2SYS (Pierrot et al. 2006) to simulate experimental variations in pCO_2 and pH that approximate values within the range of pre-industrial levels of pCO_2, ~270 ppm, to levels predicted for the year 2100 of ~800 ppm (IPCC 2001) and the effects on carbonate system parameters. Results of these simulations represent starting conditions for these seawater chemistry perturbation experiments and do not reflect the effect of biological organisms or calcification on seawater chemistry (this will be addressed briefly during discussion). Experimental set 1 simulates adjustments to the pH and inorganic carbon species performed using addition of known quantities of a strong monoprotic acid or base such as hydrochloric acid or sodium hydroxide, respectively. Experimental set 3 simulates the effect of allowing experiments from set 1 to re-equilibrate with atmospheric pCO_2. For experimental set 2, pCO_2 adjustments are simulated using addition of CO_2 gas via bubbling of seawater to achieve target pCO_2 concentrations. Experimental set 4 simulates the effect of allowing experiments from set 2 to re-equilibrate with atmospheric pCO_2.

Target values for carbonate system parameters, temperature, salinity, total P, and total Si for all experiments are from scenarios derived using Seacarb for the years 1766, 2007, and 2100 in Gattuso and Lavigne (2009), and re-analyzed using CO2SYS. Pressure is held constant at 0 dbars, and a calcium concentration of 10.12 μmol kg^{-1} is assumed. Starting seawater chemistry for all experimental manipulations is approximated at pre-industrial conditions with a TCO_2 of

1994 μmol kg^{-1}, TA of 2326 μmol kg^{-1}, pCO_2 of 267 μatm, and pH of 8.2. ***Experimental conditions for each set are shown in table 1.*** CO2SYS is used to calculate carbonate system parameters for all simulation experiments. For this exercise, use dissociation constants for the carbonate system, K1 and K2, from Mehrbach et al. (1973) refit by Dickson and Millero (1987), and for K_{HSO4} from Dickson (1990). Total pH scale (pH_T) is used for all calculations.

Step 1: Enter dissociation constants and pH scale using drop down menus on the input page of the MS Excel macro file for CO2SYS.

Step 2: Input experimental parameters for set 1: acid additions

Experimental set 1 simulates 3 experimental conditions whereby pH and carbonate system parameters are adjusted by addition of a strong, monoprotic acid, and maintained at that pH in a closed system with no exchange of carbon into or out of the system. Hydrochloric acid, 0.1 N, is added to adjust the pH from 8.194 to 8.065, and 7.792, and TCO_2 is held constant at 1994.4 μmol kg^{-1}. Input parameters for these experiments are entered on the data page of the CO2SYS macro file (table 2). Enter salinity, temperature, pressure, total P, total Si under their respective columns on rows 4, 5, and 6 of the data input spreadsheet using experimental conditions described above. Since TCO_2 is held constant, at 1994.4 μmol kg^{-1}, enter this value under the TCO_2 column for each of these three rows. Enter pH of 8.194, 8.065, and 7.792 under the pH column of the spreadsheet. Leave data columns for TA, fCO_2, and pCO_2 blank for this simulation. Press "start" on the data entry page to calculate results. Results for input conditions for this simulation are shown in table 3 (rows 4, 5, and 6). Output condition results are identical to input condition results because input and output conditions were the same and are, thus, not shown in table 3.

Step 3: Calculate the volume of acid needed to achieve target pH conditions.

The volume of acid needed to achieve experimental conditions can be approximated using the difference in TA from starting seawater conditions and the TA value at the target pH to determine the number of moles of H^+ needed to balance the total alkalinity change, then dividing by the concentration (normality) of stock acid (0.1N HCl) (see equation 1).

Eqn. 1. Liters of HCl added (L kg^{-1} SW) = ΔTA (mols kg^{-1} SW)/[H^+] (mol L^{-1})

This approximation can be made because it is a closed system and no other constituents besides [H^+] that affect total alkalinity are added (see definition of total alkalinity, e.g. Dickson et al. 2007, Zeebe and Wolf-Gladrow 2001). Experimental parameters and the volume of acid added to each system are listed in table 1.

Step 4: Input experimental parameters for set 2: CO_2 gas additions

The experimental set 2 simulation assumes a closed system whereby pH and carbonate system parameters are adjusted by addition of ~100% CO_2 gas via bubbling of seawater with known concentrations of CO_2. This experimental approach is the preferred methodology because it most closely resembles the effect of elevated atmospheric pCO_2 equilibrating with surface seawater (reference Gattuso and Lavigne, 2009). CO_2 bubbling can be achieved by either bubbling seawater with standardized CO_2 gas at the desired pCO_2 concentration and allowing carbonate system parameters to equilibrate, or by adding a discrete amount of

concentrated CO_2 gas to the closed tank and equilibrating seawater to achieve the desired CO_2 and total carbon concentrations. In the first approach, as gas is constantly added to the system, the head space of the experimental tank can be vented using a one-way valve to prevent pressurization of the system, or left open to the atmosphere during addition of CO_2 gas, then closed upon equilibration. In the second approach, the tank can be constantly bubbled in a closed loop system using an air pump, and a discrete volume of CO_2 gas added to the air stream. The practice exercise for set 2 is based on addition of a discrete volume of concentrated CO_2 gas. No venting is required if the volume of gas added is small relative to the total volume of the system and the total system volume and pressure change is negligible. A gas bag, or balloon, may also be attached to the head space of the experimental chamber to dampen pressure change effects.

Total alkalinity of seawater is a conservative property and does not change with the addition or subtraction of CO_2. Therefore, total alkalinity in all of these experiments is held constant. Use a starting seawater TA of 2326 μmol kg^{-1}, and enter this value on rows 7, 8, and 9 under the TA column heading in the CO2SYS spreadsheet. Enter salinity, temperature, pressure, total P, and total Si on these 3 rows under their respective columns in the spreadsheet as in set 1. Enter target values for pCO_2 (see table 1) as input data under the pCO_2 column of the spreadsheet. Data columns for TCO_2, pH, and fCO_2 are left blank for this simulation (Table 2). Press "start" on the data entry page to calculate results. Results for experimental set 2 are shown in Table 3 (rows 7, 8, and 9).

Step 5: Calculate the volume of CO_2 gas needed to achieve target pCO_2 conditions

Discrete volumes of CO_2 gas added to each experiment can be calculated by multiplying the difference in TCO_2 (in g C kg^{-1} SW) between starting seawater conditions and the TCO_2 of seawater at the target pCO_2 value times the density of CO_2 gas (1.808 g CO_2 L^{-1}) at standard atmospheric temperature and pressure (STP) (see equation 2). The ideal gas law (PV=nRT) can be used to calculate the volume of gas needed at different temperatures and pressures.

Eqn. 2 Liters of CO_2 gas added at STP kg^{-1} SW = ΔTCO_2 (mols kg^{-1} SW) x 44.01g CO_2 mol^{-1} x 1.808 g $CO_{2(g)}$ L^{-1}

Step 6: Input experimental parameters for set 3: re-equilibration of set 1 results to atmospheric pCO_2.

Experimental set 3 demonstrates the changes that occur to acid addition perturbation experiments of set 1 if the system is left open to the atmosphere and not controlled with a pH-stat after making chemical adjustments to the system. Experimental sets 3 and 4 show the importance of maintaining a controlled system and careful monitoring of chemical parameters through the duration of experiments. Inadequate control and monitoring of experimental conditions is a common error in perturbation experiments, and these two experimental exercises represent "worst-case scenarios". Input parameters for set 3 experiments are derived from the total alkalinity results of experimental set 1 and the assumption that each experiment was allowed to re-equilibrate with an assumed atmospheric pCO_2 of 384 μatm. Enter salinity, temperature, pressure, total P, and total Si on rows 10, 11, and 12 under their respective columns in the CO2SYS spreadsheet as in sets 1 and 2. Enter values obtained for total alkalinity in experimental set 1 results as input data under the TA column of the spreadsheet on rows 10, 11, and 12. Enter pCO_2 of 384 μatm for each of the 3 rows. Data columns for TCO_2, pH, and fCO_2

are left blank for this simulation (table 2). Press "start" on the data entry page to calculate results. Results for experimental set 3 are shown in table 3 (rows 10, 11, and 12).

Step 7: Input experimental parameters for set 4: re-equilibration of set 2 results to atmospheric pCO_2.

Experimental set 4 demonstrates the changes that occur to CO_2 bubbling perturbation experiments of set 2 if the system is left open to the atmosphere and allowed to re-equilibrate with atmospheric pCO_2 after making chemical adjustments to the system. For these experiments, total alkalinity is again held constant at the total alkalinity result value from set 2 (2326 μmol kg^{-1}), and atmospheric pCO_2 of 384 μatm is assumed. Enter input parameters for salinity, temperature, pressure, total P, and total Si from experimental set 2 on rows 13, 14, and 15 under their respective columns in the spreadsheet. Enter total alkalinity of 2326 μmol kg^{-1} and pCO_2 of 384 μatm on each of these 3 rows under their respective columns, and leave data columns for TCO_2, pH, and fCO_2 blank (Table 2). Press "start" on the data entry page to calculate results. Results for experimental set 4 are shown in Table 3 (rows 13, 14, and 15).

Table 4 lists the differences between values acquired in CO2SYS experiments and target values.

Other useful equations/information that may be discussed…time permitting:

Total carbon and total alkalinity can be increased by adding HCO_3^- and/or CO_3^{2-}. Amounts needed can be approximated from the differences in TA and TCO_2 between target and starting values via:

Eqn. 3 ΔTCO_2 = μmols kg^{-1} SW of total carbon needed

$\Delta TA - \Delta TCO_2$ = μmols kg^{-1} SWof CO_3^{2-} needed

$\Delta TCO_2 - (\Delta TA - \Delta TCO_2)$ = μmols kg^{-1} SW of HCO_3^- needed.

Total alkalinity can also be adjusted without changing total carbon by adding strong acid or base. The amount needed is determined by the difference in TA between target and starting values equation 1 above.

Reducing total carbon (and total alkalinity) can be achieved by adding acid to an open system, then allowing carbon to outgas as CO_2. The amount of acid needed is determined using equation 1, the amount of CO_2 that needs to be expelled can be approximated from ΔTCO_2 between target and starting values.

Background and reference material:

Dickson, A.G. 1990. Standard potential of the reaction: AgCl(s) + 1/2H_2(g) = Ag(s) + HCl (aq), and the standard acidity constant of the ion HSO4- in synthetic seawater from 273.15 to 318.15 K. Journal of Chemical Thermodynamics 22:113-127.

Dickson, A.G. and Millero, F.J. 1987. A comparison of the equilibrium constants for the dissociation of carbonic acid in seawater media. Deep-Sea Research 34:1733-1743.

Dickson, A.G., Sabine, C.L., and Christian, J.R. (eds.) 2007. Guide to best practices for ocean CO_2 measurements. PICES Special Publication 3, 191 pp.

Gattuso, J.P. and Lavigne, H. 2009. Perturbation experiments to investigate the impact of ocean acidification: approaches and software tools. Biogeoscience Discussions 6:4413-4439.

IPCC. 2001. Houghton, J.T., Ding, Y., Griggs, D.J., Noguer, M., van der Linden, P.J., Dai, X., Maskell, K., and Johnson, C.A. (eds.). Climate Change 2001: The Scientific Basis. Contribution of Working Group I to the Third Assessment Report of the Intergovernmental Panel on Climate Change. United Kingdom and New York: Cambridge University Press, 881 pp.

Mehrbach, C., Culberson, C.H., Hawley, J.E., and Pytkowicz, R.M. 1973. Measurement of the apparent dissociation constants of carbonic acid in seawater at atmospheric pressure. Limnology and Oceanography 18:897-907.

Pierrot, D.E., Lewis, E., and Wallace, D.W.R. 2006. Ms Excel program developed for CO2 system calculations. ORNL/CDIAC-105a. Carbon Dioxide Information Analysis Center, Oak Ridge National Laboratory, U.S. Department of Energy, Oak Ridge, Tennessee.

Zeebe, R.E. and Wolf-Gladrow, D. 2001. CO2 in Seawater: Equilibrium, Kinetics, Isotopes. In D. Halpern (ed.), Elsevier Oceanography Series 65, Elsevier Ltd.: San Diego, 349 pp.

A quick start guide for CO2sys EXCEL Macro is available at
http://cdiac.ornl.gov/ftp/co2sys/CO2SYS_calc_XLS/CO2SYS%20Macro%20Instructions.doc

Table 1. Target values and experimental parameters for CO2SYS practical exercises 1 through 4.

Target values from Gattuso and Lavigne (2009) via Seacarb:

Year	T (^oC)	Salinity	[1]Total P	[1]Total Si	[1]TA	pCO_2 (μatm)	[1]TCO_2	pH	[1]$[HCO_3^-]$	[1]$[CO_3^{2-}]$	[1]$[CO_2]$	Ω_A
1766	18.3	34.9	0.66	7.35	2326	267	1994	8.2	1754	231	9.05	3.6
2007	18.9	34.9	0.63	7.35	2325	384	2064	8.07	1865	186	12.8	2.9
2100	21.4	34.7	0.55	7.35	2310	793	2162	7.79	2020	118	24.7	1.8

[1]10^{-6} mol kg^{-1}

Target values from Gattuso and Lavigne (2009) via CO2SYS (using TA and pCO_2 input from above):

Year	T (^oC)	Salinity	[1]Total P	[1]Total Si	[1]TA	pCO_2 (μatm)	[1]TCO_2	pH	[1]$[HCO_3^-]$	[1]$[CO_3^{2-}]$	[1]$[CO_2]$	Ω_A
1766	18.3	34.9	0.66	7.35	2326	267	1994.4	8.194	1753.5	231.9	9.05	3.59
2007	18.9	34.9	0.63	7.35	2325	384	2064.4	8.065	1863.6	187.0	12.8	2.90
2100	21.4	34.7	0.55	7.35	2310	793	2162.1	7.792	2019.4	118.1	24.7	1.85

[1]10^{-6} mol kg^{-1}. Note: slight differences due to choice of constants.

CO2SYS PRACTICE EXERCISES:

SET 1 (rows 4-6 in CO2SYS spreadsheet, table 2): ACID ADDITION, CLOSED SYSTEM

- closed system
- Starting seawater pH and TCO_2 of 8.194 and 1994.4 μmol kg^{-1}, respectively
- TCO_2 constant at 1994.4 μmol kg^{-1}
- $[H^+]$ added as 0.1 N HCl to decrease pH, increase pCO_2 to target values for 1766, 2007, and 2100
- Temperature, salinity, pH, TCO_2, total P, and total Si as per Gattuso and Lavigne (2009) scenarios for 1766, 2007, 2100.

Volume of 0.1N HCl added to starting seawater for each experiment in set 1.

pH	8.194	8.065	7.792
mL HCl kg^{-1} SW	0	0.759	1.910

SET 2 (rows 7-9 in CO2SYS spreadsheet, table 2): CO_2 ADDITION, CLOSED SYSTEM

- closed system
- TA held constant at starting seawater condition (result from set 1 of 2326.0 μmol kg^{-1})
- Discrete volumes of CO_2 added to achieve CO2SYS pCO_2 targets for 1766, 2007, and 2100.
- pH and TCO_2 allowed to equilibrate to CO_2 addition
- Temperature, salinity, total P, and total Si same as set 1.

Volume of CO_2 gas added to starting seawater for each experiment in set 2

pCO_2 (μatm)	267	384	793
mL CO_2 kg^{-1} SW @STP	0	1.701	4.430

SET 3 (rows 10-12 in CO2SYS spreadsheet, table 2): ACID ADDITION, RE-EQUILIBRATED TO 384.0 μatm

- Set 1 results re-equilibrated with atmospheric pCO_2 of 384.0 μatm
- Input TA results from acid addition set 1
- Input pCO_2 of 384.0 μatm for all experiments
- Open system
- Temperature, salinity, total P, and total Si same as set 1

SET 4 (rows 13-15 in CO2SYS spreadsheet, table 2): CO_2 ADDITION, RE-EQUILIBRATED TO 384.0 μatm

- Set 2 results re-equilibrated with atmospheric pCO_2 at 384.0 μatm
- TA input from set 2 (2326.0 μmol kg^{-1})
- pCO_2 input of 384.0 μatm
- Open system
- Temperature, salinity, total P, and total Si same as set 1

Table 2. Input data for CO2SYS practice exercises 1 through 4.

	A	B	C	D	E	F	G	H	I	J	K	L	M
1	START	START	START	START	START	START	START	START	START	START	START	START	START
2	INPUT CONDITIONS					OUTPUT CONDITIONS		DATA (leave empty if no data)					
3	Salinity	t(oC)	P (dbars)	Total P (µmol/kgSW)	Total Si (µmol/kgSW)	t(oC)	P (dbars)	TA (µmol/kgSW)	TCO2 (µmol/kgSW)	pH (Chosen Scale)	fCO2 (µatm)	pCO2 (µatm)	Clea Dat <--
4	34.9	18.3	0	0.66	7.35	18.3	0		1994.4	8.194			Clea Resu ---
5	34.9	18.9	0	0.63	7.35	18.9	0		1994.4	8.065			
6	34.7	21.4	0	0.55	7.35	21.4	0		1994.4	7.792			
7	34.9	18.3	0	0.66	7.35	18.3	0	2326.0				267.0	
8	34.9	18.9	0	0.63	7.35	18.9	0	2326.0				384.0	
9	34.7	21.4	0	0.55	7.35	21.4	0	2326.0				793.0	
10	34.9	18.3	0	0.66	7.35	18.3	0	2326.0				384.0	
11	34.9	18.9	0	0.63	7.35	18.9	0	2250.1				384.0	
12	34.7	21.4	0	0.55	7.35	21.4	0	2135.0				384.0	
13	34.9	18.3	0	0.66	7.35	18.3	0	2326.0				384.0	
14	34.9	18.9	0	0.63	7.35	18.9	0	2326.0				384.0	
15	34.7	21.4	0	0.55	7.35	21.4	0	2326.0				384.0	

Table 3. Results for CO2SYS practice exercises 1 through 4.

	V	W	X	Y	Z	AA	AB	AC	AD	AE	AF	AG	AH	AI	AJ	AK
2	***RESULTS (Input Conditions)***															
3	TA in (µmol/kgSW)	TCO2 in (µmol/kgSW)	pH in	fCO2 in (µatm)	pCO2 in (µatm)	HCO3 in (µmol/kgSW)	CO3 in (µmol/kgSW)	CO2 in (µmol/kgSW)	B Alk in (µmol/kgSW)	OH in (µmol/kgSW)	P Alk in (µmol/kgSW)	Si Alk in (µmol/kgSW)	Revelle in	ΩCa in	ΩAr in	xCO2 in (dry at 1 atm) (ppm)
4	2326.0	1994.4	8.194	266.1	267.0	1753.5	231.9	9.1	102.6	5.1	0.8	0.3	9.246	5.54	3.59	272.5
5	2250.1	1994.4	8.065	369.9	371.2	1801.3	180.7	12.4	82.4	4.0	0.7	0.3	10.404	4.32	2.80	379.2
6	2135.0	1994.4	7.792	729.0	731.5	1862.7	108.9	22.8	51.1	2.7	0.6	0.2	13.353	2.61	1.70	750.0
7	2326.0	1994.4	8.194	266.1	267.0	1753.5	231.9	9.1	102.6	5.1	0.8	0.3	9.246	5.54	3.59	272.5
8	2326.0	2064.3	8.065	382.7	384.0	1864.3	187.1	12.8	82.5	4.0	0.7	0.3	10.493	4.47	2.90	392.3
9	2326.0	2176.4	7.795	790.4	793.0	2032.1	119.6	24.7	51.4	2.7	0.6	0.2	13.602	2.87	1.87	813.1
10	2326.0	2069.1	8.065	382.7	384.0	1872.3	183.8	13.0	81.4	3.8	0.7	0.3	10.608	4.39	2.84	392.0
11	2250.1	2000.9	8.052	382.7	384.0	1811.4	176.7	12.8	80.6	3.9	0.7	0.3	10.548	4.22	2.74	392.3
12	2135.0	1886.8	8.032	382.7	384.0	1701.7	173.1	12.0	81.4	4.7	0.6	0.3	10.193	4.16	2.71	393.7
13	2326.0	2069.1	8.065	382.7	384.0	1872.3	183.8	13.0	81.4	3.8	0.7	0.3	10.608	4.39	2.84	392.0
14	2326.0	2064.3	8.065	382.7	384.0	1864.3	187.1	12.8	82.5	4.0	0.7	0.3	10.493	4.47	2.90	392.3
15	2326.0	2045.0	8.065	382.7	384.0	1832.3	200.7	12.0	86.4	5.0	0.6	0.3	10.069	4.82	3.14	393.7

Table 4. Difference between target and experimental values for carbonate system parameters.

Practice set	Year	TA in (µmol/kg SW)	TCO2 in (µmol/kg SW)	pH in	pCO2 in (µatm)	HCO3 in (µmol/kg SW)	CO3 in (µmol/kg SW)	CO2 in (µmol/kg SW)	ΩCa in	ΩAr in	xCO2 in (dry at 1 atm) (ppm)
CO2SYS Targets	1766	2326.0	1994.4	8.2	267.0	1753.5	231.9	9.1	5.5	3.6	272.5
	2007	2325.0	2063.4	8.1	384.0	1863.6	187.0	12.8	4.5	2.9	392.3
	2100	2310.0	2162.1	7.8	793.0	2019.4	118.1	24.7	2.8	1.8	813.1
		ΔTA	**ΔTCO2**	**ΔpH**	**ΔpCO2**	**ΔHCO3**	**ΔCO3**	**ΔCO2**	**ΔΩCa in**	**ΔΩAr in**	**ΔxCO2**
Set 1	1766	0.0	0.0	0.0	0.0	0.0	0.0	0.0	0.0	0.0	0.0
Acid	% Diff.	-	-	-	-	-	-	-	-	-	-
Addition	2007	-74.9	-69.0	0.0	-12.8	-62.4	-6.3	-0.4	-0.1	-0.1	-13.1
	% Diff.	3.2	3.3	0.0	3.3	3.3	3.3	3.3	3.3	3.3	3.3
	2100	-175.0	-167.8	0.0	-61.5	-156.7	-9.2	-1.9	-0.2	-0.1	-63.1
	% Diff.	7.6	7.8	0.0	7.8	7.8	7.8	7.8	7.8	7.8	7.8
Set 2	1766	0.0	0.0	0.0	0.0	0.0	0.0	0.0	0.0	0.0	0.0
CO_2	% Diff.	-	-	-	-	-	-	-	-	-	-
Bubbling	2007	1.0	0.8	0.0	0.0	0.7	0.1	0.0	0.0	0.0	0.0
	% Diff.	0.0	0.0	0.0	0.0	0.0	0.1	0.0	0.1	0.1	0.0
	2100	16.0	14.2	0.0	0.0	12.7	1.5	0.0	0.0	0.0	0.0
	% Diff.	0.7	0.7	0.0	0.0	0.6	1.3	0.0	1.3	1.3	0.0
Set 3	1766	0.0	74.7	-0.1	117.0	118.8	-48.1	4.0	-1.1	-0.7	119.4
Re-eq.	% Diff.	0.0	3.7	1.6	43.8	6.8	20.7	43.8	20.7	20.7	43.8
Acid	2007	-74.9	-62.6	0.0	0.0	-52.2	-10.3	0.0	-0.2	-0.2	0.0
Addition	% Diff.	3.2	3.0	0.2	0.0	2.8	5.5	0.0	5.5	5.5	0.0
	2100	-175.0	-275.3	0.2	-409.0	-317.6	55.1	-12.7	1.3	0.9	-419.3
	% Diff.	7.6	12.7	3.1	51.6	15.7	46.7	51.6	46.7	46.7	51.6
Set 4	1766	0.0	74.7	-0.1	117.0	118.8	-48.1	4.0	-1.1	-0.7	119.4
Re-eq.	% Diff.	0.0	3.7	1.6	43.8	6.8	20.7	43.8	20.7	20.7	43.8
CO_2	2007	1.0	0.8	0.0	0.0	0.7	0.1	0.0	0.0	0.0	0.0
Bubbling	% Diff.	0.0	0.0	0.0	0.0	0.0	0.1	0.0	0.1	0.1	0.0
	2100	16.0	-117.2	0.3	-409.0	-187.1	82.7	-12.7	2.0	1.3	-419.3
	% Diff.	0.7	5.4	3.5	51.6	9.3	70.0	51.6	70.0	70.0	51.6

Δparameter = difference in concentration from target values for each year ([value] - [target]).

OCB OCEAN ACIDIFICATION SHORT COURSE

OUTLINE FOR LARVAL MOLLUSC OCEAN ACIDIFICATION EXPERIMENTS

Instructors: Anne Cohen, Dan McCorkle

TAs: Meredith White, Kathryn Rose

DAY 1: SETUP

You will need:

- 16 (or 20) pre-labeled 1L beakers with lids (4 treatments: ambient, 50, 840 and 2280 ppm CO_2; with 3 replicates of each condition and also organism-free controls at each treatment level). Beakers are arranged randomly on countertop.
- 16 (20) pre-labeled acid cleaned vials, and syringe(s) and syringe filters for small volume alkalinity samples
- 2 sets of sample bottles pre-labeled for large volume alkalinity and salinity
- Calibrated pH meter and temperature-compensating electrode (see "calibrating the pH meter below")
- Room temperature set to 23°C (for bay scallops) – could be in water baths to minimize temperature fluctuations
- Onset T logger(s) for temperature records
- Set mass flow controllers, and check pCO_2 levels with Qubit CO_2 analyzer

Step 1 Fill cubitainers; initial samples:

- Fill large cubitainer(s) with filtered seawater, to minimize initial variability in seawater chemistry
- Collect samples from these cubitainers for large-volume alkalinity and DIC, and for salinity (3 rinses)
- Fill two large glass bottles with filtered sea water; allow to overflow for the amount of time it takes to fill each bottle
- Immediately poison each Alk/DIC sample (50 µL of saturated $HgCl_2$)

Step 2: Fill beakers, initial samples

- Fill each beaker with 800 ml (800g) filtered sea water from cubitainer, using the balance
- Bubble compressed air/CO_2 mix from the mass flow controller gas lines into each beaker. Insert lines through hole in lid of beaker.

Step 3: Take initial Small Volume Alkalinity

- Rinse syringe using 1-2 ml seawater from desired cup (filter is not necessary); fill syringe with 10ml seawater from beaker
- Attach 0.45 µm syringe filter unit, rinse filter with 1-2 mL of sample

- Push 2 – 3 ml of water into a pre-labeled alkalinity vial, rinse and discard; fill the vial with remaining 5-7mL in the syringe, refill the syringe, and (using the same filter) add 5-10 more mL from the same beaker
- Poison the sample with 10 µL of saturated $HgCl_2$
- Close all vials tightly and seal with electrical tape
- Repeat this procedure for all experimental beakers.
- You can keep using the same syringe and filter, as long as you rinse both as you sample each new cup.

Step 4: Initial pH Measurements

3 measurements should be taken for each beaker as follows:

- Calibrating the pH meter. We use a T-compensating electrode ("ATC", automatic temperature compensation). Still, maintain buffers at same temperature as experiments
- Soak pH electrode in pH 7 buffer solution for at least 10-15 minutes. Ensure electrode does not touch the sides or bottom and that the bulb is submerged
- Push the calibrate button on the pH meter
- When stable (stops blinking) adjust reading to desired pH
- Push calibrate again
- Rinse pH meter with distilled water and blot lightly with a kimwipe or napkin
- Submerge electrode in pH 10 buffer
- When stable, adjust to desired pH (10.025)
- Push measure button on pH meter and wait for slope to appear
- A slope between 92-100% is acceptable; record this value
- Allow the electrode to soak in seawater for at least 1/2 hour, then take readings from each beaker. (Be patient; wait 1 minute, then record readings at 1 min or 30 sec intervals until stable. By systematic (use a watch) and record all readings, not just the final one.)

Day 2: Inoculating the experiments

- Repeat small volume alkalinity sampling from each beaker
- Repeat pH calibration and measurements
- Call the hatchery to check on the status of the spawn.
- When fertilization has begun, drive out to Dennis to collect the eggs.
- Bring the eggs back to the lab immediately (~3 hours)
- Back at ESL lab, determine density of eggs using counting cell slides and inoculate each beaker to have 5-10 eggs/mL (about 5000-6000 eggs per cup). Make sure the water in the bucket containing the larvae is well mixed each time you sample the bucket.

Day 3: Monitoring

- Repeat pH calibration and measurements

Day 4: Harvesting (first thing in the morning)

- Small volume alkalinity samples
- Turn off CO_2
- Carefully decant water from each beaker into a 45 µm sieve; rinse cup at least three times and sieve contents
- Rinse sieve with ethanol (repeat)
- Decant into an acid-cleaned vial using the ethanol
- Fill each vial to 5ml with ethanol.

Day 5: Quantification of calcification by image analysis

- Make sure vial contents are well mixed. Use an Eppendorf pipette to transfer 0.5 ml subsample from the vial to a **glass** counting slide (not plastic).
- Wait a minute or two for the larvae to settle.
- Using the inverted or petrographic microscopes, check for shelled larvae using the polarizer (shells are D-shaped and birefringent)
- Create a folder on the computer into which you will save your images.
- Photograph each shell at 10X magnification using SPOT digital camera. Add a scale bar to each image.
- Use SPOT to measure shell length (from center of hinge to rim) and hinge length for each sample. The hinge should be about 50 µm in length.

Friday, November 6, 2009
Lectures, coral calcification experimental setup, larval mollusk inoculations, lab tour

Morning

Time	Activity
8:30 am	**Lecture**. Algal culturing overview. (Iglesias-Rodriguez). MBL Speck Auditorium
10:00 am	Coffee Break
10:30 am	**Lecture**. Calcification overview, measurements, and background for biological experiments (Cohen/Miller)
12:00 pm	Lunch (Swope Cafeteria, MBL)

Afternoon/Evening

Time	Group G	Group H	Group I
1:15 pm	Shuttle MBL to ESL	Break	Shuttle MBL to Watson
1:30 pm	**Lab**. Coral calcification exp't setup (Holcomb, ESL 10)		**Tour**. Joan Bernhard's lab – CO_2 enrichment exp'ts with benthic foraminifera and other exp'ts (Watson 230)
2:15 pm		Shuttle MBL to ESL	
2:30 pm	Walk to Watson lab	**Lab**. Coral calcification exp't setup (Holcomb, ESL 10)	Break/Walk to ESL
2:45 pm	**Tour**. Joan Bernhard's lab – CO_2 enrichment exp'ts with benthic foraminifera and other exp'ts (Watson 230)		
3:30 pm		Break/Walk to Watson lab	**Lab**. Coral calcification exp't setup (Holcomb, ESL 10)
3:45 pm	Shuttle Watson to MBL		
4:00 pm	Break	**Tour**. Joan Bernhard's lab – CO_2 enrichment exp'ts with benthic foraminifera and other exp'ts (Watson 230)	
4:30 pm			Shuttle ESL to MBL
5:00 pm		Shuttle Watson to MBL	
5:15 pm	Dinner (Swope Cafeteria, MBL)		
7:00 pm	Shuttle MBL to ESL	Break	Break
7:15 pm	**Lab**. Take T1 samples for coral* (Holcomb, ESL 10);		
8:00 pm		Shuttle MBL to ESL	

	inoculate mollusk larvae (White/McCorkle, ESL 10)		
8:15 pm	Shuttle ESL to MBL	**Lab**. Take T1 samples for coral* (Holcomb, ESL 10); inoculate mollusk larvae (White/McCorkle, ESL 10)	
8:30 pm	Done for evening		
9:00 pm			Shuttle MBL to ESL
9:15 pm		Shuttle ESL to MBL	**Lab**. Take T1 samples for coral* (Holcomb, ESL 10); inoculate mollusk larvae (White/McCorkle, ESL 10)
9:30 pm		Done for evening	
10:15 pm			Shuttle ESL to MBL

***Coral T1-T4 (Fri-Sun) sampling: this will involve a subgroup of 3 from each group (G/H/I) so that each person gets a chance to sample**

Algal culturing

UNIVERSITY OF Southampton
School of Ocean and Earth Science

Débora Iglesias-Rodríguez
National Oceanography Centre, Southampton.

National Oceanography Centre, Southampton
UNIVERSITY OF SOUTHAMPTON AND NATURAL ENVIRONMENT RESEARCH COUNCIL

Talk outline

- Phytoplankton
- The basics in culturing algae
- Knowing your organism
- Method of manipulation
- Sampling considerations
- Evolutionary considerations

Phytoplankton

- Eukaryotic and prokaryotic species present in freshwater and marine environments.
- Phytoplankton live in the upper layer of the water column.
- The structure and abundance of the phytoplankton populations are controlled by inorganic nutrients (N, P, Si, Fe).
- Some species form blooms.
- On short time-scales, phytoplankton growth and division are tightly linked to the diel cycle.

Phytoplankton distribution

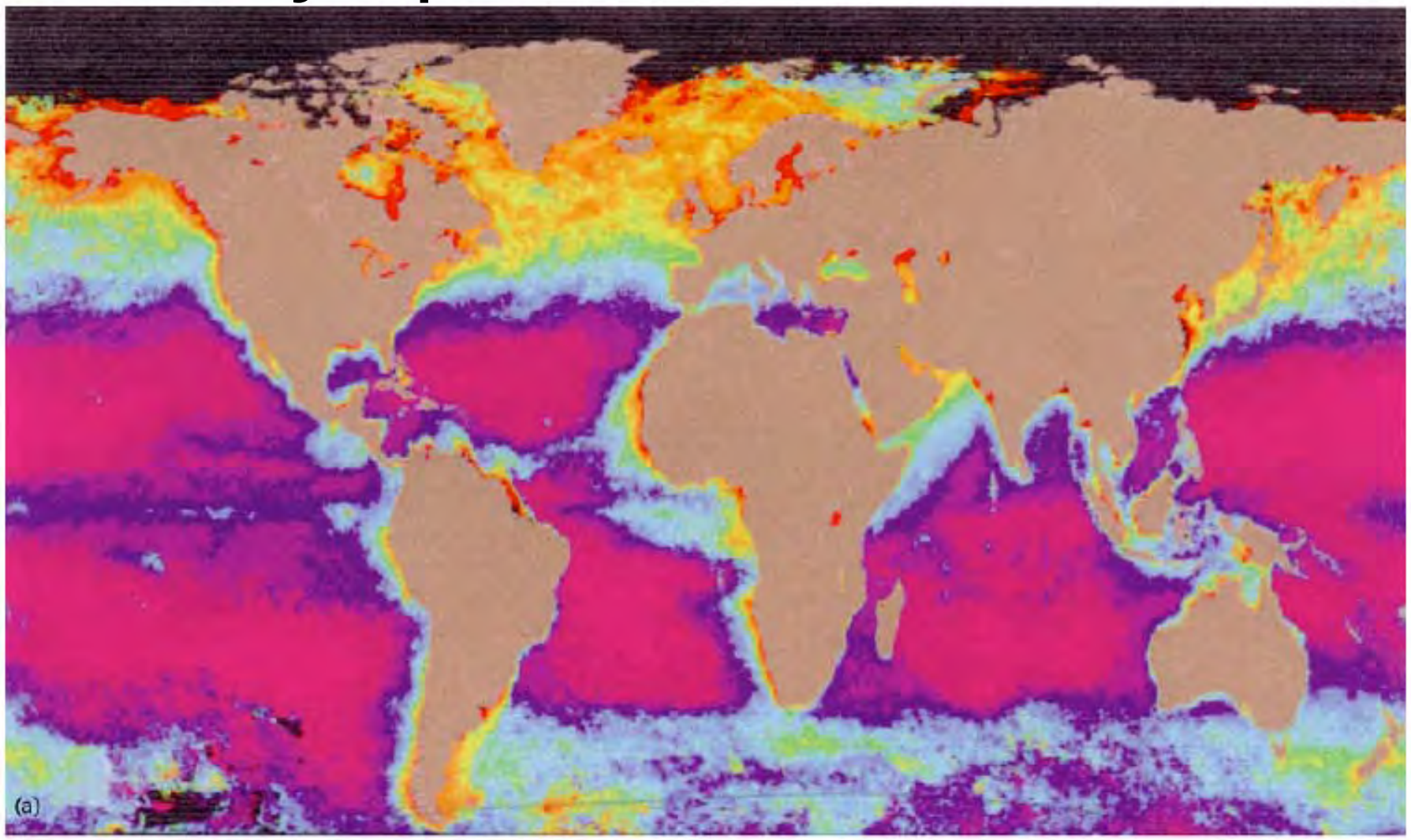

Vaulot, 2001.

Phytoplankton Size Structure and Ecosystem Function

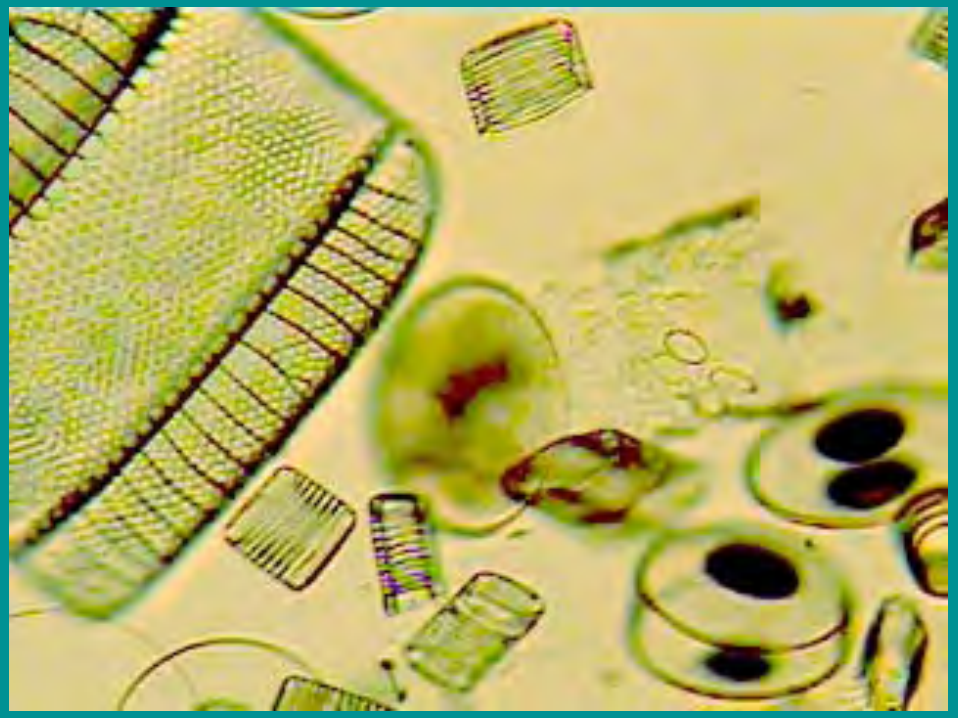

COCCOLITHOPHORES

DINOFLAGELLATES

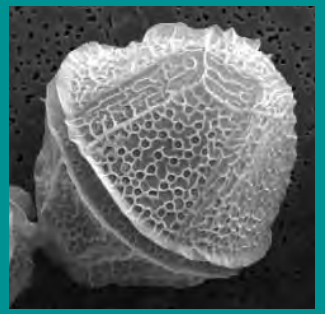

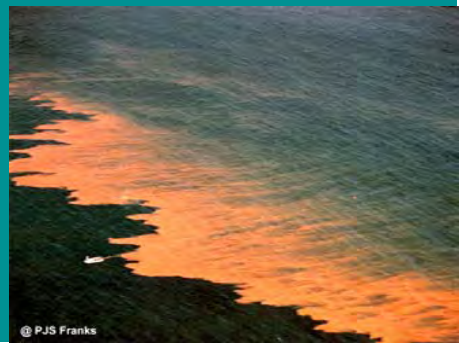

Factors controlling primary production in the oceans

- Light
- Nutrients (C, N, P, Si, trace metals, vitamins)
- Temperature: more important in selecting for species
- Physical processes (e.g., eddies, vertical mixing)

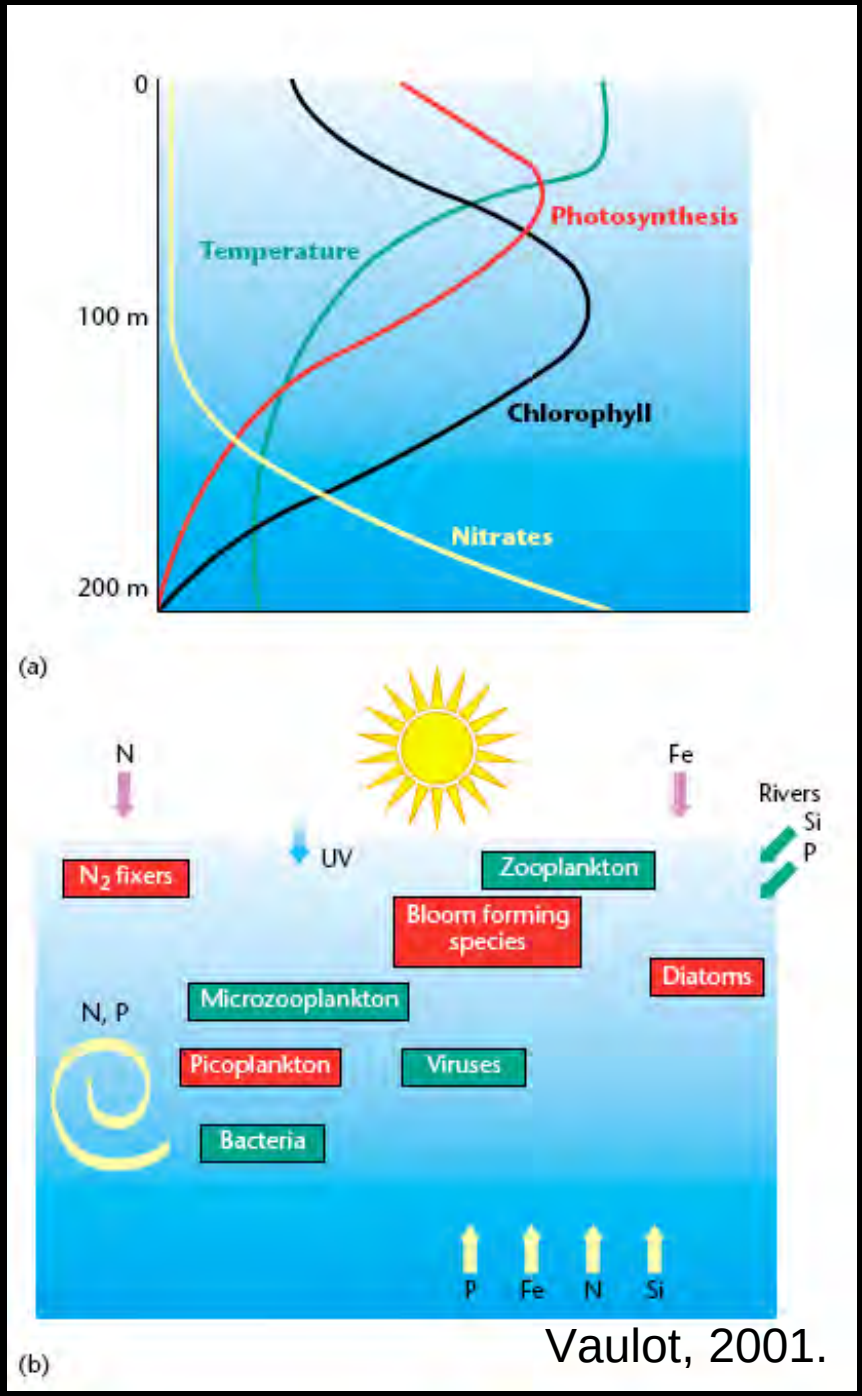

Vaulot, 2001.

Phytoplankton functional groups and global biogeochemical cycles

Algal evolution and the origin and spread of plastids by endosymbiosis

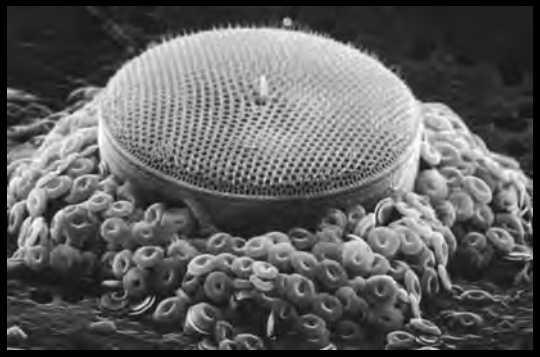

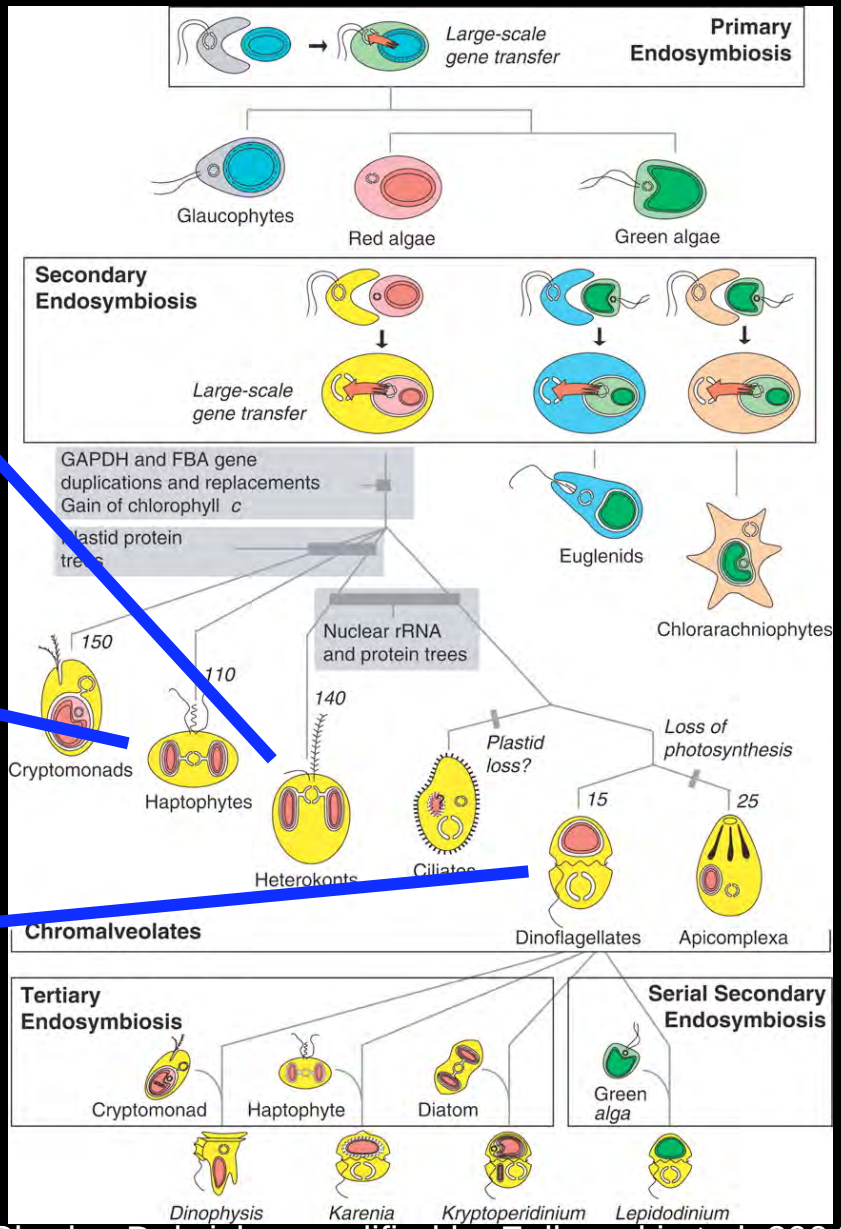

Diatom,: www.palomar.edu/ oceanography/iron.htm,
Coccolithophore image courtesy of Jeremy Young, Natural History Museum, London.Dinoflagellate: http://marinebio.org/Oceans/TheForests/

Charles Delwiche, modified by Falkowski et al, 2004.

Generation times in functional groups (autotrophs and heterotrophs)

Organism	Generation time
Coccolithophores	Days
(autotrophic)	
Foraminifera	Weeks
(heterotrophs)	
Pteropods	Months
(heterotrophs)	

The basics in culturing algae

- Decide on type of culturing approach (batch *versus* semi-continuous *versus* continuous)

- Decide on the variables to monitor

- Do you have sufficient information about your model organism?

- Will you be able to compare your data with the relevant published results?

- Before getting started pick your colleagues' brains!

Batch cultures

Cultures start with known physico-chemical conditions that evolve over a time period without additional manipulation

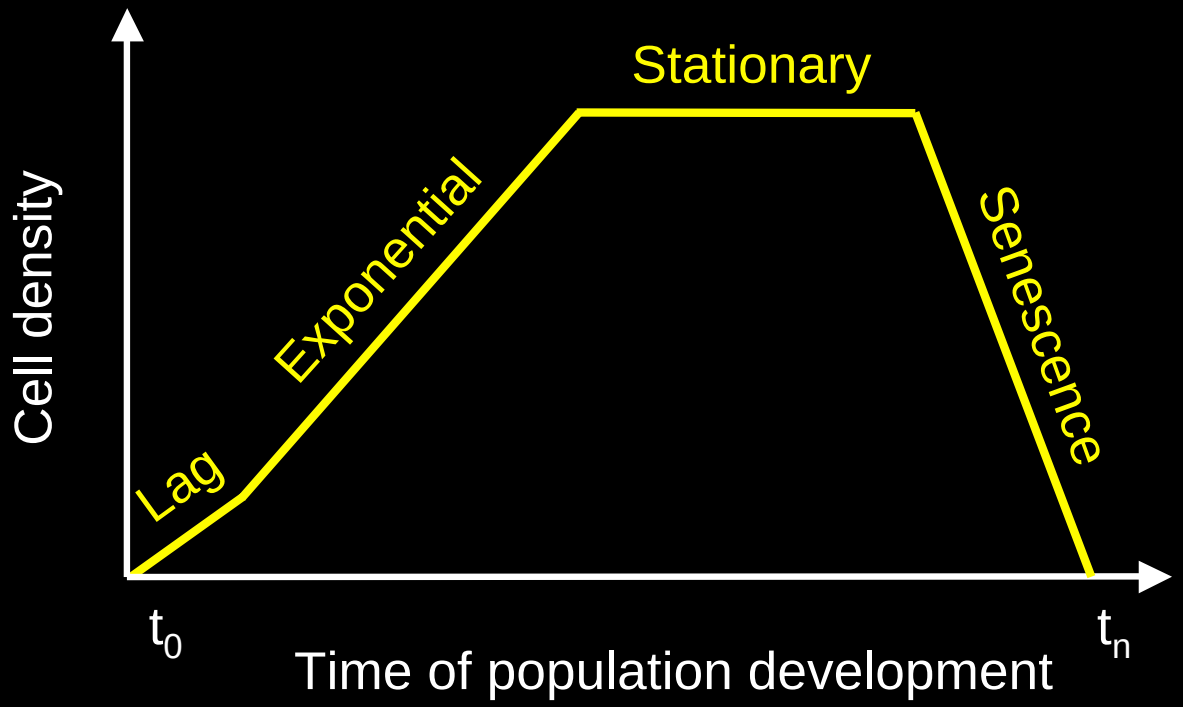

Conditions at $t_0 \neq$ conditions at t_n

Semicontinuous cultures

Cultures are kept exponentially-growing by subculturing within a few generations

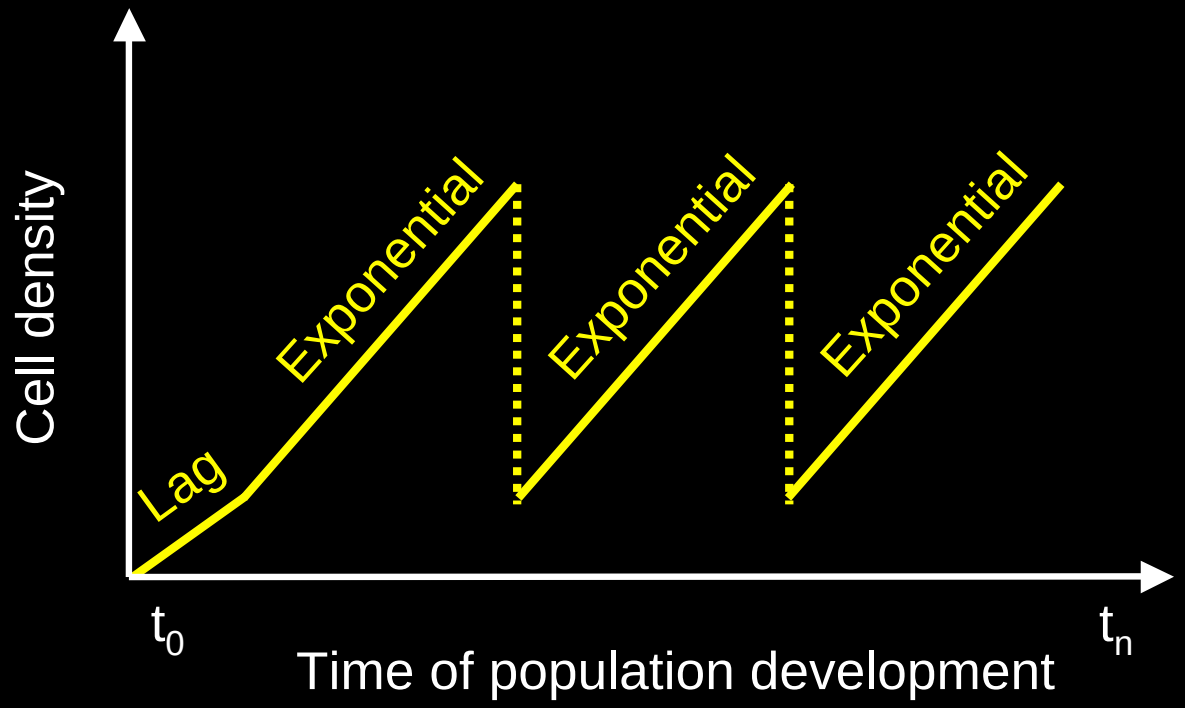

Conditions at $t_0 \neq$ conditions at t_n but range of change is constant

Continuous cultures

Cultures are kept at ~constant conditions

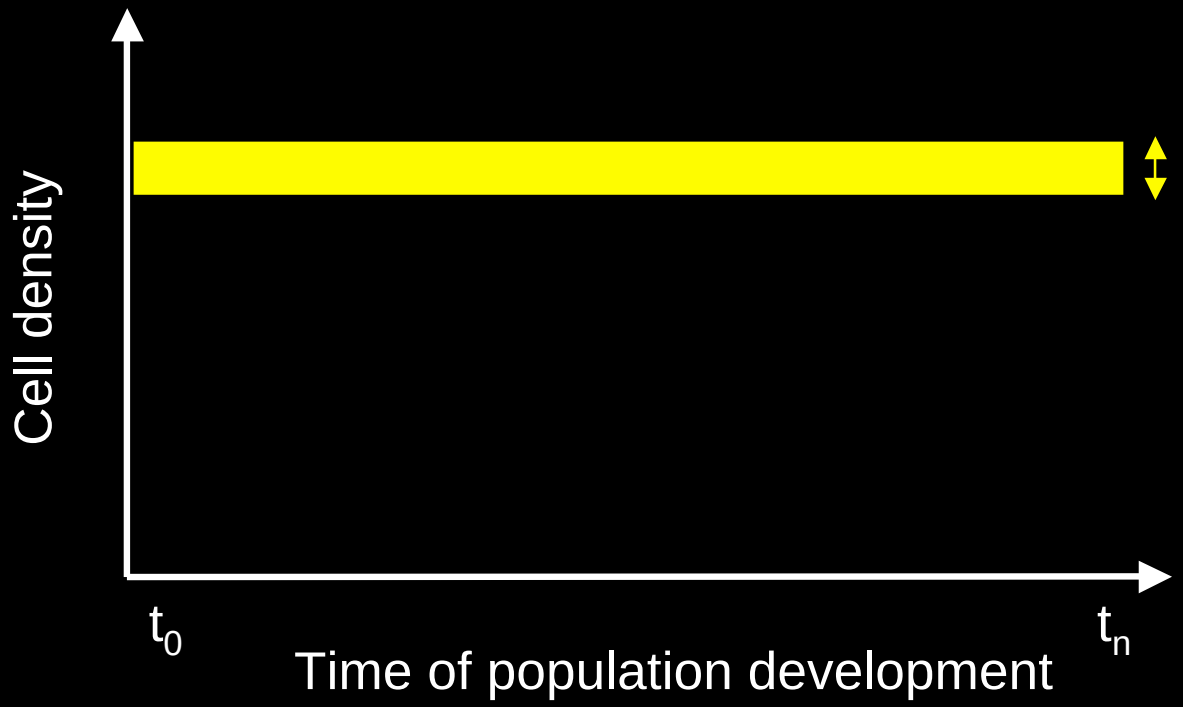

Conditions at $t_0 \approx$ conditions at t_n

Effect of climate-relevant variables on physiology (calcification)

- Lab cultures (phycological research over the last century and recent work, e.g., Riebesell et al., 2000; Langer et al., 2006; Iglesias-Rodriguez et al., 2008; Shi et al., 2009).

- Shipboard experiments (e.g., Tortell et al., 2002; Engel et al., 2005)

- Mesocosms (e.g., DeLille et al., 2005)

How long should my experiment be?

- How long is a long-term experiment?
- How many changes can be detected during the acclimation phase?
- Continuous *versus* batch approaches
- Different questions require different approaches

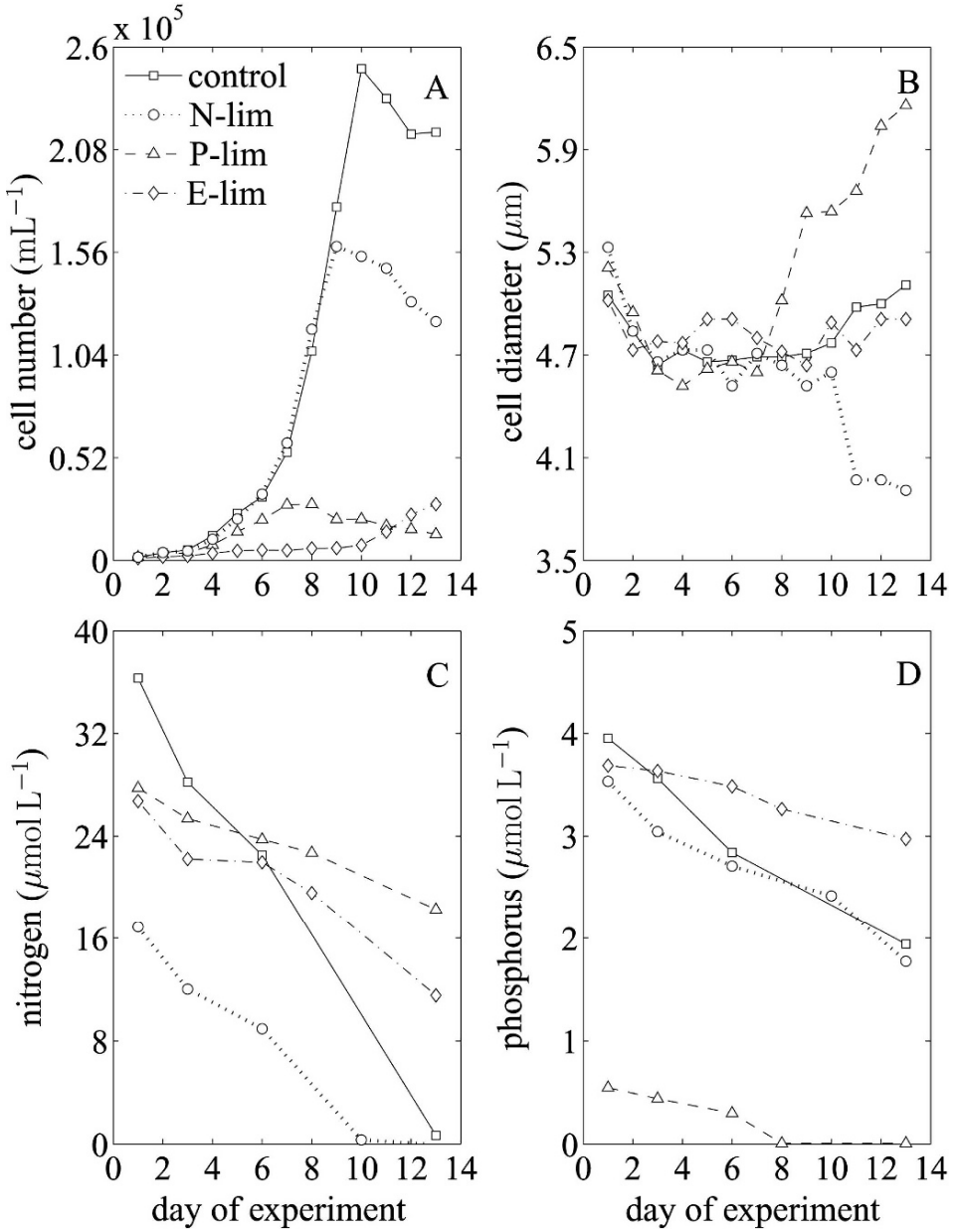

Müller et al., 2008.

Decide on the variables to monitor

- Adjust volumes and bubbling rates accordingly and ensure headspace is kept relatively constant

- Account for changes in irradiance as a result of changes in cell density and volume

- Conduct trials to ensure conditions are known during experiment and/or calculate uptake rates and threshold for limitation of growth and physiological performance (e.g., cell quota calculations, light limitation, optimal irradiance)

Monitor growth and assess stage

- Knowledge on cell quota - assess the growth stage of the culture

- Monitor nutrient changes during growth.

Example: if testing the effect of ocean acidification under nutrient replete conditions in batch cultures, test under exponential growth phase several times during growth

Knowing your model organism?

- What do you know about its cell biology? (e.g., life cycle, reproductive patterns, cyst formation, cellular quotas for nutrients)

- Always remember to check under the microscope - what you ordered from the culture collection may have changed/may be contaminated/may have undergone changes in life cycle stages

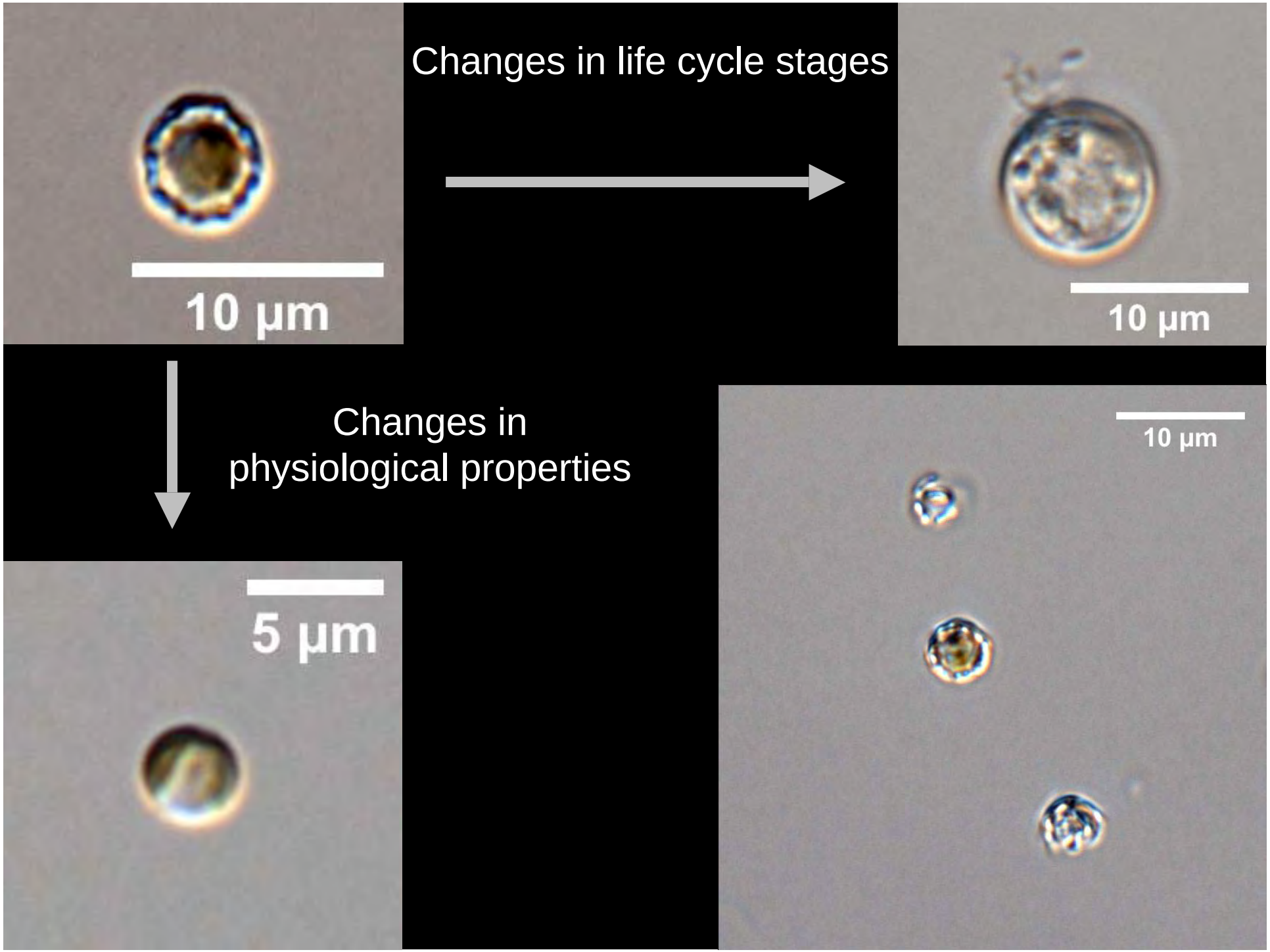
Changes in life cycle stages
10 µm
10 µm
Changes in
physiological properties
5 µm
10 µm

How representative are these types in the population?

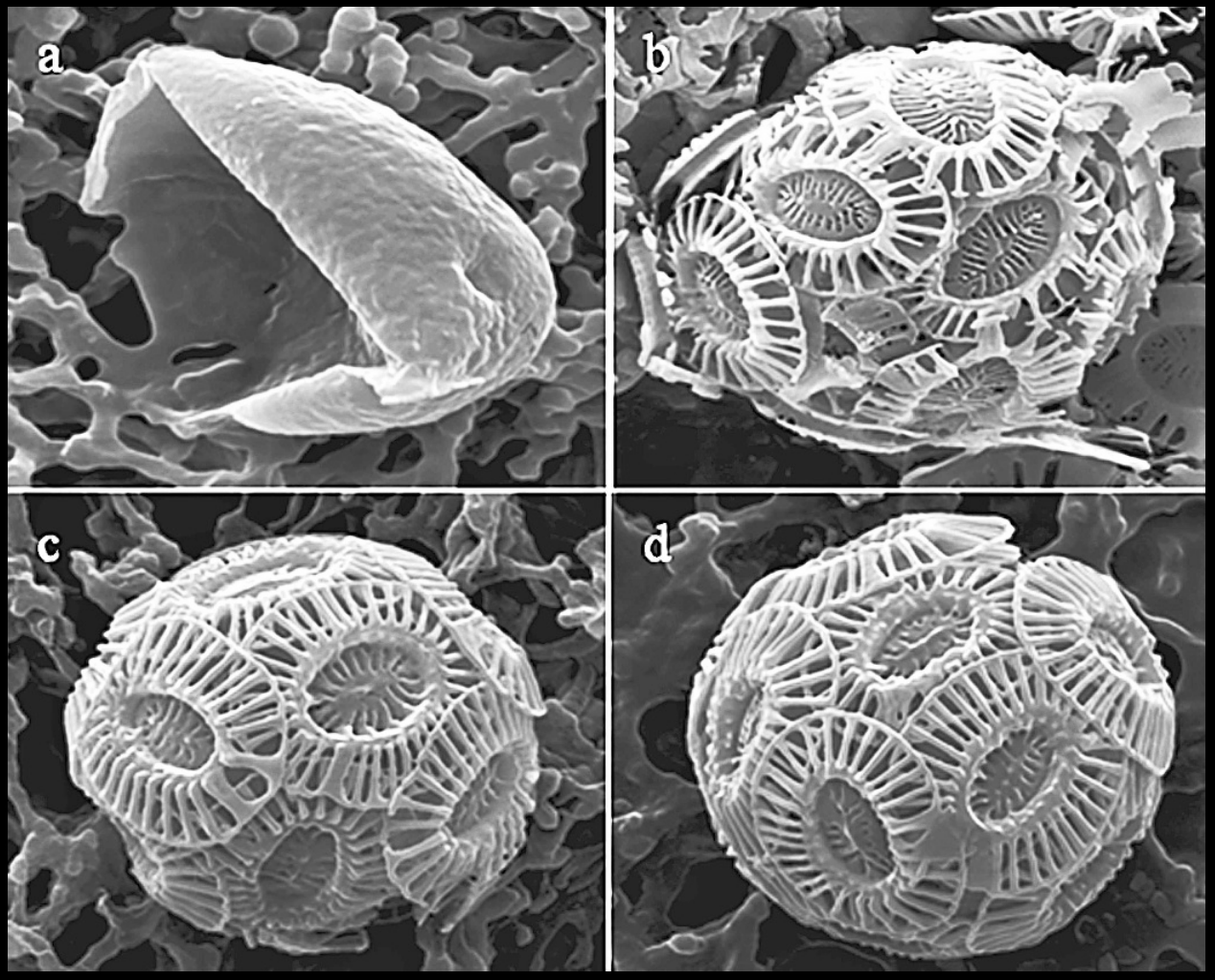

Trimborn *et al*., 2006.

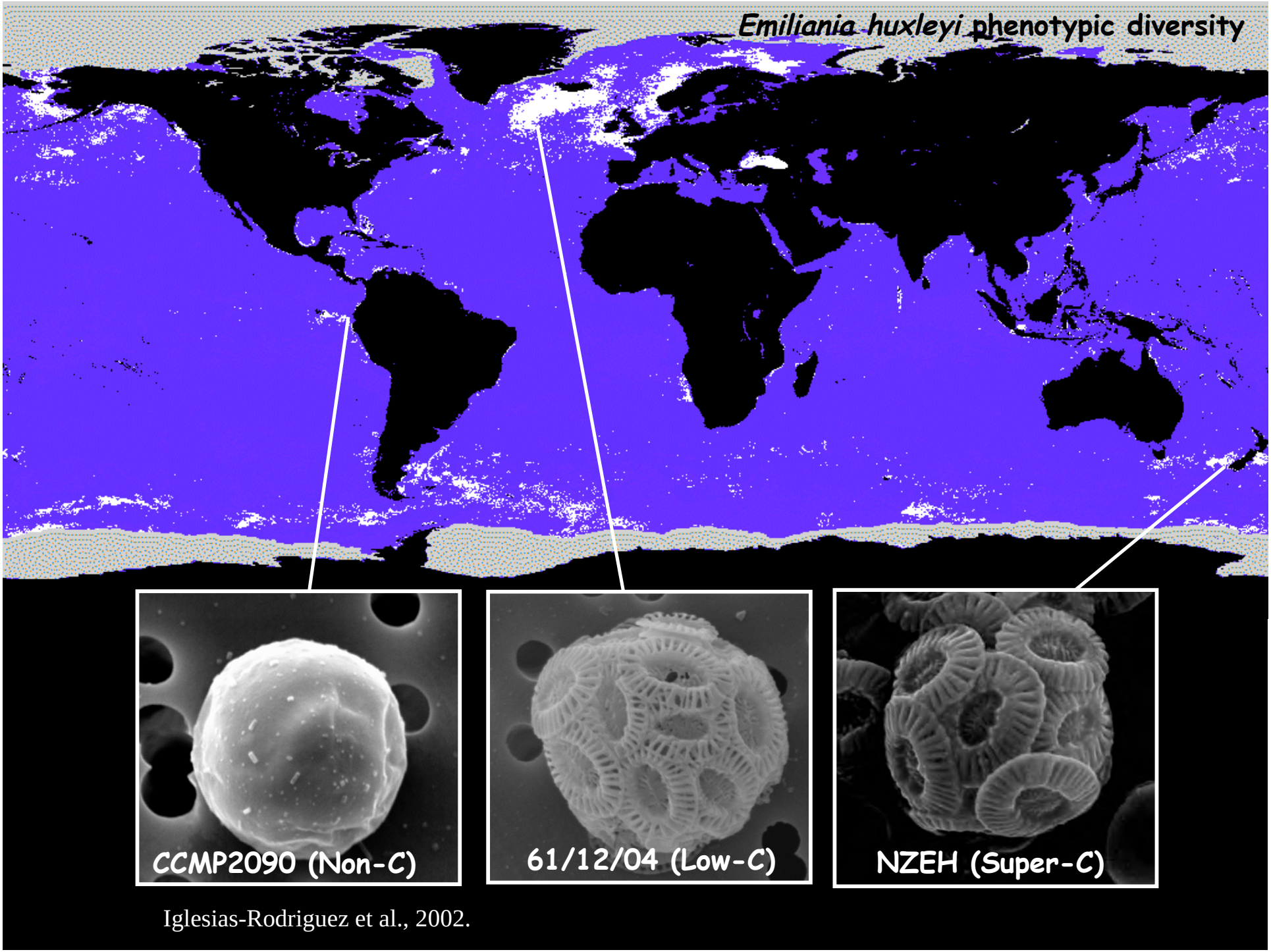

Iglesias-Rodriguez et al., 2002.

Viruses

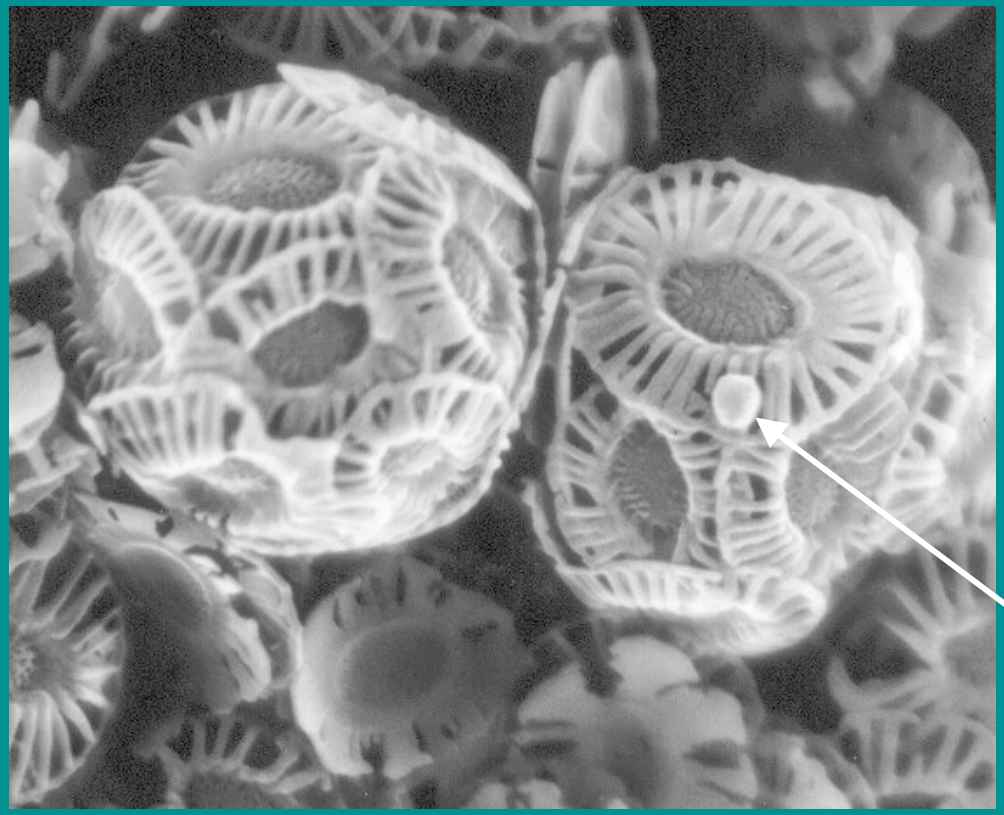

Emiliania huxleyi

- Contains biosynthetic genes for ceramide, a known inducer of PCD via a sphingolipid pathway

- Infection of Ehux374 with EhV86 triggered caspase activation.

Emiliania huxleyi virus

EhV1 infection of “sensitive” Ehux374 and “resistant” Ehux373

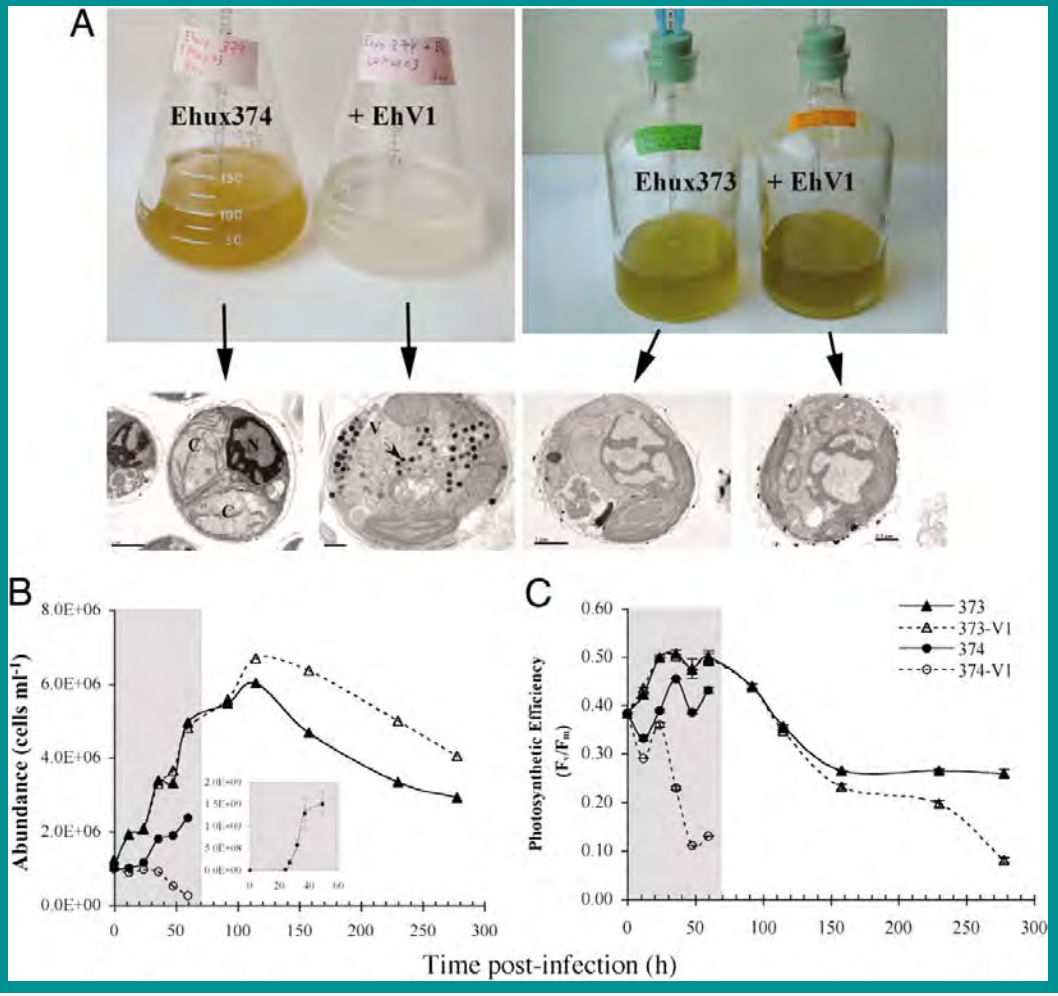

Bidle K D et al. PNAS 2007;104:6049-6054

PNAS

Intraspecific and intraclonal variability

Example: scintillon numbers by confocal microscopy

- Clonal culture *Lingulodinium polyedrum*
- 14% of cells do not contain scintillons (green)
- Only 20% have more than 10 scintillons
- Literature values of 300 scintillons per cell
- Reports of BL and non BL strains of same species

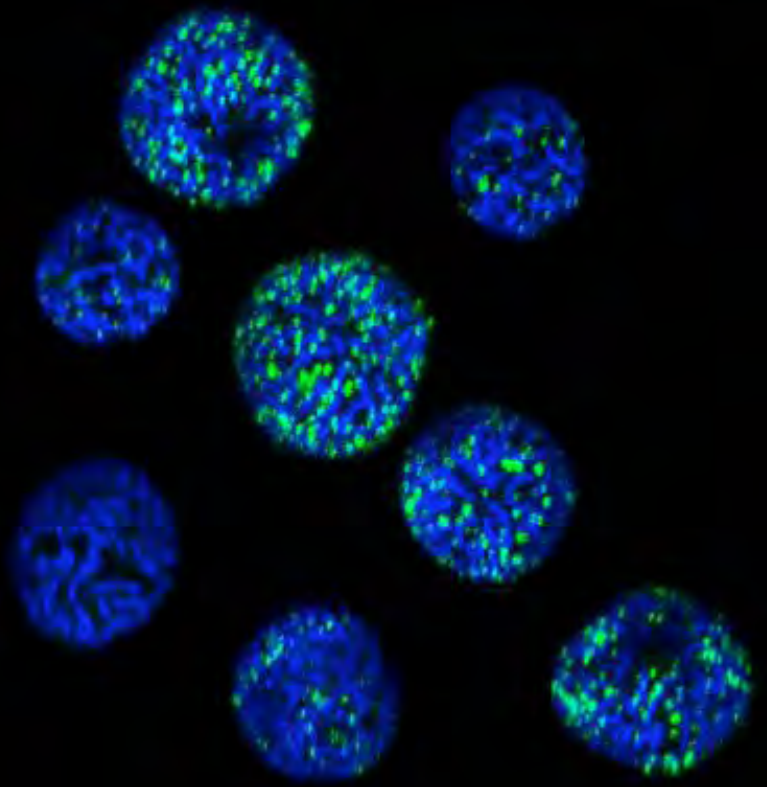

Blue = chlorophyll

Green = luciferin

Iain Dickson, pers. com.

Variability in cell synchrony

• Synchronization of cell population under constant conditions (Pascual & Caswell 1997) was explained by the fact that nutrient assimilation and division are consecutive processes in the cell cycle, the latter process taking place after the completion of the former (Vaulot et al. 1987).

• Inherent variability within and between independent experiments.

• When reporting on morphological traits via the use of images, provide numerical values, e.g. contribution of a phenotype to the total.

Changes in population structure ?

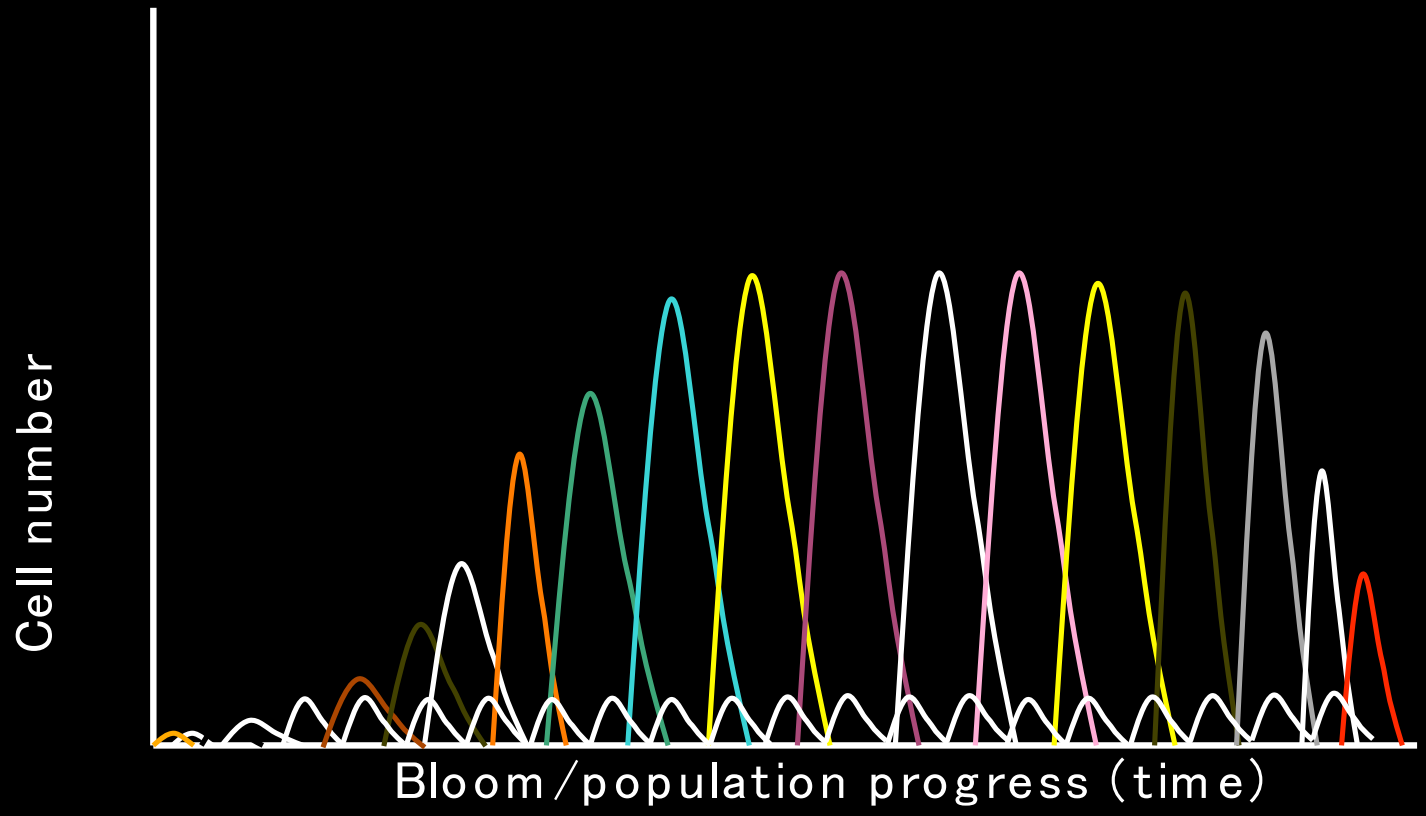

Diversity and the carbon cycle

Bloom vs non-bloom populations

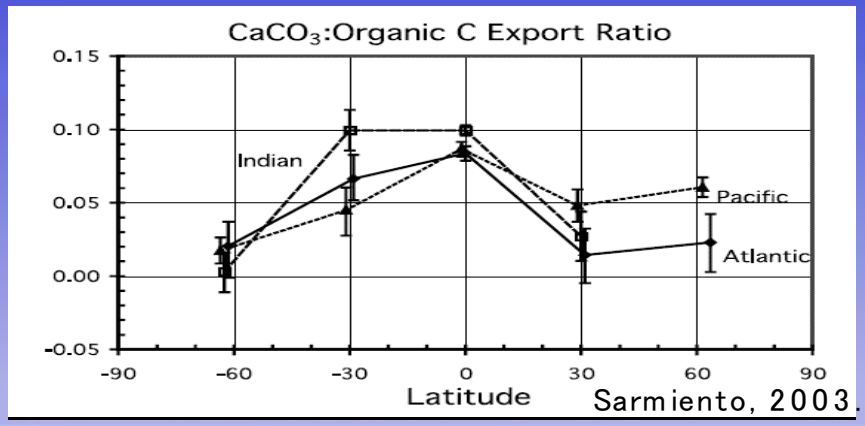

What is the composition of blooms?

- Blooms are not clonal (more than one type)

- Pops are highly diverse (Iglesias-Rodriguez 2002, 2006, Baker *et al*., 2008; Frommlet and Iglesias-Rodriguez, 2008).

How do blooms impact upon carbon chemistry?

$$Ca^{2+} + 2HCO_3^- \Leftrightarrow CaCO_3 + H_2O + CO_2$$
$$6CO_2 + 6H_2O + light \rightarrow C_6H_{12}O_6 + 6O_2$$

Coccolithophores

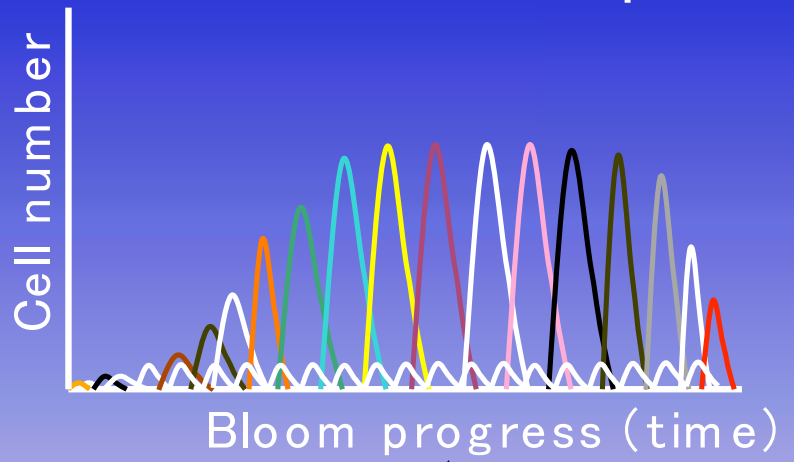

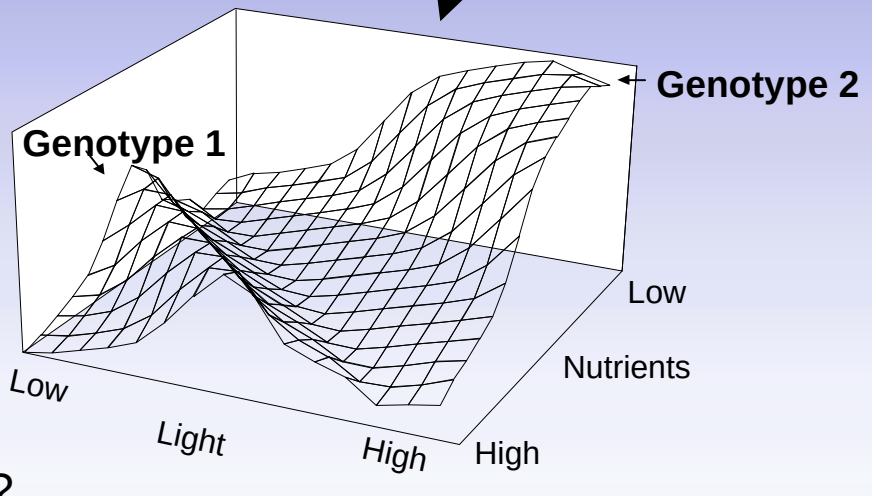

How representative are clones of natural populations?

Associated changes in long-term cultures

- Thousands- millions in a liter of water
- Several generations in a year
- When microorganisms evolve, how do we find them?

From lab cultures to the field

From the lab to the field


Mid-scale incubations


Monocultures


Photobioreactors

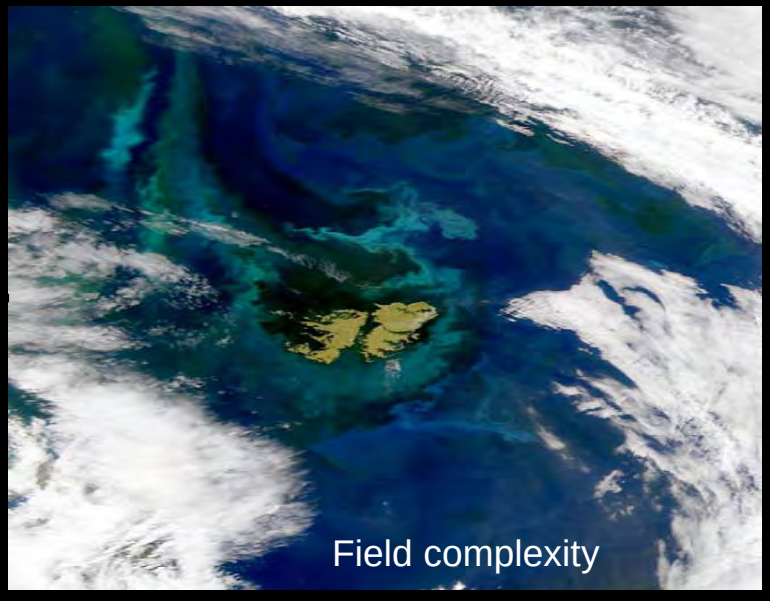
Field complexity

Method of manipulation

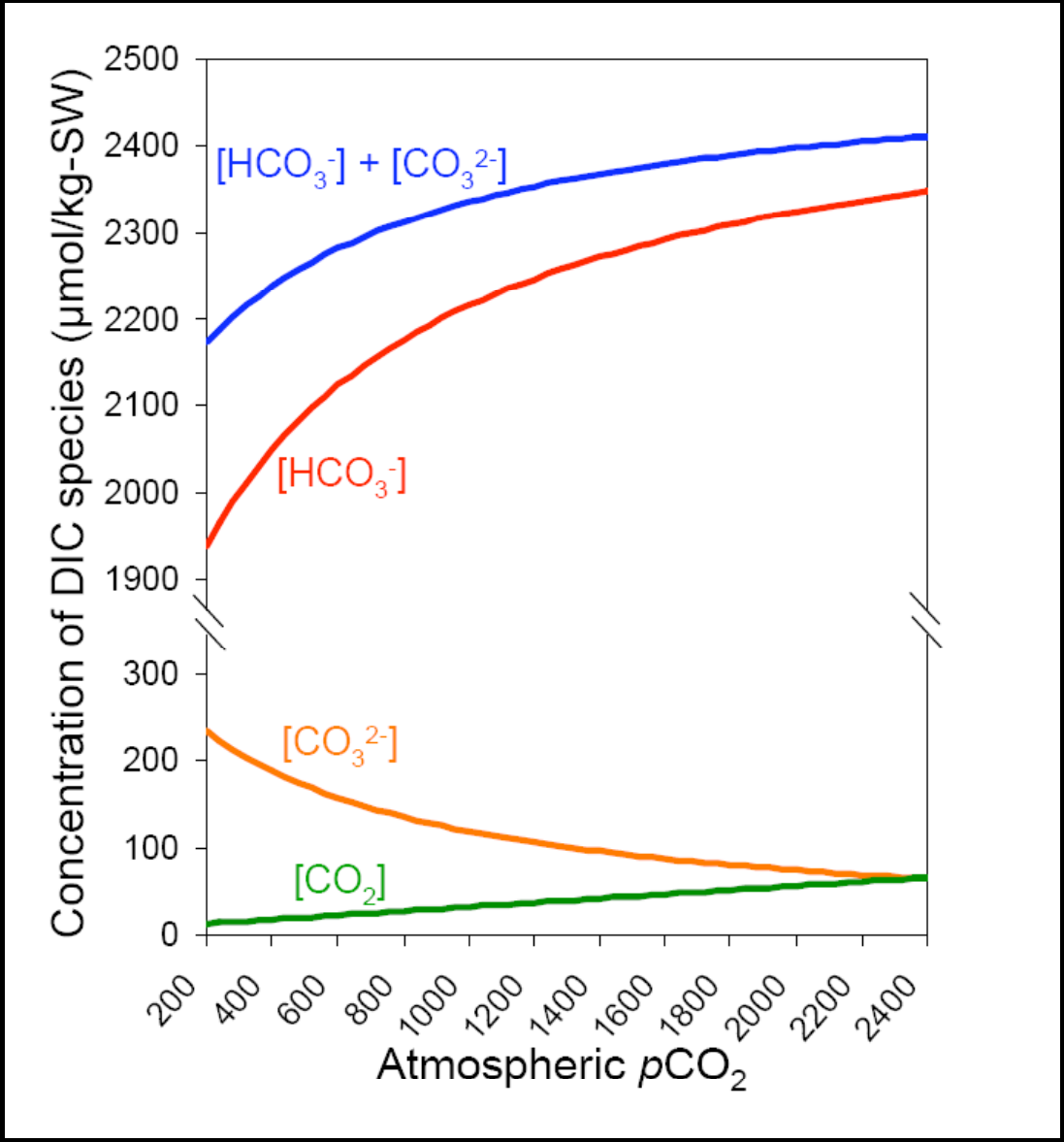

Iglesias-Rodriguez ,Buitenhuis, Gibbs, Lampitt, Lebrato, Raven, Ries, Schofield, in prep.

Bubbling considerations

- Potential mechanical effect of bubbling (Shi et al., 2009).
- Measure flow rate, monitor pH.
- Use blanks an check t_0 conditions an how these evolve through and end of experiment.

CO_2 incubation experiments

385ppmv CO_2

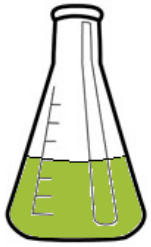

1500ppmv CO_2

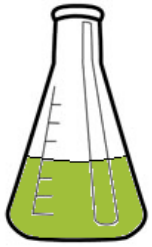

Decide on replicas (at least three)

Cell concentration maximum (e.g., 50,000/mL)

14.7 L cultures

Integration of results with complementary physiological and chemical measurements

Mechanisms behind the response to ocean acidification

Considerations

• Bubbling must be gentle (Shi et al., 2009) and cells must be checked for physiological stress (e.g., measure maintenance of photosynthetic health (Fv:Fm) using FRRF, check cells under microscope.

• Do you know your organism's physiology?

• In calcifying organisms, Mg tends to substitute for Ca in the lattice. Does your organism form "low-Mg calcite" (%$MgCO_3$ < 4) or "high-Mg calcite" (> 4)?

• Since calcite solubility increases with Mg substitution (Morse et al, 2006) - what is the mineralogy of your calcifier? (Lebrato et al., in review).

Physiological unknowns in calcifiers

- Calcification generates H^+ if using bicarbonate (no advantage and potential dissolution effect)

- Calcification does not generates H^+ if using carbonate (more susceptibility to decreasing pH??)

- Proton pumps: push protons in and out of membranes (energy cost)

- Ca^{+2} ATPases: controled by changes in Ca^{+2} availability and calcification rates in the calcification ‘vesicle’

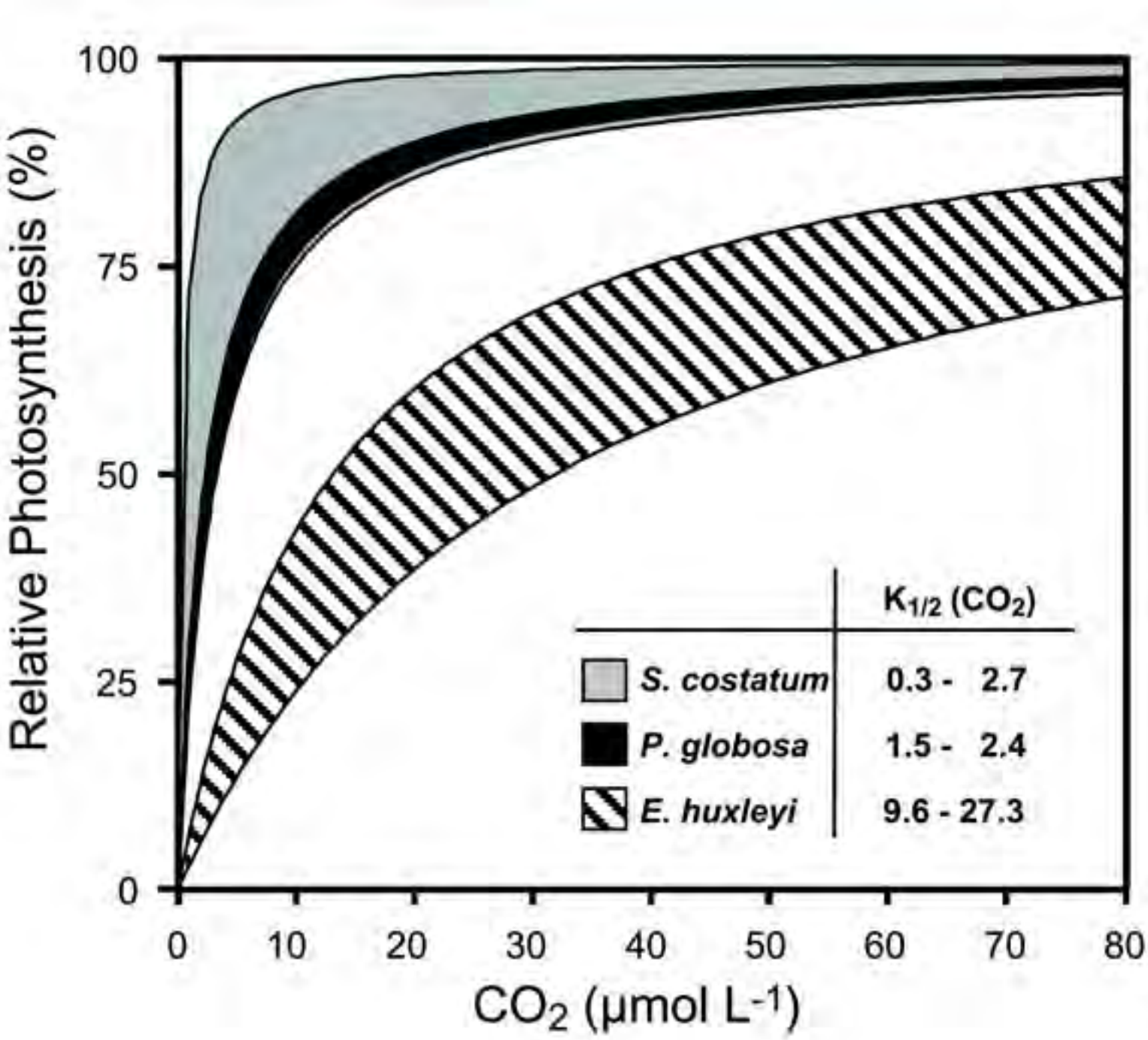
Relative Photosynthesis (%)
100
75
50
25
0
0
10
20
30
40
50
60
70
80
CO2 (µmol L-1)
K1/2 (CO2)
S. costatum
0.3 - 2.7
P. globosa
1.5 - 2.4
E. huxleyi
9.6 - 27.3

Will you be able to compare your data with the relevant published results?

- Can you justify using similar conditions? (e.g., medium, light irradiance, temperature)

- Weight improving existing methodology *versus* data comparison with previous work

Meta-approaches

Diversity of marine microbial communities: ‘metagenomics’ (Venter et al. 2004, Delong et al. 2006, Sogin et al. 2006)

Functional properties of marine communities: ‘proteomics’ (Jones, Edwards, Skipp, O’Connor, Iglesias-Rodriguez, 2009)

If cells are in the water, what are they doing?

Genome → Genes → Static

Proteome → Function → Evolving

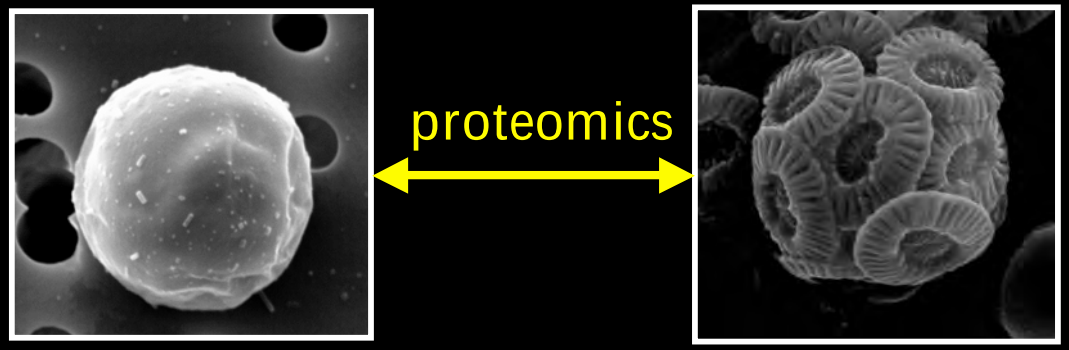

Before getting started pick your colleagues' brains!

- Particularly important in ocean acidification manipulations - check with the chemists, biologists, geologists

- Not such a thing as too much planning!

- Back up plan - e.g., collect samples for SEM to check whether there are any changes in cell morphology, volume, shape. Check what 'easy' extra-sampling you can do that will save you time

Sampling considerations

- Ensure there is sufficient replication (at least three)

- Time of sampling: implications of harvesting during day/night, be consistent

- Consider if the time length of sampling will impact upon your measurement, e.g., centrifugation time, moving cultures to a room with different temperature for harvesting - think about how harvesting time may affect the outcome

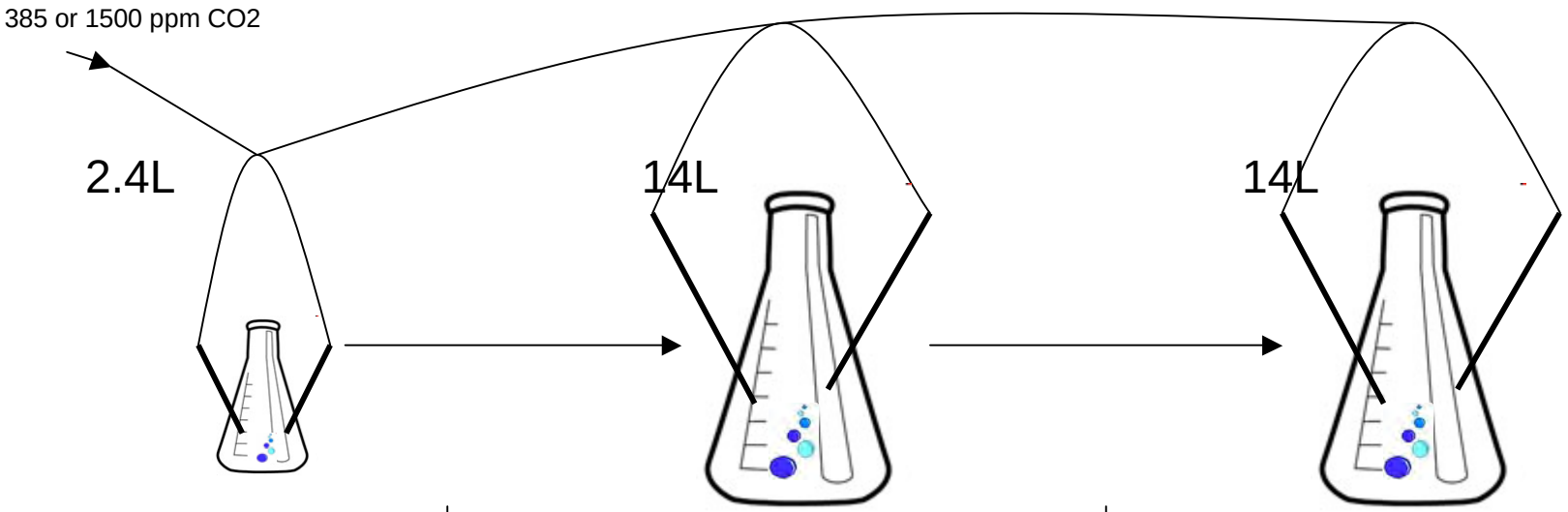

2-3 days in exponential

5/6 generations

3/4 generations

Sampling:

Before adding culture

Before transfer to 14L culture

- SEM
- Nutrients
- pH
- Salinity
- Temperature

Sampling:

Before starting bubbling

- DIC/Alk
- Nutrient
- pH
- Salinity
- Temperature

Before adding culture

- DIC/Alk
- Nutrient
- pH
- Salinity
- Temperature

Before transfer to 14L culture

- DIC/Alk
- Nutrient
- pH
- Salinity
- Temperature
- PIC
- POC
- SEM
- FRRF

Sampling:

Before starting bubbling

- DIC/Alk
- Nutrient
- pH
- Salinity
- Temperature

Before adding culture

- DIC/Alk
- Nutrient
- pH
- Salinity
- Temperature

Final harvest

- DIC/Alk
- Nutrient
- pH
- Salinity
- Temperature
- PIC
- POC
- SEM
- FRRF
- Proteins for iTRAQ

Jones, pers. com.

About ten generations of evolution!!

OA impact on coccolithophores

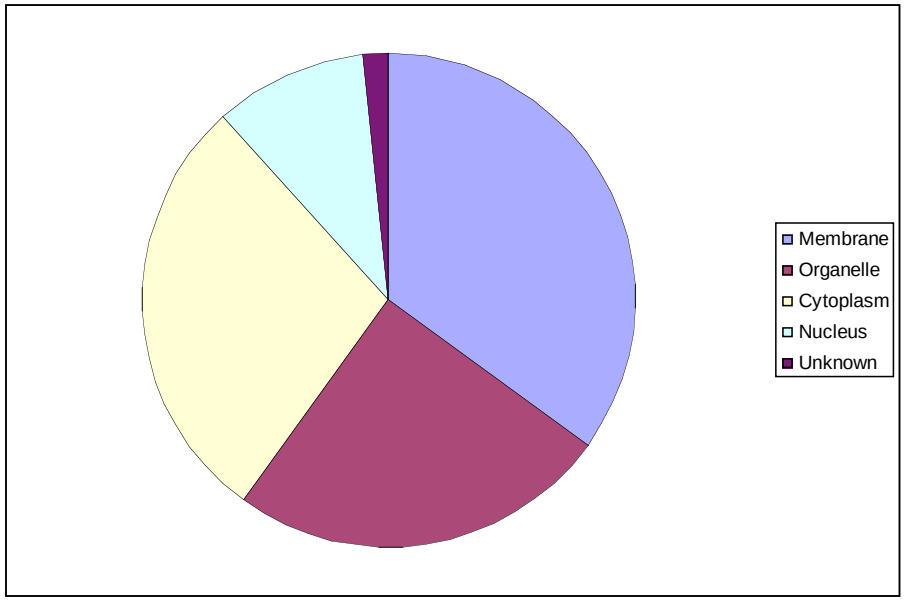

Subcellular location by protein cluster

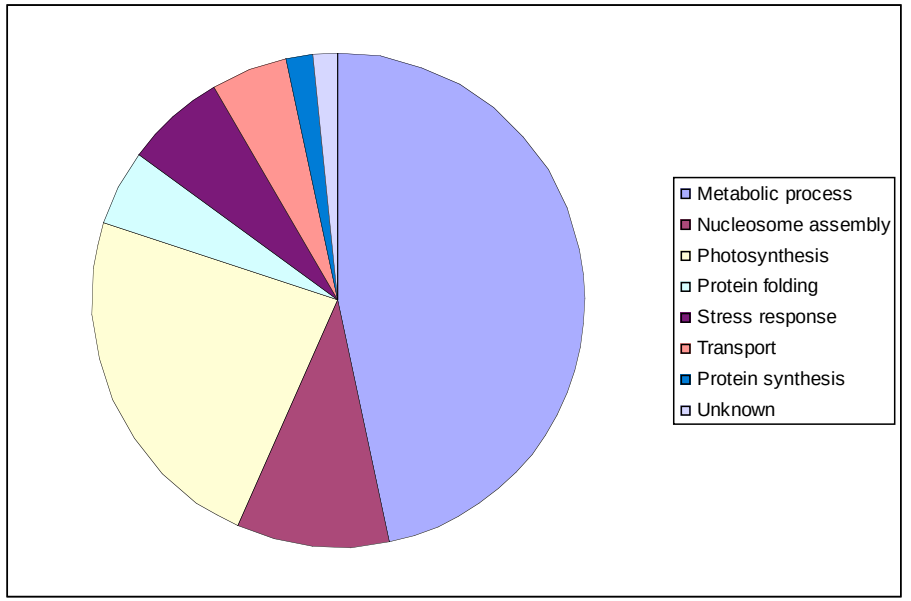

Biological process by protein cluster

Jones et al., Proteomics, in review.

Sample preparation and number

- Crucial to obtaining relevant results

- Can influence downstream applications ($\Rightarrow$ it requires thorough experimental planning to save time and money!)

- Assess qualitative (list of parameters) *versus* quantitative (up and down regulation of processes) patterns

- Statistical considerations

Preserving the *in vivo* properties - do you need to halt the process? Case sudy: proteomic analysis.

- Eukaryote protein synthesis inhibitors - geneticin (G418) and cycloheximide)

- Snap/flash freezing in liquid nitrogen

- Storage facilities important; often -80 ^{o}C with molecular samples

New '-omics' approaches

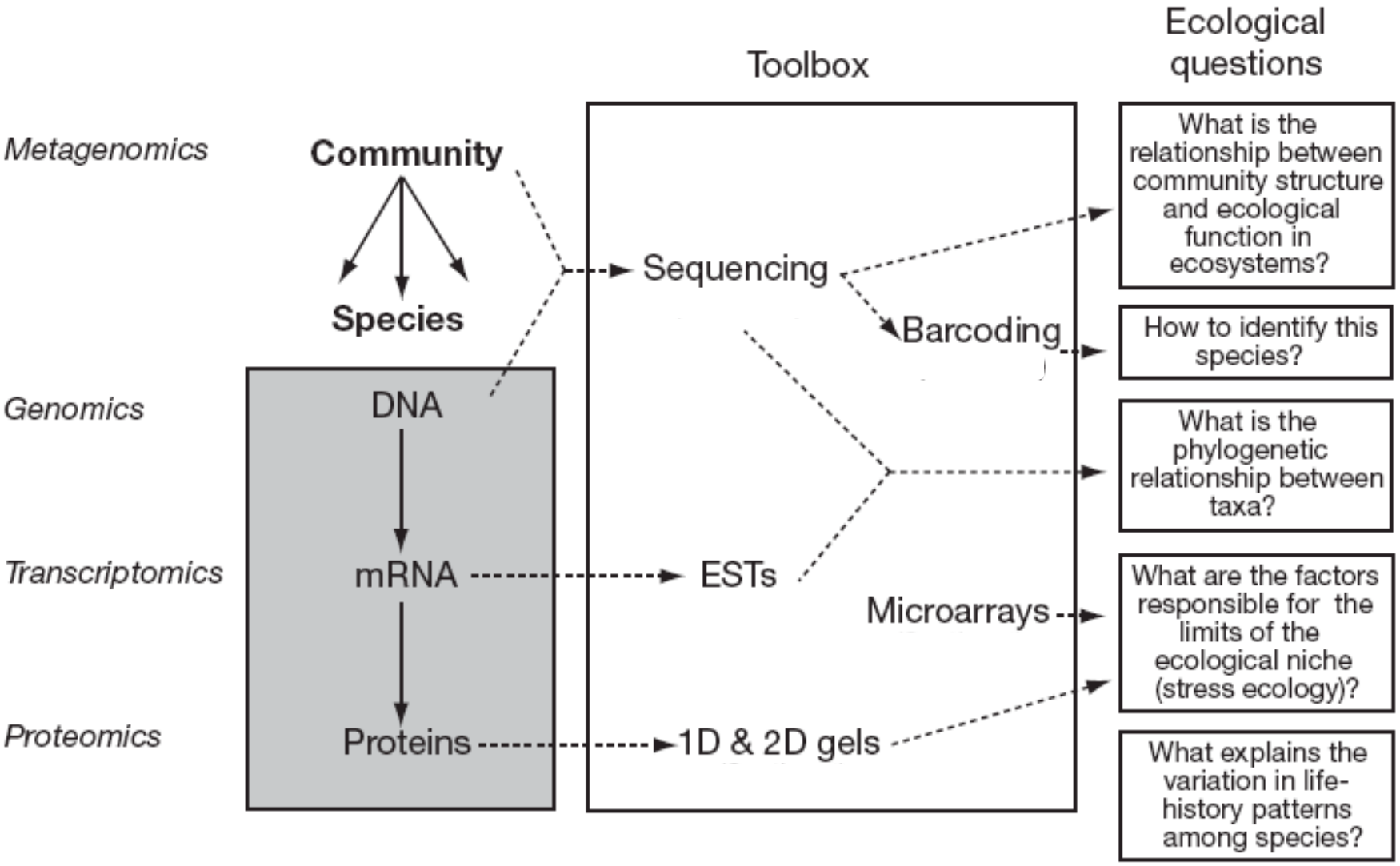

Dupont et al., 2008.

Molecular considerations

- A gene may remain present in the clone kept in the lab, but is either silent (not expressed) or expressed but producing an inactive product.
- A single mutation may activate the gene (no longer silent) or result in an active product.
- Further mutations can then make the microbe better at using new nutrient conditions.

Case study

Lenski's group (Michigan State University) has evolved 12 *E. coli* cultures in low nutrient broth, transferring daily, since 1988. He has achieved 40,000 generations of evolution - what has he discovered?

Lenski's results

- Bacteria become fitter within the first 2000 generations
- Cells become bigger
- Most of the gain comes from five different genes that have mutated
- After 20,000 generations, his group sequenced 918,700 bases from 50 isolates- they found 10 changes, all in ones with a "mutator" phenotype

Evolutionary considerations

- Can we assess evolutionary adaptation?
- How old is your strain?
- How much has your strain changed in culture?

How do we link different levels of organization, e.g., biological-geological, regional-global?

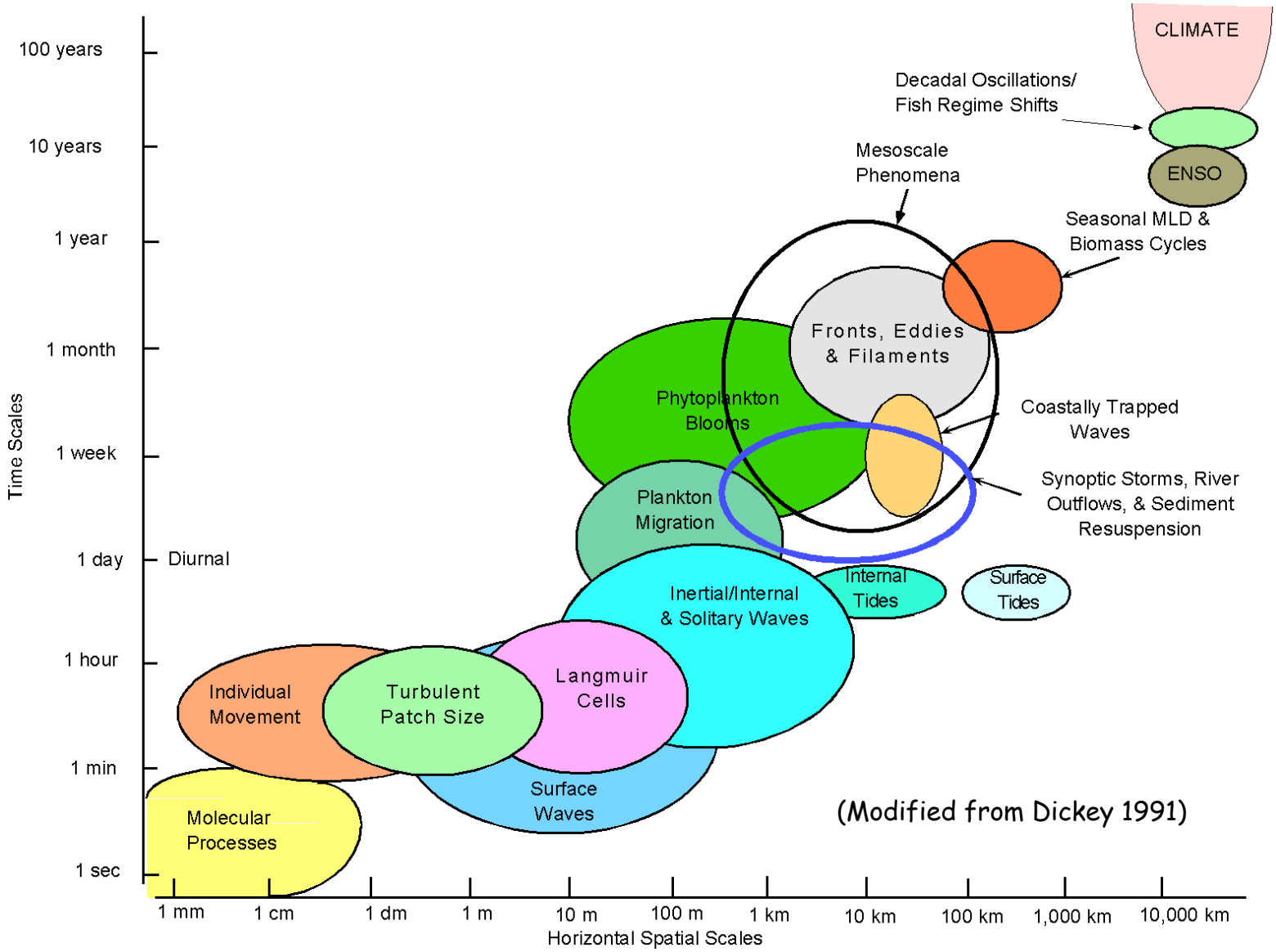

Acclimation - how?

Adaptation - who wins?

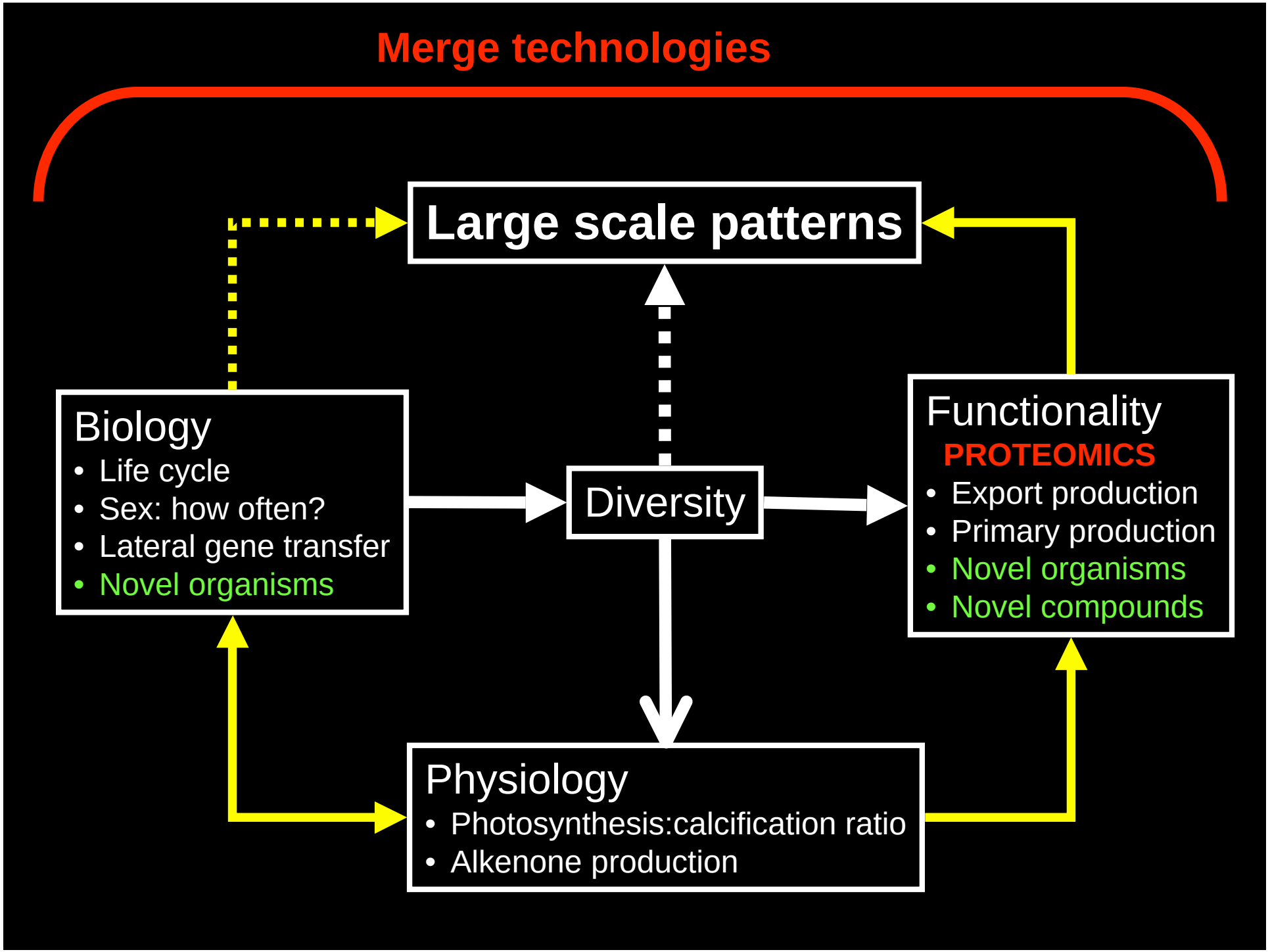
Merge technologies
Large scale patterns
Biology
• Life cycle
• Sex: how often?
• Lateral gene transfer
• Novel organisms
Diversity
Functionality
PROTEOMICS
• Export production
• Primary production
• Novel organisms
• Novel compounds
Physiology
• Photosynthesis:calcification ratio
• Alkenone production

Co-authors, NOC team and collaborators

NOC, Southampton (UK)
Bethan Jones
Daria Hinz
Alex Poulton
Darryl Green
John Allen
Toby Tyrrell
Sam Gibbs
David O'Connor (CPR, UoS)
Paul Skipp (CPR, UoS)
John Gittins
Nigel Eastwood

UW (USA)
Virginia Armbrust (UW)
Ger van den Engh (UW)
Jarred E. Swalwell (UW)
Eric Rehm (UW)

Roscoff (France)
Peter von Dassow (Roscoff)

Oxford University (UK)
Paul Halloran
Ros Rickaby

NOAA (USA)
Chris Brown

Rutgers (USA)
Oscar Schofield
Paul Falkowski

Earth, Ocean & Planetary Sciences
University of Wales Cardiff (UK)
Elena Colmenero-Hidalgo
Karin Boessenkool
Ian Hall

University of Dundee
John Raven

NOC
Ed Hill
Jacky Wood
Kim Marshall-Brown
Mike Douglas

THE ROYAL SOCIETY

NATURAL ENVIRONMENT RESEARCH COUNCIL

Coccolife Series, Rosa Seaoane, Vigo, Spain.

OCB Ocean Acidification short course
Instructor: Anne Cohen

Lecture outline

- Biomineralization strategies in corals, mollusks and other marine calcifying invertebrates; commonalities and important differences that could influence the potential impact of ocean acidification on shell formation. The role of mineralogy, crystal morphology and biomineralization mechanisms.
- Differences between larval and adult shell/skeletal formation that could influence responses and sensitivities to ocean acidification
- Experimental abiogenic (inorganic) carbonates as model systems for understanding biogenic mineralization; identifying important differences between abiogenic and biogenic mineralization; and what we can learn from low temperature abiogenic carbonate precipitation about the mechanisms by which OA impacts shell/skeletal formation.
- Summary of what we think we know and understand about impacts of OA on calcification based on experiments and possible ramifications for future health and sustainability of marine ecosystems; contradictions from experimental and field data; the potential role of nutrients and temperature in modulating or exacerbating the impact of OA on calcification.
- Advantages and challenges of using larval organisms to study the impact of OA on calcification
- Overview of larval coral and larval mollusk experiments including techniques to quantify calcification rates of larval organisms, and how to identify impacts of OA on the potential to build normal shells and skeletons.
- Overview of techniques used to quantify calcification and shell growth by adult corals and mollusks, including buoyant weighing, alkalinity depletion, isotope spiking and fluorescent dyes

Background papers (not exhaustive)

Cohen AL, McConnaughey TA (2003), A Geochemical Perspective on Coral Mineralization. In: Biomineralization. Dove PM, Weiner S, deYoreo JJ (Eds) Reviews in Mineralogy and Geochemistry Vol. 54 pp 151-187

Cohen, A. L., D. C. McCorkle, S. de Putron, G. A. Gaetani, and K. A. Rose (2009), Morphological and compositional changes in the skeletons of new coral recruits reared in acidified seawater: Insights into the biomineralization response to ocean acidification, Geochem. Geophys. Geosyst., 10, Q07005, doi:10.1029/2009GC002411.

Holcomb M, Cohen A, Gabitov R, Hutter J. (2009), Compositional and morphological features of aragonite precipitated experimentally from seawater and biogenically by corals, Geochimica Cosmochimica Acta 73: 4166-4179 doi:10.1016/j.gca.2009.04.015

Kurihara, H., S. Katoh and A. Ishimatsu (2007). The impacts of acidification on the early development of oyster Crassostrea gigas. Aquatic Biology 1, p91-98

Langdon, C., and M. J. Atkinson (2005), Effect of elevated pCO_2 on photosynthesis and calcification of corals and interactions with seasonal change in temperature/irradiance and nutrient enrichment, J. Geophys. Res., 110, C09S07, doi:10.1029/2004JC002576.

Ries JB, Cohen AL and McCorkle DC. Marine calcifiers exhibit mixed responses to CO_2-induced ocean acidification. Geology, 2009, in press.

Geochemistry Geophysics Geosystems G3
AN ELECTRONIC JOURNAL OF THE EARTH SCIENCES
Published by AGU and the Geochemical Society

Article
Volume 10, Number 7
24 July 2009
Q07005, doi:10.1029/2009GC002411
ISSN: 1525-2027

Morphological and compositional changes in the skeletons of new coral recruits reared in acidified seawater: Insights into the biomineralization response to ocean acidification

Anne L. Cohen and Daniel C. McCorkle
Woods Hole Oceanographic Institution, Woods Hole, Massachusetts 02543, USA (acohen@whoi.edu)

Samantha de Putron
Bermuda Institute of Ocean Sciences, Saint George's GE 01, Bermuda

Glenn A. Gaetani and Kathryn A. Rose
Woods Hole Oceanographic Institution, Woods Hole, Massachusetts 02543, USA

[1] We reared primary polyps (new recruits) of the common Atlantic golf ball coral *Favia fragum* for 8 days at 25°C in seawater with aragonite saturation states ranging from ambient (Ω = 3.71) to strongly undersaturated (Ω = 0.22). Aragonite was accreted by all corals, even those reared in strongly undersaturated seawater. However, significant delays, in both the initiation of calcification and subsequent growth of the primary corallite, occurred in corals reared in treatment tanks relative to those grown at ambient conditions. In addition, we observed progressive changes in the size, shape, orientation, and composition of the aragonite crystals used to build the skeleton. With increasing acidification, densely packed bundles of fine aragonite needles gave way to a disordered aggregate of highly faceted rhombs. The Sr/Ca ratios of the crystals, measured by SIMS ion microprobe, increased by 13%, and Mg/Ca ratios decreased by 45%. By comparing these variations in elemental ratios with results from Rayleigh fractionation calculations, we show that the observed changes in crystal morphology and composition are consistent with a >80% decrease in the amount of aragonite precipitated by the corals from each "batch" of calcifying fluid. This suggests that the saturation state of fluid within the isolated calcifying compartment, while maintained by the coral at levels well above that of the external seawater, decreased systematically and significantly as the saturation state of the external seawater decreased. The inability of the corals in acidified treatments to achieve the levels of calcifying fluid supersaturation that drive rapid crystal growth could reflect a limit in the amount of energy available for the proton pumping required for calcification. If so, then the future impact of ocean acidification on tropical coral ecosystems may depend on the ability of individuals or species to overcome this limitation and achieve the levels of calcifying fluid supersaturation required to ensure rapid growth.

Components: 7568 words, 8 figures, 1 table.

Keywords: ocean acidification; coral; Sr/Ca; calcification; Mg/Ca; biomineralization.

Index Terms: 0419 Biogeosciences: Biomineralization; 4916 Paleoceanography: Corals (4220).

Received 29 January 2009; **Revised** 26 May 2009; **Accepted** 8 June 2009; **Published** 24 July 2009.

Cohen, A. L., D. C. McCorkle, S. de Putron, G. A. Gaetani, and K. A. Rose (2009), Morphological and compositional changes in the skeletons of new coral recruits reared in acidified seawater: Insights into the biomineralization response to ocean acidification, *Geochem. Geophys. Geosyst.*, *10*, Q07005, doi:10.1029/2009GC002411.

1. Introduction

[2] The rising concentration of CO_2 in Earth's atmosphere is changing the carbonate chemistry of the ocean [*Orr et al.*, 2005]. As CO_2 levels continue to rise over the next century, the surface water carbonate ion concentration ($[CO_3^{2-}]$) is expected to decrease by almost 50% relative to preindustrial levels [*Feely et al.*, 2004]. In laboratory studies, multiple taxa of marine calcifying organisms exhibit high sensitivity to changes in seawater $[CO_3^{2-}]$. The response of tropical corals is particularly well documented: under controlled experimental conditions, their calcification rates show a roughly linear decline with decreasing seawater $[CO_3^{2-}]$ [e.g., *Langdon and Atkinson*, 2005]. These observations have significant implications for the survival of tropical coral reef ecosystems, but our predictive capabilities are limited by a lack of understanding of the pathways by which seawater saturation state affects coral calcification.

[3] Physicochemical models for accretion of coral skeleton typically invoke precipitation of aragonite from modified seawater within an extracellular calcifying compartment, sandwiched between the base of the tissue and either the substrate or the tip of existing skeleton. Inherent in these models is that the $[CO_3^{2-}]$ of seawater in the coral's calcifying region [*Braun and Erez*, 2004] is actively elevated above typical oceanic saturation states, thus facilitating crystal nucleation and growth. This could be achieved with plasma membrane Ca^{2+}-ATPase, an obligatory Ca^{2+}-H^+ exchanger [*Zoccola et al.*, 2004] that removes two H^+ ions for every Ca ion transported into the calcifying space, a process that can quickly and effectively elevate fluid saturation significantly above that of ambient seawater. Although direct measurements of the saturation state of fluid within the calcifying space (the so-called "calcifying fluid") have not been made, in situ measurements of the calcifying fluid pH imply that $[CO_3^{2-}]$ within the calcifying space during light-enhanced calcification may be at least as high as 1200 μmolkg^{-1}, five times higher than that of ambient seawater [*Al-Horani et al.*, 2003]. Under such conditions, aragonite precipitation is rapid [*Burton and Walter*, 1987], allowing the coral to build a sturdy skeleton of densely packed bundles of fine aragonite needles. However, despite this evidence that calcification occurs at significantly elevated aragonite saturation states, calcification appears to be strongly sensitive to very small changes in the saturation state of the external seawater environment. For example, mature colonies reared over a period of weeks in seawater with a 10% reduction in $[CO_3^{2-}]$ exhibited a 50% reduction in calcification [*Langdon et al.*, 2000]. The results of this and subsequent studies have fueled concern over the future plight of coral reefs and the ecosystems they support under increasing anthropogenic CO_2 in the atmosphere [*Kleypas et al.*, 2006].

[4] To examine the mechanism whereby changes in seawater $[CO_3^{2-}]$ influences coral calcification, we tracked early skeletal development by new recruits (spat) of the brooding coral *Favia fragum* at 25°C and four saturation states for a period of 8 days postsettlement. Early calcification involves initiation of skeletogenesis by a previously non-calcifying planktonic planula (coral larva), and therefore offers a unique opportunity to precisely pinpoint the timing of aragonite formation and the subsequent development of skeletal components under a range of conditions. Further, because all skeletal accretion occurs during the experiment, observed changes in the morphology and chemistry of harvested crystals among different treatments can be linked directly with manipulated changes in aquarium conditions.

[5] Normal development of the primary skeleton starts with deposition, directly onto the substrate, of radiating arrays of fine aragonite crystals that fuse to form a thin, circular plate (basal plate) [*Vandermeulen and Watabe*, 1973; *Le Tissier*, 1988]. Desmoid processes anchor the tissue to the plate [*Le Tissier*, 1988], and later, as the sides of the plate are built upward into a shallow bowl, it may serve to seal the calcifying space from the external seawater environment, enabling the coral polyp to effectively elevate the saturation state of the calcifying fluid to achieve rapid calcification. Subsequent accretion of skeletal components of the

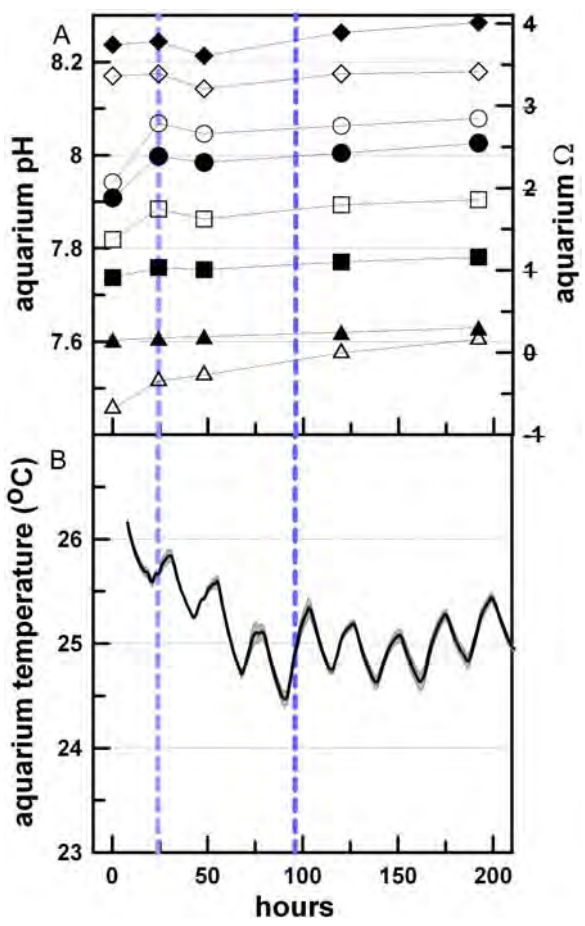

Figure 1. Tank conditions. (a) The pH(NBS) (solid symbols) and seawater saturation state with respect to aragonite (Ω, open symbols) measured in the experimental aquaria over the course of the experiment. (b) Average seawater temperatures logged in the four experimental aquaria over the course of the experiment. Error bars are the 1σ standard error. Vertical broken lines indicate when, during the course of the experiment, the settled larvae were introduced into the aquaria (light blue) and when aragonite was first detected on harvested tiles from the control tank (dark blue).

corallite (the primary and secondary septa, the corallite wall and columella) occurs above the basal plate [*Le Tissier*, 1988]. These components are built of dense bundles of fine (<1 μm diameter) aragonite fibers which are also the building blocks of the adult skeleton [e.g., *Wells*, 1956; *Constantz*, 1989; *Gladfelter*, 1983]. The early initiation of calcification and rapid subsequent growth of these skeletal components which support, protect and elevate the tissue from the substrate, are crucial steps in the successful recruitment and survival of coral spat [*Babcock and Mundy*, 1996; *Zilberberg and Edmunds*, 2001].

2. Experimental and Analytical Methods

[6] Gravid colonies of *F. fragum* were collected from the Bermudian reef and placed in covered outdoor flow-through aquaria where they released mature worm-like planula larvae over several days starting 22 July 2007. Larvae were transferred within 6 h to small (0.25 l) plastic settlement containers filled with ambient and acidified seawater from the experimental aquaria (see below) and containing preconditioned ceramic tiles. Preconditioning was achieved by leaving the tiles on racks on nearby reefs for 4–6 weeks to obtain the necessary biofilms and algae to induce settlement. Within 24 h following the first release, approximately 80% of the previously motile larvae had settled onto the tiles and metamorphosed into a doughnut-shaped primary polyp, approximately 1mm in diameter and firmly attached to the substrate. The tiles, each hosting 30–45 primary polyps, were immediately transferred to static, 30 L aquaria containing unfiltered reef seawater preadjusted via HCl addition to alkalinity values of 2421 ± 74, 1862 ± 50, 1181 ± 55, and 506 ± 118 ueq/kg, and set by continuous bubbling with laboratory air, yielding carbonate ion concentrations of 238 ± 16, 154 ± 8, 67 ± 10, and 14 ± 7, corresponding to aragonite saturation states of: $\Omega = 3.71 \pm 0.23$ (unmodified), $\Omega = 2.40 \pm 0.11$, $\Omega = 1.03 \pm 0.16$, and $\Omega = 0.22 \pm 0.11$ (Figure 1a). The zooxanthellate primary polyps were reared in the aquaria for 8 days, at an average water temperature of 25°C (Figure 1b) on a 12h/12h light/dark cycle and light levels 61 ± 6 $\mu Em^{-2}s^{-1}$. The timing of skeletal development was checked by successive harvesting of sets of tiles followed by immersion for several hours in a 10% sodium chlorite solution diluted with reef seawater. All remaining tiles were harvested after 8 days.

[7] Water samples were collected from the aquaria at the beginning and end of the experiment, and poisoned immediately after collection. Alkalinity (Alk) and dissolved inorganic carbon (DIC) were measured using a closed cell titration on ~100 mL samples, standardized using certified reference materials obtained from Dr. A Dickson (SIO); the precision of the titrations was ±0.2% for both alkalinity and DIC in ambient seawater, but only ±0.6% and ±1.7% (Alk and DIC, respectively) in

the most strongly acidified treatment. This resulted in an uncertainty in calculated saturation state of roughly ±0.5% at ambient conditions and ±16% in the lowest-Ω treatment. In addition, pH in each aquarium was monitored daily using a Radiometer combination electrode; the $pH_{(NBS)}$ values were 8.17 ± 0.006, 8.04 ± 0.03, 7.87 ± 0.015 and 7.54 ± 0.02, consistent with values calculated from the large-volume titrations.

[8] The small size of the larval corals prohibited direct measurement of calcification rate by alkalinity anomaly or buoyant weight methods. To estimate the extent of skeletal development in each treatment, we quantified both the cross-sectional area and weight of the primary and secondary septa, and when developed, the columella within each corallite. Cross-sectional area was obtained by photographing each 8-day-old corallite and using image histogram and photographic software tools (Photoshop®) to estimate the total area of skeleton visible in the photograph. Corallite weights, a more direct measure of the amount of aragonite accreted by each polyp during the experiment, were obtained by removing all visible skeleton, excluding the basal plate, from a minimum of five corallites on each tile using a 0.5 mm fine forceps and a fine brush. The skeletal components were weighed on a Mettler-Toledo microbalance, then mounted in epoxy, polished and prepared for element ratio analysis by secondary ion mass spectrometry (SIMS). A Cameca 3f ion microprobe employing a ~4 nA primary O^- beam, 20 μm in diameter and accelerated at 12.5 keV was used for all element ratio analyses. Following a 3 min preburn to remove the Au coat, a single spot was occupied while measuring secondary ion intensities for ^{24}Mg, ^{42}Ca, and ^{88}Sr within a 30 eV window centered on an 80 eV offset from the peak of the energy distribution. This energy filtering reduces molecular interferences to <0.1% [*Hart and Cohen*, 1996]. The mass spectra for Mg, Ca, and Sr were determined to be free from significant isobaric interferences through a comparison of measured isotope ratios with natural abundances. Isotope ratios were converted to molar ratios using working curves constructed from three carbonate standards: a carbonatite crystal (OKA), a calcite crystal (0875) and an aragonite crystal (AG1) with Mg/Ca ratios of 0.27–4.47 mmol/mol and Sr/Ca ratios of 0.56–19.3 mmol/mol. The composition of each standard was determined by solution ICP-MS [*Holcomb et al.*, 2009]. Routine instrument precision for $^{24}Mg/^{42}Ca$ and $^{88}Sr/^{42}Ca$ are 1.2% and 0.3%, respectively.

3. Acid Addition Versus pCO_2 Manipulation

[9] In this study, seawater $[CO_3^{2-}]$ was manipulated by HCl addition rather than by CO_2 enrichment, which would be more similar to the global uptake of fossil fuel CO_2 by the oceans. There is a fundamental chemical difference between these two approaches that could, in theory, influence the calcification response, depending on both the biomineralization mechanism involved and the availability of an alternative source of dissolved inorganic carbon (DIC) for calcification. While data from our companion pCO_2 experiments with new coral recruits indicate that the calcification response is identical whether HCl or CO_2 is used to manipulate seawater saturation state (S. de Putron et al., manuscript in preparation, 2009), it is worthwhile to clarify the differences between these two techniques.

[10] Manipulation of seawater $[CO_3^{2-}]$ by elevating the pCO_2 of the aquarium seawater increases the dissolved inorganic carbon concentration (DIC) and bicarbonate concentration $[HCO_3^-]$ of the solution. In contrast, addition of HCl lowers the alkalinity of the aquarium seawater. In our experiment, the pCO_2 of the low-alkalinity seawater was then set by bubbling with laboratory air (pCO_2 ~450 ppm). The resulting equilibrium DIC and $[HCO_3^-]$ concentrations are substantially lower than in the initial seawater, and much lower than in seawater where the same low initial $[CO_3^{2-}]$ has been achieved by CO_2 enrichment. If an organism calcifies by modifying the chemistry of a small volume of seawater-derived calcifying fluid, and if no DIC is added to this calcifying fluid during the calcification process, then no matter how much energy the organism expends to increase the pH of the calcifying fluid by removing protons, the final $[CO_3^{2-}]$ of that fluid can never be pushed above its initial DIC concentration. This places a relatively low upper limit on the potential saturation state of the calcifying fluid in acid addition experiments (Figure 2a). In contrast, if the experimental saturation state is lowered by pCO_2 enrichment, then the $[CO_3^{2-}]$ and saturation state of the calcifying fluid can reach much higher values (Figure 2b). The calculations shown in Figure 2 are for an idealized, closed system calcifying space with no DIC addition. However, if sufficient metabolic CO_2 is available for calcification, then the corals in acid

addition experiments may not experience the closed system DIC limitation seen in Figure 2a. Such DIC addition could happen, for example, because of diffusion of metabolic CO_2 into the calcifying region as the pH of the calcifying fluid increases and its pCO_2 drops, as proposed by *McConnaughey and Falk* [1991] and *Cohen and McConnaughey* [2003]. Indeed, results from at least three studies suggest that DIC addition to the site of calcification is likely. First, data published by *Furla et al.* [2000] indicate that metabolic CO_2 is likely a significant source of DIC for calcification in zooxanthellate corals. Second, in a direct comparison of different saturation state manipulation methods, *Schneider and Erez* [2006] did not observe any limitation to calcification arising from acid addition. And finally, our own data from recent CO_2 enrichment experiments with *Favia* and *Porites* new recruits, in which we elevated pCO_2 to produce external saturation states as low as $\Omega = 1.4$, show reductions in calcification comparable to the reductions seen in our acid addition experiments with similar saturation states (S. de Putron et al., manuscript in preparation, 2009).

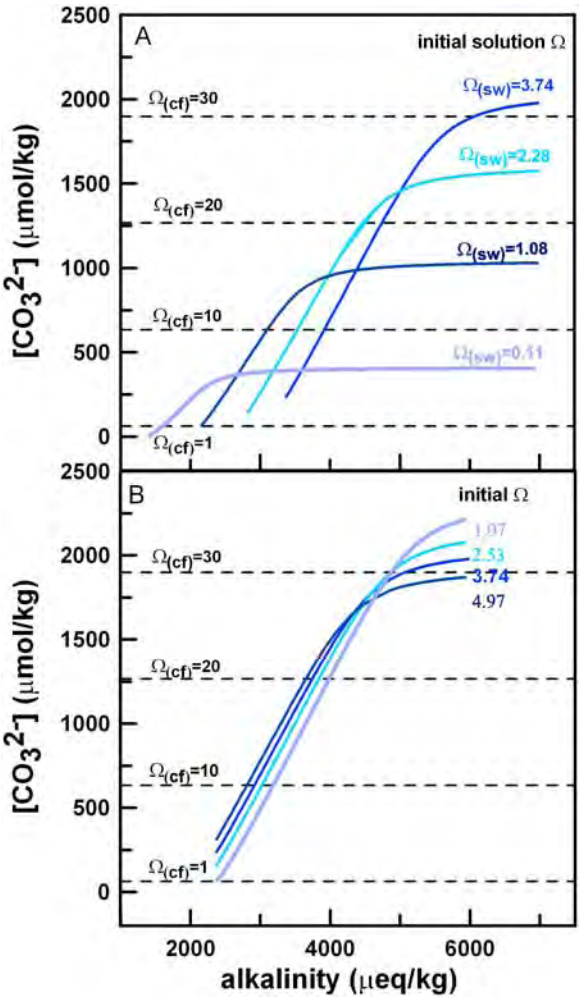

Figure 2. Model calculations of the carbonate ion concentration in the calcifying fluid as a function of calcifying fluid alkalinity illustrate the potential for DIC limitation when solution carbonate chemistry is manipulated by (a) acid addition rather than by (b) CO_2 enrichment. The increase in alkalinity (x axis) is equal to proton removal from the calcifying space by the coral. All calculations were carried out using a spreadsheet implementation of the CO2SYS program of *Lewis and Wallace* [1998], with the dissociation constants of *Roy et al.* [1993]. In both sets of calculations the DIC of the calcifying fluid (cf) was held at the concentration in the appropriate aquarium, and salinity (36.8 psu) and temperature (27°C) were held constant (values are hypothetical and do not exactly match conditions in our experimental aquaria). In Figure 2a, when solution saturation state is set by acid additions at fixed initial pCO_2, low-Ω treatments have low initial alkalinity and DIC concentrations. The maximum carbonate ion concentration (and thus the maximum saturation state) that can be attained can be no higher than the DIC initially present in the solution (asymptotic values of the curves). In Figure 2b, this potential limitation does not occur when solution Ω is lowered by CO_2 enrichment: high-pCO_2 (low-Ω) treatments have high initial DIC concentrations, and thus higher maximum carbonate ion concentrations. The initial DIC will still place an upper limit on the final Ω, assuming no DIC addition to the calcifying fluid, but these asymptotic Ω values are much higher than in acid addition experiments.

4. Results

[11] Aragonite was accreted by corals in all treatments, including those reared under strongly undersaturated conditions (Figure 3). In the ambient tanks, aragonite was first detected on the tiles approximately 3 days after settlement. However, in the $\Omega = 1.04$ and $\Omega = 0.22$ treatments, aragonite was first detected on the tiles between 4 and 5 days after settlement, and subsequent skeletal development was visibly depressed. The shape of the basal plate, circular under normal conditions (Figure 3a), became increasingly distorted with decreasing saturation state, possibly reflecting anatomical distortions of the basal disc (Figures 3c and 3d). In the strongly undersaturated seawater ($\Omega = 0.22$), basal plates, if present, were ill defined and lacked a well-developed rim. This combination may have made it difficult for the primary polyps to effectively seal the calcifying region from the external seawater, contributing both to the delay in onset of

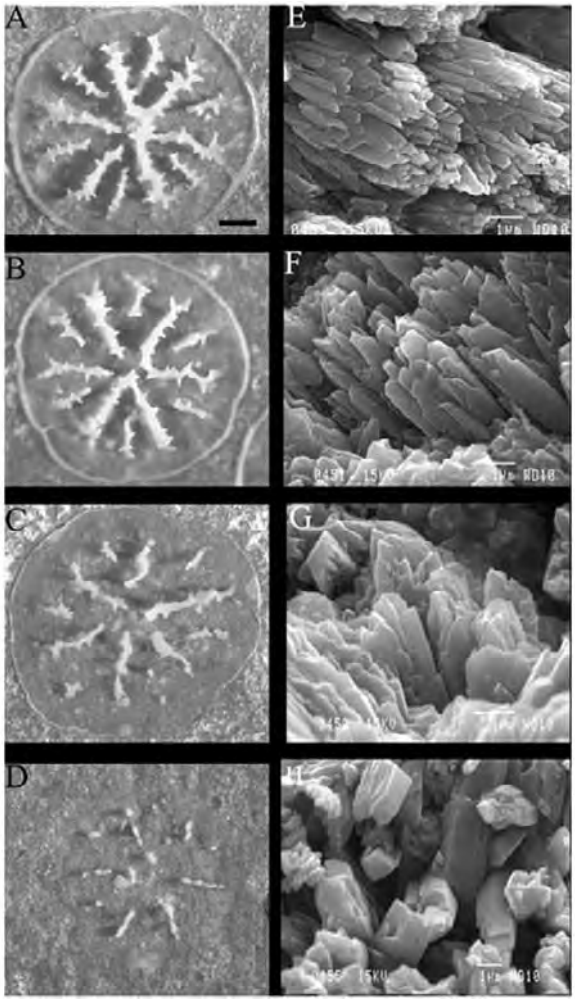

Figure 3. (a–d) Progressive changes in the mesoscale skeletal development, including distortion of basal plate and retardation of septal development, of 8-day-old corallites of *Favia fragum* with decreasing seawater saturation state. Visible changes in the amount of aragonite produced by the corals are quantified by cross-sectional area analysis and weighing of individual corallites (see Figure 5). (e–h) Progressive changes in the morphology and orientation of crystals within the corallites are documented by scanning electron microscopy imaging of broken faces of primary septa. In Figures 3a and 3e, $\Omega = 3.71$ (control); in Figures 3b and 3f, $\Omega = 2.40$; in Figures 3c and 3g, $\Omega = 1.03$; and in Figures 3d and 3h, $\Omega = 0.22$. In Figure 3a, scale bar is 200 μm.

skeletogenesis and to the reduction in growth rate once calcification was initiated.

[12] Raman spectroscopy identified all crystals precipitated by the larval corals as aragonite, even in the strongly undersaturated seawater experiment ($\Omega = 0.22$). However, Scanning Electron Microscope (SEM) images of broken faces of septa show that morphological features of the aragonite crystals vary systematically with changing saturation state of the aquarium seawater (Figures 3e–3h). Crystals in the control skeletons (precipitated at $\Omega = 3.71$) were long, thin blades, the long or c axis of each crystal oriented in parallel with its neighboring crystals, and organized into discrete densely packed bundles that are characteristic of corals in the wild [e.g., *Wells*, 1956; *Constantz*, 1989; *Gladfelter*, 1983] (Figure 3e). As the saturation state of the external seawater decreased, crystals became shorter and thicker, their orientation became increasingly random, and the discrete fiber bundles disappeared. Crystals accreted in the lowest saturation state experiments ($\Omega = 0.22$) were highly faceted rhombs rather than fine blades (Figure 3h). The minimal skeleton built of these crystals lacked the ordered microstructure of skeleton grown at ambient conditions, and crumbled to the touch (Figures 4a and 4b).

[13] Visible changes in the mesoscale skeletal development were quantified using both the cross-sectional area of skeletal deposits and the average corallite weight (Figure 5). The cross-sectional area of skeleton deposited by primary polyps in seawater with moderately lowered saturation state ($\Omega = 2.40$) was more than 20% less than the control, and in strongly undersaturated seawater ($\Omega = 0.22$), skeletal development was 75% less than the control. The average weight of skeletal elements in each corallite was reduced by 26% at $\Omega = 2.40$ and by 95% at $\Omega = 0.22$.

[14] Average Mg/Ca and Sr/Ca ratios of skeleton accreted by corals at ambient conditions are 6.6 ± 0.4 mmol/mol and 9.8 ± 0.3 mmol/mol, respectively, similar to that measured in the skeletons of adult Bermudan *Diploria labyrinthiformis* by SIMS ion microprobe [*Gaetani and Cohen*, 2006] (Table 1 and Figure 6). However, a systematic change in skeletal composition occurred with changing seawater saturation state, despite the strictly isothermal conditions. Average Mg/Ca ratios of the skeletons reared at constant and equivalent temperature decrease by 45%, from 6.6 ± 0.4 mmol/mol to 3.6 ± 0.5 mmol/mol, and average Sr/Ca ratios increase by 13%, from 9.8 ± 0.3 mmol/mol to 11.2 ± 0.3, as the saturation state of seawater in the tanks decreased from $\Omega = 3.71$ to $\Omega = 0.22$.

5. Discussion

[15] Recently there has been a great deal of interest in the possibility that changes in the saturation state

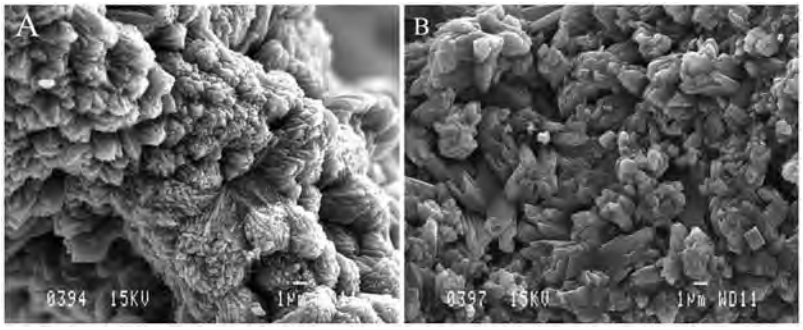

Figure 4. (a) Skeleton accreted by the corals under ambient conditions ($\Omega = 3.71$) consists of organized bundles of fine (submicron) fibers, as do the skeletons of corals grown in the wild. As the saturation state of the aquarium seawater decreased, the morphology and arrangement of crystals changed. (b) In the lowest saturation state treatment ($\Omega = 0.22$) the minimal skeleton accreted consisted of a disordered aggregate of highly faceted rhombs.

of the oceans, caused by increasing levels of atmospheric CO_2, may impact the ability of marine calcifying organisms to build their shells and skeletons. Experimental and field studies of a wide range of marine calcifying taxa suggest that calcification by many, although not all, organisms studied [*Iglesias-Rodriguez et al.*, 2008; J. Ries et al., Marine calcifiers exhibit mixed response to CO_2-induced ocean acidification, submitted to *Geology,* 2009] is strongly dependent on seawater saturation state (Ω). The negative impact of decreasing Ω on calcification by the scleractinian corals is well documented in several studies of mature colonies and at least one study of juveniles [*Albright et al.*, 2008]. Experimental studies using both HCl and pCO_2 [e.g., *Schneider and Erez*, 2006] show that coral calcification responds similarly to both methods of $[CO_3^{2-}]$ manipulation. While the sensitivity of calcification to changes in Ω differs among different studies, many experiments to date report between 40% and 60% decline in calcification with a 10% drop in Ω (as summarized by *Langdon and Atkinson* [2005]). This strong sensitivity of coral calcification to very small changes in seawater saturation state raises questions about the nature of the linkages between coral biomineralization processes and conditions in the external seawater environment.

[16] Evidence based on in situ microelectrode measurements of calcifying fluid pH [*Al-Horani et al.*, 2003] as well as the chemistry and morphology of aragonite crystals that make up the coral skeleton [*Holcomb et al.*, 2009] suggests that, under normal conditions, corals elevate the saturation state of fluid within the calcifying compartment as much as 7 times above that of the ambient seawater in order to precipitate aragonite. Therefore, it is not immediately obvious why coral calcification, which occurs in a compartment that is isolated from the external environment, should respond so strongly to changes in seawater $[CO_3^{2-}]$ much smaller than the changes incurred by the organism itself. A mechanistic understanding of the coral calcification response to ocean acidification is therefore critical to predicting how different species on different reefs experiencing multiple, dif-

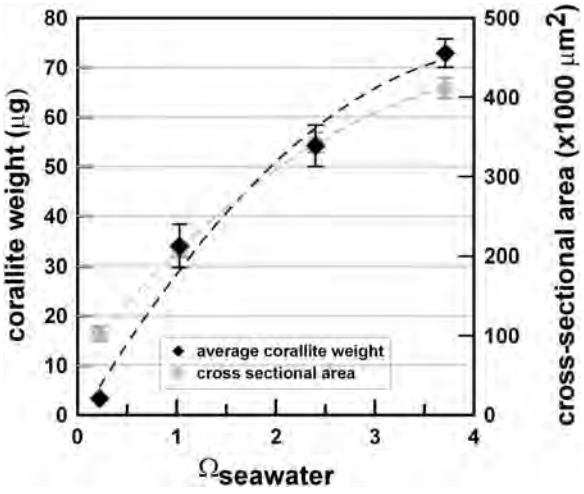

Figure 5. Average corallite size (cross-sectional area) and weight of aragonite precipitated by the new coral recruits in the experimental aquaria. The cross-sectional area of corallites was estimated in Photoshop® by selecting all skeletal components above the basal plate (i.e., including primary and secondary septa and columella if present) and using the histogram tool to quantify the cross-sectional area. Weights were obtained by removing the entire corallite, including the basal plate if present, from the tile using a pair of fine forceps and a fine brush. A minimum of five corallites were used for each weight estimate. Error bars are the 1σ standard error.

Table 1. Average Mg/Ca and Sr/Ca Ratios of Aragonite Accreted by New *Favia fragum* Recruits Reared in 25°C Seawater Over a Range of Aragonite Saturation States[a]

$\Omega_{seawater}$	Mg/Ca (mmol/mol)	Standard Error	Sr/Ca (mmol/mol)	Standard Error
3.71	6.567	0.387	9.771	0.283
2.40	6.214	0.273	9.841	0.178
1.03	5.058	0.220	10.469	0.251
0.22	3.624	0.482	11.223	0.319

[a] Element ratios were generated by in situ Secondary Ion Mass Spectrometric (ion microprobe) analyses of aragonite from 5 corallites in each experiment. The standard error is the standard deviation divided by the square root of n.

ferent stressors will respond to global environmental change over the next century.

[17] In this study, skeletal accretion by juvenile corals reared from the larval stage in experimental aquaria showed a strong response to changes in seawater saturation state induced by HCl addition and continuous bubbling with laboratory air. Initiation of calcification was delayed and subsequent growth was visibly depressed in the treatment tanks relative to the control. On the basis of measurements of the amount of aragonite accreted by polyps over the study period, an approximately 18% drop in calcification occurred per unit drop in seawater saturation state. This sensitivity is consistent with that reported for other zooxanthellate scleractinia in experimental and field studies [*Langdon and Atkinson*, 2005].

[18] Our results demonstrate that corals are able to accrete aragonite even under strongly undersaturated conditions, attesting to the extent of organismal control over conditions within the calcifying compartment. This observation contrasts with results from most experiments with mature coral colonies, in which calcification was not detected below saturation states of ~1 (see review by *Langdon and Atkinson* [2005]). Nevertheless, in the young coral skeletons, changes in crystal morphology were apparent long before $\Omega_{aragonite}$ dropped below 1. As the saturation state of the experimental seawater decreased from $\Omega = 3.71$ to $\Omega = 2.40$, aragonite needles within each fiber bundle became visibly shorter and wider, and as Ω approached 1, the integrity of the fiber bundles was lost altogether. Under strongly undersaturated conditions, the densely packed bundles of fine needles characteristic of a normal skeleton gave way to randomly oriented highly faceted rhombs.

[19] Similar, systematic changes have been observed in the morphology of carbonates precipitated from seawater at varying aragonite supersaturations [*Holcomb et al.*, 2009] and in silicate minerals grown from a silicate melt at varying undercoolings, which is analogous to supersaturation [e.g., *Lofgren*, 1971, 1980]. In aragonites precipitated experimentally from seawater at 25°C, *Holcomb et al.* [2009] found that dense, closed spherulites containing long, thin blades of aragonite precipitated from the seawater solution when the saturation state was relatively high ($\Omega \sim 25$), whereas coarse open spherulites containing highly faceted crystals precipitated when the saturation state was relatively low ($\Omega \sim 6$). This suggests a change in the growth kinetics of the crystals in response to the changing saturation state of the solution from which they grew. In general, the higher the precipitation rate, the greater the departure of the crystal form from the equilibrium shape [*Burton et al.*, 1951; *Keith and Padden*, 1963; *Lofgren*, 1971, 1980]. In aragonites, this means a shift from the equilibrium orthorhombic shape to long, thin blades. Using the abiogenic aragonites as a framework for interpreting morphological changes observed in the coral crystals, we suggest that the observed changes in the coral skeleton reflect changes in the saturation state of the coral's calcifying fluid. This in turn implies that as the saturation state of seawater in the experimental

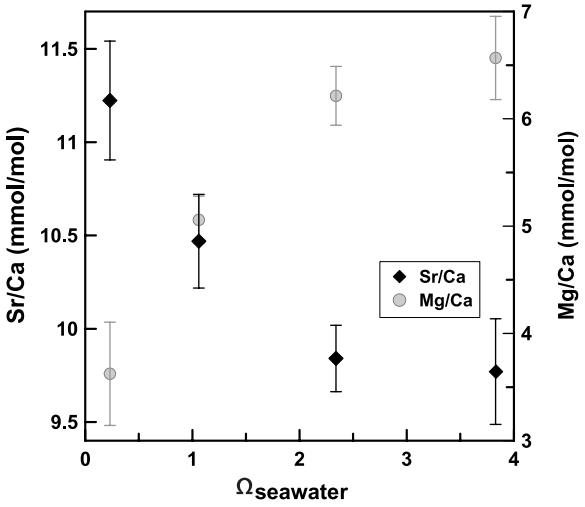

Figure 6. Sr/Ca (solid diamonds) and Mg/Ca (gray circles) ratios of aragonite accreted by the new coral recruits in the four experimental aquaria as a function of the saturation state of the seawater in which the corals were reared (see Table 1). Data were generated by SIMS ion microprobe analyses of septa; each point is the mean value of five analyses. The error bars are the 1σ standard error.

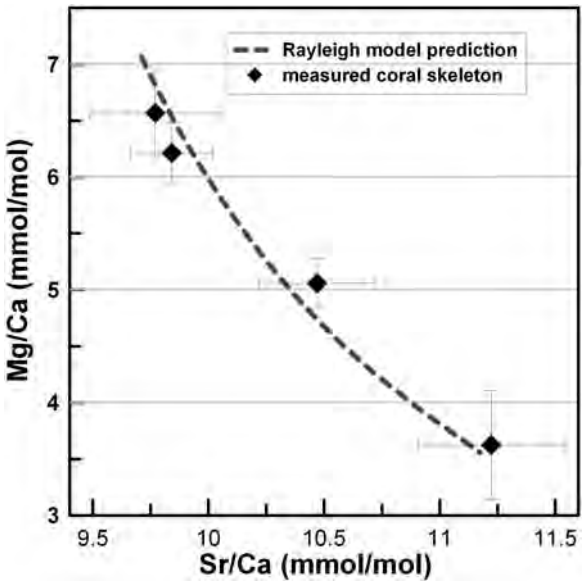

Figure 7. Variations in elemental ratios (Mg/Ca and Sr/Ca) (see Table 1) of skeleton accreted by new coral recruits in the experimental aquaria (solid diamonds) compared with results from Rayleigh fractionation calculations (dashed line) (see Appendix A). The Rayleigh distillation equation (1) [*Rayleigh*, 1896] relates the average concentration of an element *i* in the aragonite ($\overline{C}_i^{Aragonite}$) to its concentration in the calcifying fluid as precipitation begins (C_i^0), the mass fraction of the initial fluid remaining at a given point during aragonite precipitation (*FL*), and the Nernst aragonite-seawater partition coefficient for element *i* ($D_i^{Aragonite\text{-}Seawater}$). The Rayleigh equation accurately predicts the coral composition when the mass fraction of aragonite precipitated by the corals (*1-FL* in equation (1)) decreases from 0.07% to <0.01% as the aragonite saturation state of seawater in the tanks drops from $\Omega = 3.71$ to $\Omega = 0.22$.

aquaria decreased, the saturation state of the coral's internal calcifying fluid also decreased.

[20] Systematic changes in the Sr/Ca and Mg/Ca ratios of the coral skeletons provide further insight into the mechanism by which changes in seawater saturation state affect coral calcification. As seawater saturation state decreased in the experimental aquaria, Sr/Ca ratios of the skeletons increased by 13% and Mg/Ca ratios decreased by 45%. Both the trend and the relative magnitude of changes in Sr/Ca and Mg/Ca ratios are consistent with a Rayleigh distillation process in which compositional variability in the coral skeleton is driven primarily by changes in the mass fraction of aragonite precipitated by the coral from an isolated "batch" or reservoir of calcifying fluid (hereafter referred to as the "mass fraction") [*Gaetani and Cohen*, 2006; *Cohen et al.*, 2006; *Gagnon et al.*, 2007]. The data were modeled using the following solution to the Rayleigh distillation equation [*Rayleigh*, 1896]:

$$\frac{\overline{C}_i^{Aragonite}}{\overline{C}_{Ca}^{Aragonite}} = \frac{C_i^0}{C_{Ca}^0}\,\frac{1 - FL^{D_i^{Aragonite-Seawater}}}{1 - FL^{D_{Ca}^{Aragonite-Seawater}}} \quad (1)$$

where $\overline{C}_i^{Aragonite}$ is the average concentration of element *i* in the aragonite, C_i^0 is the concentration of element *i* in the calcifying fluid as precipitation begins, FL the mass fraction of the initial fluid remaining at a given point during aragonite precipitation, and $D_i^{Aragonite\text{-}Seawater}$ is the Nernst aragonite-seawater partition coefficient for element *i*. In this study, the known variables are the composition of the aragonite ($\overline{C}_i^{Aragonite}$) and the Nernst aragonite-seawater partition coefficients ($D_i^{Aragonite\text{-}Seawater}$) which were derived independently from abiogenic aragonite precipitated from seawater at controlled growth rates [*Gabitov et al.*, 2006] (Appendix A). A global minimization was carried out to solve equation (1) for the mass fraction of aragonite precipitated from each batch of calcifying fluid (1-FL), the initial composition of the calcifying fluid (C_i^0) and the growth rate of the crystals (see Appendix A).

[21] In Figure 7, we compare the measured variations in elemental ratios with results from our Rayleigh fractionation calculations. The results from our calculations show that the compositional variability observed in the coral skeletons can be explained by variations in the mass fraction of aragonite (1-FL) precipitated by the corals from each batch of calcifying fluid brought into the calcifying space. The results from our calculations also indicate that the mass of aragonite precipitated decreased from ~0.07% of the initial mass of a batch of calcifying fluid to <0.001% as the saturation state of the aquarium seawater decreases from $\Omega = 3.71$ to $\Omega = 0.22$. This corresponds to roughly 70% and 0.1% of the Ca^{2+} initially present in the calcifying fluid. The results from our calculations also indicate that crystal growth rates decreased by ~30% between the ambient and strongly undersaturated seawater treatments and that in all the experiments, regardless of seawater saturation state, the Mg/Ca and Sr/Ca ratios of the coral's calcifying fluid at the start of precipitation were very close to seawater values (5.3 mol/mol and 8.9 mmol/mol, respectively).

[22] In Figure 8, we compare the mass fraction aragonite precipitated by the corals as predicted by the Rayleigh model with the actual weight of the corallites as a function of the saturation state of the

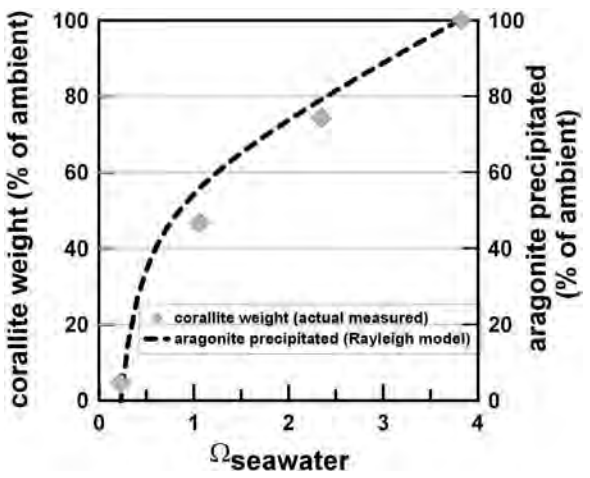

Figure 8. The mass fraction aragonite precipitated by the primary polyps as predicted by the Rayleigh calculations, compared with the actual weight of the corallites as a function of the aragonite saturation state of the aquarium seawater. Both parameters are expressed as a percentage of the ambient. Corallite weight and percent aragonite precipitated at ambient Ω are set at 100%.

aquarium seawater. Although coral calcification rate depends on both the mass fraction of aragonite precipitated and the rate at which the calcifying fluid is replenished in the calcifying compartment, our data indicate that at least in these juvenile corals, the amount of skeleton produced by each corallite over the 8 day period is closely related to the mass fraction of aragonite precipitated from each batch of calcifying fluid.

[23] Accretion of aragonite even in strongly undersaturated seawater demonstrates that the coral elevates the saturation state of the calcifying fluid significantly above that of the external seawater. So, how do changes in the saturation state of seawater cause large changes in the saturation state of the calcifying fluid? One possibility is that primary polyps of *Favia fragum* have a limited ability to raise the saturation state of the seawater brought into their calcifying space, reflecting either a limit to the amount of energy available for proton pumping, or a more fundamental limit to the rate of proton pumping regardless of the polyp's energy budget. In either case, as the aragonite saturation state of the external seawater drops, the polyp's ability to raise the saturation state of the calcifying fluid decreases, and leads to aragonite precipitation at lower rates than are necessary to build an orderly skeleton of fine fiber bundles.

[24] The IPCC business-as-usual emissions scenario A2 predicts that the saturation state of the midlatitude surface oceans could drop by almost 50% by 2100 A.D. [*Caldeira and Wickett*, 2005]. If this happens our data suggest that, unless corals can increase the rate of proton pumping, possibly by diverting more energy to this task, a significant drop in the rate of skeleton building by new coral recruits could occur over the next century, and by 2300 A.D., rates of early calcification could be too slow to sustain growth of a normal skeleton.

Appendix A

[25] The Mg/Ca and Sr/Ca ratios of aragonite precipitated from an isolated reservoir of calcifying fluid are described by a solution to the Rayleigh distillation equation [*Rayleigh*, 1896]:

$$\frac{\overline{C}_i^{Aragonite}}{\overline{C}_{Ca}^{Aragonite}} = \frac{C_i^0}{C_{Ca}^0}\,\frac{1 - FL^{D_i^{Aragonite-Seawater}}}{1 - FL^{D_{Ca}^{Aragonite-Seawater}}} \tag{A1}$$

where $\overline{C}_i^{Aragonite}$ is the average concentration of element i in the aragonite, C_i^0 is the concentration of element i in the calcifying fluid as precipitation begins, FL is the mass fraction of the initial fluid remaining at any point during aragonite precipitation, and $D_i^{Aragonite\text{-}Seawater}$ is the Nernst aragonite-seawater partition coefficient for element i. Kinetics exerts the principal control on element distribution during carbonate precipitation at low temperatures, so that partition coefficients vary with crystal growth rate [*Lorens*, 1981; *Watson*, 2004; *Gaetani and Cohen*, 2006; *Gabitov et al.*, 2008]. *Gabitov et al.* [2006] carried out abiogenic precipitation experiments at 25°C and determined the partitioning of Mg, Sr and Ca between aragonite and seawater at linear crystal growth rates of 2.7–117 μm/d. Results from these experiments were fit to a logarithmic functional form to derive expressions that describe growth rate–dependent partitioning:

$$C_{Mg}^{Aragonite}/C_{Mg}^{Seawater} = 0.2616 \times \ln(r) + 0.2882 \; r^2 = 0.9199 \tag{A2}$$

$$C_{Sr}^{Aragonite}/C_{Sr}^{Seawater} = 275.2 \times \ln(r) + 1423.99 \; r^2 = 0.9051 \tag{A3}$$

$$C_{Ca}^{Aragonite}/C_{Ca}^{Seawater} = 191.2 \times \ln(r) + 1237.78 \; r^2 = 0.8693 \tag{A4}$$

where C is weight concentration and r is crystal growth rate in microns per day.

[26] Calculations were carried out as follows. First, equations describing the growth rate–dependent partitioning of Mg, Sr and Ca between aragonite and seawater (equations (A2)–(A4)) were substituted into equation (A1) to derive a growth rate–dependent Rayleigh equation for each elemental ratio obtained by analyzing the coral skeleton. The concentrations of Mg and Sr in the calcifying fluid were treated as unknowns, and normalized to a Ca concentration of 394 ppm. Elemental ratios in the calcifying fluid at the beginning of precipitation were assumed to be independent of seawater saturation state. In order to avoid local minima, functional forms were assumed for the relationships between saturation state (Ω) and FL or r. Global minimization calculations resulted in the following empirical relationships:

$$FL = 0.9996 - 8.34 \times 10^{-5}\Omega + 8.57 \times 10^{-5}\Omega^{-1} \quad \text{(A5)}$$

$$r = 68.52\Omega^{0.11} \quad \text{(A6)}$$

A simple polynomial was used to describe the relationship between FL and Ω because our current understanding of coral biomineralization does not provide a theoretical basis for predicting the functional form. The functional form of the relationship between r and Ω was taken from the empirical rate equation [e.g., *Mucci and Morse*, 1983; *Burton and Walter*, 1987], except that saturation state was used in place of supersaturation. Because the actual saturation state of the calcifying fluid is unknown, coefficients derived from fitting our data to this equation do not have the same physical significance as would be the case for controlled precipitation experiments.

[27] Combining equations (A1)–(A6) results in a series of independent equations that are mathematically overconstrained: each of the 4 Sr/Ca and Mg/Ca ratios (averaged from 5 analyses of coral per treatment) provides 2 known quantities (Mg/Ca and Sr/Ca ratios) for a total of $2 \times 4 = 8$ constraints, and the unknown quantities are the Mg/Ca and Sr/Ca ratios of the calcifying fluid at the onset of precipitation, and coefficients for equations relating FL and r to Ω, for a total of 7. The minimized quantity was the sum of the squared percentage difference between the measured ratios and those predicted by the Rayleigh model:

$$\sum \left(100 \times \left(i/Ca_{Rayleigh} - i/Ca_{Measured}\right)/i/Ca_{Measured}\right)^2 \quad \text{(A7)}$$

where $i/Ca_{Rayleigh}$ and $i/Ca_{Measured}$ are the element-to-calcium ratio predicted by the Rayleigh equation and measured in the coral skeleton, respectively.

Acknowledgments

[28] The authors are grateful for technical assistance from Louis Kerr (Scanning Electron Microscopy), Nobuchimi Shimizu (Secondary Ion Mass Spectrometery), and Rebecca Belastock (Alk/DIC analyses) and for the constructive comments of reviewers which greatly improved the manuscript. This study was supported by NSF OCE-0648157 and NSF OCE-0823527 and the Bermuda Institute for Ocean Sciences.

References

Albright, R., B. Mason, and C. Langdon (2008), Effect of aragonite saturation state on settlement and post-settlement growth of *Porites astreoides* larvae, *Coral Reefs*, *27*, 485–490, doi:10.1007/s00338-008-0392-5.

Al-Horani, F. A., S. M. Al-Moghrabi, and D. de Beer (2003), The mechanism of calcification and its relation to photosynthesis and respiration in the scleractinian coral *Galaxea fascicularis*, *Mar. Biol. Berlin*, *142*, 419–426.

Babcock, R. C., and C. Mundy (1996), Coral recruitment: Consequences of settlement choice for early growth and survivorship in two scleractinians, *J. Exp. Mar. Biol. Ecol.*, *206*, 179–201, doi:10.1016/S0022-0981(96)02622-6.

Braun, A., and J. Erez (2004), Preliminary observations on sea water utilization during calcification in scleractinian corals, *Eos Trans. AGU*, *85*(47), Fall Meet. Suppl., Abstract B14B–04.

Burton, E. A., and L. M. Walter (1987), Relative precipitation rates of aragonite and Mg calcite from seawater: Temperature or carbonate ion control?, *Geology*, *15*, 111–114, doi:10.1130/0091-7613(1987)15<111:RPROAA>2.0.CO;2.

Burton, W. K., N. Cabrera, and F. C. Frank (1951), The growth of crystals and the equilibrium structure of their surfaces, *Philos. Trans. R. Soc. London, Ser. A*, *243*, 299–358.

Caldeira, K., and M. E. Wickett (2005), Ocean model predictions of chemistry changes from carbon dioxide emissions to the atmosphere and ocean, *J. Geophys. Res.*, *110*, C09S04, doi:10.1029/2004JC002671.

Cohen, A. L., and T. A. McConnaughey (2003), A geochemical perspective on coral mineralization, in *Biomineralization*, *Rev. in Mineral. Geochem.*, vol. 54, edited by P. M. Dove, S. Weiner, and J. J. deYoreo, pp. 151–187, Mineral. Soc. of Am., Washington, D. C.

Cohen, A. L., G. A. Gaetani, T. Lundälv, B. H. Corliss, and R. Y. George (2006), Compositional variability in a cold-water scleractinian, *Lophelia pertusa*: New insights into "vital effects," *Geochem. Geophys. Geosyst.*, *7*, Q12004, doi:10.1029/2006GC001354.

Constantz, B. R. (1989), Skeletal organisation in *Acropora*, in *Origin, Evolution and Modern Aspects of Biomineralization in Plants and Animals*, edited by R. E. Crick, pp. 175–200, Plenum, New York.

Feely, R. A., C. L. Sabine, K. Lee, W. Berelson, J. Kleypas, V. J. Fabry, and F. J. Millero (2004), Impact of anthropogenic CO_2 on the $CaCO_3$ system in the oceans, *Science*, *305*, 362–366, doi:10.1126/science.1097329.

Furla, P., I. Galgani, I. Durand, and D. Allemand (2000), Sources and mechanisms of inorganic carbon transport for

coral calcification and photosynthesis, *J. Exp. Biol.*, *203*, 3445–3457.

Gabitov, R. I., A. L. Cohen, G. A. Gaetani, and M. Holcomb (2006), Growth rate dependence of Mg, Sr, and U incorporation into aragonite: Experimental constraints on the origin of vital effects, *Eos Trans. AGU*, *87*(52), Fall Meet. Suppl., Abstract B13B–1076.

Gabitov, R. I., G. A. Gaetani, E. B. Watson, A. L. Cohen, and H. L. Ehrlich (2008), Experimental determination of growth rate effect on U^{6+} and Mg^{2+} partitioning between aragonite and fluid at elevated U^{6+} concentration, *Geochim. Cosmochim. Acta*, *72*, 4058–4068, doi:10.1016/j.gca.2008.05.047.

Gaetani, G. A., and A. L. Cohen (2006), Element partitioning during precipitation of aragonite from seawater: A framework for understanding paleoproxies, *Geochim. Cosmochim. Acta*, *70*, 4617–4634, doi:10.1016/j.gca.2006.07.008.

Gagnon, A. C., J. F. Adkins, D. P. Fernandez, and L. F. Robinson (2007), Sr/Ca and Mg/Ca vital effects correlated with skeletal architecture in a scleractinian deep-sea coral and the role of Rayleigh fractionation, *Earth Planet. Sci. Lett.*, *261*, 280–295, doi:10.1016/j.epsl.2007.07.013.

Gladfelter, E. H. (1983), Skeletal development in Acropora cervicornis. Diel patterns of calcium carbonate accretion, *Coral Reefs*, *2*, 91–100, doi:10.1007/BF02395279.

Hart, S. R., and A. L. Cohen (1996), An ion probe study of annual cycles of Sr/Ca and other trace elements in corals, *Geochim. Cosmochim. Acta*, *60*, 3075–3084, doi:10.1016/0016-7037(96)00154-8.

Holcomb, M., A. L. Cohen, R. I. Gabitov, and J. L. Hutter (2009), Compositional and morphological features of aragonite precipitated experimentally from seawater and biogenically by corals, *Geochim. Cosmochim. Acta*, *73*, 4166–4179, doi:10.1016/j.gca.2009.04.015.

Iglesias-Rodriguez, M. D., et al. (2008), Phytoplankton calcification in a high-CO_2 world, *Science*, *320*, 336–340, doi:10.1126/science.1154122.

Keith, H. D., and F. J. Padden (1963), A phenomological theory of spherulitic crystallization, *J. Appl. Phys.*, *34*, 2409–2421, doi:10.1063/1.1702757.

Kleypas, J. A., R. A. Feely, V. J. Fabry, C. Langdon, C. L. Sabine, and L. L. Robbins (2006), Impacts of ocean acidification on coral reefs and other marine calcifiers: A guide for future research, report, 88 pp., Natl. Sci. Found., Arlington, Va.

Langdon, C., and M. J. Atkinson (2005), Effect of elevated pCO_2 on photosynthesis and calcification of corals and interactions with seasonal change in temperature/irradiance and nutrient enrichment, *J. Geophys. Res.*, *110*, C09S07, doi:10.1029/2004JC002576.

Langdon, C., T. Takahashi, C. Sweeney, D. Chipman, J. Goddard, F. Marubini, H. Aceves, H. Barnett, and M. J. Atkinson (2000), Effect of calcium carbonate saturation state on the calcification rate of an experimental coral reef, *Global Biogeochem. Cycles*, *14*(2), 639–654.

Le Tissier, M. D. A. (1988), Patterns of formation and the ultrastructure of the larval skeleton of *Pocillopora damicornis*, *Mar. Biol. Berlin*, *98*, 493–501, doi:10.1007/BF00391540.

Lewis, E., and D. W. R. Wallace (1998), Program developed for CO_2 system calculations, *ORNL/CDIAC-105*, Carbon Dioxide Inf. Anal. Cent., Oak Ridge Natl. Lab., U.S. Dep. of Energy, Oak Ridge, Tenn.

Lofgren, G. (1971), An experimental study of plagioclase crystal morphology: Isothermal crystallization, *Am. J. Sci.*, *274*, 243–273.

Lofgren, G. (1980), Experimental studies on the dynamic crystallization of silicate melts, in *Physics of Magmatic Processes*, edited by R. B. Hargraves, pp. 487–565, Princeton Univ. Press, Princeton, N. J.

Lorens, R. B. (1981), Sr, Cd, Mn and Co distribution coefficients in calcite as a function of calcite precipitation rate, *Geochim. Cosmochim. Acta*, *45*, 553–561, doi:10.1016/0016-7037(81)90188-5.

McConnaughey, T. A., and R. H. Falk (1991), Calcium-proton exchange during algal calcification, *Biol. Bull.*, *180*, 185–195, doi:10.2307/1542440.

Mucci, A., and J. W. Morse (1983), The incorporation of Mg^{2+} and Sr^{2+} into calcite overgrowths: Influences of growth rate and solution composition, *Geochim. Cosmochim. Acta*, *47*, 217–233, doi:10.1016/0016-7037(83)90135-7.

Orr, J. C., et al. (2005), Anthropogenic ocean acidification over the twenty-first century and its impact on calcifying organisms, *Nature*, *437*, 681–686, doi:10.1038/nature04095.

Rayleigh, J. W. S. (1896), Theoretical considerations respecting the separation of gases by diffusion and similar processes, *Philos. Mag.*, *42*, 77–107.

Roy, R. N., L. N. Roy, K. M. Vogel, C. Portermoore, T. Pearson, C. E. Good, F. J. Millero, and D. M. Campbell (1993), The dissociation-constants of carbonic-acid in seawater at salinities 5 to 45 and temperatures 0°C to 45°C, *Mar. Chem.*, *44*, 249–267, doi:10.1016/0304-4203(93)90207-5.

Schneider, K., and J. Erez (2006), The effect of carbonate chemistry on calcification and photosynthesis in the hermatypic coral *Acropora eurystoma*, *Limnol. Oceanogr.*, *51*, 1284–1293.

Vandermeulen, J. H., and N. Watabe (1973), Studies on reef corals. I. Skeleton formation by newly settled planula larva of *Pocillopora damicornis*, *Mar. Biol. Berlin*, *23*, 47–57, doi:10.1007/BF00394111.

Watson, E. B. (2004), A conceptual model for near-surface kinetic controls on the trace-element and stable isotope composition of abiogenic calcite crystals, *Geochim. Cosmochim. Acta*, *68*, 1473–1488, doi:10.1016/j.gca.2003.10.003.

Wells, J. W. (1956), Scleractinia, in *Treatise on Invertebrate Paleontology, part F, Coelenterata*, edited by R. C. Moore, pp. F328–F479, Geol. Soc. of Am., New York.

Zilberberg, C., and P. J. Edmunds (2001), Competition among small colonies of Agaricia: The importance of size asymmetry in determining competitive outcome, *Mar. Ecol. Prog. Ser.*, *221*, 125–133, doi:10.3354/meps221125.

Zoccola, D., E. Tambutté, E. Kulhanek, S. Puverel, J. Scimeca, D. Allemand, and S. Tambutté (2004), Molecular cloning and localization of a PMCA P-type ATPase from the coral *Stylophora pistillata*, *Biochim. Biophys. Acta*, *1663*, 117–126, doi:10.1016/j.bbamem.2004.02.010.

Available online at www.sciencedirect.com
ScienceDirect
Geochimica et Cosmochimica Acta 73 (2009) 4166–4179
Geochimica et Cosmochimica Acta
www.elsevier.com/locate/gca

Compositional and morphological features of aragonite precipitated experimentally from seawater and biogenically by corals

Michael Holcomb [a,*], Anne L. Cohen [a], Rinat I. Gabitov [a,b,1], Jeffrey L. Hutter [c]

[a] Dept. Marine Geology and Geophysics, Woods Hole Oceanographic Institution, Woods Hole, MA 02543, USA
[b] Dept. Earth and Environmental Sciences, Rensselaer Polytechnic Institute, Troy, NY 12180, USA
[c] Dept. Physics and Astronomy, The University of Western Ontario, London, Ont., Canada N6A 3K7

Received 26 January 2009; accepted in revised form 8 April 2009; available online 3 May 2009

Abstract

The morphology and composition of abiogenic (synthetic) aragonites precipitated experimentally from seawater and the aragonite accreted by scleractinian corals were characterized at the micron and nano scale. The synthetic aragonites precipitated from supersaturated seawater solutions as spherulites, typically 20–100 μm in diameter, with aggregates of sub-micron granular materials occupying their centers and elongate (fibrous) needles radiating out to the edge. Using Sr isotope spikes, the formation of the central granular material was shown to be associated with high fluid pH and saturation state whereas needle growth occurred at lower pH and saturation state. The granular aggregates have significantly higher Mg/Ca and Ba/Ca ratios than the surrounding fibers.

Two types of crystals are identified in the coral skeleton: aggregates of sub-micron granular material and bundles of elongate (fibrous) crystals that radiate out from the aggregates. The granular materials are found in "centers of calcification" and in fine bands that transect the fiber bundles. They have significantly higher Mg/Ca and Ba/Ca ratios than the surrounding fibers.

The observed relationship between seawater saturation state and crystal morphology and composition in the synthetic aragonites was used as a framework to interpret observations of the coral skeleton. We propose that coral skeletal growth can be viewed as a cyclical process driven by changes in the saturation state of the coral's calcifying fluids. When saturation state is high, granular crystals precipitate at the tips of the existing skeletal elements forming the centers of calcification. As the saturation state decreases, aragonitic fibres grow in bundles that radiate out from the centers of calcification.

1. INTRODUCTION

Early studies of the ultrastructure of the scleractinian coral skeleton identified two distinct structures: the centers of calcification which appear as dark spots in petrographic thin-section, and the clusters of fibrous crystals which radiate out from the centers (e.g., Ogilvie, 1896; Vaughan and Wells, 1943; Wells, 1956). The centers of calcification and their clusters of fibers are called sclerodermites and are considered to be the basic building blocks of the skeleton (Wells, 1956). Bryan and Hill (1941) noted the striking similarity between spherulitic morphologies observed in a range of mineral systems, and coral sclerodermites. Both exhibit fibrous crystals radiating from a common center. Spherulitic growth in mineral systems is associated with diffusion-controlled growth from highly supersaturated solutions (Keith and Padden, 1963; Chernov, 1984). Such observations led Barnes (1970) and Constantz (1986), among others, to describe the precipitation of aragonite by scleractinian corals as a process analogous to crystal growth from highly supersaturated solutions.

* Corresponding author. Fax: +1 (508) 457 2150.
E-mail address: mholcomb@whoi.edu (M. Holcomb).
[1] Present address: Division of Geology and Planetary Sciences, California Institute of Technology, Pasadena, CA 91125, USA.

0016-7037/$ - see front matter © 2009 Elsevier Ltd. All rights reserved.
doi:10.1016/j.gca.2009.04.015

Over the past few decades, a range of imaging and analytical techniques have been employed to examine coral skeletons. SEM imaging of materials occupying the centers of calcification showed that these are morphologically distinct from the surrounding fibers. The materials at the centers of calcification have been variously described as small, nano-crystals, very fine, or granular (e.g. Wainwright, 1964; Constantz, 1986; Cohen et al., 2001; Clode and Marshall, 2003). Selective analyses of centers of calcification and adjacent fibers indicate that centers of calcification are also compositionally distinct. Several elements, notably Mg, Sr, S, Ba, and N, are enriched in the centers of calcification (e.g. Cuif et al., 2003; Gagnon et al., 2007; Meibom et al., 2004, 2006, 2007) and several isotope ratios, such as $\delta^{13}C$, $\delta^{18}O$, and $\delta^{11}B$, are depleted in centers of calcification (e.g. Adkins et al., 2003; Rollion-Bard et al., 2003; Meibom et al., 2006; Blamart et al., 2007) relative to the surrounding fibers. These findings have been used to support the hypothesis that centers of calcification are formed by a process distinct from that responsible for the formation of fibers (e.g. Meibom et al., 2006) and, thus, the formation of aragonite by corals is a process distinct from the inorganic precipitation of aragonite from a highly supersaturated solution. Lacking from these studies, however, is a comparison between coral aragonite and synthetic aragonite precipitated from a highly supersaturated solution.

Here, results from such a study are presented. A range of imaging techniques: light microscopy, fluorescence microscopy, scanning electron microscopy (SEM) and atomic force microscopy (AFM), as well as elemental measurements using secondary ion mass spectrometry (SIMS) were employed to characterize the morphology and chemistry of synthetic (i.e. precipitated experimentally from seawater) and biogenic aragonites (i.e. precipitated by tropical corals).

2. METHODS

2.1. Synthetic aragonite precipitates

Techniques employed for precipitating synthetic aragonites from seawater were adopted from Kinsman and Holland (1969), as modified by Gaetani and Cohen (2006). The details for some of the experiments employed in this study differ slightly, so the specifics of each experiment are briefly described below.

Aragonite was precipitated from 0.45 μm filtered Vineyard Sound (Woods Hole, MA, USA) seawater (salinity 30.8–32.1). A PTFE or PET beaker containing 600 ml of filtered seawater was placed into a Lauda RE-106 isothermal bath, and stirred continuously with a PTFE stirrer. Note that initial experiments showed no effect of the plastic type on the development of a run, so later runs used transparent PET which allowed the onset of crystallization to be more readily assessed. Several different experiments were conducted, each representing one of three categories of experiments.

2.1.1. Timing of precipitate formation

To establish the relationship between fluid chemistry, crystal morphology and crystal composition, a pair of Sr isotope spikes were used in Experiment 1 to constrain the timing of precipitation. In Experiment 1, seawater was held at 25 °C in a PTFE beaker and stirred continuously at 40 rpm. Evaporated seawater and a 0.04 M Na_2CO_3 (Alfa Aesar) solution were introduced simultaneously at a rate of 4.8 ml h^{-1} for 37.5 h. Evaporated seawater was prepared by placing seawater in a PTFE beaker held in a 80 °C water bath (for some experiments, concentrated seawater was prepared in a polypropylene beaker held at 60 °C—similar results were obtained with both methods) until half the mass had been lost. The evaporated seawater was used to maintain the salinity at a roughly constant value as the 0.04 M Na_2CO_3 solution was added (initial salinity 31.85, final salinity 31.88). During this experiment, strontium isotope spikes (^{84}Sr and ^{86}Sr) were introduced at separate times into the seawater mixture. These spikes are incorporated into the growing crystals and serve as a marker from which the timing and rate of crystal growth can be determined. After the first 65 ml were added, 100 μl of a ^{84}Sr solution was added to nearly double the ^{84}Sr concentration. After the final Na_2CO_3 addition, 100 μl of ^{86}Sr was added to approximately double the ^{86}Sr concentration. Precipitation of aragonite was allowed to proceed for an additional 24 h after pumping stopped. Precipitates were separated from solution by filtration through a 0.7 μm glass fiber filter and rinsed briefly with distilled water and ethanol. Sr isotopes were purchased from Oak Ridge National Lab.

2.1.2. Cyclic saturation states

In Experiments 2 and 3, the saturation state was cycled over the course of each run by pulsed addition of Na_2CO_3 to produce precipitates with alternating regions of growth formed at high and low saturation states (bands). Experiment 2 was conducted under variable salinity conditions at either 55 °C or 65 °C. A 0.01 M Na_2CO_3 solution was added to the beaker of seawater in two 125 ml steps, 1 day apart, at a rate of ~1 ml min^{-1}, and the solution was stirred at 120 rpm. This experiment is described in detail by Gaetani and Cohen (2006). In Experiment 3, a ~0.04 M Na_2CO_3 solution and evaporated seawater were added in two steps to seawater (initial salinity 31.3, final 32.1) held in a PET beaker in a 25°C water bath. The solution was stirred continuously at 120 rpm. ^{84}Sr, ^{86}Sr and ^{137}Ba isotope spikes were added at different times over the course of each run. Pumping durations, volumes, times of isotope spike addition and solution chemistry are given in the electronic annex Table EA1, Fig. EA1 and EA2.

2.1.3. Effect of pumping rate on morphology

To examine the effects of saturation state on the morphology of precipitates, Experiments 4, 5, 6 and 7 were conducted using different pumping rates to generate different 'steady state' conditions under which the bulk of the precipitate formed in each experiment. In Experiments 4, 5 and 6, a syringe pump was used to continuously add a ~0.04 M Na_2CO_3 solution and evaporated seawater to seawater in a PTFE beaker (final salinities ranged from 31.4 to 32.8). Experiments 4–6 were conducted at 25 °C while stirring at 120 rpm. Pumping rates for the bulk of each experiment were: high = 360 ml h^{-1} for Experiment 4, intermedi-

ate = 2 ml h^{-1} for Experiment 5, and low = 0.2 ml h^{-1} for Experiment 6. Injection volumes ranged from 76 to 181 ml. Aragonite seed crystals (fish otoliths, cleaned by sonication and ground to 5–300 μm) were added to Experiment 6 in an effort to speed nucleation. Precipitation was allowed to continue for 21–35 h after pumping stopped.

In Experiment 7, a ~0.04 M Na_2CO_3 solution and evaporated seawater were added continuously at a rate of 0.4 ml/h to seawater (initial salinity 31.3, final 33.5) held in a PET beaker in a 25 °C water bath. The solution was stirred continuously at 120 rpm. Isotope spikes (^{84}Sr, ^{86}Sr, and ^{137}Ba) were added at different times over the course of the run. Pumping durations, volumes, times of isotope spike addition and solution chemistry are given in the Table EA1, Fig. EA1 and EA2.

2.1.4. Growth conditions of the synthetic aragonites

Solution pH (NBS scale) was monitored throughout aragonite synthesis Experiments 1, 3, 4, 5, 6, and 7 (Table 1, Fig. 1a, Electronic annex Table EA-1, Fig. EA-1). Saturation state was also determined periodically by measuring alkalinity and calcium concentration, data are presented in Fig. 1a, Table EA-1 and Figure EA-1. Solution pH increased as Na_2CO_3 was added until nucleation occurred. Following nucleation, solution pH fell to a quasi-steady state value related to pumping rate (Fig. EA-2). At the end of each experiment, when pumping of the Na_2CO_3 solution ceased, the pH of each experimental solution dropped but remained above the initial value (~8.0). Saturation states follow a trend similar to that seen in pH data (Table EA-1). Solution chemistry for some of the runs and starting materials are provided in Table EA-1. Raman spectra of the precipitates reveal a peak at ~705 cm^{-1}, consistent with the presence of aragonite (e.g. Clarkson et al., 1992). Raman data are presented in Fig. EA-3.

2.2. Coral samples

The skeletons of three coral species *Diploria labyrinthiformis* (brain coral), *Porites lutea* and *Porites solida* were examined. *D. labyrinthiformis* (sample #BER002) was collected live from John Smith's Bay, Bermuda at a depth of 13 m (Cohen et al., 2004). *Porites lutea* (sample #JA4) was collected live from Johnston Atoll, north central Pacific (Cohen et al., 2001). *Porites solida* (sample #141-B05-53) was provided by Dr David Barnes (AIMS). *Porites solida* was collected live in June 1989 from the Great Barrier Reef, Australia (151°E, 21°S) (Cohen and Hart, 1997).

Table 1
pH (NBS scale) values measured near the time of nucleation, and following nucleation while pumping continued (representing the period during which most growth occurred) for each synthetic precipitation run. Nucleation represents the peak in pH values, while growth is an average of pH values measured following nucleation, standard deviation is given in parenthesis.

Run	Nucleation	Growth
Experiment 1.	9.2	8.9 (.1)
Experiment 4. high pumping rate	9.6	9.5 (.1)
Experiment 5. intermediate pumping rate	9.2	8.8 (.2)
Experiment 6. low pumping rate	8.9	8.3 (.2)
Experiment 7. low pump rate	8.7	8.16 (.02)

2.3. Polishing of synthetic and coral aragonites

All samples were placed inside 2.5 cm Al rings and imbedded in Epo-thin epoxy (Buehler) prior to polishing. Double sided adhesive tape (Buehler) was used to hold specimens and rings in place as epoxy was added. Corals were prepared by breaking ~1 cm^2 sections of coral skeleton, roughly parallel to the axis of growth, and placing the sections on the adhesive. Synthetic aragonites were mounted by applying a light dusting of grains to the adhesive. Polishing was done on nylon cloths with alumina (Mark V Laboratories) suspended in heptane (Alfa Aesar), except for the coral used for light microscopy and SIMS analysis, which was prepared commercially (OMNI Laboratories). A small amount of water was used to initially apply the alumina grit. Each specimen was polished through a range of grit sizes down to 0.3 μm, or 0.05 μm for specimens imaged with Atomic Force Microscopy. Following mechanical polishing, a final polish with 0.02 μm colloidal silica was applied to all samples, with the exception of those used in the acridine staining experiments (see below). Colloidal silica is a water-based polishing compound, hence there is dissolution of the aragonite in addition to mechanical abrasion. An initial comparison of different techniques revealed that a colloidal silica etch on the synthetic grains gave good AFM images (Fig. EA-4). In addition to the dissolution induced by the colloidal silica, corals were etched for 30–50 s prior to AFM imaging using 0.1% formic acid and 3% gluteraldehyde in water (Cuif et al., 2003). Etching was stopped by rinsing with water. This additional etching step improved contrast between features in coral samples, as observed in preliminary comparisons of different techniques (Fig. EA-5). Samples for SEM imaging were either mounted on SEM stubs without any further preparation, or were polished as above and etched for 10s with .1 N HCl.

2.4. Imaging

2.4.1. Light microscopy and scanning electron microscopy (SEM)

Polished sections of corals and synthetic aragonites were examined in reflected and transmitted light with a Nikon Eclipse E 600 Polarizing microscope equipped with a Spot Insight color CCD camera. SEM imaging of Au/Pd coated samples (both polished and unpolished) was done using a JEOL 840 scanning electron microscope. Accelerating voltage was 15 kV unless otherwise specified.

2.4.2. Acridine orange staining

Acridine orange staining of polished sections of corals and synthetic aragonites was carried out following the protocol of Stolarski (2003). Acridine orange is a dye used to stain coral skeletons and regions retaining acridine orange are thought to have high concentrations of organic materials. Corals were etched prior to staining by placing samples in distilled water overnight to lightly etch the surface. Sam-

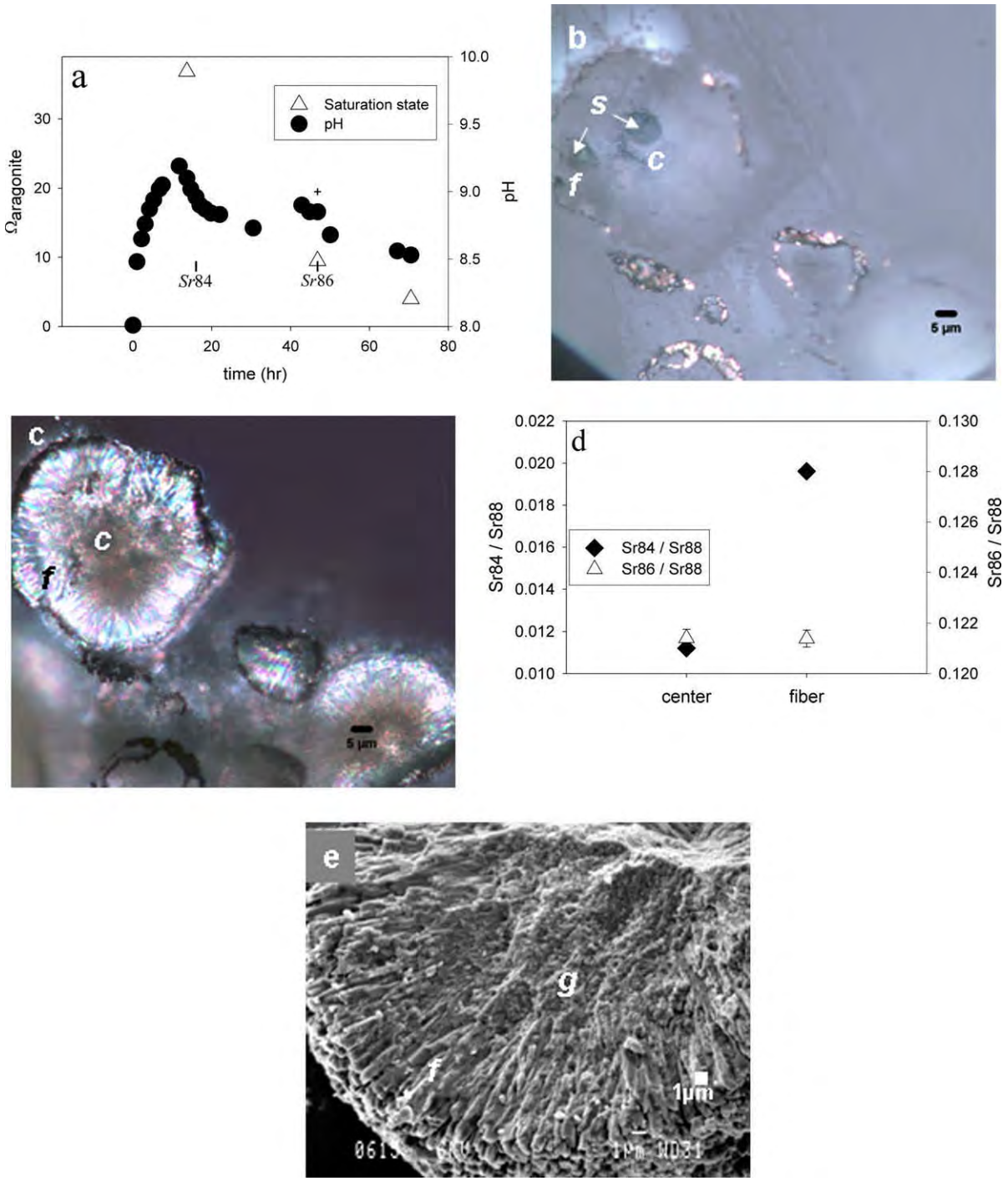

Fig. 1. Precipitation conditions, light microscopy images, isotope ratios, and SEM images for synthetic aragonite grains formed in Experiment 1. (a) Saturation state (open triangles) and pH (black circles) over the course of Experiment 1, the time at which pumping stopped is indicated by the cross, the times at which isotope spikes were added are indicated by vertical lines labeled with the isotope added. Errors are small relative to symbol size. (b) A grain with ionprobe spots (*s*) near the center (*c*), and in a fibrous region (*f*) imaged with reflected light. (c) The same grain shown in b, imaged with cross-polarized transmitted light, which better shows the fibers (*f*). (d) Sr isotope ratios determined for the same spots used for M/Ca data in Fig. 4. Sr84/88 ratios (black circles) are significantly higher in the fibers than the centers ($p < 0.01$), while Sr86/88 ratios (open triangles) show no significant difference. Points are means, error bars are standard error. (e) SEM image of a grain formed in Experiment 1, which shows fibers (*f*) radiating out from a granular center (*g*). Accelerating voltage for this image is 6 kV.

ples were overlain with a 1% acridine orange (Alfa Aesar) aqueous solution, allowed to sit for 5 min, briefly rinsed, blotted dry and imaged on a Zeiss Axiovert inverted microscope using a mercury vapor UV source and FITC short pass filter set. Images were captured using either a Sony color CCD camera or a Canon Digital Rebel XTi camera.

2.4.3. Atomic force microscopy (AFM)

AFM imaging of polished sections of corals and synthetic aragonites was conducted at The University of Western Ontario using a Veeco MultiMode AFM and at Woods Hole Oceanographic Institution using a Veeco Dimension 3100 AFM equipped with silicon nitride tips (Veeco NP-S, with a ~10 nm radius of curvature, and BudgetSensors, with a ~20 nm radius of curvature, respectively). All images were acquired in contact mode. Image capture and processing were performed using Digital Instruments NanoScope software.

2.5. Secondary ion mass spectrometry (SIMS ion microprobe)

M/Ca (Mg/Ca, Sr/Ca, and Ba/Ca) ratios of the coral *Porites lutea* and synthetic aragonite formed in Experiment 1 were analyzed with a Cameca 3f Ion Microprobe. Following a 3-min pre-burn to remove the gold coating, a single spot on the coral sample was illuminated with the primary ion beam while measuring secondary ion intensities for ^{24}Mg, ^{88}Sr, ^{138}Ba and ^{42}Ca (Gaetani and Cohen, 2006). A 2.5 nA O-primary ion beam, ~10 μm in diameter, was accelerated at 12.7 keV. Secondary ion intensities were measured using a −80 eV offset from the peak of the energy distribution. This energy filtering reduces molecular interferences to <0.1% (Hart and Cohen, 1996).

In addition to the M/Ca ratios, $^{84}Sr/^{88}Sr$ and $^{86}Sr/^{88}Sr$ ratios were also determined in the synthetic aragonite grains in order to locate the isotope spikes. Individual synthetic aragonite grains were targeted with a 4nA O-primary ion beam, ~7 μm in diameter, accelerated at 12.7 keV. Secondary ion intensities (^{24}Mg, ^{84}Sr, ^{86}Sr, ^{88}Sr, ^{138}Ba and ^{40}Ca) were measured using a −90 eV offset from the peak of the energy distribution. Ion probe intensity ratios were converted to molar ratios using the carbonatite standard OKA, which was assumed to be homogeneous with a Mg/Ca ratio of 4.47 mmol/mol, a Sr/Ca ratio of 19.3 mmol/mol and a Ba/Ca ratio of 1.61 mmol/mol (Gaetani and Cohen, 2006). At least eight measurements of the OKA standard were made each day samples were measured, average intensity ratios measured at the time of coral data collection were: 0.202, 2.62 and 0.16 for $^{24}Mg/^{42}Ca$, $^{88}Sr/^{42}Ca$ and $^{138}Ba/^{42}Ca$, respectively; at the time of synthetic aragonite measurements, values were: 0.0018, 0.014 and 0.00072 for $^{24}Mg/^{40}Ca$, $^{88}Sr/^{40}Ca$ and $^{138}Ba/^{40}Ca$, respectively. In all cases, standard errors were less 3%. Means were compared using a t-test (Zar, 1984).

3. RESULTS

3.1. Synthetic aragonite

The individual grains formed in Experiment 1 are roughly circular; in polarized light, the center (*c*) of each grain is distinguished by a dark region (Fig 1c). Radiating out from this center are aragonite fibers (*f*). The morphology of the grains is consistent with the spherulitic morphology found in a range of minerals i.e. a radially disposed array of acicular crystals that emerge from a common center or nucleation region (e.g., Cross, 1891; Iddings 1891), typical of crystals formed rapidly from a supersaturated or supercooled solution (Lofgren, 1971; Sunagawa, 1987; Lowenstam and Weiner, 1989). Using SEM (Fig 1e), it can be seen that the material found in the center is sub-micron in size and has a granular (*g*) appearance, while the fibers (*f*) radiating out from the center are ~1 μm wide and several microns long.

3.1.1. Timing of growth

The Sr isotope ratios in the center of each grain formed during Experiment 1 reflect natural abundances (Fig. 1d), indicating that the centers formed prior to the addition of the ^{84}Sr isotope spike. The ^{84}Sr spike is present in the fibrous aragonite between the centers and the edge of the spherulite, indicating that fibers formed after the centers but prior to the addition of ^{86}Sr (Fig. 1d). High ^{86}Sr was found only at the edges of a few spherulites, indicating that very little aragonite precipitated following the addition of ^{86}Sr (data not shown).

The presence of spikes allows the crystal morphology to be correlated with the solution chemistry. In Experiment 1, solution pH increased as Na_2CO_3 was added until nucleation occurred (Fig. 1a). The granular centers of the aragonite grains formed during this high pH period (pH ~9.2), as indicated by the absence of the ^{84}Sr spike. Following nucleation, solution pH fell to a quasi-steady state value related to pumping rate. Fibrous aragonite grew during this period when pH was ~8.9, as indicated by the presence of the ^{84}Sr but absence of ^{86}Sr spikes (Fig. 1b–d). Very little aragonite was deposited near the end of the experiment after pumping stopped when pH was ~8.6, as indicated by the scarcity of elevated ^{86}Sr.

3.1.2. Stepped pumping produces banded spherulites

Fig. 2a represents a cross section through a composite of three synthetic aragonite grains formed in Experiment 2 at 65 °C. Fig. 2b shows a cross section through a single synthetic aragonite grain formed in Experiment 3 at 25 °C. The two pumping cycles used in each of these experiments lead to two cycles of high and low saturation state over the course of aragonite precipitation. The synthetic aragonite grains precipitated in these experiments are similar to those in Fig. 1c, but an additional feature, a single dark band running perpendicular to the axis of fiber growth, is present (Fig. 2a and b). In these spherulites, the dark band is located ~15 μm from the outer edge of each grain formed in Experiment 2, and ~4 μm from the edge for grains formed in Experiment 3.

Fig. 2c shows a fluorescence image of a synthetic aragonite grain, grown in Experiment 2 by cyclic pumping, stained with acridine orange. Addition of acridine orange results in increased fluorescence associated with the center (*c*) and dark bands (arrow) observed in light microscopy.

Fig. 2d shows an SEM image of a polished, HCl etched aragonite grain formed in Experiment 3 by cyclic pumping. The central region is composed of granular to finely fibrous material. Fine fibers radiate out from the center and become larger till reaching the band (arrow). Following the band, fibers again radiate out to the edge of the aragonite grain.

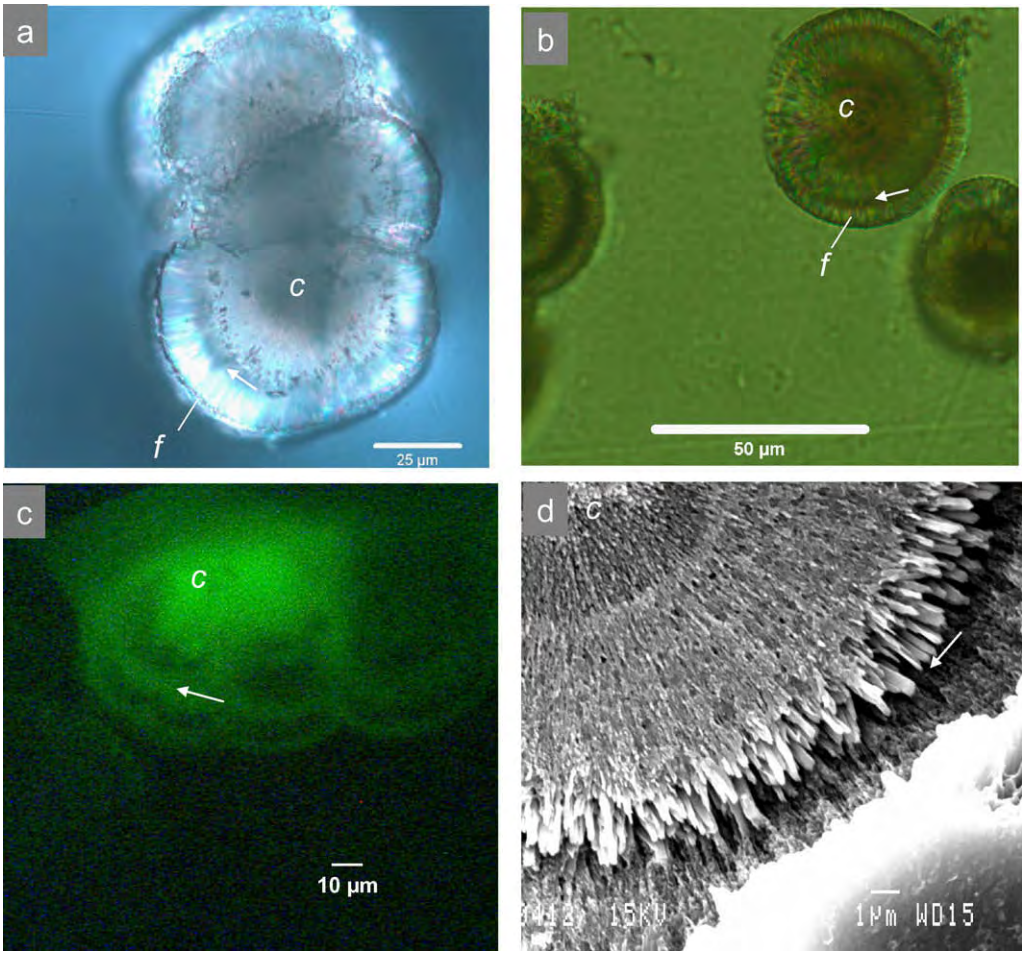

Fig. 2. Light microscopy and SEM images of synthetic aragonites formed in Experiments 2 (a,c) and 3 (b,d). (a and b) Transmitted polarized light micrographs of polished sections showing bands (indicated by arrows) perpendicular to the direction of fibrous aragonite (*f*) growth and centers (*c*) in synthetic aragonite grains formed in: a. Experiment 2 at 65 °C, and b. Experiment 3. (c) Fluorescence microscopy image showing fluorescent bands (arrow) and center (*c*) in an acridine orange stained synthetic aragonite grown in Experiment 2 at 65 °C. (d) SEM image of a synthetic aragonite grain formed in Experiment 3 showing a center (c), and a band (arrow) with fibers on either side of the band. Specimen was polished and etched with .1 N HCl for 10 s.

3.1.3. SEM imaging

SEM images of synthetic aragonites precipitated in Experiment 4 (Fig. 3a), 5 (Fig 3b), 6 (seeded, Fig. 3d) and 7 (Fig. 3c) at high (Fig. 3a), medium (Fig. 3b), and low (Fig. 3c and d) pumping rates reveal a systematic change in crystal morphology with pumping rate, and thus pH (Fig. EA 1,2). Synthetic aragonite grains formed in the high pumping rate run (~pH 9.5) lack well-defined crystals, and are composed of very fine fibers (Fig. 3a). Synthetic grains grown at intermediate pumping rates (pH ~8.8) are composed of well-defined aragonite blades, 1–2 µm wide and several microns long and there are clear grain boundaries between individual fibers (Fig. 3b). Synthetic aragonites precipitated in the low pumping rate runs (pH ~8.2 for Fig. 3c, ~8.3 for Fig. 3d) are composed of broad (~2 µm wide), highly faceted fibers that are widely separated (Fig. 3c and d). The fibers emerge from a common center, as shown in Fig. 3c and the inset in Fig. 3d.

3.1.4. AFM imaging

AFM height images of synthetic aragonite grains etched with colloidal silica show similar changes in crystal morphology with pumping rate to those seen with SEM (Fig. 4). In all images, height is on a scale of 0–400 nm, with the highest regions shown as white, lowest as black. The length-scale, in microns, is shown on the *x* and *y* axes of each image.

In Fig. 4a, an AFM image of two synthetic aragonite grains precipitated with two stepped additions of sodium carbonate (Experiment 2) is shown. The grains have roughly circular centers (*c*) (only partly visible at the base of the image) surrounded by two layers of fibrous aragonite (*f*). A darker region of granular material, ~10 µm wide (arrow), separates the inner and outer fibrous layers. Granular materials are sub-micron in size, while fibers are micron scale features—typically 8 µm long, and 0.7 µm wide.

Fig. 4b shows a synthetic aragonite formed in a high pumping rate run (pH ~9.5, Experiment 4). The entire sur-

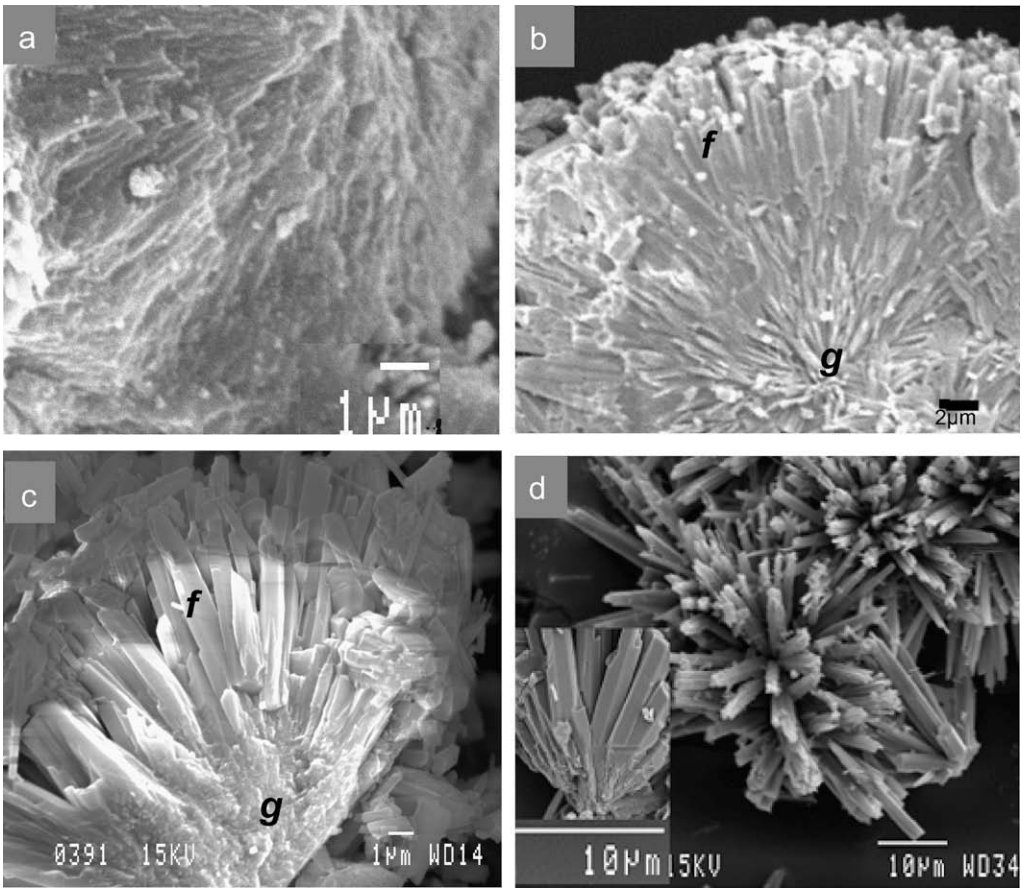

Fig. 3. SEM images of synthetic aragonite grains formed in Experiments 4 (a), 5 (b), 7 (c), 6 (d) showing two crystal morphologies—granular (*g*) and blade-like fibers (*f*). (a) Aragonite grain formed at a high pumping rate in Experiment 4 exhibiting a granular to finely fibrous surface. (b) Aragonite grain formed at a moderate pumping rate in Experiment 5, exhibiting blade like crystals. (c) A low pumping rate grain grown without seed crystals in Experiment 7 showing widely spaced blades arising from a granular center. (d) A low pumping rate grain grown with seed crystals in Experiment 6 showing widely spaced blades arising from a common center (inset). Accelerating voltages are 6 kV for (b) and the inset in (d), all others are at 15 kV.

face of the grain is rough and granular (*g*), lacking defined fibers. In Fig. 4c, a synthetic aragonite formed in a low pumping rate (pH ~8.3, Experiment 6) run is imaged. Granular material (*g*) is restricted to near the center of

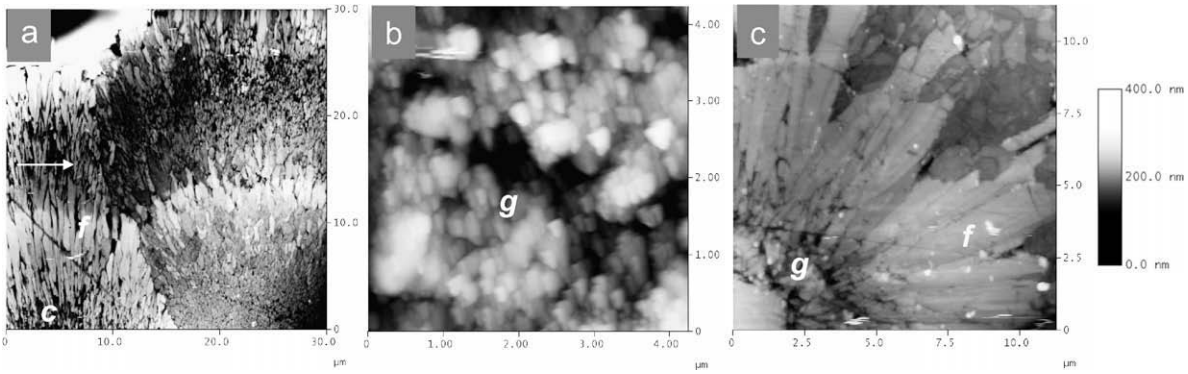

Fig. 4. AFM height images of synthetic aragonite grains from Experiment 2 (a), 4 (b), and 6 (c) showing centers (*c*), dark bands (arrows), granular (*g*) and fibrous aragonite (*f*). (a) Banded synthetic aragonite formed in Experiment 2. (b) Synthetic aragonite precipitated in Experiment 4 at high pumping rate showing a rough, granular surface. (c) Synthetic aragonite precipitated at low pumping rate (Experiment 6) showing blade-like fibers (*f*) and a granular center (*g*). All specimens were polished with colloidal silica.

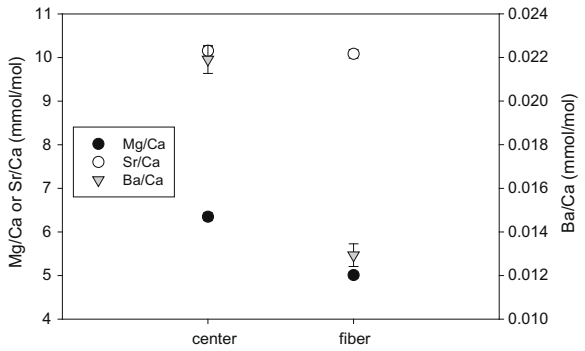

Fig. 5. M/Ca ratios determined with SIMS at centers and in fibers of synthetic aragonite grains formed in Experiment 1. Mg/Ca and Ba/Ca ratios are higher at centers than in adjacent fibers ($p < 0.01$). Sr/Ca ratios show no significant difference with respect to location. Symbols represent means of 4 different grains (3 for Ba), error bars represent 1 standard error.

the grain. The bulk of the grain is made up of broad well-defined fibers (*f*) that emerge from the granular materials and radiate outward to the edge (Fig. 4c).

3.1.5. M/Ca ratios

Mg/Ca, Sr/Ca, and Ba/Ca ratios in centers and fibers of synthetic aragonites grown in Experiment 1 were measured by SIMS ion microprobe (Fig. 5). Discrete analyses of centers of synthetic grains were possible with the 7 μm diameter analytical spot. Similarly, discrete analyses of aragonite fibers emerging from the centers of synthetic aragonite grains were made. The Mg/Ca and Ba/Ca ratios are higher in the centers of the grains (6.35 ± 0.09 and 0.022 ± 0.001 mmol/mol, respectively) than in the surrounding fibers (5.01 ± 0.07 and 0.013 ± 0.001 mmol/mol, respectively) ($p < 0.01$). Sr/Ca ratios show no significant difference between centers (10.2 ± 0.1 mmol/mol) and fibers (10.1 ± 0.1 mmol/mol).

3.2. Coral aragonite

3.2.1. Light microscopy

In Fig. 6a, the arrangement of aragonite crystals in a coral skeleton is seen in a cross section through a synapticulum or horizontal cross-bar of *Porites solida*. In polarized light, the center of calcification (*c*) appears dark with poorly defined edges. Radiating outward from the center of calcification are aragonite fibers (*f*). This observation is consistent with the description of coral sclerodermites (Wells, 1956). In this section, the fibers are interrupted by fine dark bands (arrow), ~2 μm apart and aligned perpendicular to the axis of crystal extension.

3.2.2. Fluorescence imaging

Fig. 6b shows a fluorescence image of a section of the coral *Diploria labyrinthiformis* stained with acridine orange. There is an increase in fluorescence associated with the centers of calcification (*c*) and dark bands (arrow) following acridine staining. This observation is consistent with that of Stolarski (2003).

3.2.3. SEM imaging

Fig. 7 shows SEM images of dissepiments (horizontal sheets) in the skeletons of *Diploria labyrinthiformis* (Fig. 7a) and *Porites lutea* (Fig. 7b). The dissepiments are composed of two layers (as identified by Barnes, 1971). The primary (base) layer is built of small granular materials (*g*), <1 μm diameter. The secondary layer is composed of broad blade-like fibers (*f*), each ~1–2 μm wide and several microns long.

3.2.4. AFM imaging

In Fig. 8, AFM height images of skeletal cross sections of *Diploria* (Fig. 8a and c) and *Porites* (Fig. 8b,d) reveal centers of calcification as regions of low relief (dark) and bands of aragonite fibers as regions of higher

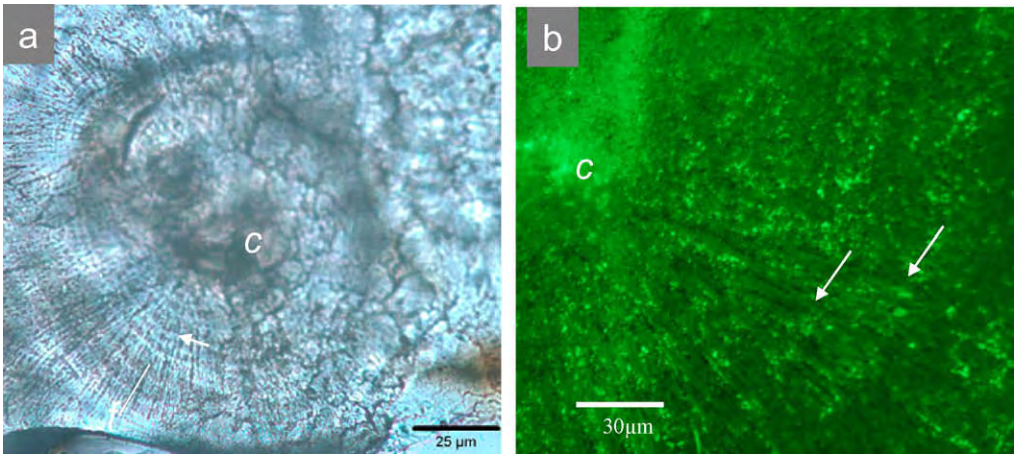

Fig. 6. Light microscopy images of corals. (a) Transmitted polarized light micrograph of polished section showing bands (arrow) perpendicular to the direction of fibrous aragonite (*f*) growth and center of calcification (*c*) in *Porites lutea.* (b) Fluorescence microscopy image showing fluorescent bands (arrows) and center (*c*) in an acridine orange stained *Diploria labyrinthiformis* specimen. (For interpretation of the references to color in this figure legend, the reader is referred to the web version of this paper.)

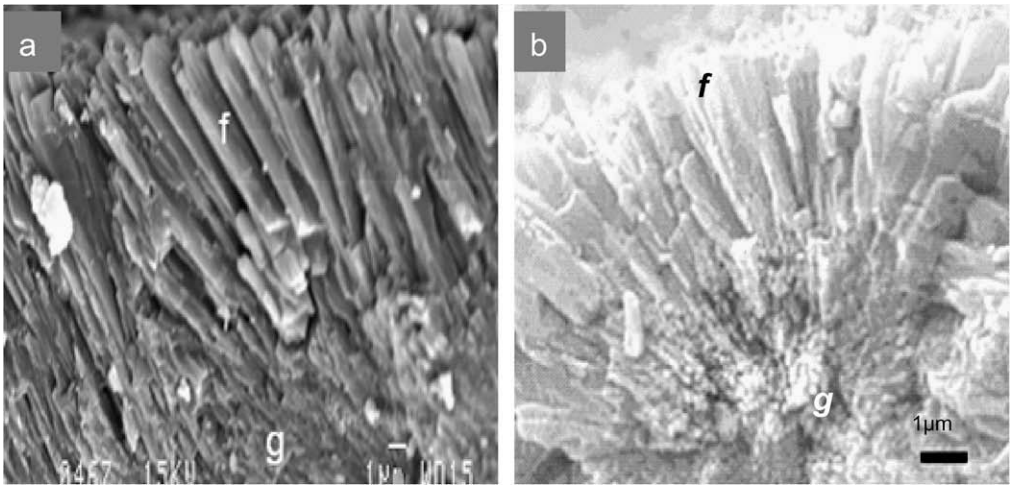

Fig. 7. SEM images showing two crystal morphologies in coral dissepiments—granular (*g*) and blade-like fibers (*f*) in a: *Diploria labyrinthiformis*, (b) *Porites lutea.*

relief (light). Fine dark bands that transect the aragonite fibers are also visible as regions of low relief. Materials occupying centers of calcification (Fig. 8d) and dark bands (Fig. 8c) are small and granular in texture. Conversely, in both species, the light bands are packed with larger elongated fibers

In Fig. 8a, a cross section through a *Diploria* septotheca, the direction of vertical growth is from the lower right to the upper left of the image. Centers of calcification (*c*) appear crescent-shaped, and form a line of discrete dark crescents up the middle of the septum. Centers of calcification are continuous with fine dark bands (arrow) that extend toward the edge of the septotheca. The width of the fine bands decreases with distance from the centers of calcification. Near the centers of calcification, the fine bands are 5.3 ± 0.4 μm ($n = 10$) wide. At the outer edge of the septotheca, the width of the bands is not discernible. As the width of the dark bands decrease, the distinction between light bands of aragonite fibers and the dark bands that interrupt them becomes less distinct. Near the center of the septotheca, the transition between light fibrous bands and fine dark bands is abrupt. Toward the edge of the septotheca, the fibers appear continuous, cutting across dark bands.

In the *Porites* septum, the centers of calcification are oval rather than crescent shaped (Fig. 8b). Fine dark bands (arrows) are present in the fibers but these are not as clearly defined in this *Porites* specimen as they are in the *Diploria* skeleton.

3.2.5. *M/Ca ratios*

Selective analysis of Mg/Ca, Sr/Ca, and Ba/Ca ratios in centers of calcification and surrounding fibers of a *Porites* skeleton are shown in Fig. 9. Mg/Ca, Sr/Ca, and Ba/Ca ratios are higher in the centers of calcification (4.91 ± 0.02, 8.98 ± 0.03, and 0.0058 ± 0.0001 mmol/mol, respectively) than in adjacent fibers (3.88 ± 0.01, 8.63 ± 0.03, and 0.0034 ± 0.0001 mmol/mol, respectively). For all M/Ca ratios measured, the value for the centers was significantly higher than for the fibers ($p < 0.01$).

4. DISCUSSION

4.1. Synthetic aragonite

Synthetic aragonite crystal morphology and composition are coupled to the pH and saturation state of the fluid from which the crystals grew. Within a single spherulite, the centers packed with sub-micron sized granular materials form when the saturation state of the fluid is very high. Growth of fibrous crystals outward from the centers occurs when the saturation state of the fluid has decreased following nucleation. The supersaturation achieved prior to nucleation depends on the rate at which Na_2CO_3 is added; the faster the addition of Na_2CO_3, the higher the saturation state achieved prior to nucleation, consistent with the work of Prieto and others (1989, 1994). In addition, the morphology of the spherulite (i.e., open, coarse versus closed, fine) and the size and shape of the aragonite needles within the spherulites change systematically with the pH (saturation state) of the seawater in which they grew. In the high pH, high saturation state experiments, fine closed spherulites form that contain densely packed fibers with ill-defined grain boundaries (Fig. 3a). Conversely, spherulites formed at low pH are typically open and coarse, containing fewer, broad, faceted fibers (Fig. 3b). This observation is consistent with systematic variations in crystal morphologies observed in non-$CaCO_3$ minerals and polymers with increasing degrees of supercooling or with increasing supersaturation (e.g., Keith and Padden, 1963; Lofgren, 1971, 1974; Chernov, 1984; Sunagawa, 1987), and reflects the crystal morphology that allows the maximum growth rate under those conditions (e.g., Tiller, 1964). The formation of smooth sides and development of facets in the lower pumping rate experiments likely reflects a change in growth mechanism, with a rough interface associated with spherulitic growth transitioning to a smooth interface dominated by dislocation growth controlling step flow on faceted crystals (e.g. Sunagawa, 1981, Sunagawa, 1987; Prieto et al., 1989).

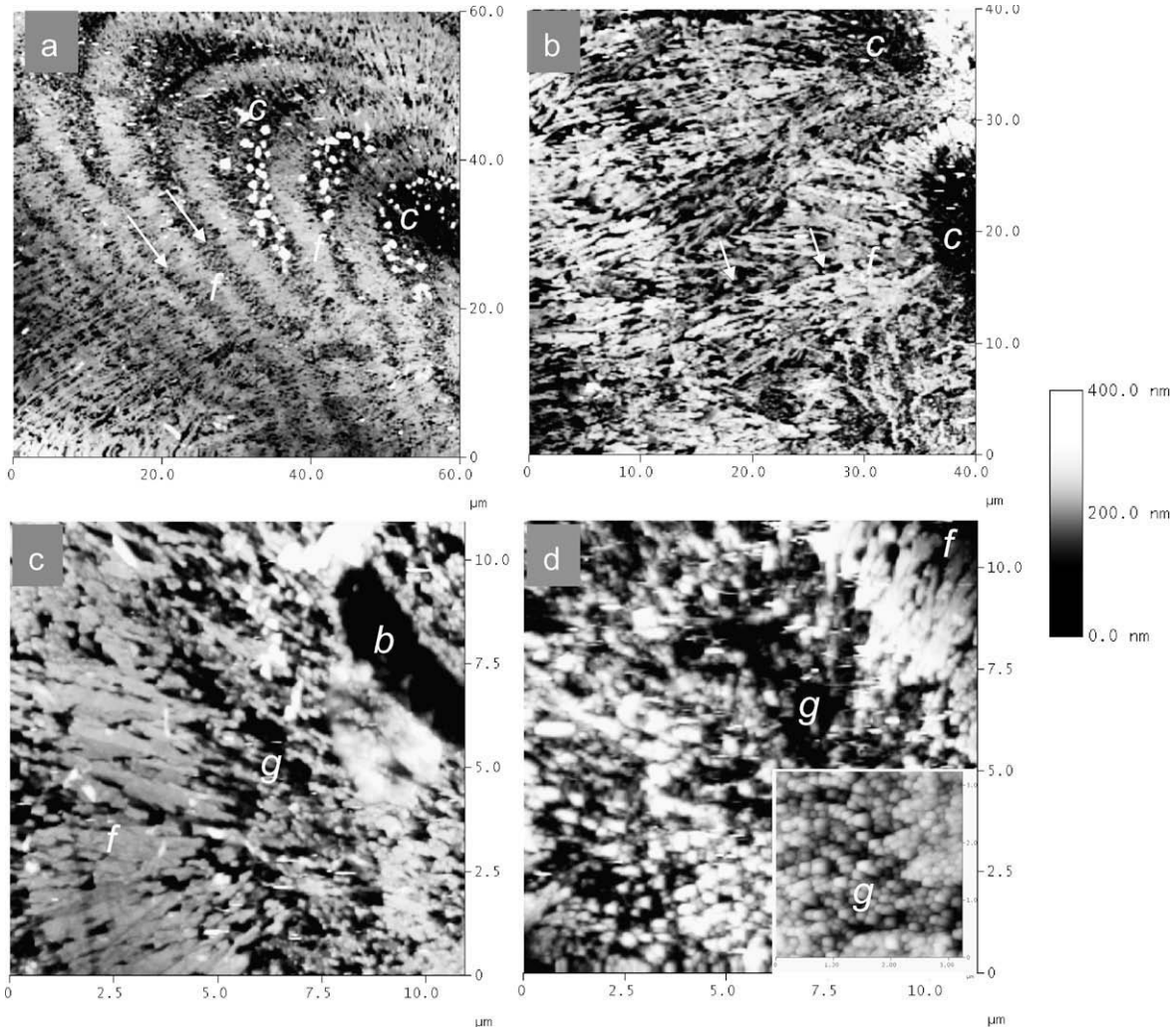

Fig. 8. AFM height images of corals centers (*c*), dark bands (arrows), and fibrous aragonite (*f*). (a) *Diploria labyrinthiformis* septotheca showing a banded region of the skeleton prepared with an acid etch, note the transition from complete separation of fibers by dark bands near centers, to fibers cutting across bands near the edges. (b) *Porites solida* showing centers of calcification and banded growth. (c) Magnified view of *Diploria* showing a granular band (*g*), a fibrous band (*f*) and a boring (*b*). (d) Magnified view of *Porites solida* center with higher magnification inset. Specimen preparation was as follows: for a and c, final polish was with .05 μm alumina on a microcloth, followed by etching 50 s with .1% formic acid, 3% gluteraldehyde, etching stopped by rinsing with water; for (b) and (d), a 30 s etch was used.

Measurements of Mg/Ca, Sr/Ca, and Ba/Ca show that the Mg/Ca and Ba/Ca ratios are significantly elevated at the center of the spherulite relative to the fibers (Fig. 5). In each experiment, the highest saturation state occurs at the onset of nucleation, thus the center of each spherulite contains crystals expected to have the highest growth/precipitation rate (Burton and Walter, 1987) (though it should be noted that growth mechanism and relative areas of different crystal faces also change, and could influence composition as well). This relationship between crystal growth rate and M/Ca ratio is consistent with the growth rate dependency expected for Mg/Ca and Ba/Ca, as all M/Ca ratios are expected to increase with higher growth rates due to more efficient entrapment of an impurity enriched mineral surface layer composition at higher crystal growth rates (Watson 2004; Gaetani and Cohen, 2006). Gabitov et al. (2006, 2008) showed that the growth dependence of Mg/Ca in aragonite is much higher than that of Sr/Ca. Therefore, the absence of a significant elevation of Sr/Ca in the centers found in this study is consistent with their data.

4.2. Coral aragonite

Data presented here concur with earlier observations that coral sclerodermites consist of aragonite needles radiating out from regions of fine granular materials or 'nanocrystals' (Figs. 6–8) (Vaughan and Wells, 1943; Wainwright, 1964; Constantz, 1986; Cohen et al., 2001; Clode and Marshall, 2003). The sub-micron-sized granular materials are found at the base of dissepiments (Fig. 7a,b), in the centers of calcification (Fig. 8) and in the fine bands that cut across aragonite fibers (Fig. 8).

Regions associated with granular materials are also associated with an increase in fluorescence following acri-

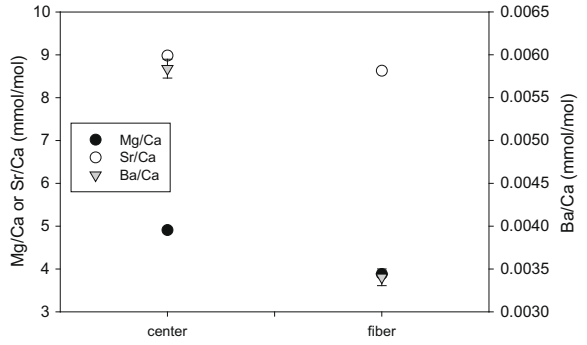

Fig. 9. M/Ca ratios measured near centers and in adjacent fibrous aragonite of *Porites lutea*. Mg/Ca, Sr/Ca, and Ba/Ca ratios are higher at centers than in adjacent fibers ($p < 0.01$). Symbols represent the average of measurements taken at 4 different locations within a single specimen; error bars represent 1 standard error.

dine orange staining (Fig. 6b), which is consistent with the results of Gautret et al. (2000) and Stolarski (2003). Mg/Ca, Sr/Ca, and Ba/Ca ratios are found to increase at the centers of calcification relative to adjacent fibers (Fig. 9), which is consistent with the findings of Meibom et al. (2004, 2006).

4.3. Results of inorganic precipitation experiments in relation to coral skeleton morphology and composition

Aragonite crystals formed by experimental precipitation from a supersaturated seawater solution and the aragonite crystals formed by living corals during skeletogenesis share several morphological and compositional features. Both the synthetic aragonites precipitated in this study and the coral sclerodermites are composed of two distinct types of crystals: sub-micron-sized granular materials and larger elongate fibrous crystals that radiate out from the granular materials. Granular materials are found near the centers of synthetic grains, in the centers of calcification of corals, and in dark bands found both in corals, and in the synthetic aragonites formed by stepped additions of Na_2CO_3. Higher Mg/Ca and Ba/Ca ratios and acridine orange staining correspond to regions of granular materials in both synthetic aragonite (Fig. 2c, 5) and corals (Fig. 6b, 9).

Since the composition and morphology of crystals provide insights into the conditions under which they grew (e.g., Lofgren, 1971; Reddy and Nancollas, 1976; Marsh, 1988; Prieto et al., 1997; Marsh, 1998; Cohen and McConnaughey, 2003; Tong et al., 2004; Wasylenki et al., 2005), the observed crystal morphologies and compositions associated with known conditions in the synthetic experiments may be useful in assigning possible conditions of formation of naturally formed precipitates.

The similarity between the finely fibrous to granular materials at the centers of spherulites (Fig. 4a), grains formed at very high pH (Fig. 4b) and materials occupying centers of calcification, fine bands, and the base layer of dissepiments in coral skeletons (Fig. 8), suggests that these regions in the coral represent material formed at substantially elevated saturation states. The morphology of fibrous aragonite in coral skeletons (Fig. 7a and b) is consistent with that of aragonites grown in the mid pumping (moderate precipitation) rate experiment (Fig. 3b): tightly spaced but with distinct boundaries between fibers. This may suggest that fibrous growth in corals occurs at a saturation state below that needed to induce nucleation but substantially above that of ambient seawater.

4.3.1. Band formation in corals and synthetic aragonite

The formation of alternating bands of fibrous crystals and granular materials in synthetic aragonites precipitated in Experiments 2 and 3 resulted from the stepped addition of Na_2CO_3 which caused the saturation state of the seawater solution to cycle during the experiment. Addition of the first volume of Na_2CO_3 elevated the solution pH (supersaturation), initiating nucleation and the formation of granular materials at the center of the spherulites. Following nucleation, the solution pH dropped, enabling fibers to grow and radiate outward from the center. Addition of a second volume of Na_2CO_3 solution elevated the solution pH, favoring nucleation over elongation of pre-existing crystals and forming a fine band of granular materials followed again by radial growth (Fig. 4a).

Such a cycling of fluid saturation state may explain the formation of microscale bands of alternating fibers and granular materials within the coral skeleton (Jell, 1974; Sorauf and Jell, 1977; Risk and Pearce, 1992). The coral crystal morphologies reported here (Fig. 8a–c) are consistent with repeated cycles of high and moderate saturation states. Variations in rates of ion pumping or internal fluid flow could generate both spatial and temporal variations in saturation state. Zooxanthellate coral calcification rates (e.g. Kawaguti and Sakumoto, 1948; Goreau, 1959; Barnes and Chalker, 1990), and the internal pH of the coral (Al-Horani et al., 2003), are both known to change substantially over light dark cycles. Thus, the microscale bands (often called daily growth bands) within zooxanthellate coral skeletons may be the product of daily cycles in saturation state.

A model to explain the banding patterns seen in *Diploria* is presented in Fig. 10. In *Diploria,* the banding patterns are characterized by thick regions of granular material near the center of a skeletal element, with a gradual thinning of the granular band away from the center, transitioning to fibrous growth and a loss of bands (Fig. 8a). This pattern could be explained by the presence of a highly supersaturated fluid adjacent to where the granular centers form, transitioning to a moderate saturation state far from the centers, where fibers are continuous. The region of highest saturation state would be associated with the fastest growth and, thus, the thickest band of granular material. Moving down that saturation state gradient, growth would slow, shifting from granular to fibrous material. At different times, a more uniform, moderate, saturation state could exist throughout the calcifying environment, generating a band of fibrous crystals.

The proposed cycle in saturation state could account for both the high Mg/Ca ratios at centers of calcification, and the alternating micron-scale bands of high and low Mg/Ca ratios reported by Meibom et al. (2004). This is consistent

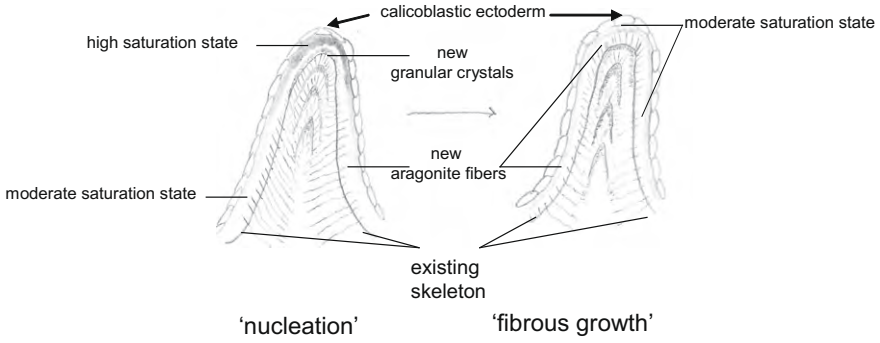

Fig. 10. Schematic representation of the cycle in saturation state of the calcifying 'fluid', and the crystals formed in *Diploria labyrinthiformis*. During 'nucleation' periods, high saturation state adjacent to nascent centers leads to the formation of granular materials at centers. Moving away from centers, the saturation state drops, leading to a transition from the high saturation state granular materials to the lower saturation state fibrous crystals. Between 'nucleation' periods, fibrous growth occurs, during which the calcifying 'fluid' experiences a more uniform, moderate saturation state, and the crystals formed throughout the skeleton are fibrous.

with the suggestion of Tsukamoto and Tsukamoto (1996) that growth rate variation could account for some of the variability in Mg/Ca ratios and is similar to the explanation proposed by Eggins et al. (2004), which attributes daily Mg/Ca bands in foraminifera to cycles in pH.

Cycles in the saturation state of the calcifying environment can also give rise to fine-scale heterogeneity in isotope ratios. Differences in $\delta^{13}C$ and $\delta^{18}O$ between centers and fibers, as well as fine-scale heterogeneity in the composition of coral fibers may, in part, be due to diffusion kinetics favoring the lighter isotope in the faster growing regions (Rollion-Bard et al., 2003; Meibom et al., 2006). The calcification model proposed by Adkins et al. (2003) expands upon the diffusion model to incorporate multiple carbon sources which contribute to skeletal $\delta^{13}C$ in a pH dependent manner. Similarly elevations in the pH of the calcifying fluid induce depletion of $\delta^{18}O$. This model is compatible with the compositional response of aragonite precipitates to variations in saturation state proposed here. In the Adkins et al. (2003) model, high pH in the calcifying environment is associated with light $\delta^{13}C$ and $\delta^{18}O$ and rapid growth rate. Assuming that saturation state of the precipitating fluid is linked to pH, centers of calcification and bands of granular crystals should have a lighter $\delta^{13}C$ and $\delta^{18}O$ signature relative to fibers.

Some independent observations appear to contradict the proposed model. For example, Blamart et al. (2007) show that centers of calcification have lower boron isotope ratios than adjacent fibers, which the authors interpret to mean that crystals in centers of calcification form at a lower pH than the surrounding fibers. However, factors controlling the boron isotope ratios of coral skeletons are not well-understood and considerable variability has been found between different coral species, even when grown under similar environmental conditions (e.g. Vengosh et al., 1991; Pagani et al., 2005; Klochko et al., 2006, 2009; Xiao et al., 2006; Blamart et al., 2007). In two separate studies, Clode and Marshall (2002) and Tambutté et al. (2007) examined the interface between the skeleton and the calicoblastic ectoderm, and found, in freeze-fractured specimens, that the membrane lays flush with the skeletal surface with the possible exception of nanometer scale spaces. Tambutté et al. (2007) interpreted this as the absence of a reservoir in which saturation state could be regulated, however that nanometer scale volumes are sufficient for saturation state to control crystal formation cannot be ruled out.

The results presented here show that features of coral skeletons such as: banding patterns, fibrous and granular materials, Mg/Ca ratios, and acridine fluorescence patterns, can be reproduced by manipulating the saturation state. Our results suggest that these features cannot be used as firm evidence of organic materials (e.g., templates) controlling crystal growth. Cycles in saturation state may not be the only factor controlling the morphology and chemistry of coral crystals. By using synthetic aragonite spherulites as a control material, it may be possible to identify coral features that cannot be reproduced by manipulating saturation state alone and, thus, may be indicative of biological control over and above controlling saturation state within the calcifying environment.

4.4. Differences

Despite the numerous similarities between synthetic aragonites and coral skeletons, there are some key differences. The most significant of these for sample preparation is the greater apparent solubility of the synthetic aragonites (Fig. EA 4,5). This may be due to coral-derived organic materials decreasing the solubility of the coral skeleton or it may be a reflection of the much smaller size of individual spherulites (<100 μm diameter for a spherulite, versus millimeters for a coral), making them more vulnerable to dissolution.

5. SUMMARY

The morphology and composition of synthetic aragonitic spherulites precipitated experimentally from seawater is shown to change systematically with the pH (saturation state) of the precipitation environment. Spherulites progress from coarse open structures at pH values near seawater to fine closed structures at high pH. The highest pH precipitates have a granular appearance, similar to the

granular appearance of centers of calcification and bands in corals, whereas coral fibers resemble synthetic fibers grown at lower pH. Variations in elemental ratios coincide with the morphological variations, suggesting that the saturation state influences both the morphology and composition of the precipitate. The similarities observed between portions of the coral skeleton and synthetic aragonites grown under varying controlled chemical conditions may prove useful in interpreting the coral biomineralization process. These observations suggest that the saturation state beneath the calicoblastic epithelium is not homogenous, and that there may be regular cycles in the saturation state within the calcifying environment which lead to the formation of centers of calcification and fine bands within the coral skeleton.

ACKNOWLEDGMENTS

The authors are grateful for the insightful comments of AE Alfonso Mucci and the anonymous reviewers that greatly improved the manuscript, to Shailesh Nene (UWO) for assistance with AFM imaging, Louie Kerr (MBL) for help on the SEM, and Nobuchimi Shimizu (WHOI) for help with SIMS analysis Jerzy Blustajn, Zhengrong Wang and Scot Birdwhistell for assistance with ICP-MS, David Wellwood for salinities, and Joanne Goudreau for alkalinity data. Greg Hirth and Glenn Gaetani (WHOI) provided insightful discussions and materials. Glenn Gaetani made his laboratory available for sample preparation. Sheri White, Dawn Moran, Becky Gast, Karen Casciotti, and Ben Van Mooy (WHOI) provided equipment that made this work possible. Financial support was provided by a WHOI Interdisciplinary Award #39040300, a WHOI Coastal Ocean Institute Award to MH, and by NSF OCE-0648157. This material is based upon work supported under a National Science Foundation Graduate Research Fellowship.

APPENDIX A. SUPPLEMENTARY DATA

Supplementary data associated with this article can be found, in the online version, at doi:10.1016/j.gca.2009.04.015.

REFERENCES

Adkins J. F., Boyle E. A., Curry W. B. and Lutringer A. (2003) Stable isotopes in deep-sea corals and a new mechanism for vital effects. *Geochim. Cosmochim. Acta* **67**, 1129–1143.

Al-Horani F. A., Al-Moghrabi S. M. and de Beer D. (2003) The mechanism of calcification and its relation to photosynthesis and respiration in the scleractinian coral Galaxea fascicularis. *Mar. Biol.* **142**, 419–426.

Barnes D. J. (1970) Coral skeletons: an explanation of their growth and structure. *Science* **170**, 1305–1308.

Barnes D. J. (1971) A study of growth, structure and form in modern coral skeletons. Ph. D. thesis, Univ. Newcastle upon Tyne.

Barnes D. J. and Chalker B. E. (1990) Calcification and photosynthesis in reef building corals and algae. In *Coral Reefs: Ecosystems of the World*, vol. 25 (eds. Z. Dubinsky and D. W. Goodall). Elsevier. pp. 109–131.

Blamart D., Rollion-Bard C., Meibom A., Cuif J.-P., Juillet-Leclerc A. and Dauphin Y. (2007) Correlation of boron isotopic composition with ultrastructure in the deep-sea coral Lophelia pertusa: implications for biomineralization and paleo-pH. *Geochem. Geophys. Geosyst.* **8**, Q12001.

Bryan W. H. and Hill D. (1941) Spherulitic crystallization as a mechanism of skeletal growth in the hexacorals. *Proc. R. Soc. Queensland* **LII**, 78–92.

Burton E. A. and Walter L. M. (1987) Relative precipitation rates of aragonite and Mg calcite from seawater: temperature or carbonate ion control? *Geology* **15**, 111–114.

Chernov A. A. (1984) *Modern Crystallography III Crystal Growth*. Springer-Verlag, New York.

Clarkson J. R., Price T. J. and Adams C. J. (1992) Role of metastable phases in the spontaneous precipitation of calcium carbonate. *J. Chem. Soc. Faraday Trans.* **88**, 243–249.

Clode P. L. and Marshall A. T. (2002) Low temperature FESEM of the calcifying interface of a scleractinian coral. *Tissue Cell* **34**, 187–198.

Clode P. L. and Marshall A. T. (2003) Skeletal microstructure of Galaxea fascicularis exsert septa: a high-resolution SEM study. *Biol. Bull.* **204**, 146–154.

Cohen A. L. and Hart S. R. (1997) The effect of colony topography on climate signals in coral skeleton. *Geochim. Cosmochim. Acta* **61**, 3905–3912.

Cohen A. L., Layne G. D., Hart S. R. and Lobel P. S. (2001) Kinetic control of skeletal Sr/Ca in a symbiotic coral: implications for the paleotemperature proxy. *Paleoceanography* **16**, 20–26.

Cohen A. L. and McConnaughey T. A. (2003) Geochemical perspectives on coral mineralization. *Rev. Mineral. Geochem. Biomineralization* **54**, 151–187.

Cohen A. L., Smith S. R., McCartney M. S. and van Etten J. (2004) How brain coral record climate: an integration of skeletal structure, growth and chemistry of Diporia labrynthiformis from Bermuda. *Mar. Ecol. Prog. Ser.* **271**, 147–158.

Constantz B. R. (1986) Coral skeleton construction: a physiochemically dominated process. *Palaios* **1**, 152–157.

Cross W. (1891) Constitution and origin of spherulites in acid eruptive rocks. *Washington Philos. Soc. Bull.* **11**, 411–444.

Cuif J.-P., Dauphin Y., Doucet J., Salome M. and Susini J. (2003) XANES mapping of organic sulfate in three scleractinian coral skeletons. *Geochim. Cosmochim. Acta* **67**, 75–83.

Eggins S. M., Sadekov A. and Deckker P. D. (2004) Modulation and daily banding of Mg/Ca in Orbulina universa tests by symbiont photosynthesis and respiration: a complication for seawater thermometry? *Earth Planet. Sci. Lett.* **225**, 411–419.

Gabitov R. I., Cohen A. L., Gaetani G. A., Holcomb M. and Watson E. B. (2006) The impact of crystal growth rate on element ratios in aragonite: an experimental approach to understanding vital effects. *Geochim. Cosmochim. Acta* **70s,** A187.

Gabitov R. I., Gaetani G. A., Watson E. B., Cohen A. L. and Ehrlich H. L. (2008) Experimental determination of temperature and growth rate effects on U6+ and Mg2+ partitioning between aragonite and fluid. *Geochim. Cosmochim. Acta* **72**, 4058–4068.

Gaetani G. A. and Cohen A. L. (2006) Element partitioning during precipitation of aragonite from seawater: a framework for understanding paleoproxies. *Geochim. Cosmochim. Acta* **70**, 4617–4634.

Gagnon A. C., Adkins J. F., Fernandez D. P. and Robinson L. F. (2007) Sr/Ca and Mg/Ca vital effects correlated with skeletal architecture in a scleractinian deep-sea coral and the role of Rayleigh fractionation. *Earth. Planet. Sci. Lett.* **261**, 280–295.

Gautret P., Cuif J.-P. and Stolarski J. (2000) Organic components of the skeleton of scleractinian corals—evidence from in situ acridine orange staining. *Acta Palaeontologica Polonica* **45**, 107–118.

Goreau T. F. (1959) The physiology of skeleton formation in corals I. A method for measuring the rate of calcium deposition by corals under different conditions. *Biol. Bull.* **116**, 59–75.

Hart S. R. and Cohen A. L. (1996) An ion probe study of annual cycles of Sr/Ca and other trace elements in corals. *Geochim. Cosmochim. Acta* **60**, 3075–3084.

Iddings J. P. (1891) Spherulitic crystallization. *Washington Philos. Soc. Bull.* **11**, 445–463.

Jell J. S. (1974) The microstructure of some scleractinian corals. In *Proceedings of 2nd International Coral Reef Symposium*, vol. 2. pp. 301–320.

Kawaguti S. and Sakumoto D. (1948) The effect of light on the calcium deposition of corals. *Bull. Oceanograph. Inst. Taiwan* **4**, 65–70.

Keith H. D. and Padden F. J. J. (1963) A phenomenological theory of spherulitic crystallization. *J. Appl. Phys.* **34**, 2409–2421.

Kinsman D. J. J. and Holland H. D. (1969) The co-precipitation of cations with CaCO3—IV. The co-precipitation of Sr2+ with aragonite between 16 and 96 C. *Geochim. Cosmochim. Acta* **33**, 1–17.

Klochko K., Kaufman A. J., Yao W., Byrne R. H. and Tossell J. A. (2006) Experimental measurement of boron isotope fractionation in seawater. *Earth Planet. Sci. Lett.* **248**, 276–285.

Klochko K., Cody G. D., Tossell J. A., Dera P. and Kaufman A. J. (2009) Re-evaluating boron speciation in biogenic calcite and aragonite using ^{11}B MAS NMR. *Geochim. Cosmochim. Acta* **73**, 1890–1900.

Lofgren G. (1971) Spherulitic textures in glassy and crystalline rocks. *J. Geophys. Res.* **76**, 5635–5648.

Lofgren G. (1974) An experimental study of plagioclase crystal morphology: isothermal crystallization. *Am. J. Sci.* **274**, 243–273.

Lowenstam H. A. and Weiner S. (1989) *On Biomineralization*. Oxford University Press, New York. pp. 207–251.

Marsh B. D. (1988) Crystal size distribution (CSD) in rocks and the kinetics and dynamics of crystallization I theory. *Contrib. Mineral. Petrol.* **99**, 277–291.

Marsh B. D. (1998) On the interpretation of crystal size distributions in magmatic systems. *J. Petrol.* **39**, 553–599.

Meibom A., Cuif J.-P., Hillion F., Constantz B. R., Juillet-Leclerc A., Dauphin Y., Watanabe T. and Dunbar R. B. (2004) Distribution of magnesium in coral skeleton. *Geophys. Res. Lett.* **31**, L23306.

Meibom A., Yurimoto H., Cuif J.-P., Domart-Coulon I., Houlbreque F., Constantz B., Dauphin Y., Tambutte E., Tambutte S., Allemand D., Wooden J. and Dunbar R. (2006) Vital effects in coral skeletal composition display strict three dimensional control. *Geophys. Res. Lett.* **33**, L1160.

Meibom A., Mostefaoui S., Cuif J.-P., Dauphin Y., Houlbreque F., Dunbar R. and Constantz B. (2007) Biological forcing controls the chemistry of reef-building coral skeleton. *Geophys. Res. Lett.* **34**, L02601.

Ogilvie M. M. (1896) Microscopic and systematic study of Madreporarian types of corals. *Phil. Trans. R. Soc. Lond. B* **187**, 83–345.

Pagani M., Lemarchand D., Spivack A. and Gaillardet J. (2005) A critical evaluation of the boron isotope-pH proxy: the accuracy of ancient ocean pH estimates. *Geochim. Cosmochim. Acta* **69**, 953–961.

Prieto M., Fernandez-Diaz L. and Lopez-Andres S. (1989) Supersaturation evolution and first precipitate location in crystal growth in gels; application to barium and strontium carbonates. *J. Cryst. Growth* **98**, 447–460.

Prieto M., Putnis A., Fernandez-Diaz L. and Lopez-Andres S. (1994) Metastability in diffusing-reacting systems. *J. Cryst. Growth* **142**, 225–235.

Prieto M., Fernandez-Gonzalez A., Putnis A. and Fernandez-Diaz L. (1997) Nucleation, growth, and zoning phenomena in crystallizing (Ba, Sr)CO3, Ba (SO4, CrO4), (Ba, Sr) SO4, and (Cd, Ca) COa solid solutions from aqueous solutions. *Geochim. Cosmochim. Acta* **61**, 3383–3397.

Reddy M. M. and Nancollas G. H. (1976) The crystallization of calcium carbonate: IV. The effect of magnesium, strontium and sulfate ions. *J. Cryst. Growth* **35**, 33–38.

Risk M. J. and Pearce T. H. (1992) Interference imaging of daily growth bands in massive corals. *Nature* **358**, 572–573.

Rollion-Bard C., Blamart D., Cuif J.-P. and Juillet-Leclerc A. (2003) Microanalysis of C and O isotopes of azooxanthellate and zooxanthellate corals by ion microprobe. *Coral Reefs* **22**, 405–415.

Sorauf J. E. and Jell J. S. (1977) Structure and incremental growth in the ahermatypic coral Desmophyllum cristagalli from the North Alantic. *Paleontology* **20**, 1–19.

Stolarski J. (2003) Three-dimensional micro- and nanostructural characteristics of the scleractinian coral skeleton: a biocalcification proxy. *Acta Palaeontologica Polonica* **48**, 497–530.

Sunagawa I. (1981) Characteristics of crystal growth in nature as seen from the morphology of mineral crystals. *Bull. Mineral.* **104**, 81–87.

Sunagawa I. (1987) *Morphology of Crystals Part B.* Terra Scientific Publishing Co. Tokyo.

Tambutté E., Allemand D., Zoccola D., Meibom A., Lotto S., Caminiti N. and Tambutté S. (2007) Observations of the tissue-skeleton interface in the scleractinian coral Stylophora pistillata. *Coral Reefs* **26**, 517–529.

Tiller W. A. (1964) Dendrites. *Science* **146**, 871–879.

Tong H., Ma W., Wang L., Wan P., Hu J. and Cao L. (2004) Control over the crystal phase, shape, size and aggregation of calcium carbonate via a L-aspartic acid inducing process. *Biomaterials* **25**, 3923–3929.

Tsukamoto S. and Tsukamoto H. (1996) Variability of trace elements in a daily banded coral. *Geograph. Rep. Tokyo Metropol. U* **31**, 167–172.

Vaughan T. W. and Wells J. W. (1943) Revision of the suborders families, and genera of the scleracinia. *Geological Society of America special papers*. p. 44.

Vengosh A., Kolodny Y., Starinsky A., Chivas A. R. and McCulloch M. T. (1991) Co-precipitation and isotopic fractionation of boron in modern biogenic carbonates. *Geochim. Cosmochim. Acta* **55**, 2901–2910.

Wainwright S. A. (1964) Studies of the mineral phase of coral skeleton. *Exp. Cell Res.* **34**, 213–230.

Wasylenki L. E., Dove P. M. and Yoreo J. J. D. (2005) Effects of temperature and transport conditions on calcite growth in the presence of Mg2: implications for paleothermometry. *Geochim. Cosmochim. Acta* **69**, 4227–4236.

Watson E. B. (2004) A conceptual model for near-surface kinetic controls on the trace-element and stable isotope composition of abiogenic calcite crystals. *Geochim. Cosmochim. Acta* **68**, 1473–1488.

Wells J. W. (1956) Scleractinia. In *Treatise on Invertebrate Paleontology*. pp. 328–444.

Xiao Y. K., Shirodkar P. V., Zhang C. G., Wei H. Z., Liu W. G. and Zhou W. J. (2006) Isotopic fractionation of boron in growing corals and its palaeoenvironmental implication. *Curr. Sci.* **90**, 414–420.

Zar J. H. (1984) *Biostatistical Analysis*. Prentice-Hall, Englewood Cliffs, NJ.

Associate editor: Alfonso Mucci

Marine calcifiers exhibit mixed responses to CO_2-induced ocean acidification

Justin B. Ries*, Anne L. Cohen, and Daniel C. McCorkle
Department of Geology and Geophysics, Woods Hole Oceanographic Institution, Woods Hole, Massachusetts 02543, USA

ABSTRACT

Anthropogenic elevation of atmospheric carbon dioxide (pCO_2) is making the oceans more acidic, thereby reducing their degree of saturation with respect to calcium carbonate ($CaCO_3$). There is mounting concern over the impact that future CO_2-induced reductions in the $CaCO_3$ saturation state of seawater will have on marine organisms that construct their shells and skeletons from this mineral. Here, we present the results of 60 d laboratory experiments in which we investigated the effects of CO_2-induced ocean acidification on calcification in 18 benthic marine organisms. Species were selected to span a broad taxonomic range (crustacea, cnidaria, echinoidea, rhodophyta, chlorophyta, gastropoda, bivalvia, annelida) and included organisms producing aragonite, low-Mg calcite, and high-Mg calcite forms of $CaCO_3$. We show that 10 of the 18 species studied exhibited reduced rates of net calcification and, in some cases, net dissolution under elevated pCO_2. However, in seven species, net calcification increased under the intermediate and/or highest levels of pCO_2, and one species showed no response at all. These varied responses may reflect differences amongst organisms in their ability to regulate pH at the site of calcification, in the extent to which their outer shell layer is protected by an organic covering, in the solubility of their shell or skeletal mineral, and whether they utilize photosynthesis. Whatever the specific mechanism(s) involved, our results suggest that the impact of elevated atmospheric pCO_2 on marine calcification is more varied than previously thought.

INTRODUCTION

Surface ocean pH has already decreased by 0.1 units since the industrial revolution, and it is predicted to decline another 0.3–0.4 units by the end of this century (Brewer, 1997). This translates to a nearly 50% reduction in the carbonate ion concentration [CO_3^{2-}] of surface seawater, resulting in aragonite and high-Mg calcite undersaturation in the high-latitude oceans. The effect of CO_2-induced ocean acidification on marine calcification is currently the subject of intense scientific investigation with regard to both the immediate future (cf. Gattuso et al., 1998; Langdon et al., 2000; Langdon and Atkinson, 2005; Kleypas et al., 2006; see the GSA Data Repository[1]) and the geologic past (Knoll et al., 2007; Zhuravlev and Wood, 2008).

METHODS

To investigate the impact of ocean acidification on a range of benthic marine calcifiers, we reared 18 calcifying species for 60 d in isothermal (25 °C; see the Data Repository for discussion) experimental seawaters equilibrated with average pCO_2 values (±SD) of 409 (±6), 606 (±7), 903 (±12), and 2856 (±54) ppm, corresponding to modern pCO_2, and ~2, 3, and 10 times pre-industrial levels (~280 ppm), respectively, and yielding average seawater saturation states (±SD) of 2.5 (±0.4), 2.0 (±0.4), 1.5 (±0.3), and 0.7 (±0.2) with respect to aragonite (see the Data Repository for detailed methods). These carbonate system parameters were selected to represent the range of values predicted for the coming millennium (Brewer, 1997; Feely et al., 2004) and to span those reported to have occurred since mid-Cretaceous time (ca. 110 Ma; Royer et al., 2004; Tyrrell and Zeebe, 2004). The organisms' net rates of calcification (total calcification minus total dissolution) under the various pCO_2 treatments were estimated from changes in their buoyant weight and verified with dry weight measurements after harvesting (Fig. 1; see Fig. DR1, Table DR3, and additional methods in the GSA Data Repository).

RESULTS

In ten of the 18 species (temperate corals, pencil urchins, hard clams, conchs, serpulid worms, periwinkles, bay scallops, oysters, whelks, soft clams; Figs. 1I–1R), net calcification decreased with increasing pCO_2 (reduced $CaCO_3$ saturation state). And in six of the ten negatively impacted species (pencil urchins, hard clams, conchs, periwinkles, whelks, soft clams; Figs. 1J–1L, 1N, and 1Q–1R), we observed net dissolution of the shell in the highest pCO_2 treatment, for which the experimental seawater was undersaturated with respect to aragonite and high-Mg calcite. However, in four of the 18 species (limpets, purple urchins, coralline red algae, calcareous green algae; Figs. 1D–1G), net calcification increased relative to the control under intermediate pCO_2 levels (605 and 903 ppm), and then declined at the highest pCO_2 level (2856 ppm). In three species (crabs, lobsters, and shrimps; Figs. 1A–1C), net calcification was greatest under the highest level of pCO_2 (2856 ppm). And one species, the blue mussel (Fig. 1H), exhibited no response to elevated pCO_2.

Our experiments revealed six general calcification response patterns to elevated pCO_2 (Fig. 1; Fig. DR3; Table 1): positive (Figs. 1A and 1B); threshold-positive (no change under intermediate pCO_2, positive under highest pCO_2; Fig. 1C); parabolic (positive under intermediate pCO_2, negative under highest pCO_2; Figs. 1D–1G); neutral (no change; Fig. 1H); threshold-negative (little or no change under intermediate pCO_2, negative under highest pCO_2; Figs. 1I–1L); and negative (Figs. 1M–1R). A combination of factors, including the organisms' ability to regulate pH at the site of calcification, the extent of organic-layer coverage of their external shell, their biomineral solubility, and whether they utilize photosynthesis, may contribute to the disparity of these response patterns.

FACTORS EXPLAINING VARIABLE RESPONSES AMONGST ORGANISMS

Regulation of pH at the Site of Calcification Converts HCO_3^- to CO_3^{2-}

Many calcifying organisms, including scleractinian corals (Al-Horani et al., 2003; Cohen and McConnaughey, 2003), coralline red algae (Borowitzka, 1987; McConnaughey and Whelan, 1997), calcareous green algae (Borowitzka, 1987; McConnaughey and Whelan, 1997; De Beer and Larkum, 2001), foraminifera (Rink et al., 1998), and crabs (Cameron, 1985) are thought to facilitate $CaCO_3$ precipitation by elevating pH at the site of calcification. This reduction in [H^+] converts HCO_3^- to CO_3^{2-}, elevating [CO_3^{2-}] within calcifying compartments.

Microelectrode data (Rink et al., 1998; De Beer and Larkum, 2001; Al-Horani et al., 2003) show elevated pH—up to 2 units above external seawater—at sites of calcification in several marine calcifiers. These

*Current address: Department of Marine Sciences, 333 Chapman Hall, Campus Box 3300, University of North Carolina–Chapel Hill, Chapel Hill, North Carolina 27599, USA

[1]GSA Data Repository item 2009279, supplementary information, Table DR1, Figures DR1 and DR2, is available online at www.geosociety.org/pubs/ft2009.htm, or on request from editing@geosociety.org or Documents Secretary, GSA, P.O. Box 9140, Boulder, CO 80301, USA.

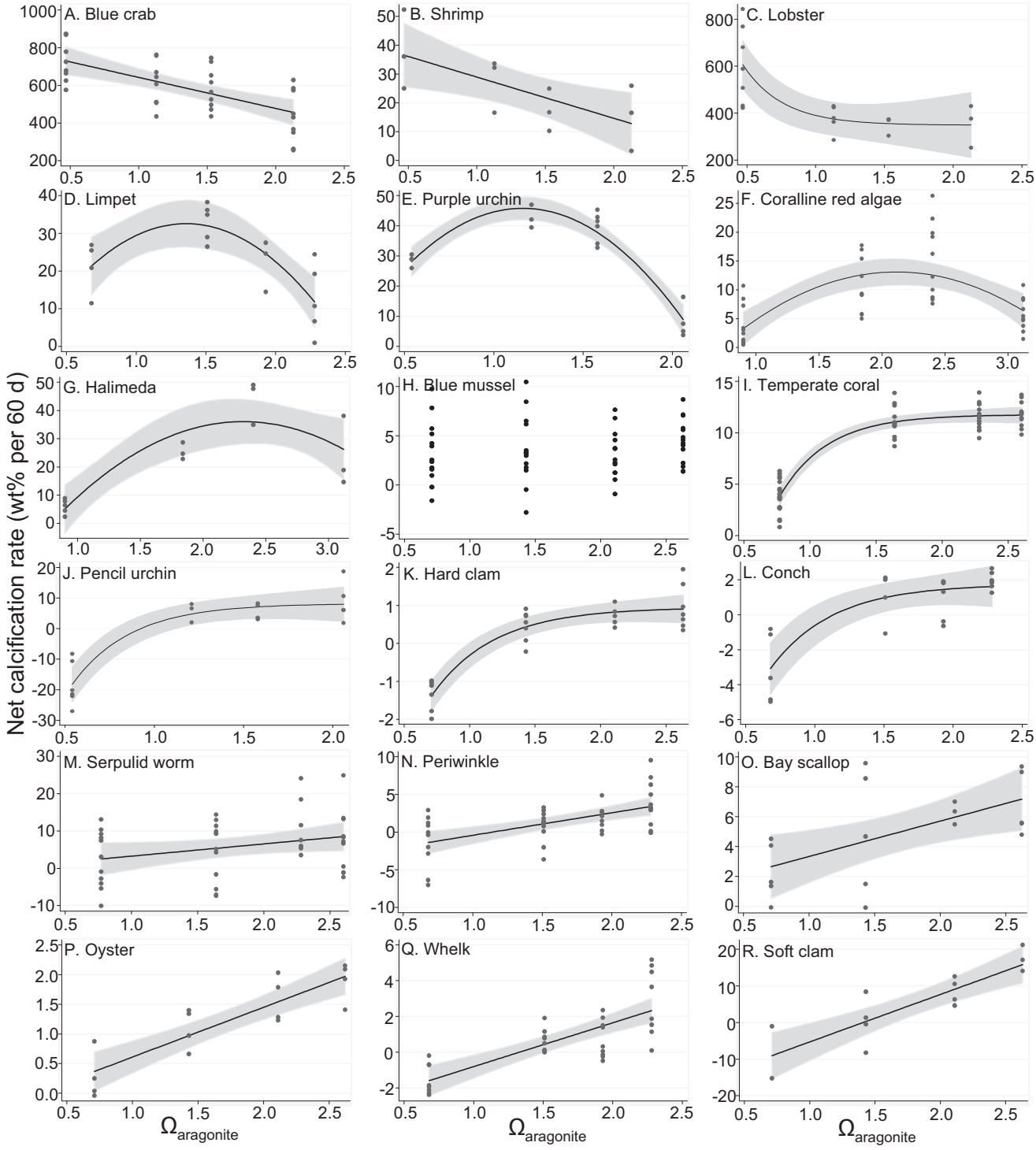

Figure 1. Calcification response patterns for 18 species of calcifying organisms subjected for 60 d to CO_2-induced reductions in $CaCO_3$ saturation state of seawater. Net rates of calcification(+)/dissolution(–) were estimated from buoyant weighing (verified with dry weight measured after harvesting) and are expressed as a percentage of the organisms' initial buoyant weight (see GSA Data Repository Fig. DR1 and Tables DR1 and DR3 [see footnote 1]). *Halimeda* growth is in mg/day, since all algae emerged under experimental conditions (i.e., initial weight was zero). Linear, quadratic, and exponential regression analyses were used to examine relationship between net calcification rate and aragonite saturation state (Table 1). These regressions were calculated using least squares method and adjusted for clustering within tanks with generalized estimating equations, which employ Huber-White sandwich estimator of variance in place of standard estimator of variance to increase rigor of test for statistical significance (Rogers, 1993; see GSA Data Repository). The regression analysis (linear, quadratic, or exponential) that yielded the lowest mean squared error for each species is plotted above (see Table 1 and Table DR5). All plotted regressions are statistically significant ($p<\leq0.05$); 95% confidence intervals are shown in gray. Regression analyses are intended to show general trends – the locations of the break-in-slope of the exponential curves (B, I-L) are not precisely constrained by the available data. $\Omega_{aragonite} = [Ca^{2+}][CO_3^{2-}]/K^*_{sp}$, where K^*_{sp} is the stoichiometric solubility product of aragonite. $\Omega_{aragonite}$ was calculated from measured values of temperature, salinity, alkalinity, and pH (see Table DR2 [see footnote 1]) using Roy et al. (1993) values for carbonic acid constants K_1 and K_2 (see GSA Data Repository [see footnote 1]), the Mucci (1983) value for K^*_{sp}, and pressure (P) = 1.015 atm.

TABLE 1. REGRESSION ANALYSES OF $\Omega_{ARAGONITE}$ VS. NET CALCIFICATION RATE AND SUMMARY OF CALCIFICATION-RELEVANT TRAITS

Organism	Scientific name	Panel	Best-fit Regression*					Response§	Mineralogy#	Cover**	Photo††
		(Fig. 1)	Regression	Type	p†	R^2	RMSE				
Crab	*Callinectes sapidus*	A	$y = -165x + 807$	LIN	0.00	0.41	120.71	positive	HMC	high	no
Shrimp	*Penaeus plebejus*	B	$y = -14.3x + 43.3$	LIN	0.01	0.47	9.98	positive	HMC	high	no
Lobster	*Homarus americanus*	C	$y = 1296e^{-344x} + 348$	EXP	0.00	0.57	112.11	threshold(+)	HMC	high	no
Limpet	*Crepidula fornicata*	D	$y = -24.4x^2 + 66.3x - 12.5$	QUAD	0.00	0.59	7.17	parabolic	Arag>LMC	low	no
Purple urchin	*Arbacia punctulata*	E	$y = -45.7x^2 + 106x - 15.9$	QUAD	0.00	0.91	4.65	parabolic	HMC	high	no
Coralline red alga	*Neogoniolithon* sp.	F	$y = -6.66x^2 + 28.2x + -16.7$	QUAD	0.03	0.43	4.86	parabolic	HMC	high	yes
Halimeda	*Halimeda incrassata*	G	$y = -15.4x^2 + 71.2x - 46.6$	QUAD	0.02	0.74	8.73	parabolic	Arag	high	yes
Blue mussel	*Mytilus edulis*	H	no significant trend (p>0.05)	NONE	n/a	n/a	n/a	neutral	LMC>Arag	mod	no
Temperate coral	*Oculina arbuscula*	I	$y = -67.2e^{-277x} + 11.8$	EXP	0.00	0.87	1.43	threshold(-)	Arag	high	yes
Pencil urchin	*Eucidaris tribuloides*	J	$y = -137e^{-304x} + 8.25$	EXP	0.02	0.84	5.68	threshold(-)	HMC	low	no
Hard clam	*Mercenaria mercenaria*	K	$y = -10.3e^{-210x} + 0.94$	EXP	0.00	0.83	0.44	threshold(-)	Arag≫HMC	low	no
Conch	*Strombus alatus*	L	$y = -21.9e^{-222x} + 1.75$	EXP	0.00	0.69	1.37	threshold(-)	Arag>LMC	low	no
Serpulid worm	*Hydroides crucigera*	M	$y = 1.64x - 0.02$	LIN	0.05	0.08	3.93	negative	Arag + HMC	low	no
Periwinkle	*Littorina littorea*	N	$y = 2.99x - 3.41$	LIN	0.00	0.34	2.55	negative	LMC>Arag	mod	no
Bay scallop	*Argopecten irradians*	O	$y = 2.37x - 0.97$	LIN	0.00	0.34	2.61	negative	LMC	low	no
Oyster	*Crassostrea virginica*	P	$y = 0.84x - .23$	LIN	0.00	0.76	0.36	negative	LMC	low	no
Whelk	*Urosalpinx cinerea*	Q	$y = 2.45x - 3.26$	LIN	0.01	0.58	1.28	negative	Arag>LMC	low	no
Soft clam	*Mya arenaria*	R	$y = 13.0x - 18.2$	LIN	0.00	0.73	5.31	negative	Arag≫HMC	low	no

*Regressions in bold are plotted in Fig. 1. Linear regression is bold if statistically significant ($p < 0.05$). Quadratic regression is bold if it generates a significant improvement in fit (Ward $\chi^2 \leq 0.05$) over linear regression. "Intcpt" = y-intercept of the regression; p—p value; R^2—correlation coefficient.

†Ward χ^2—p value of the Ward chi-square test for improvement of fit of quadratic regression over linear regression.

§Response—generalized calcification response pattern exhibited by organisms reared under elevated pCO_2; organisms are ranked in increasingly negative order

#Mineralogy—polymorph of $CaCO_3$ in shell or skeleton (see GSA Data Repository for references [see text footnote 1]), confirmed with X-ray diffraction and scanning electron microscopy; HMC—high-Mg calcite (>4 mol% $MgCO_3$); LMC—low-Mg calcite (<4 mol% $MgCO_3$); Arag—aragonite.

**Cover—extent to which shell or skeleton is covered by organic layer.

††Photo—whether organism utilizes CO_2 via photosynthesis.

localized increases in pH may be achieved in various ways, for example, via conventional proton channeling, Ca^{2+}-activated proton-translocating ATPase, light-induced proton-pumping, transcellular symporter and co-transporter proton-solute shuttling, cellular extrusion of hydroxyl ions (OH^-) into the calcifying medium, and CO_2 utilization via photosynthesis (Borowitzka, 1987; McConnaughey and Whelan, 1997; De Beer and Larkum, 2001; Cohen and McConnaughey, 2003).

The decrease in seawater pH that will accompany the forecasted rise in anthropogenic pCO_2 will reduce the $[CO_3^{2-}]$ of seawater, and, for many organisms, there is experimental evidence that a reduction in seawater $[CO_3^{2-}]$ will inhibit calcification, and perhaps cause dissolution of existing shell (cf. Gattuso et al., 1998; Langdon et al., 2000; Langdon and Atkinson, 2005; Kleypas et al., 2006). It is also possible, however, that calcification in some organisms will be enhanced under elevated pCO_2. If seawater is the source of the organism's calcifying fluid, then the concentration of dissolved inorganic carbon (DIC) in this fluid will increase as pCO_2 increases. Organisms able to maintain an elevated pH at their site of calcification, despite reduced external pH, will convert much of this increased DIC, occurring primarily as HCO_3^-, to CO_3^{2-}. These organisms may experience a final $[CO_3^{2-}]$ at their site of calcification that is only slightly less than, and possibly equal to or greater than, that attained under present-day pCO_2—depending upon the efficiency of their specific proton-regulating mechanism. Alternatively, organisms such as coccolithophores may utilize HCO_3^- directly in calcification (Iglesias-Rodriguez et al., 2008), although mesocosm experiments suggest that reef-building organisms lack this ability (Langdon et al., 2000; Schneider and Erez, 2006). Nonetheless, the ability to convert HCO_3^- to CO_3^{2-} via proton regulation at the site of calcification, and/or utilize HCO_3^- directly in calcification, may explain, in part, why some of the organisms investigated in our experiments exhibited enhanced calcification under conditions of elevated pCO_2.

Of the calcifiers that have been investigated in microelectrode studies, those reported to maintain their calcifying fluids at higher pH (corals: 9.3 [Al-Horani et al., 2003; Fig. 1I] and calcareous green algae: 8.8–10.5 [De Beer and Larkum, 2001; Fig. 1G]) were generally less negatively affected by elevated pCO_2 in our experiments than those reported to maintain their calcifying fluid at lower pH (bivalve molluscs: pH = 7.33–8.53 [Crenshaw, 1972; Figs. 1K, 1O–1R]). These observations are consistent with the hypothesis that organisms able to maintain an elevated pH and, thus, elevated $[CO_3^{2-}]$ at their site of calcification could be less negatively impacted by CO_2-induced reductions in the $CaCO_3$ saturation state of seawater.

Protective External Organic Layer

Most calcifying marine organisms produce some type of external organic layer that separates their shell or skeleton from ambient seawater. Crustacea enclose their carapace within a relatively thick epicuticle, urchins cover their tests with an epidermis, algae precipitate $CaCO_3$ in spaces bound by cortical tissue, corals nucleate aragonite beneath several layers of epithelial tissue, and molluscs cover their shells with periostracum. The structure and composition of these protective organic layers vary widely amongst organisms. Through visual inspection, we have classified the organisms investigated in this study by their extent of organic-layer coverage (Table 1; high = total coverage; moderate = majority coverage; low = minority coverage). Organisms that accrete shell or skeleton that remains totally covered by an external organic layer, such as the crustacea (Figs. 1A–1C), purple urchins (Fig. 1E), coralline red algae (Fig. 1F), calcareous green algae (Fig. 1G), blue mussel (Fig. 1H), and temperate corals (Fig. 1I), generally exhibited greater resilience to elevated pCO_2 than those producing shell that is largely exposed to ambient seawater after deposition, such as the conchs (Fig. 1L), serpulid worms (Fig. 1M), periwinkles (Fig. 1N), scallops (Fig. 1O), oysters (Fig. 1P), whelks (Fig. 1Q), and clams (Figs. 1K and 1R).

$CaCO_3$ Polymorph Mineralogy

It is also predicted that organisms utilizing the more soluble forms of $CaCO_3$—aragonite and high-Mg calcite—would be more adversely affected by elevated pCO_2 than those utilizing the less soluble low-Mg calcite form (Morse et al., 2007). Although we did not observe a direct relationship between skeletal mineral solubility and vulnerability to elevated

pCO_2 (Table 1) under the intermediate pCO_2 levels (606 and 903 ppm), mineralogy did come into play for the highest pCO_2 level (2856 ppm). Of the six species that exhibited net dissolution under these conditions (pencil urchin, hard clam, conch, periwinkle, whelk, and soft clam; Figs. 1J–1L, 1N, and 1Q–1R), five of these secrete shells that are composed predominantly of the more soluble aragonite (hard clam, conch, whelk, soft clam) and high-Mg calcite (pencil urchin) polymorphs.

Fertilization of Photosynthesis

The coralline red (Fig. 1F) and calcareous green algae (Fig. 1G) investigated in this study both exhibited increased net calcification under the intermediate pCO_2 levels (606 and 903 ppm), and the temperate corals (Fig. 1I), which contain photosynthetic symbionts, exhibited no response over this range. This suggests that the direct utilization of CO_2 via photosynthesis may also influence an organism's calcification response to CO_2-induced reductions in saturation state (Table 1). While the relationship between photosynthesis and calcification is complex, increased CO_2 in seawater may increase the organism's rate of photosynthesis (Bowes, 1993; Iglesias-Rodriguez et al., 2008), potentially increasing the amount of energy available for converting HCO_3^- to CO_3^{2-} via pH regulation at the site of calcification. The parabolic calcification response patterns exhibited by the coralline red algae (Fig. 1F) and calcareous green algae (Fig. 1G) in our experiments, which peaked between 600 and 1100 ppm pCO_2, are consistent with previous work showing that pCO_2 is only limiting for photosynthesis in marine algae at partial pressures less than 1000 ppm (Bowes, 1993).

IDENTIFICATION OF OCEAN ACIDIFICATION EVENTS IN THE GEOLOGIC PAST

Past ocean acidification events, reportedly associated with intervals of intense global volcanism, have been invoked as potential drivers of mass extinctions throughout the Phanerozoic Eon (e.g., Knoll et al., 2007). The present study, by identifying both positive and negative responses to elevated pCO_2 for a wide range of organisms, offers a unique, polyphyletic fingerprint for identifying such CO_2-induced extinction events in the fossil record.

CONCLUSIONS

Our experiments suggest that the response of calcifying marine organisms to elevated atmospheric pCO_2 will be variable and complex. However, with the data at hand, it is difficult to predict how these changes in calcification will impact organisms' survival, reproductive success, and overall ecosystem health. Even those organisms showing enhanced calcification under elevated pCO_2 could be negatively impacted by the decline of less CO_2-tolerant species within their ecosystems. We have only begun to generate the data needed to assess CO_2-driven impacts on organisms and ecosystems in the geologic past, and to anticipate the effects of anthropogenic ocean acidification in the decades and centuries ahead.

ACKNOWLEDGMENTS

We thank G. Piniak (National Oceanic and Atmospheric Administration), J. Diamond (Marine Biological Laboratory), O. Zmora (University of Maryland, Center of Marine Biotechnology), and R. Crowley (Stonington Lobster Hatchery) for generously providing experimental specimens. M. Holcomb provided critical feedback on the design and implementation of the experiments. This work was funded by Woods Hole Oceanographic Institution (to Ries and Cohen) and the National Science Foundation (to Cohen and McCorkle).

REFERENCES CITED

Al-Horani, F.A., Al-Moghrabi, S.M., and De Beer, D., 2003, The mechanism of calcification and its relation to photosynthesis and respiration in the scleractinian coral *Galaxea fascicularis*: Marine Biology (Berlin), v. 142, p. 419–426.

Borowitzka, M.A., 1987, Calcification in algae—Mechanisms and the role of metabolism: Critical Reviews in Plant Sciences, v. 6, no. 1, p. 1–45.

Bowes, G., 1993, Facing the inevitable: Plants and increasing atmospheric CO_2: Annual Review of Plant Physiology and Plant Molecular Biology, v. 44, no. 1, p. 309–332, doi: 10.1146/annurev.pp.44.060193.001521.

Brewer, P.G., 1997, Ocean chemistry of the fossil fuel CO_2 signal: The haline signal of "business as usual": Geophysical Research Letters, v. 24, p. 1367–1369, doi: 10.1029/97GL01179.

Cameron, J.N., 1985, Post-moult calcification in the blue crab (*Callinectes sapidus*): Relationships between apparent net H^+ excretion, calcium and bicarbonate: The Journal of Experimental Biology, v. 119, p. 275–285.

Cohen, A.L., and McConnaughey, T.A., 2003, A geochemical perspective on coral mineralization, *in* Dove, P.M., Weiner S., and De Yoreo, J.J., eds., Biomineralization: Reviews in Mineralogy and Geochemistry, v. 54, p. 151–187.

Crenshaw, M.A., 1972, The inorganic composition of molluscan extrapallial fluid: The Biological Bulletin, v. 143, p. 506–512.

De Beer, D., and Larkum, A.W.D., 2001, Photosynthesis and calcification in the calcifying alga *Halimeda discoidea* studied with microsensors: Plant, Cell, and Environment, v. 24, no. 1, p. 1209–1217.

Feely, R.A., Sabine, C.S., Lee, K., Berelson, W., Kleypas, J., Fabry, V.J., and Millero, F.J., 2004, Impact of anthropogenic CO_2 on the $CaCO_3$ system in the oceans: Science, v. 305, no. 5682, p. 362–366, doi: 10.1126/science.1097329.

Gattuso, J.P., Frankignoulle, M., Bourge, I., Romaine, S., and Buddemeier, R.W., 1998, Effect of calcium carbonate saturation of seawater on coral calcification: Global and Planetary Change, v. 18, no. 1–2, p. 37–46.

Iglesias-Rodriguez, M.D., Halloran, P.R., Rickaby, R.E.M., Hall, I.R., Colmenero-Hidalgo, E., Gittins, J.R., Green, D.R.H., Tyrrell, T., Gibbs, S.J., von Dassow, P., Rehm, E., Armbrust, E.V., and Boessenkool, K.P., 2008, Phytoplankton calcification in a high-CO_2 world: Science, v. 320, no. 5874, p. 336–340, doi: 10.1126/science.1154122.

Kleypas, J.A., Feely, R.A., Fabry, V.J., Langdon, C., Sabine, C.L., and Robbins, L.L., 2006, Impacts of Ocean Acidification on Coral Reefs and Other Marine Calcifiers: A Guide for Future Research: Report of a workshop held 18–20 April 2005, St. Petersburg, Florida, sponsored by the National Science Foundation, National Oceanic and Atmospheric Administration, and the U.S. Geological Survey: http://www.healthyreefs.org/pdf/communicati.pdf, 88 p.

Knoll, A.H., Bambach, R.K., Payne, J.L., Pruss, S., and Fischer, W.W., 2007, Paleophysiology and end-Permian mass extinction: Earth and Planetary Science Letters, v. 256, p. 295–313, doi: 10.1016/j.epsl.2007.02.018.

Langdon, C., and Atkinson, M.J., 2005, Effect of elevated pCO_2 on photosynthesis and calcification of corals and interactions with seasonal change in temperature/irradiance and nutrient enrichment: Journal of Geophysical Research, v. 110, p. C09S07, doi: 10.1029/2004JC002576.

Langdon, C., Takahashi, T., Sweeney, C., Chipman, D., Goddard, J., Marubini, F., Aceves, H., Barnett, H., and Atkinson, M.J., 2000, Effect of calcium carbonate saturation state on the calcification rate of an experimental coral reef: Global Biogeochemical Cycles, v. 14, no. 2, p. 639–654, doi: 10.1029/1999GB001195.

McConnaughey, T.A., and Whelan, J.F., 1997, Calcification generates protons for nutrient and bicarbonate uptake: Earth-Science Reviews, v. 42, no. 1–2, p. 95–117.

Morse, J.W., Arvidson, R.S., and Luttge, A., 2007, Calcium carbonate formation and dissolution: Chemical Reviews, v. 107, p. 342–381, doi: 10.1021/cr050358j.

Mucci, A., 1983, The solubility of calcite and aragonite in seawater at various salinities, temperatures, and one atmosphere total pressure: American Journal of Science, v. 283, p. 780–799.

Rink, S., Kuhl, M., Bijma, J., and Spero, H.J., 1998, Microsensor studies of photosynthesis and respiration in the symbiotic foraminifer *Orbulina universa*: Marine Biology (Berlin), v. 131, p. 583–595, doi: 10.1007/s002270050350.

Rogers, W.H., 1993, Regression standard errors in clustered samples: Stata Technical Bulletin, v. 13, p. 19–23.

Roy, R.N., Roy, L.N., Vogel, K.M., Porter-Moore, C., Pearson, T., Good, C.E., Millero, F.J., and Campbell, D.M., 1993, The dissociation constants of carbonic acid in seawater at salinities 5 to 45 and temperatures 0 to 45°C: Marine Chemistry, v. 44, p. 249–267, doi: 10.1016/0304-4203(93)90207-5.

Royer, D.L., Berner, R.A., Montañez, I.P., Tabor, N.J., and Beerling, D.J., 2004, CO_2 as a primary driver of Phanerozoic climate: GSA Today, v. 14, no. 3, p. 4–10, doi: 10.1130/1052-5173(2004)014<4:CAAPDO>2.0.CO;2.

Schneider, K., and Erez, J., 2006, The effect of carbonate chemistry on calcification and photosynthesis in the hermatypic coral *Acropora eurystoma*: Limnology and Oceanography, v. 51, no. 3, p. 1284–1293.

Tyrrell, T., and Zeebe, R.E., 2004, History of carbonate ion concentration over the last 100 million years: Geochimica et Cosmochimica Acta, v. 68, no. 17, p. 3521–3530, doi: 10.1016/j.gca.2004.02.018.

Zhuravlev, A.Y., and Wood, R.A., 2008, Eve of biomineralization: Controls on skeletal mineralogy: Geology, v. 36, p. 923–926, doi: 10.1130/G25094A.1.

Manuscript received 7 March 2009
Revised manuscript received 16 July 2009
Manuscript accepted 21 July 2009

Printed in USA

GSA-DR material for Ries et al. (2009, Geology 37: 1131-1134)

1. Experimental growth conditions

Organisms were grown for 60 days in 24 38-Liter glass aquaria filled with 0.2 μm-filtered seawater obtained from Great Harbor in Vineyard Sound off the coast of Cape Cod, Massachusetts. The aquaria were divided into six sets of four, which were continuously equilibrated with air-CO_2 gas mixtures (± SD) of 409 (± 6), 606 (± 7), 903 (± 12), and 2856 (± 54) ppm pCO_2, yielding average seawater saturation states (± SD) of 2.5 (±0.4), 2.0 (±0.4), 1.5 (±0.3), and 0.7 (±0.2) with respect to aragonite and 3.8 (±0.5), 3.1 (±0.7), 2.3 (±0.4), and 1.1 (±0.2) with respect to calcite (Table DR2).

Organisms were grouped in the same sets of aquaria as follows: set 1 - *Callinectes sapidus* (blue crab) and *Homarus americanus* (american lobster); set 2 - *Penaeus plebeju*s (edible shrimp), *Littorina littorea* (periwinkle), *Urosalpinx cinerea* (whelk), *Crepidula fornicata* (limpet), and *Strombus alatus* (conch); set 3 - *Halimeda incrassata* (calcareous

green alga) and *Neogoniolithon* sp. (coralline alga); set 4 - *Eucidaris tribuloides* (tropical urchin) and *Arbacia punctulata* (temperate urchin); set 5 - *Hydroides crucigera* (feather duster worm) and *Oculina arbuscula* (temperate coral); set 6 - *Mercenaria mercenaria* (quahog), *Mytilus edulis* (blue mussel), *Mya arenaria* (softshell clam), *Argopecten irradians* (bay scallop), and *Crassostrea virginica* (eastern oyster).

The experimental seawaters were maintained at 25 ± 1ºC using 50-watt electric heaters. Each tank was continuously filtered with polyester fleece and activated carbon at the rate of 600 L/hour. Aquaria sets 2, 3, and 5 were illuminated with 10 hours/day of 426 Watts per square meter (W/m^2) irradiance (T8, 8000K aquarium spectrum lamps), aquaria sets 4 and 6 were illuminated with 10 hours/day of 213 W/m^2 irradiance (T8, 8000K aquarium spectrum lamps), and aquaria set 1 was not illuminated. Each aquarium and attached filtration system was covered with plastic wrap to facilitate equilibration between the gas mixtures and the experimental seawaters and to minimize evaporative water-loss. Seventy-five percent seawater changes (using seawater pre-equilibrated with the experimental air-CO_2 mixtures) were made approximately every 14 days.

Heterotrophic organisms were fed every other day as follows (Table DR4): 900 mg wet weight (mg w-wt) frozen brine shrimp to each *Callinectes sapidus* (blue crab) and *Homarus americanus* (american lobster); 210 mg w-wt edible shrimp to each *Penaeus plebeju*s (edible shrimp); 10 mg dry weight (mg d-wt) green algae to each *Littorina littorea* (periwinkle), *Urosalpinx cinerea* (whelk), *Crepidula fornicata* (limpet); 50 mg d-wt green algae to each *Strombus alatus* (conch); 90 mg d-wt green algae to each

Eucidaris tribuloides (tropical urchin) and *Arbacia punctulata* (temperate urchin); 90 mg w-wt frozen brine shrimp to each *Hydroides crucigera* (feather duster worm); 330 mg w-wt frozen brine shrimp to each *Oculina arbuscula* (temperate coral); 290 mg w-wt puréed frozen brine shrimp and 10 mg d-wt puréed green algae to each *Mercenaria mercenaria* (quahog), *Mytilus edulis* (blue mussel), *Mya arenaria* (softshell clam), *Argopecten irradians* (bay scallop), and *Crassostrea virginica* (eastern oyster).

2. Maintenance of seawater at 25ºC

A seawater temperature of 25ºC was employed in these experiments because this value falls within the narrow range of temperatures that is experienced by all of the organisms investigated in this study at some point during the year (Table DR4). Furthermore, a fixed water temperature is necessary to maintain an equivalent range of aragonite saturation states amongst the six sets of aquaria, as temperature plays an important role in determining the effect of pCO_2 on the aragonite saturation state of seawater (Morse and Mackenzie, 1990). Nevertheless, we recognize that temperature stress could potentially modify an organism's response to pCO_2-induced reductions in $CaCO_3$ saturation state. However, it is unlikely that the wide range of calcification responses observed in our experiments (Fig. 1) results from differential temperature stress, as both positive and negative calcification response patterns were exhibited by tropical as well as temperate species (Fig. 1; Table DR4).

3. Carbonate system manipulation and constraint

The experimental air-CO_2 gases (± SD) of 409 (± 6), 606 (± 7), 903 (± 12), and 2856 (± 54) ppm pCO_2 were formulated using *Cole-Parmer* mass flow controllers (catalog #: K-32907-51; K-32661-16; 00119FB). These air-CO_2 gas mixtures were introduced to the aquaria with 6-inch micro-porous air-stones secured to the base of the aquaria at approximately 30 cm depth. Salinity, temperature, and pH of the experimental seawaters were measured weekly, while alkalinity of the experimental seawaters and pCO_2 of the mixed gases were measured biweekly. Aragonite saturation state, DIC, and pCO_2 were calculated from these measured parameters. Average (± standard deviation) values of the measured and calculated carbonate system parameters are presented in Table DR2.

a. Measured parameters (Table DR2)

Mixed-gas pCO_2 was measured with a *Qubit S151* infrared pCO_2 analyzer calibrated with certified air-CO_2 mixed-gas standards (precision = ±2.0%; accuracy = ±1.8%). Temperature was measured with a partial-immersion mercury-glass thermometer (precision = ±0.3%, accuracy = ±0.4%). Salinity was determined from the measurement of total dissolved solids (TDS) and/or using a refractometer calibrated with simultaneous determinations of TDS (precision = ±0.3%; accuracy = ±0.4%). Alkalinity of seawater in each aquarium was determined biweekly via small (precision = ±0.5%, accuracy = ±0.5%) and/or large volume Gran titrations (precision = ±0.3%, accuracy = ±0.3%) calibrated with certified Dickson alkalinity standards. Seawater pH was determined weekly using an *Orion* pH electrode/meter calibrated with certified NBS pH standards of 4.01, 7.00, and 10.01 (precision = ±0.01; accuracy = ±0.02).

The alkalinity in several sets of tanks was greater for treatments equilibrated with the highest pCO_2 (2856 ppm) than for tanks equilibrated with lower pCO_2 (409, 606, 903 ppm; see Table DR2). This was caused by the dissolution of $CaCO_3$ occurring in response to the undersaturated conditions ($\Omega arag < 1$) maintained within the highest pCO_2 treatments. This should not pose a problem to the interpretation of the results because the calcification response patterns are plotted as a function of the saturation state of seawater with respect to aragonite. Since this parameter is calculated from both the pH and alkalinity of the seawater, it accounts for any effects that the increased alkalinity would have on the aragonite saturation state of the experimental seawaters.

b. Calculated parameters (Table DR2)

Aragonite saturation states and DIC of the experimental seawaters, and pCO_2 of the mixed gases, were calculated from the measured values of temperature, salinity, alkalinity and pH using the program CO2SYS (Pierrot et al, 2006) with Roy et al. (1993) values for carbonic acid constants K1 and K2, Mucci (1983) value for the stoichiometric aragonite solubility product, and pressure = 1.15 atm. Differences amongst $\Omega_{aragonite}$ for the experimental seawaters equilibrated with the four pCO_2 levels are statistically significant ($p \leq 0.05$) for each of the six sets of tanks (Table DR2). Dissolved inorganic carbon (DIC) calculated from simultaneous measurements of pH, alkalinity, temperature, and salinity had an average %-difference of 1.7% relative to DIC values determined at the start of the experiment by large volume Gran Titration (Bradshaw et al., 1981)

calibrated with certified Dickson DIC standards (precision = ±0.1%, accuracy = ±0.1%; Fig. DR2).

4. Selection of dissociation constants for CO2SYS carbonate system calculations

We recognize that the choice of carbonate dissociation constants will influence the calculated carbonate system parameters, including the two parameters of most relevance to this study - carbonate ion concentration and aragonite saturation state. For example, using carbonate dissociation constants from Roy et al. (1993) in these calculations results in higher carbonate ion concentrations (by 6.6 ± 2.5 μmol/kg $CO_3^{=}$), and lower aqueous CO_2 and HCO_3^- concentrations (by 0.2 ± 0.1 and 13.3 ± 5.1 μmol/kg HCO_3^-), than those calculated using dissociation constants from Dickson and Millero (1987). As a result, using Roy et al (1993) constants with alkalinity and pH as inputs yields a higher estimate of the aragonite saturation state of the 24 aquaria (by 0.11 ± 0.04 μmol/kg) than using the Dickson and Millero (1987) constants. However, this difference is small relative to the differences amongst the aragonite saturation states corresponding to the four pCO_2 levels employed in our experiments. Recalculating our saturation state values with different sets of constants does not visibly alter our figures or the trends they show, nor will it materially alter our discussion of or conclusions from these experiments.

5. Specimen collection

Organisms were collected, pursuant to local, state, and federal regulations, from the following US localities (Table DR4): *Callinectes sapidus* (blue crab) from the Chesapeake Bay, Maryland; *Homarus americanus* (american lobster) from the Gulf of Maine;

Penaeus plebejus (edible shrimp), *Eucidaris tribuloides* (tropical urchin), and *Arbacia punctulata* (temperate urchin) from the Atlantic Ocean off the coast of Florida; *Littorina littorea* (periwinkle), *Urosalpinx cinerea* (whelk), *Crepidula fornicata* (limpet), *Mytilus edulis* (blue mussel), and *Crassostrea virginica* (eastern Oyster) from Buzzards Bay, Massachusetts; *Strombus alatus* (conch) from the Gulf of Mexico off the coast of Florida; *Hydroides crucigera* (feather duster worm), *Mercenaria mercenaria* (quahog), *Mya arenaria* (softshell clam), and *Argopecten irradians* (bay scallop) from Nantucket Sound off the coast of Massachusetts; and *Oculina arbuscula* (temperate coral) from the Atlantic Ocean off the coast of North Carolina. After collection, organisms were transported by airplane, boat, or automobile to the Environmental Systems Laboratory at the Woods Hole Oceanographic Institution, where they were immediately placed in holding tanks equilibrated with ambient pCO_2 (~409 ppm). After approximately 14 days of acclimatization to the laboratory conditions, healthy specimens were transferred to the experimental seawaters for an additional 14 days of acclimatization prior to the official start of the experiment.

6. Buoyant weighing technique

A buoyant weighing method (precision = ±0.3%; accuracy varies from ±0.4% to ±6.2%, depending on type of organism – see Fig. DR1 and Table DR3) was employed to estimate the organisms' net rates of calcification/dissolution under the experimental conditions (Table DR1). Specimens were suspended at 15 cm depth in an aquarium filled with 0.2 µm-filtered seawater (T = 25 ºC, Sal = 32 ppt) by a hook or basket attached to an aluminum wire hanging from a *Cole Parmer* bottom-loading scale. Net calcification rates were

calculated as the %-weight difference between the specimens' buoyant weight at the beginning and end of the 60-day experiment. This percentage change in the buoyant weight of these organisms will reflect their total calcification minus their $CaCO_3$ lost through dissolution, molting, or abrasion. This is referred to in the text as their "net calcification/dissolution rate." Measured changes in buoyant weight were generally on the order of hundreds or thousands of milligrams, well above the milligram precision of the scale. Sixty-day calcification rates were normalized to the specimen's initial size by dividing the specimen's calcification rate by its buoyant weight at the beginning of the experiment (Fig. 1; Table DR1).

The buoyant weighing method for estimating dry $CaCO_3$ weight was calibrated for each of the organisms investigated in this study by plotting each specimen's final buoyant weight against its final dry $CaCO_3$ weight (Fig. DR1; Table DR3), which was estimated as the dry weight of the organism's shell or skeleton after tissue, chitin, and vegetative material had been removed via combustion for 6 hours at 550ºC (Heiri et al., 2001). Buoyant weight and dry $CaCO_3$ weight are highly correlated ($R^2 > 0.96$, $p < 0.0001$; Table DR3) and plot on a straight line passing near the origin for each of the species investigated (Fig. DR1). This indicates that a statistically-significant relationship exists between buoyant weight and dry $CaCO_3$ weight and that this relationship is relatively constant (linear) regardless of the size of the specimen or the pCO_2 conditions under which it was grown.

We recognize that the buoyant weighing method of estimating net calcification or dissolution is limited by various factors, including (a) the potential for unintended measurement of organic material attached to the shell or skeleton that is of a density unequal to that of seawater and (b) measurement of shell material that changes density throughout the molting cycle (e.g., crustacea). However, since the buoyant weight calibration curves are based upon the specimens actually employed in the experiments, and therefore include the range of molt stages, differences in tissue density, etc. actually measured, any error in the buoyant weight method associated with these factors will be manifest as a deviation from the regressed calibration curve. Thus, the average %-error of the $CaCO_3$ vs. buoyant wt. regressions quantifies the potential error imparted by these complicating factors for each of the organisms investigated. Critically, these errors range only from 0.4 to 6.2% (Table DR3). Thus, given the excellent correlation between buoyant weight and dry $CaCO_3$ weight observed for each of the organisms investigated in this study (Fig. DR1, Table DR3), combined with the need to make non-destructive determinations of shell/skeletal mass at the beginning of the experiment, buoyant weight constitutes a viable and justified approach to estimating net rates of calcification or dissolution for the organisms investigated in these experiments.

7. Survivorship

A linear regression of average calcification rate (y; wt-%/60-day) vs. survival rate (x; %) for the species investigated (data obtained from Table DR1) reveals a weak, inverse relationship ($y = -251.8x + 258.5$; $R^2 = 0.087$; $p=0.01$) between these variables, such that calcification rates marginally decline with increasing survival rates. Thus, ancillary tank

stress, as estimated by reduced survivorship, appears not to have resulted in reductions in net rates of calcification.

A linear regression of survival rate (y; %) vs. saturation state (x) for the species investigated (data obtained from Table DR1) reveals that there is no significant relationship between these variables ($y = 0.017x + 0.746$; $R^2 = 0.004$; $p=0.61$). Thus, the reduced survivorship exhibited by organisms under the various pCO_2 treatments appears not to have resulted directly from increased levels of stress associated with reduced $CaCO_3$ saturation states, reduced pH, and/or elevated DIC.

8. Previous investigations of closely related species

Previous investigations of species that are the same or closely related to those investigated in the present study have been conducted by Berge et al. (2006; *Mytilus edulis*), Gazeau et al. (2007; *Mytilus edulis and Crassostrea gigas*), and Shirayama and Thornton (2005; *Strombus luhuanus*). While a thorough review of all previous acidification studies is beyond the scope of the present work, we will briefly summarize the findings of these particularly relevant works and discuss how they compare with the results of the present study.

Berge et al. (2006) observed a significant ($p<0.05$) decrease in the rate of shell extension in *Mytilus edulis* when subjected to a range of pCO_2 levels corresponding to a seawater pH of 6.7, 7.1, 7.4, 7.6, and 8.1. However, over the range of pH levels that we investigated (7.4, 7.6, 8.1), Berge et al (2006) did not identify a statistically significant

($p<0.05$) change in the rate of shell extension in either large or small specimens. These results are consistent with the results of our study, in which *Mytilus edulis* did not exhibit a statistically significant ($p<0.05$) change in net calcification rate when subjected to conditions of elevated pCO_2 spanning a comparable range. However, it is difficult to directly compare the results of Berge et al.'s (2006) work with the present work because Berge et al. measured shell extension rate while we measured net calcification rate (estimated from changes in buoyant weight).

Gazeau et al. (2007) observed a decrease in net rate of calcification (inferred from changes in alkalinity) in *Mytilus edulis* and *Crassostrea gigas* when subjected to a range of pCO_2 comparable to that investigated in the present work. Their observed negative response by *Mytilus edulis* contrasts with the neutral response that we observed. The negative response that they observed for *Crassostrea gigas* is consistent with the negative response that we observed for *Crassostrea virginica*. However, it is difficult to compare the results of their study with the present study because their study was carried out over a period of two hours, while our study took place over 60 days. The negative responses that they observed may be partly attributable to the mussel's initial shock of being placed in extremely chemically-modified seawater, without any period of acclimatization.

Shirayama and Thornton (2005) observed decreases in both the rate of change in wet weight and shell height of *Strombus luhuanus* when reared in seawaters equilibrated with 560 ppm pCO_2. These results are consistent with the results of the present study on *Strombus alatus*. However, direct comparison of the two experiments is complicated by

the fact that Shirayama and Thornton (2005) measured changes in wet weight (which is largely determined by organic tissue mass) and shell height, as opposed to changes in shell mass.

9. Huber-White sandwich estimator of variance

Because specimens of a given species exposed to a given pCO_2 were all reared in the same aquarium, there exists the possibility that the net calcification rates for these specimens would be more tightly clustered about the mean than if they had each been reared in separate tanks. This would be expected to occur if, for instance, there was something unique about each aquarium, beyond its prescribed carbonate chemistry, that caused the response of the inhabiting specimens to be abnormally similar to each other. This would reduce the variance of the measurements, thereby artificially increasing the likelihood that a regression through the data would pass a test for significance that is based upon a model of normal probability distribution.

We controlled for this so-called "clustering" within tanks by employing Generalized Estimating Equations that employ the Huber-White sandwich estimator of variance, also known as the Robust Covariance Matrix, in place of the standard estimator of variance (Rogers, 1993). Essentially, instead of employing statistical parameters that assume that the data will be normally distributed about the mean (via the standard estimator of variance), the Huber-White estimator of variance uses a Taylor Series Expansion to adjust the statistical parameters so that they are based on the actual distribution of the data in each of the tanks – thus subjecting the data to a more rigorous test for significance

(i.e., one that is *more* difficult to pass). In all cases, the p-value generated using the Huber-White estimator of variance was greater than that generated using the standard estimator of variance, which is indicative of a more rigorous test for significance. This conservative approach minimizes the likelihood of committing a type 1 statistical error.

10. Polymorph mineralogy of investigated organisms presented in Table 1

Polymorph of $CaCO_3$ (aragonite, low-Mg calcite, high-Mg calcite) in shell or skeleton of investigated organisms was originally reported in Clarke and Wheeler (1917), Chave (1954), and/or Lowenstam (1954, 1964) and confirmed in the present study by x-ray diffraction and scanning electron microscopy.

11. Captions for supplementary figures

Figure DR1. Plots of buoyant weight (x-axis) vs. dry $CaCO_3$ weight (y-axis) of species investigated in the present study. These measurements are highly correlated ($R^2 > 0.96$, $p < 0.0001$) and plot on a straight line passing through the origin, indicating that a statistically significant relationship exists between buoyant weight and dry $CaCO_3$ weight and that this relationship is relatively constant (pursuant to the statistics presented in Table DR3), regardless of the size of the specimen or the pCO_2 conditions under which it was grown. Dry $CaCO_3$ weight is the dry weight of the organism's shell or skeleton after tissue or vegetative material had been removed via combustion for 6 hours at 550ºC (Heiri et al., 2001). Regressions were calculated using the least-squares method.

Figure DR2. Plot of dissolved inorganic carbon (DIC) measured from large volume Gran titration (Bradshaw et al., 1981; y-axis) vs. DIC calculated from temperature, salinity, pH, and alkalinity (x-axis) for all 24 experimental seawaters on 8/31/2008. The two methods yielded DIC values that were highly correlated ($R^2 = 0.9937$; average %-difference = 1.7%). Linear regression was calculated using the least-squares method.

Figure DR3. Graphical summary of the calcification response patterns exhibited by organisms grown in experimental seawaters spanning a range of $CaCO_3$ saturation states: positive (A); threshold-positive (B); neutral (C); parabolic (D); threshold-negative (E); and negative (F). Aragonite saturation state and pCO_2 increase in the direction of arrows.

12. Headings for supplementary tables

Table DR1. Average aragonite saturation state (Ω_{arag}), survival rate, number of surviving individuals upon which net calcification rates are based (n), and average net calcification (+)/dissolution (-) rate obtained from buoyant weighing. SD is standard deviation.

Table DR2. Average measured pCO_2, salinity (Sal), temperature (Temp), alkalinity (Alk), and pH and average calculated dissolved inorganic carbon (DIC), pCO_2, aragonite saturation state (Ω_{arag}), and student's t-test statistics (t-test, P-value) for differences in Ω_{arag} at given pCO_2 vs. next lowest pCO_2 for each aquaria in the 60-day experiment. SD is standard deviation.

Table DR3. Calibration of the buoyant weight method, including the least-squares linear regression through the buoyant weight (x) and dry $CaCO_3$ weight (y) data, the correlation coefficient of the regression (R^2), and the average %-error of the regression (absolute value of the difference between the measured and predicted dry $CaCO_3$ weight divided by the measured dry $CaCO_3$ weight).

Table DR4. Collection site, annual water temperature range (National Oceanic and Atmospheric Administration, 2008), food (during experiment), and stage of development of the organisms investigated in the present study.

Table DR5. Linear, quadratic, and exponential regression analyses of $\Omega_{aragonite}$ vs. net calcification rate for each of the 18 species investigated in the present study, calculated using the least squares method. The regression analysis (linear, quadratic, or exponential) that yielded the lowest square root of the mean squared error for a given species (i.e., "Best-fit") is shown in bold and plotted in figure 1 of the text. "p" = p-value; "R^2" = correlation coefficient; "RMSE" = square root of the mean squared error.

Table DR6. Detailed weight data for organisms investigated in the experiments. Initial and final buoyant weight refers to buoyant weight at the beginning and end of the experiment, respectively. Initial and final dry weight of $CaCO_3$ refers to dry weight of $CaCO_3$ at the beginning and end of the experiment, respectively. Dry weight of $CaCO_3$ is estimated from the buoyant weights using the empirically derived calibration curves (Fig. DR1, Table DR3).

References Cited

Berge, J.A., Bjerkeng, B., Pettersen, O., Schaanning, M.T., and Øxnevad, S., 2006, Effects of increased sea water concentrations of CO_2 on growth of the bivalve *Mytilus edulis*. Chemosphere, v. 62, 4 p. 681-687.

Bradshaw, A.L., Brewer, P.G., Shafer, D.K., and Williams, R.T., 1981, Measurements of total carbon dioxide and alkalinity by potentiometric titration in the GEOSECS program. Earth and Planetary Science Letters, v. 55, 1 p. 99-115.

Chave, K.E., 1954, Aspects of the Biogeochemistry of magnesium, 1. Calcareous marine organisms. Journal of Geology, v. 62, p. 266-283.

Clarke, F.W., and Wheeler, W.C., 1917, The inorganic constituents of marine invertebrates. United States Geological Survey Professional Paper, v. 102, p. 1–56.

Dickson, A.G., and Millero, F.J., 1987, A comparison of the equilibrium constants for the dissociation of carbonic acid in seawater media. Deep-sea Research, v. 34, 10 p. 1733-1743.

Gazeau, F., Quiblier, C., Jansen, J.M., Gattuso, J.P., Middleburg, J.J., and Heip, C.H.R., 2007, Impact of elevated CO_2 on shellfish calcification. Geophysical Research Letters, v. 34, p. L07603.

Heiri, O.O., Lotter, A.F., and Lemcke, G., 2001, Loss on ignition as a method for estimating organic and carbonate content in sediments: reproducibility and comparability of results. Journal of Paleolimnology, v. 25, 1 p. 101-110.

Lowenstam, H.A., 1964, Coexisting calcites and aragonites from skeletal carbonates of marine organisms and their strontium and magnesium contents, in Y. Miyake and T.

Koyama, eds., Recent researches in the fields of hydrosphere, atmosphere and nuclear geochemistry: Tokyo, p. 373-404.

Lowenstam, H.A., 1954, Factors affecting the aragonite:calcite ratios in carbonate-secreting marine organisms. Journal of Geology, v. 62, p. 284-322.

Morse, J.W., and Mackenzie, F.T., 1990, Geochemistry of Sedimentary Carbonates v. 48: Amsterdam, Elsevier, 707 p.

Mucci, A., 1983, The solubility of calcite and aragonite in seawater at various salinities, temperatures, and one atmosphere total pressure. American Journal of Science, v. 283, p. 780-799.

National Oceanic and Atmospheric Administration. National Oceanic and Atmospheric Administration Integrated Ocean Observing System 2008 http://ioos.noaa.gov/program/products.html.

Pierrot, D., Lewis, E., and Wallace, D. W. R., 2006, *MS Excel Program Developed for CO_2 System Calculations*. ORNL/CDIAC-105a. Carbon Dioxide Information Analysis Center, Oak Ridge National Laboratory, U.S. Department of Energy, Oak Ridge, Tennessee.

Roy, R.N., Roy, L.N., Vogel, K.M., Porter-Moore, C., Pearson, T., Good, C.E., Millero, F.J., and Campbell, D.M., 1993, The dissociation constants of carbonic acid in seawater at salinities 5 to 45 and temperatures 0 to 45°C. Marine Chemistry, v. 44, p. 249-267.

Shirayama, Y., and Thornton, H., 2005, Effect of increased atmospheric CO_2 on shallow water marine benthos. Journal of Geophysical Research, v. 10, p. C09S08.

Figure DR1

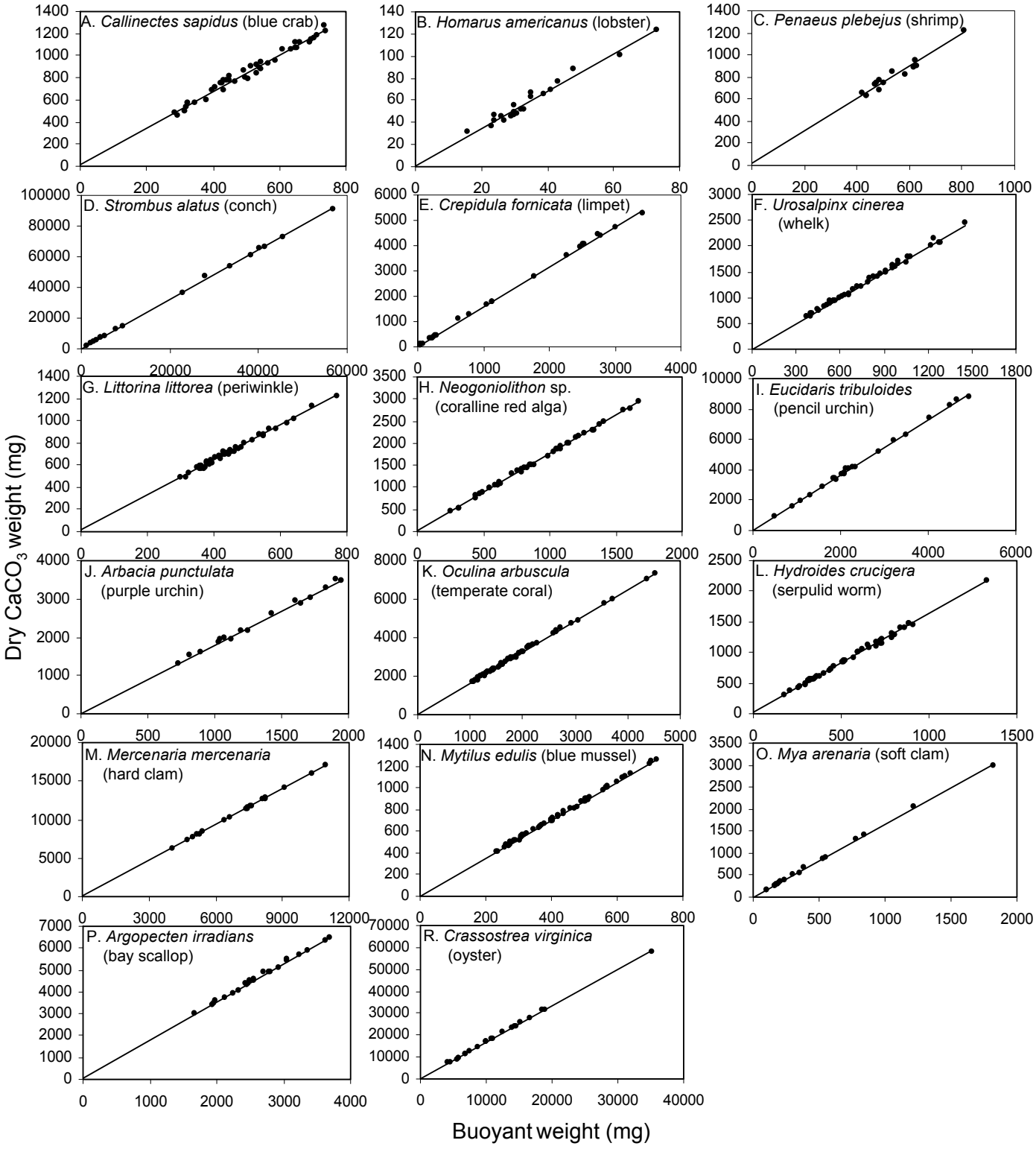
A. Callinectes sapidus (blue crab)
B. Homarus americanus (lobster)
C. Penaeus plebejus (shrimp)
D. Strombus alatus (conch)
E. Crepidula fornicata (limpet)
F. Urosalpinx cinerea (whelk)
G. Littorina littorea (periwinkle)
H. Neogoniolithon sp. (coralline red alga)
I. Eucidaris tribuloides (pencil urchin)
J. Arbacia punctulata (purple urchin)
K. Oculina arbuscula (temperate coral)
L. Hydroides crucigera (serpulid worm)
M. Mercenaria mercenaria (hard clam)
N. Mytilus edulis (blue mussel)
O. Mya arenaria (soft clam)
P. Argopecten irradians (bay scallop)
R. Crassostrea virginica (oyster)
Dry CaCO3 weight (mg)
Buoyant weight (mg)

Figure DR2

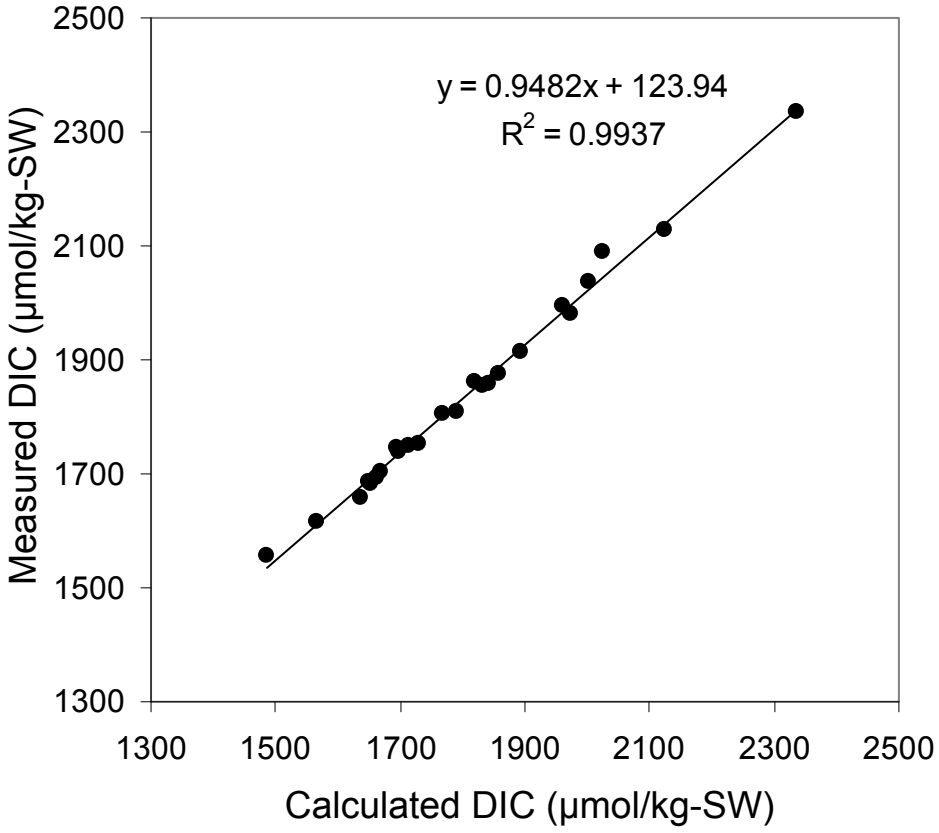
y = 0.9482x + 123.94
R2 = 0.9937
Measured DIC (µmol/kg-SW)
Calculated DIC (µmol/kg-SW)
2500
2300
2100
1900
1700
1500
1300
1300
1500
1700
1900
2100
2300
2500

Figure DR3

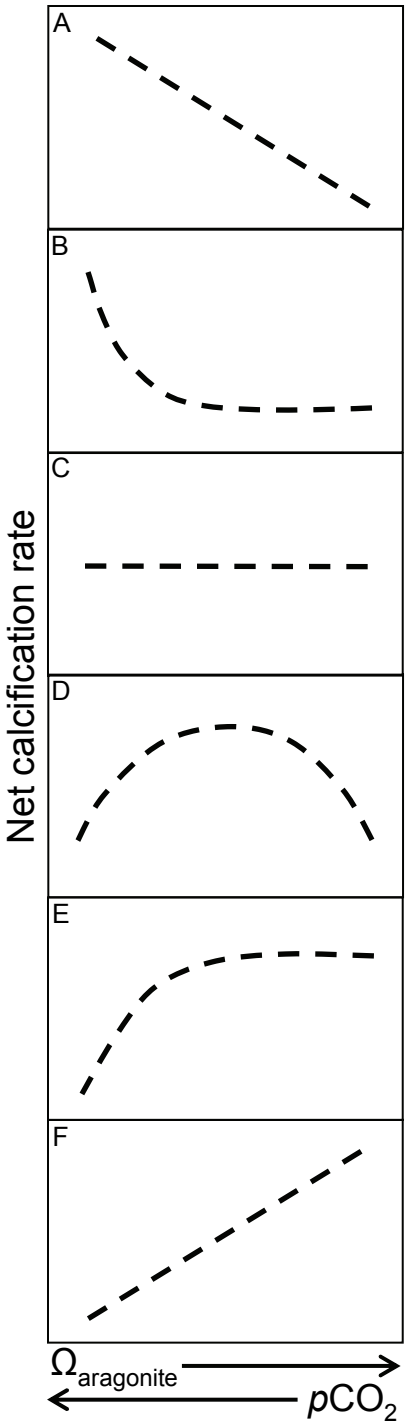

Table DR1

Organism	Scientific name	Ωarag	SD	Survival rate	n	Net calcification (AVG)	SD
						(wt-%/60-day)	(wt-%/60-day)
Lobster	*Homarus americanus*	2.13	0.38	25%	3	353.0	91.0
Lobster	*Homarus americanus*	1.53	0.39	25%	3	349.5	39.6
Lobster	*Homarus americanus*	1.13	0.25	42%	5	376.3	58.6
Lobster	*Homarus americanus*	0.47	0.07	58%	7	606.1	164.6
Crab	*Callinectes sapidus*	2.13	0.38	75%	9	433.8	138.0
Crab	*Callinectes sapidus*	1.53	0.39	83%	10	598.2	116.7
Crab	*Callinectes sapidus*	1.13	0.25	75%	9	600.9	117.3
Crab	*Callinectes sapidus*	0.47	0.07	67%	8	724.0	109.2
Shrimp	*Penaeus plebejus*	2.13	0.38	100%	3	15.3	11.4
Shrimp	*Penaeus plebejus*	1.53	0.39	100%	3	17.3	7.4
Shrimp	*Penaeus plebejus*	1.13	0.25	100%	3	27.5	9.4
Shrimp	*Penaeus plebejus*	0.47	0.07	100%	3	37.8	13.7
Conch	*Strombus alatus*	2.28	0.19	100%	6	2.0	0.5
Conch	*Strombus alatus*	1.93	0.26	83%	5	0.8	1.2
Conch	*Strombus alatus*	1.51	0.20	83%	5	1.2	1.4
Conch	*Strombus alatus*	0.68	0.12	83%	5	-3.1	2.0
Limpet	*Crepidula fornicata*	2.28	0.19	71%	5	12.4	9.5
Limpet	*Crepidula fornicata*	1.93	0.26	43%	3	22.2	6.8
Limpet	*Crepidula fornicata*	1.51	0.20	71%	5	33.0	5.0
Limpet	*Crepidula fornicata*	0.68	0.12	57%	4	21.2	7.0
Whelk	*Urosalpinx cinerea*	2.28	0.19	67%	8	2.9	1.9
Whelk	*Urosalpinx cinerea*	1.93	0.26	75%	9	0.7	1.1
Whelk	*Urosalpinx cinerea*	1.51	0.20	67%	8	0.7	0.6
Whelk	*Urosalpinx cinerea*	0.68	0.12	67%	8	-1.5	0.9
Periwinkle	*Littorina littorea*	2.28	0.19	100%	12	3.8	2.9
Periwinkle	*Littorina littorea*	1.93	0.26	75%	9	1.9	1.6
Periwinkle	*Littorina littorea*	1.51	0.20	92%	11	0.9	2.1
Periwinkle	*Littorina littorea*	0.68	0.12	83%	10	-1.2	3.4
Coralline red alga	*Neogoniolithon sp.*	3.12	0.22	83%	10	5.7	2.9
Coralline red alga	*Neogoniolithon sp.*	2.40	0.42	92%	11	14.5	6.6
Coralline red alga	*Neogoniolithon sp.*	1.84	0.13	83%	10	10.7	4.7
Coralline red alga	*Neogoniolithon sp.*	0.90	0.05	92%	11	3.6	3.5
Halimeda	*Halimeda incrassata*	3.12	0.22	100%	3	23.9	12.5
Halimeda	*Halimeda incrassata*	2.40	0.42	100%	3	43.9	7.8
Halimeda	*Halimeda incrassata*	1.84	0.13	100%	3	25.4	3.0
Halimeda	*Halimeda incrassata*	0.90	0.05	100%	5	6.0	2.6
Pencil urchin	*Eucidaris tribuloides*	2.06	0.35	83%	5	8.7	6.4
Pencil urchin	*Eucidaris tribuloides*	1.58	0.30	67%	4	5.6	2.7
Pencil urchin	*Eucidaris tribuloides*	1.21	0.14	50%	3	5.6	3.1
Pencil urchin	*Eucidaris tribuloides*	0.54	0.06	100%	6	-18.3	7.3
Purple urchin	*Arbacia punctulata*	2.06	0.35	67%	4	8.2	5.7
Purple urchin	*Arbacia punctulata*	1.58	0.30	100%	6	39.4	5.0
Purple urchin	*Arbacia punctulata*	1.21	0.14	50%	3	42.8	3.8
Purple urchin	*Arbacia punctulata*	0.54	0.06	67%	4	28.5	1.9
Coral	*Oculina arbuscula*	2.60	0.26	58%	11	11.8	1.2
Coral	*Oculina arbuscula*	2.28	0.18	79%	15	11.6	1.2
Coral	*Oculina arbuscula*	1.64	0.18	63%	12	11.1	1.5
Coral	*Oculina arbuscula*	0.77	0.07	89%	17	3.8	1.7
Serpulid worm	*Hydroides crucigera*	2.60	0.26	92%	11	3.5	4.1
Serpulid worm	*Hydroides crucigera*	2.28	0.18	78%	7	5.5	3.8
Serpulid worm	*Hydroides crucigera*	1.64	0.18	100%	12	2.3	4.0
Serpulid worm	*Hydroides crucigera*	0.77	0.07	92%	11	1.3	3.8
Hard clam	*Mercenaria mercenaria*	2.63	0.30	100%	7	1.0	0.6
Hard clam	*Mercenaria mercenaria*	2.11	0.41	71%	5	0.7	0.3
Hard clam	*Mercenaria mercenaria*	1.43	0.15	100%	7	0.5	0.4
Hard clam	*Mercenaria mercenaria*	0.71	0.05	86%	6	-1.4	0.4
Blue mussel	*Mytilus edulis*	2.63	0.30	100%	15	4.4	2.2
Blue mussel	*Mytilus edulis*	2.11	0.41	87%	13	3.1	2.5
Blue mussel	*Mytilus edulis*	1.43	0.15	93%	14	3.6	3.4
Blue mussel	*Mytilus edulis*	0.71	0.05	93%	14	3.1	3.2
Soft clam	*Mya arenaria*	2.63	0.30	50%	3	17.5	3.5
Soft clam	*Mya arenaria*	2.11	0.41	83%	5	7.7	3.6
Soft clam	*Mya arenaria*	1.43	0.15	67%	4	0.2	6.9
Soft clam	*Mya arenaria*	0.71	0.05	33%	2	-8.1	6.9
Bay scallop	*Argopecten irradians*	2.63	0.30	67%	5	6.9	2.1
Bay scallop	*Argopecten irradians*	2.11	0.41	50%	3	6.3	0.8
Bay scallop	*Argopecten irradians*	1.43	0.15	83%	5	4.8	4.2
Bay scallop	*Argopecten irradians*	0.71	0.05	83%	5	2.3	1.9
Oyster	*Crassostrea virginica*	2.63	0.30	67%	4	1.9	0.3
Oyster	*Crassostrea virginica*	2.11	0.41	67%	4	1.6	0.4
Oyster	*Crassostrea virginica*	1.43	0.15	67%	4	1.1	0.3
Oyster	*Crassostrea virginica*	0.71	0.05	67%	4	0.3	0.4

Table DR2

	MEASURED										CALCULATED							
Tank	***p*CO2**	**SD**	**Sal**	**SD**	**Temp**	**SD**	**Alk**	**SD**	**pH**	**SD**	**DIC**	**SD**	***p*CO2**	**SD**	**Ωarag**	**SD**	**t-test**	**P-value**
Lobster/Crab/Shrimp (I)	409	5.66	32.0	0.169	24.9	0.179	1860	156.7	8.03	0.0562	1678	139.64	526	63	2.13	0.380	n/a	n/a
Lobster/Crab/Shrimp (II)	606	7.26	31.8	0.148	25.0	0.141	1849	131.0	7.85	0.0962	1732	119.26	839	171	1.53	0.388	2.49	0.0188
Lobster/Crab/Shrimp (III)	903	11.74	32.1	0.969	25.0	0.152	1817	161.9	7.72	0.0575	1744	154.98	1146	124	1.13	0.247	1.92	0.0484
Lobster/Crab/Shrimp (IV)	2856	53.73	31.9	0.187	25.1	0.114	1817	171.2	7.31	0.0348	1860	169.23	3103	217	0.47	0.074	5.76	0.0011
Conch/Limpet/Whelk/Periwinkle (I)	409	5.66	31.8	0.088	25.1	0.110	1770	107.5	8.09	0.0304	1568	100.95	420	46	2.28	0.187	n/a	n/a
Conch/Limpet/Whelk/Periwinkle (II)	606	7.26	31.8	0.228	24.9	0.152	1798	141.8	8.00	0.0719	1634	147.12	561	137	1.93	0.263	2.42	0.0231
Conch/Limpet/Whelk/Periwinkle (III)	903	11.74	31.9	0.191	24.9	0.148	1849	62.8	7.86	0.0734	1733	77.91	831	168	1.51	0.199	2.81	0.0130
Conch/Limpet/Whelk/Periwinkle (IV)	2856	53.73	31.7	0.110	24.9	0.134	2079	124.2	7.42	0.0659	2097	111.49	2758	316	0.68	0.123	8.02	0.0000
Coralline red alga/Halimeda (I)	409	5.66	31.8	0.207	25.0	0.055	2008	56.5	8.19	0.0317	1738	50.35	359	32	3.12	0.221	n/a	n/a
Coralline red alga/Halimeda (II)	606	7.26	31.7	0.118	25.0	0.152	1987	127.3	8.05	0.0604	1786	100.71	526	68	2.40	0.420	3.41	0.0071
Coralline red alga/Halimeda (III)	903	11.74	31.5	0.155	25.1	0.164	2044	53.2	7.91	0.0286	1903	45.91	802	48	1.84	0.129	2.81	0.0187
Coralline red alga/Halimeda (IV)	2856	53.73	31.8	0.258	24.9	0.130	2354	37.0	7.49	0.0216	2350	33.21	2593	106	0.90	0.050	15.33	0.0000
Pencil urchin/Purple urchin (I)	409	5.66	31.9	0.269	25.1	0.122	1744	146.8	8.04	0.0574	1563	126.86	473	67	2.06	0.347	n/a	n/a
Pencil urchin/Purple urchin (II)	606	7.26	31.8	0.099	25.0	0.152	1751	168.3	7.90	0.0510	1623	144.58	686	35	1.58	0.302	2.37	0.0228
Pencil urchin/Purple urchin (III)	903	11.74	31.7	0.286	24.9	0.114	1792	116.6	7.77	0.0241	1707	107.63	999	44	1.21	0.136	2.46	0.0244
Pencil urchin/Purple urchin (IV)	2856	53.73	31.7	0.218	25.0	0.148	1891	78.2	7.36	0.0328	1921	73.47	2854	159	0.54	0.060	10.01	0.0000
Coral/Serpulid worm (I)	409	5.66	31.7	0.208	25.0	0.191	1960	29.7	8.11	0.0628	1738	46.83	450	83	2.60	0.263	n/a	n/a
Coral/Serpulid worm (II)	606	7.26	31.6	0.353	24.9	0.129	2012	36.7	8.03	0.0376	1824	31.62	573	52	2.28	0.175	2.00	0.0509
Coral/Serpulid worm (III)	903	11.74	31.7	0.426	24.9	0.141	2027	29.9	7.85	0.0519	1907	29.70	915	110	1.64	0.183	5.04	0.0012
Coral/Serpulid worm (IV)	2856	53.73	31.5	0.633	25.2	0.058	2071	48.3	7.48	0.0332	2070	40.33	2377	128	0.77	0.067	9.00	0.0004
Clams/Mussel/Scallop/Oyster (I)	409	5.66	32.1	0.288	25.1	0.148	1833	125.3	8.15	0.0404	1598	112.11	370	46	2.63	0.299	n/a	n/a
Clams/Mussel/Scallop/Oyster (II)	606	7.26	31.7	0.199	25.1	0.110	1862	141.3	8.02	0.0803	1684	126.47	547	119	2.11	0.408	2.31	0.0272
Clams/Mussel/Scallop/Oyster (III)	903	11.74	31.9	0.251	25.0	0.158	1856	91.7	7.83	0.0452	1749	87.20	892	108	1.43	0.151	3.51	0.0085
Clams/Mussel/Scallop/Oyster (IV)	2856	53.73	31.9	0.240	25.0	0.084	2063	42.6	7.45	0.0370	2071	50.88	2551	256	0.71	0.050	10.11	0.0001

Table DR3

Organism	Scientific name	Buoyant (x) vs. $CaCO_3$ wt (y) (mg)	R^2	AVG %-err
Lobster	*Homarus americanus*	y = 1.687x + 0.5583	0.9684	6.202%
Crab	*Callinectes sapidus*	y = 1.649x + 13.83	0.9782	3.558%
Shrimp	*Penaeus plebejus*	y = 1.468x + 13.20	0.9521	3.745%
Conch	*Strombus alatus*	y = 1.608x - 38.29	0.9993	1.323%
Limpet	*Crepidula fornicata*	y = 1.578x + 12.76	0.9994	5.339%
Whelk	*Urosalpinx cinerea*	y = 1.653x + 5.449	0.9951	1.986%
Periwinkle	*Littorina littorea*	y = 1.576x + 10.13	0.9909	1.925%
Coralline red alga	*Neogoniolithon* sp.	y = 1.745x + 8.957	0.9985	1.815%
Pencil urchin	*Eucidaris tribuloides*	y = 1.830x - 27.03	0.9986	1.465%
Purple urchin	*Arbacia punctulata*	y = 1.787x + 17.37	0.9933	2.144%
Coral	*Oculina arbuscula*	y = 1.612x + 33.78	0.9991	1.131%
Serpulid worm	*Hydroides crucigera*	y = 1.614x + 14.95	0.9967	2.150%
Hard clam	*Mercenaria mercenaria*	y = 1.551x - 7.818	0.9997	0.408%
Blue mussel	*Mytilus edulis*	y = 1.750x + 2.759	0.9985	1.121%
Soft clam	*Mya arenaria*	y = 1.661x - 6.619	0.9994	3.107%
Bay scallop	*Argopecten irradians*	y = 1.744x + 62.49	0.9958	1.108%
Oyster	*Crassostrea virginica*	y = 1.654x + 249.0	0.9989	1.997%

Table DR4

Organism	Scientific name	Collection site	Ann temp range (ºC)	Food	Age
Lobster	*Homarus americanus*	Gulf of Maine, ME	1 - 26	*Artemia* sp.	juvenile
Crab	*Callinectes sapidus*	Chesapeake Bay, MD	3 - 32	*Artemia* sp.	juvenile
Shrimp	*Penaeus plebejus*	Atlantic Ocean, FL	20 - 32	*Artemia* sp.	adult
Conch	*Strombus alatus*	Gulf of Mexico, FL	20 - 30	green algae	adult
Limpet	*Crepidula fornicata*	Buzzards Bay, MA	3 - 28	green algae	adult
Whelk	*Urosalpinx cinerea*	Buzzards Bay, MA	3 - 28	green algae	adult
Periwinkle	*Littorina littorea*	Buzzards Bay, MA	3 - 28	green algae	adult
Coralline red alga	*Neogoniolithon* sp.	Atlantic Ocean, FL	20 - 32	autotrophic	adult
Halimeda	*Halimeda incrassata*	Atlantic Ocean, FL	20 - 32	autotrophic	adult
Pencil urchin	*Eucidaris tribuloides*	Atlantic Ocean, FL	20 - 32	green algae	adult
Purple urchin	*Arbacia punctulata*	Nantucket Sound, MA	1 - 27	green algae	adult
Coral	*Oculina arbuscula*	Atlantic Ocean, NC	15 - 30	*Artemia* sp.	adult
Serpulid worm	*Hydroides crucigera*	Nantucket Sound, MA	1 - 27	*Artemia* sp.	adult
Hard clam	*Mercenaria mercenaria*	Nantucket Sound, MA	1 - 27	*Artemia* +algae	adult
Blue mussel	*Mytilus edulis*	Buzzards Bay, MA	3 - 28	*Artemia* +algae	adult
Soft clam	*Mya arenaria*	Nantucket Sound, MA	1 - 27	*Artemia* +algae	adult
Bay scallop	*Argopecten irradians*	Nantucket Sound, MA	1 - 27	*Artemia* +algae	adult
Oyster	*Crassostrea virginica*	Buzzards Bay, MA	3 - 28	*Artemia* +algae	adult

Table DR5

Organism	Linear				Quadratic				Exponential				Best-fit	Calcification
	Regression	p	R^2	RMSE	Regression	p	R^2	RMSE	Regression	p	R^2	RMSE		response
Crab	**y = -165x + 807**	**0.00**	**0.41**	**120.71**	y = -41.0x^2 - 57.9x + 752	0.00	0.41	121.74	y = -119$e^{60.6x}$ + 871	0.33	0.41	121.58	linear	positive
Shrimp	**y = -14.3x + 43.3**	**0.01**	**0.47**	**9.98**	y = 5.61x^2 - 28.8x + 50.6	0.00	0.49	10.30	y = 48.0$e^{-70.7x}$ + 3.71	0.27	0.49	10.33	linear	positive
Lobster	y = 173x + 649	0.05	0.43	126.40	y = 181x^2 - 620x + 856	0.00	0.56	114.79	**y = 1296e^{-344x} + 348**	**0.00**	**0.57**	**112.11**	exponential	threshold(+)
Limpet	y = -5.67x + 31.4	0.43	0.11	10.22	**y = -24.4x^2 + 66.3x - 12.5**	**0.00**	**0.59**	**7.17**	y = -0.001e^{518x} + 27.1	0.53	0.41	8.64	quadratic	parabolic
Purple urchin	y = -9.93x + 43.9	0.50	0.15	13.42	**y = -45.7x^2 + 106x - 15.9**	**0.00**	**0.91**	**4.65**	y = 639$e^{-1.56x}$ - 595	0.51	0.15	13.44	quadratic	parabolic
Coralline red alga	y = 1.82x + 4.94	0.57	0.06	6.17	**y = -6.66x^2 + 28.2x + -16.7**	**0.03**	**0.43**	**4.86**	y = -750e^{-523x} + 10.5	0.00	0.23	5.57	quadratic	parabolic
Halimeda	y = 11.6x + 0.04	0.18	0.43	12.42	**y = -15.4x^2 + 71.2x - 46.6**	**0.02**	**0.74**	**8.73**	y = - 23340e^{-242x} + 3228	0.62	0.63	1039.75	quadratic	parabolic
Blue mussel	y = 0.53x + 2.67	0.12	0.02	2.84	y = 0.51x^2 - 1.18x + 3.82	0.09	0.02	2.86	y = -1806$e^{-0.03x}$ + 1809	0.12	0.02	2.84	none	neutral
Temperate coral	y = 4.56x + 1.19	0.01	0.74	1.97	y = -3.93x^2 + 17.4x - 7.22	0.00	0.86	1.46	**y = -67.2e^{-277x} + 11.8**	**0.00**	**0.87**	**1.43**	exponential	threshold(-)
Pencil urchin	y = 18.1x - 25.1	0.01	0.73	7.21	y = -16.2x^2 + 59.4x - 45.3	0.00	0.83	5.89	**y = -137e^{-304x} + 8.25**	**0.02**	**0.84**	**5.68**	exponential	threshold(-)
Hard clam	y = 1.12x - 1.73	0.04	0.67	0.60	y = -0.94x^2 + 4.28x - 3.89	0.00	0.81	0.46	**y = -10.3e^{-210x} + 0.94**	**0.00**	**0.83**	**0.44**	exponential	threshold(-)
Conch	y = 3.01x - 4.60	0.01	0.62	1.48	y = -2.00x^2 + 8.87x - 8.11	0.00	0.68	1.40	**y = -21.9e^{-222x} + 1.75**	**0.00**	**0.69**	**1.37**	exponential	threshold(-)
Serpulid worm	**y = 1.64x - 0.02**	**0.05**	**0.08**	**3.93**	y = -0.35x^2 + 2.80x - 0.81	0.08	0.09	3.99	y = -9.27$e^{-28.1x}$ + 8.64	0.82	0.08	3.99	linear	negative
Bay scallop	**y = 2.37x - 0.97**	**0.00**	**0.34**	**2.61**	y = -0.94x^2 + 5.52x - 1.14	0.00	0.36	2.66	y = -10.3$e^{-80.3x}$ + 8.13	0.00	0.36	2.66	linear	negative
Periwinkle	**y = 2.99x - 3.41**	**0.00**	**0.34**	**2.55**	y = 1.00x^2 - 0.01x - 1.65	0.00	0.35	2.57	y = 1.49$e^{69.3x}$ - 3.52	0.03	0.35	2.57	linear	negative
Oyster	**y = 0.84x - .23**	**0.00**	**0.76**	**0.36**	y = -0.21x^2 + 1.55x - 0.71	0.00	0.78	0.36	y = -3.67$e^{-53.2x}$ + 2.80	0.00	0.78	0.36	linear	negative
Whelk	**y = 2.45x - 3.26**	**0.01**	**0.58**	**1.28**	y = 0.69x^2 + 0.47x - 2.09	0.01	0.59	1.28	y = -168.6$e^{-1.485x}$ + 165.3	0.01	0.58	1.28	linear	negative
Soft clam	**y = 13.0x - 18.2**	**0.00**	**0.73**	**5.31**	y = 2.46x^2 + 4.57x - 12.1	0.00	0.73	5.31	y = 14.6$e^{42.3x}$ - 27.2	0.06	0.74	5.43	linear	negative

Table DR6

Organism	Ωarag	Buoyant Weight		Dry Weight of CaCO3	
		Initial (mg)	Final (mg)	Initial (mg)	Final (mg)
Lobster	2.13	34	120	58	203
Lobster	2.13	34	162	58	274
Lobster	2.13	32	170	55	287
Lobster	1.53	37	149	63	253
Lobster	1.53	34	161	58	272
Lobster	1.53	35	165	60	279
Lobster	1.13	34	131	58	221
Lobster	1.13	36	191	61	322
Lobster	1.13	34	178	58	302
Lobster	1.13	33	153	56	258
Lobster	1.13	32	153	55	259
Lobster	0.47	37	225	63	380
Lobster	0.47	35	330	60	558
Lobster	0.47	37	193	63	326
Lobster	0.47	34	295	58	499
Lobster	0.47	35	241	60	407
Lobster	0.47	34	181	58	306
Lobster	0.47	37	289	63	488
Crab	2.13	145	518	253	868
Crab	2.13	144	522	251	875
Crab	2.13	142	958	248	1593
Crab	2.13	144	672	251	1123
Crab	2.13	145	1056	253	1755
Crab	2.13	142	780	248	1301
Crab	2.13	143	644	250	1075
Crab	2.13	146	774	255	1290
Crab	2.13	143	978	250	1627
Crab	1.53	145	830	253	1383
Crab	1.53	147	1215	256	2017
Crab	1.53	144	1031	251	1715
Crab	1.53	145	907	253	1510
Crab	1.53	145	965	253	1604
Crab	1.53	143	765	250	1275
Crab	1.53	142	847	248	1411
Crab	1.53	147	1244	256	2064
Crab	1.53	143	1077	250	1790
Crab	1.53	142	1200	248	1993
Crab	1.13	144	875	251	1456
Crab	1.13	139	1036	243	1722
Crab	1.13	145	887	253	1476
Crab	1.13	146	1253	255	2080
Crab	1.13	142	1225	248	2034
Crab	1.13	145	1117	253	1855
Crab	1.13	144	879	251	1463
Crab	1.13	144	1019	251	1694
Crab	1.13	139	744	243	1241
Crab	0.47	145	1107	253	1839
Crab	0.47	144	974	251	1620
Crab	0.47	142	1030	248	1713
Crab	0.47	141	1366	246	2267
Crab	0.47	145	1130	253	1877
Crab	0.47	147	1213	256	2014
Crab	0.47	143	1257	250	2086
Crab	0.47	149	1451	260	2406
Shrimp	2.13	406	420	610	630
Shrimp	2.13	345	435	520	652
Shrimp	2.13	537	625	801	931
Shrimp	1.53	483	533	723	796
Shrimp	1.53	380	475	571	711
Shrimp	1.53	401	468	602	700
Shrimp	1.13	429	500	643	747
Shrimp	1.13	476	629	712	937
Shrimp	1.13	366	489	551	731
Shrimp	0.47	595	810	887	1202
Shrimp	0.47	288	439	436	658
Shrimp	0.47	495	619	740	922
Conch	2.28	2292	2330	3648	3708
Conch	2.28	3585	3631	5727	5800
Conch	2.28	9277	9524	14879	15276
Conch	2.28	33906	34531	54482	55487
Conch	2.28	37959	38872	61000	62468
Conch	2.28	45328	46222	72849	74286
Conch	1.93	1322	1317	2087	2079

Table DR6 (continued)

Organism	Ωarag	Buoyant Weight		Dry Weight of CaCO3	
		Initial (mg)	Final (mg)	Initial (mg)	Final (mg)
Conch	1.93	4594	4565	7349	7303
Conch	1.93	8123	8229	13023	13194
Conch	1.93	41103	41888	66055	67317
Conch	1.93	33973	34591	54590	55585
Conch	1.51	2862	2831	4563	4514
Conch	1.51	5430	5484	8693	8780
Conch	1.51	22612	23083	36321	37079
Conch	1.51	45020	45978	72354	73895
Conch	1.51	56354	57481	90580	92391
Conch	0.68	3174	3138	5065	5007
Conch	0.68	4862	4822	7779	7715
Conch	0.68	30137	28672	48422	46066
Conch	0.68	42249	40718	67897	65436
Conch	0.68	43183	41029	69401	65936
Crepidula	2.28	2580	2752	4084	4355
Crepidula	2.28	1896	2260	3004	3579
Crepidula	2.28	909	1131	1447	1797
Crepidula	2.28	264	293	430	474
Crepidula	2.28	50	51	92	93
Crepidula	1.93	902	1124	1436	1786
Crepidula	1.93	1968	2510	3119	3973
Crepidula	1.93	168	193	279	317
Crepidula	1.51	2177	3010	3448	4762
Crepidula	1.51	1869	2546	2962	4030
Crepidula	1.51	464	626	745	1001
Crepidula	1.51	194	245	318	399
Crepidula	1.51	166	214	275	351
Crepidula	0.68	2720	3413	4305	5398
Crepidula	0.68	833	1057	1328	1681
Crepidula	0.68	248	277	404	449
Crepidula	0.68	643	777	1027	1238
Whelk	2.28	693	727	1151	1207
Whelk	2.28	1011	1057	1677	1752
Whelk	2.28	1128	1141	1870	1891
Whelk	2.28	788	816	1307	1355
Whelk	2.28	1320	1341	2188	2221
Whelk	2.28	1255	1256	2080	2082
Whelk	2.28	1313	1337	2176	2216
Whelk	2.28	873	918	1449	1523
Whelk	1.93	1016	1013	1684	1680
Whelk	1.93	526	525	875	874
Whelk	1.93	656	666	1091	1106
Whelk	1.93	1130	1151	1873	1909
Whelk	1.93	581	581	966	966
Whelk	1.93	592	589	983	978
Whelk	1.93	416	422	693	703
Whelk	1.93	1029	1032	1706	1711
Whelk	1.93	585	599	973	996
Whelk	1.51	1275	1281	2113	2123
Whelk	1.51	1530	1532	2535	2538
Whelk	1.51	1005	1014	1667	1682
Whelk	1.51	1023	1035	1696	1716
Whelk	1.51	484	485	806	807
Whelk	1.51	880	880	1460	1460
Whelk	1.51	1311	1321	2172	2189
Whelk	1.51	765	780	1271	1295
Whelk	0.68	689	676	1144	1123
Whelk	0.68	591	578	982	961
Whelk	0.68	1157	1154	1917	1914
Whelk	0.68	713	697	1184	1157
Whelk	0.68	1014	1007	1681	1670
Whelk	0.68	711	706	1181	1173
Whelk	0.68	625	610	1039	1015
Whelk	0.68	661	648	1098	1076
Periwinkle	2.28	522	538	832	858
Periwinkle	2.28	364	386	583	619
Periwinkle	2.28	764	772	1215	1227
Periwinkle	2.28	413	428	662	685
Periwinkle	2.28	549	567	875	903
Periwinkle	2.28	592	621	943	989
Periwinkle	2.28	428	441	685	705
Periwinkle	2.28	432	432	691	690
Periwinkle	2.28	421	461	674	737
Periwinkle	2.28	694	695	1104	1105
Periwinkle	2.28	451	484	721	773

Table DR6 (continued)

Organism	Ωarag	Buoyant Weight		Dry Weight of CaCO3	
		Initial (mg)	Final (mg)	Initial (mg)	Final (mg)
Periwinkle	2.28	571	587	910	936
Periwinkle	1.93	455	467	727	747
Periwinkle	1.93	362	361	580	579
Periwinkle	1.93	381	384	610	616
Periwinkle	1.93	409	415	655	664
Periwinkle	1.93	445	446	712	713
Periwinkle	1.93	383	393	613	629
Periwinkle	1.93	419	431	670	689
Periwinkle	1.93	358	375	574	601
Periwinkle	1.93	311	318	500	511
Periwinkle	1.51	369	378	592	606
Periwinkle	1.51	390	403	625	645
Periwinkle	1.51	485	492	775	786
Periwinkle	1.51	429	434	686	693
Periwinkle	1.51	526	516	839	823
Periwinkle	1.51	541	548	863	874
Periwinkle	1.51	380	391	609	626
Periwinkle	1.51	539	548	859	874
Periwinkle	1.51	475	476	759	760
Periwinkle	1.51	451	454	720	726
Periwinkle	1.51	666	642	1059	1021
Periwinkle	0.68	376	380	602	609
Periwinkle	0.68	423	432	677	690
Periwinkle	0.68	363	363	582	582
Periwinkle	0.68	353	363	566	582
Periwinkle	0.68	351	326	563	524
Periwinkle	0.68	348	351	558	563
Periwinkle	0.68	446	438	714	700
Periwinkle	0.68	453	451	724	721
Periwinkle	0.68	367	357	589	572
Periwinkle	0.68	572	536	912	855
Coralline red alga	3.12	727	763	1278	1340
Coralline red alga	3.12	1498	1554	2623	2721
Coralline red alga	3.12	1545	1618	2706	2832
Coralline red alga	3.12	1199	1216	2100	2131
Coralline red alga	3.12	738	778	1296	1367
Coralline red alga	3.12	572	588	1008	1035
Coralline red alga	3.12	926	1005	1625	1763
Coralline red alga	3.12	779	843	1368	1480
Coralline red alga	3.12	898	995	1576	1745
Coralline red alga	3.12	1123	1198	1969	2099
Coralline red alga	2.4	1207	1307	2115	2290
Coralline red alga	2.4	907	1087	1592	1906
Coralline red alga	2.4	926	1040	1625	1824
Coralline red alga	2.4	1032	1135	1810	1990
Coralline red alga	2.4	1085	1293	1902	2265
Coralline red alga	2.4	1124	1209	1970	2119
Coralline red alga	2.4	982	1067	1722	1871
Coralline red alga	2.4	1344	1562	2354	2735
Coralline red alga	2.4	548	670	965	1178
Coralline red alga	2.4	402	508	711	895
Coralline red alga	2.4	315	342	558	606
Coralline red alga	1.84	735	772	1292	1356
Coralline red alga	1.84	1056	1117	1851	1958
Coralline red alga	1.84	763	858	1341	1506
Coralline red alga	1.84	482	567	849	998
Coralline red alga	1.84	598	690	1052	1213
Coralline red alga	1.84	770	814	1353	1429
Coralline red alga	1.84	562	613	990	1079
Coralline red alga	1.84	869	1016	1525	1782
Coralline red alga	1.84	1238	1353	2169	2370
Coralline red alga	1.84	727	794	1278	1394
Coralline red alga	0.9	550	553	969	974
Coralline red alga	0.9	237	239	423	426
Coralline red alga	0.9	468	508	826	895
Coralline red alga	0.9	1303	1320	2282	2312
Coralline red alga	0.9	1110	1137	1946	1993
Coralline red alga	0.9	424	455	749	803
Coralline red alga	0.9	1030	1061	1806	1860
Coralline red alga	0.9	834	862	1464	1513
Coralline red alga	0.9	461	465	813	820
Coralline red alga	0.9	330	365	584	646
Coralline red alga	0.9	621	629	1093	1107
Halimeda	3.12	n/a	n/a	n/a	n/a
Halimeda	3.12	n/a	n/a	n/a	n/a

Table DR6 (continued)

Organism	Ωarag	Buoyant Weight		Dry Weight of CaCO3	
		Initial (mg)	Final (mg)	Initial (mg)	Final (mg)
Pencil urchin	2.06	1669	1701	3028	3086
Pencil urchin	2.06	1215	1443	2196	2614
Pencil urchin	2.06	2637	2800	4799	5096
Pencil urchin	2.06	2436	2586	4430	4705
Pencil urchin	2.06	4016	4445	7322	8107
Pencil urchin	1.58	1844	1899	3347	3448
Pencil urchin	1.58	1379	1494	2497	2707
Pencil urchin	1.58	1555	1672	2819	3032
Pencil urchin	1.58	3503	3629	6383	6614
Pencil urchin	1.21	1740	1880	3157	3413
Pencil urchin	1.21	2704	2885	4921	5252
Pencil urchin	1.21	5723	5842	10446	10664
Pencil urchin	0.54	1119	816	2020	1466
Pencil urchin	0.54	893	702	1607	1258
Pencil urchin	0.54	1518	1356	2751	2455
Pencil urchin	0.54	2809	2579	5114	4692
Pencil urchin	0.54	5058	3942	9229	7187
Pencil urchin	0.54	5395	4308	9846	7856
Purple urchin	2.06	618	720	1123	1304
Purple urchin	2.06	1260	1308	2269	2355
Purple urchin	2.06	1324	1391	2383	2502
Purple urchin	2.06	884	951	1597	1716
Purple urchin	1.58	486	707	886	1280
Purple urchin	1.58	539	762	980	1379
Purple urchin	1.58	963	1278	1738	2302
Purple urchin	1.58	987	1324	1781	2383
Purple urchin	1.58	1089	1555	1963	2797
Purple urchin	1.58	1203	1683	2168	3025
Purple urchin	1.21	589	822	1070	1486
Purple urchin	1.21	778	1144	1409	2062
Purple urchin	1.21	826	1174	1494	2116
Purple urchin	0.54	742	968	1344	1748
Purple urchin	0.54	774	974	1400	1759
Purple urchin	0.54	1352	1743	2433	3132
Purple urchin	0.54	1398	1801	2515	3237
Coral	2.60	1463	1620	2393	2645
Coral	2.60	1790	1966	2920	3203
Coral	2.60	1446	1618	2364	2642
Coral	2.60	1999	2225	3256	3620
Coral	2.60	1294	1468	2119	2400
Coral	2.60	2961	3318	4807	5382
Coral	2.60	2644	2917	4296	4736
Coral	2.60	2505	2830	4072	4596
Coral	2.60	2402	2686	3906	4364
Coral	2.60	2007	2282	3269	3712
Coral	2.60	3403	3793	5520	6148
Coral	2.28	1668	1863	2722	3036
Coral	2.28	1424	1579	2330	2580
Coral	2.28	1884	2106	3071	3428
Coral	2.28	2394	2647	3893	4300
Coral	2.28	3964	4340	6424	7030
Coral	2.28	1370	1545	2243	2525
Coral	2.28	1763	1965	2876	3201
Coral	2.28	3192	3548	5179	5752
Coral	2.28	1906	2131	3106	3469
Coral	2.28	2284	2518	3716	4092
Coral	2.28	1623	1831	2650	2985
Coral	2.28	1958	2212	3190	3600
Coral	2.28	2644	3012	4296	4889
Coral	2.28	3269	3670	5303	5950
Coral	2.28	1302	1436	2133	2348
Coral	1.64	1989	2180	3240	3548
Coral	1.64	1727	1916	2818	3122
Coral	1.64	2346	2604	3815	4231
Coral	1.64	1180	1329	1935	2176
Coral	1.64	2174	2377	3538	3866
Coral	1.64	1704	1885	2780	3072
Coral	1.64	1571	1742	2566	2842
Coral	1.64	1677	1857	2737	3027
Coral	1.64	1802	2034	2939	3313
Coral	1.64	2145	2443	3492	3972
Coral	1.64	2617	2919	4252	4739
Coral	1.64	1912	2078	3116	3384
Coral	0.77	2082	2177	3391	3543
Coral	0.77	1661	1765	2711	2879

Table DR6 (continued)

Organism	Ωarag	Buoyant Weight		Dry Weight of CaCO3	
		Initial (mg)	Final (mg)	Initial (mg)	Final (mg)
Coral	0.77	1851	1902	3018	3100
Coral	0.77	2200	2231	3580	3630
Coral	0.77	1822	1837	2971	2995
Coral	0.77	2368	2430	3850	3951
Coral	0.77	1815	1895	2960	3089
Coral	0.77	1717	1787	2802	2914
Coral	0.77	2170	2250	3532	3661
Coral	0.77	1833	1884	2989	3071
Coral	0.77	2354	2495	3828	4056
Coral	0.77	2651	2803	4308	4552
Coral	0.77	2096	2170	3412	3532
Coral	0.77	1329	1349	2176	2208
Coral	0.77	1872	1977	3052	3221
Coral	0.77	1977	2080	3220	3387
Serpulid worm	2.60	750	800	1226	1306
Serpulid worm	2.60	499	516	821	848
Serpulid worm	2.60	339	337	562	559
Serpulid worm	2.60	458	475	755	782
Serpulid worm	2.60	584	623	957	1020
Serpulid worm	2.60	1379	1362	2240	2213
Serpulid worm	2.60	555	579	911	949
Serpulid worm	2.60	834	836	1361	1364
Serpulid worm	2.60	744	775	1216	1266
Serpulid worm	2.60	917	912	1495	1487
Serpulid worm	2.60	323	363	536	601
Serpulid worm	2.28	449	462	739	761
Serpulid worm	2.28	876	892	1430	1455
Serpulid worm	2.28	538	569	883	933
Serpulid worm	2.28	711	738	1163	1206
Serpulid worm	2.28	932	957	1520	1560
Serpulid worm	2.28	325	364	539	602
Serpulid worm	2.28	358	391	593	646
Serpulid worm	1.64	822	840	1342	1371
Serpulid worm	1.64	668	701	1093	1146
Serpulid worm	1.64	331	346	548	573
Serpulid worm	1.64	371	361	614	598
Serpulid worm	1.64	402	431	664	711
Serpulid worm	1.64	788	760	1287	1242
Serpulid worm	1.64	367	391	608	646
Serpulid worm	1.64	403	422	666	696
Serpulid worm	1.64	618	653	1012	1069
Serpulid worm	1.64	765	785	1250	1282
Serpulid worm	1.64	504	500	829	822
Serpulid worm	1.64	559	538	917	883
Serpulid worm	0.77	730	710	1193	1161
Serpulid worm	0.77	411	403	679	665
Serpulid worm	0.77	229	228	385	383
Serpulid worm	0.77	706	735	1155	1201
Serpulid worm	0.77	832	863	1358	1408
Serpulid worm	0.77	427	447	705	736
Serpulid worm	0.77	812	824	1325	1345
Serpulid worm	0.77	390	370	644	612
Serpulid worm	0.77	299	319	498	530
Serpulid worm	0.77	918	966	1497	1574
Serpulid worm	0.77	598	590	981	967
Hard clam	2.63	1787	1815	2764	2807
Hard clam	2.63	5104	5128	7908	7945
Hard clam	2.63	5501	5608	8523	8690
Hard clam	2.63	7625	7699	11819	11933
Hard clam	2.63	7548	7595	11698	11772
Hard clam	2.63	10537	10617	16335	16459
Hard clam	2.63	8263	8292	12808	12852
Hard clam	2.11	5426	5472	8409	8479
Hard clam	2.11	6814	6862	10560	10636
Hard clam	2.11	6610	6647	10245	10302
Hard clam	2.11	8316	8407	12890	13032
Hard clam	2.11	11378	11425	17639	17712
Hard clam	1.43	842	849	1298	1308
Hard clam	1.43	3006	2999	4654	4644
Hard clam	1.43	5381	5402	8338	8370
Hard clam	1.43	4901	4946	7594	7664
Hard clam	1.43	7792	7848	12077	12164
Hard clam	1.43	9432	9484	14621	14702
Hard clam	1.43	8570	8577	13285	13295
Hard clam	0.71	4415	4355	6840	6747

Table DR6 (continued)

Organism	Ωarag	Buoyant Weight		Dry Weight of CaCO3	
		Initial (mg)	Final (mg)	Initial (mg)	Final (mg)
Hard clam	0.71	3851	3775	5966	5847
Hard clam	0.71	4908	4820	7605	7468
Hard clam	0.71	8632	8547	13381	13249
Hard clam	0.71	8485	8390	13152	13005
Hard clam	0.71	9439	9340	14632	14479
Blue mussel	2.63	308	314	542	552
Blue mussel	2.63	221	237	390	418
Blue mussel	2.63	290	302	511	532
Blue mussel	2.63	253	263	446	462
Blue mussel	2.63	260	273	458	481
Blue mussel	2.63	311	318	547	560
Blue mussel	2.63	397	419	697	736
Blue mussel	2.63	445	470	781	826
Blue mussel	2.63	460	492	808	865
Blue mussel	2.63	593	617	1041	1083
Blue mussel	2.63	476	518	836	909
Blue mussel	2.63	558	566	980	993
Blue mussel	2.63	418	437	734	767
Blue mussel	2.63	590	599	1036	1050
Blue mussel	2.63	676	705	1186	1236
Blue mussel	2.11	281	285	495	501
Blue mussel	2.11	355	369	625	648
Blue mussel	2.11	256	275	450	484
Blue mussel	2.11	254	257	447	453
Blue mussel	2.11	318	315	559	554
Blue mussel	2.11	353	369	620	648
Blue mussel	2.11	395	404	695	710
Blue mussel	2.11	550	570	965	1001
Blue mussel	2.11	360	370	633	650
Blue mussel	2.11	612	644	1074	1129
Blue mussel	2.11	473	505	831	887
Blue mussel	2.11	705	720	1237	1263
Blue mussel	2.11	568	571	997	1002
Blue mussel	1.43	263	291	464	512
Blue mussel	1.43	229	234	404	413
Blue mussel	1.43	319	323	560	569
Blue mussel	1.43	368	399	647	701
Blue mussel	1.43	260	269	458	473
Blue mussel	1.43	382	405	671	712
Blue mussel	1.43	368	380	647	668
Blue mussel	1.43	440	438	773	769
Blue mussel	1.43	320	311	562	547
Blue mussel	1.43	429	457	753	802
Blue mussel	1.43	406	420	714	738
Blue mussel	1.43	498	507	875	890
Blue mussel	1.43	606	627	1063	1100
Blue mussel	1.43	490	505	861	887
Blue mussel	0.71	344	363	604	639
Blue mussel	0.71	315	310	554	545
Blue mussel	0.71	290	318	510	560
Blue mussel	0.71	281	286	495	503
Blue mussel	0.71	291	307	513	539
Blue mussel	0.71	401	400	704	703
Blue mussel	0.71	334	348	588	611
Blue mussel	0.71	410	420	721	738
Blue mussel	0.71	443	478	778	839
Blue mussel	0.71	551	557	967	977
Blue mussel	0.71	488	501	857	879
Blue mussel	0.71	395	402	694	707
Blue mussel	0.71	493	513	865	901
Blue mussel	0.71	703	701	1233	1230
Soft clam	2.63	248	301	405	493
Soft clam	2.63	687	784	1135	1296
Soft clam	2.63	1559	1825	2582	3025
Soft clam	2.11	174	185	283	301
Soft clam	2.11	147	165	237	267
Soft clam	2.11	373	390	612	641
Soft clam	2.11	477	527	785	868
Soft clam	2.11	1161	1215	1921	2011
Soft clam	1.43	169	168	274	273
Soft clam	1.43	214	197	349	320
Soft clam	1.43	544	551	897	909
Soft clam	1.43	782	848	1292	1401
Soft clam	0.71	121	103	195	164

Table DR6 (continued)

Organism	Ωarag	Buoyant Weight		Dry Weight of CaCO3	
		Initial (mg)	Final (mg)	Initial (mg)	Final (mg)
Soft clam	0.71	354	350	581	575
Bay scallop	2.62	2011	2124	3570	3766
Bay scallop	2.62	1842	1930	3275	3429
Bay scallop	2.62	2565	2708	4537	4786
Bay scallop	2.62	2794	3056	4935	5391
Bay scallop	2.62	2566	2797	4538	4940
Bay scallop	2.11	1866	1969	3318	3496
Bay scallop	2.11	2314	2476	4098	4381
Bay scallop	2.11	2627	2793	4643	4934
Bay scallop	1.43	2258	2451	4001	4338
Bay scallop	1.43	2391	2503	4233	4428
Bay scallop	1.43	2567	2565	4539	4535
Bay scallop	1.43	3016	3061	5322	5400
Bay scallop	1.43	3372	3695	5944	6507
Bay scallop	0.71	2301	2338	4075	4140
Bay scallop	0.71	1887	1972	3353	3501
Bay scallop	0.71	2151	2238	3813	3966
Bay scallop	0.71	3636	3634	6404	6400
Bay scallop	0.71	3198	3242	5640	5716
Oyster	2.62	6761	6902	11431	11665
Oyster	2.62	12210	12472	20444	20878
Oyster	2.62	13709	13972	22923	23359
Oyster	2.62	14318	14519	23930	24264
Oyster	2.11	4100	4152	7030	7117
Oyster	2.11	9833	10009	16512	16803
Oyster	2.11	16417	16751	27403	27954
Oyster	2.11	18634	18863	31069	31449
Oyster	1.43	4476	4506	7652	7701
Oyster	1.43	5513	5566	9367	9456
Oyster	1.43	10980	11127	18410	18653
Oyster	1.43	14999	15208	25057	25404
Oyster	0.71	5896	5898	10001	10005
Oyster	0.71	7532	7598	12707	12816
Oyster	0.71	8798	8820	14800	14837
Oyster	0.71	9930	9926	16673	16666

Calcification Overview (Part II)

Lecturer: Whitman Miller (Smithsonian Environmental Research Center)

Date: 06 November 2009

Title: Measuring Calcification in Biological Experiments – Mollusks

Topics:

1. **Calcification in Mollusks – Overview and Background**
2. **Indirect Measurements – Shell growth**
    a. Light Microscopy measurements – tracking individuals
    b. Image Analysis – population measures (central tendency and variance)
3. **Scanning Electron Microscopy – fine scale measures**
4. **Direct Measurements – quantifying calcium carbonate**
    a. Inductively Coupled Plasma/Optical Emissions Spectrometry – per capital mass
    b. Total Alkalinity Anomaly Method – measuring rates of calcification (cursory summary)
5. **Some examples from larval oyster experiments**
6. **Supplementary Reading:**
    a. Weiss IM, Tuross N, Addadi L and S Weiner 2002. Mollusc larval shell formation: amorphous calcium carbonate is a precursor phase for aragonite. J. Exp. Zool. 293:478-491 (.pdf supplied)

JOURNAL OF EXPERIMENTAL ZOOLOGY 293:478–491 (2002)

Mollusc Larval Shell Formation: Amorphous Calcium Carbonate Is a Precursor Phase for Aragonite

INGRID MARIA WEISS,[1] NOREEN TUROSS,[2] LIA ADDADI,[1] AND STEVE WEINER[1]*
[1]*Department of Structural Biology, Weizmann Institute of Science, 76100 Rehovot, Israel*
[2]*Smithsonian Center for Materials Research and Education, Suitland, Maryland 20746*

ABSTRACT The larval shells of the marine bivalves *Mercenaria mercenaria* and *Crassostrea gigas* are investigated by polarized light microscopy, infrared spectroscopy, Raman imaging spectroscopy, and scanning electron microscopy. Both species contain similar shell ultrastructures. We show that larval shells contain amorphous calcium carbonate (ACC), in addition to aragonite. The aragonite is much less crystalline than nonbiogenic aragonite. We further show that the initially deposited mineral phase is predominantly ACC that subsequently partially transforms into aragonite. The postset juvenile shell, as well as the adult shell of *Mercenaria* also contains aragonite that is less crystalline than nonbiogenic aragonite. We conclude that ACC fulfills an important function in mollusc larval shell formation. It is conceivable that ACC may also be involved in adult shell formation. *J. Exp. Zool. 293:478–491, 2002.*

Molluscs form a diverse array of mineralized deposits, in addition to their shells. These are used for many different purposes (Lowenstam and Weiner, '89). The adult mollusc shell itself is highly variable. It comprises calcite or aragonite, or both, and is built up of one or more shell layers, each of which may have a different ultrastructure (Bøggild, '30; Kobayashi, '69; Taylor et al., '73; Watabe, '88; Bandel, '90; Carter, '90). In contrast, mollusc larval shells all contain aragonite (Schmidt, '24; Stenzel, '64; Cather, '67; Ivester, '72; LaBarbera, '74; Carriker and Palmer, '79; Carter, '80; Eyster, '82, '86; Bandel, '90) and have similar, if not identical ultrastructures (Carriker and Palmer, '79; Iwata, '80; Waller, '81; Castilho et al., '89). This implies that the larval shell is highly conserved during evolution (Taylor, '73). Larval shells may therefore provide information on basic strategies of mollusc shell formation.

The formation of the larval shell is initiated by a specialized group of ectodermal cells in the early embryo, the shell field (Kniprath, '79; Iwata, '80). When shell field cells invaginate to form the shell gland, the remaining surface cells start to produce the outermost organic shell layer, the periostracum (Eyster and Morse, '84). Specific cell-cell interactions are necessary to coordinate the onset of this process (Cather, '67; McCain, '92). The inner part of the shell gland then everts in an inside-out manner while transforming into the larval mantle epithelium (Neff, '72; Kniprath, '79, '81; Bielefeld and Becker, '91). During this process, the periostracum spans the whole shell field epithelial surface. Only then is crystalline calcium carbonate detected for the first time (Eyster, '86). The onset of shell mineralization occurs during the trochophore larval stage. This usually occurs about 20 hr after fertilization (LaBarbera, '74; Iwata, '80), although it can be delayed for several days (Eyster, '86). The shell is called the prodissoconch I (for review on terminology, see Jablonski and Lutz, '80). The bivalve prodissoconch I is enlarged until the embryo is entirely enfolded and able to close its two valves. Transformation into the motile veliger larva then

Grant sponsor: Deutsche Forschungsgemeinschaft; Grant number: WE2629/2-1; Grant sponsor: Smithsonian Institution; Grant sponsor: Minerva Foundation.
*Correspondence to: S. Weiner, Department of Structural Biology, The Weizmann Institute of Science, 76100 Rehovot, Israel. E-mail: steve.weiner@weizmann.ac.il
Received 1 March 2002; Accepted 22 May 2002
Published online in Wiley InterScience (www.interscience.wiley.com). DOI: 10.1002/jez.90004

occurs. The veliger larva enlarges prodissoconch I to form prodissoconch II (Carriker and Palmer, '79; Waller, '81). After metamorphosis into the postset juvenile stage, the shell is called the dissoconch. The transition from trochophore to veliger larval stage occurs about the second or third day after fertilization, and metamorphosis in general takes place between days 10–17. Here, too, there is much variability in the timing of these events among individuals of the same species, and even more when comparing different species or genera. In terms of studying changes in biomineralization during development, the mollusc shell has another advantage. The larval prodissoconchs I and II are preserved during metamorphosis and are integrated into the juvenile and adult shell. Thus, each shell is essentially a record of the entire shell formation process.

In general, the mollusc larval shell comprises three mineralized layers, as is revealed by scanning electron microscopy (Carriker and Palmer, '79; Waller, '81). There is an outer prismatic layer below the periostracum, and an inner prismatic layer adjacent to the mantle epithelium. A so-called homogeneous layer with globular structures of 200–500 nm diameter is embedded between the two prismatic layers. In some cases, the outer prismatic layer is very thin or totally absent (Castilho et al., '89). The other two layers may vary greatly in thickness. This variability is somewhat dependent on the location and age of the shell, but in general applies to both prodissoconchs I and II.

Schmidt ('24) used polarized light microscopy to show that the aragonite crystals of the larval shell have their c-axes oriented perpendicular to the shell surface. Medakovic et al. ('97) noted that the peaks obtained from a powder X-ray diffraction pattern of the larval shells of *Ostrea edulis* are relatively broad as compared to the adult. They attributed the broad peaks to the presence of an amorphous tissue (periostracum and organic matrix). An EXAFS study of the larval shell of a freshwater snail, *Biomphalaria*, was interpreted as showing the presence of amorphous calcium carbonate with a nascent aragonitic structure (Hasse et al., 2000).

Here, we use polarized light microscopy, infrared spectroscopy, and Raman imaging spectroscopy to investigate the mineral phase of the larval shells of the marine bivalves *Mercenaria mercenaria* and *Crassostrea gigas* during their development. We use scanning electron microscopy to compare the observed mineralogical changes to their ultrastructures.

MATERIALS AND METHODS

Larval shells of *Mercenaria mercenaria* were obtained from the Harbor Branch Oceanographic Institution (Ft. Pierce, FL). The freshly collected, live larvae were shock frozen in liquid nitrogen three, six, nine, and 13 days after spawning, and they were stored frozen at -20°C. Larvae of *Crassostrea gigas* were obtained from The National Center for Mariculture (Eilat, Israel). Larvae were collected two, three, and nine days after spawning. They were freshly frozen at -70°C immediately after collection and stored in aliquots at -20°C. Nonbiogenic aragonite was obtained from two sources: deposits on the walls of containers in which water was boiled (scale), and the Lisan Formation sediments, Israel. The latter is a precipitate from Dead Sea water.

Samples were thawed at room temperature prior to use. If necessary, larvae were washed in deionized water (DDW) several times, and they were air dried in some cases. For removal of larval tissue, shells were treated with 2.5% sodium hypochlorite for 5–15 minutes while gently shaking and washed in DDW several times. This treatment is known not to affect amorphous calcium carbonate in other organisms (Lowenstam, '89; Aizenberg et al., '95). During this treatment, most of the shells separated into the two valves. The mineralized material showed the same characteristics in polarized light for at least 1–2 cycles of freezing/thawing or when stored air dry at room temperature for several months.

For the etching procedure, purified and dried larval shells were cross-sectioned individually with a razor blade. Cross-sections were exposed to a drop of DDW for 12 hours on a glass slide in a humid atmosphere. The liquid was removed, and the samples were washed in DDW several times and air dried.

For polarized light microscopy, a Leica binocular microscope equipped with an Applitec MSV-700L signal transducer was used at a magnification of $50\times$. All polarized light images were taken at half maximum light source, gain 0, shutter speed 1/50 and black level 0 (usual mode), or black level 250 (signal enhanced mode). The software ''NIH image'' was used for image processing. High resolution (image size 3,040 $\times$ 2,016 pixels) polarized light images of shell edges were

produced using a Nikon Labophot2-Pol Microscope equipped with a Nikon 40/0.65 (160/0.17) P objective and a FUJI FinePix S1 Pro digital camera.

Raman imaging spectroscopy was performed both on freshly thawed, wet, and ten-minute UV-light pre-exposed larvae, or sodium hypochlorite treated, purified, and dried larval shells. The specimens were placed on glass or silicon slides. The Renishaw Raman imaging spectrometer incorporates a Leica microscope with objectives of $20\times$ and $50\times$ magnification. Both were used with reflected white light for focusing on the object. The light source of the microscope was then transferred to a diode laser (780 nm) at the same magnification. Each spectrum was obtained from a ten second scan in the range 100–2,000 cm^{-1}. For each shell, between 10–25 spectra per location were analyzed. We noted a wider distribution of values mainly at the shell center and edge locations (defined as position 1 and 5 in the Results). This behavior might be related to either structural differences in the material or to the different angles to which the surface is exposed in relation to the laser beam.

For scanning electron microscopy (SEM), cleaned, air-dried larval shells were mounted on carbon double-sided tape attached to aluminum stubs and gold-coated. A JEOL 6400 scanning electron microscope (SEM) was used. Cross-sections were obtained by cutting larval valves mounted on carbon tape on small brass cubes with a razor blade. One half of the valve was removed or smashed with a needle. The cube was then mounted with silver paste on aluminum stubs, but rotated 90° to expose the larval shell cross section in top view. Gold-coated cross-sections were observed using a Philips XL-30 environmental scanning electron microscope (ESEM) in high-resolution high vacuum mode.

For infrared spectroscopy (IR), the dried and ground samples were mounted in KBr pellets. Infrared absorption spectra were obtained using a MIDAC Fourier transform infrared (FTIR) spectrometer at 2 cm^{-1} resolution.

RESULTS

Mercenaria mercenaria

Larval shells of *Mercenaria mercenaria*, three or more days old (Fig. 1), consist of two morphologically different stages. The prodissoconch I, corresponding to the trochophora larval stage, is deposited first. It has a smooth outer surface and measures up to 80–100 μm in diameter. The veliger stage prodissoconch II has an outer surface showing growth rings. There is a sharply defined transition between the two shell zones. The prodissoconch II constitutes about half of the shell after three days of development (Fig. 1b). The three day old larval shells are about 2–4 μm in thickness. After nine days, the prodissoconch II has enlarged to 250–300 μm in diameter (Fig. 1a), and the average thickness is 3–5 μm. Even then, *Mercenaria* larval shells appear transparent in the light microscope. The thickness of the three and nine day old shells are fairly uniform, although detailed measurements inevitably show that the thickness close to the forming edge is greater than the older portions of prodissoconch II. Between nine and 13 days, larvae begin to transform into the juvenile, and their shells enlarge to 350 μm during this so-called postset stage.

Initial information on the nature of the larval shell mineral phase was obtained using polarized light microscopy (Fig. 2). Under identical observation conditions, nine day old shells are a lot more birefringent than three day old ones. Weak birefringence could be observed for the three day old shells, but only after considerable signal enhancement. The birefringence of *Mercenaria* larval shells disappears within 25 min after treatment with 10 mM EDTA and is therefore due to the mineral phase. The differences in birefringence show that the older larval shells do contain a much larger proportion of crystalline calcium carbonate than the younger shells.

Raman imaging spectra obtained from adult *Mercenaria* shells (Fig. 3d) are very similar to those of nonbiogenic aragonite (Fig. 3e). They contain four peaks at 156 cm^{-1} and 205 cm^{-1} (translational lattice modes of the carbonate ion) and at 703 cm^{-1} and 1,087 cm^{-1} (symmetric stretch internal mode of the carbonate ion). Raman imaging spectra obtained from freshly thawed and untreated nine day old *Mercenaria* larval shells in sea water vary between two extremes. Some show the four peaks characteristic of crystalline aragonite (compare Fig. 3c,e). Note that after normalization of the spectra to the same 1,087 cm^{-1} peak height, the peaks at 156 cm^{-1} and 205 cm^{-1} (translational lattice modes of the carbonate ion) are much smaller than the 156 cm^{-1} and 205 cm^{-1} peaks in nonbiogenic aragonite. At the other extreme, we obtained spectra in which only the 703 cm^{-1} and the 1,087 cm^{-1} peaks are present, together with a broad baseline rise in the area around 150–250 cm^{-1}. An example is

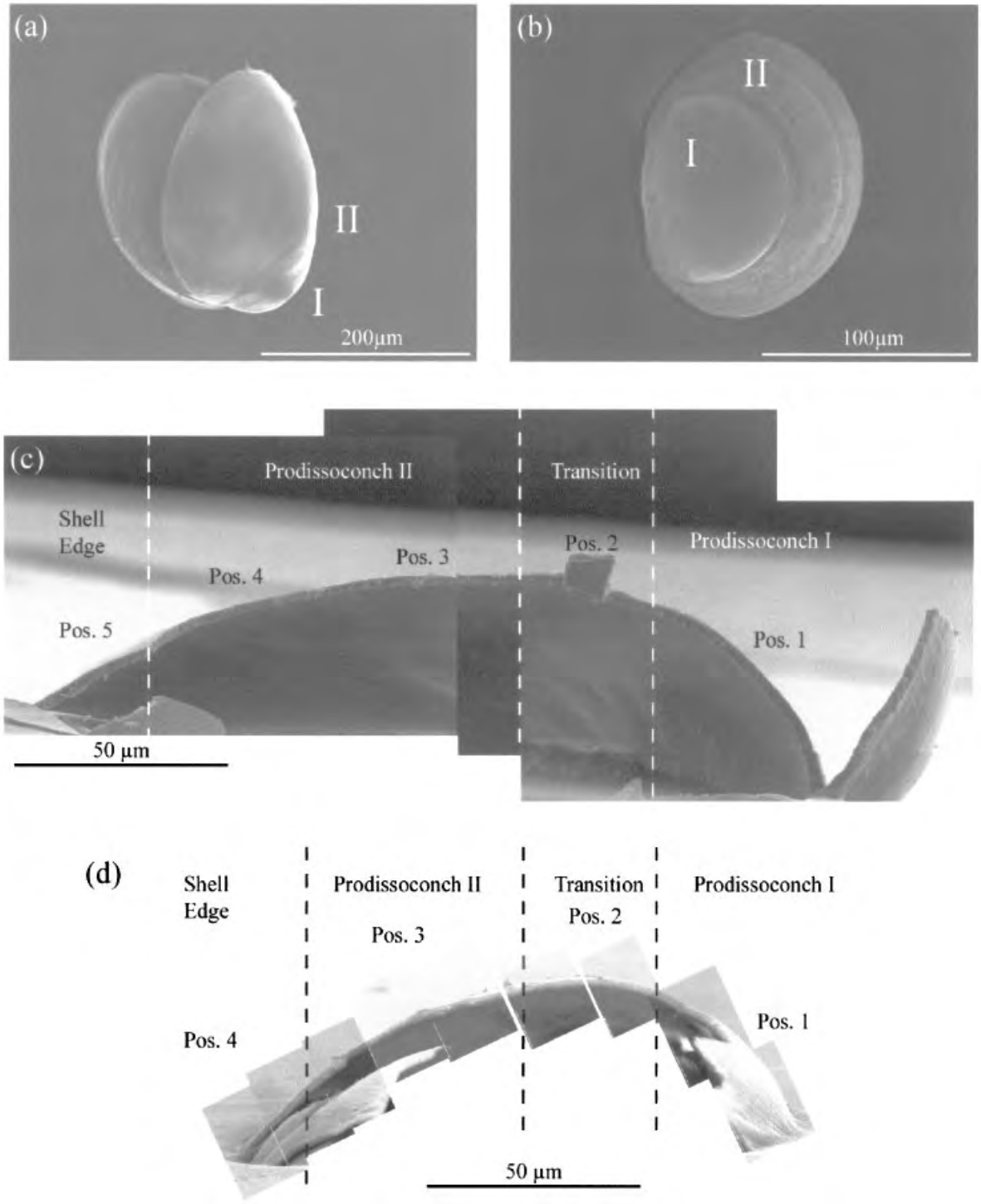

Fig. 1. Scanning electron micrographs of the larval shells of *Mercenaria mercenaria*. (**a**) Nine day old larval shell. I – prodissoconch I; II – prodissoconch II. (**b**) Three day old larval shell. I – prodissoconch I; II – prodissoconch II. (**c**) Nine day old larval shell cross-section. Positions 1–5 indicate areas where Raman imaging spectroscopy was performed. Dotted lines indicate a rough division of the larval shell into several developmental stages: prodissoconch I, transition between I and II, prodissoconch II, and shell edge. (**d**) Three day old larval shell cross-section. Positions 1–4 indicate areas where Raman imaging spectroscopy was performed. Dotted lines indicate a rough division of the larval shell into several developmental stages as described above. Note that the scales of (c) and (d) are the same, and that each designated position for Raman imaging is approximately the same distance from the shell apex irrespective of the age of the shell. Thus, as the shell grows, additional positions are added. Abbreviation: Pos. - Shell position.

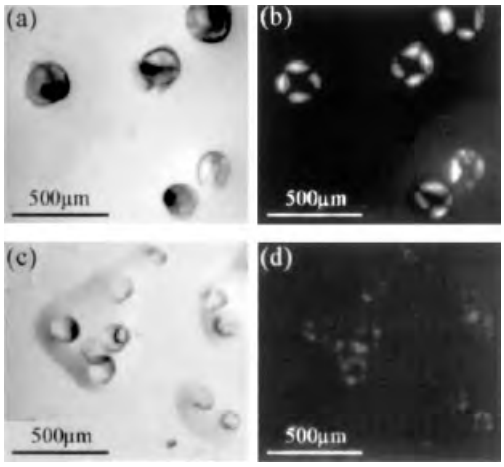

Fig. 2. Larval shells of *Mercenaria mercenaria* observed by plain and crossed polarized light. (**a**) Plain polarized light image of nine day old shells. (**b**) Crossed polarized light image of nine day old shells. (**c**) Plain polarized light image of three day old shells. (**d**) Crossed polarized light image of three day old shells after significant signal enhancement (see Materials and Methods section). The un-enhanced image is completely dark.

shown from a nine day old larval shell (Fig. 3b). Spectra of this type are characteristic of the family of amorphous calcium carbonate (ACC) phases, an example of which is shown from the spicules of the ascidian *Pyura* (Fig. 3a). We note that in the *Pyura* ACC spectrum (Fig. 3a), the peak at 1,087 cm^{-1} is broader than that obtained from the larval shells (Fig. 3b,c) and there is no clearly detectable peak at 703 cm^{-1}. Even though these are certainly significant differences, we regard spectra of this type, namely not having the peaks at 156 cm^{-1} and 205 cm^{-1}, but having a peak at 1,087 cm^{-1}, as indicating the presence of an ACC phase.

Raman spectra from different locations on three, six, and nine day old *Mercenaria* larval shells produced spectra characteristic of ACC (Fig. 3b), as well as those with reduced intensity lattice mode peaks (Fig. 3c). The 13 day old shells never produced spectra characteristic of ACC, but only those of the type shown in Figure 3c. The distribution of the two types of spectra even in a single shell is very complex. In order to understand this phenomenon better, we collected data from specific positions on the shells (defined in Fig. 1). We quantified the reduction in peak intensity by calculating the ratio of intensities of the 205 cm^{-1} and 1,087 cm^{-1} peaks ($I_{205}/I_{1,087}$ ratio) and defining the ratio for nonbiogenic aragonite as 1.0 and ACC as zero. The results are shown in Fig. 4 with error bars (n = 10–25), and in Figure 5 in the form of a three-dimensional plot. Note too that the ratio for the adult *Mercenaria* shell is 0.98 $\pm$ 0.16 (Fig. 4), which does not differ from that of nonbiogenic aragonite. We first discuss the changes that take place with increasing age at a given location in the larval shells, and then we discuss the trends as the larva grows.

At shell position 1 (prodissoconch I), there is a remarkable and significant change from the three day old to the six day old shells (t-test results: $P < 0.003$). The former produced mainly ACC type

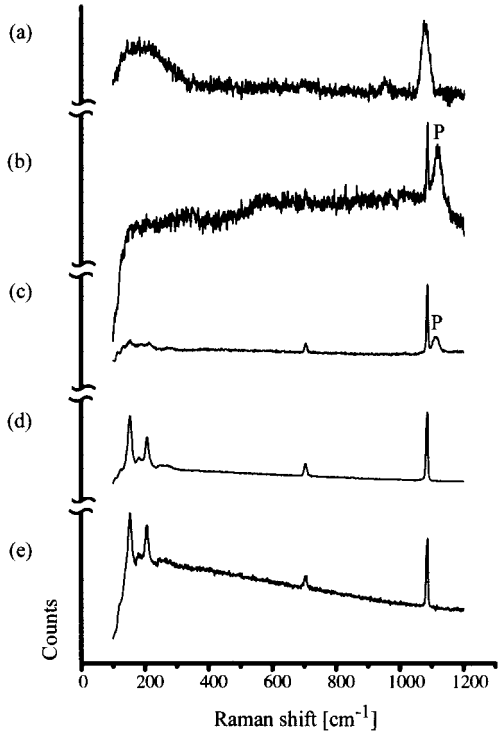

Fig. 3. Raman imaging spectra normalized to the same 1,087 cm^{-1} peak height. (**a**) Raman spectrum from the spicules of *Pyura pachydermatina*, containing only ACC (Aizenberg et al., '96). Note the characteristic peak for calcium carbonate at 1,087 cm^{-1}. (**b**) Raman spectrum obtained from a nine day old *Mercenaria* larval shell (position 3). The absence of the peaks at 150 cm^{-1} and 205 cm^{-1} indicates that this spectrum is derived from ACC. The peak at 1,110 cm^{-1} marked with "P" is from the periostracum and is not related to calcium carbonate. (**c**) Raman spectrum taken from a different nine day old *Mercenaria* larval shell (position 3) with peaks characteristic of aragonite. The peaks at 150 cm^{-1} and 205 cm^{-1} are small relative to the peaks at 703 cm^{-1} and 1,087 cm^{-1}; characteristics that differentiate this spectrum from that of nonbiogenic aragonite (Fig. 3e). This sample was not treated chemically. The small peak at 1,110 cm^{-1} marked with "P" is from the periostracum. (**d**) Raman spectrum obtained from an adult *Mercenaria* shell. (**e**) Raman spectrum of nonbiogenic aragonite (scale).

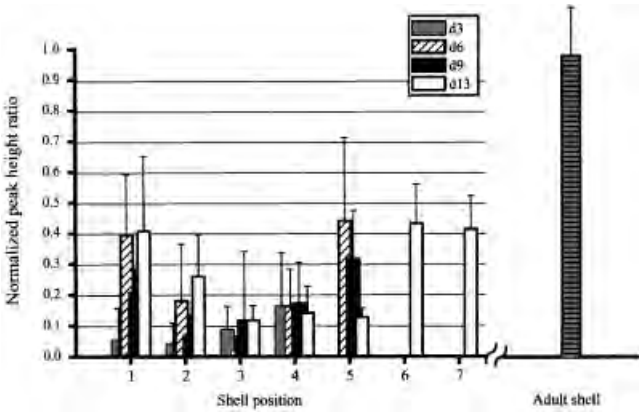

Fig. 4. Quantification of Raman imaging spectroscopy data obtained from *Mercenaria* larval shells. The y-axis shows the peak height ratios of peaks 205 cm^{-1}/1,087 cm^{-1}. Values were normalized to the peak height ratios obtained from nonbiogenic aragonite (Fig. 3e). The error bars represent one standard deviation (n = 10–25). The x-axis shows the different positions of larval shells as indicated in Fig. 1c,d. Different ages of larval shells (d3 - three day old; d6 - six day old etc.) are indicated by different shades of gray or the filled pattern. Note that positions 1–4 are present in three day old shells, whereas the older shells have additional positions due to their larger sizes. The peak height ratio for adult *Mercenaria* is also shown.

spectra, whereas the latter produced mainly spectra of type 3c. The normalized $I_{205}/I_{1,087}$ ratio increases from 0.05 $\pm$ 0.16 to 0.40 $\pm$ 0.20. This indicates that most of the first formed mineral of prodissoconch I is ACC, which subsequently transforms into a more crystalline phase. From the six day old to the nine day old larvae, there is a reduction in the ratio, and this again increases in the 13 day old larvae. These changes presumably reflect the dynamics of the addition of ACC and its subsequent transformation.

Shell position 2 follows the same trends as shell position 1, and shell positions 3 and 4 show consistently low ratios that do not change much on the average with increasing age. We infer that this, too, reflects two concomitant processes that balance out—namely the deposition of ACC and the transformation of a small portion of the ACC into a more crystalline product.

The shell edge positions reflect the last deposited mineral phase prior to freezing the animals. Surprisingly, the mineral phase at the shell edge inevitably has a higher $I_{205}/I_{1,087}$ ratio as compared to the positions some distance from the shell edge.

Figure 5 clearly shows that the $I_{205}/I_{1,087}$ ratio changes systematically from the prodissoconch I (position 1) through prodissoconch II and out to the shell edge. The same trends are seen for the six, nine, and 13 day old larvae. The latter is already considered an adult animal. The only exception is position 1 of the three day old larvae, which comprises mostly ACC.

Mercenaria larval shell cross-sections were studied using scanning electron microscopy (SEM). We noted that the samples were all much more sensitive to beam damage than the adult shells. Our observations of the ultrastructure are consistent with those previously reported, namely we observed an inner prismatic layer, a central granular-homogeneous layer, and, in prodissoconch I, an outer prismatic layer adjacent to the periostracum (Carriker and Palmer, '79; Waller, '81). We will refer to the granular-homogeneous layer as simply ''granular.'' Figure 6 compares the prodissoconch I cross-sections at shell position 1 of the three day old and nine day old larvae. The overall thickness has increased, and the relative proportions of the prismatic layers as compared to the granular layer have also increased. Note that the Raman spectra from this location in the three day old indicate that ACC is the predominant mineral phase. We do note that in these fracture surfaces, the prism outlines are better defined in

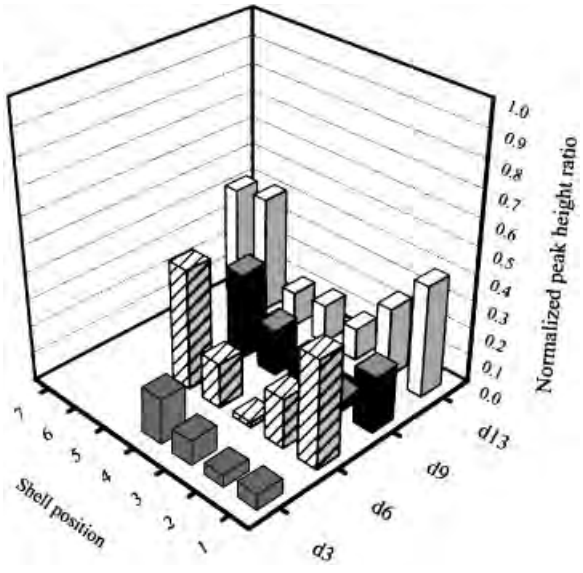

Fig. 5. Three-dimensional plot of the quantification of Raman imaging data of *Mercenaria* larval shells from Fig. 4. The changes in peak height ratios for each position on the shell can be followed over the developmental period from three days (d3) to six days (d6), to nine days (d9), and to 13 days (d13). Furthermore, the trends within shells of a particular age can also be followed more clearly from prodissoconch I (shell position 1) to the shell edge (shell positions 4–7, according to age).

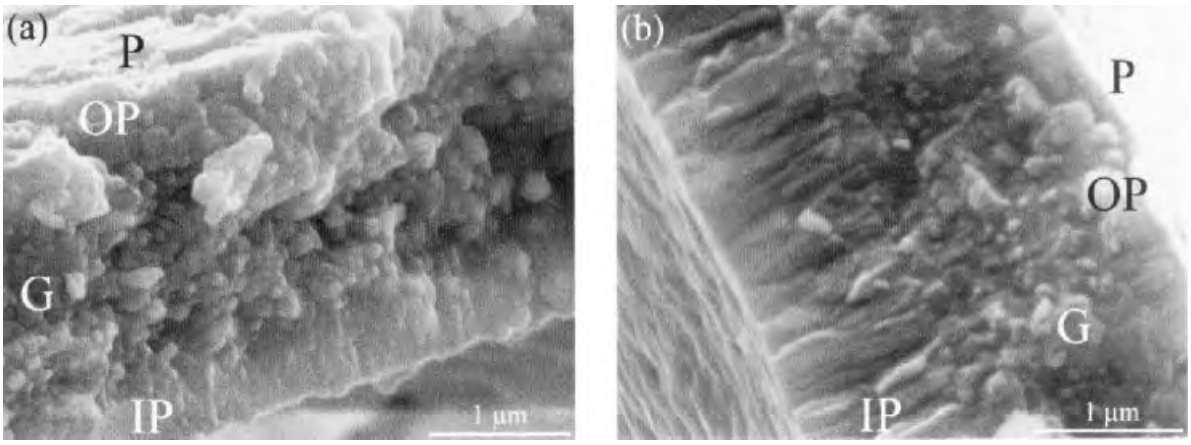

Fig. 6. SEM images taken in ''high resolution'' mode of cross sections of three and nine day old *Mercenaria* larval shells. (**a**) Prodissoconch I (position 1) of a three day old *Mercenaria* larval shell, showing the three shell layers; the outer prismatic layer (OP), the granular-homogeneous layer (G), and the inner prismatic layer (IP). The first formed organic periostracum (P) is extremely thin and covers the outer shell surface. It may have been partially removed during sample preparation. (**b**) Prodissoconch I (position 1) of a nine day old *Mercenaria* larval shell. The layers are indicated as described in (a). Note that the thickening of the shell from three days to nine days in this position is due to additional inner prismatic layer (IP). The thickness of the granular layer (G) stays more or less constant, but the texture of this layer appears more condensed in the nine day old shell. The outer prismatic layer (OP) is very thin in both cases.

the nine day old as compared to the three day old and that the spherical structures, often characteristic of amorphous minerals, are less prominent in the granular layer. These differences may reflect the larger proportion of ACC in the three day old shell as compared to the nine day old shell. Figure 7a shows the center of prodissoconch II (shell position 4) from a nine day old larval shell. The inner prismatic layer is overlain by the granular layer. There is no outer prismatic layer in this view, but we have on occasion observed it beneath the periostracum. Figure 7b,c are cross-sectional views close to the shell edge and almost at the shell edge, respectively. There is no visible, prismatic layer at the very edge, and away from the edge it increases in thickness and the prisms are better defined in the fracture surface. The granular layer at the shell edge (Fig. 7c) shows a platy structure oblique to the shell surface. It is superimposed on the spherical structures. This platy structure is not evident in the center of prodissoconch II (Fig. 7a), where the granular layer is dominated by arrays of spherical structures. There is no well defined boundary between the inner prismatic layer and the granular layer.

To both confirm the presence of ACC and study its distribution in the two shell layers, etching experiments were performed. These experiments exploit the fact that crystalline calcium carbonate is hardly affected by etching in water, while ACC is affected by exposure to water even at neutral pH (Aizenberg et al., '96). Nine day old larval shells, cut longitudinally to expose their cross-sections, were examined by SEM after incubation in a drop of water for 12 hours at room temperature (Fig. 7d). Conspicuous dissolution of mineral is evident, especially in the granular layer, but it is detectable also in the prismatic layer. Furthermore, the residual mineral in the granular layer appears to be predominantly in the form of thin prisms oriented perpendicular to the shell surface and parallel to the prisms of the prismatic layer. This is in agreement with the Raman spectroscopy data and confirms the presence of ACC in both layers.

Crassostrea gigas

The adult *Crassostrea* shell is composed almost entirely of calcite (Stenzel, '63) and has an ultrastructure quite different from that of adult *Mercenaria*, and therefore it cannot be used for comparison to the larval shell. The shells of the three day and nine day old *Crassostrea* larvae are much smaller than their *Mercenaria* counterparts (Fig. 8a,b). In fact, three day old *Crassostrea* shells consist mainly of prodissoconch I (Fig. 8b). The structures observed in cross-section of prodissoconchs I and II are essentially the same as those observed in *Mercenaria*, including the changes from the shell edge to the center in both layers.

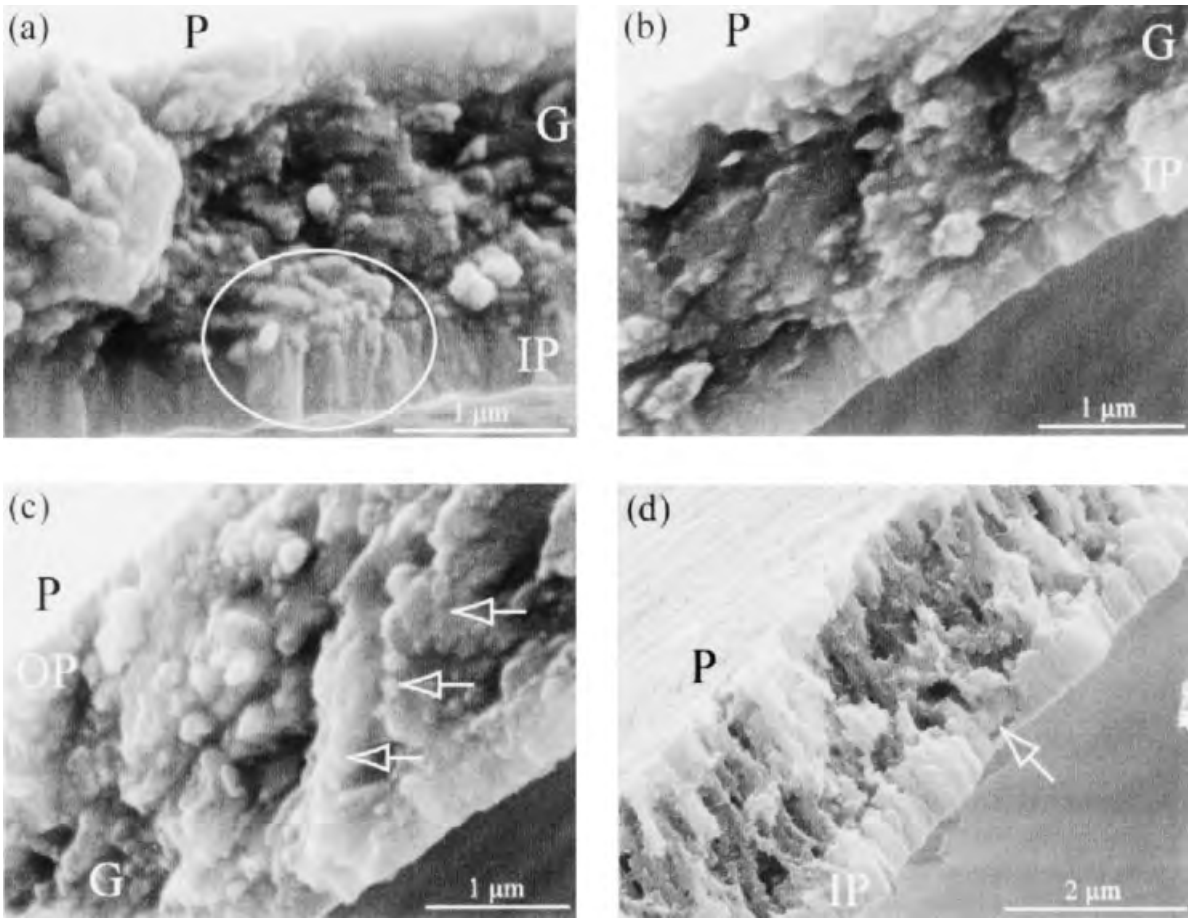

Fig. 7. SEM images taken in ''high resolution'' mode of nine day old *Mercenaria* larval shell cross sections. (**a**) Prodissoconch II at a central position (position 4) with well developed inner prismatic layer. Note that there is no well defined boundary between the inner prismatic (IP) and the granular layer (G) (see area designated in oval). The periostracum (P) is located on the outer surface. (**b**) Prodissoconch II close to the shell edge. The inner prismatic layer (IP) is thinner than in the center (a) and the single prisms are not as well defined as in (a). (**c**) Shell edge. No inner prismatic layer is evident. The granular layer (G) and a thin outer prismatic (OP) layer are present. The arrows indicate the superimposed platy structure oblique to the shell surface. (**d**) Etched cross section of Prodissoconch II close to the transition region (position 3). The etching affects mainly the granular layer and also the prismatic layer (arrow). Remaining parts appear rod-like and are more or less oriented perpendicular to the shell surface.

The latter, however, were observed even more clearly in *Crassostrea* and are shown in Fig. 9 for a nine day old shell. Figure 9a is from an area close to the edge. The prisms are well defined, whereas at the edge (Fig 9b), the prisms are poorly defined. The granular layer in both views shows the platy structure with an oblique orientation relative to the shell surface. At high magnification, the irregular nature of the interface between the inner prismatic and the granular layer can be seen close to the shell edge (Fig. 9c) and at the shell edge (Fig. 9d).

The mineralogy of the *Crassostrea* larval shells could not be analyzed by Raman imaging spectroscopy due to intrinsic fluorescence. Infrared (IR) spectroscopy was therefore used. The disadvantages of IR as compared to Raman spectroscopy are that IR spectra cannot be recorded separately from single shell locations, and the shells are subjected to drying and grinding. A typical IR spectrum obtained from nine day old *Crassostrea* larval shells is shown in Fig. 10b. This is compared to spectra of ACC from *Pyura pachydermatina* (Aizenberg et al., '96) (Fig. 10a), *Mercenaria* six day old larval shells (Fig. 10c), aragonite from adult *Mercenaria* (Fig. 10d), and nonbiogenic aragonite (Fig. 10e). The spectra are scaled such that the 713 cm^{-1} peaks all have the same height

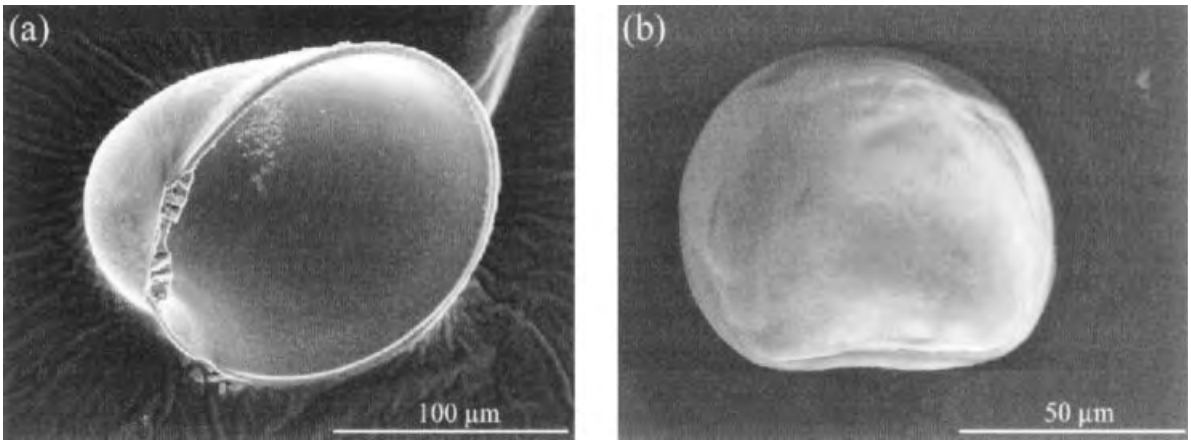

Fig. 8. Scanning electron micrographs of *Crassostrea* larval shells. (**a**) Nine day old *Crassostrea* larval shell. Note that it is much smaller than *Mercenaria* shells of the same age (Fig. 1a). (**b**) Three day old *Crassostrea* larval shell. Note that it consists mainly of Prodissoconch I and a small transition zone to Prodissoconch II.

(ν_4 modes of the carbonate ion). The ACC spectrum was scaled to have the same integrated area under the baseline rise in this region. Under these normalized conditions, the peak ratios and widths of the 713 cm^{-1} and 700 cm^{-1} doublets do not vary (ACC excluded). As ACC does not have distinct peaks in the lattice frequency region, the doublet around 700 cm^{-1} must be due to crystalline aragonite. It should be accompanied by a peak at 856 cm^{-1} in at least the same ratio as in (e), if the aragonite is comparably crystalline. The peak at 856 cm^{-1}, however, varies, with the height progressively decreasing and the width increasing from nonbiogenic aragonite (that we assume is fully crystalline) to the adult shells, and finally to the larval shells. These observations are thus consistent with these larval shells containing, in addition to ACC, an aragonite phase that is in itself disordered, rather than a mixture of pure, well crystallized aragonite and pure ACC. The differences observed above have been quantified by determining the peak height ratios between ν_2 and ν_4 peaks of the IR spectra (Fig. 11). The peak height ratio of nonbiogenic aragonite is centered around 5.5. Pure ACC spectra obtained from *Pyura pachydermatina* have peak height ratios centered at 1.8. With a ratio of 4.7, the adult *Mercenaria* has values significantly (t-test results: $P < 0.001$) lower than the nonbiogenic aragonite. The *Crassostrea* larval shells are in the range of 2.2–3.3. In conclusion, these IR results indicate that larval shells of *Crassostrea gigas* contain aragonite that is less crystalline than nonbiogenic aragonite. They are not inconsistent with the presence of ACC in the shell as well.

DISCUSSION

We show here that both *Mercenaria mercenaria* and *Crassostrea gigas* larval shells have similar ultrastructures, namely an inner prismatic layer overlain by a thicker granular layer. At some locations, there is also an outer prismatic layer adjacent to the periostracum. Raman spectra of the prodissoconch I of *Mercenaria* show that three day old larvae are composed mainly of ACC, which transforms after several more days into a more crystalline phase with peaks characteristic of aragonite. The presence of ACC in both shell layers is confirmed by etching experiments in water. Thickening of the larval shell occurs by the addition of more ACC, which subsequently transforms into the more crystalline phase. Interestingly, in the older shells, the addition of new material at the shell edge involves the deposition of more crystalline material as compared to the central parts of the younger shells. Infrared spectra of different age *Crassostrea* larval shells indicate that they are composed mainly of ACC, together with an aragonitic phase that is also less crystalline than nonbiogenic aragonite.

Raman imaging spectroscopy provides information on the nature of the mineral phases of *Mercenaria* larval shells and their distributions. Major limitations of the technique are the presence of fluorescent compounds that overwhelm the Raman signal, as occurred in the *Crassostrea* larval shells, and the unknown sampling volume. As the surface of the larval shell is never totally flat and homogeneously transparent to the laser beam, the volume sampled is unknown and

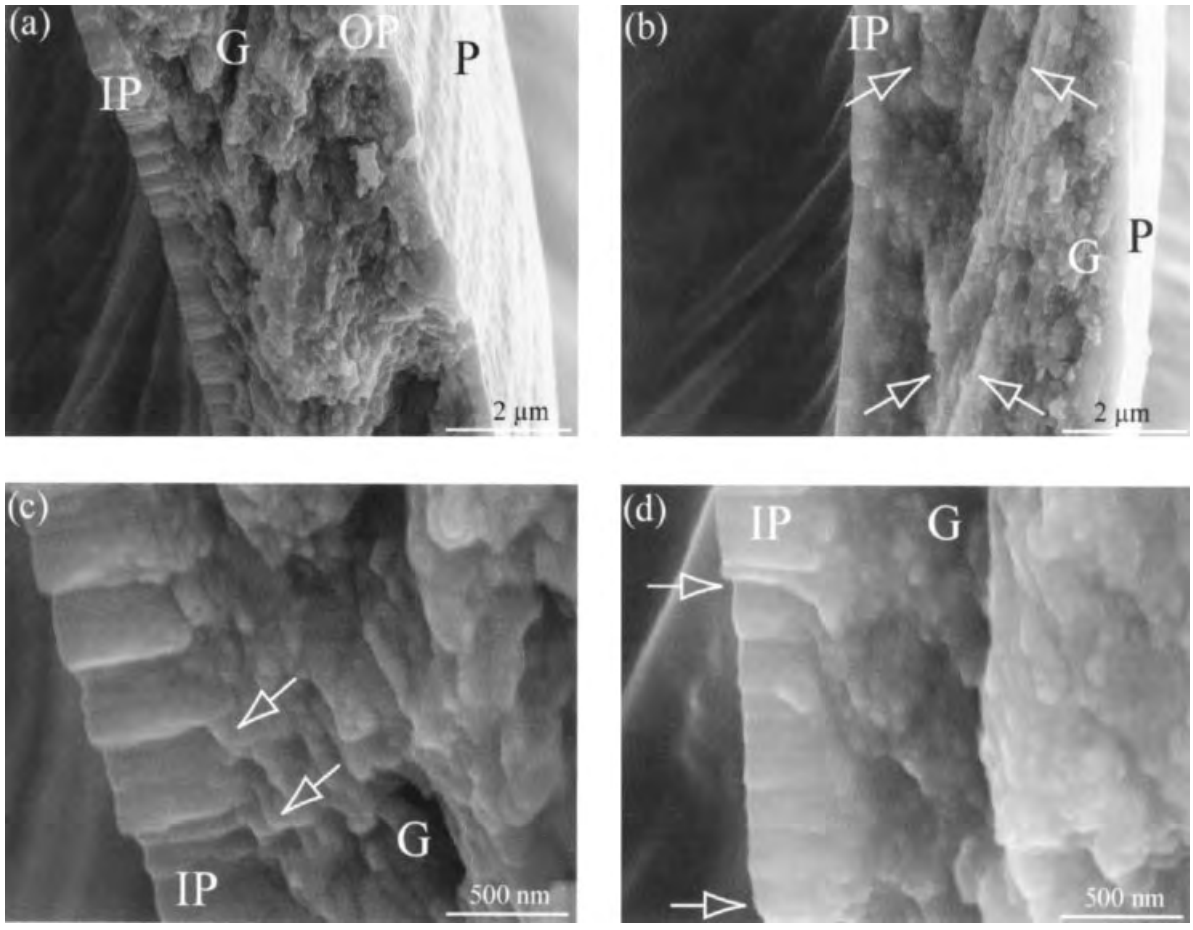

Fig. 9. SEM images taken in ''high resolution'' mode of nine day old *Crassostrea* larval shell cross sections, showing the center of Prodissoconch II and the shell edge. The periostracum is located on the outer shell surface. (**a**) Center of Prodissoconch II, showing the inner prismatic layer (IP), the granular layer (G), and the outer prismatic layer (OP). The superimposed oblique structure to the granular layer is even more pronounced than in *Mercenaria* (Fig. 7c). (**b**) View of shell edge. The inner prismatic layer (IP) is thinner than in (a), and the individual prisms are not well defined. The granular layer (G) shows the superimposed oblique structure as indicated by arrows. (**c**) Higher magnification view of the center of Prodissoconch II. There is no well defined boundary between the inner prismatic layer (IP) and the granular layer (G) (arrows). The prisms are well defined with sharp outlines. (**d**) Higher magnification view of the shell edge. The prisms of the prismatic layer (IP) and the granules of the granular layer (G) are less well defined than in (c), and again the boundary between the two layers is not sharp. Note that the prisms become better defined (upper arrow) with increasing distance from the shell edge (lower arrow). The ultrastructure is similar to that of *Mercenaria* (Fig. 7). Abbreviation: P, Periostracum.

probably variable. In these analyses, this is of particular importance close to the shell edge, as at this location the shell is always oriented at high angles to the laser beam. As we also do not know the depth of penetration of the beam, we analyzed the inside and outside of the surfaces separately, but did not detect any systematic differences. It should also be taken into consideration that crystalline phases may produce much more intense signals compared to amorphous phases.

Many of the Raman spectra obtained, especially from position 1 of the *Mercenaria* prodissoconch I shell, only have peaks at 703 cm^{-1} and 1,087 cm^{-1}. Amorphous calcium carbonate only has the 1,087 cm^{-1} peak, and in all the ACC phases we have examined to date by Raman spectroscopy, the 1,087 cm^{-1} peak of ACC is broader than that of the larval shells observed here. We have also shown (using mainly EXAFS) that each biogenic ACC phase we have studied has a different structure (Levi-Kalisman et al., 2000, 2002). We thus assume that the differences in Raman spectra between the larval shell ACC phase and that of *Pyura*, for example (namely, the broad 1,087 cm^{-1} peak and the presence of a small 703 cm^{-1} peak), are due to the fact that the larval ACC phase also

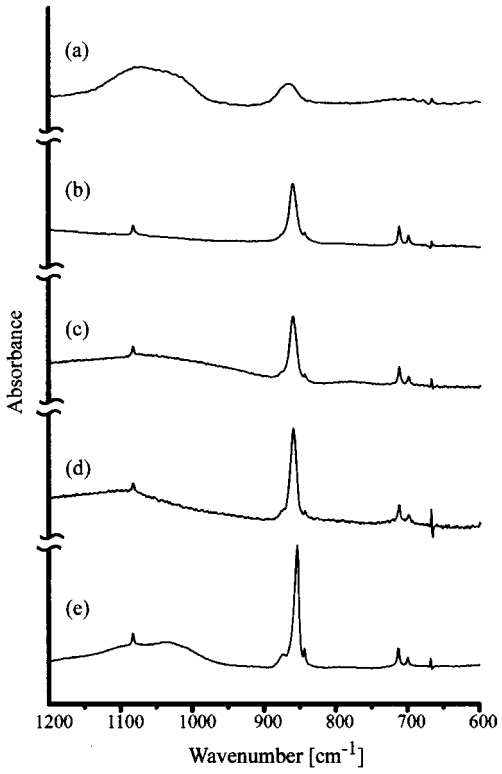

Fig. 10. IR spectra of different samples normalized to equal peak heights at 713 cm^{-1}. The ACC spectrum was scaled to have the same integrated area under the baseline rise in the 713 cm^{-1} and 700 cm^{-1} region. (**a**) IR spectrum from biogenic ACC (*Pyura pachydermatina*) (Aizenberg et al., '96). (**b**) IR spectrum from nine day old *Crassostrea* larval shells. (**c**) IR spectrum from six day old *Mercenaria* larval shells. (**d**) IR spectrum from adult *Mercenaria* shell. (**e**) IR spectrum from nonbiogenic aragonite (Lisan Formation, Israel). Note the broadening and decrease in height of the 856 cm^{-1} peak from nonbiogenically formed aragonite shown in (e) to ACC shown in (a).

has unique structural characteristics. Hasse et al. (2000) used EXAFS analyses of the mineral phase of the fresh-water gastropod larval shell to show that it is composed of ACC. They concluded that it has a nascent aragonitic structure. It would be difficult to interpret EXAFS spectra of these larval shells if indeed, as we observed here, they too are composed of both ACC and a somewhat disordered aragonite phase.

All the Raman spectra that do possess the four peaks characteristic of aragonite differ from nonbiogenic aragonite spectra, in that the peak intensities of the two translational lattice modes relative to the 1,087 cm^{-1} peak are much less intense than in fully crystalline aragonite. This could be due to two possibilities: that this mineral phase is a poorly ordered aragonite, or that this second phase is a mixture of fully crystalline aragonite and ACC. The infrared spectra of the *Crassostrea* larval shells, however, show that one phase is aragonite, which is less ordered than nonbiogenic aragonite. Thus, combining the IR and Raman data, we conclude that the shells of both larval species contain ACC and a poorly ordered aragonite phase. This conclusion is consistent with the observation that the birefringence of the larval shell edge shows the presence of islands of highly birefringent material in a bulk phase, which is isotropic (Fig 12). Iwata ('80) observed something similar in *Haliotis* larval shells and interpreted this to be crystals of aragonite in an organic matrix phase. We suggest that it is more likely to be crystals of poorly ordered aragonite in ACC.

The striking difference in birefringence between the three day old *Mercenaria* larval shells and the nine day old larval shells attests to the presence of a lot more crystalline mineral in the older larvae than in the younger ones. We thus conclude that the ACC is transforming into aragonite. This is demonstrated by the Raman spectra obtained from prodissoconch I, which was initially mainly ACC, but subsequently contained much more crystalline aragonite. The trends that we observed in the Raman spectra at other locations within the

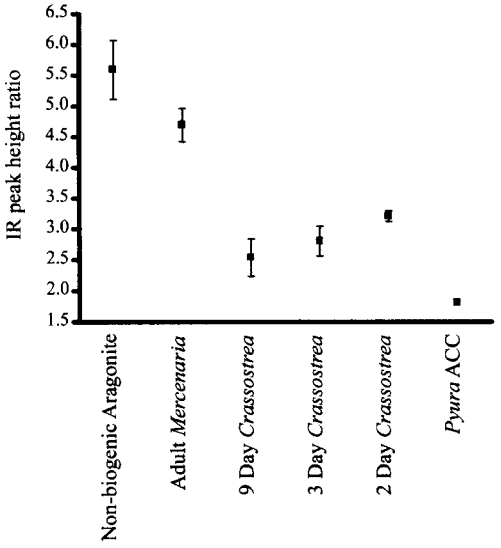

Fig. 11. Quantification of IR spectroscopy data shown in Fig. 10. The y-axis shows the peak height ratio of peaks 856 cm^{-1}/713 cm^{-1}. The error bars reflect the mean and one standard deviation (n = 3–16). Note that adult *Mercenaria* gives values slightly lower than nonbiogenic aragonite, indicating that there are significant differences between the two aragonite phases. Abbreviation: ACC, Amorphous calcium carbonate.

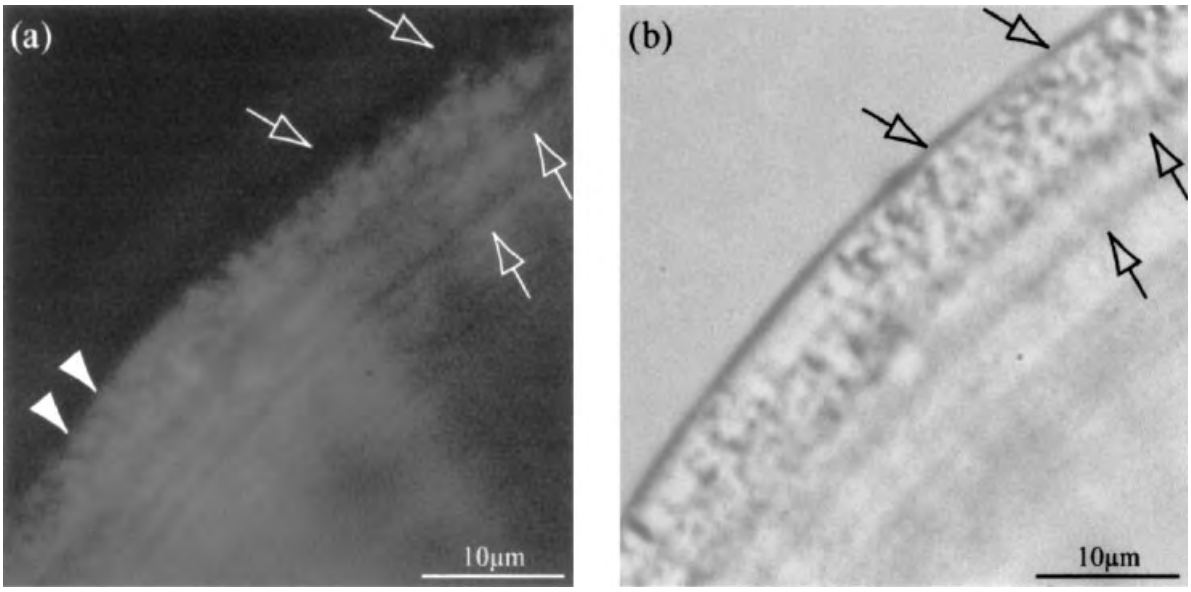

Fig. 12. Polarized light microscopy of a nine day old *Mercenaria* larval shell edge at 400× magnification. (**a**) Crossed polarizer image showing birefringent granular structures. These are light areas embedded in a black isotropic matrix. Two examples are indicated by the white filled arrowheads. The downward pointing, unfilled arrows mark an area where the shell edge is entirely isotropic. The upward pointing arrows show two growth lines for reference. (**b**) Plane polarized image of the same area as in (a), indicating the isotropic area of the shell edge seen in (a) (downward pointing arrows) and the same growth rings (upward pointing arrows) shown in (a).

same shell are consistent with thickening of the inner prismatic layer occurring by the addition of ACC, and the subsequent partial transformation of this ACC to more crystalline aragonite. This thickening is apparently very active in the central parts of the shell. Hence, in these regions, we consistently observed a larger proportion of ACC (Fig. 5). This transformation process may also be occurring in the granular layer. Furthermore, in the 13 day old larval shell, no Raman spectra indicative of only ACC were recorded, implying that by this stage, enough of the ACC had transformed such that every volume sampled contained crystalline aragonite.

A most curious observation is that the last deposited mineral phase at the shell edge inevitably produces Raman spectra that indicate a higher proportion of crystalline material than in the shell center. It is conceivable that this indicates that the shell formation process of prodissoconch II differs from that of prodissoconch I. We, however, tend to prefer the more parsimonious interpretation— namely that it also forms via a transient ACC precursor phase. As the inner prismatic layer does not reach to the very shell edge, the pure ACC that initially forms this layer does not contribute to these spectra. Furthermore, high resolution polarized light images show that in certain individuals, there is a very thin rim at the shell edge that is isotropic (Fig. 12), whereas in exactly the same position in other individuals the shell edge is birefringent. This is consistent with a discontinuous mechanism of shell enlargement involving a first deposited ACC phase that rapidly transforms into a crystalline phase.

The material that forms at the shell edge makes up the granular layer. In fact, we noticed that the ultrastructure of this granular layer close to the shell edge of the more mature larvae does have a more platy and less spheroidal texture as compared to the granular layer closer to the prodissoconch I/II boundary (Figs. 6,7). It thus appears that in the older larvae, the proportion of aragonite per se deposited at the shell edge is higher than in the younger larvae— a conclusion consistent with the Raman spectra from the edge and central regions (Fig. 5). It is not inconceivable that this is the mode of formation of the adult as well— namely, the formation of islands of aragonite enveloped by ACC. This could account for the fact that even the adult mineral phase is not as crystalline as pure inorganic aragonite.

We note that the ultrastructure of the larval shell does not always reflect the mineralogical nature of the shell as revealed by Raman spectroscopy. The first-formed prismatic layer close to the

shell edge has no discernible prisms, suggesting that it is composed entirely of ACC. However, even the well developed prismatic structure of the three day old prodissoconch I is also shown to be composed mainly of ACC. We also noted that there is no clear-cut boundary between the inner prismatic layer and the granular layer. This may indicate that the inner prismatic layer increases in thickness at the expense of the granular layer, in addition to the formation of new material by the associated cells. We also noted that the entire larval shell is susceptible to radiation damage when examined in the SEM. The radiation damage may cause dehydration or internal conformational changes. Amorphous calcium carbonate would be much more susceptible to radiation damage than aragonite. This suggests that, irrespective of shell layer or location, ACC is a major component of the mineral phase. The etching experiments performed on nine day old larval shells confirm that ACC is present in both layers, although it appears to be more abundant in the granular layer.

We showed that the larval shells of two bivalve taxa are very similar in ultrastructure and mineral phases. We therefore assume that other bivalve larvae and possibly mollusc larvae in general will have these basic properties. The larva of the gastropod *Biomphalaria* is reported to be composed entirely of ACC (Hasse et al., 2000). It should be noted that the sea urchin larval spicule formation process is also reported to involve a transformation of ACC into a crystalline polymorph of calcium carbonate— in this case, calcite (Beniash et al., '97). As the molluscs and the echinoderms are on two different branches of the animal phylogenetic tree (Peterson et al., 2000), it is conceivable that the involvement of ACC in calcium carbonate mineral formation in invertebrate animal skeleton formation may be a lot more widespread than has previously been thought.

ACKNOWLEDGMENTS

We thank Sefi Raz for helpful discussions and for her assistance in some Raman experiments. We also thank Raphael Fridman and Muki Shpigel from The National Center for Mariculture, Eilat, Israel, for providing spawn of *Crassostrea gigas* and assistance in *Crassostrea gigas* larval culture. We thank John Scarpa from Harbor Branch Oceanographic Institution, Ft. Pierce, FL for *Mercenaria* larvae. This work supported by grants from: Deutsche Forschungsgemeinschaft (I.M.W., WE2629/2-1); Smithsonian Institution (S.W., Burch fellowship); Minerva Foundation. S.W. is incumbent of the Dr. Walter and Dr. Trude Borchardt Professorial Chair in Structural Biology, and L.A. is incumbent of the Dorothy and Patrick E. Gorman Professorial Chair of Biological Ultrastructure.

LITERATURE CITED

Aizenberg J, Hanson J, Ilan M, Leiserowitz L, Koetzle TF, Addadi L, Weiner S. 1995. Morphogenesis of calcitic sponge spicules— a role for specialized proteins interacting with growing crystals. FASEB J 9:262–268.

Aizenberg J, Lambert G, Addadi L, Weiner S. 1996. Stabilization of amorphous calcium carbonate by specialized macromolecules in biological and synthetic precipitates. Adv Mater 8:222–226.

Bandel K. 1990. Shell structure of the gastropoda excluding archaeogastropoda. In: Carter JG, editor. Skeletal biomineralization: patterns, processes and evolutionary trends. New York: Van Nostrand Reinhold. p 117–134.

Beniash E, Aizenberg J, Addadi L, Weiner S. 1997. Amorphous calcium carbonate transforms into calcite during sea urchin larval spicule growth. Proc R Soc Lond B Biol Sci 264: 461–465.

Bielefeld U, Becker W. 1991. Embryonic development of the shell in *Biomphalaria glabrata* (Say). Int J Dev Biol 35: 121–131.

Bøggild OB. 1930. The shell structure of the mollusks. K Dan Vidensk Selsk Skr Naturvidensk Math Afd 9:233–326.

Carriker MR, Palmer RE. 1979. Ultrastructural morphogenesis of prodissoconch and early dissoconch valves of the oyster *Crassostrea virginica*. Proc Natl Shellfish Assoc 69:103–128.

Carter JG. 1980. Environmental and biological controls of bivalve shell mineralogy and microstructure. In: Rhoads D, Lutz R, editors. Skeletal growth of aquatic organisms. New York and London: Plenum Press. p 69–113.

Carter JG. 1990. Shell microstructural data for the bivalvia. In: Carter JG, editor. Skeletal biomineralization: patterns, processes and evolutionary trends. New York: Van Nostrand Reinhold. p 297–411.

Castilho F, Machado J, Reis ML, Sa C. 1989. Ultrastructural study of the embryonic and larval shell of *Anodonta cygnea*. Can J Zool 67:1659–1664.

Cather JN. 1967. Cellular interactions in the development of the shell gland of the Gastropod, *Ilyanassa*. J Exp Zool 166:205–224.

Eyster LS. 1982. Embryonic shell formation in the Nudibranch *Aeolidia papillosa*. Am Zool 22:981.

Eyster LS. 1986. Shell inorganic composition and onset of shell mineralization during Bivalve and Gastropod embryogenesis. Biol Bull 170:211–231.

Eyster LS, Morse MP. 1984. Early shell formation during molluscan embryogenesis, with new studies on the Surf Clam, *Spisula solidissima*. Am Zool 24:871–882.

Hasse B, Ehrenberg H, Marxen JC, Becker W, Epple M. 2000. Calcium carbonate modifications in the mineralized shell of the freshwater snail *Biomphalaria glabrata*. Chem Eur J 6:3679–3685.

Ivester MS. 1972. Ultrastructural study of larval shell formation in *Nassarius obsoletus*. Am Zool 12:717.

Iwata K. 1980. Mineralization and architecture of the larval shell of *Haliotis discus hannai* Ino, (Archaeogastropoda). Jour Fac Sci Hokkaido Univ ser IV 19:305–320.

Jablonski D, Lutz RA. 1980. Molluscan larval shell morphology: ecological and paleontological applications. In: Rhoads D, Lutz R, editors. Skeletal growth of aquatic organisms. New York and London: Plenum Press. p 323–377.

Kniprath E. 1979. The functional morphology of the embryonic shell-gland in the conchiferous molluscs. Malacologia 18:549–552.

Kniprath E. 1981. Ontogeny of the molluscan shell field: a review. Zoologica Scripta 10:61–79.

Kobayashi I. 1969. Internal microstructure of the shell of bivalve molluscs. Am Zool 9:663–372.

LaBarbera M. 1974. Calcification of the first larval shell of *Tridacna squamosa* (Tridacnidae: Bivalvia). Mar Biol 25:233–238.

Levi-Kalisman Y, Raz S, Weiner S, Addadi L, Sagi I. 2000. X-ray absorption spectroscopy studies on the structure of a biogenic ''amorphous'' calcium carbonate phase. J Chem Soc Dalton Trans:3977–3982.

Levi-Kalisman Y, Raz S, Weiner S, Addadi L, Sagi I. 2002. Structural differences between biogenic amorphous calcium carbonate phases using X-ray absorption spectroscopy. Adv Funct Mater 12:43–48.

Lowenstam HA. 1989. Spicular morphology and mineralogy in some pyuridae (Ascidiaceae). Bull Marine Sci 45:243–252.

Lowenstam HA, Weiner S. 1989. On biomineralization. New York: Oxford Univ. Press.

McCain ER. 1992. Cell interactions influence the pattern of biomineralization in the *Ilianassa obsoleta* (Mollusca) embryo. Dev Dyn 195:188–200.

Medakovic D, Popovic S, Grzeta B, Plazonic M, Hrs-Brenko M. 1997. X-ray diffraction study of calcification processes in embryos and larvae of the brooding oyster *Ostrea edulis*. Marine Biol 129:615–623.

Neff JM. 1972. Ultrastructure of the outer epithelium of the mantle in the clam *Mercenaria mercenaria* in relation to calcification of the shell. Tissue Cell 4:591–600.

Peterson KJ, Cameron RA, Davidson EH. 2000. Bilaterian origins: significance of new experimental observations. Dev Biol 219:1–17.

Schmidt WJ. 1924. Die Bausteine des Tierkörpers in Polarisiertem Lichte. Bonn: Friedrich Cohen.

Stenzel HB. 1963. Aragonite and calcite as constituents of adult oyster shells. Science 142:232–233.

Stenzel HB. 1964. Oysters: composition of the larval shell. Science 145:155–156.

Taylor JD. 1973. The structural evolution of the bivalve shell. Palaeontology 16:519–534.

Taylor JD, Kennedy WJ, Hall A. 1973. The shell structure and mineralogy of the bivalvia. Bull Br Mus Nat Hist (Zool) 22:253–294.

Waller TR. 1981. Functional morphology and development of veliger larvae of the European oyster, *Ostrea edulis* Linne. Smithsonian Contrib Zool 328:1–70.

Watabe N. 1988. Shell structure. In: The mollusca. Academic Press. p 69–104.

OCB OCEAN ACIDIFICATION SHORT COURSE

CORAL CALCIFICATION EXPERIMENT

Michael Holcomb (WHOI)

In this exercise, students will have the opportunity to collect alkalinity, pH, and DIC samples for estimating coral calcification rates. In addition to measuring carbonate system parameters, NH_3 will be measured to allow alkalinity to be corrected for NH_3 excretion. Alkalinity values will be corrected for evaporation using evaporation rate estimates from changes in container weight.

Supplies/equipment to be prepared in advance:

- 12 labeled slides with *Astrangia poculata* colonies, 3 blank slides
- 15 1L labeled containers with lids (PET food service containers) pre-soaked in seawater, rinsed with fresh water and dried (Group G will use containers 1-5, group H: 6-10, group I: 11-15)
- 1 constant temperature water bath with temperature logger and positions for 15 1L containers and a 10cm flow cell connected to a USB4000 spectrophotometer and fiber optic light source for pH measurement
- Airlines to supply air to each container
- Jugs with filtered seawater, containing ambient seawater or seawater supplemented with sodium bicarbonate (sufficient to increase alkalinity by ~500 µmol/kg) each bubbled with air and kept in a constant temperature bath.
- washed scintillation vials for alkalinity samples (60), DIC vials (60), nutrient vials (20), washed 10ml syringes (32) for spectrophotometric pH measurements (and stock solution of m-cresol purple (~0.9mM)), 1 25ml syringe and syringe filter for NH_3 samples
- 1 (or more) balances with 1kg capacity
- Conductivity meter

<u>Step 1: set up:</u>

- weigh each of the 1L containers with lid and airstone
- add 800-900 ml seawater from the appropriate jug (group G: ambient, group H: elevated alkalinity, group I: ambient)
- weigh the container with water
- remove the coral (or blank slide) assigned to the container from the water (be careful not to touch the coral), allow water to drain off slide briefly and add to the container, close container
- re-weigh container
- Place container in water bath and connect airline
- Measure initial salinity (conductivity meter) on the source seawater – pour water from the jug into a 100 ml beaker, place probe in beaker, press read button until successive readings stabilize at the same value

Step 2: samples (T1-T4)

- remove each container from the bath, dry off container, weigh, and take samples

Samples:

- For all samples, make sure the exterior of the container or syringe being used for sampling is clean and dry to avoid introducing contaminants
- pH samples: rinse 2 10ml syringes twice with a few ml of water from the container, (discard rinsings). Fill syringes with 10ml from the container, add pH indicator (50 µl to one, 100 µl to the other) and introduce a small bubble with the pH indicator to make mixing easier, cap the syringe, shake to mix and place in the constant temperature bath.
- DIC: dip a glass DIC vial into the container, fill to near the top of the vial (fill slowly, try to minimize bubbles and splashing). Leave ~ 1ml air space, add 10 µl of saturated $HgCl_2$. Cap tightly, mix, and place in refrigerator.
- Alkalinity: dip a HDPE alkalinity vial into the container, fill to near the top, cap tightly and place in refrigerator.
- Ammonia: rinse the syringe with a few ml of sample, fill the 25ml syringe with 20ml water (water will only be taken from a subset of containers, group G: sample containers 2 and 5, group H: 8 and 10, group I: 14), attach the syringe filter and force 10ml through the filter to rinse, collect the next Xml in the appropriate tube for NH_3 samples.
- Following sampling, re-weigh container and return to bath

Step 2.1: pH measurement

- Spectrasuite will be pre-configured to save each spectrum in the OCB folder (open folder to see current file number)
- Fill the seawater syringe with water from the jug used to fill your containers.
- remove the distilled water syringe from the brown luer fitting (input)
- Make sure there is a bead of water at the end of the seawater syringe and on the input fitting to avoid introducing air bubbles.
- Inject most of the seawater (inject slowly – a few seconds for each ml) being careful not to introduce any bubbles
- block the light path (place Al foil in slit on the light source)
- Make sure spectrasuite is in spectrum mode (click button S)
- collect spectrum (play/pause button – green triangle and double bars)
- set as dark (click dark light bulb button)
- remove Al foil from light path
- collect spectrum, set as reference (click yellow light bulb button)
- switch to absorbance mode (click blue A button)
- remove seawater syringe and attach first sample syringe, inject ~5ml of sample being careful not to introduce bubbles and collect spectrum – repeat for each sample
- If a bubble does get into the light path (indicated by a rise in background absorbance), remove the sample syringe, inject seawater till the bubble moves through (check by collecting spectra) if the bubble persists, use the syringe on the outlet side of the flow cell to pull water through the cell. If neither approach works,

a dilute soap solution may be used to clear the bubble (use distilled water for this, use distilled water following the soap solution to rinse the cell). Once the bubble has been cleared, the remaining ~5ml of sample may be injected to get a usable spectrum

- Once all samples have been run, use the DI syringe to inject 8ml of distilled water to flush the seawater out of the cell.

Step 3: take down (T4)

- At the end of the exercise (T4), take final samples
- check the salinity and temperature on each container (conductivity meter)
- return corals to holding tank

OCB OCEAN ACIDIFICATION SHORT COURSE

OUTLINE FOR LARVAL MOLLUSC OCEAN ACIDIFICATION EXPERIMENTS

Instructors: Anne Cohen, Dan McCorkle

TAs: Meredith White, Kathryn Rose

Please refer to full protocol under Thursday November 5 tab.

Protocol for Algal Culturing

Meredith White (WHOI)

Note: This protocol is appropriate to grow algae to be used in larval culture. It is not precise enough if the point of your experiment is measuring algae growth. There are specifics in this protocol that pertain to the set up at WHOI, but you can adapt it to your set-up.

Generally

Primary →	Secondary →	Tertiary		→ Quaternary
Test tube →	Erlenmeyer Flask →	Erlenmeyer Flask *or* Fernbach Flask		→ Carboy
~10 mL →	~ 50 mL →	~ 500 mL	~1L	→ 12 L

NOTE:
- ~1-2 week for culture to grow up (1-2 week per arrow)
- Throw out cultures that are more than 2 weeks old
- Transfer your primary culture every 7-10 days
  - Whenever you start a new culture, the volume of algae that you add should be about 10% of the total culture volume

Nutrients

Kent's F/2 algal media A (vitamins and minerals) and B (phosphate, nitrogen) say add 2 tsp of each to 20 gallons of water. This is equivalent to 130 μL of each part to 1 L water. Carly used 135 μL of each to 1 L water, so that's what I'll do.

This is a really really small amount of nutrients to seawater, so you could either make many liters at once or make a dilute solution of the stock nutrients. I make a dilute solution. I.e., if I'm making 1 L of media, I want to be able to add 1 mL of each nutrient instead of adding 130 μL of each.

DILUTE NUTRIENT SOLUTION:

In ESL
(DO FOR BOTH PARTS A & B)
Since you can only autoclave jars that are 2/3 full, make about 700 mL solution in a 1 L jar. Use a 1 L autoclavable jar with lid. Using a graduated cylindar, add 95 mL of pure nutrient solution and 605 mL DI water (fill to 700 mL mark). Close jar and invert several times. LABEL! (This is the same as 135 mL nutrients into 1 L solution.)

In Redfield
Bring dilute nutrient solutions to Redfield right away (since there's a nutrient solution, it's a perfect condition for algae or bacteria to grow, so you want to treat it right away). Autoclave solutions on the liquid cycle for 20 minutes (autoclave cycle 3). Don't leave it in the autoclave because if it cools slowly, the nutrients can precipitate out. Bring them back to ESL and store them in the refrigerator. **Note:** Vitamins often break down with heat, but if you don't autoclave these dilute nutrient solutions, they could become contaminated and cause

problems later. Following this procedure, I have not had problems with algae not growing due to lack of nutrients.

Laminar Flow Hood
All algae culture transfers should be performed under laminar flow hood. The hood should be cleaned with isopropyl alcohol solution or 70% Ethanol (on top of hood) and paper towels each time. Turn on the light and flow with the switch WAY in the back above hood.

Quick Overview
This is the protocol that I have developed for myself for my algal culturing at WHOI. I had input from Phil Alatalo and Carly Strasser. This is not mean to be a be-all-end-all guide to algae culture, but its methods do work, at least for me. Some things are specific to the facility at WHOI, but you can adapt it to your facility. I might be overly meticulous about this, but it works for me. You can play around with it and see where you can cut corners (maybe not having all three stages of culture).

At WHOI, we have an algae culture room in ESL equipped with a wall bank of full-spectrum fluorescent lights. In the summer, many people are using the room and it is necessary to have this many lights. If you are growing only a small volume, you may be able to get by with a small fixture holding two fluorescent bulbs that sits on the benchtop.

I usually prepare about 3-4 weeks worth of media at one time. I get about 5 L of filtered seawater (FSW) and add 5 mL of each of my dilute nutrient solutions. This 5 L of media is then distributed among the primary culture test tubes and secondary and tertiary culture flasks. Caps/stoppers are placed loosely on all and they are all autoclaved for 20 minutes on the liquid cycle. I store them labeled in a cabinet until I'm ready to use them.

Every week and a half to two weeks, I transfer the algae to new cultures so it doesn't get too old. When I transfer, I keep at least one flask of the old culture in case something goes wrong and my algae dies. I transfer the primary cultures to the secondary cultures, the secondary cultures to the tertiary cultures, and the tertiary cultures to the quaternary cultures. If I'm only maintaining my cultures, but not using them, I do not keep quaternary cultures and I usually only have 1-2 replicates for each stage. I restart primary cultures from the tertiary cultures. Here's a table to help explain:

Protocol for Algal Culturing – MMW

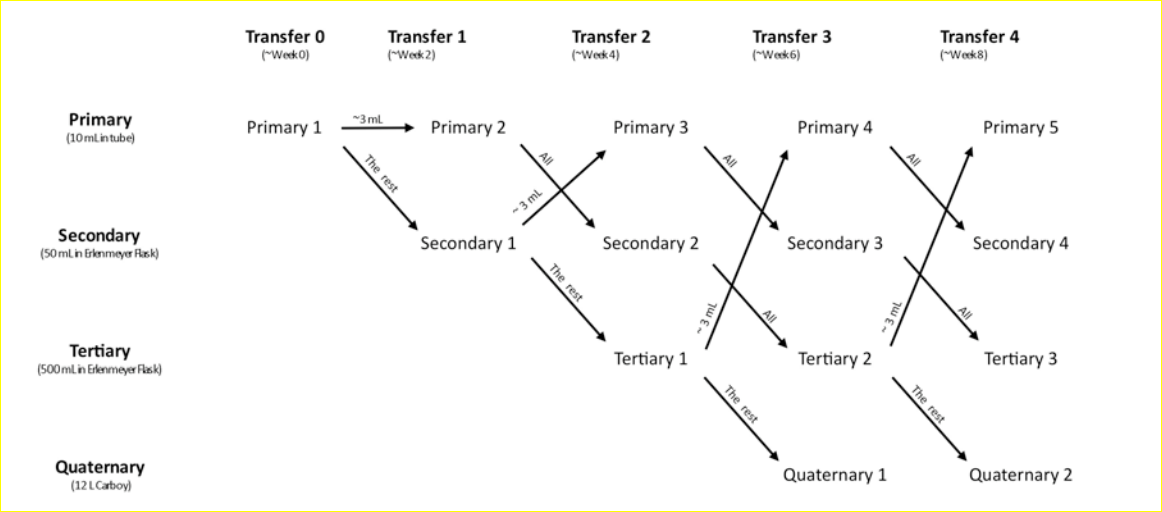

Test tube preparation (Primary Culture)
The primary culture is SACRED! It needs to be kept clean and healthy at all times. Never let all primary cultures die – have at least 2-3 going at any given time.

In ESL
- Add about 10 mL of FSW to the pyrex tube
- Add 10 μL of each dilute nutrient solution (A & B) to the tube using a micropipetter

In Redfield
- Autoclave for 20 minutes on the liquid cycle (cycle 3)
- Remove from autoclave promptly to avoid precipitation of nutrients

In ESL
- Wait for the media to cool to room temperature (at least overnight) – store (covered) as long as necessary before inoculating

Inoculation (Under Laminar Flow Hood)
- Use a sterile disposable pipette to add ~3 mL of initial algal culture to inoculate the new culture (I usually use 3 mL from the current tertiary culture)
- Cover with foam stopper, label and place tubes in front of lights (we use full-spectrum fluorescent lights that are kept on all the time).

Erlenmeyer flask preparation (Secondary Culture)
In ESL
- Add about 50 mL of FSW to the 125 mL autoclavable Erlenmeyer flask
- Add 50 μL each of dilute nutrient solution (A & B) to the flask using a micropipetter
- Put a foam stopper in and loosely cover with aluminum foil

For a bigger flask:
- Add about 500 mL of FSW to a 1 L autoclavable Erlenmeyer flask
- Add 500 μL each of dilute nutrient solution (A & B) to the flask using a micropipetter
- Put a foam stopper in and loosely cover with aluminum foil

In Redfield
- Autoclave for 20 minutes on the liquid cycle (cycle 3)

- Remove from autoclave promptly to avoid precipitation of nutrients

In ESL

- Wait for the media to cool to room temperature – store (covered) as long as necessary before inoculating

Inoculation (Under Laminar Flow Hood)

- Pour the contents of the primary culture tube into the flask (make sure that you have started a new primary culture!)
- Cover with foam stopper, label, and place flask in front of lights

Fernbach flask preparation (Secondary Culture)

In ESL

- Add about 1 L of FSW to the 2 L autoclavable Fernbach flask
- Add 1 mL each of dilute nutrient solution (A & B) to the flask using a sterile disposable pipette
- Put a foam stopper in and loosely cover with aluminum foil

In Redfield

- Autoclave for 20 minutes on the liquid cycle (cycle 3)
- Remove from autoclave promptly to avoid precipitation of nutrients

In ESL

- Wait for the media to cool to room temperature – store (covered) as long as necessary before inoculating

Inoculation (Under Laminar Flow Hood)

- You should start a new Fernbach flask either from a secondary culture.
- Pour the contents (~ 50 mL) of the secondary culture flask into the new flask
- Cover with foam stopper, label, and place flask in front of lights

Carboy preparation (Tertiary Culture)

Carboys are not autoclavable because they are too big. We sterilize by bleaching them.

In ESL

- Wash a glass or plastic carboy with filtered seawater

Sterilize

- Fill the carboy with FSW
- Add 1 mL bleach per 2 L water (so if the carboy is 12 L, add 6 mL bleach) using a graduated cylinder. This kills all bacteria.
- Put a sterile pipette on the end of an air-tube and put into the carboy. Try to get it close to the bottom to prevent bacteria film from developing.
- Loosely cover with a plastic beaker
- Let it bleach overnight
- Neutralize the chlorine by adding 1 mL of 1 M sodium thiosulfate pentahydrate ($Na_2S_2O_3 \cdot 5H_2O$) for every mL of bleach. So, if you added 6 mL of bleach, add 6 mL of 1 M $Na_2S_2O_3 \cdot 5H_2O$. The chlorine is neutralized very quickly, but I usually wait about 2 hours before adding new algae.

Nutrients

- Add 1 mL of each dilute nutrient solution (A & B) per L FSW to the carboy using a sterile disposable pipette (so if the carboy is 12 L, add 12 mL of each nutrient).

Inoculation (not in hood)

- You should start a new tertiary flask from a secondary culture
- Pour the contents (~ 500 mL or 1 L) of the tertiary culture flask into the carboy. There should be enough algae that there is a faint color visible
- Label and place carboy in front of lights

Sodium thiosulfate preparation

We want a 1 M solution of $Na_2S_2O_3 \cdot 5H_2O$ (MW: 248.19 g/mol)

- Add 248.19 g $Na_2S_2O_3 \cdot 5H_2O$ to a 1 L volumetric flask
- Add some DI water to the flask and swirl to dissolve solids. Continue to add DI water to fill the flask to the line.
- Transfer to a storage bottle and label
- Autoclave the storage bottle for 20 minutes on the liquid cycle (cycle 3)
- Allow to cool to room temperature before using

Notes on Autoclaving

- There are fast and slow cycles. Fast cycles release the pressure quickly and are suitable for solids. Slow cycles release the pressure slowly and are suitable for liquids.
- Cycle 1: Solid (20 min)
- Cycle 2: Solid (45 min)
- Cycle 3: Liquid (20 min)
- Cycle 4: Liquid (45 min)
- Liquids should be autoclaved in a bin incase any spills out of the container
- Lids on liquid containers should always be very loose. If they are tight, the bottle could explode.
- Liquids should only fill 2/3 of the container or else it will spill out.

Saturday, November 7, 2009
Lectures, monitoring coral and larval mollusk experiments

Morning

Time	Activity
8:45 am	Shuttle MBL to ESL
9:00 am	**Lab**. T2 sampling for coral and monitor pH of mollusks (3 person subgroups of Groups G, H, I) (Holcomb, ESL 10)
10:00 am	Shuttle ESL to MBL
10:30 am	**Lecture**. Radioisotope Techniques for measuring coccolithophore calcification (Balch) and PIC methods for quantifying calcification (Iglesias-Rodriguez), MBL Speck Auditorium
12:00 pm	Lunch (Swope Cafeteria, MBL)

Afternoon

Time	Activity
1:15 pm	Shuttle MBL to ESL
1:30 pm	**Lab**. T3 sampling for coral (3 person subgroups of Groups G, H, I) (Holcomb, ESL 10)
2:30 pm	Shuttle ESL to MBL
2:45 pm	Break
4:00 pm	**Lecture**. Measuring calcification in the field. (Langdon). MBL Speck Auditorium
5:30 pm	Dinner (Swope Cafeteria, MBL)

OCB OCEAN ACIDIFICATION SHORT COURSE

OUTLINE FOR LARVAL MOLLUSC OCEAN ACIDIFICATION EXPERIMENTS

Instructors: Anne Cohen, Dan McCorkle

TAs: Meredith White, Kathryn Rose

Please refer to full protocol under Thursday November 5 tab.

OCB OCEAN ACIDIFICATION SHORT COURSE

CORAL CALCIFICATION EXPERIMENT

Michael Holcomb (WHOI)

Please refer to full protocol under Friday November 6 tab.

Radioisotope techniques for measuring coccolithophore calcification

Instructor: Barney Balch

1. Overview of various methods to estimate coccolithophore calcification, with and without isotopes

2. Safe handling procedures with isotopes

3. Sample collection

4. Water handling
    a. To Pre-screen or not to pre-screening water samples?
    b. Bottles
        i. Types
        ii. cleaning
    c. Care in sample handling

5. Incubation conditions
    a. Simulated in situ incubations
        i. Temperature control
        ii. Light quantity
        iii. Light quality
    b. In situ incubations

6. How long to incubate?

7. Difference technique
    a. Origins (Paasche, 1963)
    b. Materials
    c. Basics
    d. Preparing samples for counting
    e. Advantages
    f. Limitations
    g. Costs
    h. Accuracy, Precision, Sensitivity

8. Micro-diffusion technique
    a. Origins (Paasche and Brubaak, 1994)
    b. Materials
    c. Basics
        i. Fastidiously clean manipulation is critical
        ii. Interstitial water in filter
        iii. Controls for micro-diffusion efficiency

        iv. Checks of isotope specific activity
        v. Preparing samples for counting
        vi. Controls for reagent contamination
    d. Advantages
    e. Limitations
    f. Costs
    g. Accuracy, Precision, Sensitivity

9. Blank vs. time zero's

10. Dark calcification

11. Equations for calculating calcification and assumptions

12. Why isn't foraminifera and pteropod calcification included in these techniques?

PIC methods for quantifying calcification

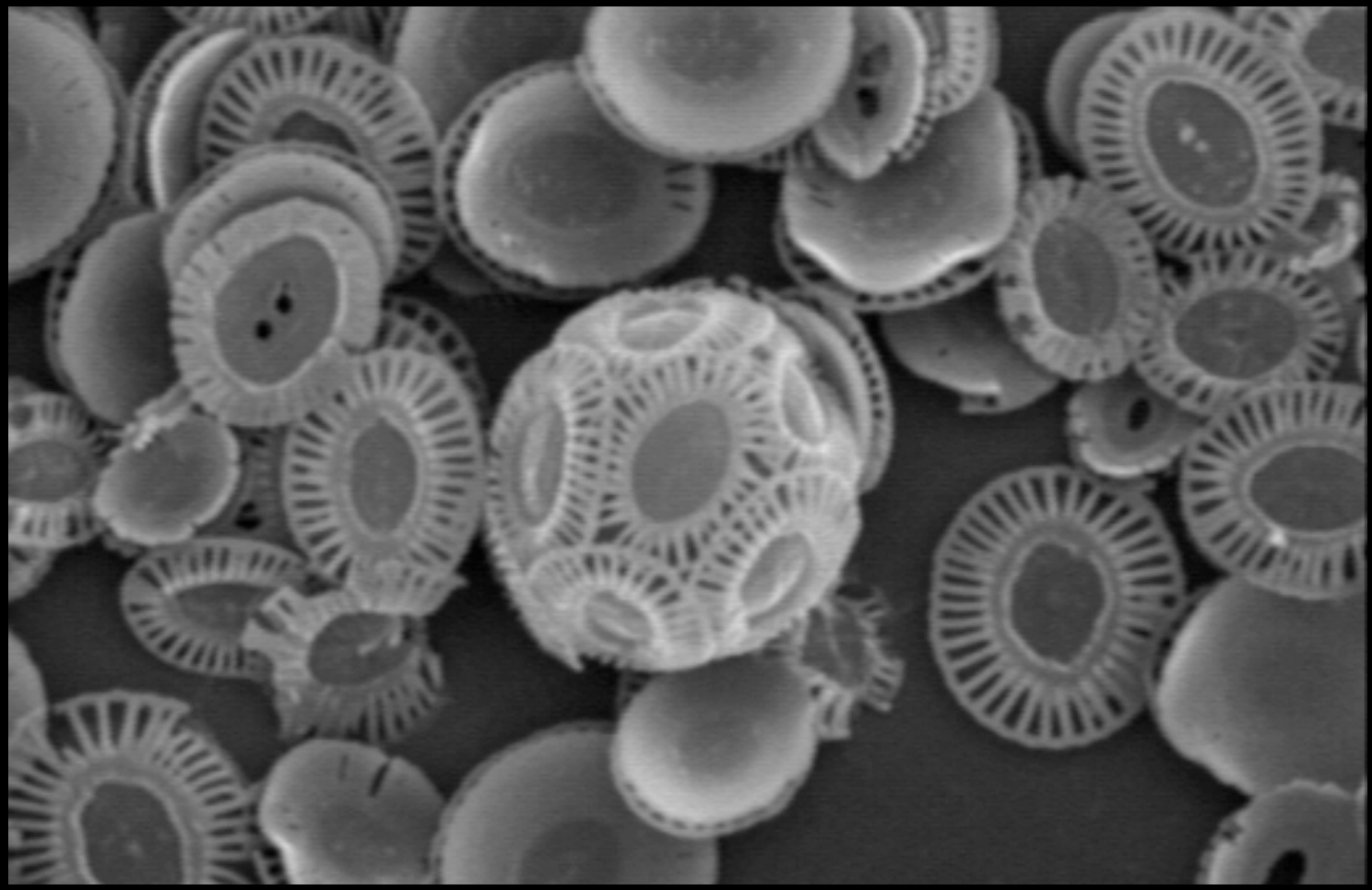

Débora Iglesias-Rodríguez
National Oceanography Centre, Southampton.

Indirect calculation of PIC

- Aliquot cultures are filtered onto pre-combusted glass fiber filters (GF/C)

- One of two replicate filter sets are treated with 0.4 M HNO_3 to dissolve the coccoliths and both filters are then analyzed for particulate carbon on a CHN analyzer.

- The concentration of PIC is determined from the difference between the total particulate carbon and the particulate organic carbon concentration.

Direct calculation of particulate inorganic carbon

- Aliquots of cultures are filtered through 0.22 µm polycarbonate filters

- Filters are washed (before and after filtration) with dilute ammonium hydroxide solution (pH ~9) to remove seawater. NaOH is avoided as sodium is used as a proxy of seawater contamination.

- $CaCO_3$ is dissolved using 0.4 M HNO_3 (Romil UpA grade) and keeping the tubes in a rotating platform overnight

Particulate inorganic carbon analysis

• The resulting solution is filtered through 0.45 µm hydrophilic PTFE membranes and analyzed using a Perkin Elmer Optima 4300 DV inductively coupled plasma - optical emission spectrometer (ICP-OES)

• Calibrations are conducted using standard solutions bracketing the range of concentrations measured.

• Sodium concentration was used as a proxy for seawater contamination.

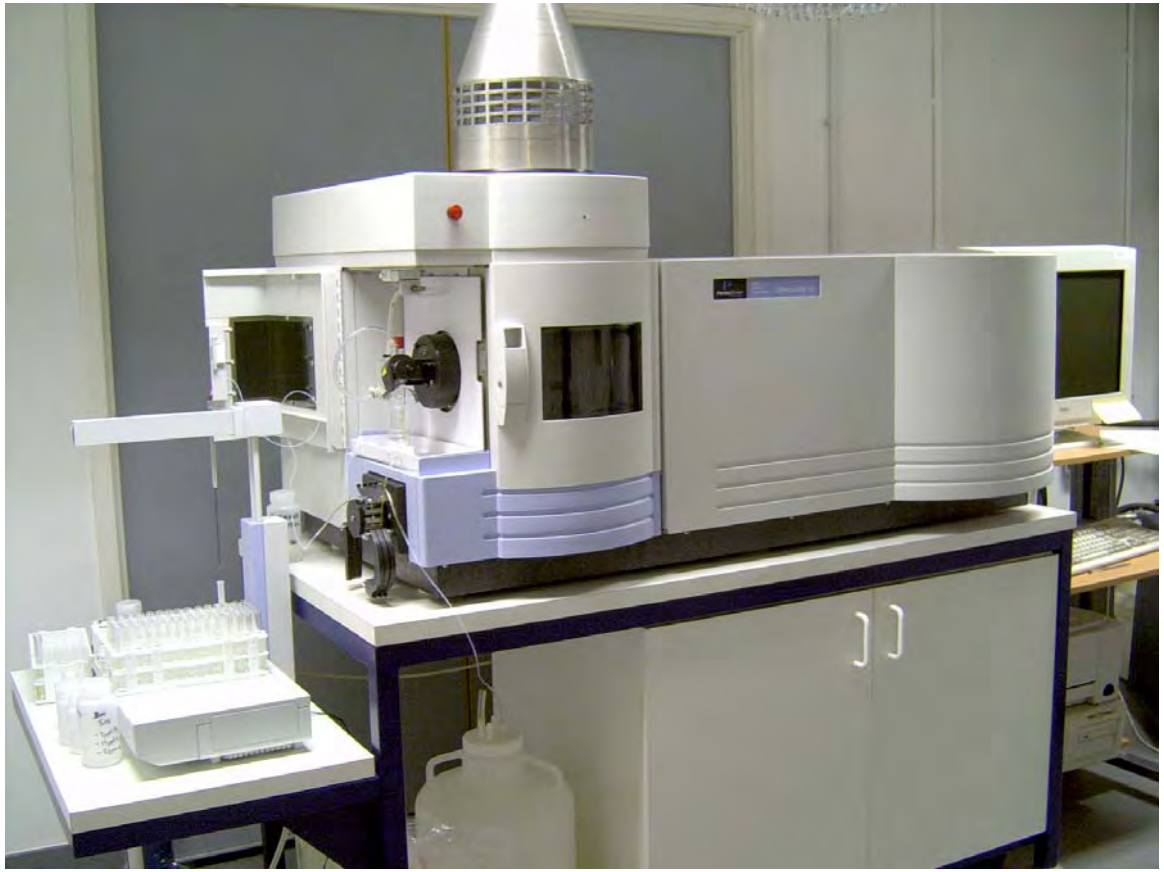

Normalization of PIC

- Typically, rates are expressed per cell basis (cellular calcification, e.g. pmol C cell^{-1} d^{-1}) (biologicaly relevant)

- Growth rates of the culture under nutrient-saturated conditions are based on cell counts made at the same time of day each day

$$\mu = \ln\left(C_{t+1}/C_t\right) + D$$

where m and D are the growth rate and dilution rate (d^{-1}), respectively, and C_{t+1}/C_t is the ratio of cell counts on successive days. Adjustments must be made to the dilution rate.

- Normalization to organic carbon should accompany cellular measurements of PIC (biogeochemically relevant)

Limitations in inferring $CaCO_3$ from Ca^{2+} measurements

- Magnesium tends to substitute Ca in the calcite lattice, forming “low-Mg calcite” when %$MgCO_3$ <4, and “high-Mg calcite” when it is >4.

- Calcifiers incorporate substantial amounts of Mg, which is often produced as $MgCO_3$ (Weber, 1969; Vinogradov, 1953; Chave, 1954; Lowenstam, 1954, 1964; Clarke, 1917).

- The degree of Mg incorporation varies widely amongst different organisms, as well as amongst different skeletal components within a single organism (Ries, 2004).

- Mg incorporation is also known to be largely influenced by seawater Mg/Ca (Ries, 2004) and temperature (Chave, 1954).

Merely calculating the saturation state as:

$$\Omega = [Ca^{2+}][CO_3^{2-}]/K_{sp}$$

of the biomineral (calcite or aragonite) **<u>is not adequate</u>** for estimating the organism's susceptibility to elevated pCO_2.

$CaCO_3$ calculations from Ca^{2+} measurements could underestimate calcification

Implications on dissolution of biomineral - susceptibility of organisms to high CO_2

- The saturation state of seawater with respect to Mg calcite:

$\Omega = [Mg^{2+}]^{x} [Ca^{2+}]^{(1-x)} [CO_3^{2-}]/K_x$
(Plummer and Mackenzie, 1974).

x = mol fraction of Mg ions, and K_x is the equilibrium constant with respect to Mg calcite (ion activity product at equilibrium since stoichiometric solubility products have not been determined).

$$\Omega = [Mg^{2+}]^{x} [Ca^{2+}]^{(1-x)} [CO_3^{2-}]/K_x$$

Mg is five times more abundant than Ca in seawater:

- substituting Mg for Ca in the above equation will effectively increase the ion concentration product for high Mg calcite
- However, this increase is offset by a proportionally greater increase in the solubility product for high Mg calcite.

The solubility of Mg calcite in seawater will exceed that of aragonite when $MgCO_3$ in calcite exceeds about 11 mole %

[modelling work suggests that Mg calcite with greater than 17 mole % $MgCO_3$ will be undersaturated in surface seawater by the year 2230 (Morse et al, 2006)].

Tipping points - WP9 re-analysis (Lebrato et al. pers. Com)

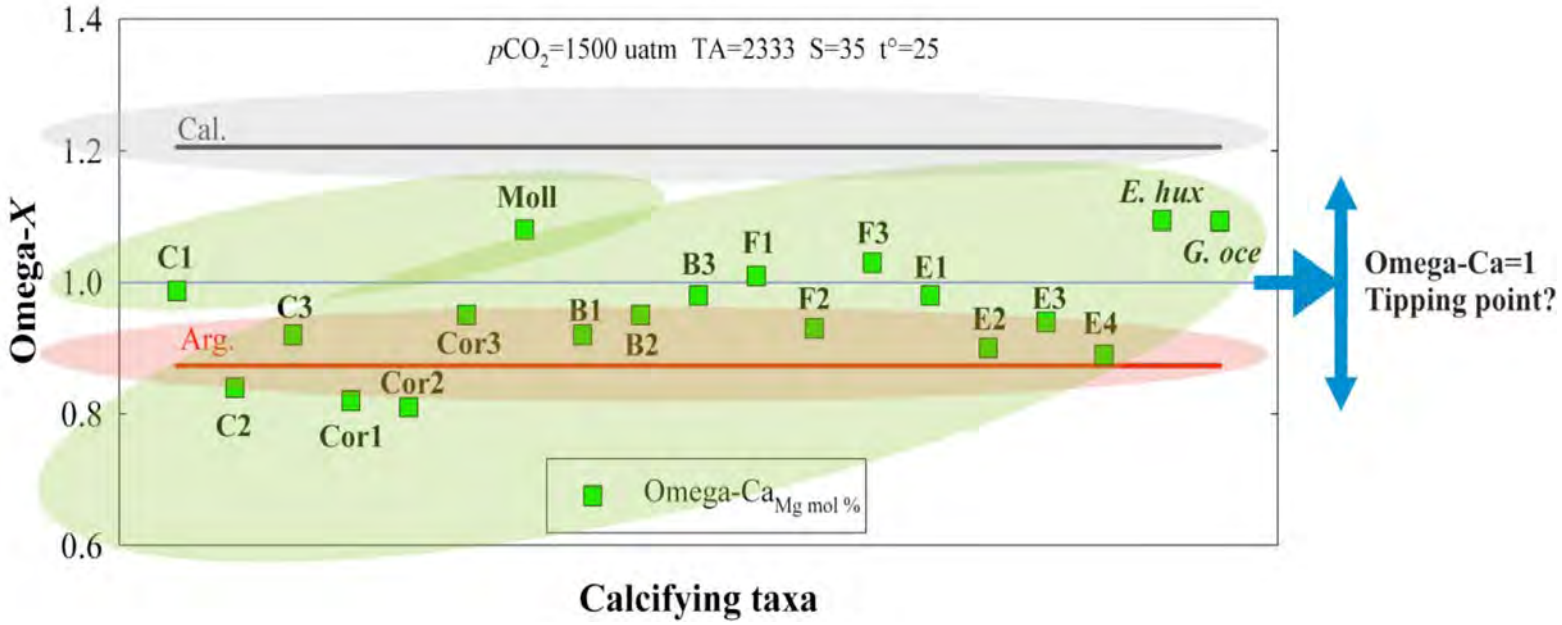

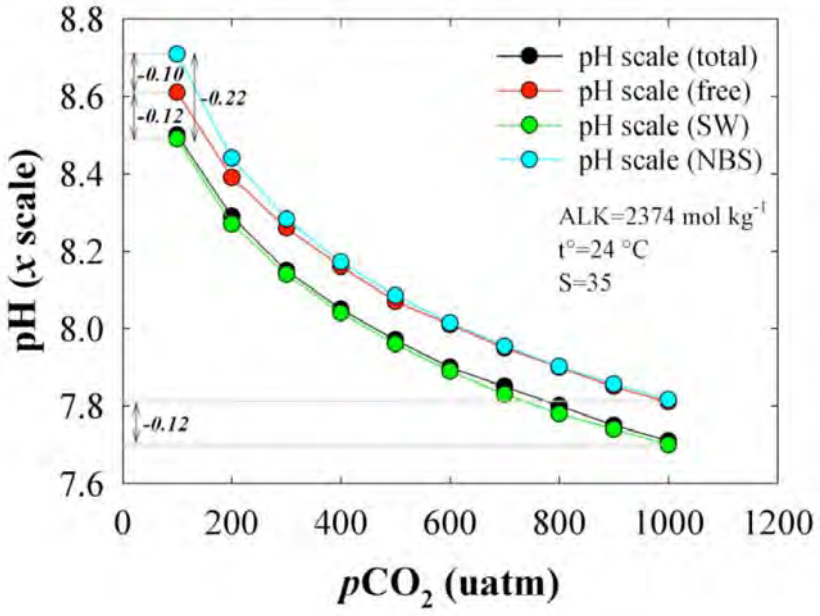

- Need to report the pH scale to avoid confounding tipping points
- Saturation states need to be more clearly defined and developed within the concept of a species depending on the Mg content
- Avoid possible confounding tipping points at Omega=1
- We need to re-assess if this is relevant for model outputs

Technical recommendation

• Determine co-variation of calcium and magnesium incorporation into biomineral in response to environmental conditions (effect of nutrient availability, diurnal cycles (sampling time), temperature, Mg:Ca ratios).

Future needs

• Characterization of Mg contribution to the biomineral in calcifiers

• Develop new technologies to ‘clean’ chlorophyll fraction and potential cellular contributors to Mg other than the biomineral fraction

Measuring calcification in the field

Instructor: Chris Langdon

1. Planktonic organisms and systems
    a. ^{45}Ca or ^{14}C incorporation into the biogenic $CaCO_3$
    b. Increase in shell size or mass over time
    c. Instantaneous growth rate time standing stock
    d. Changes in concentration of particulate Ca or inorganic carbon PIC over time
    e. Sediment trap flux of $CaCO_3$
2. Benthic organisms and systems
    a. ^{45}Ca or ^{14}C incorporation into the biogenic $CaCO_3$
    b. Buoyant weight increase in skeletal mass
    c. Coral density banding (linear growth between annual bands times skeletal density)
    d. Change in skeleton and shell dimension or mass
    e. Staining skeleton or shell using Alizarin Red or Calcein followed weeks or months later by sacrificing the organism and measuring the increment of growth
    f. Calcimass technique - the product of the calcium carbonate mass of the organism times the turnover rate of the organism
    g. Enclosing the organism or portion of a community and measuring the calcification and photosynthesis from change in TA, DIC, O_2 or the incorporation of ^{45}C or ^{14}C into the skeleton
        i. Small enclosures of 1-5 liters
        ii. Enclosures of several cubic meters such as the Monaco coral mesoocosm, the Bergen plankton mesocosms, HIMB flume and the USGS SHARQ that are sufficient to enclose a small natural community under conditions that permit control of the carbonate chemistry and precise measurements of community calcification and photosynthesis
        iii. An enclosure of several thousand cubic meters that permits long term experimentation and allows organisms to complete their life cycle
    h. Stagnant water method – calcification computed from change in TA over a portion of a reef while the water is at slack tide
    i. Eulerian method – calcification computed from difference in TA of water flowing across a portion of a reef measured before and after the water flows over the reef
    j. Lagrangian method – calcification computed from the change in TA of a water mass as it flows over a portion of a reef
    k. TA depletion/residence time method – draw down in salinity normalized TA divided by the residence time of the water mass over the reef

    l. Sedimentological or geological thickness of a carbonate sediment or coral reef framework divided by the time – measure of accumulation or accretion
3. Scaling up to regional and global estimates
    a. Remote sensing techniques to characterize water types, bloom occurrences and dimensions
    b. Remote sensing techniques to characterize different bottom communities
4. Other important measurements
    a. Light
    b. Temperature
    c. Water motion
    d. Food availability
    e. Grazing
    f. Affects of pH and changing carbonate chemistry on other biological processes
        i. Sperm motility
        ii. Fertilization
        iii. Larval development
        iv. Larval settlement
        v. Growth rate of early life history stages
        vi. Photosynthesis
        vii. Respiration

Sunday, November 8, 2009
Monitoring coral and larval mollusk experiments

Morning Free

Afternoon

Time	Activity
1:15 pm	Shuttle MBL to ESL
1:30 pm	**Lab**. T4 sampling for coral and monitor pH of mollusks (3 person subgroups of Groups G, H, I), end coral exp't (Holcomb, ESL 10)
3:30 pm	Shuttle ESL to MBL
3:45 pm	Break
5:00 pm	Dinner (Swope Cafeteria, MBL)

OCB OCEAN ACIDIFICATION SHORT COURSE

OUTLINE FOR LARVAL MOLLUSC OCEAN ACIDIFICATION EXPERIMENTS

Instructors: Anne Cohen, Dan McCorkle

TAs: Meredith White, Kathryn Rose

Please refer to full protocol under Thursday November 5 tab.

OCB OCEAN ACIDIFICATION SHORT COURSE

CORAL CALCIFICATION EXPERIMENT

Michael Holcomb (WHOI)

Please refer to full protocol under Friday November 6 tab.

Monday, November 9, 2009
Larval mollusk harvesting, lectures, MBL Marine Resources Center tour

Morning

<table>
<tr><th>Time</th><th>Group G</th><th>Group H</th><th>Group I</th></tr>
<tr><td>8:15 am</td><td>Shuttle MBL to ESL</td><td rowspan="2">Break</td><td rowspan="4">Break</td></tr>
<tr><td>8:30 am</td><td rowspan="3">Lab. Harvest mollusks (Cohen/Rose, ESL 10)</td></tr>
<tr><td>9:15 am</td><td>Shuttle MBL to ESL</td></tr>
<tr><td>9:30 am</td><td rowspan="4">Lab. Harvest mollusks (Cohen/Rose, ESL 10)</td></tr>
<tr><td>10:00 am</td><td>Shuttle ESL to MBL</td><td></td></tr>
<tr><td>10:15 am</td><td rowspan="5">Break</td><td>Shuttle MBL to ESL</td></tr>
<tr><td>10:30 am</td><td rowspan="3">Lab. Harvest mollusks (Cohen/Rose, ESL 10)</td></tr>
<tr><td>11:00 am</td><td>Shuttle ESL to MBL</td></tr>
<tr><td>11:15 am</td><td rowspan="2">Break</td></tr>
<tr><td>12:00 pm</td><td>Shuttle ESL to MBL</td></tr>
<tr><td>12:15 pm</td><td colspan="3">Lunch (Swope Cafeteria, MBL)</td></tr>
</table>

Afternoon

Time	Activity
1:30-3:00 pm	**Lecture/Demo/Hands-on**. Ocean Data View (Schlitzer, MBL Speck Auditorium)
3:00 pm	Shuttle MBL to Watson (for Tour 2 at 3:15 pm)
3:15-4:00 pm	**Tour 1*** MBL Marine Resources Center (Ed Enos, MRC)
3:15-4:15 pm	**Tour 2.** Algal Culturing Lab (John Waterbury, WHOI Watson 102)
4:00-4:15 pm	Shuttle MBL to Watson (for Tour 2 at 4:15 pm)
4:15-4:30 pm	Shuttle Watson to MBL
4:15-5:15 pm	**Tour 2.** Algal Culturing Lab (John Waterbury, WHOI Watson 102)
5:15-5:30 pm	Shuttle Watson to MBL
5:30 pm	Dinner (Swope Cafeteria, MBL)

Notes:
***Tour 1 will only be conducted once, so if you would like to do both tours, you will need to catch the 4:00 pm shuttle to WHOI and do the 4:15 pm tour of the Waterbury lab.**

OCB OCEAN ACIDIFICATION SHORT COURSE

OUTLINE FOR LARVAL MOLLUSC OCEAN ACIDIFICATION EXPERIMENTS

Instructors: Anne Cohen, Dan McCorkle

TAs: Meredith White, Kathryn Rose

Please refer to full protocol under Thursday November 5 tab.

OCB Ocean Acidification Course
Ocean Data View lecture
Instructor: Reiner Schlitzer

This course shows how to use the Ocean Data View software for the analysis and display of GLODAP, CARINA or participant's own carbon data. In addition to original, measured quantities, participants will calculate and visualize derived parameters, such as the saturation states of calcite and aragonite, and the concentrations of individual carbon species. Most of the available time will be devoted to working on exercises.

In preparation for this, course participants should download and install on their laptop computers the latest version of the Ocean Data View software (v4.2.1), as well as the CARINA and GLODAP ODV data collections:

1. Software

Download ODV 4.2.1 from
http://odv.awi.de/en/software/download/. Choose the version for your computer platform (Windows, Mac OS X or Linux) and follow the installation instructions. Registration is required to get access to the download site.

2. Data

Download the CARINA data from
http://odv.awi.de/en/data/ocean/carina_bottle_data/

Download the GLODAP data from
http://odv.awi.de/en/data/ocean/glodap_bottle_data/

Then follow the installation instructions.

Participants new to ODV are strongly encouraged to try running ODV on the CARINA and GLODAP datasets before they come to the course.

The getting started document
(http://odv.awi.de/fileadmin/user_upload/odv/misc/GettingStarted.pdf)

ODV User's Guide
(http://odv.awi.de/fileadmin/user_upload/odv/misc/odv4Guide.pdf)

should help get you acquainted with the software. Context-sensitive help is available from inside ODV.

Participants are also strongly encouraged to bring their own data. Practicing the import of new data into ODV is part of the course.

Tuesday, November 10, 2009
Lectures, cellular pH regulation experiment, and larval microscopy

Morning

Time	Activity
8:30 am	**Lecture**. Biogeochemical modeling introduction (Doney) MBL Speck Auditorium
10:00 am	Coffee Break
10:30 am	**Lecture.** Physiology (Seibel) MBL Speck Auditorium
12:00 pm	Lunch (Swope Cafeteria, MBL)

Afternoon

<table>
<tr><th>Time</th><th>Group G</th><th>Group H</th><th>Group I</th></tr>
<tr><td>1:15 pm</td><td>Shuttle MBL to Clark</td><td rowspan="2">Break</td><td>Shuttle MBL to ESL</td></tr>
<tr><td>1:30 pm</td><td rowspan="3">Lab. Larval mollusk microscopy (Cohen/Rose, Clark 120)</td><td rowspan="3">Shuttle MBL to ESL</td><td rowspan="3">Lab. Set up and begin cellular pH experiment (Seibel, ESL 10)</td></tr>
<tr><td>2:15 pm</td></tr>
<tr><td>2:30 pm</td><td rowspan="4">Lab. Set up and begin cellular pH experiment (Seibel, ESL 10)</td><td>Walk ESL to Clark</td></tr>
<tr><td>2:45 pm</td><td rowspan="3">Break/Walk Clark to ESL</td><td rowspan="3">Lab. Larval mollusk microscopy (Cohen/Rose, Clark 120)</td></tr>
<tr><td>3:00 pm</td></tr>
<tr><td>3:30 pm</td><td rowspan="3">Lab. Set up and begin cellular pH experiment (Seibel, ESL 10)</td><td>Walk ESL to Clark</td></tr>
<tr><td>4:00 pm</td><td rowspan="3">Lab. Larval mollusk microscopy (Cohen/Rose, Clark 120)</td><td>Shuttle Clark to MBL</td></tr>
<tr><td>4:15 pm</td><td rowspan="3">Break</td></tr>
<tr><td>4:30 pm</td><td>Shuttle ESL to MBL</td></tr>
<tr><td>4:45 pm</td><td rowspan="2">Break</td><td rowspan="2">Shuttle Clark to MBL</td></tr>
<tr><td>5:15 pm</td></tr>
<tr><td>5:30 pm</td><td colspan="3">Dinner (Swope Cafeteria, MBL)</td></tr>
</table>

Chapter 9

Global Ocean Carbon Cycle Modeling

Scott C. Doney · Keith Lindsay · J. Keith Moore

9.1 Introduction

One of the central objectives of the Joint Global Ocean Flux Study (JGOFS) is to use data from the extensive field effort to improve and evaluate numerical ocean carbon cycle models. Substantial improvements are required in the current suite of numerical models if we are to understand better the present ocean biogeochemical state, hindcast historical and paleoclimate variability, and predict potential future responses to anthropogenic perturbations. Significant progress has been made in this regard, and even greater strides are expected over the next decade as the synthesis of the JGOFS data sets are completed and disseminated to the scientific community. The goals of this chapter are to outline the role of modeling in ocean carbon cycle research, review the status of basin to global-scale modeling, and highlight major problems, challenges, and future directions.

Marine biogeochemical models are quite diverse, covering a wide range of complexities and applications from simple box models to global 4-D (space and time) coupled physical-biogeochemical simulations, and from strict research tools to climate change projections with direct societal implications. Model development and usage are strongly shaped by the motivating scientific or policy problems as well as the dynamics and time/space scales considered. A common theme, however, is that models allow us to ask questions about the ocean we could not address using data alone. In particular, models help researchers quantify the interactions among multiple processes, synthesize diverse observations, test hypotheses, extrapolate across time and space scales, and predict future behavior.

A well posed model encapsulates our understanding of the ocean in a mathematically consistent form. Many, though not all, models can be cast in general form as a coupled set of time-dependent advection, diffusion, reaction equations:

$$\frac{\partial X}{\partial t} + \vec{u}\nabla X - \nabla(K\nabla X) = \text{sources/sinks} \qquad (9.1)$$

where X refers to a set of prognostic or predicted variables (e.g., temperature, phytoplankton biomass, dissolved inorganic carbon). The second and third terms on the left hand side of the equation describe the physical processes of advection and mixing, respectively. All of the chemical and biological interactions are subsumed into the final source/sink term(s) on the right hand side, which often involve complex interactions among a number of prognostic variables. In addition, the model may require external boundary conditions (e.g., solar radiation, wind stress, dust deposition) and, for time varying problems, initial conditions. The model equations are then solved numerically by integrating forward in time for X.

Numerical models cannot capture all of the complexity of the real world. Part of the art of modeling is to abstract the essence of a particular problem, balancing model complexity with insight. Many processes must be either parameterized in a simple fashion or neglected altogether. For example, the biophysical details of photosynthesis, though quite well known, may not necessarily be crucial and certainly not sufficient for simulating the seasonal bloom in the North Atlantic. On the other hand, a number of key processes (e.g., phytoplankton mortality, the controls on community structure) are not well characterized and are often used as model tuning parameters.

As opposed to much of ocean physics, fundamental relationships either are not known or may not exist at all for much of marine biogeochemistry. Therefore, ocean biogeochemical modeling is inherently data driven. The JGOFS field data are invaluable in this regard, providing the basis for highlighting model deficiencies, developing improved parameterizations, and evaluating overall model performance. The desire for increasing model realism and sophistication must be tempered by the realization that models can quickly outstrip the ability to parameterize the appropriate processes or evaluate the overall simulation. Inverse methods and data assimilation will certainly help in this regard, but the true benefits will only be gained when the underlying models rest on a sound, mechanistic basis.

Broadly speaking, much of current ocean carbon cycle modeling can be condensed into a few overarching scientific questions that match well with the other individual chapters of this book. These include: What are

the physical and biological controls on primary, new and export production? What are the roles of multiple limiting nutrients, mesoscale variability and trophic structure? How are organic and inorganic carbon transported, transformed and remineralized below the surface layer? How much anthropogenic carbon does the ocean take up and where? How does ocean biogeochemistry respond to climate variability and are there feedbacks on climate change? Ocean carbon modeling is a diverse and growing field and can not be covered comprehensively in a single chapter. Rather, we present an overview of the current state and major issues involving ocean biogeochemical and ecosystem modeling drawing mostly on specific examples from the NCAR modeling program.

Historically, global ocean biological and chemical modeling has evolved along three related, though often distinct, paths. First, a number of early efforts were directed toward improving oceanic anthropogenic carbon uptake estimates, building on simple box models and coarse resolution ocean physical general circulation models (GCMs). Transient tracer simulations (radiocarbon, tritium, chlorofluorocarbons) developed in conjunction as a way to assess model physical circulation and mixing. Second, biogeochemical carbon cycle models, while often relying on the same physical model frameworks, were developed to improve our understanding of the dynamics controlling large-scale biogeochemical fields (e.g., surface pCO_2, subsurface nutrient, oxygen and dissolved inorganic carbon distributions) and their responses to climate variability and secular change (e.g., glacial-interglacial transition and greenhouse warming). The treatment of biological processes in this class of models has been rather rudimentary in most cases. Third, marine ecosystem models have been focused much more on the details of biological interactions within the upper ocean, tracking the controls on upper ocean primary and export production as well as the flow of mass and energy though the marine food web. These models often are created for specific biogeographical regions commonly based on local surface or 1-D time-series data sets. More recently, ecosystem models have been extended to basin and global scale. One of the most important trends in the field is the unification of these three approaches, leading ultimately to a coherent modeling framework linking ocean physics, biology and chemistry over a range of time and space scales.

9.2 Anthropogenic Carbon Uptake, Transient Tracers, and Physics

An initial and ongoing focus of ocean biogeochemical modeling research is to quantify the rate at which the ocean takes up transient tracers and excess anthropogenic CO_2. The water column and upper few meters of marine sediments contain the largest mobile, natural reservoir of carbon on time-scales of 10^2 to 10^5 years. With about 50 times more carbon than that stored in the atmosphere (Fig. 9.1) (Sarmiento and Sundquist

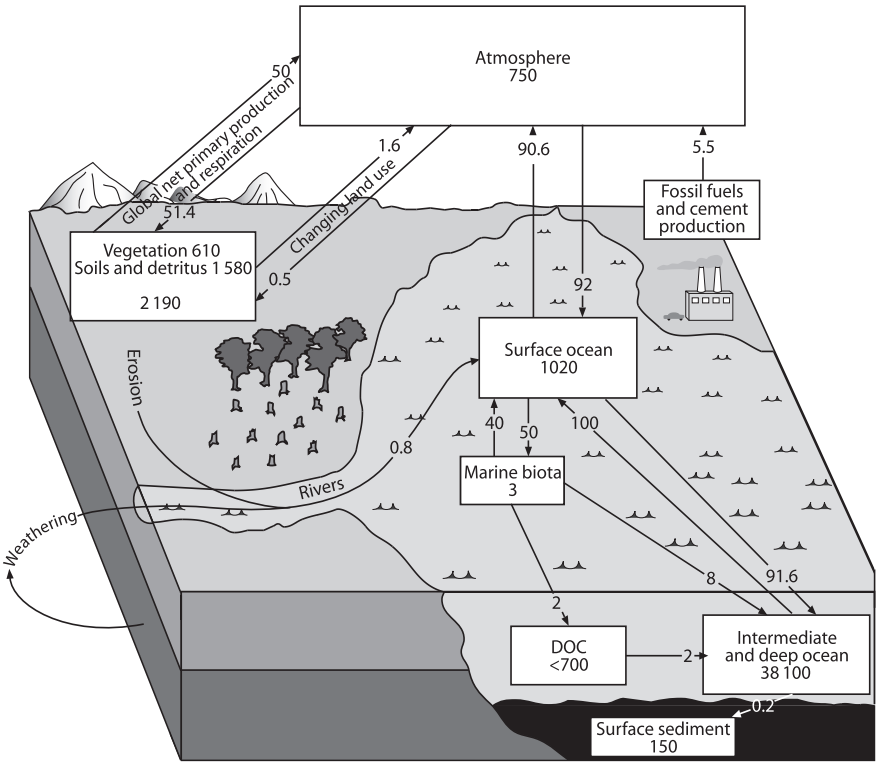

Fig. 9.1.
Schematic of present global carbon cycle budget. The budget includes the natural background cycle as well as anthropogenic perturbations. Reservoir sizes are given in units of Pg C (1 Pg equals 10^{15} g), while fluxes are given in Pg C yr^{-1} (adapted from Schimel et al. (1995) and US CCSP (1999))

1992; Siegenthaler and Sarmiento 1993), the ocean will serve as the ultimate sink for about 90% of human fossil fuel emissions (Archer et al. 1998). Anthropogenic carbon uptake is often computed as a passive perturbation to the natural dissolved inorganic carbon (DIC) field (Sarmiento et al. 1992), a fairly reasonable assumption for the pre-industrial to the present time period. Under these conditions (i.e., fixed circulation and background biogeochemical cycles), net carbon uptake is simply a matter of ocean physics, primarily determined by the ventilation time-scales exposing deep water to the surface and, to a much lesser degree, air-sea gas exchange. The invasion into the ocean of transient tracers such as radiocarbon, tritium, and the chlorofluorocarbons provides a direct, often quite dramatic illustration of ocean ventilation and is commonly used either to calibrate/evaluate ocean physical models or as proxies for anthropogenic CO_2 uptake.

Early attempts to calculate ocean CO_2 uptake in the 1970s and 1980s relied heavily on ocean box and 1-D advection diffusion models of varying complexity (Oeschger et al. 1975; Siegenthaler and Oeschger 1978; Siegenthaler and Joos 1992). This class of models represents, in a fairly crude, schematic form, the basics of ocean thermocline ventilation and thermohaline circulation. The crucial model advection and mixing parameters are typically set by calibrating simulated transient tracer distributions (tritium, natural and bomb radiocarbon) to observations. More recently, such models have mostly been supplanted by full 3-D general circulation models for the anthropogenic CO_2 question. But because they are simple to construct (and interpret) and computationally inexpensive, box models and a related derivative the 2-D, zonally averaged basin model (Stocker et al. 1994) continue to be used today for a number of applications requiring long temporal integrations including paleoceanography (Toggweiler 1999; Stephens and Keeling 2000) and climate change (Joos et al. 1999). Some caution is advised, however, as recent studies (Broecker et al. 1999; Archer et al. 2000) clearly demonstrate that box model predictions for key carbon cycle attributes can differ considerably from the corresponding GCM results.

Ocean general circulation model studies of anthropogenic carbon uptake date back to the work of Maier-Reimer and Hasselmann (1987) and Sarmiento et al. (1992), and the number of model estimates (and modeling groups) for CO_2 uptake has increased significantly over the 1990s. For example, more than a dozen international groups are participating in the IGBP/GAIM Ocean Carbon Model Intercomparison Project (OCMIP; *http://www.ipsl.jussieu.fr/OCMIP/*). These numerical experiments are closely tied to and greatly benefit from efforts to evaluate ocean GCMs using hydrographic (Large et al. 1997; Gent et al. 1998) and transient tracer data (Toggweiler et al. 1989a,b; Maier-Reimer 1993; England 1995; Heinze et al. 1998; England and Maier-Reimer 2001). More recently, empirically based methods have been developed for estimating anthropogenic carbon distributions directly from ocean carbon and hydrographic observations (Gruber et al. 1996; Gruber 1998; Wanninkhof et al. 1999; Watson this volume). With the completion of the high quality, JGOFS/WOCE global CO_2 survey (Wallace 1995, 2001), a baseline can be constructed for the world ocean for the pre-industrial DIC field and the anthropogenic carbon perturbation as of the mid-1990s, an invaluable measure for testing numerical model skill and monitoring future evolution.

As an example of this class of carbon uptake simulations, the large-scale patterns of anthropogenic CO_2 air-sea flux and integrated water column inventory from the NCAR CSM Ocean Model (Large et al. 1997; Gent et al. 1998) are shown in Fig. 9.2. The regions of highest anthropogenic carbon uptake – equatorial upwelling bands, western boundary currents, high latitude intermediate and deep water formation regions – are associated with the transport of older subsurface waters to the air-sea interface (Doney 1999). Although the maximum specific uptake rates are found in the subpolar North Atlantic, the area is relatively small, and the integrated uptake of the Southern Ocean and Equatorial band are larger. The anthropogenic DIC water column anomaly is stored primarily in the thermocline and intermediate waters of the subtropical convergence zones and the lower limb of the North Atlantic thermohaline circulation as illustrated by the second panel of Fig. 9.2 and Fig. 9.3, a depth vs. latitude comparison of field data derived and model simulated anthropogenic DIC. The two meridional sections follow the thermohaline overturning circulation from the northern North Atlantic to the Southern Ocean and then back to the northern North Pacific. The model simulates in a reasonable fashion the patterns from empirical estimates except perhaps in the subpolar and intermediate depth North Atlantic, which may reflect problems with the model formation of North Atlantic Deep Water (Large et al. 1997).

At present, most numerical models predict a similar net uptake of anthropogenic CO_2 for the 1990s of approximately 2 Pg C yr^{-1} (1 Pg C equals 10^{15} g C) (Orr et al. 2001), a result supported by atmospheric biogeochemical monitoring and a variety of other techniques (Schimel et al. 1995; Keeling et al. 1996; Rayner et al. 1999). The models, however, show considerable regional differences, particularly in the Southern Ocean (Orr et al. 2001). The agreement of the NCAR model with empirical basin inventories is quite good (Table 9.1), suggesting that at least at this scale the NCAR model transport is relatively skillful.

While based on a more complete description of ocean physics, the coarse resolution, global GCMs used for these carbon studies still require significant parameterization of sub-gridscale phenomenon such as deep wa-

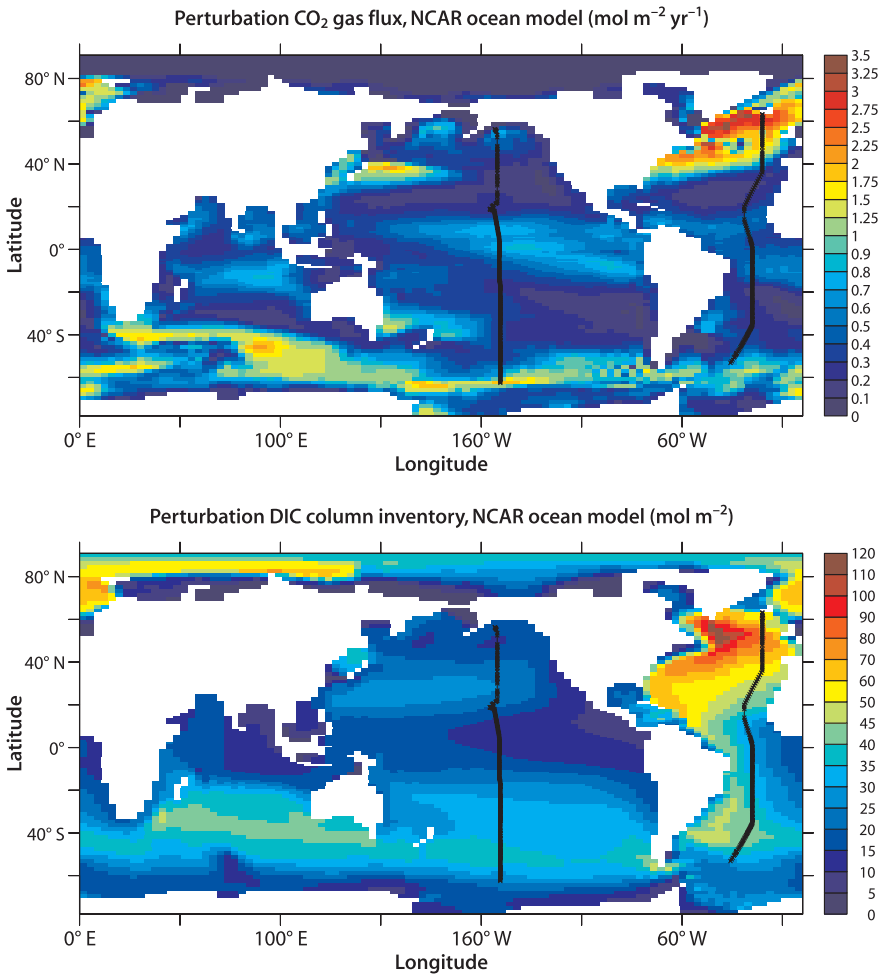

Fig. 9.2.
Spatial distributions of model simulated ocean anthropogenic (perturbation) carbon. Simulated fields are shown for (*top*) air-sea flux (mol C m^{-2} yr^{-1}) and (*bottom*) water column inventory (mol C m^{-2}) for 1990 from the NCAR CSM Ocean Model. The two *lines* indicate the Atlantic and Pacific transects used for the horizontal sections in Fig. 9.3 and 9.7

ter formation, surface and bottom boundary layer physics, and mixing rates along and across density surfaces (isopycnal and diapycnal diffusion). The ongoing OCMIP effort is comparing about a dozen current generation global ocean carbon models among themselves and against ocean observations. Completed analysis of OCMIP Phase 1 and early results from Phase 2 demonstrate significant differences among the models in the physical circulation and simulated chlorofluorocarbon (Dutay et al. 2001), radiocarbon, and current and projected future anthropogenic CO_2 fields (Orr et al. 2001). The largest model-model differences and model-data discrepancies are found in the Southern Ocean, reflecting differences in the relative strength and spatial patterns of Antarctic Mode (Intermediate) Waters and Antarctic Bottom Water (AABW) (Dutay et al. 2001). Models using horizontal mixing rather than an isopycnal scheme (Gent and McWilliams 1990) tend to overestimate convective mixing in the region of the Antarctic Circumpolar Current (Danabasoglu et al. 1994). Not surprisingly, the formation of AABW appears quite sensitive to the under-ice, surface freshwater fluxes in the deep water formation zones (Doney and Hecht 2002); ocean models without active sea ice components appear to have weak AABW formation while many of the interactive ocean-sea ice models tend to have way too much bottom water production.

These known deficiencies in ocean GCM physics hamper quantitative model-data comparisons of biogeochemical and ecosystem dynamical models as well. Uncertainties in the physical flow field, particularly vertical velocity (Harrison 1996), mixing and convection, affect a variety of biogeochemical processes – nutrient supply, boundary layer stability and mean light levels, downward transport of transient tracers, anthropogenic carbon and semi-labile dissolved organic matter – and thus obscure the validation of tracer and biogeochemical components. The refinement of global ocean GCMs is an on-going process, and substantial progress will likely arise from improved treatments of surface boundary forcing and subgrid-scale physics (McWilliams 1996; Haidvogel and Beckmann 1999; Griffes et al. 2000). Transient tracers and biogeochemistry can contribute in this regard by providing additional, often orthogonal, constraints on model performance to traditional physical measures (Gnanadesikan 1999; Gnanadesikan and

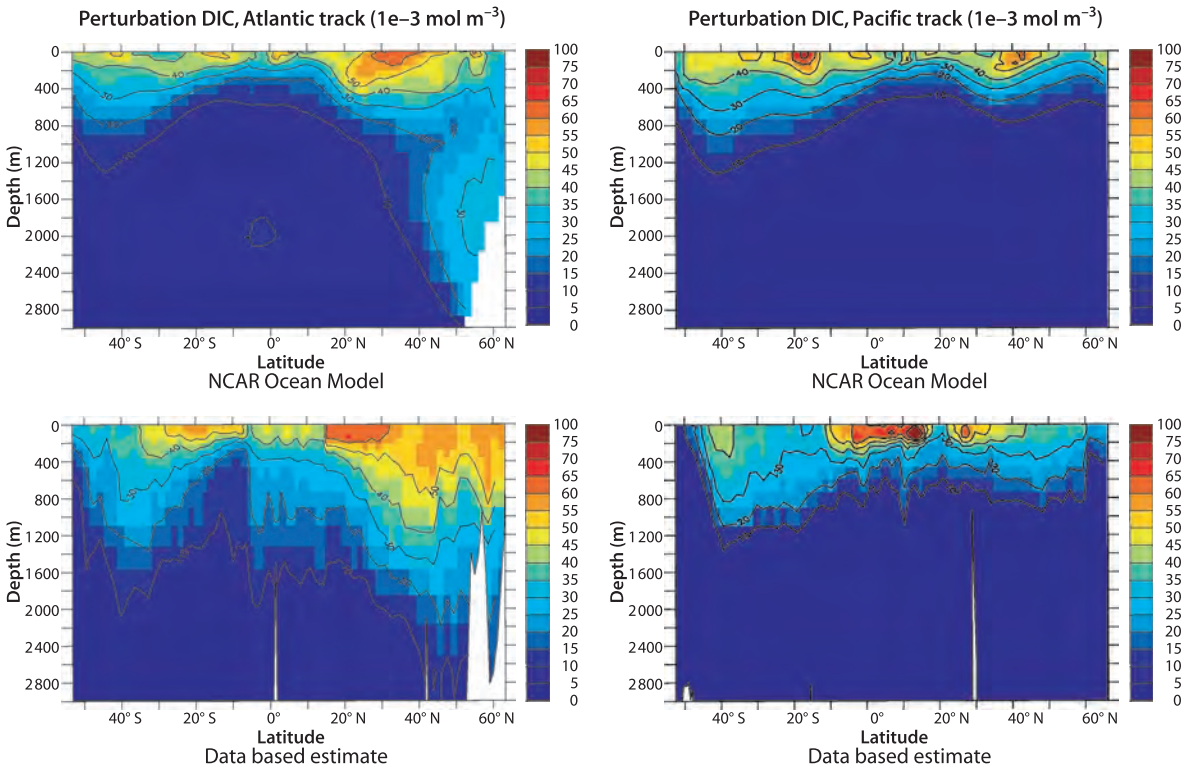

Fig. 9.3. Depth vs. latitude contour plots of anthropogenic CO_2 (mmol C m^{-3}). The panels show the simulated results from the NCAR CSM ocean model and the empirical, observation based estimates (N. Gruber 2000, pers. comm.) each for an Atlantic and Pacific section along the main path of the thermohaline circulation (see Fig. 9.2). Note that depth is limited to 3000 m

Table 9.1.
Estimated basin inventories of anthropogenic DIC (Pg C)

Ocean	NCAR CSM ocean model	Data-based C* estimates	Data reference
Indian	22.1	20 ±3	Sabine et al. (1999)
Atlantic	39.5	40 ±6	Gruber (1998)
Pacific	46.7	46 ±5?	Feely and Sabine (pers. comm.)
Total	108.4	106 ±8?	Feely and Sabine (pers. comm.)

Toggweiler 1999). The incorporation of active biology tests new facets of the physical solutions, especially the surface air-sea fluxes and boundary layer dynamics (Large et al. 1994; Doney 1996; Doney et al. 1998) and their interaction with the interior mesoscale field (Gent and McWilliams 1990).

The desired horizontal resolution for ocean carbon cycle models is often a contentious issue, involving tradeoffs between model fidelity/realism and computational constraints. Most global climate models used for long integrations (i.e., the multi-decade to centennial and longer timescales often of interest to the ocean carbon community) have relatively coarse horizontal resolution of one to a few degrees and thus do not explicitly represent key processes such as deep-water overflows and mesoscale eddies. Increasing the resolution of this class of models is an important objective but is not a general panacea for a number of reasons. First, computational costs increase dramatically; for every factor of two increase in horizontal resolution, the integration time goes up by roughly a factor of 8. Basin-scale, eddy-resolving biological simulations at such resolution are only now becoming computationally feasible and only for short integrations. Second, very high resolution on the order of 1/10° appears to be required to correctly capture the dynamics (not just presence) of the mesoscale eddies (e.g., eddy kinetic energy; eddy-mean flow interactions) (Smith et al. 2000), and some numerical errors persist even as resolution is decreased (Roberts and Marshall 1998). One solution is to incorporate the effect of the unresolved processes using more sophisticated sub-grid scale parameterizations. For example, the Gent and McWilliams (1990) isopycnal mixing scheme tends to greatly reduce the resolution dependence and improves, in both eddy permitting and non-eddy resolving solutions, the simulated meridional heat transport, an important physical diagnostic likely relevant for nutrients and carbon as well as heat.

Another important, and often overlooked, numerical issue is the tracer advection scheme (Haidvogel and Beckmann 1999; Griffes et al. 2000). The centered difference schemes used in most 3-D ocean general circulation models, while conserving first and second moments of the tracer distribution, tend to produce dispersive errors (e.g., under and overshoots, ripples, nonpositive definite tracer fields), which can be particularly troubling for biogeochemical and biological properties that have sharp vertical gradients (Oschlies and Garçon 1999). Oschlies (2000), for example, demonstrates that the common problem of equatorial nutrient trapping (Najjar et al. 1992) is primarily numerical and can be solved by increasing vertical resolution and/or implementing more sophisticated advection methods. The wide range of alternative advection schemes (e.g., third order upwinding, flux corrected transport) mostly use some amount of diffusion (only first order accurate) to suppress the dispersion errors. The main differences in the methods are the magnitude of the dissipation, whether it is applied uniformly or selectively in space and time, and the exact numerical implementation (Webb et al. 1998; Hecht et al. 2000).

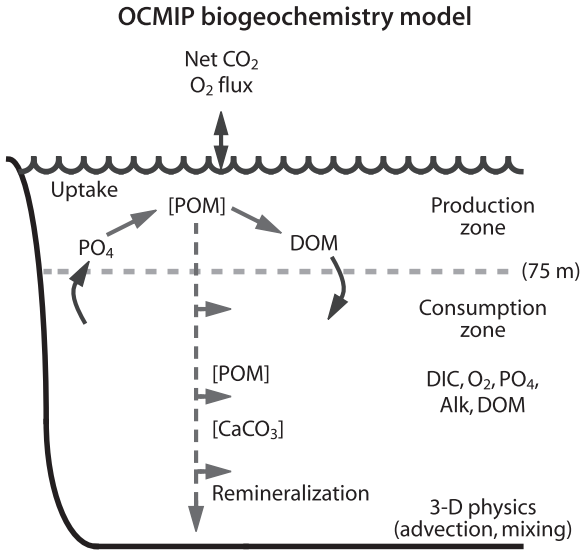

Fig. 9.4. Schematic of OCMIP global ocean carbon biogeochemical model. For more details see text and (*http://www.ipsl.jussieu.fr/OCMIP*)

9.3 Global Biogeochemical Cycles

The net anthropogenic ocean carbon uptake occurs on top of the large background DIC inventory and ocean gradients, air-sea fluxes, biological transformations, and internal transports driven by the natural carbon cycle (Fig. 9.1). Beginning with a series of global biogeochemical simulations in the early 1990s (Bacastow and Maier-Reimer 1990; Najjar et al. 1992; Maier-Reimer 1993), numerical models have played key roles in estimating basin and global-scale patterns and rates of biogeochemical processes (e.g., export production, remineralization). The primary measure for evaluating such models has been the large-scale fields of inorganic nutrients, oxygen, and DIC (Levitus et al. 1993; Conkright et al. 1998; Wallace 2001). As more robust global estimates of biogeochemical rates (e.g., new production, Laws et al. 2000) are developed from the JGOFS field data and satellite remote sensing, they too are being included in model-data comparisons (Gnanadesikan et al. 2001). Numerical biogeochemical models are also valuable tools for exploring specific hypotheses (e.g., iron fertilization; Joos et al. 1991), estimating interannual variability (Le Quéré et al. 2000), and projecting future responses to climate change (Sarmiento et al. 1998).

With a few exceptions (Six and Maier-Reimer 1996), the treatment of biology in these global biogeochemical models to date has been rather rudimentary. This is exhibited in Fig. 9.4 by a schematic of the biotic carbon model from OCMIP Phase 2. The OCMIP model consists of five prognostic variables, a limiting nutrient PO_4, dissolved inorganic carbon DIC, total alkalinity TALK, semi-labile dissolved organic matter DOM, and dissolved oxygen. Upper ocean production (0–75 m) is calculated by restoring excess model PO_4 toward a monthly nutrient climatology (Louanchi and Najjar 2000). The production is split with 1/3 going into rapidly sinking particles and the remainder into the DOM pool. The sinking particles are remineralized in the subsurface consumption zone (>75 m) using an empirical particle flux depth curve similar in form (though with different numerical parameters; Yamanaka and Tajika 1996) to that found by Martin et al. (1987) from sediment trap data. The DOM decays back to phosphate and DIC using first order kinetics with a 6 month time-scale throughout the water column. Most of the DOM is remineralized within the surface production zone but a fraction is mixed or subducted downward prior to decay and thus contributes to overall export production. Surface $CaCO_3$ production is set at a uniform 7% of particulate organic matter production, and all of the $CaCO_3$ is export as sinking particles which are remineralized with a deeper length-scale relative to organic matter. The relative uptake and release rates of PO_4, DIC, and O_2 from the organic pools are set by fixed, so-called Redfield elemental ratios, and CO_2 and O_2 are exchanged with the atmosphere via surface air-sea gas fluxes computed using the quadratic wind-speed gas exchange relationship of Wanninkhof (1992).

Despite its simplicity, the OCMIP model captures to a degree many of the large-scale ocean biogeochemical

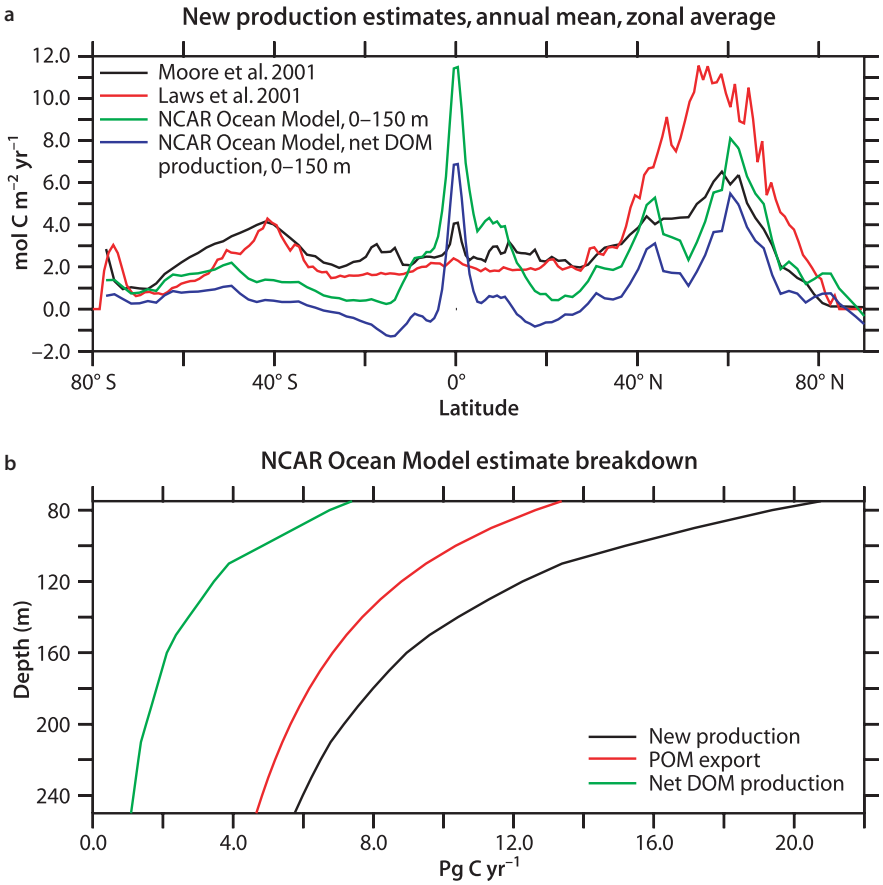

Fig. 9.5.
Annual averaged new production estimates. In the *upper panel* (**a**) the NCAR model total production (particle plus net semi-labile DOM creation) and net DOM creation computed to 150 m are compared against recent new/export production estimates from Laws et al. (2000) (satellite primary production and ecosystem model based *f*-ratios) and Moore et al. (2002a) (global ecosystem model including DOM loss from downwelling and seasonal mixed layer shoaling). In the *lower panel* (**b**), the NCAR model global integral total, particle and DOM new production rates are shown as a function of the bottom limit of the depth integration

patterns found in nature. The model, zonally averaged, total new production (particle export plus net DOM production) is compared in Fig. 9.5a with recent new/export production estimates from Laws et al. (2000) (satellite primary production and ecosystem model based *f*-ratios) and Moore et al. (2002a,b) (global ecosystem model; see below for more details). The NCAR model estimate has been recomputed at 150 m rather than 75 m as specified in the OCMIP formulation to be more consistent with data based and the other model estimates. The global integrated new production estimates from the GCM (9.6 Pg C at 150 m), satellite diagnostic calculation (12.6 Pg C), and ecosystem model (11.9 Pg C) are comparable but with significant regional differences. The Moore et al. and Laws et al. curves have similar patterns with high values in the Northern Hemisphere temperate and subpolar latitudes, low levels in the tropics and subtropics and slightly elevated rates in the Southern Ocean around 40° S. The GCM results are considerably larger in the equatorial upwelling band and lower in the subtropics, reflecting in part net production, horizontal export and subsequent remineralization of organic matter. The Laws et al. (2000) estimates are based on two components: satellite derived primary production rates from CZCS ocean color data and the Behrenfeld and Falkowski (1997) algorithm, and a functional relationship of *f*-ratio to temperature and primary production from an ecosystem model. As discussed by Gnanadesikan et al. (2001), the Laws et al. (2000) values in the equatorial region are sensitive to assumptions about the maximum growth rate as a function of temperature (and implicitly nutrients), and alternative formulations can give higher values.

A significant fraction of the GCM export production at mid- to high latitudes is driven by net DOM production followed by downward transport (global integral at 150 m of 2.4 Pg C) (Fig. 9.5a and 9.5b). This has been observed in the field at a number of locations (Carlson et al. 1994; Hansell and Carlson 1998), and is thought to be an important mechanism north of the Antarctic Polar Front supporting a significant fraction of the organic matter remineralization in the upper thermocline (Doval and Hansell 2000). Because the semi-labile DOM in the model is advected by the horizontal currents, the local sum of new production and remineralization do not always balance leading to regional net convergence/divergence of nutrients and DIC. Some ocean inversion transport estimates, for example, suggest that there are net horizontal inputs of organic nutrients into subtropical areas from remote sources (Rintoul and Wunsch 1991). Another factor to consider when looking at the model production estimates and model-data compari-

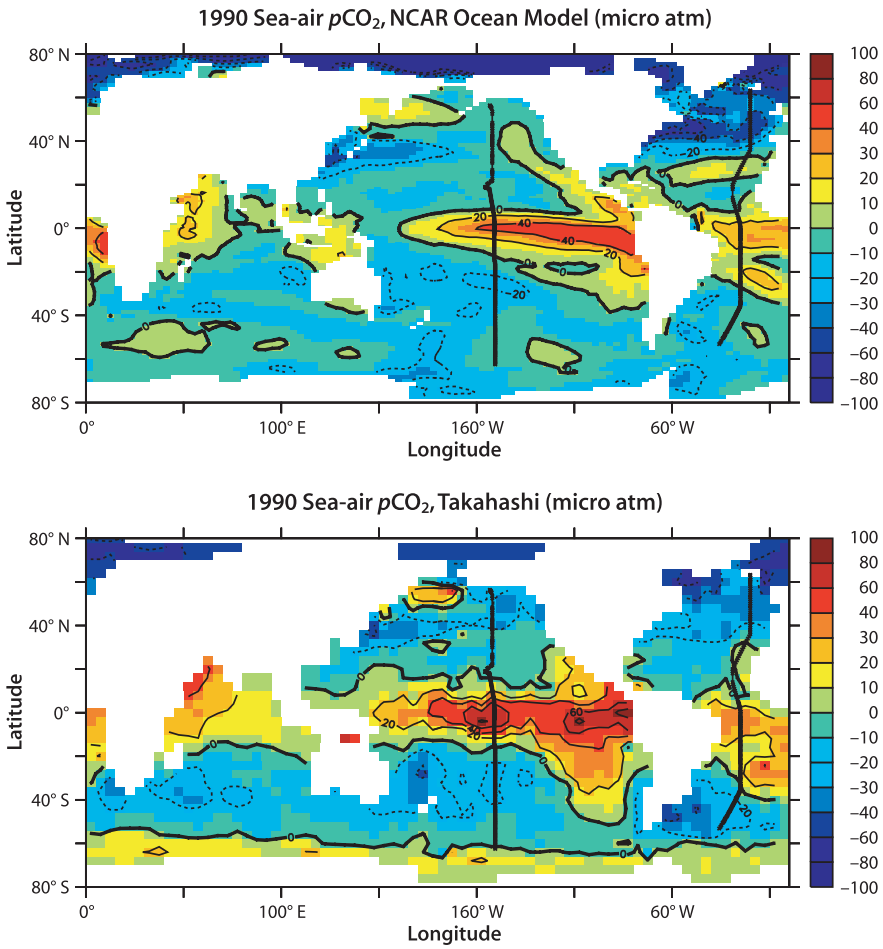

Fig. 9.6.
Spatial distributions of present (1990), annual mean surface sea-air pCO_2 difference (µatm) from (*top*) the NCAR CSM Ocean Model and (*bottom*) the Takahashi et al. (1997) climatology. The two *lines* indicate the Atlantic and Pacific transects used for the horizontal sections in Fig. 9.3 and 9.7

sons is the sensitivity of new production to the depth surface chosen for the vertical integral. The cumulative (surface to depth) new production drops off significantly with depth below 75 m in the model because of the assumed rapid decrease in the sinking particle flux and relatively shallow penetration of DOM governed mostly by seasonal convection (Fig. 9.5b). For most field studies, the vertical mixing and advection terms are difficult to quantify, and the new production is computed typical at either the base of the euphotic zone (100 m to 125 m) or the shallowest sediment trap (~150 m).

Another important measure of model skill is the surface water pCO_2 field (Sarmiento et al. 2000), which can be compared to extensive underway pCO_2 observations (Takahashi et al. 1997, 1999) and atmospheric CO_2 data sets (Keeling et al. 1996; Rayner et al. 1999). The model surface water pCO_2 field is the thermodynamic driving force for air-sea gas exchange and is governed by biological DIC drawdown, physical transport, surface temperature (and salinity), and air-sea fluxes. Figure 9.6 shows the annual mean air-sea ΔpCO_2 field from the model for 1990 (pre-industrial equilibrium plus anthropogenic perturbation) and the Takahashi et al. (1997) climatology. The large-scale patterns are similar with CO_2 outgassing from the equatorial regions, where cold DIC rich water is brought to the surface by upwelling, and CO_2 uptake in the western boundary currents, Antarctic Circumpolar Current, and North Atlantic deep water formation zones. The most striking regional model-data difference is the predicted larger (smaller) model uptake in the Southern Ocean (North Atlantic), compared to the Takahashi et al. (1997) climatology, and the indication of net outgassing right along the Antarctic coast in the observations. Interestingly, the model Southern Ocean results are more in line with recent atmospheric inversion results from the IGBP/GAIM atmospheric transport model intercomparison, TRANSCOM (S. Denning, per. comm. 2000). All three approaches (ocean model, pCO_2 data climatology, and atmospheric inversion) have their own unique uncertainties and potential biases, and more effort should be given to resolving these apparent discrepancies using a combination of improved numerical models and enhanced field data collection.

The model subsurface nutrient, DIC and oxygen fields can also be compared with observations, in this case historical hydrographic data sets and the JGOFS/WOCE global CO_2 survey. The preindustrial DIC results are

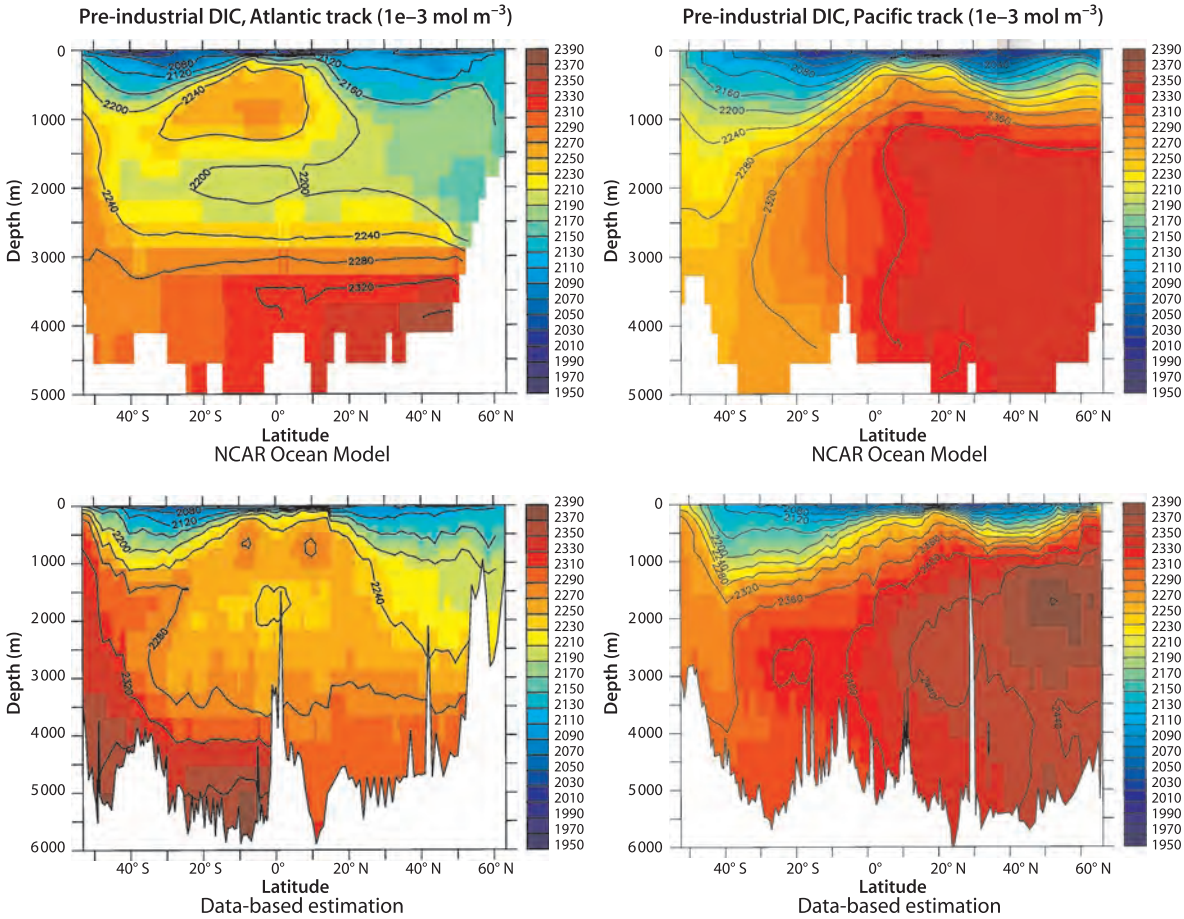

Fig. 9.7. Depth vs. latitude contour plots of pre-industrial DIC (mmol C m^{-3}). The panels show the simulated results from the NCAR CSM ocean model and observed DIC fields with the anthropogenic DIC component removed using the C* technique (N. Gruber 2000, pers. comm.) for an Atlantic and Pacific section along the main path of the thermohaline circulation (see Fig. 9.6)

shown in the same format as for anthropogenic DIC (Fig. 9.3), i.e., meridional sections in the Atlantic and Pacific (Fig. 9.7). The model surface to deep water DIC vertical gradient, which is comparable to the observations, results from contributions of about 2/3 from the biological export ('biological pump') and 1/3 from the physics ('solubility pump'). The horizontal gradients in the deep-water are determined by a mix of the thermohaline circulation and the subsurface particle remineralization rate, and the NCAR-OCMIP model captures most of the broad features. Several of the key model-data differences can be ascribed, at least partly, to problems with the model physics (e.g., too shallow outflow of North Atlantic Deep Water, Large et al. 1997; overly weak production of Antarctic bottom water, Doney and Hecht 2002). The WOCE/JGOFS carbon survey and historical data sets can also be used to estimate the horizontal transport of biogeochemical species within the ocean (e.g., Brewer et al. 1989; Rintoul and Wunsch 1991; Broecker and Peng 1992; Holfort et al. 1998; Wallace 2001), providing another constraint for ocean biogeochemical models (Murnane et al. 1999; Sarmiento et al. 2000; Gruber et al. 2001).

9.4 Ecosystem Dynamics

If the simple OCMIP biogeochemical model captures the zeroth-order state of the ocean carbon cycle then what are the important areas for progress? An obvious deficiency of the OCMIP straw man is the lack of explicit, prognostic biological dynamics to drive surface production, export and remineralization. By linking to a fixed surface nutrient climatology, we have avoided specifying the details of how the surface nutrient field is controlled (e.g., grazing, iron fertilization, mesoscale eddies) or how it might evolve under altered forcing. While useful for the purposes of OCMIP, clearly a more mechanistic approach is desired for many applications. For example, looking toward the next several centuries, future changes in ocean circulation and biogeochemistry may lead to large alterations in the background carbon cycle that could strongly impact projected ocean carbon sequestration (Denman et al. 1996; Sarmiento et al. 1998; Doney and Sarmiento 1999; Boyd and Doney 2003). Realistic projections will require coupled ecosys-

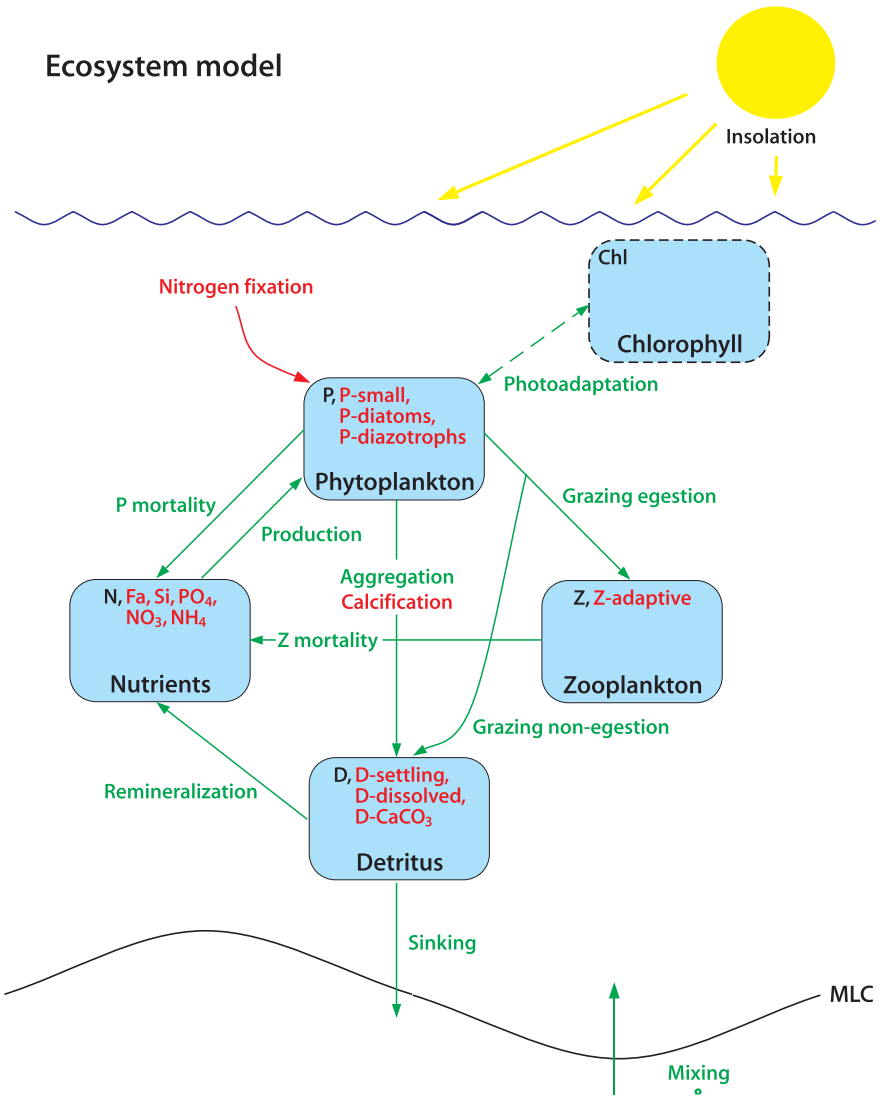

Fig. 9.8.
Schematic of a simple marine ecosystem model originally developed for the Bermuda Atlantic Time-Series Study site (Doney et al. 1996; Doney et al., pers. comm.) and (in *red*) the recent extension by Moore et al. (2001a)

tem-biogeochemical models that include the main processes thought to be sensitive to climate change (e.g., atmospheric dust, nitrogen fixation, community structure).

As an example of a typical marine ecosystem, consider the schematic shown in Fig. 9.8. The model developed for vertical 1-D simulations of the Sargasso Sea by Doney et al. (1996) incorporates five prognostic variables: phytoplankton, zooplankton, nutrient, detritus and chlorophyll (a so-called PZND model). As is common, the model aggregates populations and species of organisms into broadly defined trophic compartments. The equations are based on the flow of a single limiting currency, in this case the concentration of nitrogen (mol N m^{-3}), among compartments rather than individual organisms. The various source/sink terms (e.g., photosynthesis, zooplankton grazing, detrital remineralization) are calculated using standard, though not always well agreed upon, sets of empirical functional forms and parameters derived either from limited field data or laboratory experiments, the latter often with species and conditions of limited relevance to the actual ocean (Fasham 1993; Evans and Fasham 1993; Evans and Garçon 1997). This type of compartment ecosystem model has been used extensively in oceanography (Steele 1974) and theoretical ecology (May 1973; Case 2000) since the early 1970s but has roots much further back in the literature (e.g., Riley 1946; Steele 1958). The area was revitalized about the time of the inception of JGOFS by the seminal work of Evans and Parslow (1985), Frost (1987), Fasham et al. (1990), and Moloney and Field (1991).

Despite its simplifications, the PZND model (Fig. 9.8) does an adequate job capturing the vertical structure and broad seasonal patterns of bulk biogeochemical properties in Bermuda field data (e.g., chlorophyll – Fig. 9.9; nitrate; Doney et al. 1996). Specific features include: a winter phytoplankton bloom following nutrient injection via deep convection; low surface nutrients and chlorophyll during the stratified summer period; and the formation of a sub-

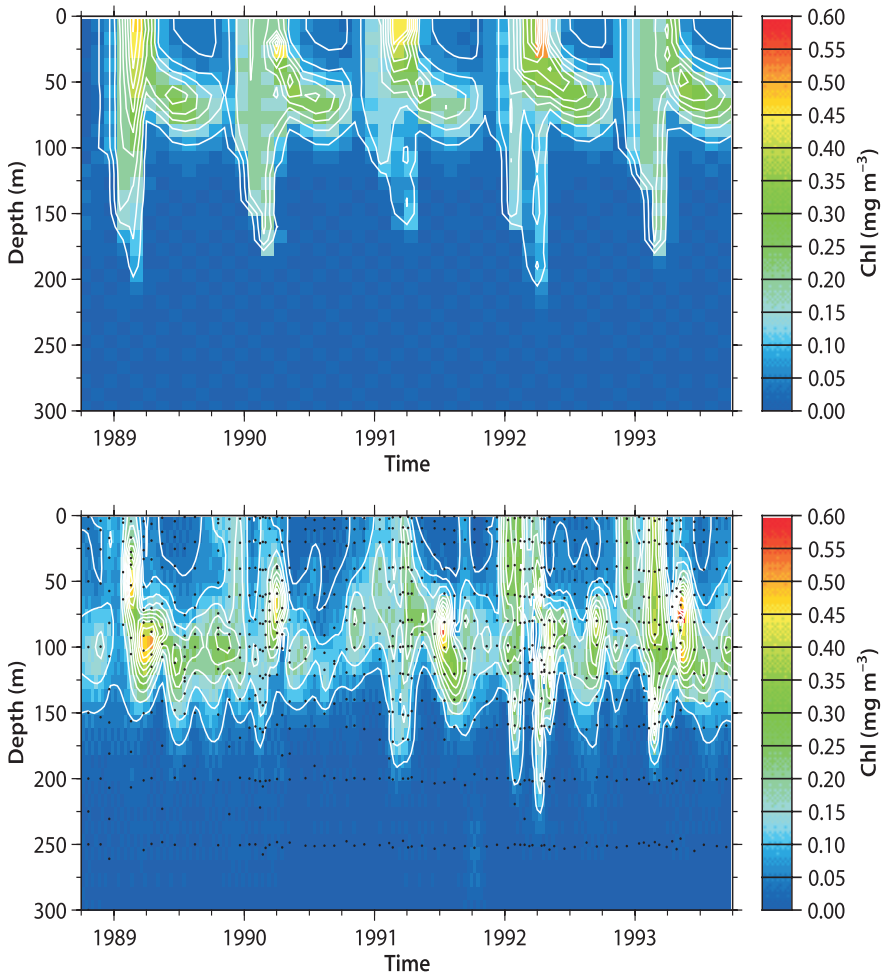

Fig. 9.9.
A comparison of the modeled and observed time-depth chlorophyll distribution for the Bermuda Atlantic Time-Series Study site in the western subtropical North Atlantic. The 1-D coupled biological-physical model is based on Doney et al. (1996) and Doney (1996)

surface chlorophyll maximum at the top of the nutricline. The 1-D coupled biological-physical model, based on surface forcing and physics described by Doney (1996), also reproduces aspects of the observed interannual variability driven by the depth of the winter convection.

Variants on the PZND theme have been successfully applied in vertical 1-D form in a diverse range of biogeographical regimes from oligotrophic subtropical gyres (Bissett et al. 1994) to seasonal bloom regimes (Fasham 1995) to subarctic high-nitrate, low chlorophyll regions (McClain et al. 1996; Pondaven et al. 2000). The construction of the 1-D physical framework (vertical mixing, temperature etc.) requires explicit consideration (Archer 1995; Doney 1996; Evans and Garçon 1997), but in general 1-D coupled models have resulted in useful test-beds for exploring ecological processes and implementing biological data assimilation techniques. It has been known for a while that the relatively simple PZND dynamics belie the ecological complexity of the real system, and recent idealized and local 1-D coupled models include increasing levels of ecological sophistication. Models are incorporating a range of factors such as: size and community structure (Armstrong 1994, 1999a; Bissett et al. 1999), iron limitation (Armstrong 1999b; Leonard et al. 1999; Denman and Pena 1999; Pondaven et al. 2000), and nitrogen fixation (Hood et al. 2001; Fennel et al. 2002). One problem, however, is that most 1-D coupled models are developed and evaluated for a single site, and the generality of these models and their derived parameter values for basin and global simulations remains an open question.

Early three-dimensional basin and global scale calculations (Sarmiento et al. 1993; Six and Maier-Reimer 1996) were conducted with single, uniform PZND ecosystem models applied across the entire domain. These experiments demonstrated that large-scale features such as the contrast between the oligotrophic subtropical and eutrophic subpolar gyres could be simulated qualitatively. Some problems arose, however, with the details. For example, the incorporation of the Fasham et al. (1990) model into a North Atlantic circulation model by Sarmiento et al. (1993) showed too low production and biomass in the oligotrophic subtropics and too weak a spring bloom at high latitudes. The Six and Maier-Reimer (1996) result required careful tuning of the phytoplankton growth temperature sensitivity and zoo-

plankton grazing in order to control biomass in the Southern Ocean HNLC (high nitrate-low chlorophyll) regions. A number of coupled 3-D ecosystem models now exist for regional (Chai et al. 1996; McCreary et al. 1996; Ryabchenko et al. 1998; Dutkiewicz et al. 2001) and global (Aumont et al., pers. comm.) applications, and these 3-D ecosystem models are beginning to include many of the features already addressed in 1-D, including multiple nutrient limitation and community structure (Christian et al. 2001a,b; Gregg et al. 2002). Often, however, these models are not used to fully explore the coupling of upper ocean biology and subsurface carbon and nutrient fields because of the short integration time (a few years) or limited horizontal/vertical domain.

The next step is to combine reasonably sophisticated components for both ecosystem and biogeochemical dynamics in a global modeling framework. The exact form of such a model is yet to be determined. Based on the new insights emerging from JGOFS and other recent field studies, a minimal model can be envisioned covering those basic processes that govern surface production, export flux, subsurface remineralization, and the (de)coupling of carbon from macronutrients (multinutrient limitation; size structure and trophic dynamics; plankton geochemical functional groups; microbial loop and dissolved organic matter cycling; particle transport and remineralization).

As part of such a project, we have developed an intermediate complexity, ecosystem model incorporated within a global mixed layer framework (Moore et al. 2002a,b). The model biology is simulated independently at each grid point and then composited to form global fields. The model has a low computational overhead, and thus can be used for extensive model evaluation and exploration. Sub-surface nutrient fields are from climatological databases, and the mixed layer model captures the local processes of turbulent mixing, vertical advection at the base of the mixed layer, seasonal mixed layer entrainment/detrainment, but not horizontal advection. Other forcings include sea surface temperature, percent sea ice cover, surface radiation, and the atmospheric deposition of iron (Fung et al. 2000; Fig. 9.10). The physical forcings are prescribed from climatological databases (Levitus et al. 1994; Conkright et al. 1998) and the NCAR CSM Ocean Model (NCOM) (Large et al. 1997). A preliminary version of the ecosystem model also has been tested in a fully coupled, 3-D North Atlantic Basin configuration (Lima et al. 1999), and the full ecosystem model is currently being implemented in the new global NCAR-Los Alamos model. The mixed layer ecosystem model is discussed in some detail to highlight new modeling directions and approaches to model-data evaluation.

The ecosystem model (Fig. 9.8) is adapted from Doney et al. (1996) and consists of eleven main compartments, small phytoplankton, diatoms, and diazotrophs; zooplankton; sinking and non-sinking detrital classes; and dissolved nitrate, ammonia, phosphorus, iron, and silicate. The small phytoplankton size class is meant to generically represent nano- and pico-sized phytoplankton, with parameters designed to replicate the rapid and highly efficient nutrient recycling found in many subtropical, oligotrophic (low nutrient) environments. The small phytoplankton class may be iron, phosphorus, nitrogen, and/or light-limited. The larger phytoplankton class is explicitly modeled as diatoms and may be limited by silica as well. Many of the biotic and detrital compartments contain multiple elemental pools to track flows through the ecosystem. The model has one zooplankton class which grazes the three phytoplankton groups and the large detritus. Phytoplankton growth rates are determined by available light and nutrients using a modified form of the Geider et al. (1998) dynamic growth model. Carbon fixation rate is governed by internal cell nutrient quotas (whichever nutrient is currently most-limiting), and the cell quotas computed relative to carbon are allowed to vary dynamically as the phytoplankton adapt to changing light levels and nutrient availability. There is good laboratory evidence for a relationship between cell quotas (measured as nutrient/C ratios) and specific growth rates (Sunda and Huntsman 1995; Geider et al. 1998). Photoadaptation is modeled according to Geider et al. (1996, 1998) with a dynamically adaptive Chl/C ratio. The diazotrophs are assumed to fix all required nitrogen from N_2 gas following Fennel et al. (2002) and are limited by iron, phosphorus, light or temperature. Calcification is para-

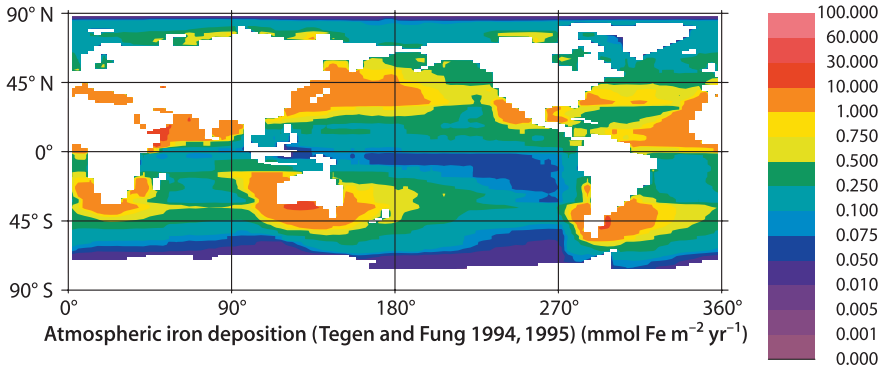

Fig. 9.10.
Annual mean map of atmospheric iron deposition to the ocean adapted from Tegen and Fung (1995) model estimates (reprinted from Deep-Sea Res II 49, Moore et al. (2002) Iron cycling and nutrient limitation patterns in surface waters of the world ocean. pp 463–507, © 2002, with permission from Elsevier Science)

meterized as a time-varying fraction of the small (pico/nano) plankton production as a function of ambient temperature and nutrient concentrations. Based on Harris (1994) and Milliman et al. (1999) we assume that grazing processes result in substantial dissolution of $CaCO_3$ in the upper water column.

The model output is in generally good agreement with the bulk ecosystem observations (e.g., total biomass; productivity; nutrients) across diverse ecosystems that include both macro-nutrient and iron-limited regimes and very different physical environments from high latitude sites to the mid-ocean gyres. The detailed, local data sets from JGOFS and historical time-series stations (Kleypas and Doney 2001) have been important for developing parameterizations, testing hypotheses, and evaluating model performance. As an example, a comparison of model simulated and observed mixed layer seasonal cycle for nitrate is shown in Fig. 9.11 for nine locations across the globe. The time-series stations and regional JGOFS process studies (e.g., EqPAC, Arabian Sea) often provide invaluable constraints on biological fluxes (primary productivity profiles, export flux, zooplankton grazing, not shown) as well, parameters that are typically sampled too sparsely to construct global data sets. The variables that are available from observations on a global scale are more limited, including seasonal (now monthly) nutrient fields (Conkright et al. 1998), satellite remotely sensed surface chlorophyll (McClain et al. 1998) (Fig. 9.12) and diagnostic model derived products such as satellite based integrated primary production (Behrenfeld and Falkowski 1997) and *f*-ratio (Laws et al. 2000) estimates. Compared with the satellite estimates, the model produces realistic global patterns of both primary and export production.

The incorporation of iron limitation plays a critical part in the model skill of reproducing the observed high nitrate and low phytoplankton biomass conditions in the Southern Ocean and the subarctic and equatorial Pacific regions. A small number of desert regions (e.g., China, Sahel), mostly in the Northern Hemisphere, provide the main sources of atmospheric dust (and thus iron) to the ocean, and the estimated iron deposition rate to oceanic HNLC environments can be orders of magnitude lower than other locations (Fig. 9.10). At such low deposition rates, upwelling of subsurface iron likely contributes a significant fraction of the total bioavailable

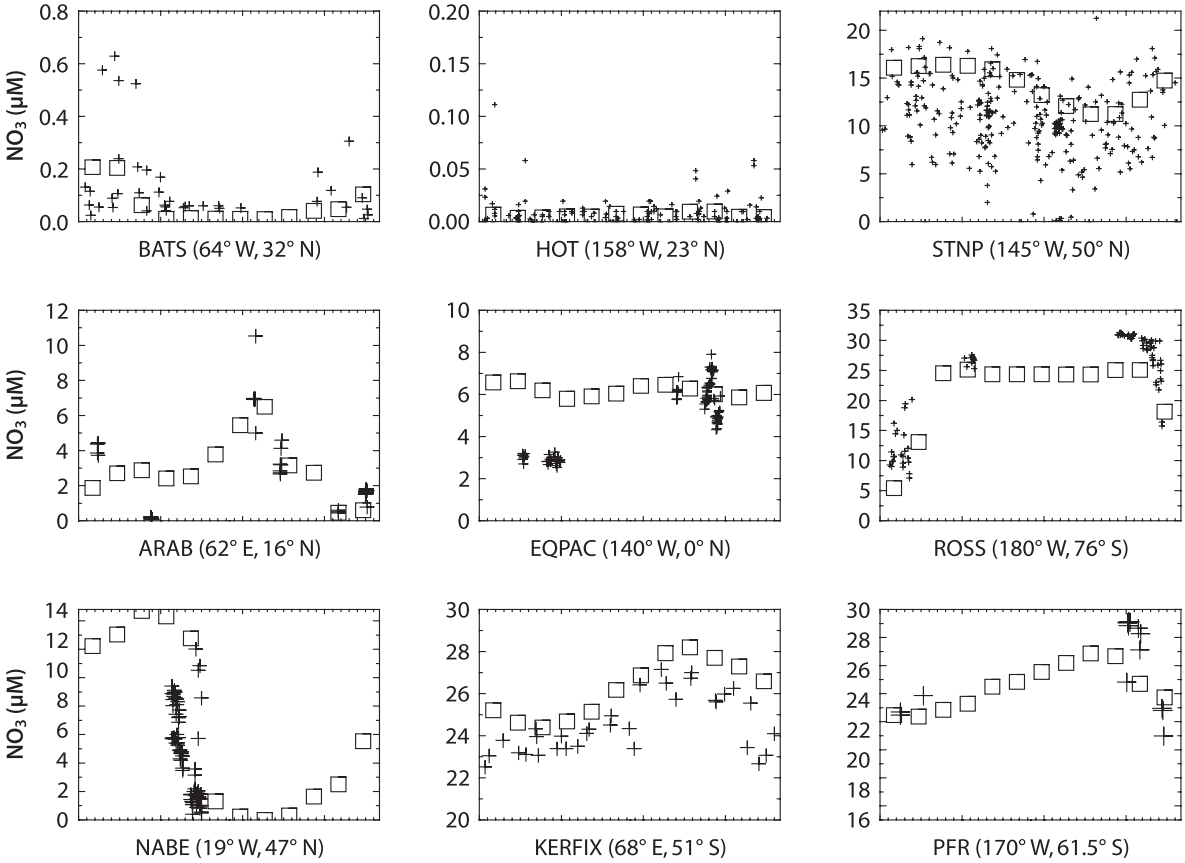

Fig. 9.11. Comparison of simulated and observed seasonal nitrate cycle at nine JGOFS time-series stations across a range of biogeographical regimes (Kleypas and Doney 2001). The model results are from a global mixed layer ecosystem model with uniform biological coefficients (reprinted from Deep-Sea Res II 49, Moore et al. (2002) An intermediate complexity marine ecosystem model for the global domain. pp 403–462, © 2002, with permission from Elsevier Science)

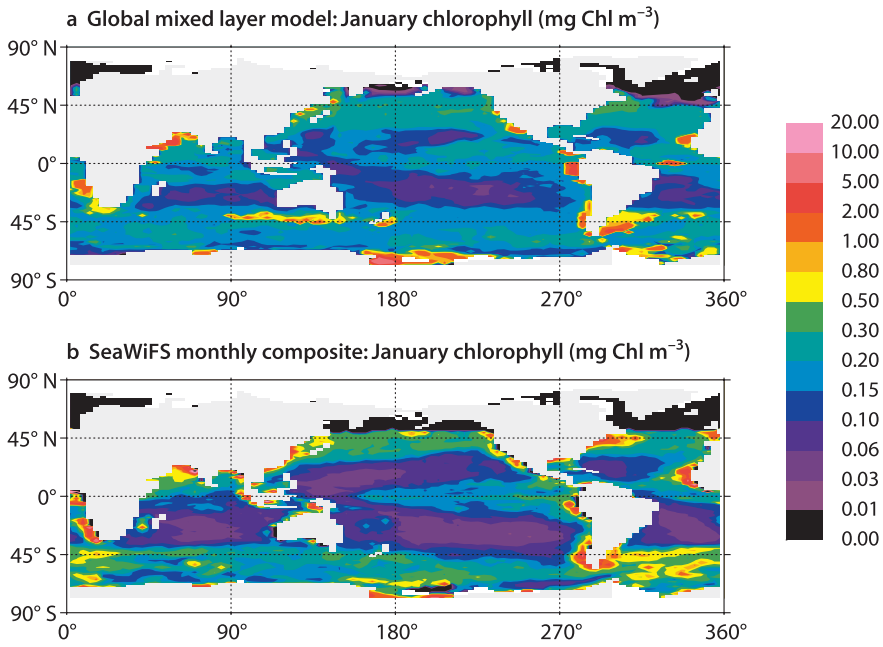

Fig. 9.12. Global field of monthly mean surface chlorophyll concentration for January from SeaWiFS and a global mixed layer ecosystem model (reprinted from Deep-Sea Res II 49, Moore et al. (2002) Iron cycling and nutrient limitation patterns in surface waters of the world ocean. pp 463–507, © 2002, with permission from Elsevier Science)

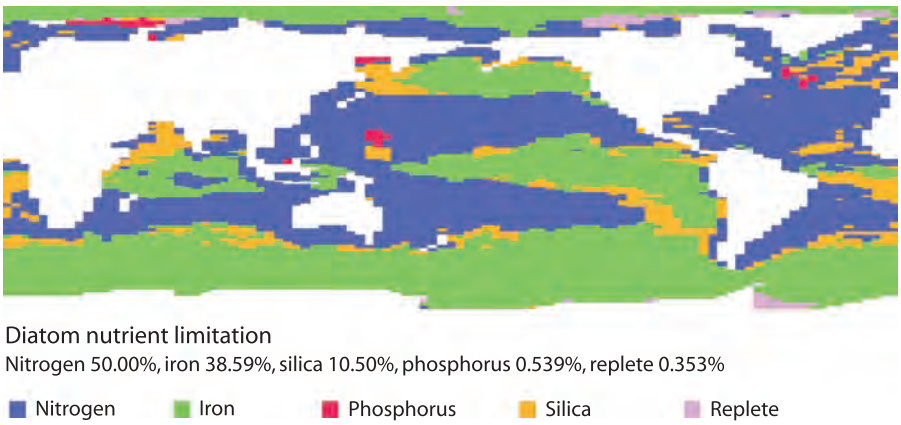

Fig. 9.13. Ecosystem model simulated nutrient limitation patterns during summer months in each hemisphere (June–August in the Northern Hemisphere, December–February in the Southern Hemisphere) for diatoms. The global fractional area limited by each nutrient is listed below the plot. Nutrient replete areas (here arbitrarily defined as areas where all nutrient cell quotas are >90% of their maximum values) are largely restricted to areas of extreme light-limitation under permanently ice-covered regions (reprinted from Deep-Sea Res II 49, Moore et al. (2002) Iron cycling and nutrient limitation patterns in surface waters of the world ocean. pp 463–507, © 2002, with permission from Elsevier Science)

iron. In the model, these regions are characterized by strong iron limitation of diatom growth and modest iron limitation and strong grazing pressure on the small phytoplankton. The observed low chlorophyll and low nitrate levels in oligotrophic gyres are also simulated well, but the model does not fully capture the strong blooms in some of the coastal upwelling regions, most likely a result of the weak vertical velocities input from the coarse resolution physics model.

Models should allow us to do more than simply replicate what is already known, by posing new (and testable) hypotheses of how the ocean functions at the system level. As an example, the global mixed layer model predicts the degree and time/space patterns of nutrient limitation. Not too surprisingly, the model suggests that both small phytoplankton and diatoms are iron limited in the classic HNLC regions (40% and 52% of the global surface area, respectively for the two phytoplankton groups), while the mid-ocean subtropical gyres are typically nitrogen or, to much smaller degree, phosphorus limited (Fig. 9.13). Diatom silica limitation is exhibited in the subantarctic and North Atlantic waters with bands of silica-iron co-limitation along the edges of the tropics. The variable cell quota approach allows for easy diagnosis of varying degrees of nutrient stress, which can be compared in the near future with global nutrient stress fields to be derived from the MODIS natural fluorescence measurements (Letelier and Abbott 1996).

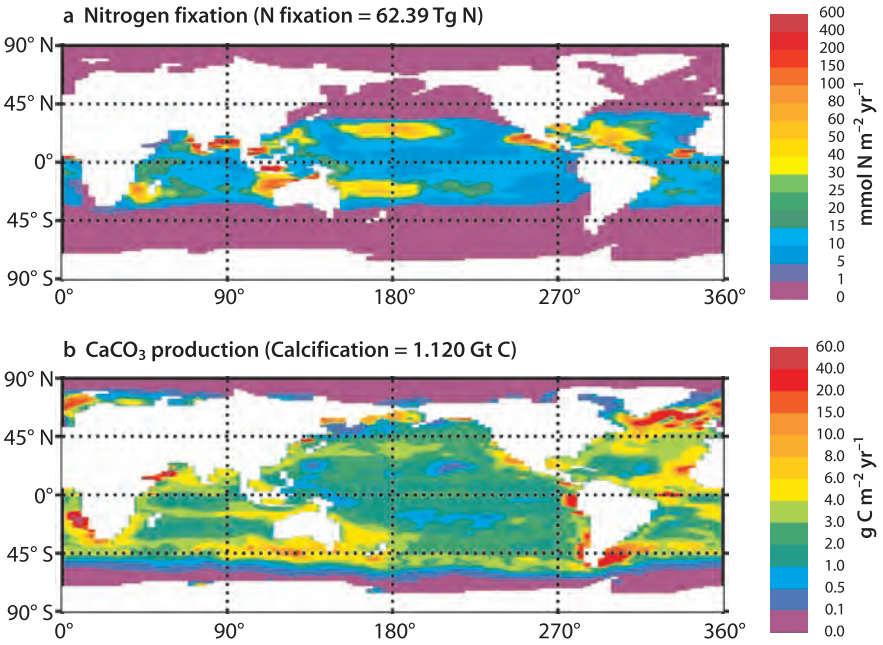

Fig. 9.14.
Model simulated annual mean nitrogen fixation and calcification fields (reprinted from Deep-Sea Res II 49, Moore et al. (2002) Iron cycling and nutrient limitation patterns in surface waters of the world ocean. pp 463–507, © 2002, with permission from Elsevier Science)

The other new aspect of the global model is the inclusion of community structure through planktonic geochemical functional groups, namely diatoms (export flux and silica ballast), diazotrophs (nitrogen fixation), and calcifiers (alkalinity and ballast). The model spatial patterns of annual nitrogen fixation (Fig. 9.14) agree well with the limited information known from in situ work (Capone et al. 1997), high trichodesmium biomass and/or nitrogen fixation rates reported in the Caribbean Sea and eastern tropical North Atlantic (Lipschulz and Owens 1996) as well as in the subtropical North Pacific (Letelier and Karl 1996, 1998; Karl et al. 1997). The total model nitrogen fixation of 58 Tg N, which accounts only for the mixed layer production, is somewhat less than, though of comparable magnitude to, the 80 Tg N estimate of Capone et al. (1997) and the Gruber and Sarmiento (1997) geochemical estimates of >100 Tg N.

The parameterization of phytoplankton calcification is an active research topic, but the spatial patterns shown in Fig. 9.14 are generally similar to those estimated by Milliman (1993) and Milliman et al. (1999). $CaCO_3$ production/export is lower in the mid-ocean gyres and higher in the North Atlantic, coastal upwelling zones and mid-latitude Southern Ocean waters. The high latitude North Atlantic in particular is known to be a region with frequent coccolithophore blooms (Holligan et al. 1993). The model production/export is lower in the equatorial Pacific and Indian ocean compared with Milliman et al. (1999), but the global sinking export of 0.46 Gt C is in good agreement with their integrated estimate.

Two main factors limiting progress on ecosystem modeling are the conceptualization of key processes at a mechanistic level and the ability to verify model behavior through robust and thorough model-data comparisons (Abbott 1995). The phytoplankton iron limitation story is an illuminating example. Atmospheric dust/iron deposition flux estimates vary considerably (perhaps as large as a factor of ten or more in some areas) and the bioavailable fraction of the dust iron is not well known. Surface and subsurface ocean iron measurements are limited (particularly from a global modeler's perspective), and there remain serious analytical and standardization issues. Organic ligands may play a role in governing both bioavailability and subsurface iron concentrations. Not enough is known about the effect of iron limitation and variability on species competition at ambient low iron levels. A host of other processes may be relevant, but are currently poorly characterized, including: iron release by photochemistry and zooplankton grazing, release of iron from ocean margin sediments, and iron remineralization from sinking particles.

9.5 Other Topics

In a recent review paper, Doney (1999) described a set of key marine ecological and biogeochemical modeling issues to be addressed in the next generation of numerical models: multi-element limitation and community structure; large-scale physical circulation; mesoscale space and time variability; land, coastal, and sediment exchange with the ocean; and model-data evaluation and data assimilation. In the preceding three sections we have presented in some detail the nature of several of these challenges and specific initial progress made by our group. Below we more briefly outline some of the remaining items.

9.5.1 Mesoscale Physics

The ocean is a turbulent medium, and mesoscale variability (scales of 10 to 200 km in space and a few days to weeks in time) is a ubiquitous feature of ocean biological fields such as remotely sensed ocean color. Based on new in situ measurement technologies (Dickey et al. 1998) and mesoscale biogeochemical models (McGillicuddy and Robinson 1997; Oschlies and Garçon 1998; Spall and Richards 2000; Lima et al. 2002) it has become clear that mesoscale variability is not simply noise to be averaged over, but rather a crucial factor governing the nature of pelagic ecosystems. The ecological impacts of disturbance are diverse, and the initial research emphasis on the eddy enhancement of new nutrient fluxes to the euphotic zone (McGillicuddy et al. 1998; Fig. 9.15) is broadening to include light limitation, community structure, organic matter export, and subsurface horizontal transport effects as well (Garçon et al. 2001).

Quantifying the large-scale effect of such variability will require concerted observational, remote sensing and numerical modeling programs with likely heavy reliance on data assimilation. The computational demands of truly eddy resolving basin to global calculations are significant, however. Recent high resolution physical simulations of the North Atlantic show that dramatic improvement in eddy statistics and western boundary current dynamics is reached only at 1/10 of a degree resolution (Smith et al. 2000), and even higher resolution may be needed for biology if submesoscale (0.5–10 km) processes are as important as suggested by preliminary results (Levy et al. 1999; Mahadevan and Archer 2000; Lima et al. 2002). Over the near term, long time-scale equilibrium and climate simulations will be limited primarily to non-eddy resolving models in which submesoscale and mesoscale eddy effects will have to be incorporated via subgrid-scale parameterizations (Levy et al. 1999; Lima et al. 2002).

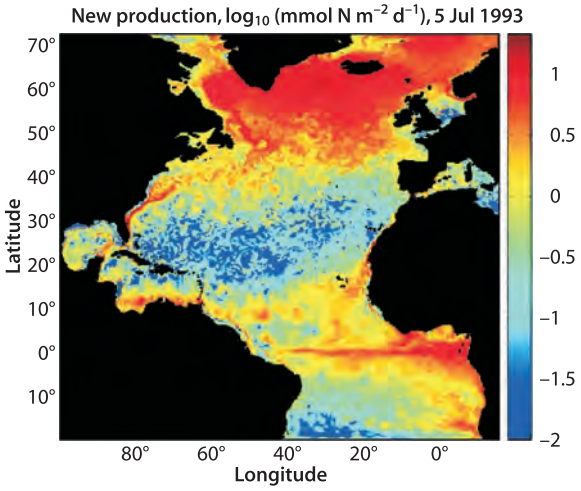

Fig. 9.15. Daily snapshot of new production from a Los Alamos-POP 1/10° mesoscale simulation of the North Atlantic (Dennis McGillicuddy, pers. comm.)

9.5.2 Climate Variability and Secular Change

A key measure for the skill of numerical models is their ability to accurately hind-cast oceanic responses to natural climate variability on timescales from the seasonal cycle to multiple decades. Large-scale modeling studies, with some exceptions, have tended to focus primarily on the mean state of the ocean. Biological oceanographic time series exhibit significant variability on interannual to interdecadal scales associated with physical climate phenomenon such as the El Niño-Southern Oscillation (ENSO) and the Pacific Decadal Oscillation (PDO) (Venrick et al. 1987; Karl et al. 1995; McGowan et al. 1998; Karl 1999). The ecosystem response to physical forcing may be quite nonlinear, manifesting in the North Pacific, for example, as a major biological regime shift in the mid-1970s due to the PDO (Francis and Hare 1994). Comparable climate related biological shifts are also inferred for the North Atlantic (Reid et al. 1998). Retrospective models can help explain the underlying mechanisms of such phenomena (Polovina et al. 1995). Because of an interest in separating terrestrial and oceanic signals in the atmospheric CO_2 network, there is also a growing effort to model the oceanic contribution to atmospheric variability, which appears to be small except for the tropical ENSO signal (Rayner et al. 1999; Le Quéré et al. 2000).

Numerical models are also being used to project the potential marine biogeochemical responses to anthropogenic climate change (Sarmiento et al. 1998; Matear and Hirst 1999). Coupled ocean-atmosphere model simulations differ considerably in their details, but most models suggest general warming of the upper ocean and thermocline, increased vertical stratification in both the low latitude (warming) and high latitude (freshening) surface waters, and weakening of the thermohaline circulation. Combined, the physical effects lead to a 30–40% drop in the cumulative anthropogenic CO_2 uptake over the next century partly compensated by changes in the strength of the natural biological carbon pump. Given the low level of biological sophistication used in these early simulations, such projections must be considered preliminary, demonstrating the potential sensitivity of the system and posing important questions to be addressed through future research.

Preliminary ecosystem simulations (Bopp et al. 2001) show different regional climate change responses to enhanced stratification with decreased subtropical pro-

ductivity (nutrient limited) and increased subpolar productivity (light limited) reminiscent of the PDO signal (Polovina et al. 1995). Other environmental factors to consider include alterations of aeolian trace metal deposition due to changing land-use and hydrological cycle, variations in cloud cover and solar and UV irradiance, coastal eutrophication, and lower surface water pH and carbonate ion concentrations due to anthropogenic CO_2 uptake (Kleypas et al. 1999). The decadal time-scale biogeochemical and ecological responses to such physical and chemical forcings are not well understood in detail, and prognostic numerical models will be relied on heavily along with historical and paleoceanographic climate variability reconstructions (Doney and Sarmiento 1999; Boyd and Doney 2003).

9.5.3 Land, Coastal Ocean, and Sediment Interactions

The coastal/margins zone interacts strongly and complexly with the land, adjacent atmosphere, continental shelves and slopes, and open-ocean. The specific rates of productivity, biogeochemical cycling, and organic/inorganic matter sequestration are higher than those in the open ocean, with about half of the global integrated new production occurring over the continental shelves and slopes (Walsh 1991; Smith and Hollibaugh 1993). The high organic matter deposition to, and close proximity of the water column to, the sediments raises the importance of sedimentary chemical redox reactions (e.g., denitrification, trace metal reduction and mobilization), with implications for the global carbon, nitrogen, phosphorus and iron cycles. Finally, the direct and indirect human perturbations to the coastal environment (e.g., pollution, nutrient eutrophication, fisheries) are large, with important impacts on marine ecosystems (harmful algal blooms, coral reefs, spawning grounds) and society (e.g., commercial fisheries, tourism, and human health and aesthetics).

Because of the topographic complexity, smaller time/space scales, and specific regional character of coastal environments, basin to global scale models typically do not fully account for biogeochemical fluxes and dynamics on continental margins and in the coastal ocean. Thus coastal/open-ocean exchange and the large-scale influence on the ocean are not well quantified except in a few locations (Falkowski et al. 1994; Liu et al. 2000). Regional coastal ecosystem models have been moderately successful (Robinson et al. 2001; Fig. 9.16), and an obvious next step is to meld open ocean and coastal domains through more adaptable grid geometries such as unstructured (spectral) finite element grids (Haidvogel et al. 1997) or by embedding regional domain, higher-resolution models (Spall and Holland 1991). Dynamic marine sediment geochemistry models (Heinze et al. 1999) are needed both for the coastal problem and for large-scale paleoceanographic applications, an example being the compensation of the sediment $CaCO_3$ to changes in ocean carbon chemistry on millennial time-scales (Archer and Maier-Reimer 1994; Archer et al. 2000).

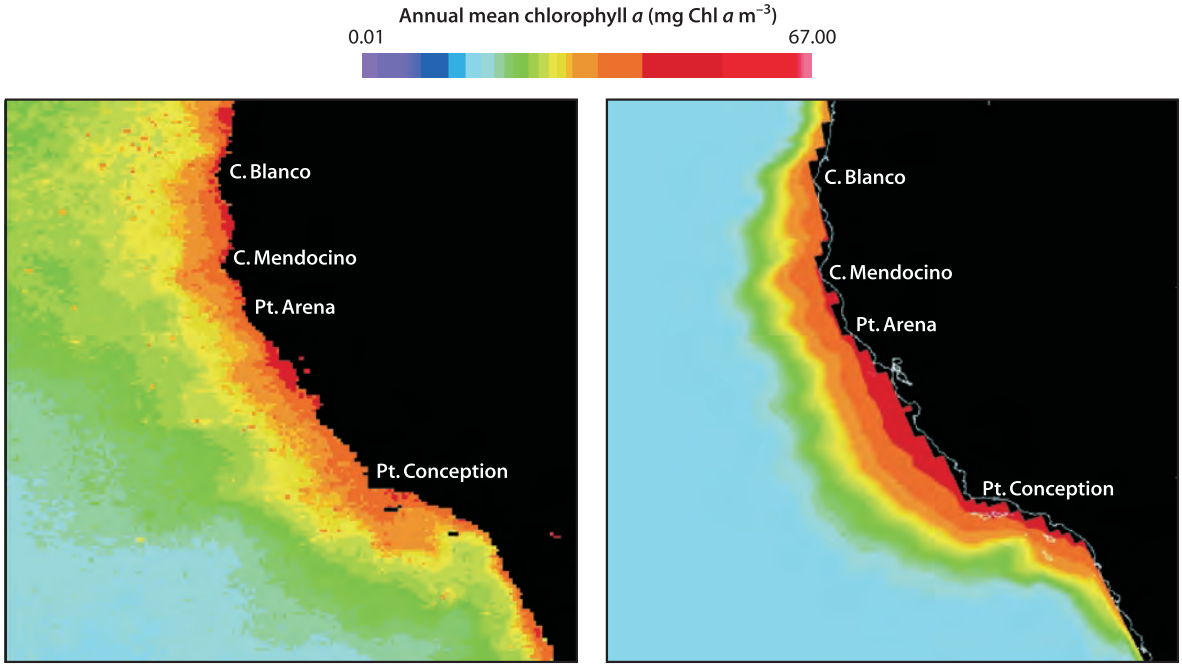

Fig. 9.16. Annual mean chlorophyll for the California Current coastal region from SeaWiFs and the UCLA regional coastal ecosystem model ROMS (James McWilliams, pers. comm.)

9.5.4 Inverse Modeling and Data Assimilation

The emerging techniques of inverse modeling and data assimilation, which more formally compare and meld model results and data, are becoming essential in model development and evaluation (U.S. JGOFS 1992; Kasibhatla et al. 2000). In theory data assimilation provides a solution, if it exists, that is dynamically consistent with both the observations and model equations within the estimated uncertainties. Much of the art of data assimilation lies in assigning relative error weights to different data types and to the model equations themselves, the so-called cost function problem (U.S. JGOFS 1992). A number of recent studies have used this approach to better constrain or optimize parameters for marine biogeochemical box and one-dimensional models, particularly with time series data (Matear 1995; Fasham and Evans 1995; Hurtt and Armstrong 1996; Spitz et al. 1998; Fennel et al. 2001). Applications to three-dimensional models are more limited but include efforts to assimilate satellite ocean color data into ecosystem models (Ishizaka 1990) or to estimate poorly measured fluxes such as dissolved organic phosphorus transport/remineralization (Matear and Holloway 1995), surface export production (Schlitzer 2000), and air-sea oxygen fluxes (Gruber et al. 2001) from the large-scale nutrient distributions and physical circulation flow fields. The utility of data assimilation will continue to grow with the import and refinement of numerical methods from meteorology and physical oceanography to interdisciplinary problems (Robinson 1996) and with the availability of automated software systems for generating the required model adjoints (Giering and Kaminski 1998).

9.6 Summary

Numerical models are essential tools for understanding the complex physical, biological and chemical interactions that govern the ocean carbon cycle. They are also crucial for extrapolating local/regional relationships to the global scale and for projecting the effects and feedbacks on the ocean carbon cycle of past and potential future climate change. As outlined in this chapter, the field of marine biogeochemical modeling is alive and vigorous, benefiting greatly from the surge of new data and concepts arising from the decade long international JGOFS field effort. The boundaries of the three quasi-independent lines of research (i.e., anthropogenic CO_2 transient tracer uptake; biogeochemical cycling; and ecosystem dynamics) that characterized numerical modeling historically are being blurred, and integrated regional and global 3-D eco-biogeochemical models are emerging. These models are based on the new paradigms of multi-element cycling, community structure and geochemical functional groups (e.g., nitrogen fixers, calcifiers), key to addressing hypotheses of how the ocean might alter or drive long term changes in atmospheric CO_2. Growing utilization of retrospective or hindcasting experiments will be used to evaluate model skill relative to historical interannual and paleoclimate variability. Significant progress is also being made in process and regional models on issues such as biological-physical sub- and mesoscale interactions as well as coastal ecosystem and biogeochemical dynamics.

A number of major challenges remain for the next decade(s):

Ecological sophistication. Ocean models must be grounded at a more fundamental level by ecological and evolutionary hypotheses. The current emphasis is often on simulating chemical and biochemical analyses: phytoplankton treated simply as concentrations of pigments and organic carbon, zooplankton as grazers, and physics as a mechanism for providing nutrients. A more mechanistic understanding is needed of how individual organisms and species interact to form pelagic ecosystems, how food webs affect biogeochemical fluxes, and how the structure of food webs and corresponding biogeochemical fluxes will change in the coming decades.

High frequency variability. The importance of high frequency spatial and temporal variability (e.g., fronts, mesoscale eddies) on the large-scale carbon cycle needs to be better characterized. This will require a combination of subgrid-scale parameterizations, nested models, and dedicated very high-resolution computations.

Land-ocean-sediment interactions. Explicit treatment of the biologically and biochemically active regions along continents needs to be incorporated. At present, coastal modeling is often 'parochial' in the sense that each region is treated as unique both physically and ecologically. The computational approaches will be similar to those outlined for mesoscale dynamics.

Model-data fusion. Models must be confronted more directly with data using a hierarchy of diagnostic, inverse, and data assimilation methods. While technically challenging, data assimilation holds the promise of creating evolving, 4-D 'state estimates' for the ocean carbon cycle. Further, assimilation methods (e.g., parameter optimization) can be used to demonstrate that some models or functional forms are simply incompatible with observations, thus offering some hope for focusing the current and growing model plethora.

Global carbon cycle. The ocean is only one component of the global carbon cycle, and independent and often complementary estimates of key measures of ocean carbon dynamics are being developed by scientists working in other disciplines. Examples include air-sea CO_2

fluxes based on atmospheric inversions and seasonal marine net community production based on atmospheric O_2/N_2 ratios. Similar to progress made in ocean-atmosphere modeling, one solution is to emphasize and attempt to reconcile model fluxes that occur between the ocean-atmosphere and land-ocean. Another is to actively pursue adding integrated carbon cycle dynamics into coupled (ocean-atmosphere-land) climate models.

Acknowledgements

We would like to thank our numerous colleagues and collaborators who have contributed to this chapter through formal and informal discussions, comments, and research material. We especially thank P. Falkowski, D. Feely, I. Fung, D. Glover, N. Gruber, J. Kleypas, I. Lima, F. Mackenzie, D. McGillicuddy, J. McWilliams, C. Sabine, and S. Smith. We also thank the editor of this volume, M. Fasham, and an anonymous reviewer for providing guidance and suggestions on the text. This work is supported in part by a NASA US Ocean Carbon Model Intercomparison Project (OCMIP Phase II) grant (NASA W-19,274), a NOAA-OGP Global Carbon Cycle grant (NOAA-NA96GP0360), and the NSF US JGOFS Synthesis and Modeling Project management grant (NSF 97308). The National Center for Atmospheric Research is sponsored by the US National Science Foundation.

References

Abbott MR (1995) Modeling the southern ocean ecosystem. GLOBEC Planning Report, 18, U.S. Global Ocean Ecosystem Dynamics (GLOBEC) Program, Berkeley, California, 63 pp

Archer D (1995) Upper ocean physics as relevant to ecosystem dynamics: a tutorial. Ecol Appl 5:724–739

Archer D, Maier-Raimer E (1994) Effect of deep-sea sedimentary calcite preservation on atmospheric CO_2 concentration. Nature 367:260–263

Archer D, Kheshgi H, Maier-Reimer E (1998) Dynamics of fossil fuel CO_2 neutralization by marine $CaCO_3$. Global Biogeochem Cy 12:259–276

Archer D, Eshel G, Winguth A, Broecker W (2000) Atmospheric CO_2 sensitivity to the biological pump in the ocean. Global Biogeochem Cy 14:1219–1230

Armstrong RA (1994) Grazing limitation and nutrient limitation in marine ecosystems: steady state solutions of an ecosystem model with multiple food chains. Limnol Oceanogr 39:597–608

Armstrong RA (1999a) Stable model structures for representing biogeochemical diversity and size spectra in plankton communities. J Plankton Res 21:445–464

Armstrong RA (1999b) An optimization-based model of iron-light ammonium colimitation of nitrate uptake and phytoplankton growth. Limnol Oceanogr 44:1436–1446

Bacastow R, Maier-Reimer E (1990) Ocean-circulation model of the carbon cycle. Clim Dynam 4:95–125

Behrenfeld MJ, Falkowski PG (1997) Photosynthetic rates derived from satellite-based chlorophyll concentration. Limnol Oceanogr 42:1–20

Bissett WP, Meyers MB, Walsh JJ (1994) The effects of temporal variability of mixed layer depth on primary productivity around Bermuda. J Geophys Res 99:7539–7553

Bissett WP, Walsh JJ, Carder KL (1999) Carbon cycling in the upper waters of the Sargasso Sea: I. Numerical simulation of differential carbon and nitrogen fluxes. Deep-Sea Res Pt I 46:205–269

Bopp L, Monfray P, Aumont O, Dufresne J-L, Le Treut H, Madec G, Terray L, Orr JC (2001) Potential impact of climate change on marine export production. Global Biogeochem Cy 15:81–99

Boyd P, Doney S (2003) The impact of climate change and feedback process on the ocean carbon cycle. Chap. 7. Springer-Verlag, (this volume)

Brewer PG, Goyet C, Dyrssen D (1989) Carbon dioxide transport by ocean currents at 25° N latitude in the Atlantic Ocean. Science 246:477–479

Broecker WS, Peng T-H (1992) Interhemispheric transport of carbon dioxide by ocean circulation. Nature 356:587–589

Broecker W, Lynch-Stieglitz J, Archer D, Hofmann M, Maier-Reimer E, Marchal O, Stocker T, Gruber N (1999) How strong is the Harvardton-Bear constraint? Global Biogeochem Cy 13:817–820

Capone DG, Zehr JP, Paerl HW, Bergman B, Carpenter EJ (1997) Trichodesmium: a globally significant cyanobacterium. Science 276:1221–1229

Carlson CA, Ducklow HW, Michaels AF (1994) Annual flux of dissolved organic carbon from the euphotic zone in the northwest Sargasso Sea. Nature 371:405–408

Case TJ (2000) An illustrated guide to theoretical ecology. Oxford University Press 4, 49 pp

Chai F, Lindley ST, Barber RT (1996) Origin and maintenance of high nutrient condition in the equatorial Pacific. Deep-Sea Res Pt II 42:1031–1064

Christian JR, Verschell MA, Murtugudde R, Busalacchi AJ, McClain CR (2001a) Biogeochemical modelling of the tropical Pacific Ocean. I. Seasonal and interannual variability. Deep-Sea Res Pt II 49:509–543

Christian JR, Verschell MA, Murtugudde R, Busalacchi AJ, McClain CR (2001b) Biogeochemical modelling of the tropical Pacific Ocean. II. Iron biogeochemistry. Deep-Sea Res Pt II 49:545–565

Conkright ME, Levitus S, O'Brien T, Boyer TP, Stephens C, Johnson D, Stathoplos L, Baranova O, Antonov J, Gelfeld R, Burney J, Rochester J, Forgy C (1998) World ocean atlas database 1998; CD-ROM data set documentation. National Oceanographic Data Center, Silver Spring, MD

Danabasoglu G, McWilliams JC, Gent PR (1994) The role of mesoscale tracer transports in the global ocean circulation. Science 264:1123–1126

Denman K, Hofmann E, Marchant H (1996) Marine biotic responses to environmental change and feedbacks to climate. In: Houghton JT, Meira LG Filho, Callander BA, Harris N, Kattenberg A, Maskell K (eds) Climate change 1995. IPCC, Cambridge University Press, pp 487–516

Denman KL, Pena MA (1999) A coupled 1-D biological/physical model of the northeast subarctic Pacific Ocean with iron limitation. Deep-Sea Res Pt II 46:2877–2908

Dickey T, Frye D, Jannasch H, Boyle E, Manov D, Sigurdson D, McNeil J, Stramska M, Michaels A, Nelson N, Siegel D, Chang G, Wu J, Knap A (1998) Initial results from the Bermuda testbed mooring program. Deep-Sea Res Pt I 45:771–794

Doney SC (1996) A synoptic atmospheric surface forcing data set and physical upper ocean model for the U.S. JGOFS Bermuda Atlantic Time-Series Study (BATS) site. J Geophys Res 101: 25615–25634

Doney SC (1999) Major challenges confronting marine biogeochemical modeling. Global Biogeochem Cy 13:705–714

Doney SC, Hecht MW (2002) Antarctic bottom water formation and deep water chlorofluorocarbon distributions in a global ocean climate model. J Phys Oceanogr 32:1642–1666

Doney SC, Sarmiento JL (eds) (1999) Synthesis and modeling project; ocean biogeochemical response to climate change. U.S. JGOFS Planning Report 22, U.S. JGOFS Planning Office, Woods Hole, MA, 105 pp

Doney SC, Glover DM, Najjar RG (1996) A new coupled, one-dimensional biological-physical model for the upper ocean: applications to the JGOFS Bermuda Atlantic Time Series (BATS) site. Deep-Sea Res Pt II 43:591–624

Doney SC, Large WG, Bryan FO (1998) Surface ocean fluxes and water-mass transformation rates in the coupled NCAR Climate System Model. J Climate 11:1422–1443

Doval M, Hansell DA (2000) Organic carbon and apparent oxygen utilization in the western South Pacific and central Indian Oceans. Mar Chem 68:249–264

Dutay J-C, Bullister JL, Doney SC, Orr JC, Najjar R, Caldeira K, Champin J-M, Drange H, Follows M, Gao Y, Gruber N, Hecht MW, Ishida A, Joos F, Lindsay K, Madec G, Maier-Reimer E, Marshall JC, Matear RJ, Monfray P, Plattner G-K, Sarmiento J, Schlitzer R, Slater R, Totterdell IJ, Weirig M-F, Yamanaka Y, Yool A (2001) Evaluation of ocean model ventilation with CFC-11: comparison of 13 global ocean models. Ocean Modelling 4: 89–120

Dutkiewicz S, Follows M, Marshall J, Gregg WW (2001) Interannual variability of phytoplankton abundances in the North Atlantic. Deep-Sea Res Pt II 48:2323–2344

England MH (1995) Using chlorofluorocarbons to assess ocean climate models. Geophys Res Lett 22:3051–3054

England MH, Maier-Reimer E (2001) Using chemical tracers to assess ocean models. Rev Geophys 39:29–70

Evans GT, Fasham MJR (ed) (1993) Towards a model of ocean biogeochemical processes. Springer-Verlag, New York

Evans GT, Garçon VC (ed) (1997) One-dimensional models of water column biogeochemistry. JGOFS Report 23/97, 85 pp., JGOFS, Bergen, Norway

Evans GT, Parslow JS (1985) A model of annual plankton cycles. Biolo Oceanogr 3:327–347

Falkowski PG, Biscaye PE, Sancetta C (1994) The lateral flux of biogenic particles from the eastern North American continental margin to the North Atlantic Ocean. Deep-Sea Res Pt II 41: 583–601

Fasham MJR (1993) Modelling the marine biota. In: Heimann M (ed) The global carbon cycle. Springer-Verlag, Heidelberg, pp 457–504

Fasham MJR (1995) Variations in the seasonal cycle of biological production in subarctic oceans: a model sensitivity analysis. Deep-Sea Res Pt I 42:1111–1149

Fasham MJR, Evans GT (1995) The use of optimisation techniques to model marine ecosystem dynamics at the JGOFS station at 47° N and 20° W. Philos T Roy Soc B 348:206–209

Fasham MJR, Ducklow HW, McKelvie SM (1990) A nitrogen-based model of plankton dynamics in the oceanic mixed layer. J Mar Res 48:591–639

Fennel K, Losch M, Schröter J, Wenzel M (2001) Testing a marine ecosystem model: sensitivity analysis and parameter optimization. J Marine Syst 28:45–63

Fennel K, Spitz YH, Letelier RM, Abbott MR, Karl DM (2002) A deterministic model for N_2-fixation at the HOT site in the subtropical North Pacific. Deep-Sea Res II 49:149–174

Francis RC, Hare SR (1994) Decadal-scale regime shifts in the large marine ecosystems of the North-east Pacific: a case for historical science. Fish Oceanogr 3:279–291

Frost BW (1987) Grazing control of phytoplankton stock in the subarctic Pacific: a model assessing the role of mesozooplankton, particularly the large calanoid copepods, *Neocalanus* spp. Mar Ecol Prog Ser 39:49–68

Fung IY, Meyn SK, Tegen I, Doney SC, John JG, Bishop JKB (2000) Iron supply and demand in the upper ocean. Global Biogeochem Cy 14:281–295

Garçon VC, Oschlies A, Doney SC, McGillicuddy D, Waniek J (2001) The role of mesoscale variability on plankton dynamics. Deep-Sea Res Pt II 48:2199–2226

Geider RJ, MacIntyre HL, Kana TM (1996) A dynamic model of photoadaptation in phytoplankton. Limnol Oceanogr 41:1–15

Geider RJ, MacIntyre HL, Kana TM (1998) A dynamic regulatory model of phytoplankton acclimation to light, nutrients, and temperature. Limnol Oceanogr 43:679–694

Gent PR, McWilliams JC (1990) Isopycnal mixing in ocean circulation models. J Phys Oceanogr 20:150–155

Gent PR, Bryan FO, Danabasoglu G, Doney SC, Holland WR, Large WG, McWilliams JC (1998) The NCAR Climate System Model global ocean component. J Climate 11:1287–1306

Giering R, Kaminski T (1998) Recipes for adjoint code construction. Acm t math software 24:437–474

Gnanadesikan A (1999) A global model of silicon cycling: sensitivity to eddy parameterization and dissolution. Global Biogeochem Cy 13:199–220

Gnanadesikan A, Toggweiler JR (1999) Constraints placed by silicon cycling on vertical exchange in general circulation models. Geophys Res Lett 26:1865–1868

Gnanadesikan A, Slater R, Gruber N, Sarmiento JL (2001) Oceanic vertical exchange and new production: a comparison between models and observations. Deep-Sea Res Pt II 49:363–401

Gregg WW (2002) Tracking the SeaWiFS record with a coupled physical/biogeochemical/radiative model of the global oceans. Deep-Sea Res Pt II 49:81–105

Griffes SM, Böning C, Bryan FO, Chassignet EP, Gerdes R, Hasumi H, Hirst A, Treguer A-M, Webb D (2000) Developments in ocean climate modelling, vol. 2. pp 123–192

Gruber N (1998) Anthropogenic CO_2 in the Atlantic Ocean. Global Biogeochem Cy 12:165–191

Gruber N, Sarmiento JL (1997) Global patterns of marine nitrogen fixation and denitrification. Global Biogeochem Cy 11: 235–266

Gruber N, Sarmiento JL, Stocker TF (1996) An improved method for detecting anthropogenic CO_2 in the oceans. Global Biogeochem Cy 10:809–837

Gruber N, Gloor M, Fan SM, Sarmiento JL (2001) Air-sea flux of oxygen estimated from bulk data: implications for the marine and atmospheric oxygen cycle. Global Biogeochem Cy 15(4): 783–803

Haidvogel DB, Beckmann A (1999) Numerical ocean circulation modeling. Imperial College Press, London, 318 pp

Haidvogel DB, Curchitser E, Iskandarani M, Hughes R, Taylor M (1997) Global modeling of the ocean and atmosphere using the spectral element method. Atmos Ocean 35:505–531

Hansell DA, Carlson CA (1998) Net community production of dissolved organic carbon. Global Biogeochem Cy 12:443–453

Harris RP (1994) Zooplankton grazing on the coccolithophore *Emiliania huxleyi* and its role in inorganic carbon flux. Mar Biol 119:431–439

Harrison DE (1996) Vertical velocity variability in the tropical Pacific: a circulation model perspective for JGOFS. Deep-Sea Res Pt II 43:687–705

Hecht MW, Wingate BA, Kassis P (2000) A better, more discriminating test problem for ocean tracer transport. Ocean Modelling 2:1–15

Heinze C, Maier-Reimer E, Schlosser P (1998) Transient tracers in a global OGCM: source functions and simulated distributions. J Geophys Res 103:15903–15922

Heinze C, Maier-Reimer E, Winguth AME, Archer D (1999) A global oceanic sediment model for long-term climate studies. Global Biogeochem Cy 13:221–250

Holfort J, Johnson KM, Wallace DWR (1998) Meridional transport of dissolved inorganic carbon in the South Atlantic Ocean. Global Biogeochem Cy 12:479–499

Holligan PM, Fernandez E, Aiken J, Balch WM, Boyd P, Burkill PH, Finch M, Groom SB, Malin O, Muller K, Purdie DA, Robinson C, Trees CC, Turner SM, van del Wal P (1993) A biogeochemical study of the coccolithophore *Emiliania huxleyi* in the North Atlantic. Global Biogeochem Cy 7:879–900

Hood RR, Bates NR, Olson DB (2001) Modeling the seasonal to interannual biogeochemical and N_2 fixation cycles at BATS. Deep-Sea Res Pt II 48:1609–1648

Hurtt GC, Armstrong RA (1996) A pelagic ecosystem model calibrated with BATS data. Deep-Sea Res Pt II 43:653–683

Ishizaka J (1990) Coupling of Coastal Zone Color Scanner data to a physical-biological model of the Southeastern U.S. continental shelf ecosystem, 3, nutrient and phytoplankton fluxes and CZCS data assimilation. J Geophys Res 95:20201–20212

Joos F, Siegenthaler U, Sarmiento JL (1991) Possible effects of iron fertilization in the Southern Ocean on atmospheric CO_2 concentration. Global Biogeochem Cy 5:135–150

Joos F, Plattner O-K, Schmittner A (1999) Global warming and marine carbon cycle feedbacks on future atmospheric CO_2. Science 284:464–467

Karl DM (1999) A sea of change: biogeochemical variability in the North Pacific subtropical gyre. Ecosystems 2:181–214

Karl DM, Letelier R, Hebel D, Tupas L, Dore J, Christian J, Winn C (1995) Ecosystem changes in the North Pacific subtropical gyre attributed to the 1991–1992 El Niño. Nature 378:230–234

Karl D, Letelier R, Tupas L, Dore J, Christian J, Hebel D (1997) The role of nitrogen fixation in biogeochemical cycling in the subtropical North Pacific Ocean. Nature 388:533–538
Kasibhatla P, Heimann M, Rayner P, Mahowald N, Prinn RG, Hartley DE (ed) (2000) Inverse methods in global biogeochemical cycles. AGU Geophysical. Monograph Series, American Geophysical Union, Washington D.C., 324 pp
Keeling RF, Piper SC, Heimann M (1996) Global and hemispheric CO_2 sinks deduced from changes in atmospheric O_2 concentration. Nature 381:218–221
Kleypas JA, Doney SC (2001) Nutrients, chlorophyll, primary production and related biogeochemical properties in the ocean mixed layer – a compilation of data collected at nine JGOFS sites. NCAR Technical Report, NCAR/TN–447+STR, 53 pp
Kleypas JA, Buddemeier RW, Archer D, Gattuso J-P, Langdon C, Opdyke BN (1999) Geochemical consequences of increased atmospheric carbon dioxide on coral reefs. Science 284:118–120
Large WG, McWilliams JC, Doney SC (1994) Oceanic vertical mixing: a review and a model with a nonlocal boundary layer parameterization. Rev Geophys 32:363–403
Large WG, Danabasoglu G, Doney SC, McWilliams JC (1997) Sensitivity to surface forcing and boundary layer mixing in a global ocean model: annual-mean climatology. J Phys Oceanogr 27:2418–2447
Laws EA, Falkowski PG, Smith WO Jr., Ducklow H, McCarthy JJ (2000) Temperature effects on export production in the open ocean. Global Biogeochem Cy 14:1231–1246
Le Quéré C, Orr JC, Monfray P, Aumont O, Madec G (2000) Interannual variability of the oceanic sink of CO_2 from 1979 though 1997. Global Biogeochem Cy 14:1247–1265
Leonard CL, McClain CR, Murtugudee R, Hofmann EE, Harding JLW (1999) An iron-based ecosystem model of the central equatorial Pacific. J Geophys Res 104:1325–1341
Letelier RM, Abbott MR (1996) An analysis of chlorophyll fluorescence for the Moderate Resolution Imaging Spectrometer (MODIS). Remote Sens Environ 58:215–223
Letelier R, Karl D (1996) Role of *Trichodesmium* spp. in the productivity of the subtropical North Pacific Ocean. Mar Ecol Prog Ser 133:263–273
Letelier R, Karl D (1998) *Trichodesmium* spp. physiology and nutrient fluxes in the North Pacific subtropical gyre. Aquat Microb Ecol 15:265–276
Levitus S, Conkright ME, Reid JL, Najjar RG, Mantilla A (1993) Distribution of nitrate, phosphate and silicate in the world oceans. Prog Oceanogr 31:245–273
Levitus S, Burgett R, Boyer T (1994) World atlas 1994. NOAA Atlas NESDIS, U.S. Dept. of Commerce, Washington D.C.
Levy M, Memery L, Madec G (1999) Combined effects of mesoscale processes and atmospheric high-frequency variability on the spring bloom in the MEDOC area. Deep-Sea Res Pt I 47:27–53
Lima I, Doney S, Bryan F, McGillicuddy D, Anderson L, Maltrud M (1999) Preliminary results from an eddy-resolving ecosystem model for the North Atlantic. EOS, Transactions AGU, 80(49), Ocean Sciences Meeting Supplement, OS28
Lima ID, Olson DB, Doney SC (2002) Biological response to frontal dynamics and mesoscale variability in oligotrophic environments: a numerical modeling study. J Geophys Res (in press)
Lipschultz F, Owens NJP (1996) An assessment of nitrogen fixation as a source of nitrogen to the North Atlantic. Biogeochemistry 35:261–274
Liu K-K, Atkinson L, Chen CTA, Gao S, Hall J, Macdonald RW, Talaue McManus L, Quiñones R (2000) Exploring continental margin carbon fluxes on a global scale. EOS, Transactions of the American Geophysical Union 81:641–644
Louanchi F, Najjar RG (2000) A global monthly mean climatology of phosphate, nitrate and silicate in the upper ocean: spring–summer production and shallow remineralization. Global Biogeochem Cy 14:957–977
Mahadevan A, Archer D (2000) Modeling the impact of fronts and mesoscale circulation on the nutrient supply and biogeochemistry of the upper ocean. J Geophys Res 105:1209–1225
Maier-Reimer E (1993) Geochemical cycles in an ocean general circulation model. Preindustrial tracer distributions. Global Biogeochem Cy 7:645–677
Maier-Reimer E, Hasselmann K (1987) Transport and storage in the ocean – an inorganic ocean-circulation carbon cycle model. Clim Dynam 2:63–90
Martin JH, Knauer GA, Karl DM, Broenkow WW (1987) VERTEX: carbon cycling in the northeast Pacific. Deep-Sea Res 34:267–285
Matear RJ (1995) Parameter optimization and analysis of ecosystem models using simulated annealing: a case study at Station P. J Mar Res 53:571–607
Matear RJ, Hirst AC (1999) Climate change feedback on the future oceanic CO_2 uptake. Tellus B 51:722–733
Matear RJ, Holloway G (1995) Modeling the inorganic phosphorus cycle of the North Pacific using an adjoint data assimilation model to assess the role of dissolved organic phosphorus. Global Biogeochem Cy 9:101–119
May RM (1973) The stability and complexity of model ecosystems. Princeton University Press, Princeton New Jersey, 265 pp
McClain CR, Arrigo K, Turk D (1996) Observations and simulations of physical and biological processes at ocean weather station P, 1951–1980. J Geophys Res 101:3697–3713
McClain CR, Cleave ML, Feldman GC, Gregg WW, Hooker SB, Kuring N (1998) Science quality SeaWiFS data for global biosphere research. Sea Technol 39:10–14
McCreary JP, Kohler KH, Hood RR, Olson DB (1996) A four compartment ecosystem model of biological activity in the Arabian Sea. Prog Oceanogr 37:193–240
McGillicuddy DJ Jr., Robinson AR (1997) Eddy-induced nutrient supply and new production. Deep-Sea Res Pt I 44:1427–1450
McGillicuddy DJ Jr., Robinson AR, Siegel DA, Jannasch HW, Johnson R, Dickey TD, McNeil J, Michaels AF, Knap AH (1998) Influence of mesoscale eddies on new production in the Sargasso Sea. Nature 394:263–266
McGowan JA, Cayan DR, Dorman LM (1998) Climate-ocean variability and ecosystem response in the Northeast Pacific. Science 281:210–217
McWilliams JC (1996) Modeling the oceanic general circulation. Annu Rev Fluid Mech 28:215–248
Milliman JD (1993) Production and accumulation of calcium carbonate in the ocean: budget of a nonsteady state. Global Biogeochem Cy 7:927–957
Milliman JD, Troy PJ, Balch WM, Adams AK, Li YH, Mackenzie FT (1999) Biologically mediated dissolution of calcium carbonate above the chemical lysocline? Deep-Sea Res Pt I 46:1653–1669
Moloney CL, Field JG (1991) The size-based dynamics of plankton food webs. I. A simulation model of carbon and nitrogen flows. J Plankton Res 13:1003–1038
Moore JK, Doney SC, Kleypas JA, Glover DM, Fung IY (2001a) An intermediate complexity marine ecosystem model for the global domain. Deep-Sea Res Pt II 49:403–462
Moore JK, Doney SC, Kleypas JA, Glover DM, Fung IY (2001b) Iron cycling and nutrient limitation patterns in surfce waters of the world ocean. Deep-Sea Res Pt II 49:463–507
Murnane RJ, Sarmiento JL, Le Quéré C (1999) Spatial distribution of air-sea CO_2 fluxes and the interhemispheric transport of carbon by the oceans. Global Biogeochem Cy 13:287–305
Najjar RG, Sarmiento JL, Toggweiler JR (1992) Downward transport and fate of organic matter in the ocean: simulations with a general circulation model. Global Biogeochem Cy 6:45–76
Oeschger H, Siegenthaler U, Guglemann A (1975) A box-diffusion model to study the carbon dioxide exchange in nature. Tellus 27:168–192
Orr JC, Maier-Reimer E, Mikolajewicz U, Monfray P, Sarmiento JL, Toggweiler JR, Taylor NK, Palmer J, Gruber N, Sabine CL, Le Quéré C, Key RM, Boutin J (2001) Estimates of anthropogenic carbon uptake from four three-dimensional global ocean models. Global Biogeochem Cy 15:43–60
Oschlies A (2000) Equatorial nutrient trapping in biogeochemical ocean models: the role of advection numerics. Global Biogeochem Cy 14:655–667
Oschlies A, Garçon V (1998) Eddy-induced enhancement of primary production in a model of the North Atlantic Ocean. Nature 394:266–269
Oschlies A, Garçon V (1999) An eddy-permitting coupled physical-biological model of the North Atlantic-1. Sensitivity to advection numerics and mixed layer physics. Global Biogeochem Cy 13:135–160

Polovina JJ, Mitchum GT, Evans GT (1995) Decadal and basin-scale variation in mixed layer depth and the impact on biological production in the Central and North Pacific, 1960–88. Deep-Sea Res Pt I 42:1701–1716
Pondaven P, Ruiz-Pino D, Jeandel C (2000) Interannual variability of Si and N cycles at the time-series station KERFIX between 1990 and 1995 – a 1-D modelling study. Deep-Sea Res Pt I 47:223–257
Rayner PJ, Enting IG, Francey RJ, Langenfelds R (1999) Reconstructing the recent carbon cycle from atmospheric CO_2, $d13C$ and O2/N2 observations. Tellus B 51:213–232
Reid PC, Edwards M, Hunt HG, Warner AJ (1998) Phytoplankton change in the North Atlantic. Nature 391:546
Riley GA (1946) Factors controlling phytoplankton populations on Georges Bank. J Mar Res 6:54–73
Rintoul SR, Wunsch C (1991) Mass, heat, oxygen and nutrient fluxes and budgets in the North Atlantic Ocean. Deep-Sea Res 38 (suppl.) S355–S377
Roberts M, Marshall D (1998) Do we require adiabatic dissipation schemes in eddy-resolving ocean models? J Phys Oceanogr 28:2050–2063
Robinson AR (1996) Physical processes, field estimation and an approach to interdisciplinary ocean modeling. Earth-Sci Rev 40:3–54
Robinson AR, McCarthy JJ, Rothschild BJ (2001) The sea: biological-physical interactions in the ocean. John Wiley & Sons, New York
Ryabchenko VA, Gorchakov VA, Fasham MJR (1998) Seasonal dynamics and biological productivity in the Arabian Sea euphotic zone as simulated by a three-dimensinoal ecosystem model. Global Biogeochem Cy 12:501–530
Sabine CL, Key RM, Goyet C, Johnson KM, Millero FJ, Poisson A, Sarmiento JL, Wallace DWR, Winn CD (1999) Anthropogenic CO_2 inventory in the Indian Ocean. Global Biogeochem Cy 13:179–198
Sarmiento JL, Sundquist ET (1992) Revised budget for the oceanic uptake of anthropogenic carbon dioxide. Nature 356:589–593
Sarmiento JL, Wofsy SC (1999) A U.S. Carbon Cycle Science Plan. (U.S. CCSP 1999), U.S. Global Change Research Program, Washington DC, 69 pp
Sarmiento JL, Orr JC, Siegenthaler U (1992) A perturbation simulation of CO_2 uptake in an ocean general circulation model. J Geophys Res 97:3621–3646
Sarmiento JL, Slater RD, Fasham MJR (1993) A seasonal three-dimensional ecosystem model of nitrogen cycling in the North Atlantic euphotic zone. Global Biogeochem Cy 7:417–450
Sarmiento JL, Hughes TMC, Stouffer RJ, Manabe S (1998) Simulated response of the ocean carbon cycle to anthropogenic climate warming. Nature 393:245–249
Sarmiento JL, Monfray P, Maier-Reimer E, Aumont O, Murnane RJ, Orr JC (2000) Sea-air CO_2 fluxes and carbon transport: a comparison of three ocean general circulation models. Global Biogeochem Cy 14:1267–1281
Schimel D, Enting IG, Heimann M, Wigley TML, Raynaud D, Alves D, Siegenthaler U (1995) CO_2 and the carbon cycle. In: Houghton JT, Meira Filho LG, Bruce J, Lee H, Callander BA, Haites E, Harris N, Maskell K (eds) Climate change 1994. Intergovernmental Panel on Climate Change. Cambridge University Press, pp 39–71
Schlitzer R (2000) Applying the adjoint method for global biogeochemical modeling. In: Kasibhatla P, et al. (eds) Inverse methods in global biogeochemical cycles. AGU Geophysical Monograph Series, American Geophysical Union, Washington D.C., pp 107–124
Siegenthaler U, Joos F (1992) Use of a simple model for studying oceanic tracer distributions and the global carbon cycle. Tellus B 44:186–207
Siegenthaler U, Oeschger H (1978) Predicting future atmospheric carbon dioxide levels. Science 199:388–395
Siegenthaler U, Sarmiento JL (1993) Atmospheric carbon dioxide and the ocean. Nature 365:119–125
Six KD, Maier-Reimer E (1996) Effects of plankton dynamics on seasonal carbon fluxes in an ocean general circulation model. Global Biogeochem Cy 10:559–583
Smith RD, Maltrud ME, Bryan FO, Hecht MW (2000) Numerical simulation of the North Atlantic at 1/10°. J Phys Oceanogr 30:1532–1561
Smith SV, Hollibaugh JT (1993) Coastal metabolism and the oceanic organic carbon balance. Rev Geophys 31:75–89
Spall MA, Holland WR (1991) A nested primitive equation model for oceanic applications. J Phys Oceanogr 21:205–220
Spall SA, Richards KJ (2000) A numerical model of mesoscale frontal instabilities and plankton dynamics. I. Model formulation and initial experiments. Deep-Sea Res Pt I 47:1261–1301
Spitz YH, Moisan JR, Abbott MR, Richman JG (1998) Data assimilation and a pelagic ecosystem model: parameterization using time series observations. J Marine Syst 16:51–68
Steele JH (1958) Plant production in the northern North Sea. Mar Res 7:1–36
Steele JH (1974) The structure of marine ecosystems. Harvard University Press, Cambridge, MA, 128 pp
Stephens BB, Keeling RF (2000) The influence of Antarctic sea ice on glacial/interglacial CO_2 variations. Nature 404:171–174
Stocker TF, Broecker WS, Wright DG (1994) Carbon uptake experiments with a zonally-averaged global ocean circulation model. Tellus B 46:103–122
Sunda WG, Huntsman SA (1995) Iron uptake and growth limitation in oceanic and coastal phytoplankton. Mar Chem 50:189–206
Takahashi T, Feely RA, Weiss RF, Wanninkhof RH, Chipman DW, Sutherland SC, Takahashi TT (1997) Global air-sea flux of CO_2, An estimate based on measurements of sea-air pCO_2 difference. P Natl Acad Sci USA 94:8929–8299
Takahashi T, Wanninkhof RH, Feely RA, Weiss RF, Chipman DW, Bates N, Olafson J, Sabine C, Sutherland SC (1999) Net air-sea CO_2 flux over the global oceans: an improved estimate based on the sea-air pCO_2 difference. In: Center for Global Environmental Research, National Institute for Environmental Studies (ed) Proceedings of the 2nd International Symposium on CO_2 in the Oceans. Tsukuba, Japan, pp 9–15
Tegen I, Fung I (1995) Contribution to the atmospheric mineral aerosol load from land surface modification. J Geophys Res 100:18,707–18,726
Toggweiler JR (1999) Variation of atmospheric CO_2 by ventilation of the ocean's deepest water. Paleoceanography 14:571–588
Toggweiler JR, Dixon K, Bryan K (1989a) Simulations of radiocarbon in a coarse-resolution world ocean model; 1. Steady state pre-bomb distribution. J Geophys Res 94:8217–8242
Toggweiler JR, Dixon K, Bryan K (1989b) Simulations of radiocarbon in a coarse-resolution world ocean model; 2. Distributions of bomb-produced carbon-14. J Geophys Res 94:8243–8264
US Joint Global Ocean Flux Study (US JGOFS) (1992) Report of the U.S. JGOFS Workshop on Modeling and Data Assimilation. Planning Report Number 14, U.S. JGOFS Planning Office, Woods Hole, MA, 28 pp
Venrick EL, McGowan JA, Cayan DR, Hayward TL (1987) Climate and chlorophyll *a*: longterm trends in the central North Pacific Ocean. Science 238:70–72
Wallace DWR (1995) Monitoring global ocean carbon inventories. Ocean Observing System Development Panel Background, Texas A&M University, College Station, TX, 54 pp
Wallace DWR (2001) Storage and transport of excess CO_2 in the oceans: the JGOFS/WOCE Global CO_2 survey. In: Siedler G, Gould J, Church J (eds) Ocean circulation and climate: observing and modeling the global ocean. Academic Press, New York
Walsh JJ (1991) Importance of continental margins in the marine biogeochemical cycling of carbon and nitrogen. Nature 350:53–55
Wanninkhof R (1992) Relationship between wind speed and gas exchange over the ocean. J Geophys Res 97:7373–7382
Wanninkhof R, Doney SC, Peng T-H, Bullister J, Lee K, Feely RA (1999) Comparison of methods to determine the anthropogenic CO_2 invasion into the Atlantic Ocean. Tellus B, 51:511–530
Watson AJ, Orr JC (2003) Carbon dioxide fluxes in the global ocean. Springer-Verlag, (this volume)
Webb DJ, deCuevas BA, Richmond CS (1998) Improved advection schemes for ocean models. J Atmos Ocean Tech 15:1171–1187
Yamanaka Y, Tajika E (1996) The role of the vertical fluxes of particulate organic matter and calcite in the oceanic carbon cycle: studies using an ocean biogeochemical general circulation model. Global Biogeochem Cy 10:361–382

Contents

Chapter 8

Integration of ODE's and 0-D (Box) Models

> "God does not care about our mathematical difficulties; He integrates empirically." *Albert Einstein*

Up to now we have been talking about data analysis, interpreting one's data with an underlying model in mind or exploring one's data looking for clues as to what model might apply. Now we transition into modeling, building models to generate, for lack of a better word, *computa* (also known as *model output* or sometimes *synthetic data*). We will start with simple models written in the form of ordinary differential equations (ODE), these are characterized by a single, independent variable (*e.g*, time or space). Ordinary differential equations can be written in general form as:

$$\frac{dC}{dx} = f(C, x, \text{constants}) \tag{8.1}$$

In this chapter, we show how to compute $C(x)$ from a single ODE or a set of coupled ODEs and present some important applications, namely *box models*.

8.1 ODE Categorization

The study of differential equations is aided by a system of categorization that, if nothing else, makes them easier to talk about. Differential equations are broken down by type, order, degree, homogeneity, linearity, and boundary conditions, the last of which is perhaps the most important when it comes to numerically solving differential equations.

8.1.1 Types

Differential equations are broadly divided into two kinds: ordinary and partial. This chapter will focus on ordinary differential equations (ODE) and Chapter **??** will introduce a key technique for numerically dealing with partial differential equations (*i.e.*, finite difference equations). Ordinary differential equations occur when the dependent variable (C, for concentration or y or N, the thing

we are modeling) is a function of a single independent variable (x or t, the dimension over which our model is varying). Partial differential equations (PDE) occur when the dependent variable is a function of multiple independent variables (x, y, z, *etc.*), but only one of which is allowed to vary in the evaluation of a specific differential operator. In short, if the equations contain an ordinary d as the differential operator, then the equation is an ordinary differential equation, if the differential operator is one of those funny "backward sixes", ∂, then it's a partial differential equation.

8.1.2 Order

The order of a differential equation is given by the highest-order derivative of the dependent variable. For example:

$$\frac{d^3C}{dx^3} + \left(\frac{dC}{dx}\right)^2 - e^{-\lambda C} = 0 \tag{8.2}$$

is a third order ODE.

8.1.3 Degree

The degree of a differential equation is given by the highest exponent of the highest-order derivative of the dependent variable, once the equation has been cleared of fractions and radicals in the dependent variable and derivatives. As an example:

$$\left(\frac{d^3C}{dx^3}\right)^2 + \left(\frac{d^2C}{dx^2}\right)^5 + \frac{C}{x^2+1} = e^x \tag{8.3}$$

is a third order ODE of degree two.

8.1.4 Homogeneous and nonhomogeneous equations

A homogeneous ODE is one in which every term contains the dependent variable or its derivative. For example:

$$a_2\frac{d^2C}{dx^2} + a_1\frac{dC}{dx} + a_\circ C = 0 \tag{8.4}$$

is homogeneous if the a's are constant or functions of x only. An equation of the form:

$$a_2\frac{d^2C}{dx^2} + a_1\frac{dC}{dx} + a_\circ C = x^2 \tag{8.5}$$

is nonhomogeneous (or inhomogeneous) because there is a term which does not depend on the dependent variable (C).

Remembering from calculus, the sum of solutions to a differential equation are solutions to the differential equation, we can use the relationship between homogeneous and inhomogeneous

differential equations when solving analytically. The solution to an homogeneous differential equation is a general class of solutions. To find the specific solution for an inhomogeneous differential equation solve the homogeneous equation first, then add the particular solution (usually based on boundary or initial conditions) for the inhomogeneous term.

8.1.5 Linear and nonlinear equations

This distinction follows the same definition we use in describing other kinds of equations. Equations 8.4 and 8.5 are linear so long as the a's are constant or a function of x only. Some other examples are:

$$\frac{dN}{dt} = -\lambda N \tag{8.6}$$

$$F = -D\frac{dC}{dx} \tag{8.7}$$

as first order, linear, homogeneous differential equations. You may recognize Eqn 8.6 as the radioactive decay equation and Eqn 8.7 as Fick's First Law.

8.1.6 Initial and boundary value problems

Simply put, *initial value* problems are differential equation problems where all C_i are given at an initial time (or x) and the problem is to find or predict all C_i until some final time (or x). *Boundary value* problems typically have multiple x's (or t's) specified around the boundary of the modeling domain and the trick is the solve for all positions within the domain simultaneous. Initial value problems have a starting point and are integrated forward (in time or space) to a final position. Boundary value problems cannot be solved in this manner (*i.e.*, integrating inward from the edges) as this tends to be a numerically unstable thing to do and there's no guarantee that everything will match when we get to the center. Typically this is done with iterative techniques or matrix inversions that converge on a stable answer.

8.2 Examples of Box Models (0-D)

Box models are ubiqutous in ocean biology and geochemistry as simple "teaching tools" to research grade investigations (Case, 1999). Frequently the "type" of box model comes down to the type of equations (differential equations) that describe the system you are modeling. The solution you come up with can vary from analytical to complicated numerical solutions. Because biological models are important in any understanding of the biogeochemical processes that occur at the earth's surface and because they provide good examples of the various types of equations that occur in 0-D box models, we will use them in this section to illustrate some basic model "types".

8.2.1 Exponential growth models

Here we discuss simple homogeneous ordinary differential equations of one dependent and one independent variable (usually time, the *zero*-D refers normally to spatial dimensions). Consider simple birth-death biological models (sometimes called *exponential growth* models); the deterministic birth model can be written as:

$$\frac{dN}{dt} = \mu N \tag{8.8}$$

where N is the number of individuals (population) or the concentration of biomoass and μ is the birth (growth) rate. A deterministic loss model can be written as:

$$\frac{dN}{dt} = -\lambda N \tag{8.9}$$

where here λ is the death rate but could also reflect other loss process such a removal *via* sinking or advection out of the system. Simple birth-death models are just the sum of the two:

$$\frac{dN}{dt} = \mu N - \lambda N = (\mu - \lambda)\, N \tag{8.10}$$

which, of course, can be solved analytically as:

$$N = N_\circ e^{(\mu-\lambda)t} \tag{8.11}$$

Box models based on analytical solutions like this assume that nothing limits growth. If $\mu > \lambda$, the population grows to infinity, and if $\lambda > \mu$, then the population will become extinct. The population is only stable when $\mu = \lambda$.

8.2.2 Carrying capacity models

The next step is to move to equations where something in the environment keeps the population from growing without bounds; this can be represented as a *carrying capacity* of the environment. We introduce something to limit growth (other than death) to the equation(s). We rewrite the birth-death equation as:

$$\frac{dN}{dt} = N f(N) \tag{8.12}$$

where

$$f(N) = \mu - sN \tag{8.13}$$

and μ and s are positive constants. This is the simplest linear representation of an inhibitory effect, because as N gets large df/dt becomes negative. Recombining we get:

$$\frac{dN}{dt} = N(\mu - sN) \tag{8.14}$$

which is also known as the *logistic equation*. If we let μ be the net growth rate in unlimited conditions (absence of regulation) and s be the effect of a N-sized population on growth, then we can define $k = \mu/s$ as the carrying capacity. This gives:

$$f(N) = \mu\left(1 - \frac{N}{k}\right) \tag{8.15}$$

and

$$\frac{dN}{dt} = \mu N\left(1 - \frac{N}{k}\right) \tag{8.16}$$

Now this has, up to now, all been for a single population. How do the equations change for two (or more) tracers that interact? Again population dynamics provide some good examples.

8.2.3 Coupled linear 1$^{\text{st}}$ order ODEs

Coupled ODEs arise when there is interaction between the dependent variables. This is when the RHS of the ODE for variable N_1 contains terms with other dependent variables. Consider competition which comes into play when there are two or more populations competing for the same resource(s) (*e.g.*, space, light, nutrients, computer time). First let's consider the logistic growth equation rewritten for two populations:

$$\begin{aligned} \frac{dN_1}{dt} &= (\mu_1 - s_{11}N_1 - s_{12}N_2)N_1 \\ \frac{dN_2}{dt} &= (\mu_2 - s_{21}N_1 - s_{22}N_2)N_2 \end{aligned} \tag{8.17}$$

where s_{11} refers to competition within species (*i.e.*, members of N_1 competing amongst themselves) and s_{21} competition between species (N_1 *vs.* N_2). This can be simplified by assuming that within species and between species competition is basically the same for any given resource (*i.e.*, $s_{11}s_{22} = s_{12}s_{21}$).

$$\begin{aligned} \frac{dN_1}{dt} &= [\mu_1 - s_1(N_1 + pN_2)]\, N_1 \\ \frac{dN_2}{dt} &= [\mu_2 - s_2(N_1 + pN_2)]\, N_2 \end{aligned} \tag{8.18}$$

where p is an amplification factor that can be either ≥ 1 or < 1. Now all of this assumes that the two competing populations are in competition for a resource rather than one another. What do the

equations look like when a *predator-prey* type of relation exists? Predation, after all, is only an intense form of competition.

Let's let N_1 be the prey population and N_2 be the predator population. Then:

$$\begin{aligned} \frac{dN_1}{dt} &= N_1(\mu_1 - b_1 N_2) \\ \frac{dN_2}{dt} &= N_2(-s_2 + b_2 N_1) \end{aligned} \tag{8.19}$$

where μ_1 is the prey growth rate, s_2 the predator death rate, b_1 the rate prey is eaten by predators, and b_2 the rate at which the predator grows from eating the prey. This is known as the *Lotka-Volterra* predator-prey model.

8.2.4 Higher order ODEs

It can be shown that any higher order ODE can be rewritten as a set of coupled first order ODEs. Take for example:

$$\frac{d^2y_1}{dt^2} - \mu(1 - y_1^2)\frac{dy_1}{dt} + y_1 = 0 \tag{8.20}$$

if we let $dy_1/dt = y_2$ then:

$$\frac{d^2y_1}{dt^2} = \frac{dy_2}{dt} \tag{8.21}$$

Through substitution:

$$\begin{aligned} \frac{dy_1}{dt} &= y_2 \\ \frac{dy_2}{dt} &= \mu(1 - y_1^2)y_2 - y_1 \end{aligned} \tag{8.22}$$

where we have converted the original equation into a pair (or system) of *coupled*, first order ODEs. This example is known as the *van der Pol equation*.

8.3 Analytical Solutions

Before we dive into the numerical techniques that exist for integrating ODEs, we would be remiss indeed if we failed to mention that many ODE's do have analytical solutions as well. We will discuss here three of the most common "tricks" used to find analytical solutions to ordinary differential equations.

Now some of you may be wondering why we discuss analytical solutions at all, isn't this a book about numerical techniques? Yes it is, but analytical solutions can be very useful in testing

numerical methods. Many times your problem can be simplified to an ODE that has an analytical solution. Even if the simplified form is not close enough to your real problem to be a useful solution, testing to make sure your numerical and analytical forms give the same results will give you confidence in your numerical solution of the more complex problem. Further, analytical solutions of simpler equations can be used to bracket your solution space.

A word about finding analytical solutions. It can be intellectually challenging and it can also be very time consuming. Most of the ODE's (that have an analytical solution) have been collected in extensive tables of integrals, published by the CRC and others. This amounts to the ultimate trick in finding analytical solutions, using standard math tabels. One particularly useful collection can be found in the *CRC Standard Mathematical Tables* (Zwillinger, 2002). There are no prizes for reinventing the wheel, and although it may not look like it, your ODE can often be rearranged to fit one of these standard forms if it has an analytical solution at all. So here is our advice — if you need (or want) an analytical solution to your differential equation, look in the standard integral tables first. Another approach, which we will not discuss in detail would be to use a symbolic math package (MATLAB, Mathematica, *etc.*).

8.3.1 Simple integration

There is a class of ODEs called *separable equations*, that are straightforward to integrate. Separable means one can group terms independently for the dependent and independent variables. Equation 8.23 familiar from radioactive decay is such an equation:

$$\frac{dN}{dt} = -\lambda N \tag{8.23}$$

because it can be rearranged and integrated thus:

$$\frac{dN}{N} = -\lambda dt \tag{8.24}$$

$$\int \frac{dN}{N} = -\int \lambda dt \tag{8.25}$$

$$\ln N = -\lambda t + c \tag{8.26}$$

where c is a constant of integration found from specific boundary conditions, in this case an initial condition (*i.e.* $N = N_\circ$ at $t = 0$). Exponentiating each side of the equation yields:

$$N = N_\circ e^{-\lambda t} \tag{8.27}$$

8.3.2 Variable replacement

Some ODE's can be analytically solved by substituting one variable for another making the equation simpler and more straightforward to solve. Later, back substitution yields the actual solution

you are after. Take for example the *Bernoulli Equation* (which describes the relationship between pressure and fluid velocity):

$$\frac{du}{dx} + Pu = Qu^n \tag{8.28}$$

where P and Q are functions only of x. By making the following substitution and rearranging, we can solve this equation. First, let:

$$\begin{aligned} z &= u^{1-n} && (8.29)\\ \frac{dz}{dx} &= (1-n)u^{-n}\frac{du}{dx} && (8.30)\\ (1-n)u^{-n}\frac{du}{dx} + (1-n)u^{-n}Pu &= (1-n)u^{-n}Qu^n && (8.31)\\ \frac{dz}{dx} + (1-n)Pz &= (1-n)Q && (8.32) \end{aligned}$$

the last of which is now a linear, first-order ODE and can be solved.

8.3.3 Trigonometric methods

There are a large body of trigonometric substitutions that are used to solve ODE's. In fact, there are so many that we are going to cover only one of the most basic trigonometric substitutions. Suppose we have a second-order, linear, homogeneous equation of the form:

$$a_2\frac{d^2y}{dx^2} + a_1\frac{dy}{dx} + a_0y = 0 \tag{8.33}$$

Here we are using x and y as generic variables. We can rewrite this equation in *operator notation* as:

$$(a_2D^2 + a_1D + a_0)y = 0 \tag{8.34}$$

If we remove y and substitute $r = D$, we can rewrite this as the *characteristic equation* of the parent differential equation:

$$a_2r^2 + a_1r + a_0 = 0 \tag{8.35}$$

and, of course, this quadratic equation has roots. The type of trigonometric substitution one uses to find solutions to these types of ODEs depends on the character of the roots. They can be real and equal, real and unequal, or complex conjugates (if the roots are complex, they will be conjugates).

In the first case ($r_1 = r_2 = r$ and $\in \mathbb{R}$):

$$y = (C_1x + C_2)e^{rx} \tag{8.36}$$

For the case when $r_1 \neq r_2$ ($r_1, r_2 \in \mathbb{R}$), the solution obtained by trigonometric substitution is:

$$y = C_1 e^{r_1 x} + C_2 e^{r_2 x} \tag{8.37}$$

In the case where the roots are complex conjugates ($r_1, r_2 \in \mathbb{C}$):

$$\begin{aligned} r_1 &= \alpha + \beta i \\ r_2 &= \alpha - \beta i \end{aligned} \tag{8.38}$$

where i is the imaginary number corresponding to $\sqrt{-1}$, a solution can be found with:

$$y = e^{\alpha x} \left(C_1 \cos \beta x + C_2 \sin \beta x \right) \tag{8.39}$$

Let's take, as an example, the following second order, linear, homogeneous differential equation:

$$\frac{d^2 y}{dx^2} + 2\frac{dy}{dx} + 2y = 0 \tag{8.40}$$

whose roots of the characteristic equation can be found to be:

$$\begin{aligned} r_1 &= -1 + i \\ r_2 &= -1 - i \end{aligned} \tag{8.41}$$

You'll note that these complex roots are conjugates of each other. Using Eqn 8.38 for solving such ODE's, we can see that $\alpha = \beta = 1$. Consequently our solution to Eqn 8.40 is:

$$y = e^{-x} \left(C_1 \cos x + C_2 \sin x \right) \tag{8.42}$$

where the two constants C_1 and C_2 in all three cases are determined from specific boundary conditions.

If the ODE is nonhomogeneous, not all hope is lost. As we reminded you in Sec 8.1.4, sums of solutions are solutions to differential equations. Here's how you can use this fact to exploit the relationship between homogeneous and nonhomogeneous ODEs. First force your nonhomogeneous, second order, linear ODE to be homogeneous by setting the single term without reference to the dependent variable to zero. Then find the general solution to the homogeneous equation as we have outlined above. Now all you need is one specific solution to your nonhomegeous ODE add the two and you have a general solution to the nonhomogeneous ODE. How do you find the specific solution? By inspection or by insight you might be able to guess at one, or you can use a technique known as parameter variation (which is beyond the scope of our book). If all of this sounds like a lot of work that also requires some luck, you are right, but if it's that complicated why not take the numerical approach? That's probably why you started this chapter in the first place.

8.4 Numerical Integration Techniques

When analytical solutions do not exist for your differential equation, numerical integration techniques can come to the rescue. The solution of a differential equation (its integration) takes on many forms and we are going to discuss three of them for ODEs in this section (numerical techniques for partial differential equations are the meat and potatoes of Chapter **??**).

8.4.1 Simple quadrature methods

We will start by looking at a simpler, but related topic — the numerical integration of a function. That is, we want to know the solution to $\int f(x)dx$ where you can evaluate the function $f(x)$ but don't have an analytical solution for the integral. If you remember back to your high school calculus you may recall being introduce to the concept of integration as a mathematical operation equivalent to finding the area underneath a curve. You may have been exposed to the idea that this action was approximated by drawing boxes underneath the curve, and as you made the width of these boxes smaller and smaller their area approached the true integral. This is essentially what quadrature means — finding the area underneath a curve when approximated by geometric constructs. If we look at Fig 8.1 we see an example of this, where the area under the curve is approximated by the sum of the areas of the rectangles constructed under it. The equally spaced abscissa are given by $x_i = x_\circ + ih$, and $f(x_i)$ is evaluated for all x_i. Sometimes it is not possible to evaluate $f(x)$ at the boundaries and in these cases open forms of the quadrature are used.

There are several forms of the closed formulas, we introduce two here that will be both useful and familiar. Both of these forms are known as closed *Newton-Cotes* forms. The first is the *trapezoidal rule*, which is given by the following formula:

$$\int_{x_1}^{x_2} f(x)dx = h\left[\frac{1}{2}f(x_1) + \frac{1}{2}f(x_2)\right] + \mathcal{O}\left(h^3\frac{d^2f}{dx^2}\right) \tag{8.43}$$

the reason for putting the 1/2 inside the brackets will become obvious when we examine the next closed Newton-Cotes quadrature. Another way of thinking about this expression is that we're multiplying h by a linear interpolation to the center of the interval. In the trapezoidal rule, the expression $\mathcal{O}(\dots)$ refers to the *order of accuracy* of the approximation. In this case, the trapezoidal rule is accurate to the order of h^3 times the second derivative of the function being integrated. The final term in Eqn 8.43 is an error estimate of the integration approximation and we see that quadrature becomes less accurate for larger steps (h) or for functions/regions with more curvature (d^2f/dx^2). As you might have noticed (and it should be no big surprise) the trapezoidal rule involves a two-point formula and is therefore exact for polynomials of order one.

Another closed form Newton-Cotes formula is known as *Simpson's rule*. It takes the following form:

$$\int_{x_1}^{x_3} f(x)dx = h\left[\frac{1}{3}f(x_1) + \frac{4}{3}f(x_2) + \frac{1}{3}f(x_3)\right] + \mathcal{O}\left(h^5\frac{d^4f}{dx^4}\right) \tag{8.44}$$

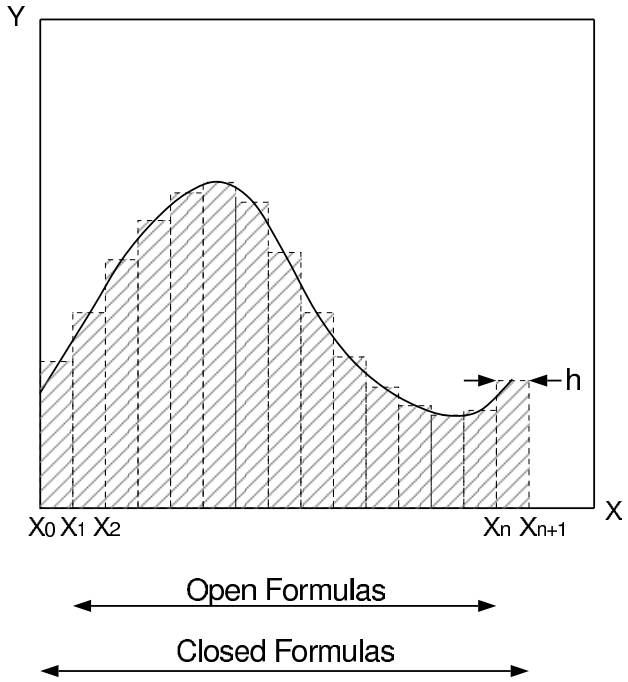

Figure 8.1: *An example of quadrature from rectangles equally spaced along the abscissa. Notice how some parts of the rectangles extend above the curve being integrated while other parts seem to be "too short". The width of each rectangle is a constant* h.

by using information from more points simultaneously, Simpson's does a better job accounting for curvature. Another way of looking at this formula is to imagine one is taking a weighted average value (with the greatest weight on the middle value) of the function. Note that the sum of the fractional weights adds to 2, which is a result of the fact that we're taking the area over a distance of $2h$. Simpson's rule is a three-point formula and exact for polynomials of order two.

Another advantage of closed forms is the ability to create "extended" versions of the form. We present here the *extended trapezoidal rule*:

$$\int_{x_1}^{x_n} f(x)dx = h\left[\frac{1}{2}f(x_1) + f(x_2) + \cdots + f(x_{n-1}) + \frac{1}{2}f(x_n)\right] + \mathcal{O}\left(\frac{(x_n - x_1)^3}{n^2}\frac{d^2 f}{dx^2}\right) \quad (8.45)$$

MATLAB provides the following quadrature/numerical integration functions:

```
trapz      - numerical integration with Trapezoidal Rule
cumtrapz   - cumulative trapezoidal numerical integration
quad       - adaptive Simpson quadrature
quadl      - adaptive Lobatto quadrature
quadgk     - adaptive Gauss-Kronrod quadrature
```

```
dblquad    - numerically evaluate double integral
triplequad - numerically evaluate triple integral
```

where the first is the trapezoidal rule and is useful for tables of numbers that represent curves that must be integrated, the second function provides an adaptive Simpson's rule quadrature of a provided function, while the third is an adaptive Lobatto quadrature. The last two are quadratures one would use for integrating double and triple integrals, respectively. The last four functions require you to provide a short m-file that will evaluate the function being integrated *i.e.*, an m-file that returns $f(x)$ similar to function files we used in Chapter **??** when fitting non-linear equations. As with all things computer, we strongly recomend the student read the online help for any of these functions before using them.

8.4.2 Initial value methods

We have shown (Section 8.2.4) that higher order ODEs can always be reduced to a system of coupled first order ODEs. Just as important, while setting up an ODE problem, are the specifications of the boundary conditions that must be satisfied at discrete, specified points, but not necessarily in between these points. As we have already seen (Section 8.1.6), there are two broad categories of boundary conditions:

Initial Value Problems : if $y = f(x)$ then $y_\circ = f(x_\circ)$ is specified and all values of $y_i = f(x_i)$ are solved up to some final $y_f = f(x_f)$.

Boundary Value Problems : again $y = f(x)$, typically some $y_\circ = f(x_\circ)$ and $y_f = f(x_f)$ are specified and must be satisfied by all $y_i = f(x_i)$ computed in between.

For the remainder of this chapter we are going to focus on the numerical solution of initial values problems. There are three broad categories of numerical integrators that can be applied to these kinds of problems. The first are the forward time stepping integrators; the most common and useful are the *Runge-Kutta* methods, a modification of *Euler*-style integrator. The second are the *extrapolation type integrators*, commonly refered to as *Bulirsch-Stoer* integrators that try to extrapolate to a zero step size. Finally the third are the *predictor-corrector* methods that store the answers along the integration path and use that information to predict the next point.

Basically initial value problems are solved numerically starting at a known value of the solution and then using the differential equation and a specified time step to march the solution forward in time to a predetermined final time. We accomplish this by rewriting:

$$\frac{dy}{dt} = f(t, y) \tag{8.46}$$

as a finite difference equation. We will get to finite difference equations in a more thorough fashion in Chapter **??**, for now just consider what the equation would look like if we replaced the dy/dt with $\Delta y/\Delta t$.

$$\Delta y = f(t, y)\Delta t \tag{8.47}$$

Notice now that we've gone over to using t as the independent variable because these methods are commonly used for time dependent problems (not just to confuse you). In this fashion we can predict changes in y with Δt steps forward, keeping in mind that Δt must be small enough to make a reasonably good approximation of the differential equation. The rest is bookkeeping.

If we write out the most straightforward implementation of this concept we get:

$$y^{n+1} = y^n + \Delta t f(t, y) \tag{8.48}$$

This is known as *Euler's Method* (we want to point out that the n's are not exponentiation, but rather refer to the time step). Although straightforward and simple, it is not recommended because it is not very accurate compared to other methods of similar computational burden and it's not very stable. Figure 8.2 shows, essentially, what's being done with Euler's method.

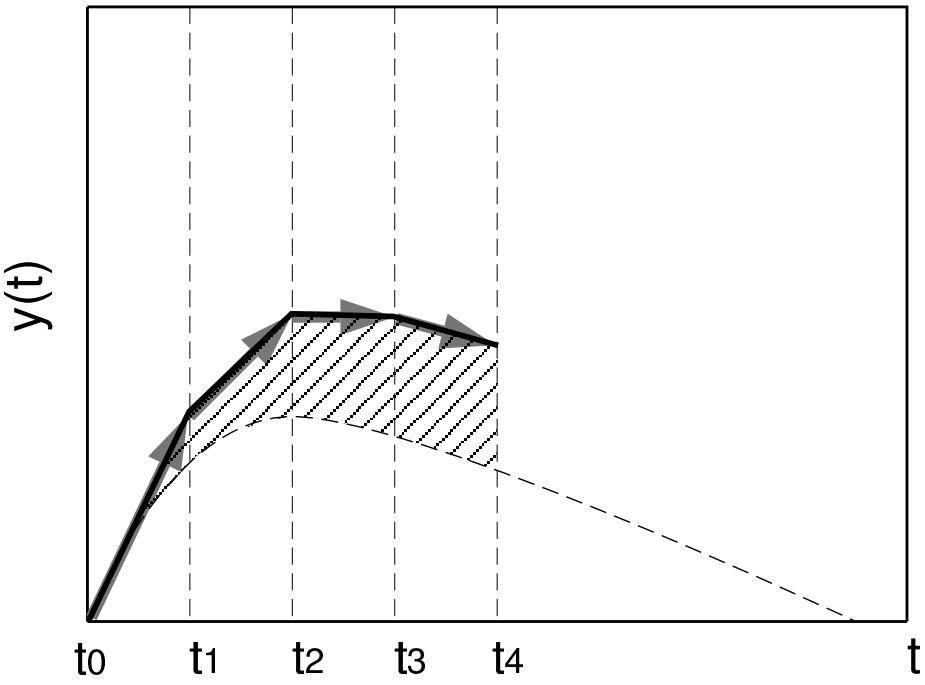

Figure 8.2: *At each time step (t_i) the derivative (the gray arrow) is evaluated and extrapolated to the next time step. The solid black line traces out the actual path this method follows while numerically integrating (truncated for clarity just beyond the third time step), the dashed curved line is the "correct" path, the hatched area represents the difference (or error) between the two. This method is first order accurate.*

But suppose we took a "trial" step only half way to the next time step and then used the derivative evaluation at the halfway point to predict the next full time step. Mathematically it

looks like:

$$k_1 = \Delta t f(t^n, y^n) \tag{8.49}$$

$$k_2 = \Delta t f\left(t^n + \frac{1}{2}\Delta t, y^n + \frac{1}{2}k_1\right) \tag{8.50}$$

$$y^{n+1} = y^n + k_2 + \mathcal{O}(\Delta t^3) \tag{8.51}$$

where $\mathcal{O}(\Delta t^3)$ refers to the truncation error of order Δt^3 that is to say the method is second order accurate. Graphically these equations look like Fig 8.3.

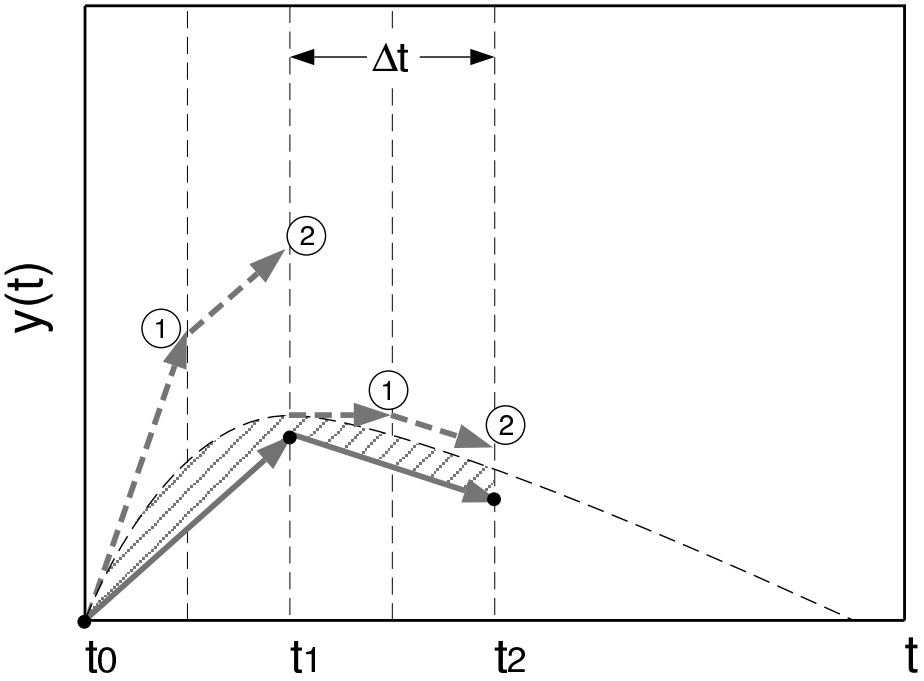

Figure 8.3: *A graphical representation of the second order Runge-Kutta method. The solid gray arrows represent the actual integration path this method follows (truncated for clarity at the t_2 time step). The curved dashed line is the "correct path" and the difference between the two is the hatched area representing the error in this method. The numbered dashed gray arrows represent the evaluations of the differential used to calculate k_1 and k_2 (two estimations per time step). The mid-point derivative evaluation acts to increase the order of the accuracy of the method to $\mathcal{O}(\Delta t^3)$. It should be noted that Figs. 8.2 and 8.3 are not to scale nor are the time steps the same exaggerated size, but an attempt was made to render the graphics so that the error area can be compared.*

This is known as the *Runge-Kutta method* of integration. When one uses only one mid-point derivative evaluation it is said to be the Runge-Kutta 23 method (2^{nd} order accurate with a truncation error of on the order of Δt^3). In MATLAB the function that performs this algorithm is `ode23`.

We can continue this argument and make two mid-point derivative evaluations, which leads to the following equations:

$$
\begin{aligned}
k_1 &= \Delta t f(t^n, y^n) && (8.52)\\
k_2 &= \Delta t f\left(t^n + \frac{1}{2}\Delta t, y^n + \frac{1}{2}k_1\right) && (8.53)\\
k_3 &= \Delta t f\left(t^n + \frac{1}{2}\Delta t, y^n + \frac{1}{2}k_2\right) && (8.54)\\
k_4 &= \Delta t f\left(t^n + \Delta t, y^n + k_3\right) && (8.55)\\
y^{n+1} &= y^n + \frac{k_1}{6} + \frac{k_2}{3} + \frac{k_3}{3} + \frac{k_4}{6} + \mathcal{O}(\Delta t^5) && (8.56)
\end{aligned}
$$

This is known as the Runge-Kutta 45 method and is implemented in MATLAB with `ode45`.

Now, a word about "higher order" methods, higher order doesn't always mean higher accuracy. The 4^{th} order Runge-Kutta is usually superior to the 2^{nd} order, but beware of the size of the time steps and the number of them because higher order *can* mean more smaller steps and that can add up to quite a bit of wall-clock time.

In MATLAB the Runge-Kutta routines all use a variable, continuously adjusted time step; you need only specify the first and last time step (and, under certain circumstances, you don't have to specify these either, see `help odefile` for more details on this advanced feature). MATLAB does give you the option of specifying the specific time steps at which you want solutions, but the underlying code will still use the variable time step method. There are versions of Runge-Kutta that are not adaptive time stepping, but you run the risk of getting really bogged down in many steps to keep it stable. The adaptive time stepping algorithm is controlled by a predetermined, desired accuracy (the variables `RelTol` and `AbsTol` in `ode23`, `ode45` and others), basically this is a truncation error. The adaptive time stepping algorithm takes small steps where the function is changing rapidly and can take really big time steps where the function is smooth and not varying much. This ability can save you time measured in factors of tens to hundreds in compute speed and wall-clock time.

Press *et al.* (2007) give such good advice as to which ODE integrator to use that we are going to repeat it (paraphased) here. In general, use Runge-Kutta when:

- you don't know any better,
- you have an intransigent problem, *i.e.*, the problem is not "smooth",
- when computational efficiency is not of paramount importance, and
- when adaptive time stepping is not a problem and may actually be a great boon.

We will provide a simple example of applying Runge-Kutta in Section 8.5.1.

8.4.3 Explicit vs. implicit

So far we have only used information or knowledge about the solution "from the past" as it were. This is what we mean by *explicit* methods, wherein we can algebraically calculate a new time step from the solutions we have calculated in earlier steps. But suppose, for a moment, you could use information "from the future", or at least from the current time step you are trying to evaluate. This is what we mean by *implicit* methods. But wait a minute! we hear you cry, how can we use information about the very thing we are trying to evaluate in the first place? Try not to worry too much about it right now, it can be done and we'll show you some of the ways it is done later in this chapter and in other chapters.

There is quite a division amoung modelers about the use of implicit *vs.* explicit methods, even amoung the authors of this book. One of us feels that this is no big deal, it is done all the time, and in fact the large, global scale general circulation models you hear so much about these days would not be possible without the use of implicit methods. Another of us feels that implicit methods should be avoided if at all possible. That one should stick to explicit methods, at least for simple numerical problems. The other author feels that one should go where the work is. If you need an implicit method, say, to make your model run in a reasonable amount of time, then by all means use one. Certainly we expect our readers to make their own, reasoned, choices.

8.5 A numerical example

Perhaps the best way of seeing how to use the MATLAB ODE solvers is to construct a simple model and work with it. We will do more of this in a later chapter, but hopefully the application will clarify both how we use the tools, and incidentally, something about how the ocean works.

8.5.1 An Example: a 2-Box Global Ocean Phosphate Model

We start with a Broecker-type two-box model of the global ocean, where we have two reservoirs consisting of a surface layer and the deep ocean (see Fig 8.4). The global ocean cycle of phosphorus is relatively simple, with phosphorus being added to the surface ocean by river inflow, and being sedimented out in the deep ocean. Phosphorus predominantly exists in the ocean in the form of an inorganic phosphate ion, although it spends time within organic pools (ignored here for the moment). There is a net overturning in our ocean model, resulting in the real ocean from sinking of deep water in the polar regions, balanced by an equivalent upwelling elsewhere (to balance water transport). In fact to balance the river input of water, there must be an equivalent amount of evaporation from the surface of the ocean (river flow must be balanced hydrologically by rainfall that finds its ultimate source in evaporation from the ocean surface).

To model the system, we need to put numbers on the phosphate fluxes in the figure, and on the volumes of the boxes (concentration changes occur as a result of fluxes divided by volumes). The phosphate fluxes are given by the water fluxes times the concentrations of phosphate in the water. Table 8.1 gives the appropriate figures for our toy model.

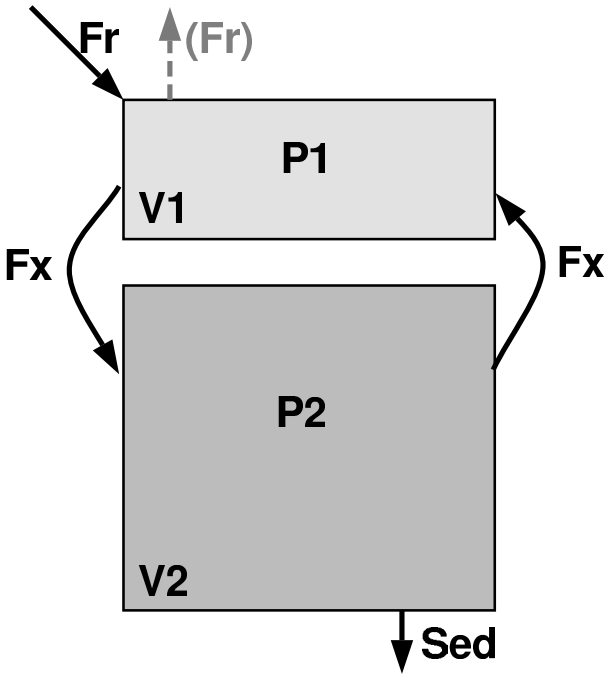

Figure 8.4: *A two box global ocean phosphate model showing water fluxes. In the implementation of this model in the text, we use the following parameters:* $V_1 = 3 \times 10^{16}$ *m*^{3}*;* $V_2 = 1 \times 10^{18} m^3$*;* $F_r = 3 \times 10^{13}$ *m*^{3} *y*$^{-1}$*; and* $F_x = 6 \times 10^{14}$ *m*^{3} *y*$^{-1}$.

Note that we have striven to maintain a consistent system of units. This is vital in a model (or any geochemical) calculation. We've chosen m^3 for volume (of box or of water), m^3 y^{-1} for a water flux, mmol for P amount, and mmol m^{-3} for P concentration. The residence time of P in the oceans is probably of order 10's of thousands of years, so we've chosen years as our time unit rather than seconds: we'll likely be integrating our ODEs for thousands to millions of years, so seconds would work but be a little inconvenient (try saying, "integrating for 10^{13} seconds ...").

So let's set up the ordinary differential equations for the two reservoirs. The equations are:

$$\frac{dP_1}{dt} = \frac{(F_R P_R - F_X P_1 + F_X P_2)}{V_1} \tag{8.57}$$

$$\frac{dP_2}{dt} = \frac{(F_X P_1 - F_X P_2 - \mathrm{Sed})}{V_2} \tag{8.58}$$

where Sed is the sedimentary flux. Inasmuch as we don't quite know what to do with this flux just yet, we'll arbitrarily say that it is 1% of the downwelling flux of P from the surface box (a not very clever choice, but it's a start), giving:

Table 8.1: Global Two Box Phosphorus Model Parameters

Name	Symbol	Flux or Volume	Description
River Water Flux	F_R	3×10^{13} m^3 y^{-1}	River flux $\sim$ 1 Sv = 10^6 m^3 s^{-1}
P Conc. In R.W.	P_R	1.5 mmol m^{-3}	
River P Flux		4.5×10^{13} mmol y^{-1}	Conc. $\times$ Water Flux
Overturning Water Flux	F_X	60×10^{13} m^3 y^{-1}	Overturning $\sim$ 20 Sv $= 20 \times 10^6$ m^3 s^{-1}
Surface Area of Oceans		3×10^{14} m^2	Approximately 70% of earth's area
Surface Box Vol.	V_1	3×10^{16} m^3	Assuming 100 m depth
Deep Box Vol.	V_2	1×10^{18} m^3	Assuming 3300 m depth

$$\frac{dP_1}{dt} = \frac{(F_R P_R - F_X P_1 + F_X P_2)}{V_1} \tag{8.59}$$

$$\frac{dP_2}{dt} = \frac{(F_X P_1 - F_X P_2 - 0.01 F_X P_1)}{V_2} \tag{8.60}$$

We now need to code this in MATLAB in order to use the ODE solver. We write a MATLAB function, which we'll call `phos2.m`.

```
function dPdt=phos2(t,P)

% PHOS2 is a function file representing a 2 box global ocean phosphate
%  model to be used by ODE23 or ODE45 to integrate the ODEs
%  NB: Output must be a column vector for the integrator to work

%
%  Value initialization
%

V=[3 100] * 1e16;       % volume of reservoirs in m3
dPdt=zeros(2,1);        % Initialize output as a column vector
Fx = 6e14;              % overturning water flux in m3 per year
Fr = 3e13;              % river water flux in m3 per year
Pr = 1.5;               % river water P concentration in mMol per m3
Sed = 0.01*Fx*P(1);     % sedimentary loss of P in deep box

%
%  difference equations
%
```

```
dPdt(1) = (Fr*Pr - Fx*P(1) + Fx*P(2))/V(1);
dPdt(2) = (Fx*P(1) - Fx*P(2) - Sed)/V(2);
```

Notice how we've split out the terms for clarity, and for future change. Now let's integrate this thing! Following our own advice we'll start with `ode45`, as it's generally the most accurate, efficient and stable of the algorithms. These routines are very easy to use. All we need to do is to specify the function name (here it's `phos2.m`), the time span for integration, and the starting values for the variables (remember, it's an initial value problem). For the sake of simplicity, we'll start with zero values. Note also that the initial value and the output of the function must be column vectors. So we do the following:

```
>> P0=[0 0]';
>> [T,P]=ode45('phos2',1e4,P0);
>> plot(T,P)
```

Note that `ode45`, like the other integrators, returns two things: a column vector of the times in the integration steps, and a multi-column vector of the variable outputs (one column per variable, each row corresponds to a time step). Also, we've chosen to integrate only for a shortish period of time, as an exploratory step. This is a prudent, standard approach.

In plotting the results, we see that it has not reached equilibrium for such a short time (in Fig. 8.5a the concentrations are still going up and have not leveled off yet). No real surprise there, a lower bound on the expected time scale of the problem can be estimated by dividing the larger reservoir by the river volume flux $V_2/F_R \sim 3 \times 10^4$ years, so we run it again with a longer integration time span:

```
>> P0=[0 0]';
>> [T,P]=ode45('phos2',1e6,P0);
>> plot(T,P)
```

Figure 8.5 shows the results, note that not surprisingly, the model has the two boxes with rather similar concentrations, and with the surface box slightly higher than the lower box. The sign of the difference is not surprising, as the input is in the surface box, and the sink is in the lower box. The size of the difference makes sense too: the removal rate is about 1% per box turnover, which gives a time-scale large relative to the turnover timescale ($V_2/F_X \sim 1,600$ years) so that they should be very similar in concentration.

This, however, is not realistic, as we know two things. First, biological production occurs in the surface ocean, using up phosphate (plus other nutrients) and resulting in a particulate flux to the deep water. It is this particulate flux that is remineralized in the deep ocean, and a fraction of which ends up in the sediments. Second, as a consequence, surface phosphate concentrations are generally much lower than deep water. Thus our model is not well formulated or realistic. Let's recast the equations in a slightly more realistic fashion.

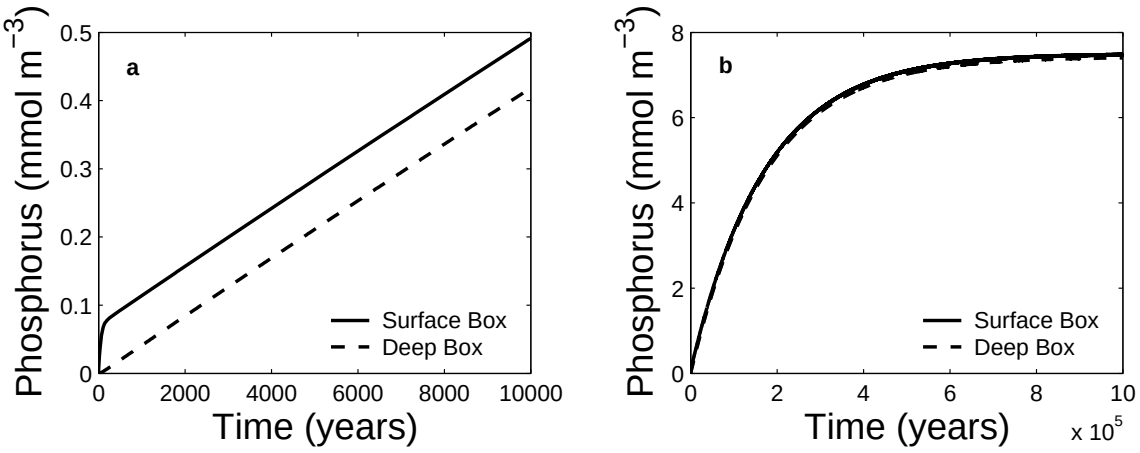

Figure 8.5: *Results of our first 2-box global phosphate model integration, a)* $t_f = 10^4$ *y and b)* $t_f = 10^6$ *y.*

$$\frac{dP_1}{dt} = \frac{(F_R P_R - F_X P_1 + F_X P_2 - \text{Production})}{V_1} \tag{8.61}$$

$$\frac{dP_2}{dt} = \frac{(F_X P_1 - F_X P_2 + 0.99 \times \text{Production})}{V_2} \tag{8.62}$$

$$\text{Production} = \frac{(P_1 V_1)}{\tau_P} \tag{8.63}$$

What we've done is assumed that the phosphate is removed from the surface box at a rate that is proportional to the amount of phosphate, $P_1 V_1$, in the box (not a bad idea, actually, since biological production is nutrient limited). We've characterized this removal rate with a time-constant (τ_P) that might be visualized as the life-time of phosphate in the surface ocean due to biological uptake. In the deep box, this loss magically reappears (by oxidation of the falling particles), but it is not 100% efficient, as some particles make it to the sediments, and are lost from the system. In fact, this results in the system approaching steady-state ($dp/dt = 0$), as the sedimentary loss must balance the river input. So we rewrite the m-file to add the biology (calling it `phos2b.m`):

```
function dPdt=phos2b(t,P)

% PHOS2b is a function file representing a 2 box global ocean phosphate
%  model with biology to be used by ODE23 or ODE45 to integrate the ODEs
%  NB: Output must be a column vector for the integrator to work

%
```

```
%  Value initialization
%

V=[3 100] * 1e16;          % volume of reservoirs in m3
dPdt=zeros(2,1);           % Initialize output as a column vector
Fx = 6e14;                 % overturning water flux in m3 per year
Fr = 3e13;                 % river water flux in m3 per year
Pr = 1.5;                  % river water P concentration in mMol per m3
Tau = 100;                 % 100 year residence time of P in the surface
Prodtvy = P(1)*V(1)/Tau;   % Production
ReminEff = 0.99;           % Remineralization efficiency

%
%  difference equations
%

dPdt(1) = (Fr*Pr - Fx*P(1) + Fx*P(2) - Prodtvy)/V(1);    % surface box
dPdt(2) = (Fx*P(1) - Fx*P(2) + ReminEff*Prodtvy)/V(2);   % deep
```

and we run it with:

```
>> [T,P]=ode45('phos2b',3e6,P0);
```

to get Fig 8.6 which shows the surface box has lower concentrations. Note something odd, however, in that it took a little longer to run than the previous experiment (perhaps half again as long). Doing a `whos` shows that the number of steps was larger, which explains it (*i.e.*, the computer took longer because it computed more time steps). Why `ode45` took so many more steps we'll let you think about it for a while.

Now we suspect that the residence time of phosphate in the surface ocean is in fact a lot shorter than 100 years. Try running the experiment again, this time setting τ_P to 1 year. What you'll find when you do this is that `ode45` takes forever to run the code. In fact, we had to kill the program with the task manager on our computer (Windows, or with `kill -9 PID` UNIX). We finally got it to run by letting it churn away for a long time. What happened? We didn't increase the computational load in the equations significantly. If you do a `whos` after running the code for a 3×10^6 year run, you find $\sim 3.7 \times 10^6$ time steps (*vs.* $\sim$110,000 for the 100 year time-constant case). It appears that the integrator has to choose smaller time steps for stability (more about this stability thing in Chapter **??**, but for the time being just think of stability as that characteristic of your model that prevents it from blowing up, generally stability, then, is a good thing).

8.5.2 Stiff equations

A word needs to said here about the problem of *stiff equations*. An ordinary differential equation (ODE) problem is said to be "stiff" when stability requirements force the solver to take a lot

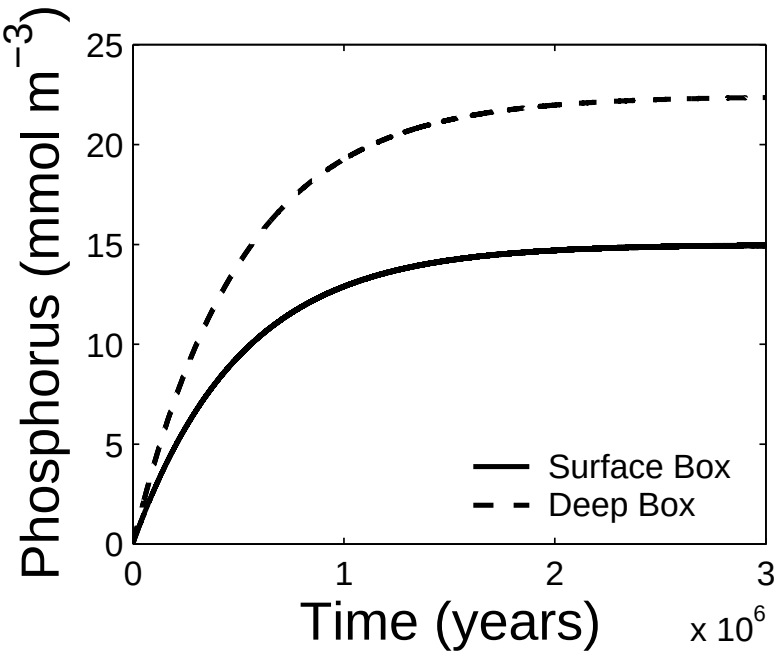

Figure 8.6: *Our two boxglobal phosphate model with more realistic biological removal of phosphorus from the surface box.*

of small time steps, this happens when you have a system of coupled differential equations that have two or more very different scales of the independent variable over which you are integrating. Another way of thinking about this is to consider what must happen when two different parts of the solution require/allow very different time steps. For example, suppose your solution was the combination of (sum of) two exponential decay curves, one that decays away very rapidly and one that decays away very slowly. Except for the few time steps away from the initial condition, the slowly decaying curve will dominate since the rapid curve will have decayed away. But because the variable time step routine will continue to meet the stability requirements for both components, you will be locked into small time steps even though the dominant component would allow much larger time steps.

Another example, more likely encountered by geochemists looking at multi-box (multi-reservoir) models is when there are two reservoirs in the system with vastly different time-scales or volumes/masses. For example if you had a two-box model of the world ocean, one surface and one deep. You might divide the surface and deep at 50-100 m. depth, resulting in a deep ocean box that is $\sim$50-100 times larger than the small box. The fluxes transferred between these two reservoirs would have a correspondingly disparate effect, so that in order to do a stable integration, you'd be constrained to take a sufficiently small step in time so not to swamp the smaller box. But you would have to integrate long enough to allow the deep box to reach equilibrium (in a steady-state

system) or change significantly (in a transient case).

This is what we mean by "stiff" equations, we get locked into taking very small time steps for a component of the solution that makes infinitesimally small contributions to the solution. In other words, we're forced to crawl when we could be leaping along to a solution.

The answer to this problem is to use implicit methods. Now we know we will warn you against implicit codes in future chapters, but there are situations where they are quite useful (see the discussion of explicit vs. implicit methods in Sections 8.4.3 and **??**). All we will say here is that for ordinary differential equations, MATLAB has provided you with quite an arsenal of ODE solvers that range from classical applications of Runge-Kutta methods to rather sophisticated implicit, multi-step ODE integrators (see Table 8.2).

How do we implement these approaches? We can use one of the stiff equation solvers in MATLAB in exactly the same way that we used `ode45`, this time we use `ode15s`, an implicit scheme that is somewhat less accurate, but far more efficient.

```
>> [T,P]=ode15s('phos2b',3e6,P0);
```

which proceeds far faster than `ode45`, and integrates over three million years in 65 steps! Of course, if you set τ_P back to 100 years `ode15s` takes 63 steps to cover the same 3×10^6 years. This routine is only first order accurate in Δt, so you might be tempted to artificially increase the resolution in time (as stability requires the adaptive time step to yield only a coarsely resolved system). Looking at the output of the integration above, we see that most of the action occurs in the first million years, so that we only need to integrate out to perhaps 1,200,000 years, and suppose we want to resolve at the century timescale. Although it's advisable to start by specifying the span to see what the minimum time step size should be for stability, we can seize control of the reported time steps by providing a column vector of the time steps, *e.g.*,

```
>> [T,P]=ode15s('phos2b',[0:100:1.2e6]',P0);
>> plot(T,P)
```

where `[0:100:1.2e6]'` creates a column vector of time intervals from zero to 1,200,000 years in 100 year steps (`whos` confirms this by reporting `T` has 12,001 elements). But if you look at a plot of the results with 65 steps *vs.* 12,001 steps they appear to plot on top of each other. It turns out that for this problem the higher time resolution results differ from the coarse on the order of 0.01 mmol P m^{-3} at 1.2×10^6 years ... small differences are expected in such a smoothly varying problem.

The question frequently arises, is MATLAB really using these extra time-steps that I am specifiying? The answer is both yes and no. So we give to you straight from the depths of the MATLAB online documentation:

> *"Specifying* `tspan` *with more than two elements does not affect the internal time steps that the solver uses to traverse the interval from* `tspan(1)` *to* `tspan(end)`*. All solvers in the ODE suite obtain output values by means of continuous extensions of the*

> *basic formulas. Although a solver does not necessarily step precisely to a time point specified in* `tspan`*, the solutions produced at the specified time points are of the same order of accuracy as the solutions computed at the internal time points. Specifying* `tspan` *with more than two elements has little effect on the efficiency of computation, but for large systems, affects memory management.*"

8.5.3 Chaotic Behavior

We should emphasize that although you may play by all the rules, *e.g.*, choosing an efficient and accurate ODE solver for your system and perhaps dealing with stiff equations sensibly, the coupled equations may in fact exhibit a chaotic (seemingly random) behavior that is not a result of your numerical scheme. While chaos is a subject outside of the scope of this book, you will likely run into well-formulated biogeochemical models that exhibit this behavior. The difficult task is to convince yourself that what you're seeing is not a result of numerical instability. A number of approaches to rule out instability include the use of a fundamentally different ODE integration algorithm and changing (reducing) step size. If you find that the "statistical" behavior of the system remains independent of the scheme choice and step size, you are likely dealing with a chaotic system. By "statistical" we remind you that you need to examine the behavior over a number of "cycles" because different pathways or initial conditions will result in variations in individual realizations, and you need to compare the ensemble behavior of your solutions.

8.6 Other methods

You may think things are doomed if Runge-Kutta fails, but common sense tells you there must be a way. After all, these systems exist, and nature somehow finds a way to integrate them. In order to deal with stiff equations efficiently, some kind of implicit or semi-implicit scheme must be used. While we are big fans of Runge-Kutta for solving ordinary differential equations, as we indicated above there are times when other methods need to be used. So that you don't fall into the trap of using a mathematical tool as a "black box" we are going to describe in this section some of the more commonly used techniques to solve ODEs *other* than Runge-Kutta.

8.6.1 Predictor-Corrector Schemes

Predictor-corrector schemes are a subset of a class of multi-step semi-implicit schemes that have some historical significance, and have been used for efficient, precision solution of smoothly varying equations with complicated structure (*i.e.* many terms on the R.H.S.). They are treated with some ambivalence in the literature these days, but are representative of a semi-implicit multi-step algorithmic approach. The most commonly used is the Adams-Bashforth-Moulton scheme. The approach is actually 3 basic steps done iteratively. As an example of the 3rd order version of this approach, the first step (the "P" or predictor step) is to make an estimate of the next step:

$$y_{n+1} = y_n + \frac{\Delta t}{12}\left(23\left.\frac{dy}{dt}\right|_n - 16\left.\frac{dy}{dt}\right|_{n-1} + 5\left.\frac{dy}{dt}\right|_{n-2}\right) + \mathcal{O}(\Delta t^4) \tag{8.64}$$

where in the above equation we've used a convenient shorthand for the time step index in the derivatives in the subscript (just checking to see if you are paying attention). In other words, we are estimating the next $(n+1)$ value of y using the current position (n) and a Simpson's rule type evaluation using the current plus the two previous derivatives. The predictor is essentially a polynomial extrapolation.

The second step is the evaluation or "E" step in which you evaluate the new derivative y'_{n+1}. You then take the corrector ("C") step to refine your estimate of y_{n+1} using:

$$y_{n+1} = y_n + \frac{\Delta t}{12}\left(5\left.\frac{dy}{dt}\right|_{n+1} + 8\left.\frac{dy}{dt}\right|_n - \left.\frac{dy}{dt}\right|_{n-1}\right) + \mathcal{O}(\Delta t^4) \tag{8.65}$$

and finally take a fourth "E" step to re-evaluate the derivative at y_{n+1}. Hence it's given the name "PECE". Of course, we do not have to keep track of all this bookkeeping as MATLAB provides us with `ode113`.

8.6.2 Bulirsch-Stoer extrapolation

The Bulirsch-Stoer algorithm for numerically integrating ordinary differential equations can achieve very high accuracy integrations with exceptional efficiency (*i.e.*, with minimal computational effort). But, as with everything else in life, there are conditions. First of all, your problem (differential equation) must be very smoothly varying. Discontinuities or sudden jumps in value will give Bulirsch-Stoer the fits. Second, there cannot be any singularities embedded within your limits of integration (any $\tan(t)$ that might approach $\pi/2$?). Third, as far as we can tell, MATLAB does not provide the Bulirsch- Stoer algorithm in its suite of `ode` integrators. So this is a reality check, do you really need to use this algorithm or is there one listed in Table 8.2 that will suffice? Having said all of that, here's an introduction to the Bulirsch-Stoer method for those that need both high accuracy and high computational efficiency.

In Chapter **??** we discussed the concepts of interpolation and extrapolation. Now imagine one could take a mid-point integration scheme, like Runge-Kutta 23, and extrapolate the effect of crossing the Δt step not with two but with an infinite number of $\Delta t = 0$ steps. We know this sounds a little bit like Xeno's paradox, but this is essentially what the *Bulirsch-Stoer* method does. Now, of course, it doesn't really take an infinite number of $\Delta t = 0$ steps; it extrapolates to the effect of $\Delta t = 0$, with a relatively few ($\mathcal{O}(20)$ at the most), reasonable sized steps.

How is this done? Bulirsch-Stoer first estimates the integration by taking a big step (nowhere near zero). It then refines the estimate by dividing that big step in two, then four, then six, *etc.* Then assuming the error of these integrations are a polynomial function of step size, it builds higher order estimates of the answer using using the polynomial recursion algorithm of Neville (Stoer and Bulirsch, 2002). As one builds up higher and higher orders of accuracy, the error (estimated from the order before) is checked, when it reaches a predetermined acceptable level, the algortihm

stops. In reality, this usually happens long, long before it reaches the extrapolated infinite number of divisions (steps).

If you feel you must have this algorithm to solve your problem, we recommend you check out the description (and code snippets) in Press *et al.* (2007).

8.6.3 Boundary value methods

When ODEs are required to satisfy boundary conditions in two different places along the independent variable axis, these problems are called "two-point boundary value problems". These methods involve iterative solutions from initial "guesses".

Earlier we said we would be concentrating on initial value problems, but there are problems and situations that cannot be solved by integrating forward from an initial condition. Some of these problems give or require certain boundary conditions be met at certain times or places in the model domain and boundary value methods are of important use in these situations. In this subsection we review some of the better known boundary value methods and suggest the interested student check out Press *et al.* (2007) if they wish to learn more.

The first type of boundary value method is known as the *shooting method*. At one boundary (call it the initial boundary) we specify values for all the dependent variables that are consistent with that boundary. We then integrate forward using initial value techniques to the other boundary (call it the final boundary) using a best guess set of parameters for the differential equation. Of course, our "shot" will have missed, but we will be able to calculate the discrepancies from the boundary conditions at the final boundary. We use this information to solve the multidimensional systems of equations and improve our initial parameters. Then we "shoot" again, and again, and again until our solution arrives at the final boundary within some predetermined accuracy and the routine terminates. In some respects, this resembles the non-linear least-squares approaches discussed in Chapter **??**, and this is not accidental. One can imagine designing a similar χ^2 minimization strategy that seeks the optimal solution iteratively. Although conceptually straightforward, the primary difference would be the evaluation step (which would be an ODE initial value integration rather than chi-squared computation) so the iteration would be more computationally expensive, but manageable for simple systems. For more complex systems, a more efficient technique must be sought.

Another type of boundary value method is known as *relaxation methods* wherein we make an initial guess at the solution of all the dependent variables in the domain. These guesses don't have to meet all of the boundary conditions, but the better our initial guess, the quicker we'll "relax" to the final solution. The relaxation involves modifying the solution of dependent variables in such a way that they come closer to agreeing with the differential equations and the boundary conditions. If this method suggests to you the solution of simultaneous equations, you are correct. If one can arrange one's space/time grid as block diagonal, sparse matrix (see Fig. **??**) the inversion can be done quickly. Oddly enough, for the right kinds of problems, this approach is faster (more efficient) than the shooting method. We'll see one more "two- point boundary value" method in a later chapter when we discuss 1-D models in sediment profiles (Chapter **??**), the *tridiagonal*

algorithm.

8.6.4 MATLAB ODE Solvers

The ODE solvers in MATLAB fall, broadly, into two types: solvers for non-stiff and stiff problems. It can be rather confusing as to which ODE routine you should use and so in Table 8.2 we include some "words of wisdom" as to which ODE routine to use for which kind of problem. This table is constructed from information found in the nearly 5,000 pages of the MATLAB *7 Function Reference* (MathWorks, 2009) and Shampine and Reichelt (1997).

REMEMBER, always start with `ode45`, if it fails or seems to be taking a long time to integrate (even if you give it a small time interval to integrate over, as a test), then consider the following. Are you asking it to integrate solutions that are very small in comparison to the accuracy tolerances either provided to you by default or explicitly given by you. If that doesn't seem to be your problem think about whether or not you may be integrating stiff equations with a method that wasn't meant to integrate stiff equations (like `ode45`). Some times the easiest thing to do is to try a different ODE solver, something like say, `ode15s`. Don't make the mistake of trying to fix your stiff equation problem by switching another non-stiff solver (like `ode23`). Be sure to look at Table 8.2 carefully and if you have more questions, the MathWorks has provided extensive documentation about their ODE solvers on their web site and this documentation may be loaded onto your machine as well.

8.7 Problems

8.1. Modify our biological, two-box model of the global phosphorus cycle to systematically step through the remineralization efficiency from 90% to 100% making note of both the time it takes to reach equilibrium (t_{eq}) and the concentration difference (ΔP) between the surface and deep box. Plot ΔP vs. t_{eq} in a separate figure window. Do the same for time-constants τ_P of 1, 5, 20, 50 and 100 years, Explain results.

References

Case, T.J., 1999, *An Illustrated Guide to Theoretical Ecology*, Oxford University Press, New York, NY, 464 pp.

Fennel, W. and T. Neumann, 2004, *Introduction to the Modelling of Marine Ecosystems*, Elsevier Oceanography Series, 72, Elsevier, Inc., San Diego, CA, 297 pp.

Hastings, A., 1997, *Population Biology, Concepts and Models*, Springer-Verlag, New York, NY, 220 pp.

Mathworks, 2009, MATLAB *7 Function Reference*, The Mathworks, Inc., Natick, MA, 4,912 pp.

Table 8.2: Summary of MATLAB ODE Solvers

Solver	Problem Type	Accuracy	Mathematical Method	Recomended uses
`ode45`	non-stiff	medium	Explicit Runge-Kutta 45 method.	Try this method first. Often this is as far as you'll need to go.
`ode23`	non-stiff	low	Explicit Runge-Kutta 23 method.	While using crude error tolerances this method may be quicker than `ode45`. Also good for the "moderately" stiff systems.
`ode113`	non-stiff	low to high	Variable order Adams-Bashforth-Moulton predictor-corrector (PECE) method.	For strict error tolerances and/or computationally difficult problems. May give better results than `ode45` at strict tolerances.
`ode15s`	stiff	low to medium	Based on numerical differentiation formulas (NDF), variable order.	If `ode45` is slow (stiff systems). Try this one if `ode45` fails. First order accurate.
`ode15i`	stiff	low to medium	Fully implicit backward differentiation (BDF), variable order.	If your problem must be formulated in a fully implicit fashion. Initial conditions must be consistent. This one is a little different than the others.
`ode23s`	stiff	low	Modified Rosenbrock method of order 2.	For stiff systems when `ode15s` fails, crude error tolerances, but higher order accuracy.
`ode23t`	moderately stiff	low	The trapezoidal rule using a "free" interpolant.	If the problem is only moderately stiff and you need a solution without numerical damping.
`ode23tb`	stiff	low	An implicit Runge-Kutta method with first stage trapezoidal rule and second stage backward differentiation formula of order 2 (TR-BDF2).	If using crude error tolerances to solve stiff systems. May work when `ode15s` fails at crude tolerances.

Press, W.H., B.P. Flannery, S.A. Teukolsky, and W.T. Vetterling, 1992, *Numerical Recipes, 2nd Edition*, Cambridge University Press, New York, , 818 pp.

Roughgarden, J., 1998, *Primer of Ecological Theory*, Prentice Hall, Upper Saddle River, NJ, 456 pp.

Shampine, L. F. and M. W. Reichelt, 1997, The MATLAB ODE Suite, *SIAM Journal on Scientific Computing*, **18**, pp 1-22.

Stoer, J. and R. Bulirsch, 2002, *Introduction to Numerical Analysis, 3rd edition*, Springer-Verlag, New York, NY, 752 pp.

Zwillinger, D., 2002, *CRC Standard Mathematical Tables and Formulae, 31st Edition*, Chapman & Hall/CRC, Boca Raton, FL, 912 pp.

Index

DRAFT, 15 May 2009. Please do not cite.

Guide for *Best Practices in Ocean Acidification Research and Data Reporting*

Please send comments directly to the lead authors, the chapter and chief editors: aoschlies@ifm-geomar.de, jcb@pml.ac.uk, marion.gehlen@lsce.ipsl.fr, uriebesell@ifm-geomar.de, fabry@csusm.edu, gattuso@obs-vlfr.fr

Chapter 4: Data reporting and data usage

Section 4.1. Modeling considerations

Lead authors: Andreas Oschlies[1], Jeremy Blackford[2], Marion Gehlen[3]

[1]Leibniz Institute of Marine Science (IFM-GEOMAR), Marine Biogeochemistry, Düsternbrooker Weg 20, 24105 Kiel, Germany.

[2]Plymouth Marine Laboratory, Prospect Place, Plymouth, PL13DH, UK.

[3]Laboratoire des Sciences du Climat et de l'Environnement, LSCE/IPSL, UMR CEA/CNRS/UVSQ, L'Orme des Merisiers, Bât. 712, 91191 Gif-sur-Yvette cedex, France.

4.1.1 Introduction

Numerical models can be viewed as a simplified representation of the real world. They comprise a system of rules that are combined with a number of initial conditions (e.g., nutrient distributions) and boundary conditions (e.g., atmospheric forcing) to make inferences about the state of affairs. A very similar procedure takes place when interpreting observations or planning experiments: the readings of instruments are translated following a set of rules into biogeochemically relevant properties, these are then arranged into a coherent picture in the mind of the scientist. Numerical models require that the rules be represented in a formal mathematical description, which has, at least in theory, the advantage of a clear and unambiguous language that should help to make models transparent and portable between different investigators.

Numerical models can be used to put data of different quality, isolated in space and in time, into a coherent context. This process can benefit from the concept of data assimilation that aims at a most efficient combination of information contained in the data with information contained in the model's rules. However, the complex theoretical and operational apparatus of data assimilation has, so far, limited its application. Probably the most widespread applications of numerical models are to explore logical consequences of hypotheses ("what if" experiments) and to identify sensitivities of integral properties to individual processes. The former category includes scenario simulation into the future.

Numerical models can basically address the same kind of scientific questions as other scientific methods. In this respect, models are just another tool, comparable to, for example, mass spectrometry. However models have a unique ability to firstly test our synthesized understanding of a given system and secondly extrapolate in time or space to regions where data is sparse. Calibrated model results can identify problems with our underlying conceptual understanding and highlight observational and experimental needs.Further, models can identify the perturbation envelope for experimental activities e.g. pH and Ω ranges and identify sensitive areas (e.g. the Arctic). Model results can also contribute to the identification of new hypotheses that require testing by data. Consequently, modelers should not be viewed as potential "end users" of experiments or observational campaigns. Though they may contribute to the analysis of individual data sets, the use of models (and of other methods) can only be justified by their ability to answer scientific questions.

Predictive models are, in general, one of the key methods for synthesizing understanding into a policy usable format. Indeed the recent emergence of climate change as a mainstream issue, which depends to a large extent on climate model scenario simulations, has enabled the far more rapid recognition of ocean acidification as a parallel concern for policy makers. As a consequence the scientific community is being challenged to produce robust and relevant science that underpins international policy development on a relatively short timescale. However whilst prediction of the carbonate system response is reasonably robust (e.g. Caldeira & Wickett 2003, Orr et al, 2005), predicting the response of ecosystems and resources is problematic and is at a very early stage (for example Blackford & Gilbert, 2007; Bourret et al, 2007; Hashioka & Yamanaka, 2007). This is due in part to the complexity of system drivers and in part to the range of effects identified and the variety of responses of different species, phyla etc. Hence a translation of results into policy poses several problems for modelers.

4.1.2 Approaches and methodologies

In contrast to ocean circulation models that rely on the well-established Newton's Laws, there are no known fundamental equations that govern marine ecosystems. There is not even consensus on biological invariants that may be used as prognostic variables of a marine ecosystem model. Traditionally, most models partition the ecosystem into nutrients, phytoplankton, zooplankton, and non-living particulate and dissolved organic matter, but more and more species and functions are found that cannot be easily mapped onto the traditional picture. One approach is to make models more complex, e.g. by adding multiple plankton functional types (PFT models). No model, simple or complex, has yet demonstrated a satisfactory ability to reproduce observed global patterns of biomass.

It is noteworthy that increased complexity comes at the cost of having to constrain more model parameters (e.g. growth rates, mortality rates, grazing rates), about which we have only very limited information. Moreover, the variety of species specific responses to acidification, noted in calcifying species (Fabry, 2008), makes a generic PFT type parameterization problematic. Aggravating in this respect is that is is unclear how such models (as well as simpler models) could adequately describe adaptation to environmental changes. Promising new modeling approaches include trait-based models in aquatic ecology. These new models let the ecosystem self-assemble from a large number of species, and biodiversity and, to some extent, adaptation are emergent feature of such models (Norberg et al., 2001; Bruggeman and Kooijman, 2007; Follows et al., 2007).

So far, there are broadly two types of modeling approaches. One attempts to build models based on mechanistic principles, i.e. some reasonably correct representation of physiological and biogeochemical processes that describe the exchange of matter and energy among the different compartments of an ecosystem model. The other is based on empirical relationships derived from culture, mesocosm or observational studies, and sometimes results from statistical regressions of simple functional relationships against measurements. The former approach has the disadvantage of requiring possibly many parameters (not all of which can be constrained without becoming empirical again), but has no a-priori reason why such models cannot be used in predictive mode, as long as the changing drivers are correctly described and incorporated into the process descriptions. The empirical approach is often unsuitable for predictive approaches as, in general, the sensitivity of these relationships to environmental change, such as warming or acidification, has not fully been established and can therefore not be properly accounted for by the models. A notable exception being empirical models based on observations that encompass future variability of environmental conditions by either considering past and present natural variability or perturbation experiments.

The carbonate system is, in contrast, well constrained, equilibrium constants are extensively published, and although there are variations in particular constants emerging from different studies a consistent, robust approach is generally possible (Zeebe & Woolf Gladrow, 2001 amongst others). Typically models use calculated dissolved inorganic carbon (DIC) and a representation of total alkalinity (TA) as the master variables from which pH, pCO2, bicarbonate, carbonate and omega are derived. On ocean basin scales this approach is reasonably robust and TA can be derived from salinity according to a number of basin-specific linear relationships. Unfortunately, these relationships are at best approximate in shelf seas as alkalinity is influenced by significant biological and riverine signals, coupled with high heterogeneity (Friis et al., 2003;

Thomas et al 2008). These processes are also susceptible to change (e.g. riverine alkalinity, Raymond & Cole, 2003) and potential changes must be factored into predictive scenarios. It is recommended that alkalinity is included in biogeochemical ocean circulation models as prognostic tracer rather than being diagnosed from empirical fits to salinity etc.

With respect to the production of biogenic particulate inorganic matter (PIC), which modelers usually associate with calcium carbonate, a large variety of parameterizations have been used. Many models assume that PIC production is proportional to primary production or export production, thereby emphasizing the role of the $CaCO_3$ cycle in the Earth system. This is fundamentally different from an attempt to assess impacts on the ecosystem level. The parameterizations used are often independent of carbonate chemistry (e.g. Schmittner et al., 2008). Some models take into account a control of PIC production by the carbonate chemistry (Heinze, 2004; Gehlen et al., 2007; Ridgwell et al., 2007, Gangstø et al., 2008) though different models use different controls (pH, CO_2, CO_3^{2-}, Ω) and different functional forms (linear, sigmoid, power law) describing either PIC production or the ratio of PIC to POC (particulate organic carbon) production. While some of the variables describing the carbonate system are temperature dependent, some models explicitly or, via primary production, implicitly include a temperature dependence in the parameterization of PIC production.

The different parameterizations of PIC production and its sensitivities to changes in temperature and carbonate chemistry can lead to very different results. When applied to a global warming scenario, different models may even predict different signs in the change of PIC production. For example, a business-as-usual emission scenario leads to a (CO_2 driven) reduction of PIC production over the next few hundred years in the model of Heinze (2004), whereas essentially the same scenario leads to a (temperature driven) increase in PIC production in the model of Schmittner et al. (2008). The former model run neglects warming effects and assumes a linear relationship between PIC production and CO_2, the later model assumes no direct impact of the carbonate chemistry on PIC production, but includes a temperature effect. Gangstø et al. (2008) include a combination of both global warming and CO_2 effects and predict an overall reduction of PIC production. To the authors' knowledge, model parameterizations have not yet been tested against experimental data sets that yield information about the combined effect of warming and acidification on calcium carbonate production and dissolution. These data sets are currently becoming available and will allow an evaluation of model parameterizations in the near future.

Other implications of acidification are relevant to element cycling and ecological questions. Phytoplankton functional groups have varying sensitivities to CO_2 availability (Tortell et al., 2002, 2008, Rost et al., 2003), with studies showing a shift away from calcifiers to diatoms at low

pH. Nutrient speciation, nitrification (Huesemann et al., 2002) and nitrogen fixation (Hutchins et al 2007, Levitan et al., 2007) are all sensitive to pH. Nutrient uptake stoichiometry may by affected by changes in community composition and vice-versa. Phytoplankton uptake and export C:N ratios have also been shown to be CO_2 sensitive (Riebesell et al 2007). These processes are generally not included in present generation models, apart from specific sensitivity studies (e.g., Oschlies et al., 2008).

4.1.3 Strengths and weaknesses

A strength of numerical models is their purely mathematical description. In principle, the clarity of this "language" should leave no room for ambiguities. However, modern numerical models have become more and more complex, culminating in several ten to hundred thousand lines of code for current coupled carbon-climate models. A normal user of such models will not be able to carefully read through the entire codes and careful checks are needed to establish with confidence that newly added model components work correctly when combined with the rest of the code. Biogeochemical tracers are, for example, not only affected by the biotic source or sink terms. They are also affected by physical transport processes such as advection, diapycnal mixing, isopycnal mixing, sometimes air-sea exchange, dilution by rain or river run-off, or sinking of particles. All these processes are commonly dealt with in different subroutines at different locations of the complex code. A common model user will, in general, not want to or not be able to go into the details of all these code parts. This is general scientific practice (not many experimentalists will know everything about the components of their measurement devices), but any flaws in the code parts or in the way they were combined may significantly affect the simulated biogeochemical tracer distributions. Apart from mass conservation, no generally accepted biogeochemical model tests are available, and the appropriate model setup will depend on the experience and prudence of the individual modeller.

Acidification is not the only factor with implications for the marine system and processes sensitive to ocean acidification are likely to impinge on climate (changes in temperature, surface fluxes, transport, light, mixing, and species interactions) and direct anthropogenic drivers such as fishing and eutrophication. This complexity underlines the utility of a modelling approach which has the potential to address multiple drivers, particularly as the strongly non-linear interaction of these vectors and the non equilibrium state of marine ecosystems makes empirical/statistical based predictions questionable. For example physical processes sensitive to climate change induce variability in carbonate system (i.e latitudinally, Orr et al, 2005 or due to upwelling, Feely et al, 2008). Altered regional rainfall patterns which, along side changes in land use and industrial processes, will modify fluvial inputs to coastal systems affecting nutrients, optical properties, inorganic carbon and alkalinity (Gypens et al, in press, Raymond & Cole, 2003). Species and communities are likely to shift their geographic ranges as temperatures increase (e.g. Beaugrand

et al., 2002), introducing different phenologies, acidification sensitivities and trophic transfer potential. There are also processes and systems directly affected by both temperature and acidification. Corals are vulnerable to both thermal stress from climate change and lowering saturation states driven by acidification (reviewed in Hoegh-Guldberg et al, 2007) with sensitivities to nutrient concentrations also identified (Langdon et al., 2005). There is also clear evidence that combined CO_2 and temperature stress induce amplified effects on higher trophic level organisms induce amplified effects (Pörtner et al 2004, 2005; Pörtner & Knust, 2007; Pörtner & Farrell, 2008).

4.1.4 Potential pitfalls

Numerical models are written in computer languages that have to be translated by machine-specific compilers into machine-readable commands. As a matter of fact, the same model may yield different results when run on different computers or even on different CPUs of the same computer. Usually, these differences are small, e.g., rounding errors at the last digit. For properly written codes this should not significantly affect the results of the simulation. Another issue are compilers, themselves computer codes with possible errors, that have different "risk options" with higher risks often being very attractive as they lead to faster performance of the code. Model results obtained under different "risk options" are often different. It is generally hoped, but rarely shown, that these differences do not significantly affect the model results. Finally some care has to be taken that the solution algorithm (e.g. Euler, Runge-Kutta, etc), in combination with the choice of timestep does not lead to unacceptably large numerical errors.

4.1.5 Suggestions for improvements

It is considered vital that the entire model code used in publications is archived and available so that experiments could be repeated. Many journals now explicitly allow for electronic supplementary material, others like EGU's new open access journal "Geoscientific Model Development" encourages publication of model descriptions. A minimum requirement should be the publication of the mathematical equations used in the respective model. From a biogeochemist's viewpoint this should be the biogeochemical source and sink terms of any coupled carbon-climate model. However, it should be kept in mind that apparent details such as the algorithms used to transport tracers may turn out to be significant for the model results, as are the initial conditions, forcing data and computational details. Similar to laboratory log books used in experimental work, it should therefore be good practice and is recommended here to archive the entire source code, make files, the compiler options, operating system and machine version used to obtain the published results. Testing of models or model components by others in the

form of collaborative projects is to be encouraged, as this encourages two way knowledge exchange.

Evaluation of models is a pre-requisite for establishing (un)certainty and model utility. Far to little attention has historically been paid to evaluation (Arhonditsis& Brett, 2004) and although more attention is being paid to evaluation recently, many publications still do not consider model correctness with any acceptable detail. One particular practice is to rely solely on visual comparisons, which have no quantitative basis. Formal evaluation metrics are readily available (Stow et al., 2008) and these provide an ability to gauge model improvements as well as identifying process, spatial or temporal problems with model construct. Other multivariate techniques (e.g. Allen & Somerfield, 2008) provide an ability to test the emergent properties of a model, for example do the relationships between key variables in the model replicate that in the observations. This approach can be useful in dynamic systems where the model setup is rarely able to exactly mimic events in space or time because of say a lack of accuracy in underlying physical models or boundary conditions, but the essential dynamics of the ecosystem model are potentially reasonable.

Evaluation can take many forms. Where observations are sparse, an evaluation of process descriptions is useful. In particular forecast scenarios which clearly cannot be evaluated per-se can be evaluated in a hindcast simulation. Evaluation can also be addressed as a stand alone publication, which allows sufficiently detailed treatment necessary especially for complex model systems (e.g. Holt et al 2005, Lewis et al, 2007, Allen et al 2008)

Despite driver uncertainties in marginal seas, the carbonate system is well constrained, formulations, parameterisations and even publically available code exists via the OCMIP protocol (http://www.ipsl.jussieu.fr/OCMIP/). Therefore an absolute requirement for models is the correct treatment of the carbonate system.

A concern is the obvious lack of biological detail in global or earth system models and the less obvious identification of the level of model complexity needed to answer the respective scientific question. Whilst complexity is often limited by computational systems and important feedback mechanisms are likely to be omitted, more complex models tend to be much more difficult to calibrate. There is a case for stronger iteration with regional, ecologically complex models that may be better constrained by the available data sets than global models and that may help to identify important processes that could be tested in global simulations. In particular, variable stoichiometry (carbon to nutrients, carbon to chlorophyll) are being identified as important qualities of marine ecosystem models.

The translation of model results to policy ready information requires some care. For example the highly variable predictions of warming from climate models initially created uncertainty in public and policy response which may have undermined the speed with which climate change became globally recognised . The IPCC approach in creating a synergistic reporting envelope is highly valuable as have the coherent messages from the "Oceans in a high CO2 world" programme for example. Specific to modeling, understanding uncertainty and rigorous evaluation are vital components for robust science. In addition, ensemble approaches which explore say parameter or driver uncertainty and deliver a probabilistic conclusion are valuable as are model–model intercomparison exercises which explore apparent disagreements in results.

4.1.6 Data reporting

The archiving of model output has to follow the general rules outlined with respect to data and metadata reporting and archiving outlined in section 4.2. Similar to protocols used in experimental work, it is therefore good practice to archive the entire code, make files, and compiler options used to obtain the published results.

4.1.7 Recommendations for standards/guidelines

1. **Report all equations, parameterizations and parameter values used in publication**
2. **Model code must be archived, ideally under version control. If possible it should be made publicly available.**
3. **Carbonate chemistry descriptions must be correct (the OCMIP protocol is recommended: http://www.ipsl.jussieu.fr/OCMIP/)**
4. **Models must be evaluated, their uncertainty documented and accounted for when drawing conclusions**

References

Allen, J.I., Holt JT, Blackford J, Proctor R 2007. Error quantification of a high-resolution coupled hydrodynamicecosystem coastal-ocean model: Part 2. Chlorophyll-a, nutrients and SPM. Journal ofMarine Systems 68, 381-404

Allen, J.I., Somerfield, P.J.,2009. A multivariate approach to model skill assessment, Journal of Marine Systems 76, ?-?

Arhonditsis, G.B., Brett, M.T., 2004. Evaluation of the current state of mechanistic aquatic biogeochemical modeling. Marine Ecology Progress Series 271, 13–26.

Beaugrand, G., Reid, P.C., Ibanez, F.,Lindley, J.A., Edwards, M., 2002. Reorganization of North Atlantic Marine Copepod Biodiversity and Climate. Science, 296, 1692-1694.

Blackford,J.C., Allen, J.I., Gilbert,F.G., 2004. Ecosystem dynamics at six contrasting sites: a generic modelling study. Journal of Marine Systems 52, 191–215.

Blackford JC, Gilbert FJ, (2007). pH variability and CO_2 induced acidification in the North Sea. Journal of Marine Systems 64, 229-241.

Bourret, A., Martin Y., Troussellier, M., 2008. Modelling the response of microbial food web to an increase of atmospheric CO_2 partial pressure in a marine Mediterranean coastal ecosystem (Brusc Lagoon, France). Ecological Modelling 208, 189-204.

Bruggeman, J., and S. A. L. M. Kooijman (2007), A biodiversity-inspired approach to aquatic ecosystem modeling, Limnol. Oceanogr., 52, 1533-1544.

Caldeira K, Wickett ME, (2003). Anthropogenic carbon and ocean pH. Nature 425, 365.

Fabry, V.J. 2008. Ocean science - Marine calcifiers in a high-CO_2 ocean Science, 320, 1020-1022.

296 Feely, R.A., Sabine, C.L., Hernandez-Ayon, J.M., Ianson, D., Hales, B., 2008. Evidence for Upwelling of Corrosive "Acidified" Water
297 onto the Continental Shelf. Science, 320, 1490-1492.

298 Friedrichs MAM, Dusenberry JA, Anderson LA, Armstrong RA, Chai F, Christian JR, Doney SC, Dunne J, Fujii M, Hood R,
299 McGillicuddy Jr DJ., Moore JK, Schartau M, Spitz YH, Wiggert JD, (2007), Assessment of skill and portability in regional marine
300 biogeochemical models: Role of multiple planktonic groups, J. Geophys. Res., 112, C08001.

301 Friis, K., A. Körtzinger, and D. W. R. Wallace, The salinity normalization of marine inorganic carbon chemistry data, Geophys. Res.
302 Lett., 30(2), 1085, doi:10.1029/2002GL015898, 2003.

303 Follows, M. J., S. Dutkiewicz, S. Grant, and S. W. Chisholm (2007), Emergent biogeography of microbial communities in a model
304 ocean, Science, 315, 1843-1846. chem.

305 Gangstø, R., Gehlen, M., Schneider, B., Bopp, L., Aumont, O., and Joos, F.(2008), Modeling the marine aragonite cycle: changes under
306 rising carbon dioxide and its role in shallow water CaCO3 dissolution, Biogeosciences, 5, 1057–1072.

307 Gehlen, M., R. Gangstø, B. Schneider, L. Bopp, O. Aumont, and C. Ethe (2007), The fate of pelagic CaCO3 production in a high CO2
308 ocean: A model study. Biogeosci., 4, 505-519.

309 Gypens, N, Borges A.V., Lancelot C. (in press). Effect of eutrophication on air-sea CO_2 fluxes in the coastal Southern North Sea: a
310 model study of the past 50 years. Global Change Biology 10.1111/j.1365-2486.2008.01773.x

311 Hashioka, T., Yamanaka, Y., 2007. Ecosystem change in the western North Pacific associated with global warming using 3D-
312 NEMURO. Ecological Modelling 202, 95–104.

313 Heinze, C. (2004), Simulating oceanic CaCO3 export production in the greenhouse, Geophy. Res. Lett., 31, L16308,
314 doi:10.1029/2004GL020613.

315 Hoegh-Guldberg, O., Mumby, P. J., Hooten, A. J., Steneck, R. S., Greenfield, P., Gomez, E., Harvell, C. D., Sale, P. F.,. Edwards, A. J,
316 Caldeira, K., Knowlton, N., Eakin, C. M., Iglesias-Prieto, R., Muthiga, N., Bradbury, R. H., Dubi, A., Hatziolos, M. E., 2007. Coral
317 Reefs Under Rapid Climate Change and Ocean Acidification, Science, 318, 1737-1742.

318 Holt, J.T., Allen, J.I., Proctor,R., Gilbert,F.G., 2005. Error quantification of a high resolution coupled hydrodynamic ecosystem coastal
319 ocean model: part 1. model overview and hydrodynamics. Journal of Marine Systems 57, 167–188.

320 Hutchins, D. A., Fu F.-X., Zhang Y., Warner M. E., Feng Y., Portune K., Bernhardt P. W., Mulholland M. R. 2007. CO_2 control of
321 Trichodesmium N2 fixation, photosynthesis, growth rates, and elemental ratios: Implications for past, present, and future ocean
322 biogeochemistry. Limnol. Oceanogr., 52, 1293–1304

323 Huesemann, M.H., Skillman, A.D., Creclius, E.A., 2002. The inhibition of marine nitrification by ocean disposal of carbon dioxide.
324 Marine Pollution Bulletin 44 (2), 142–148.

325 Langdon C, Atkinson MJ, (2005). Effect of elevated pCO_2 on photosynthesis and calcification of corals and interactions with seasonal
326 change in temperature/irradiance and nutrient enrichment. J. Geophys Res, 110, C09S07.

327 Levitan, O., Rosenberg, G., Setlik, I., Setlikova, E., Grigel, J., Klepetar, J., Prasil, O. and Berman-Frank, I. 2007. Elevated CO_2 enhances
328 nitrogen fixation and growth in the marine cyanobacterium Trichodesmium. Global Change Biology 13: 531-538.

329 Lewis K., Allen J.I., Richardson A.J., Holt J.T., (2006). Error quantification of a high resolution coupled hydrodynamic ecosystem
330 coastal-ocean model: Part3, validation with Continuous Plankton Recorder data. Journal of Marine Systems 63 209–224

331 Norberg, J., D. P. Swaney, J. Dushoff, J. Lin, R. Casagrandi, and S. A. Levin (2001), Phenotypic diversity and ecosystem functioning in
332 changing environments: A theoretical framework, PNAS, 98, 11376-11381.

333 Orr JC, Fabry VJ, Aumont O, Bopp L, Doney SC, Feely RA, Gnanadesikan A, Gruber N, Ishida A, Joos F, Key RM, Lindsay K, Maier-
334 Reimer E, Matear R, Monfray P, Mouchet A, Najjar RG, Plattner G-K, Rodgers KB, Sabine CL, Sarmiento LJ, Schlitzer R, Slater
335 RD, Totterdell IJ, Weirig M-F, Yamanaka Y, Yool A, 2005. Anthropogenic ocean acidification over the twenty-first century and its
336 impact on calcifying organisms. Nature 437, 681–686.

337 Oschlies, A., K. G. Schulz, U. Riebesell, and A. Schmittner (2008), Simulated 21st century's increase in oceanic suboxia by CO_2-
338 enhanced biological carbon export, Global Biogeochem. Cycles, 22, GB4008, doi:10.1029/2007GB003147.

339 Pörtner, H.O., Langenbuch, M. 2005, Synergistic effects of temperature extremes, hypoxia, and increases in CO_2 on marine animals:
340 From Earth history to global change. J. Geophysical Res. 110 1-15.

341 Portner, HO; Knust, R, 2007. Climate change affects marine fishes through the oxygen limitation of thermal tolerance. Science 315, 95-
342 97.

343 Pörtner, HO; Farrell, AP, 2008. Ecology Physiology and Climate Change. Science, 322, 690-692.

344 Raymond P.A., Cole J.J., 2003. Increase in the Export of Alkalinity from North America's Largest River. Science 301, 88-91

345 Ridgwell, A., I. Zondervan, J. C. Hargreaves, J. Bijma, and T. M. Lenton (2007) Assessing the potential long-term increase of oceanic
346 fossil fuel CO2 uptake due to CO2-calcification feedback, Biogeosc. 4, 481—492. Riebesell U., Schulz K. G., Bellerby R. G. J.,
347 Botros M., Fritsche P., Meyerhöfer M., Neill C., Nondal G., Oschlies A., Wohlers J., Zöllner E. 2007. Enhanced biological carbon
348 consumption in a high CO_2 ocean. Nature 450, 545-548.

349 Rost, B., Riebesell, U., Burkhardt, S., 2003. Carbon acquisition of bloom forming marine phytoplankton. Limnol. Oceanogr., 48, 55-67.

350 Schmittner, A., A. Oschlies, H. D. Matthews, and E. D. Galbraith (2008), Future changes in climate, ocean circulation, ecosystems and
351 biogeochemical cycling simulated for a business-as-usual CO$_2$ emission scenario until 4000 AD, Global Biogeochem. Cycles,
352 GB1013, doi:10.1029/2007GB002953.

353 Stow, C.A., Jolliff, J.,, McGillicuddy Jr., D.J., Doney, S.C., Allen, J.I., Friedrichs, M.A.M., Rose, K.A.,, Wallhead, P., 2009. Skill
354 assessment for coupled biological/physical models of marine systems. Journal of Marine Systems, 76, 4-15.

355 Thomas, H., Schiettecatte, L.-S., Suykens, K., Koné, Y. J. M., Shadwick, E. H., Prowe, A. E. F., Bozec, Y., Baar, H. J. W. de, Borges, A.
356 V., 2008. Enhanced ocean carbon storage from anaerobic alkalinity generation in coastal sediments. Biogeosciences Discuss., 5,
357 3575–3591.

358 Tortell P.D., DiTullio G.R., Sigman D.M., Morel F.M.M., 2002. CO_2 effects on taxonomic composition and nutrient utilization in an
359 Equatorial Pacific phytoplankton assemblage. Marine Ecology Progress Series 236, 37-43.

Tortell, P. D., Payne C. D., Li Y., Trimborn S., Rost B., Smith W. O., Riesselman C., Dunbar R. B., Sedwick P., DiTullio G. R., 2008. CO_2 sensitivity of Southern Ocean phytoplankton, Geophys. Res. Lett., 35, L04605

Zeebe, R.E.,Wolf-Gladrow, D.A., (2001). CO_2 in seawater: equilibrium, kinetics and isotopes. Elsevier Oceanography Series 65, 346.

Advances in Applied Biodiversity Science
No. 4, August 2003: pp. 59–67

CHAPTER 8

Marine Biotic Response to Elevated Carbon Dioxide

Brad A. Seibel and Victoria J. Fabry

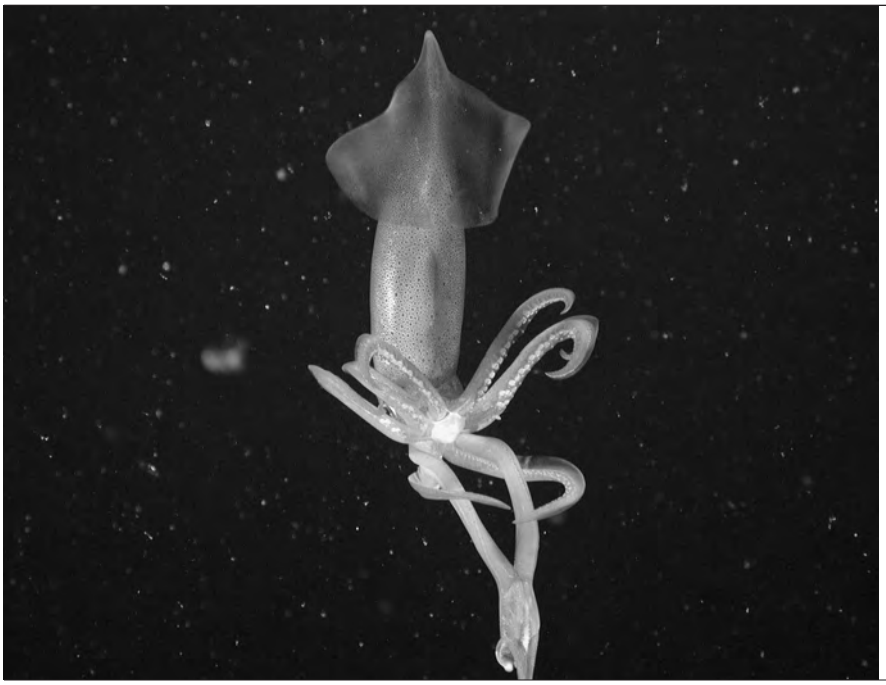

Penetration of anthropogenic CO_2 from the atmosphere to the ocean may have severe consequences for the health of marine organisms, including this midwater squid, *Gonatus onyx*.

The carbon dioxide-carbonate system is arguably the most important chemical equilibria in the ocean (Figure 8.1). It influences nearly every aspect of marine science, including ecology and, ultimately, the biodiversity of the oceans. It is largely responsible for controlling the pH of seawater and thus directly affects many other chemical equilibria as well. By the middle of this century, atmospheric carbon dioxide (CO_2) is expected to reach double its pre-industrial levels (Houghton *et al.* 2001). This expected increase in atmospheric CO_2 will, via passive diffusion, give rise to a

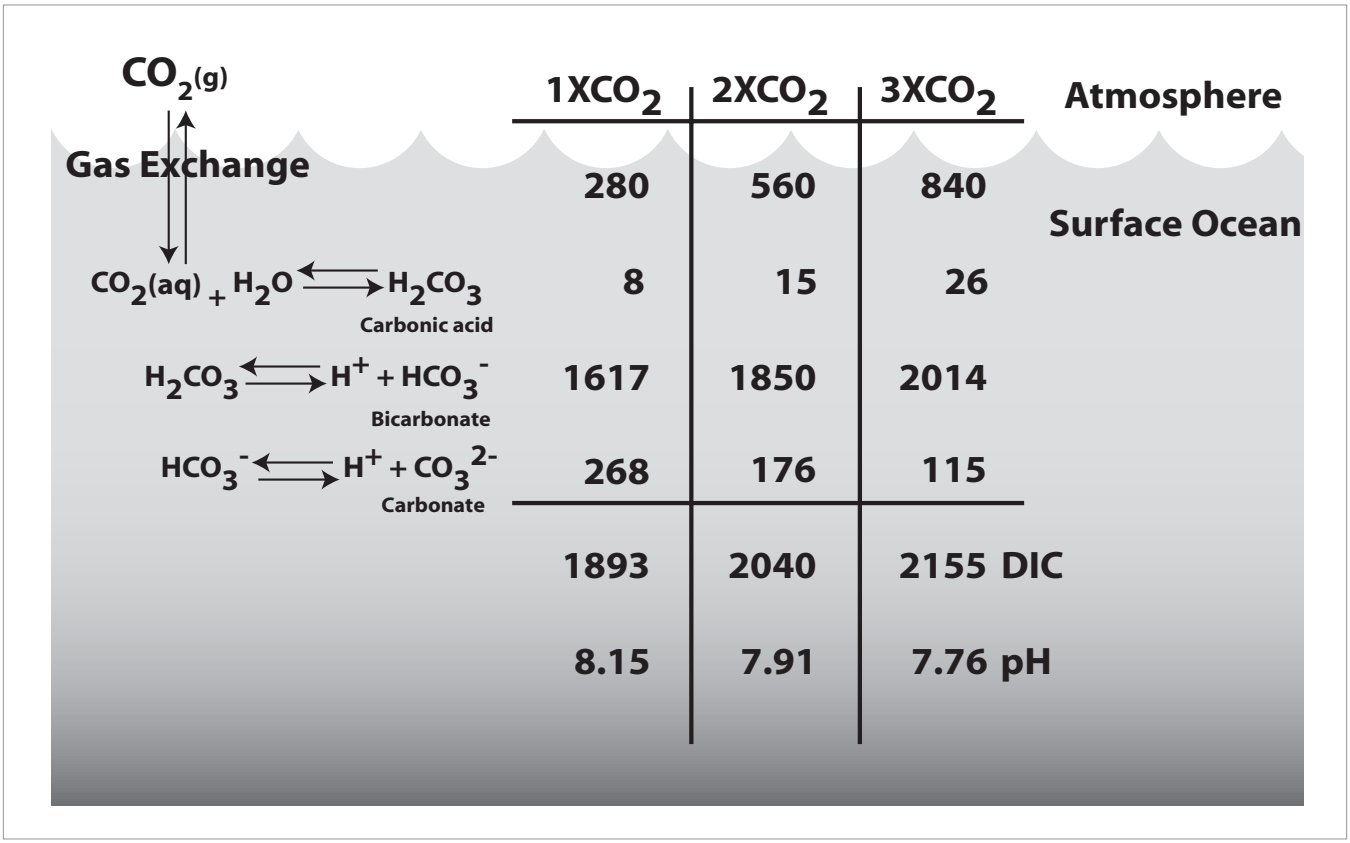

Figure 8.1. Schematic diagram of the carbon dioxide (CO_2) system in seawater. The 1 x CO_2 concentrations are for a surface ocean in equilibrium with a pre-industrial atmospheric CO_2 level of 280 ppm. The 2 x CO_2 concentrations are for a surface ocean in equilibrium with an atmospheric CO_2 level of 560 ppm. Current model projections indicate that this level could be reached sometime in the second half of this century. The atmospheric values are in units of ppm. The oceanic concentrations, which are for the surface mixed layer, are in units of μmol kg^{-1}. (Adapted from Feely *et al.* 2001 and Houghton *et al.* 2001. Courtesy of R.A. Feely).

threefold increase in surface ocean CO_2 concentrations and cause a drop in surface water pH of about 0.4 units because of the CO_2-carbonate buffer system in the ocean.

A pH reduction of approximately 0.1 unit in surface waters has occurred already due to anthropogenic CO_2 input (Goyet *et al.* 1999). Moreover, the anthropogenic CO_2 signal is apparent to depths of more than 1,000 meters in some regions of the oceans (Sabine *et al.* 1999; Feely *et al.* 2001; Sabine *et al.* 2002), with the deepest penetration occurring in areas of deep and bottom water formation. Predicted changes in pH, as well as those that have already taken place in some regions, represent a substantial fraction of the natural variation of seawater pH throughout the world's oceans (7.5 to 8.3), especially considering that pH is a log scale of the hydrogen ion concentration.

The impact of elevated CO_2 on climate and the effect of climate alterations on marine ecosystems have been given considerable attention. Considerable research effort has also been focused on elucidating the ocean's role in buffering elevated changes in atmospheric CO_2. As a vast reservoir that takes up a substantial portion of anthropogenic carbon from the atmosphere, the ocean plays a central role in the global carbon cycle (Gruber *et al.* 1996; Gruber 1998). Because of the oceans' enormous volume, purposeful disposal of CO_2 in them is being seriously considered as a means of mitigating greenhouse warming (Brewer 2000; Brewer *et al.* 1999; Seibel & Walsh 2001). However, the direct effects of anthropogenic CO_2 on marine biota have received relatively little attention to date.

Elevated CO_2 (hypercapnia) may have severe impacts on marine biota due to a direct effect on ocean chemistry. The associated decrease in seawater pH and the reduction in calcium carbonate saturation state on the health and growth of calcareous organisms in the oceans are receiving the most attention. This attention is well deserved, as these interactions will impact economically and ecologically important organisms such as corals and coccolithophorids. However, CO_2 could additionally impact all organisms to varying extents via disturbances to internal acid-base balance, oxygen transport, and metabolic processes with cascading effects on growth, reproduction, and survival. Furthermore, components of global change are synergistic and often not easily separated from each other. The potential for synergism between direct and indirect (i.e., climatic) effects of CO_2 is great. Here, we review the available literature relevant to these issues and consider the potential impacts of anthropogenic CO_2 on global ocean ecology and biodiversity.

Carbon dioxide and the marine carbonate system

Dissolved carbon dioxide readily reacts with water to form carbonic acid. This acid then dissociates in two steps to

HCO_3^- and CO_3^{2-} (Figure 8.1) resulting in an increase in the concentration of hydrogen ions, H^+, some of which combine with CO_3^{2-} to form HCO_3^{-}. Thus, total dissolved inorganic carbon (DIC) exists in seawater in three major forms: [$CO_{2\,(aq)}$], [HCO_3^-], and [CO_3^{2-}]. At a preindustrial atmospheric concentration of 280 ppm and a surface seawater pH of 8.15, the relative concentrations of the major forms of carbon are [$CO_{2\,(aq)}$] = 0.5%, [HCO_3^-]= 85%, and [CO_3^{2-}] = 14%. Within the next 50 years, the concentration of atmospheric CO_2 is expected to increase to twice the preindustrial concentration. This addition of anthropogenic CO_2 will decrease both the concentration of CO_3^{2-} and seawater pH. Carbon dioxide in seawater also interacts with calcium carbonate ($CaCO_3$) such that the addition of CO_2 enhances $CaCO_3$ dissolution. The calcium carbonate saturation state of seawater is largely determined by the [CO_3^{2-}] concentration and so will decrease, with dramatic consequences for calcareous organisms, upon addition of fossil fuel CO_2.

Values of pH in the ocean (pH = -log[H^+]) are influenced by a number of biotic and abiotic factors resulting in a range from 7.5 to about 8.3. Photosynthetic assimilation of carbon dioxide increases, while metabolic production of CO_2 decreases, seawater pH. Thus pH and CO_2 vary regionally and latitudinally with productivity, diurnally with sunlight fueling photosynthesis, and even hourly in estuaries and tide pools when cut off from the general circulation of the ocean (Burnett 1997; Millero 1996; Truchot & Duhamel-Jouve 1980). However, the tolerance of marine biota to subtle, long-term changes in CO_2 is largely unknown. Nevertheless, enough data exist to warrant some speculation regarding the relative sensitivities of various marine taxa to the gradual increase in anthropogenic CO_2 expected over the next century.

Photosynthesis and primary productivity

Most species of marine phytoplankton investigated to date are able to utilize both dissolved CO_2 and HCO_3^- during photosynthesis and, owing to the large pool of HCO_3^- in seawater, their growth generally is not limited by carbon (e.g., Burns & Beardall 1987; Rotatore *et al.* 1995; Raven 1997; Tortell *et al.* 1997; Burkhardt *et al.* 2001). Thus, unlike terrestrial systems in which elevated atmospheric CO_2 may have a fertilization effect, global net primary productivity of marine phytoplankton is not expected to be stimulated by increased dissolved [CO_2] (Raven 1994; Falkowski & Raven 1997). Species-specific differences in the efficiency of inorganic carbon acquisition (Raven 1997; Badger *et al.* 1998), however, may contribute to the competitive abilities of phytoplankton and, under conditions of elevated CO_2, may alter the species composition and succession of phytoplankton (Tortell 2000; Rost *et al.* 2003). Moreover, global warming is expected to increase thermal stratification of the upper ocean, thereby reducing the upwelling of nutrients and decreasing primary productivity (Falkowski *et al.* 1998; Cox *et al.* 2000). Shifts in species composition are likely to occur as a consequence of differential growth rates at different nutrient concentrations and values of ambient seawater pH (c.f. Hinga 2002).

In contrast to marine phytoplankton, seagrasses utilize HCO_3^- inefficiently, and their light-saturated photosynthetic rates are limited by dissolved [$CO_{2\,(aq)}$] (Zimmerman *et al.* 1997; Short & Neckles 1999; Invers *et al.* 2001). Increases in growth rates and biomass with elevated DIC concentrations have been reported in many seagrass species (c.f. Short & Neckles 1999). While these results suggest that additions to atmospheric CO_2 will lead to higher primary productivity in seagrass communities, the long-term response will depend on interactions with other potentially limiting factors such as light and nutrients.

Acid-base regulation in animals

Carbon dioxide is a waste product of routine animal metabolism whereby food molecules are broken down and converted to energy in the form of adenosine triphosphate (ATP). Animals constantly produce CO_2 in concert with the consumption of oxygen as the need for energy arises. Just as in seawater, CO_2 in the intra- and extracellular fluids will lead to reductions in pH (acidosis) with deleterious impacts on cellular function. This is why CO_2 is actively transported to gas exchange tissues (i.e., gills) and expelled. In aquatic animals, blood gases are close to equilibrium with the ambient water (Pörtner & Reipschläger 1996). Therefore, any increase in seawater CO_2 partial pressure (PCO_2) will lead directly to increases in extra- and intracellular CO_2 until a new level sufficient to restore CO_2 excretion is reached (Truchot 1987). Elevated environmental PCO_2 will lead to reductions in fluid pH with consequences for cellular metabolism and cascading impacts on activity levels, growth, reproduction, and survival.

There are several tools that organisms employ to compensate for acid-base imbalance. These tools evolved for protection against short-term elevation of acids and bases. Their effectiveness against pervasive, sustained increases in sea water PCO_2 is probably limited, as they often involve compromises in ionic balance that also impact organismal health (Cameron & Iwama 1987). Nevertheless, to the extent that short-term compensation may be indicative of long-term survivorship, it is useful to examine the capacity of marine organisms to combat environmental hypercapnia. Primary responses of organisms to internal acid-base imbalance (Figure 8.2) include metabolic production and consumption of acid-base equivalents; passive chemical buffering of intra- and extracellular fluids (including buffering via dissolution of biological calcium carbonate structures); active ion transport; CO_2 and hydrogen ion transport by extracellular respiratory proteins (e.g., hemoglobin); and suppression of metabolism to "wait out" periods of high CO_2 (see reviews in Bridges & Morris 1989; Cameron 1989; Guppy & Withers 1999; Heisler 1993; Mangum 1990; Walsh & Milligan 1989).

Metabolic pathways in living cells are tightly regulated such that the production and consumption of metabolic end-products are in balance. Species with low metabolic rates have low rates of CO_2 production and are therefore expected to tolerate only low concentrations of CO_2 and protons, all else being equal (Seibel & Walsh 2001, 2003). Of course, all else is not equal. Large variations in life-history strategies, adaptation

to variably acidic and hypercapnic waters, and phylogenetic history dictates great diversity in CO_2 and pH tolerance—at least on short time scales. However, generally speaking, animals with low metabolic rates have low capacities to buffer and transport acid-base equivalents and will therefore be relatively sensitive to hypercapnia.

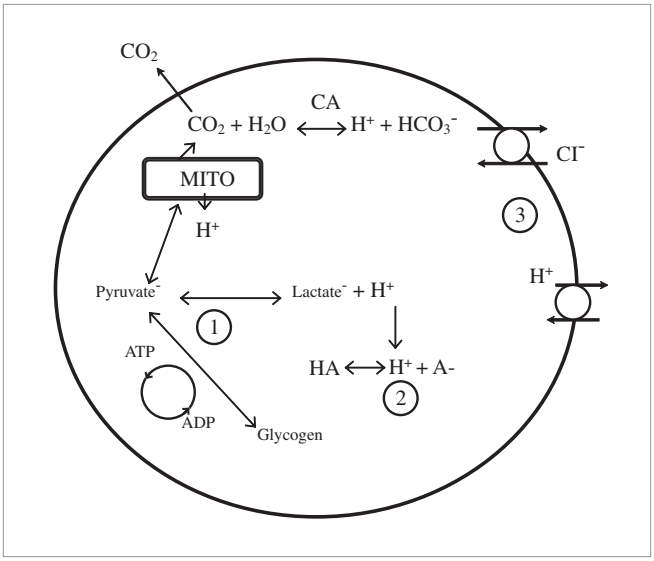

Figure 8.2. Schematic representation of an animal cell with the potential means of regulating intracellular pH. (1) Metabolic interconversion of acids and bases. (2) Buffering; HA represents a weak acid or base with dissociation constant in the physiological pH range. (3) Transport of acids and bases across cell membranes; carbonic anhydrase (CA) catalyzes the hydration of CO_2 to yield H_2CO_3 which then dissociates to H+ and HCO_3^-, which in turn dissociates to H+ and CO_3^{2-}. (The figure shows an abbreviated reaction.)

When concentrations are elevated, CO_2 readily crosses biological membranes and enters the blood and intracellular spaces. Buffering is then the only mechanism immediately available, on the order of seconds and minutes, to curtail changes in pH. Locomotory muscles of active animals, such as epipelagic fishes and cephalopods, have high activity levels of anaerobic metabolic enzymes and, consequently, have high capacity for buffering pH changes associated with anaerobically-fueled burst locomotion (Castellini & Somero 1981; Seibel *et al.* 1997). Organisms with low buffering capacity will experience greater fluctuations in intracellular pH during hypercapnia than others with higher capacity. For example, an increase in seawater PCO_2 sufficient to lower intracellular pH by 0.2 in a sluggish benthic fish may cause only a 0.02 pH unit drop in an active epipelagic fish such as tuna (c.f. Castellini & Somero 1981). Passive buffering of extracellular fluid is also provided in some cases by dissolution of $CaCO_3$ stores or exoskeletons (shells or tests). The sea mussel, *Mytilus edulis*, compensated 1% CO_2 by dissolution of its shell as indicated by increased Ca+ levels (Lindinger *et al.* 1984). Similarly, dissolution of the test buffers coelomic fluid pH changes during emersion in some sea urchins (Spicer 1995). See further discussion of $CaCO_3$ dissolution below.

In the longer-term (hours to days), compensation of acid-base imbalance relies on the ability to transport acid-base equivalent ions across cell membranes. CO_2 produced in the cells during routine metabolism is typically hydrated to form bicarbonate and protons, a reaction catalyzed by the enzyme, carbonic anhydrase. The hydrogen ions are then buffered in the intracellular space as discussed above, while the bicarbonate is transported out of the cells in exchange for Cl- via ion transport proteins. Species with ineffective ion transport capacities are poorly equipped for acid-base regulation (Heisler 1989; Walsh & Milligan 1989). Low rates of metabolism typically correlate with lower concentrations of ion transport proteins such as Na^+/K^+ and H^+-ATPases (Gibbs & Somero 1990), suggesting reduced capacities of acid-base balance. Compensation of acidosis via adjustments in ionic composition appears to be a trade-off that is not likely sustainable on longer time scales such as that associated with anthropogenic increases in seawater carbon dioxide. The fact that compensation often achieves only partial return toward control pH values may reflect a trade-off between acid-base balance and ionic and osmotic homeostasis (Cameron & Iwama 1987).

If compensation of acid-base imbalance is not achieved, reduced intra- and extracellular pH and elevated CO_2 may depress metabolism in some species (Guppy & Withers 1999; Hand 1991; Pörtner & Reipschläger 1996). Metabolic suppression is considered an adaptive strategy for survival of short-term hypercapnia and hypoxia. During periods of oxygen limitation, many organisms are able to suppress ATP demand, thereby extending the duration of tolerance. In many cases, oxygen limitation is coincident with internal acid-base disturbance. Metabolic suppression is not advantageous, however, under chronic elevations of CO_2. Metabolic suppression is typically achieved by shutting down expensive processes. Chief among these is protein synthesis (Hand 1991). Reduced protein synthesis will, by definition, reduce growth and reproductive potential. While suppression of metabolism is, under most experimental conditions, a "sublethal" reversible process, reductions in growth and reproductive output will effectively diminish the survival of the species on longer time scales.

In most macrofaunal species, respiratory proteins are circulated throughout the body to enhance oxygen delivery to the tissues for support of metabolic ATP production. Respiratory proteins are generally very sensitive to changes in pH as quantified by the Bohr coefficient ($=\Delta P_{50}/\log\Delta pH$, where the P_{50} is the oxygen partial pressure at which the protein is half saturated). Bohr coefficients of fish, crustaceans, and cephalopods are typically negative, reflecting large decreases in oxygen affinity with decreasing pH. This ensures effective release of oxygen at the tissues where cellular production of CO_2 reduces pH, and facilitates oxygen binding at the gills where CO_2 is released from the blood to the environment. In such cases, a reduction in seawater pH due to elevated CO_2 will result in a decreased ability to bind oxygen for transport to the tissues. For example, Pörtner and Reipschläger (1996) point out that, in active squids, a change in arterial pH of as much as 0.15 unit could result from the anticipated increase in seawater PCO_2 over the next century, a change sufficient to impair oxygen transport and limit the scope for activity in such species.

Some groups, such as gastropod molluscs, however, have reversed Bohr coefficients where a decrease in pH results in increased respiratory protein oxygen affinity. Such an effect is thought to be adaptive in variably hypercapnic environments, including that inside molluscan shells that may become hypercapnic and hypoxic when closed to the ambient seawater. CO_2 itself is also known to impact oxygen binding in a few cases, although the physiological function is obscure and the overall effect appears to be of less general importance than that for pH. The effect of CO_2 on oxygen affinity, when present, is typically positive (increased affinity) for hemocyanins (crustaceans and molluscs), but negative for hemoglobins (fish and some annelids) (Bridges & Morris 1989).

BIOGENIC CALCIFICATION AND CARBONATE SATURATION STATE

The major sources of oceanic calcium carbonate ($CaCO_3$) are the tests or shells precipitated by planktonic foraminifera, coccolithophorids, and euthecosomatous pteropods. In addition, coral reef ecosystems contain many benthic organisms that produce $CaCO_3$ including scleractinian corals and calcareous algae. Planktonic foraminifera and coccolithophorids precipitate $CaCO_3$ in the form of calcite, whereas pteropod molluscs, calcareous green algae, and corals produce carbonate skeletons of aragonite, a metastable form of $CaCO_3$ that is about 50 percent more soluble in seawater than calcite (Mucci 1983). Other organisms, including calcareous red algae, echinoderms, bryozoans, and benthic foraminifera, are commonly associated with reef habitats and precipitate $CaCO_3$ in the form of magnesian calcite (>5 mole % $MgCO_3$). The solubility of magnesian calcite is slightly greater than that of aragonite (Walter & Morse 1984; Bischoff *et al.* 1987). Thus, under corrosive conditions, aragonite and magnesian calcite will dissolve faster than calcite in a mixed assemblage of carbonate particles. On a local scale, the increase in $[CO_3^{-2}]$ and pH resulting from the dissolution of aragonite and magnesian calcite could confer some protection from dissolution to calcite shells.

As the saturation of each mineral form of $CaCO_3$ is largely determined by the seawater $[CO_3^{-2}]$, oceanic uptake of anthropogenic CO_2 decreases the saturation state of $CaCO_3$ in seawater (Feely *et al.* 2002; Sabine *et al.* 2002). From the preindustrial concentration of atmospheric CO_2 (1 x CO_2) to a doubling of atmospheric CO_2 (which is predicted to occur before 2100), the projected decrease in the average carbonate ion concentration of surface water is 35 percent (Figure 8.1).

Previously, carbonate chemistry was not thought to be an important factor in regulating biogenic calcification because the surface ocean is supersaturated with respect to all mineral forms of $CaCO_3$. However, recent field and laboratory studies with a variety of calcifying organisms demonstrate that the degree or extent of carbonate supersaturation has a direct and profound effect on individual species and community calcification rates (Gattuso *et al.* 1998; Langdon *et al.* 2000; Riebesell *et al.* 2000). This effect has been well-documented for corals and coral reef communities. For example, a positive correlation between $CaCO_3$ production and degree of supersaturation has been reported for coralline algae (c.f., Gattuso *et al.* 1999), reef-building coral species (Gattuso *et al.* 1998; Leclercq *et al.* 2000), and coral reef ecosystems (Langdon *et al.* 2000; Leclercq *et al.* 2002). Empirical data and model projections predict that a doubling of atmospheric CO_2 will result in a decrease in coral reef calcification of 14 to 40 percent (Gattuso *et al.* 1998; Kleypas *et al.* 1999a; Langdon *et al.* 2000; Leclercq *et al.* 2000; Leclercq *et al.* 2002). Reduced calcification of coral reef-building organisms will likely result in weaker skeletons and increased susceptibility to erosion, and may lead to shifts in species composition and community structure (Done 1999; Kleypas *et al.* 1999a).

Evidence suggests that planktonic producers of $CaCO_3$ also may show depressed calcification rates in response to increased dissolved CO_2 and decreased $[CO_3^{-2}]$ and $CaCO_3$ saturation state. In laboratory experiments, the shell weights of similarly-sized individuals of the symbiont-bearing foraminiferans *Orbulina universa* and *Globigerinoides sacculifer* varied as a function of the carbonate ion concentration of seawater (Spero *et al.* 1997; Bijma *et al.* 1999; Bijma *et al.* 2002). The positive correlation between foraminiferal shell weight and ambient $[CO_3^{-2}]$ is also observed in the paleoceanographic record as a response to known glacial-interglacial changes in atmospheric CO_2 of the past 50,000 years (Barker & Elderfield 2002).

Coccolithophorids, widely distributed throughout the world's oceans in both coastal and open ocean environments, produce highly ornate $CaCO_3$ plates, the coccoliths, which interlock on the cell surface to form a covering. On a global basis, coccolithophorids are a major oceanic producer of $CaCO_3$. Satellite images reveal that the surface blooms of coccolithophorids occur in all oceans (Brown & Yoder 1994), and each bloom can produce a massive amount of $CaCO_3$. In the North Atlantic, for example, a single bloom can cover hundreds of thousands of square kilometers of ocean surface and produce up to 1 million tons of calcite (Holligan *et al.* 1993). Experiments with laboratory cultures and field populations reveal that calcification rates of two bloom-forming species, *Emiliania huxleyi* and *Gephyrocapsa oceanica*, decrease in response to changes in seawater carbonate chemistry associated with increased atmospheric CO_2 (Riebesell *et al.* 2000; Zondervan *et al.* 2001). When the atmospheric CO_2 concentration reaches three times the preindustrial value, calcification may decrease by 16% and 45% in *E. huxleyi* and *G. oceanica*, respectively. In contrast, the photosynthetic rate of coccolithophorids may increase with increasing atmospheric CO_2 (Riebesell *et al.* 2000; Zondervan *et al.* 2001) until nutrients ultimately become limiting.

Unlike many, if not all, carbonate producers, coccolithophorids may not require calcification in order to thrive in the sea. Naked or uncalcified cells of *Emiliani huxleyi* have been maintained in laboratory cultures for decades and have also been identified in field samples from the Atlantic and Pacific Oceans using immunofluorescent techniques (e.g, Campbell *et al.* 1994). The possible functions of coccoliths are poorly understood (Young 1994; Paasche 2002).

Shelled pteropods are the most important aragonite-producing organisms in the open ocean. As a group, euthecosomatous pteropods have a cosmopolitan distribution, with species diversity highest in tropical and subtropical waters (Bé & Glimer 1977). Reliable data on pteropod abundances and aragonite production are sparse because the highly soluble shells of pteropods frequently dissolve unless care is taken in preserving plankton samples and sediment trap samples. Estimates of pteropod aragonite production derived from short-term growth experiments in various oceanic regions range from 2.1 to 6.9 mg $CaCO_3$ m^{-2} d^{-1}(Fabry 1990), similar to the range of values (1.0 to 6.5 mg $CaCO_3$ m^{-2} d^{-1}) of aragonite flux measured with sediment traps (Berner & Honjo 1981; Betzer *et al.* 1984; Fabry & Deuser 1991). In the Sargasso Sea, pteropod shells account for 15 percent of the total sinking flux of $CaCO_3$ from the upper ocean to the deep sea (Berner & Honjo 1981; Fabry & Deuser 1991). The response of these pelagic molluscs to increased dissolved CO_2 has not yet been reported; however, it is likely to be consistent with the other biogenic carbonate producers. During shell growth experiments with *Clio pyramidata*, respiratory CO_2 decreased the ambient pH in experimental containers during a 48-hour period from an initial value of 8.15 to values ranging from 7.59 to 7.39. Although animals were actively swimming during this experiment, obvious dissolution had occurred along the growing edge or aperture of the shell (Fabry, unpublished data).

BIODIVERSITY AND ECOSYSTEM RESPONSES

Table 8.1 lists a variety of organisms that may be especially sensitive to elevated CO_2 as discussed above. Animals with low metabolic rates, such as gelatinous zooplankton, that appear to lack mechanisms for compensation of acid-base imbalance may also be particularly sensitive, but no data exist at present. Organisms reliant on the $CaCO_3$ saturation state of the

Table 8.1: Examples of marine organisms sensitive to elevated CO_2 and reduced pH.

Species	Description	Seawater pH/CO2	Sensitivity	Reference
Bacteria				
Aerobic heterotrophic bacteria		7.5	Reduced growth	Reviewed in Knutzen 1981
Phytoplankton				
Cricosphaera elongata		7.4	Reduced growth rate	Reviewed by Hinga 2002
Emiliania huxleyi		7.9	Calcification reduced16%	Riebesell *et al.* 2000
		7.6	Growth rate only 10% of control pH 8.1	Reviewed in Hinga 2002
Gephyrocapsa oceanica		7.9	Calcification reduced 45%	
Gonyaulax polyedra		7.6–7.8	Mortality relative to control pH 8.2	Reviewed in Hinga 2002
Thoracosphaera hemii		7.6–7.8	Irregular growth relative to pH 8.2	
Cnidaria				
Corals		2 x CO_2 pre-industrial	40% drop in calcification	Kleypas *et al.* 1999a, Langdon *et al.* 1998
Mollusca				
Clio pyramidata	pteropod	7.56–7.39	Shell dissolution	Fabry, unpublished data
Mytilus edulis	Sea mussel	7.1 / 6.5 mm Hg	Shell dissolution	Lindinger *et al.* 1984
Pinctata fuscala	Japanese Pearl Oyster	7.7	Shell dissolution, reduced growth	Reviewed in Knutzen 1981
		>7.4	Increasing mortality	
Illex illecebrosus	Epipelagic squid	7.5 / 1.5 mm Hg	Impaired oxygen transport/reduced scope for activity due to highly sensitive respiratory protein	Pörtner & Reipschläger 1996
Arthropoda				
Euphausia pacifica	Krill	7.54, LC0	mortality observed below LC0;	Yamada & Ikeda 1999
Paraeuchaeta elongata	Mesopelagic copepod	7.41, LC0	in all cases, survival declined with	
Conchoecia sp.	Ostracod	7.79, LC0	increasing exposure time, decreasing pH	
Chaetognatha				
Sagitta elegans	Chaetognath	7.76, LC0	See above	Yamada & Ikeda 1999
Echinodermata				
Strongylocentrotus purpuratus	Urchin	High sensitivity inferred from lack of pH regulation and passive buffering via test dissolution during emersion.		cf: Burnett *et al.* 2002; Spicer 1995
Cystechinus sp.	Deep-sea urchin	7.8	80% mortality under simulated CO_2 sequestration.	Barry *et al.* 2002
Vertebrata				
Scyliorhinus canicula	Dogfish	7.7 / 1 mm Hg	Increased ventilation	Reviewed in Truchot 1987

ambient seawater for deposition of shells and tests will be most directly impacted. In all calcifying species studied to date, the calcification rate decreases with decreased $CaCO_3$ saturation state (e.g., Gattuso *et al.* 1998; Riebesell *et al.* 2000).

Impacts on the biogenic producers of aragonite (corals and pteropods) and high-magnesium calcite (benthic organisms associated with coral reef communities) may be particularly severe, as metastable forms of $CaCO_3$ are most susceptible to dissolution. Surface ocean uptake of CO_2 will reduce the aragonite saturation state in the tropics, for example, by 35 percent (Kleypas *et al.* 1999b). The aragonite saturation isoline of 3.5 will shift toward the equator by as much as 15 degrees latitude (Kleypas *et al.* 1999b). Carbonate production of reef-builders will decrease with lower $CaCO_3$ saturation state and may shift the latitudinal limits to reef development toward the equator (Kleypas *et al.* 2001).

While longterm consequences are unknown, experimental results from a marine mesocosm indicate that coral reef organisms do not acclimate to decreasing carbonate saturation state over several years (Langdon *et al.* 2000). Species' range reduction may occur within the water column, as well as with latitude. Vertical migration patterns of planktonic species such as shelled pteropod molluscs may be disrupted as anthropogenic CO_2 penetrates to depths where aragonite saturation is already low, such as in the sub-Arctic Pacific (Feely *et al.* 2002; Sabine *et al.* 2002). Thus, direct CO_2 effects may result in a narrowing and shoaling of inhabitable water for some biogenic carbonate producers.

In the open ocean, elevated CO_2 may also have substantial impacts on species and communities. As the ratio of dissolved $CO_2 : HCO_3^{-2}$ changes with increased oceanic uptake of excess atmospheric CO_2, the competitive balance among phytoplankton species with different efficiencies of DIC acquisition may shift the dominance hierarchy in species composition and succession of primary producers, impacting the food web structure and other ecosystem interactions (Tortell 2000). Potential changes in the relative contributions of diatoms versus coccolithophorids to overall primary productivity may alter the export ratio of $CaCO_3$ to organic carbon from the upper ocean to the ocean's interior. This ratio has a substantial effect on the capacity of the oceans to absorb anthropogenic CO_2 (Sarmiento *et al.* 2002) and may have contributed to glacial-interglacial changes (Archer *et al.* 2000). Ecosystem responses are difficult to predict, but will likely involve changes in community composition and structure as species' ranges and distributions shift. The synergistic impact of CO_2 with other indirect stressors, such as climatic changes and changes in sites and extent of upwelled nutrients, is likely to be substantial.

OCEAN SEQUESTRATION OF CARBON DIOXIDE

The growing concern over the potential for global warming has spurred the development of technologies for capture, storage, and disposal of carbon dioxide. In addition to a variety of terrestrial alternatives, the ocean is being evaluated as a reservoir for storage of anthropogenic carbon. Two strategies are being seriously considered: 1) enhancement of photosynthetic uptake of carbon dioxide by marine algae via iron fertilization; and 2) direct injection of carbon dioxide gas or liquid to great depths in the ocean. So-called "carbon sequestration" strategies are often portrayed as a means of enhancing "natural" processes. In contrast, evidence suggests that carbon sequestration will exacerbate and compound the disruptions to marine biological systems that passive invasion of anthropogenic CO_2 would otherwise cause (Seibel & Walsh 2001, 2003; Chisholm *et al.* 2001; Dalton 2002). Nevertheless, both methods are winning advocates, including some in high places. The United States President, George W. Bush, has stated his belief that "technology offers great promise to significantly reduce emissions—especially carbon capture, storage, and sequestration technologies" (R.A. Kerr 2001).

Iron fertilization

Over the past 15 years it has become apparent that dissolved iron concentrations in many regions of the near-surface open-ocean are very low. They may, in fact, limit phytoplankton growth rates or maximum size of phytoplankton standing crop (Martin & Fitzwater 1988; Martin & Gordon 1988; Gordon *et al.* 1997; Martin *et al.* 1994). Laboratory and shipboard experiments confirm that iron availability may limit phytoplankton growth even when macronutrients are plentiful (de Baar *et al.* 1990; Coale 1991). More recently mesoscale open-ocean iron enrichment experiments have been performed that appear to support the iron-limitation hypothesis on an ecosystem-wide scale (Martin *et al.* 1994). Adding small amounts of iron does give rise to transient, but substantial, increases in phytoplankton productivity and biomass (Coale *et al.* 1996).

Phytoplankton productivity plays a key role in the global carbon cycle by converting CO_2 to organic carbon in surface waters. The organic carbon they produce is mostly regenerated in near-surface waters via consumption and respiration by heterotrophic organisms. However, some carbon sinks to the deep ocean, creating a driving force for passive diffusion of CO_2 from the atmosphere into the ocean. In the interest of mitigating global warming due to elevated atmospheric CO_2, some have speculated that fertilization of the oceans on a large scale could increase the flux of carbon from the atmosphere to the deep sea. Iron fertilization is being seriously considered as a means of sequestering carbon in the ocean's interior, out of contact with the atmosphere. Iron fertilization was first postulated, partly in jest, by Martin who quipped "Give me half a tanker of iron, and I will give you the next ice age" (cited in Chisholm *et al.* 2001).

Thus it is now widely accepted that iron fertilization will result in increased phytoplankton productivity and biomass, and the first experiments demonstrating net transfer of CO_2 from the atmosphere into surface waters have been reported (Dalton 2002). However, these recent experiments revealed that subsequent transfer of CO_2 into deep water is only 1 percent as efficient as laboratory tests predicted. Furthermore, elevated phytoplankton stocks produced a number of other chemicals, including methyl bromide, a compound known to deplete the protective ozone layer at high altitudes, and isoprene, a hydrocarbon that generates greenhouse gases at

low altitude (Dalton 2002). These experiments also demonstrate that the amount of iron needed, and the area of ocean that would be impacted, is too large to support the commercial application of iron to the ocean as a means of mitigating climate change (Buesseler & Boyd 2003). These findings have not stopped the press and various entrepreneurs from making claims, and staking claims, on the effectiveness of iron fertilization as a means of mitigating global warming. Economic incentive to purposefully alter the ecosystem over large expanses of the Earth's surface is, at best, a dangerous proposition (Chisholm *et al.* 2001).

Direct deep-sea injection

Another method proposed to bypass the natural biological carbon pump is direct injection of carbon dioxide into the deep-sea. First proposed by Marchetti (1977) nearly 25 years ago, direct deep-sea injection of CO_2 is, like iron fertilization, gaining momentum. A variety of techniques have been suggested for delivering carbon dioxide to the ocean floor. Shallow gas injection to form a dense sinking fluid and injection of liquid CO_2 at depth forming a "lake" on the seafloor or a dissolving plume rising off the bottom are among the possible scenarios. In order to remain out of contact with the atmosphere, the CO_2 must be injected below 1,000 meters (Haugan 1997). Even so, deep-water injection is less than 100 percent effective, and models predict substantial return to the atmosphere depending on sequestration depth and location (Bacastow *et al.* 1997). The effectiveness and environmental friendliness of deep-sea CO_2 injection are dependent on the method of injection, the general circulation at depth, the depth and location of CO_2 injection, the general tolerance of deep-living organisms to reductions in pH and increased CO_2, and, most importantly, the total amount of CO_2 injected.

From the perspective of marine organisms, deep-ocean sequestration means concentrating an otherwise dilute toxin to well above lethal levels, and placing it in an environment where the organisms are less tolerant of environmental fluctuation in general and CO_2 in particular (Seibel & Walsh 2001, 2003). The impact near the injection site is clear and substantial, as indicated by recent small-scale experiments carried out on the ocean floor at 3,600 meters depth (Barry *et al.* 2002). A small (10 liter) pool of liquid CO_2 on the ocean floor killed a variety of organisms caged within 5 meters.

Localized devastation of biological communities at the injection sites is certain. Only the scale is uncertain. Haugan (1997) estimated that pH within hundreds of meters of the injection site would drop to between 5 and 7, levels that are certainly lethal for most deep-sea organisms. Others have estimated that sequestration of CO_2 equivalent to emissions from 10 standard coal-fired power plants will result in as much as 500 km^3 of seawater with pH less than 7. Still others predict much more subtle impacts. The more important question is the long-term, ocean-wide impact. If deep-ocean injection were the only strategy employed, approximately 400 gigatons of CO_2 would have to be injected by the end of next century in order to stabilize atmospheric levels at twice the pre-industrial level. Disposal of 400 gigatons of CO_2 in the ocean will reduce the pH of the entire ocean, on average, by as much as 0.3 unit, a large fraction of the natural pH variation throughout the ocean (~0.5 units). Because of the acute sensitivity of deep-sea organisms to environmental fluctuations, a 0.3 pH unit change will have large effects on some groups.

As stated above, animals with low metabolic rates are expected to be less tolerant of elevated CO_2. Research over the last 30 years has led to the general conclusion that deep-living animals have low metabolic rates due to evolved differences in lifestyle, low temperature, low food availability, and in some regions, hypoxia (Childress 1995; Seibel *et al.* 1997; Seibel & Walsh 2003). Low metabolic rates among deep-sea organisms are correlated with low buffering and ion transport capacity. Thus, deep-sea organisms are expected to be especially sensitive to environmental elevations in CO_2 (Seibel & Walsh 2001, 2003). An average decrease of only 0.1 unit has been shown to reduce survival in a variety of deep-sea macrofauna (Barry *et al.* 2002). Thus, we believe that the impact on deep-sea life will be significant, with unknown consequences for the oceanic ecosystem.

CONSERVATION LESSONS

One important lesson to be taken from the above discussion is that, regardless of any remaining disagreements over the magnitude and importance of climate change, the continued rise in atmospheric CO_2, itself, will have direct and dramatic effects on marine ecosystems. Believed to be most important is the diminished capacity for calcareous organisms, such as corals, to deposit calcium carbonate under a reduced state of carbonate saturation. Additionally, high CO_2 partial pressures may cause intracellular and blood acid-base imbalance, leading to physiological impairment in some species. The changes in pH and carbonate saturation state from pre-industrial levels are already measurable and will grow in severity without a dramatic change in global CO_2 emissions. While high CO_2 may facilitate production in some terrestrial systems by stimulating photosynthesis, most phytoplankton species in the marine environment will gain no such advantage because they are not typically carbon-limited.

The species composition of some ecosystems will change in concert with rising CO_2 as the latitudinal and vertical distribution of some species shift. These changes may result in the decline of some fisheries, both via alterations in trophic structure and direct effects on animal physiology (e.g., interference with oxygen transport in squids). The rising level of CO_2 in surface waters may also impact tourism if coral reef ecosystems are diminished due to the declining carbonate saturation state.

Reducing these impacts requires limiting global greenhouse gas levels, but some proposals for sequestering CO_2 from the atmosphere would inflict additional damage on marine systems. Direct, prolonged exposure to concentrated CO_2, such as would result near the injection site via direct ocean carbon disposal, is lethal to all organisms. Iron fertilization has also been shown to produce negative "side effects" that both exacerbate and confound the greenhouse gas problem.

For example, in recent fertilization experiments, elevated phytoplankton stocks produced a number of other chemicals, including methyl bromide, a compound known to deplete the protective ozone layer at high altitudes, and isoprene, a hydrocarbon that generates greenhouse gases at low altitude (Dalton 2002). Both sequestration proposals pose high environmental risks as they are currently formulated and, on the scale required for effective carbon sequestration, there is little prospect that these impacts could be mitigated.

The impacts of elevated carbon dioxide discussed here do not require an additional decade of study before informed decisions can be made. We have enough information to say with certainty that the rise in atmospheric CO_2 will negatively impact the marine environment. Decreased pH and carbonate saturation state in the upper ocean waters are a chemical certainty. The negative ecological impacts that will result are simply a question of time and scale.

The Journal of Experimental Biology 206, 641-650

doi:10.1242/jeb.00141

Commentary

Biological impacts of deep-sea carbon dioxide injection inferred from indices of physiological performance

Brad A. Seibel[1,*] and Patrick J. Walsh[2]

[1]*Monterey Bay Aquarium Research Institute, 7700 Sandholdt Road, Moss Landing, CA 95039, USA* and [2]*Marine Biology and Fisheries, National Institute of Environmental Health Sciences, Marine and Freshwater Biomedical Science Center, Rosenstiel School of Marine and Atmospheric Sciences, 4600 Rickenbacker Causeway, University of Miami, Miami, FL 33149, USA*

*Author for correspondence (e-mail: bseibel@mbari.org)

Accepted 12 November 2002

Summary

A recent proposal to store anthropogenic carbon dioxide in the deep ocean is assessed here with regard to the impacts on deep-living fauna. The stability of the deep-sea has allowed the evolution of species ill-equipped to withstand rapid environmental changes. Low metabolic rates of most deep-sea species are correlated with low capacities for pH buffering and low concentrations of ion-transport proteins. Changes in seawater carbon dioxide partial pressure (P_{CO_2}) may thus lead to large cellular P_{CO_2} and pH changes. Oxygen transport proteins of deep-sea animals are also highly sensitive to changes in pH. Acidosis leads to metabolic suppression, reduced protein synthesis, respiratory stress, reduced metabolic scope and, ultimately, death. Deep-sea CO_2 injection as a means of controlling atmospheric CO_2 levels should be assessed with careful consideration of potential biological impacts. In order to properly evaluate the risks within a relevant timeframe, a much more aggressive approach to research is warranted.

Key words: carbon dioxide, global warming, deep sea, hypercapnia, acid–base balance, sequestration, cephalopoda, metabolism.

Introduction

Atmospheric carbon dioxide (CO_2) has increased by 31% from pre-industrial levels (Houghton et al., 2001). A growing consensus among environmental scientists that increased atmospheric CO_2 is causing global warming has spurred the development of various strategies to control CO_2 levels in the atmosphere. United States President George W. Bush has stated his belief that "technology offers great promise to significantly reduce emissions – especially carbon capture, storage and sequestration technologies" (Kerr, 2001). The ocean is an attractive site for possible storage of CO_2 because of its enormous volume. Disposal of CO_2 in the deep-ocean, first proposed by Marchetti (1977) nearly 25 years ago, is now actively being explored (Halmann and Steinberg, 1999). The first direct experiments on the behavior of liquid CO_2 in the deep ocean (Brewer et al., 1999), and on the reaction of deep-sea organisms to CO_2 *in situ* (Tamburri et al., 2000; Barry et al., 2002), have recently been conducted.

Addition of CO_2 to seawater will result in a decrease in pH due to the bicarbonate buffer system in the ocean (equation 1):

$$CO_2 + H_2O \leftrightarrow H_2CO_3 \leftrightarrow HCO_3^- + H^+ \leftrightarrow CO_3^- + H^+ . \quad (1)$$

Reductions in pH resulting from direct ocean storage of CO_2 are estimated to range anywhere from 1.0 to 4.0 (Adams et al., 1997) and 0.01 to 0.1 (Drange et al., 2001; Haugan, 1997) pH units for acute and long-term exposure, respectively, near the injection site. These pH reductions may occur in numerous regions spanning hundreds of kilometers each, depending on the density of inputs and the method of CO_2 disposal (Caulfield et al., 1997). Disposal of sufficient CO_2 to stabilize atmospheric levels at twice the pre-industrial level by the end of this century would lower the pH of the entire ocean on average by more than 0.1 unit (Seibel and Walsh, 2001). This is a large fraction of the normal variation of pH in open seawater (7.6–8.2), especially considering that pH is a log scale of proton concentration.

A variety of disposal schemes are being discussed (Adams et al., 1997). Shallow gas injection to form a dense sinking fluid, injection of ultra-cold liquid CO_2 to form a dense ice skin-hydrate phase, formation of a lake of CO_2 on the seafloor, and dissolution of a rising plume of liquid CO_2 are among the possible scenarios. The environmental 'friendliness' of CO_2 sequestration is thought to depend primarily on the method of CO_2 injection, general circulation models at the depth and location of CO_2 injection, and the general tolerance of deep-living organisms to reductions in pH and increased CO_2 (hypercapnia). This latter point is the focus of this paper.

Environmental stability and the evolution of physiological strategies

Control of intra- and extracellular pH is a ubiquitous feature of cellular physiology, reflecting the diversity of cellular processes dependent on pH or proton gradients (Hochachka and Somero, 2002). Tight control of pH, even in the face of large environmental pH perturbations, is required for proper physiological functioning. Organisms living in variably acidic and hypercapnic environments, such as deep-sea hydrothermal vents (Goffredi et al., 1997) or estuaries (Burnett, 1997), typically have a large capacity for acid–base regulation.

However, the projected perturbations in pH and CO_2 partial pressure (P_{CO_2}) due to CO_2 disposal are large relative to the pH variation experienced by most organisms in the deep-sea. While CO_2 and pH vary diurnally, or even hourly, within some shallow-water habitats (Truchot and Duhamel-Jouve, 1980; Burnett, 1997), P_{CO_2} (pH) in most of the deep-sea, like oxygen, is dependent on regional productivity and the age of bottom water (Miyake and Saruhashi, 1956; Park, 1968) and is, thus, stable over thousands of years (Kennett and Ingram, 1995). Deep-sea animals have evolved in the absence of substantial environmental variability and, as a result, lack the capacity adaptations that facilitate regulation of their internal milieu in the face of changing environmental characteristics (Childress and Seibel, 1998; Seibel et al., 1999). Angel (1992) stated that, as a result of environmental stability, deep-sea communities "*can be expected to contain the most highly tuned species with possibly the least tolerance of environmental change of all on earth*". Haedrich (1996) affirmed this sentiment stating "*any disturbance that takes place too quickly to allow for a compensating adaptive change within the genetic potential of finely adapted deep-water organisms is likely to be harmful. Deep-water faunas are sure to be sensitive to any change that occurs over a few generations and is significantly outside the probably rather narrow range of environmental conditions under which the fauna evolved*". Therefore, even small perturbations in CO_2 or pH could have important consequences for deep-sea organismal physiology and, by extrapolation, the ecology of the entire deep sea.

Physiological responses of animals to acid–base disturbance

The physiological responses of shallow-living organisms to intra- and extracellular acidosis are well characterized (for reviews, see Roos and Boron, 1981; Somero, 1985; Cameron, 1986, 1989; Truchot, 1987; Heisler, 1989; Walsh and Milligan, 1989; Pörtner and Reipschläger, 1996). The general mechanisms used by organisms to combat acid–base imbalance are similar regardless of whether the perturbation is exogenous (environmental) or endogenous (metabolic or respiratory) in origin. Primary mechanisms for regulating acid–base balance include (1) metabolic production and consumption of protons, (2) buffering of intra- and extracellular compartments and (3) active proton-equivalent ion transport (Fig. 1; Walsh and Milligan, 1989). These

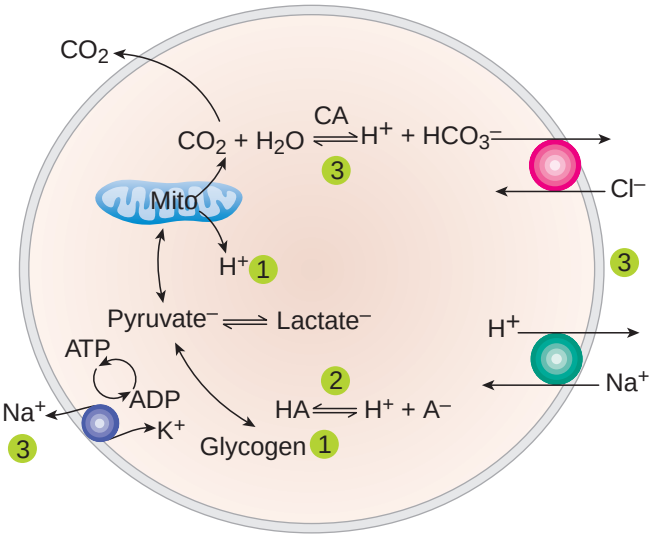

Fig. 1. Schematic representation of an animal cell with the potential means of regulating intracellular pH. (1), metabolic interconversion of acids and bases. (2), buffering; HA represents a weak acid or base with a dissociation constant in the physiological pH range. (3), transport of acids and bases across cell membranes; carbonic anhydrase (CA) catalyzes the hydration of CO_2 to yield H_2CO_3, which then dissociates to H^+, HCO_3^-, and CO_3^{2-} (an abbreviated reaction is shown).

mechanisms are highly conserved across animal phyla. In some animal groups, CO_2 and proton transport by respiratory proteins in the blood is also important (Bridges and Morris, 1989).

In the shallow-living species for which acid–base balance has been studied, elevated environmental P_{CO_2} leads directly to elevated internal P_{CO_2} until a new steady-state gradient sufficient to restore CO_2 excretion is established. When this occurs, the extracellular pH (pHe=blood pH) is depressed, and the bicarbonate concentration rises according to the bicarbonate buffer characteristics of the animal's extracellular fluid (see equation 1; Cameron, 1986). Extracellular pH and bicarbonate values directly impact intracellular pH (pHi; Pörtner et al., 1998). A secondary rise in bicarbonate ions due to active transport, ion exchange (Cameron, 1986; Cameron and Iwama, 1987; Pörtner et al., 1998) or dissolution of $CaCO_3$ exoskeletons (Lindinger et al., 1984) results in an increase in pHe towards control values over a time course of hours to days (Fig. 2). Intracellular compensation is typically completed within 48–72 h in the animals tested to date, and some return towards control values is usually observed within 24 h (Pörtner et al., 1998), often at the expense of pHe. An inability to control acid–base imbalances in the intra- and extracellular spaces may, as discussed in more detail below, lead directly to metabolic suppression, reduced scope for activity or loss of consciousness due to disruption of oxygen transport mechanisms and, ultimately, death.

Seibel and Walsh (2001) briefly reviewed the literature available for deep-sea organisms with relevance to acid–base

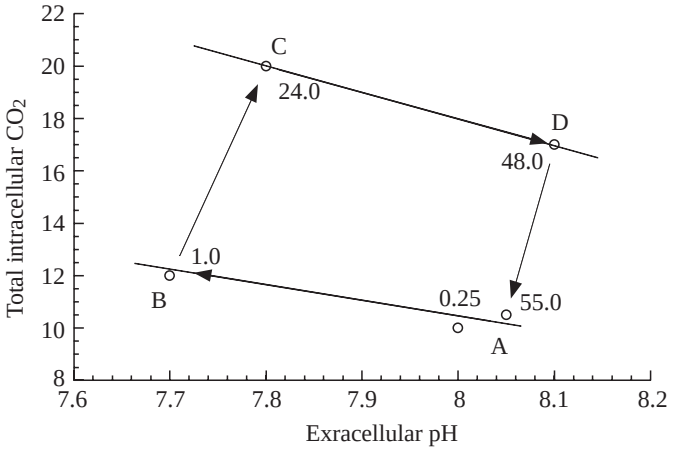

Fig. 2. A Davenport diagram, a graphical representation of the Henderson Hasselbalch equation ($pH=pK+\log[HCO_3^-]/[CO_2]$), demonstrating a typical time course for compensation of extracellular (blood) acidosis. Numbers between points represent time (h). Within 1 h of acidotic stress (A–B), extracellular pH generally drops according to the buffering capacity of the plasma. Over the next 12–24 h (B–C), bicarbonate (*y*-axis; mmol l^{-1}) is transported into the cell (or protons out) in order to shift the equilibrium towards higher pH values. Upon return to normal seawater CO_2 tensions, there is a rapid increase in pH (C–D), due again to passive reactions, followed by a slower decompensation phase (D–A) leading to restoration of the original acid–base status. Intracellular pH and bicarbonate concentrations generally follow those in the extracellular fluid. See Cameron (1989) for additional details on acid–base balance.

physiology. We concluded that, as a result of the relative environmental stability and low rates of metabolism in the deep-sea, organisms living there have little need, and thus little capacity, for robust acid–base regulation. Here, we reiterate these arguments and detail the extreme sensitivity of deep-sea organisms to even small changes in seawater chemistry. While great variation in CO_2 tolerance presumably exists within diverse animal assemblages at any given depth, enough data exist to illustrate differences in the magnitude of acid–base imbalance between generalized deep- and shallow-living species predicted to result from deep-sea injection of CO_2. However, precise thresholds for individual species cannot yet be predicted. Furthermore, it should be pointed out that regulation of acid–base balance typically occurs at the expense of ionic homeostasis and cell volume regulation (Cameron and Iwama, 1987; Whiteley et al., 2001) such that mechanisms for compensation of short-term hypercapnia may not be possible during longer exposures.

Metabolism

Over the past 30 years, a number of *in situ* studies of the oxygen consumption rates of deep-sea animals have been conducted (e.g. Smith, 1983; Smith and Hessler, 1974). Others have successfully recovered deep-sea animals and measured respiratory rates in the laboratory (for a review, see Childress, 1995; Childress and Seibel, 1998). From these studies, a general conclusion has been established that deep-living animals, both fishes and invertebrates, have low metabolic rates. In some cases, deep-living species have metabolic rates more than two orders of magnitude lower than their shallow-living relatives, even after correction for temperature

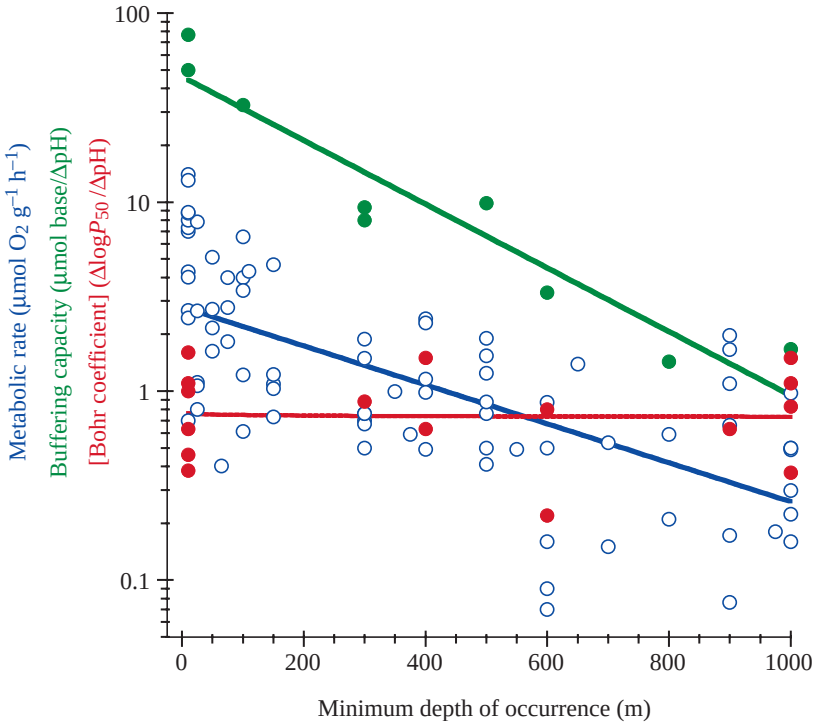

Fig. 3. Metabolic rates (open blue circles) of fishes, cephalopods and crustaceans as a function of minimum depth of occurrence (the depth below which 90% of the individuals in a population are captured). Also shown is the capacity for buffering of intracellular fluids in cephalopods (green circles) and the pH sensitivity of respiratory proteins (red circles) in crustaceans, fishes and cephalopods. Buffering capacity is measured in 'slykes', here equal to the quantity of base that must be added to a homogenate made from a 1 g sample of muscle to titrate the pH from approximately 6 to 7. The Bohr coefficient is the change in the log of respiratory oxygen affinity (P_{50}; defined as the oxygen partial pressure at which the respiratory protein is half-saturated) over the change in pH. Bohr coefficients in these animal groups are negative but are presented here as absolute values. The metabolic rates are normalized to a common body mass of 10 g and measurement temperature of 5°C using measured scaling coefficients and Q_{10} values where available or assuming a scaling coefficient of –0.25 and a Q_{10} of 2. Data are from Childress and Seibel (1998) and references therein. Note that the *y*-axis is a log scale.

differences (Fig. 3; Childress, 1995; Seibel et al., 1997). Reduced metabolism in the deep sea appears, in part, to reflect relaxed selection for locomotory capacity due to light limitation on predator–prey interactions. Some animal groups, such as infaunal invertebrates and gelatinous zooplankton, tend towards low metabolic rates regardless of depth. However, metabolism is further reduced by cold temperature and is also suppressed by limitations on food supply in some cases (Gage and Tyler, 1991). These metabolic patterns hold true to varying degrees for all phyla (Childress, 1995) and regions studied (Ikeda, 1988; Torres et al., 1994) and extend to the deepest depths of the ocean. As outlined below, a correlation is found between metabolic rate and capacity indices for acid–base balance such that we expect animals with low metabolic rates (and low capacities for burst locomotion) to have low tolerances for metabolic end products such as CO_2 and protons.

Buffering capacity

During stress conditions, such as production of protons and CO_2 during exercise, or during exogenous hypercapnia, protons may accumulate due to rate limitations of the proton-elimination pathways. Buffering is then the primary mechanism immediately available that can hold intra- and extracellular pH to values compatible with life functions (Heisler, 1989). In biological fluids, non-bicarbonate buffers are primarily protein residues characterized by pK′ values close to physiological pH (i.e. histidine). Maintenance of pHi *via* buffering of metabolic end products is imperative for conservation of protein structure and function (Somero, 1985).

The ability to buffer metabolic end products correlates with metabolic capacity. Thus, non-bicarbonate buffering capacities are as much as 100 times higher in muscles of shallow-living species than in comparable deep-living species (Fig. 3; Castellini and Somero, 1981; Morris and Baldwin, 1984; Pörtner, 1990; Seibel et al., 1997). The muscles of deep-sea organisms have low amounts of both dialyzable buffers and proteins (Somero, 1985). The consequences of reduced intracellular buffering capacity are illustrated clearly in Fig. 4. A doubling of P_{CO_2} causes only a 0.02 pH change in the intracellular space of the shallow-living squid *Stenoteuthis oualaniensis*. However, a similar increase in P_{CO_2} leads to a 0.2 pH change in the deep-living pelagic octopod *Japetella heathi*. The ability to buffer extracellular fluids against pH change is similarly dependent on the concentration of proteins in the blood (Wells et al., 1988). The majority of deep-living animals measured have extremely low extracellular protein contents compared with closely related shallow-living relatives (Douglas et al., 1976; Brix, 1983; Childress and Seibel, 1998; Seibel et al., 1999). Respiratory protein concentrations generally decrease with metabolic rate and, therefore, depth.

Ion-exchange capacity

Over the longer-term (hours to days), acid–base relevant ion transfer processes are required for elimination of H^+-equivalent ions, whether produced as metabolic end products or accumulated during environmental hypercapnia (Cameron, 1986). In crustaceans, for example, the coupled transfer of acid/base equivalents to ion exchange is the principal mechanism of acid–base regulation (Wheatly and Henry, 1992). This is why external salinity is known to influence acid–base status in some organisms (Whiteley et al., 2001). Ion transport is, in most cases, carrier mediated and thus limited by the capacity or concentration of carrier mechanisms, particularly in gas-exchange tissue (Cameron, 1986). Carriers may include Na^+/H^+ or Cl^-/HCO_3^- exchangers and pumps (i.e. ATPases). Partial correction of acidosis may also be accomplished by accumulation of HCO_3^- in the tissues and blood (Fig. 2), a process that also requires substantial ion-exchange capacity or, in some cases, modifications of gill morphology (Perry and Laurent, 1993).

Gas-exchange (e.g. gill) tissue has been identified as the primary site responsible for acid–base regulation in both fishes and invertebrates (McDonald, 1983; McDonald et al., 1991; Whiteley et al., 2001), although significant gas and ion exchange may take place across all epithelial surfaces in some organisms (e.g. cephalopods; Pörtner, 1994). Reduced gill surface area among deep-sea species may, therefore, limit ion-exchange capacity. Aside from those adapted for residence in oxygen minimum layers (Childress and Seibel, 1998), the few deep-sea species studied have much lower gill surface areas than their more-active, shallower-living counterparts (Henry et al., 1990; Marshall, 1971; Voss, 1988).

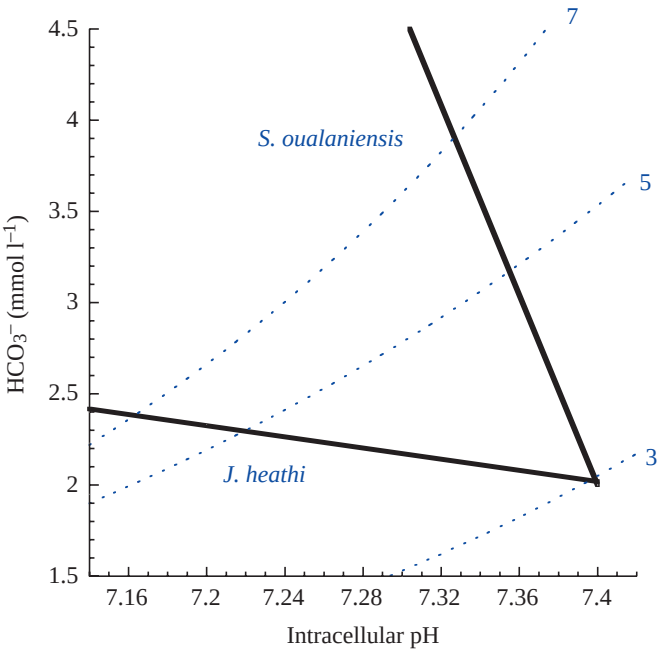

Fig. 4. Davenport diagram depicting passive buffering of intracellular pH (black lines) in two cephalopod species. Similar increases in CO_2 partial pressure (in mmHg; 1 mmHg=133.3 Pa; represented by the blue isopleths and numbers) will result in dramatically different changes in intracellular pH in shallow- (*Stenoteuthis oualaniensis*) and deep-living (*Japetella heathi*) cephalopods. Buffering data are from Seibel et al. (1997).

Gibbs and Somero (1990) reported greatly reduced capacities for active ion regulation *via* ATPases in gills of deep-sea fishes relative to shallower species. Although their study focused on Na^+/K^+-ATPases, their data show that activities of total ATPases declined with increasing depth as well. Similarly, deep-sea animals, other than those inhabiting hydrothermal vents, appear from limited data to have activities of carbonic anhydrase (CA) in gas-exchange tissue that are lower than those of shallower-living species (Henry, 1984; Kochevar and Childress, 1996). CA catalyzes the reversible hydration/dehydration reaction of CO_2 and water (equation 1) and, thus, plays an important role in CO_2 excretion and acid–base balance in marine animals by maintaining availability of H^+ and HCO_3^- for transporters (Burnett, 1997; Henry, 1984). Deep-sea species presumably have a much lower requirement for branchial ion transport due to the extreme ionic stability of seawater at depth and their low rates of metabolic and locomotory activity (Henry et al., 1990).

Oxygen transport, pH sensitivity and metabolism

Respiratory proteins in many animals are responsible for the transport of oxygen to the tissues and of CO_2 and protons to the gills for removal. The oxygen transport function of respiratory proteins (e.g. hemoglobin, Hb) is typically dependent on the pH of the blood (Bohr coefficient=$\Delta\log P_{50}\Delta pH^{-1}$, where P_{50} is the oxygen concentration at which respiratory proteins are half saturated; equation 2):

$$Hb-O_2+H^+ \leftrightarrow Hb-H^+ + O_2\,. \quad (2)$$

Protons produced in equation 1 upon addition of CO_2 reduce the affinity of respiratory proteins for O_2 according to equation 2. In some cases, the direct interaction of CO_2 with Hb can influence oxygen binding. Dependency of respiratory protein oxygen binding on pH facilitates release of oxygen at the tissues where CO_2 and protons are produced and oxygen uptake at the gills, where CO_2 is excreted (Bridges and Morris, 1989). Decreased seawater pH will diminish the effectiveness of oxygen uptake at the gills.

These interactions are well understood in a variety of organisms (see Bridges and Morris, 1989; Toulmond, 1992 for a review). However, the specific effects of CO_2 and pH on respiratory protein-mediated gas exchange vary widely between taxa. For example, limited data suggest that CO_2 increases the affinity of hemocyanin (molluscs and crustaceans) but decreases the affinity of Hb (vertebrates and annelids) for oxygen (Bridges and Morris, 1989; Toulmond, 1992). Only a few measurements of the specific effect of CO_2 on oxygen binding have been made in deep-sea species other than those inhabiting hydrothermal vents. No specific effect of CO_2 was found for vertically migrating mesopelagic shrimps (Sanders and Childress, 1990b) or for the deep-sea benthic shrimp *Glyphocrangon vicaria* (Arp and Childress, 1985). The specific CO_2 effect observed for the midwater shrimp *Notostomus gibbosus* was slight and masked by physiological concentrations of ammonium used for buoyancy in this species (Sanders et al., 1992). Regardless, increased CO_2 will result in decreased pH and a subsequent reduction of oxygen-binding affinity in most species. In addition to a large Bohr effect, many fish Hbs possess a Root effect, where a respiratory acidosis, as incurred during exposure to hypercapnia, can result in a dramatic reduction in hemoglobin-oxygen carrying capacity (up to 50%). The Root effect is thought, in some cases, to facilitate excretion of oxygen into a gas-filled swim-bladder following acid loading in the blood at the Rete Mirable. Most fishes that possess a Root effect also possess the ability to regulate red blood cell pH (pHi) during an acidosis through the release of catecholamines (adrenaline and noradrenaline) that indirectly activate Na^+/H^+ exchange (Tufts and Randall, 1989). Several deep-sea fishes investigated appear to possess a Root effect (Noble et al., 1986; Pelster, 1997). However, there are no data on whether deep-sea fishes have the ability to regulate pHi in the face of an acidosis that might be incurred during exposure to hypercapnia.

Pörtner and Reipschläger (1996) predicted that extremely active animals, in particular, squids, would be disproportionately impacted by anthropogenic decreases in seawater pH. Epipelagic squids such as *Illex illecebrosus* have extremely high rates of oxygen consumption and low blood-oxygen carrying capacity relative to fishes with intracellular respiratory proteins. Therefore, squids have little venous oxygen reserve and are highly dependent on a large Bohr shift to ensure complete release of oxygen at the tissues. Not surprisingly, pHe is tightly controlled in squids (Pörtner, 1994). A blood pH change of as little as 0.15 units is predicted to reduce the scope for activity in species such as *I. illecebrosus*, while a change of 0.25 units is lethal (Pörtner and Reipschläger, 1996).

Conversely, they argued that the specific effect of pH on oxygen binding is small in animals with low metabolic rates, such as those in the deep-sea, and that such species will be less affected by CO_2 disposal (Pörtner and Reipschläger, 1996). Although some deep-living species have respiratory proteins with low pH sensitivities (e.g. the vampire squid *Vampyroteuthis infernalis*; Seibel et al., 1999), no relationship exists between metabolic rate and the Bohr coefficient or between the Bohr coefficient and depth for a variety of deep- and shallow-living marine species (Fig. 3). The shrimp *Glyphocrangon vicaria*, for example, living on the sea floor at depths near 3000 m (oxygen=30% air saturation) has a Bohr coefficient similar to those of its shallow-living relatives despite having a low metabolic rate (Arp and Childress, 1985). Similarly, all octopodids (Cephalopoda) measured, like squids, have hemocyanins that are extremely sensitive to pH ($\Delta\log P_{50}/\Delta pH > -1.0$) regardless of depth, oxygen or metabolic rate (Bridges, 1994). For example, in the deep-sea octopod *Benthoctopus* sp., a drop in arterial pH by just 0.3 units would reduce oxygen saturation of the blood by 40% at ambient oxygen levels (Fig. 5B; A. Seibel unpublished data).

Mickel and Childress (1978) examined the effects of reduced pH on oxygen consumption of *Gnathophausia ingens*,

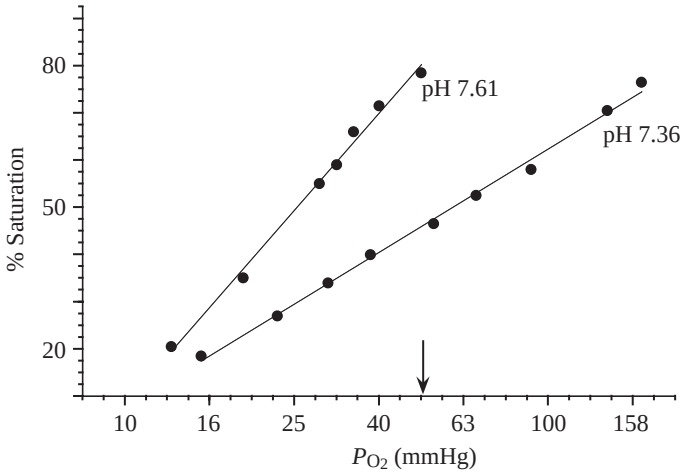

Fig. 5. Percentage hemocyanin-oxygen saturation as a function of oxygen partial pressure P_{O_2} (mmHg; 1 mmHg=133.3 Pa) at pH 7.61 and 7.36 for *Benthoctopus* sp. (B. A. Seibel, unpublished data). Ambient P_{O_2} at capture depth (51 mmHg) is indicated by an arrow. At ambient P_{O_2}, a drop in blood pH of 0.3 units results in a 40% decrease in hemocyanin saturation. All measurements were on dialyzed hemolymph at 5°C. Changes in pH were achieved by varying CO_2 concentrations, thus we cannot distinguish between pH and CO_2 effects on oxygen binding.

a crustacean living in extreme hypoxia at mid-depths off California where seawater pH values are as low as 7.6. They found no specific effect of pH on the rates of oxygen consumption or the abilities of this species to regulate its oxygen consumption rate. However, they did note a large increase in the percentage of oxygen extracted from the respiratory stream at pH 7.1 as opposed to pH 7.9. They reasoned that, as the increase in oxygen extraction does not improve the ability of *G. ingens* to regulate its oxygen uptake, there must be a loss in effectiveness of oxygen uptake at some other point along the oxygen-transport pathway at low pH. If, as is suggested by the large negative Bohr coefficient for this species (Sanders and Childress, 1990a), hemocyanin-oxygen affinity is reduced by low extracellular pH, then perhaps *G. ingens* is slowing either the respiratory or circulatory stream at low pH in order to increase the amount of oxygen extracted. Such a strategy would greatly reduce the scope for activity at low pH for this species.

Animals without well-developed circulatory systems, such as cnidarians and echinoderms, may also be sensitive to hypercapnia and reduced pH. As far as is known, they depend solely on a favorable tissue-environment gradient for CO_2 excretion. Elevated environmental P_{CO_2}, therefore, will lead directly to intracellular pH reductions. During brief bouts of environmental hypercapnia, echinoderms may use their large volume of coelomic fluid to buffer environmental changes (Spicer, 1995; Burnett et al., 2002); however, this mechanism will be ineffective during longer exposures (see below). Echinoderms and bivalves may also rely on dissolution of calcareous tests and shells to buffer pH changes (see below; Burnett et al., 2002; Lindinger et al., 1984; Spicer, 1995).

Metabolic suppression

Metabolic suppression is, in many cases, an adaptive strategy for survival of temporary energy limitation in aquatic organisms. As energy (oxygen or food) becomes limiting, ATP demand is reduced to a level that can be matched by the reduced rates of oxidative phosphorylation. Recent evidence suggests that low pH and hypercapnia are sufficient to trigger a reduction in total energy expenditure (i.e. metabolic suppression) in a variety of organisms (for a review, see Guppy and Withers, 1999), perhaps because oxygen and CO_2 are often inversely correlated in aquatic habitats (Truchot and Duhamel-Jouve, 1980). This reversible response ranges from dormancy periods lasting years in brine shrimp embryos to metabolic suppression over just minutes to hours in some intertidal organisms (Guppy and Withers, 1999).

Not all animals are able to suppress metabolism. Organisms unable to reduce oxygen demand sufficiently are subject to depletion of high-energy phosphate levels during energy limitation, resulting in death. Although not specifically investigated, metabolic suppression is suspected for midwater (mesopelagic) species migrating diurnally into low oxygen regions as well as for deep-sea benthic fauna living in burrows, crevices or shells that may become hypoxic periodically (Hunt and Seibel, 2000; Seibel and Childress, 2000). Furthermore, metabolism of some deep-living macrofauna is depressed nearly fivefold between periods of feeding (Smith and Baldwin, 1982), and many copepod species are known to overwinter in a dormant state in deep water (Alldredge et al., 1984; Hand, 1991).

The mechanisms that bring about reductions in metabolism are under active investigation. Metabolic suppression is typically associated with a decrease in pHi that may lead to rapid adjustments in pH-sensitive metabolic processes such as glycolysis in muscle tissue *via* alterations in the activities of glycolytic enzymes (reviewed by Somero, 1985). For example, phosphorylation of glycolytic enzymes is involved in the transition into dormancy in some marine molluscs (Brooks and Storey, 1997). In some cases, high CO_2 levels trigger metabolic suppression independently of pH (Hand, 1998; Pörtner et al., 1998), but reduced pH is also sometimes sufficient to trigger metabolic suppression (Hand, 1998; Kwast and Hand, 1996).

Suppression of metabolism is accomplished, at least in part, by shutting down expensive cellular processes such as protein synthesis (Guppy and Withers, 1999). For example, Reid et al. (1997) found that low pH inhibited protein synthesis in trout living in lakes rendered acidic through anthropogenic input. Mitochondrial protein synthesis in brine shrimp is also acutely sensitive to pH changes (Kwast and Hand, 1996). Metabolic suppression under conditions of environmental hypercapnia is accompanied by changes in nitrogen excretion in the marine worm *Sipunculus nudus*, which is attributable, in part, to a reduction in protein synthesis rates (Langenbuch and Pörtner, 2002). Reduced protein synthesis, by definition, restricts both growth and reproduction.

Takeuchi et al. (1997) investigated growth rate in one deep- and several shallow-living nematode species in relation to pH.

Growth rate in the deep-sea species was reduced by nearly 50% at pH 6.9, while the shallow-living species showed similar growth rates to the control at pH 6.2. This may reflect the suppression of metabolic rate due to an inability to compensate for an intracellular acidosis in the deeper-living species.

Mortality

Yamada and Ikeda (1999) recently investigated the effect of low seawater pH on zooplankton mortality, and reported that marine zooplankton are more sensitive than similar freshwater species. Furthermore, the single mesopelagic species in this study, a euchaetid copepod, was more sensitive than epipelagic species, perhaps as a result of its lower metabolic rate relative to the calanid and metridinid species with which it was compared (Thuesen et al., 1998). In the mesopelagic copepod *Paraeuchaeta elongata*, a reduction in pH of only 0.2 units from that typical at mid-depths off California is sufficient to cause 50% mortality after 6 days exposure. Mortality was directly proportional to exposure time and inversely proportional to pH (Yamada and Ikeda, 1999).

In situ investigations suggest that deep-sea echinoid (sea urchin) shells are extremely susceptible to fatal dissolution when caged near small pools of liquid CO_2 on the seafloor at 3600 m depth (Barry et al., 2002). Equation 3 demonstrates clearly how addition of CO_2 may enhance $CaCO_3$ dissolution:

$$CO_2 + H_2O + CaCO_3 \leftrightarrow 2HCO_3^- + Ca^{2+}. \quad (3)$$

Shell dissolution under modest hypercapnia can facilitate compensation of temporary acid–base imbalance. However, long-term exposure under CO_2 disposal scenarios will be fatal if CO_2 excursions are sufficient to initiate shell dissolution. Deep-sea holothuroids (sea cucumbers) were also killed by pH excursions associated with small-scale *in situ* CO_2 sequestration experiments (Barry et al., 2002). These studies suggest that echinoids and holothurians, both dominant components of the invertebrate epibenthic fauna in many areas of the deep sea (Gage and Tyler, 1991), are especially susceptible to small changes in pH (see above).

Mobility of deep-sea fauna

The most serious pH excursions (below pH 7) are expected to occur within a few hundred kilometers of the source CO_2 (Adams et al., 1997). Active avoidance is typically the first response of mobile organisms to low pH (Davies, 1991). As demonstrated above, deep-sea organisms in general have reduced locomotory capacity relative to shallower-living species. Although the majority of benthic fauna, as well as many planktonic forms, are not expected to be able to avoid a large plume of acidic seawater, some, particularly fishes, are sufficiently motile to avoid liquid CO_2 pools or plumes. However, the ability to swim does not guarantee that such species *will* avoid CO_2 plumes.

Tamburri et al. (2000) recently conducted the first *in situ* experiments attempting to directly assess the impacts of liquid CO_2 on deep-sea organisms. By mixing a fish slurry with liquid CO_2, they were able to attract fish (primarily hagfish, Myxinidae) to the liquid CO_2 itself. Hagfish appeared not to detect the CO_2 and swam directly to the beaker that contained the CO_2/fish slurry. Upon contact with the CO_2, the fish immediately lost consciousness and fell to the bottom. Rattails (*Macrouridae*), by far the dominant fishes near the deep-sea floor, rely on olfaction to find food. Studies with baited cameras on the deep-sea floor have shown that fish abundance increases dramatically, up to 1 per m^2, with the intensity of the current carrying the bait smell (Gage and Tyler, 1991). Rattails are known to root about in the ooze, sucking in the top layer of sediment and straining off small infaunal invertebrates (Gage and Tyler, 1991). Preliminary *in situ* observations suggest that rattails are also not able to detect liquid CO_2 or accompanying pH decreases. Individual rattails did, however, demonstrate dramatic reactions upon making direct contact with liquid CO_2 (B. A. Seibel, personal observation). These results are worrying because they suggest that the smell of decaying animals that is certain to accompany the initial impact from any sequestered CO_2 may attract additional scavengers.

Perspective

It is assumed that direct, prolonged, contact with liquid CO_2 will result in death and that any disposal scheme will cause mortality of at least some organisms within some distance of the injection point. The chore set forth for deep-sea biologists with respect to CO_2 sequestration is to determine what pH and CO_2 limits will be tolerated by deep-living organisms and what spatial and temporal scales are acceptable. Survival of short-term hypercapnia is dependent on the capacity to buffer, transport and eliminate acid–base equivalents, to tolerate compromised ionic balance during compensation of acidosis, and to suppress metabolism in order to wait out periods of intolerably high CO_2 or low pH. Deep-sea organisms are poorly equipped with respect to these abilities, with capacities 10–100 times lower than comparable shallow-living species. However, very few studies have directly investigated the survival of deep-sea organisms under hypercapnic conditions (Barry et al., 2002; Takeuchi et al., 1997; Yamada and Ikeda, 1999). Also important for survival of entire deep-sea ecosystems is the ability of organisms to tolerate, acclimate and adapt to subtle, prolonged elevations in CO_2. Currently, no data exist that address this issue. As stated above, deep-sea organisms are not expected to be highly plastic in their responses to environmental change.

Given the substantial research investment in deep-sea biology over the past few decades, and the relatively limited understanding of deep-sea processes that endures, a very aggressive research campaign must be initiated in order to provide the necessary information within a relevant time frame, unless a ‘no effect’ strategy is adopted.

Priorities should include:

(1) additional mechanistic studies to confirm the generality of the strategies employed to combat acid–base imbalance and

develop physiological indices useful for prediction of hypercapnic responses;

(2) studies to determine the pH and CO_2 levels below which survival is reduced and to assess the acclimatory responses of deep-living organisms over longer timescales;

(3) determination of long-term energetic (i.e. growth and reproduction) and, by extrapolation, ecological consequences of acid–base and ionic imbalance with CO_2 exposure and

(4) studies aimed at predicting potential impacts of localized CO_2 injection on ecosystem-wide processes.

Many deep-living species, if captured carefully, can be kept alive indefinitely at atmospheric pressure (e.g. Seibel and Childress, 2000). Methods are also available for successful maintenance of deep-sea animals under their respective habitat pressures in the laboratory (e.g. Girguis et al., 2002) and for laboratory culture (Omori et al., 1998; Young and George, 2000). Such methods allow long-term hypercapnia studies that are essential prior to instigating deep-sea CO_2 injection.

What can be stated with confidence, based on our present knowledge, is that shallow-living organisms are already generally intolerant of hypercapnia (Knutzen, 1981) and that deep-sea organisms will be even more so. Slow recolonization of deep-sea habitats and a tendency towards slow growth and longevity among deep-sea organisms (Gage and Tyler, 1991) suggests that recovery from any anthropogenic insult will be slow at best. Should deep-sea CO_2 injection be deemed necessary, great care and caution must be employed and further research initiated to ensure that it is done in the most environmentally benign manner possible.

This work was funded, in part, by the Rosenstiel School of Marine and Atmospheric Science Postdoctoral Fellowship to B.A.S., the National Institute of Environmental Health Sciences Marine and Freshwater Biomedical Science Center grant ES05705, a Department of Energy grant to J. Barry and Peter Brewer and by National Science Foundation grants to J. J. Childress. We thank Dr H. M. Dierssen for constructive comments on the manuscript. We thank Drs J. Company, M. Tamburri, S. Goffredi, P. Girguis, S. Haddock, P. Brewer, C. Brauner, J. Drazen and J. Barry for valuable correspondence and for sharing unpublished data and manuscripts.

References

Adams, E. E., Caulfield, J. A., Herzog, H. J. and Auerbach, D. I. (1997). Impacts of reduced pH from ocean CO_2 disposal: sensitivity of zooplankton mortality to model parameters. *Waste Man.* **17**, 375-380.

Alldredge, A. L., Robison, B. H., Fleminger, A., Torres, J. J., King, J. M. and Hamner, W. M. (1984). Direct sampling and *in situ* observation of a persistent copepod aggregation in the mesopelagic zone of the Santa Barbara Basin. *Mar. Biol.* **80**, 75-81.

Angel, M. V. (1992). Managing biodiversity in the oceans. In *Diversity of Oceanic Life: An Evaluative Review* (ed. M. N. A. Peterson), pp. 23-62. Washington, DC: The Center for Strategic and International Studies.

Arp, A. J. and Childress, J. J. (1985). Oxygen binding properties of the blood of the deep-sea shrimp, *Glyphocrangon vicaria*. *Physiol. Zool.* **58**, 38-45.

Barry, J., Seibel, B. A., Drazen, J., Tamburri, M., Lovera, C. and Brewer, P. (2002). Field experiments on direct ocean CO_2 sequestration: the response of deep-sea faunal assemblages to CO_2 injection at 3200 m off Central California. *Eos Trans. AGU* **83**, OS51F-02.

Brewer, P. G., Friederich, G., Peltzer, E. T. and Orr, F. M. J. (1999). Direct experiments on the ocean disposal of fossil fuel CO_2. *Science* **284**, 943-945.

Bridges, C. R. (1994). Bohr and Root effects in cephalopod haemocyanins – paradox or pressure in *Sepia officinalis*? In *Physiology of Cephalopod Molluscs: Lifestyle and Performance Adaptations* (ed. H. O. Pörtner, R. K. O'Dor and D. L. MacMillan), pp. 121-130. Basel, Switzerland: Gordon and Breach.

Bridges, C. R. and Morris, S. (1989). Respiratory pigments: interactions between oxygen and carbon dioxide transport. *Can. J. Zool.* **67**, 2971-2985.

Brix, O. (1983). Giant squids may die when exposed to warm currents. *Nature* **303**, 422-423.

Brooks, S. P. and Storey, K. B. (1997). Glycolytic controls in estivation and anoxia: A comparison of metabolic arrest in land and marine molluscs. *Comp. Biochem. Physiol. A* **118**, 1103-1114.

Burnett, L., Terwilliger, N., Carroll, A., Jorgensen, D. and Scholnick, D. (2002). Respiratory and acid–base physiology of the purple sea urchin, *Stronglyocentratus purpuratus*, during air exposure: presence and function of a facultative lung. *Biol. Bull.* **203**, 42-50.

Burnett, L. E. (1997). The challenges of living in hypoxic and hypercapnic aquatic environments. *Am. Zool.* **37**, 633-640.

Cameron, J. N. (1986). Acid–base equilibria in invertebrates. In *Acid–base Regulation in Animals* (ed. N. Heisler), pp. 357-394. New York: Elsevier.

Cameron, J. N. (1989). *The Respiratory Physiology of Animals*. New York: Oxford University Press.

Cameron, J. N. and Iwama, G. K. (1987). Compensation of progressive hypercapnia in channel catfish and blue crabs. *J. Exp. Biol.* **133**, 183-197.

Castellini, M. A. and Somero, G. N. (1981). Buffering capacity of vertebrate muscle: correlations with potentials for anaerobic function. *J. Comp. Physiol.* **143**, 191-198.

Caulfield, J. A., Auerbach, D. I., Adams, E. and Herzog, H. J. (1997). Near field impacts of reduced pH from ocean CO_2 disposal. *Energy Convers. Man.* **38**, 343-348.

Childress, J. J. (1995). Are there physiological and biochemical adaptations of metabolism in deep-sea animals? *Trends Ecol. Evol.* **10**, 30-36.

Childress, J. J. and Seibel, B. A. (1998). Life at stable low oxygen levels: Adaptations of animals to oceanic oxygen minimum layers. *J. Exp. Biol.* **201**, 1223-1232.

Davies, J. K. (1991). Reactions of sand smelt to low pH sea-water. *Mar. Poll. Bull.* **2**, 74-77.

Douglas, E. L., Friedl, W. A. and Pickwell, G. V. (1976). Fishes in oxygen-minimum zones: blood oxygenation characteristics. *Science* **191**, 957–959.

Drange, H., Alendal, G. and Johannessen, O. M. (2001). Ocean release of fossil fuel CO_2: a case study. *Geophys. Res. Lett.* **28**, 2637-2640.

Gage, J. D. and Tyler, P. A. (1991). *Deep-Sea Biology: A Natural History of Organisms of the Deep-sea Floor*. Cambridge: Cambridge University Press.

Gibbs, A. H. and Somero, G. N. (1990). Na^+-K^+ adenosine triphosphatase activities in gills of marine teleost fishes, changes with depth, size and locomotory activity level. *Mar. Biol.* **106**, 315-321.

Girguis, P. R., Childress, J. J., Freytag, J. K., Klose, K. and Stuber, R. (2002). Effects of metabolite uptake on proton-equivalent elimination by two species of deep-sea vestimentiferan tubeworm, *Riftia pachyptila* and *Lamellibrachia* cf *luymesi*: proton elimination is a necessary adaptation to sulfide-oxidizing chemoautotrophic symbionts. *J. Exp. Biol.* **205**, 3055-3066.

Goffredi, S. K., Childress, J. J., Desaulniers, N. T., Lee, R. W., Lallier, F. H. and Hammonds, D. (1997). Inorganic carbon acquisition by the hydrothermal vent tubeworm *Riftia pachyptial* depends upon high external P_{CO_2} and upon proton-equivalent ion transport by the worm. *J. Exp. Biol.* **200**, 883-896.

Guppy, M. and Withers, P. (1999). Metabolic depression in animals: physiological perspectives and biochemical generalizations. *Biol. Rev.* **74**, 1-40.

Haedrich, R. L. (1996). Deep-water fishes: evolution and adaptation in the Earth's largest living spaces. *J. Fish Biol.* **49**, 40-53.

Halmann, M. M. and Steinberg, M. (1999). *Greenhouse Gas Carbon Dioxide Mitigation: Science and Technology*. Washington, DC: Lewis Publishers.

Hand, S. C. (1991). Metabolic dormancy in aquatic invertebrates. In *Advances in Comparative and Environmental Physiology*, vol. 8 (ed. R. Gilles), pp. 1-47. New York: Springer-Verlag.

Hand, S. C. (1998). Quiescence in *Artemia franciscana* embryos: reversible arrest of metabolism and gene expression at low oxygen levels. *J. Exp. Biol.* **201**, 1233-1242.

Haugan, P. M. (1997). Impacts on the marine environment from direct and indirect ocean storage of CO_2. *Waste Man.* **17**, 323-327.
Heisler, N. (1989). Interactions between gas exchange, metabolism, and ion transport in animals: an overview. *Can. J. Zool.* **67**, 2923-2935.
Henry, R. P. (1984). The role of carbonic anhydrase in blood ion and acid–base regulation. *Am. Zool.* **24**, 241-251.
Henry, R. P., Handley, H. L., Krarup, A. and Perry, H. M. (1990). Respiratory and cardiovascular physiology of two species of deep-water crabs, *Chaceon fenneri* and *C. quinquidens*: in normoxia and hypoxia. *J. Crust. Biol.* **10**, 413-422.
Hochachka, P. W. and Somero, G. N. (2002). *Biochemical Adaptation*. Oxford: Oxford University Press.
Houghton, J. T., Ding, Y., Griggs, D. J., Noguer, M., van der Linden, P. J. and Xiaosu, D. (2001). Climate Change 2001: The Scientific Basis. In *PICC Third Assessment Report: Climate Change 2001*, pp. 944. Cambridge: Cambridge University Press.
Hunt, J. C. and Seibel, B. A. (2000). Life history of *Gonatus onyx* (Teuthoidea: Cephalopoda): ontogenetic changes in habitat, behavior and physiology. *Mar. Biol.* **136**, 543-552.
Ikeda, T. (1988). Metabolism and chemical composition of crustaceans from the Antarctic mesopelagic zone. *Deep-Sea Res.* **35**, 1991-2002.
Kennett, J. P. and Ingram, B. L. (1995). A 20,000-year record of ocean circulation and climate change from the Santa Barbara basin. *Nature* **377**, 510-514.
Kerr, R. A. (2001). Bush backs spending for a 'global problem'. *Science* **292**, 1978.
Knutzen, J. (1981). Effects of decreased pH on marine organisms. *Mar. Poll. Bull.* **12**, 25-29.
Kochevar, R. E. and Childress, J. J. (1996). Carbonic anhydrase in deep-sea chemoautotrophic symbioses. *Mar. Biol.* **125**, 375-383.
Kwast, K. E. and Hand, S. C. (1996). Oxygen and pH regulation of protein synthesis in mitochondria from *Artemia franciscana* embryos. *Biochem. J.* **313**, 207-213.
Langenbuch, M. and Pörtner, H. O. (2002). Changes in metabolic rate and N excretion in the marine invertebrate *Sipunculus nudus* under conditions of environmental hypercapnia: identifying effective acid–base variables. *J. Exp. Biol.* **205**, 1153-1160.
Lindinger, M. I., Lauren, D. J. and McDonald, D. G. (1984). Acid–base balance in the sea mussel, *Mytilus edulis*. III. Effects of environmental hypercapnia on intra- and extracellular acid–base balance. *Mar. Biol. Lett.* **5**, 371-381.
Marchetti, C. (1977). On geoengineering and the CO_2 problem. *Climate Change* **1**, 59-68.
Marshall, N. B. (1971). *Exploration in the Life of Fishes*. Cambridge, MA: Harvard University Press.
McDonald, D. G. (1983). The effects of H^+ upon the gills of freshwater fish. *Can. J. Zool.* **61**, 691-703.
McDonald, D. G., Freda, J., Cavdek, V., Gonzalez, R. and Zia, S. (1991). Interspecific differences in gill morphology of freshwater fish in relation to tolerance to low-pH environments. *Physiol. Zool.* **64**, 124-144.
Mickel, T. and Childress, J. J. (1978). The effect of pH on respiration and activity in the bathypelagic mysid *Gnathophausia ingens*. *Biol. Bull.* **154**, 138-147.
Miyake, Y. and Saruhashi, K. (1956). On the vertical distribution of the dissolved oxygen in the ocean. *Deep-Sea Res.* **3**, 242-247.
Morris, G. M. and Baldwin, J. (1984). pH buffering capacity of invertebrate muscle: correlations with anaerobic muscle work. *Mol. Physiol.* **5**, 61-70.
Noble, R. W., Kwiatkowski, L. D., Young, A. D., Davis, B. J., Haedrich, R. L., Tam, L. and Riggs, A. F. (1986). Functional properties of hemoglobins from deep-sea fish: correlations with depth distribution and presence of a swimbladder. *Biochim. Biophys. Acta* **870**, 552-563.
Omori, M., Norman, C. P. and Ikeda, T. (1998). Oceanic disposal of CO_2: potential effects on deep-sea plankton and micronketon – a review. *Plankton Biol. Ecol.* **45**, 87-99.
Park, K. (1968). Alkalinity and pH off the coast of Oregon. *Deep-Sea Res.* **15**, 171-183.
Pelster, B. (1997). Buoyancy at depth. In *Fish Physiology*, vol. 16 (ed. D. J. Randall and A. P. Farrell), pp. 195-237. New York: Academic Press.
Perry, S. F. and Laurent, P. (1993). Environmental effects on fish gill structure and function. In *Fish Ecophysiology* (ed. J. C. Rankin and F. B. Jensen), pp. 231-264. London: Chapman & Hall.
Pörtner, H. O. (1990). Determination of intracellular buffer values after metabolic inhibition by fluoride and nitrilotriacetic acid. *Resp. Physiol.* **81**, 275-288.
Pörtner, H. O. (1994). Coordination of metabolism acid–base regulation and haemocyanin function in cephalopods. In *Physiology of Cephalopod Molluscs: Lifestyle and Performance Adaptations* (ed. H. O. Pörtner, R. K. O'Dor and D. L. MacMillan), pp. 131-148. Basel, Switzerland: Gordon and Breach.
Pörtner, H. O. and Reipschläger, A. (1996). Ocean disposal of anthropogenic CO_2: physiological effects on tolerant and intolerant animals. In *Ocean Storage of Carbon Dioxide. Workshop 2 – Environmental Impact* (ed. B. Ormerod and M. V. Angel), pp. 57-81. Cheltenham, UK: IEA Greenhgouse Gas R&D Program.
Pörtner, H. O., Reipschläger, A. and Heisler, N. (1998). Acid–base regulation, metabolism and energetics in *Sipunculus nudus* as a function of ambient carbon dioxide level. *J. Exp. Biol.* **201**, 43-55.
Reid, S. D., Dockray, J. J., Linton, T. K., McDonald, D. G. and Wood, C. M. (1997). Effects of chronic environmental acidification and a summer global warming scenario: protein synthesis in juvenile rainbow trout (*Oncorhynchus mykiss*). *Can. J. Aquat. Sci.* **54**, 2014-2024.
Roos, A. and Boron, W. F. (1981). Intracellular pH. *Physiol. Rev.* **61**, 296-434.
Sanders, N. K. and Childress, J. J. (1990a). Adaptations to the deep-sea oxygen minimum layer: oxygen binding by the hemocyanin of the bathypelagic mysid, *Gnathophausia ingens* Dohrn. *Biol. Bull.* **178**, 286-294.
Sanders, N. K. and Childress, J. J. (1990b). A comparison of the respiratory function of the hemocyanins of vertically migrating and non-migrating oplophorid shrimps. *J. Exp. Biol.* **152**, 167-187.
Sanders, N. K., Morris, S., Childress, J. J. and McMahon, B. R. (1992). Effects of ammonia, trimethylamine, L-lactate and CO_2 on some decapod crustacean haemocyanins. *Comp. Biochem. Physiol. A* **101**, 511-516.
Seibel, B. A., Chausson, F., Lallier, F. H., Zal, F. and Childress, J. J. (1999). Vampire blood: respiratory physiology of the vampire squid (Cephalopoda: Vampyromorpha) in relation to the oxygen minimum layer. *Exp. Biol. Online* **4**, 1-10. ISSN: 1430-3418.
Seibel, B. A. and Childress, J. J. (2000). Metabolism of benthic octopods (Cephalopoda) as a function of habitat depth and oxygen concentration. *Deep-Sea Res.* **47**, 1247-1260.
Seibel, B. A., Thuesen, E. V., Childress, J. J. and Gorodezky, L. A. (1997). Decline in pelagic cephalopod metabolism with habitat depth reflects differences in locomotory efficiency. *Biol. Bull.* **192**, 262-278.
Seibel, B. A. and Walsh, P. J. (2001). Potential impacts of CO_2 injection on deep-sea biota. *Science* **294**, 319-320.
Smith, K. L., Jr (1983). Metabolism of two dominant epibenthic echinoderms measured at bathyal depths in the Santa Catalina Basin. *Mar. Biol.* **72**, 249-256.
Smith, K. L., Jr and Baldwin, R. J. (1982). Scavenging deep-sea amphipods: effects of food odor on oxygen consumption and a proposed metabolic strategy. *Mar. Biol.* **68**, 287-298.
Smith, K. L., Jr and Hessler, R. R. (1974). Respiration of benthopelagic fishes: *in situ* measurements at 1230 meters. *Science* **184**, 72-73.
Somero, G. N. (1985). Intracellular pH, buffering substances and proteins: imidazole protonation and the conservation of protein structure and function. In *Transport Processes, Iono- and Osmoregulation* (ed. R. Gilles and M. Gilles-Baillien), pp. 454-468. Berlin: Springer-Verlag.
Spicer, J. J. (1995). Oxygen and acid–base status of the sea urchin *Psammechinus miliaris* during environmental hypoxia. *Mar. Biol.* **124**, 71-76.
Takeuchi, K., Fujioka, Y., Kawasaki, Y. and Shirayama, Y. (1997). Impacts of high concentrations of CO_2 on marine organisms: a modification of CO_2 ocean sequestration. *Energy Convers. Man.* **38**, S337-S341.
Tamburri, M. N., Peltzer, E. T., Friederich, G. E., Aya, I., Yamane, K. and Brewer, P. G. (2000). A field study of the effects of CO_2 ocean disposal on mobile deep-sea animals. *Mar. Chem.* **72**, 95-101.
Thuesen, E. V., Miller, C. B. and Childress, J. J. (1998). Ecophysiological interpretation of oxygen consumption rates and enzymatic activities of deep-sea copepods. *Mar. Ecol. Prog. Ser.* **168**, 95-107.
Torres, J. J., Aarset, A. V., Donnelly, J., Hopkins, T. L., Lancraft, T. M. and Ainley, D. G. (1994). Metabolism of antarctic micronektonic crustacea as a function of depth of occurrence and season. *Mar. Ecol. Prog. Ser.* **113**, 207-219.
Toulmond, A. (1992). Chapter 9. Properties and functions of extracellular heme pigments. In *Advances in Comparative and Environmental Physiology*, vol. 13, pp. 231-256. Heidelberg: Springer-Verlag.
Truchot, J. P. (1987). *Comparative Aspects of Extracellular Acid–base Balance*. Berlin: Springer-Verlag.

Truchot, J. P. and Duhamel-Jouve, A. (1980). Oxygen and carbon dioxide in the marine intertidal environment: diurnal and tidal changes in rockpools. *Resp. Physiol.* **39**, 241-254.

Tufts, B. L. and Randall, D. J. (1989). The functional significance of adrenergic pH regulation in fish erythrocytes. *Can. J. Zool.* **67**, 235-238.

Voss, G. L. (1988). Evolution and phylogenetic relationships of deep-sea octopods (Cirrata and Incirrata). *Mollusca* **12**, 253-276.

Walsh, P. J. and Milligan, C. L. (1989). Coordination of metabolism and intracellular acid–base status: ionic regulation and metabolic consequences. *Can. J. Zool.* **67**, 2994-3004.

Wells, R. M. G., Summers, G., Beard, L. A. and Grigg, G. C. (1988). Ecological and behavioral correlates of intracellular buffering capacity in the muscles of antarctic fishes. *Polar Biol.* **8**, 323-325.

Wheatly, M. G. and Henry, R. P. (1992). Extracellular and intracellular acid–base regulation in crustaceans. *J. Exp. Zool.* **263**, 127-142.

Whiteley, N. M., Scott, J. L., Breeze, S. J. and McCann, L. (2001). Effects of water salinity on acid–base balance in decapod crustaceans. *J. Exp. Biol.* **204**, 1003-1011.

Yamada, Y. and Ikeda, T. (1999). Acute toxicity of lowered pH to some oceanic zooplankton. *Plankton Biol. Ecol.* **46**, 62-67.

Young, C. M. and George, S. B. (2000). Larval development of the tropical deep-sea echinoid *Aspidodiadema jacobyi*: phylogenetic implications. *Biol. Bull.* **198**, 387-395.

OCB OCEAN ACIDIFICATION SHORT COURSE

OUTLINE FOR LARVAL MOLLUSC OCEAN ACIDIFICATION EXPERIMENTS

Instructors: Anne Cohen, Dan McCorkle

TAs: Meredith White, Kathryn Rose

Please refer to full protocol under Thursday November 5 tab.

Wednesday, November 11, 2009
Lectures, respirometry demo, cellular pH regulation experiment, hands-on modeling

Morning

Time	Activity
8:30 am	**Lecture**. Large databases (Key). MBL Speck Auditorium
10:00 am	Coffee Break
10:30 am	**Lecture**. Genomics applications to ocean acidification research. (Fangue). MBL Speck Auditorium
12:00 pm	Lunch (Swope Cafeteria, MBL)

Afternoon

Time	Group G	Group H	Group I
1:15 pm	Shuttle MBL to ESL	Break	Shuttle MBL to Clark
1:30 pm	**Lab**. Respirometry demo and conclude cellular pH experiment (Seibel, ESL 10)		**Lab**. Hand-on Modeling (Doney, WHOI Group Training Facility, Clark 141)
2:15 pm		Shuttle MBL to Clark	
2:30 pm		**Lab**. Hand-on Modeling (Doney, WHOI Group Training Facility, Clark 141)	Walk Clark to ESL
2:45 pm	Break/Walk ESL to Clark		**Lab**. Respirometry demo and conclude cellular pH experiment (Seibel, ESL 10)
3:30 pm	**Lab**. Hand-on Modeling (Doney, WHOI Group Training Facility, Clark 141)	Break/Walk Clark to ESL	
4:00 pm		**Lab**. Respirometry demo and conclude cellular pH experiment (Seibel, ESL 10)	Shuttle ESL to MBL
4:15 pm			Break
4:30 pm	Shuttle Clark to MBL		
4:45 pm	Break		
5:15 pm		Shuttle ESL to MBL	
5:30 pm	Dinner (Swope Cafeteria, MBL)		

OCB OCEAN ACIDIFICATION SHORT COURSE

Lecture on Large Databases

Instructor: Robert Key (Princeton)

Description of lecture: Compilation, applications, and limitations of large databases

http://cdiac.ornl.gov/oceans/home.html

OCB Ocean Acidification Short Course

Genomics applications to ocean acidification research

Nann A. Fangue, Assistant Professor, UC Davis
Gretchen E. Hofmann, Professor, UC Santa Barbara

Suggested readings:

Quinn, P., Bowers, R.M., Zhang, X. et al. 2006. cDNA microarrays as a tool for identification of biomineralization proteins in the coccolithophorid *Emiliania huxleyi* (Haptophyta). Applied and Environmental Microbiology. 72 (8): 5512-5526.

Van Straalen, N.M. and D. Roelofs. 2007. An introduction to ecological genomics. Oxford University Press.

Hofmann, G.E., O'Donnell, M.J., and A.E. Todgham. 2008. Using functional genomics to explore the effects of ocean acidification on calcifying marine organisms. Marine Ecological Progress Series. 373: 219-225.

Marioni, J.C., Mason, C.E., Mane, S.M., Stephens, M. and Y. Gilad. 2008. RNA-seq: An assessment of technical reproducibility and comparison with gene expression arrays. Genome Research. 18: 1509-1517.

Shendure, J. and J. Hanless. 2008. Next-generation DNA sequencing. Nature Biotechnology. 26 (10): 1135- 1145.

Steinberg, C.E.W., Sturzenbaum, S.R., and R. Menzel. 2008. Genes and environment – Striking a fine balance between sophisticated biomonitoring and true functional environmental genomics. Science of the Total Environment. 400: 142-161.

Vera, J.C., Wheat, C.W., Fescemyer, H.W. et al. 2008. Rapid transcriptome characterization for a non-model organism using 454 pyrosequencing. Molecular Ecology. 17: 1636-1647.

Todgham, A.E. and G.E. Hofmann. 2009. Transcriptomic response of sea urchin larvae, *Stongylocentrotus purpuratus*, to CO_2-driven seawater acidification. Journal of Experimental Biology. 212: 2579-2594.

Thursday, November 12, 2009
Lectures and experimental wrap-up

Morning

Time	Activity
8:30 am	**Lecture**. Introduction to Data Management and Better Practices for Shipboard Data Management (Chandler). MBL Speck Auditorium
10:00 am	Coffee Break
10:30 am	**Lecture**. Biogeochemical Modeling Part II (Doney) MBL Speck Auditorium
12:00 pm	Lunch (Swope Cafeteria, MBL)

Afternoon

Time	Activity
1:30 pm	**Discussion**. Experimental synthesis and discussion (Langdon lead). MBL Speck Auditorium
3:30 pm	Coffee Break
4:00 pm	**Discussion.** Experimental synthesis and discussion cont'd (Langdon lead). MBL Speck Auditorium
6:00 pm	Farewell Dinner, MBL

OCB Ocean Acidification Course
Data Management Outline

Instructor: Cyndy Chandler, Biological and Chemical Oceanography Data Management Office, Woods Hole Oceanographic Institution

Introduction to Data Management and Better Practices for Shipboard Data Management

Introduction

- Why data management matters
- New funding agency requirements
- New research paradigms
- New expectations for data access

Research Cruise

- Allocation of sample (wire) time
- Allocation of sample water
- Event log
- Cruise report

Metadata Reporting

Data Reporting

- BCO-DMO example for NSF-funded research
- EPOCA data (contributed by Anne-Marin Nisumaa, EPOCA data manager)
- Contribution of data to National Data Archive Centers

Friday, November 13, 2009
Lecture, course wrap-up and evaluations

Time	Activity
8:30 am	**Lecture**. Data Reporting (Kozyr) MBL Speck Auditorium
10:00 am	Coffee Break
10:30 am	**Discussion**. Course evaluations and wrap-up (Benway/Cooley) MBL Speck Auditorium
12:00 pm	Lunch (Swope Cafeteria, MBL)

End of course.

OCB Ocean Acidification Course
Data Reporting Outline

Instructor: Alex Kozyr, Carbon Dioxide Information Analysis Center, Oak Ridge National Laboratory

Data Reporting

Introduction

- CDIAC and Global Ocean CO_2 Data Management
- Science and Technology at ORNL
- Environmental Sciences at ORNL
- CDIAC Background Basics
- Impacts
- Present Data Holdings
- CDIAC Data and Information Products
- CDIAC Most Popular Holdings and Products
- Current Data Emphasis

CDIAC Ocean Carbon Projects

- US Ocean Carbon Project Origins
- CDIAC's Role in the Global Ocean Carbon Projects

CDIAC Global Ocean CO_2 Database Components

- WOCE Database
- GLODAP Database
- CLIVAR Repeat Hydrography and Carbon Database
- VOS Underway pCO_2 Database
- Moorings and Time Series Database
- Global Coastal Program Data
- CARINA Database
- Global Surface Ocean Alkalinity Climatology Database (K. Lee)
- LDEO (Takahashi) Global Surface pCO_2 Database
- Future data synthesis projects (SOCAT, PICES)

CDIAC Search Engines

- Mercury
  Individual work with Mercury
- WAVES
  Individual work with WAVES
- LAS
  Individual work with LAS

CDIAC Data formats

How to submit data to CDIAC

CDIAC routines for data QA-QC work

CDIAC Numeric Data Packages (NDPs)